THERMOELECTRIC MAGNETOHYDRODYNAMICS

by

P.B. Dutta Gupta

A Thesis
submitted to the University of Warwick
for the Degree of Doctor of Philosophy
August, 1979

SUMMARY

The effect of the interaction of steady uniform transverse magnetic fields with the thermoelectic current in liquid metals that might exist at the nonisothermal, electically conducting interface of the metal liners, termed as TEMHD hereafter, is the subject of some theoretical and extensive experimental investigation reported in this thesis. The investigation has primarily been motivated by the possibility of significant consequences of such an effect in the lithium blankets of magnetically confined thermonuclear reactors (TNR) and the lack of any previous serious attempt to investigate this interaction experimentally.

It is shown theoretically that at high Hartmann numbers (M) in various TEMHD configurations, the flow is equivalent to the ordinary MHD flow with an inherent pressure gradient due to the thermoelectric current and magnetic field, B. How well the TEMHD interaction is effective is measured in terms of a new nondimensional number D, the ratio of thermoelectric e.m.f. and the motion (determined by viscous and inertial force balance) induced e.m.f.. Theoretical analysis for the secondary flow due to buoyancy in simple configurations shows that the secondary flow is at least an order of magnitude lower than the corresponding TEMHD flow. However, for other complex configurations there exists a B_{cr}, a function of Rayleigh and Prandtl numbers, in order to ignore the buoyancy effect.

The experimental results obtained with Hg in Cu channels, as reported in this thesis, show that even in laboratory model experiments this TEMHD interaction in liquid metals in metal containers with non-isothermal interface does produce a significant body force. This body force is measurable in terms of either the fluid flow velocity (stirring) or the static pressure gradient if the fluid flow is suitably constrained. It has been shown that these measurements provide a new method of finding experimentally the thermopower of liquid metals in magnetic fields as accurately as in conventional methods if the configuration is rightly chosen. These measurements are sensitive enough to the presence of traces of impurity to serve the purpose of determining the degree of refinement in metallurgical processes.

Since lithium has an absolute thermopower, ignoring the sign, four times that of Hg, the scaling up of the TEMHD performance in Hg-Cu combination gives an adequate simulation of the blanket system TEMHD. With the complex geometry of TNR and the magnetic field system therein, the TEMHD configurations to be considered are very varied. Initially, to avoid buoyancy driven flow, simple thermally stable stratified configurations have been adopted in the form of (i) uniform horizontal copper pipes of circular cross-section (1.25 and 2.54 cm in diameter) with a sinusoidal (first harmonic) peripheral temperature distribtuion, and (ii) horizontal straight copper pipe with a rectangular cross-section ($\simeq$ 2.5 cm square) with insulated sidewall interfaces and heated from the top and cooled at the bottom. Apart from the static pressure difference and velocity measurements, temperature oscillations are reported even in these basic thermally stable configurations which are suppressed at some field strength, B_{cr}. For a fixed heat transfer, the temperature in the TEMHD system has been found to drop with increase in B. These two unexpected experimental observations havebeen tentatively explained on the basis of finite amplitude instability due to magnetic-buoyancy force driven relaxation of isotherm curvature.

SUMMARY (continued)

In order to investigate TEMHD flow without pressure gradient, experimental investigations in (endless) annular channels with the top surface free, heated and cooled at the vertical sidewalls in uniform steady axial magnetic fields have been performed for mixed and totally conducting solid-liquid interfaces. Since in this configuration the buoyancy effect is inherently present, a few measurements of secondary flow and free surface profile are presented along with velocity and temperature measurements. The temperature at the hot wall increases with B as is normally expected, due to suppression of buoyancy induced vorticity by B. The critical magnetic field for transverse vorticity suppression and the build-up of magnetic drag by boundary layer formation has been found to occur at distinctly different values. By the choice of suitable nonlinear heating and mixed conducting interfaces, it has been shown that free shear layers could be generated. This experiment also confirms the possibility of higher TEMHD velocity as a function of B for aligned temperature gradient and B, as predicted by theoretical analysis. A discussion on the vorticity and stationary and drifting wave motion,as has been observed in these experiments, is provided.

A simple novel structure of the lithium blanket of the TOKAMAK type of TNR in the form of double spiral modules is suggested to exploit TEMHD effect to pump lithium for heat transfer purpose. Limited experimental results that could be obtained on a laboratory model, with Hg as the fluid and the module fabricated with Cu are presented.

The experimental measurements have been conducted with inclined tube manometers, flowmeters, mechanical vaned vorticity-velocity probes, pitot tube and thermoelectric potential probes. The thermoelectric potential probes,which have been invented as a modification of the ordinary potential probes to suit the TEMHD environment,provide simultaneous measurement of temperature and velocity at $B > B_{cr}$, and the calibration procedure is much easier than for the alternative methods of measurement.

A chapter on the review of literature relevant to TEMHD is provided to serve as a background of the investigation reported here, and a few areas of further investigation in TEMHD are suggested.

PREFACE

The research investigation described in this thesis was carried out in the Department of Engineering at the University of Warwick during the three academic years 1976-1979. Except where the contrary is stated, the research work described is original. Chapter 1 is introductory and Chapter 2 gives a review of previous relevant work. Where the work of others is used, a reference is given. No part of this thesis has been submitted at any other University although some part of it has been submitted to Scientific and Technical Conferences for publication in the press.

I am immensely grateful to Professor J.A. Shercliff for accepting me to work in his research laboratory. The research project on the investigation of thermoelectric effects in MHD was suggested amongst other alternatives by Professor Shercliff. I had the benefit of his advice, comments, suggestions and encouragement. Apart from the interest shown in my research work, the hospitality received from the family of Professor Shercliff, particularly that from Mrs. Daphne Shercliff, will be very kindly remembered. Professor Shercliff, in spite of his busy schedule, also read the draft of the thesis, after the sad demise of Dr. C.J.N. Alty. My thanks are due to the late Dr. C.J.N. Alty for supervising the project, though for a brief period, and for reading the first chapter of the thesis.

I have been very fortunate to have had every possible help from Mr. A.E. Webb, Senior Technician of the Engineering Department. The fabrication of the various experimental rigs, particularly that of the demountable double spiral channel module, was possible with his interest and technical expertise. Mr. Webb looked after the medical checks for mercury poisoning. Apart from getting such great help, I remain deeply indebted to Mr. Webb and Mrs. Hazel Webb for being very good friends.

Acknowledgements are due to Dr. G.A. Styles and Dr. M.H. Lewis of the Department of Physics for their help in the use of the NMR and the X-ray fluorescence test facilities. Acknowledgement is also made to Mr. A.E. Corbett for providing long strips of Mica free of cost.

Thanks are due to all the technical staff of the Department of Engineering, staff members of the Stores (Engineering, Molecular Sciences and Physics Departments) and the Library. I must apologise for not mentioning by name the many individuals who in some way or other provided help.

My visit to England was made possible by an award of a scholarship grant under the Commonwealth Scholarship and Fellowship Plan. I am indebted to the Ministry of Education, Government of India, for allowing me to accept the offer and to the authorities of the Indian Institute of Technology, Kharagpur (in particular, Professor N. Kesavamurthy) for granting the necessary leave of absence from their employment. Thanks are due to the staff members of the Commonwealth Scholarship Commission in the U.K. and to the British Council for looking after my welfare during my stay in England.

(continued)

I thank Mr. A.C. Whitehead for the photographic work. Special thanks go to Mrs. Jacynth I. McKeand for ably salvaging the typing work after the original typist retired at the beginning of Chapter 3.

Finally, with a heavy heart, I wish to record that the effort in completing the research work was made under the compulsion to honour the wishes of my father, whom I lost in 1977 and to whom I owe my education. My mother, my wife and my young son, all sacrificed their privileges in supporting me in every possible way,and saw to it that I did not go astray in my mission. Let the preface end in a doxological theme.

6th August, 1979 P.B. Dutta Gupta

CONTENTS

INDEX OF FIGURES

INDEX OF TABLES

CHAPTER 1

1. INTRODUCTION

1.1.1 INTRODUCTION TO THERMOELECTRIC MAGNETOHYDRODYNAMICS IN LIQUID METALS

Liquid metals possess high electrical and thermal conductivities and are of particular interest in nuclear reactor and power generating systems. High electrical conductivity allows the flow of these corrosive fluids to be controlled electromagnetically. When such an electrically conducting fluid flows in a magnetic field, the motion and the magnetic field interact to generate electromotive forces which in general, tend to drive electric current in the bulk of the fluid. This current produces its own magnetic field and also interacts with the total magnetic field to modify the fluid flow. The investigation of this twofold interaction in the flow of a conducting fluid in a magnetic field constitutes the study of magnetohydrodynamics. Leaving aside astrophysical events, the bulk electrical conductivity of liquid metal devices are yet not so high as to satisfy the 'frozen field line' concept and the induced magnetic field is usually small compared with the imposed field. It is obvious that in most of the applications of liquid metal magnetohydrodynamics, whether in liquid metal transportation for casting ingots or liquid metal circulation for heat transfer or in power generating apparatus, the liquid metal will be hot. These flows have been in general considered in the isothermal mode only. However, if the hot liquid metal is in contact with a dissimilar metal lining of the container and the temperature along the interface is non-uniform, then thermoelectric effects will result in current flow through the lining - liquid metal interface regions at different temperatures and heat absorption and dissipation will occur at these interface regions as well as all along the thermoelectrically driven current path in the liquid metal and in the metal lining. It is to be noted that by convention thermoelectric effects between two dissimilar elements maintained at different temperatures at their

contact interface are mentioned above, but such effects could arise in a single nonhomogeneous element (continuous variation of material composition) itself having a varied thermoelectric characteristic in the range of the temperature distribution existing along it. How these thermally driven electric currents would interact with the electromagnetic and flow fields of magnetohydrodynamics and vice-versa is the subject of this thesis and the term 'thermoelectric-magneto-hydrodynamics' (TEMHD) has been proposed to describe the effects involved. Necessarily a broader aspect of the interaction of the thermal field, electromagnetic field and the flow field (galvanothermomagnetohydrodynamics) exists but here the emphasis is only on how the magnetohydrodynamic forces affect thermoelectrically driven current in the liquid metal due to nonuniform temperatures at the interface regions of the dissimilar elements and vice versa. When the system does not differ much from the isothermal state, the new interactions discussed above would be only secondary effects and insignificant. These thermoelectric magnetohydrodynamic effects will be significant only when large temperature gradients prevail in the liquid metal in the presence of a strong magnetic field and the liquid metal and the lining material possess significant thermoelectric properties relative to one another. An analogy in terms of the significance of such secondary interaction may be drawn with the importance of Hall effect in plasma magnetohydrodynamics. Whereas the importance of Hall effect in plasma magnetohydrodynamics is firmly established, this present investigation is only the first attempt to evaluate the level of significance of the influence of thermoelectric effects in nonisothermal liquid metal systems in the presence of a magnetic field.

1.1.2 MOTIVATION FOR INVESTIGATING TEMHD

The present investigation has been motivated by the belief that TEMHD may be important in certain types of thermo-nuclear reactor -

(TNR). The presence of high temperature gradients and a strong magnetic field in the lithium surrounded by a dissimilar metal liner of the blanket in a magnetically confined TNR would generate significant thermoelectric magnetohydrodynamic effect and it is necessary to evaluate such effects before the blanket design is finalised. It is important to note that a TOKAMAK type of magnetically confined TNR using deuterium (D) and tritium (T) fuel according to the reaction

$_1D^2 + _1T^3 \longrightarrow {}_2He^4 + n + 17.6$ MeV would possibly be the first amongst the various alternative TNRs to come into operation. The lithium blanket is necessary to breed T, which does not occur in nature, according to the reactions,

$_3Li^6 + \text{'slow' } n \longrightarrow {}_1T^3 + {}_2He^4 + 4.8$ MeV

$_3Li^7 + \text{'fast' } n \longrightarrow {}_1T^3 + {}_2He^4 - 2.5$ MeV $+ n'(\text{slow})$,

to act as a neutron shield and to arrest the 14.1 MeV neutron energy. Lithium is in the form of liquid in the temperature range 186°C to 1380°C, has high specific heat and is an excellent conductor of heat. It is therefore advantageous to circulate the hot fluid through heat exchangers to raise steam for power generation or even straightaway feed into liquid metal magnetohydrodynamic generators. However, the magnetic field geometry to maintain magnetohydrodynamic stability of the confined plasma is complex, and the superconducting magnet coils have to be placed outside the blanket in order to protect them from neutron radiation. Thus the fluid has to be pumped across a strong magnetic field, causing excessive drag particularly when metal tubes are used. Since lithium has an unusually high thermoelectric power, it is interesting to consider how thermoelectricity affects the magnetohydrodynamic drag. The complex magnetic field geometry and the torus shape of the TOKAMAK type of TNR would allow various possible alternative configurations of the ducting system. This flexibility serves as an incentive to explore ways by which thermoelectric effects might be used to minimise the drag or even

to overcome it and pump the fluid. In fact then the pumping would be automatic at the expense of the available energy in the blanket itself.

In metallurgy - in the area of metal forming and crystal growth - many of the metallic materials are manufactured after they have been refined sufficiently in the molten state. Stirring is necessary to make sure that a homogeneous uniform casting with respect to the small impurity level that still remains is obtained and striation avoided. The use of alternating electromagnetic fields to stir the melt suffers from the disadvantage that the magnetic field penetration is restricted to the skin depth which decreases with increase in the frequency of the impressed electromagnetic field. If thermoelectric effects are significant and the thermoelectric currents properly aligned, a steady uniform magnetic field would suffice to induce uniform stirring throughout the body of the melt. This type of stirring is also possible in the liquid lithium blanket of the TOKAMAK reactor even if the liquid lithium is not circulated externally for heat transfer. The temperature distribution in the blanket would then be substantially different from that when the lithium is stationary. Though it might be premature to stake the claim, the possibility of TEMHD stirring of the liquid metal core of the earth and its implications for the maintenance of the terrestrial magnetic field cannot be ruled out.

Apart from the motivation arising from the practical utility applications, TEMHD itself is an interesting study of heat transfer and magnetohydrodynamic interactions in fluid flows at the non-isothermal liquid metal-metal interface. With a little effort the mathematical techniques of thermodynamics and magnetohydrodynamics can be combined through thermoelectric coupling. A thermoelectrically driven magnetohydrodynamic flow would be the dual of electrically driven magnetohydrodynamic flow, however, with variations in density, conductivity and viscosity to be taken into account.

The investigation in thermoelectricity in liquid metals has a peculiar appeal for physicists. Theoretical models of liquid metal structure based on interactions of the nearly free electrons with the ion lattices, proposed with ideas borrowed from solid state physics, are tested by comparing the theoretically predicted properties with the experimentally observed ones. Amongst the various transport properties the thermoelectric effect is an important factor in the testing of the many anomalies that have appeared in the study of liquid metals, alloys and semimetals. The effect of magnetic fields on the absolute thermoelectric power of elements with magnetic impurities at low temperature is already an important field of theoretical physics but thermoelectric effects in liquid metals at high temperatures in magnetic fields have not attracted the attention of those concerned with the evaluation of structure factors.

1.2 THE TEXT

1.2.1 SCOPE AND ASPECTS OF TEMHD CONSIDERED

In this thesis concentrated effort has been made to investigate thermoelectrically controlled magnetohydrostatic and dynamic effects in ducts of various basic shapes particularly relevant to the blanket of a TOKAMAK type TNR; the findings however have general validity and can be applied in other areas. The basic interest lies in nonrelativistic, macroscopic effects and therefore matters at the atomic dynamics level are not a matter of concern. Essentially the considerations are within the framework of classical field theory - thermal, electromagnetic and hydrodynamic. Thus radiative heat transfer is not considered. Nuclear reactions and heat sources and sinks arising out of such reactions are ignored. Since this investigation marks the beginning of experimental TEMHD, a start has been made with the simplest analytical model and variations build up as far as possible. Simplifying assumptions adopted in liquid metal magnetohydrodynamics, like treating the fluid as incompressible (that is, with velocities sufficiently low

compared to the velocity of sound), neglecting the Hall effect, ion slip and displacement current, are all retained. The cluster formation of the isotopes of the fluid, concentration gradients, electromigration and charge convection are all ignored. Emphasis is given to experimental investigations, and the analytical work substantiates the findings. The scope of the experimental work is restricted by the capacity of laboratory models and the range of parameter variations possible. All of the experimental investigations were carried out with mercury as the fluid and copper as the lining material instead of lithium and niobium, as might well be used in actual TNR blankets. This has been done for convenience in laboratory experimentation but in no way does it prevent one from scaling the results obtained to give information on the behaviour of lithium-niobium systems. Since turbulence in general is suppressed by strong magnetic fields, the most relevant study in TEMHD would basically be a laminar flow. Thus the possibility of self excitation due to turbulence and dynamo effect is ignored. In general, stable thermal stratification is used wherever possible. However, cases are included of curved flow and destabilizing thermal gradients; buoyancy forces are considered under the Oberbeck-Boussinesq approximation. The start-up process and the entry through a non-uniform magnetic field, the presence of sharp bends or expansions are all implicitly involved but this thesis concentrates on the basic studies in steady uniform strong magnetic fields. Since conducting dissimilar metal-liquid metal interface is essential for TEMHD study, a totally insulated container lining is not considered though it could be partially so.

1.2.2 GENERAL LAYOUT OF THE TEXT

Though there has been no experimental investigation in TEMHD before, yet its connection with thermodynamics and magnetohydrodynamics,

where research has been prolific requires that the survey of literature be selective if it is not to be too long. Chapter 2 deals with only the relevant general information available in the literature, critically assessed for use in the present investigation with benefit. However, when it is appropriate the discussion of the details of information is postponed to the Chapter where it is more relevant.

In Chapter 3 the basic theory of TEMHD is presented and the general equations of TEMHD starting with well developed magnetohydrodynamic equations and the Onsager's formulation of phenomenological laws of irreversible thermodynamics are developed. The relative importance of various effects is found out in terms of order of magnitude calculation and simplifying assumptions are made. The general experimental techniques, facilities and arrangements common to all the experiments are then described in the end of this Chapter. Included in this chapter is the choice of material, measurement of material properties and measurement techniques and instrumentation used during the investigations.

Chapter 4 describes investigation on the effect of thermoelectrically driven currents in straight conducting pipes of circular cross-section with alternate heating and cooling around the circumference but uniform along the length, in the presence of transverse magnetic field. Both TEMHD and static situations are analysed and experimental results presented. Some of the build-up processes are lightly touched upon.

A rather cursory treatment is given in Chapter 5 to the relatively unimportant case of a straight pipe of rectangular cross-section, with one pair of opposite sides (vertical sidewalls) of the duct-liquid metal interface electrically insulated while the other (horizontal) pair are in electrical and thermal contact with the liquid metal. Analytical and experimental results similar to those in Chapter 4 are presented.

In Chapter 6 progress is made to observations on circumferential TEMHD flow without pressure gradient in the direction of flow in an

annular channel of rectangular cross-section with radial temperature gradient driving the thermoelectric currents in a uniform axial magnetic field; this is a regime in which entry and exit effects do not arise. The effects of various boundary conditions such as partial insulation at the interface and uniform and non-uniform temperature gradients are investigated analytically and experimentally. The configuration includes a free surface which permits the flow to be observed directly and allows easy insertion and withdrawal of measuring instruments and probes.

On the basis of the information gained in Chapters 4 to 6, a technique for TEMHD pumping of liquid lithium in a double spiral channel of rectangular cross-section is suggested in Chapter 7. The design involves low external pumping power requirement for heat convection and a low stress level at the metal walls. A laboratory experimental model is described and experimental and analytical results are presented.

Chapter 8 makes recommendations for further work that could be done in the new and fertile field of thermoelectric magnetohydrodynamics following the review and final comments on the investigation reported in earlier Chapters.

CHAPTER 2

GENERAL SURVEY OF RELEVANT LITERATURE

2.1 INTRODUCTION

A brief general introduction to the relevant literature available is given in the following sections of this Chapter. It is covered under the section headings: (i) thermoelectric properties of materials and their measurement - with particular reference to liquid metals (ii) fully developed magnetohydrodynamic duct flow (iii) nonuniform,secondary flow and turbulence in magnetodydrodynamics (iv) heat transfer in magneto-hydrodynamics (v) thermoelectrically driven liquid metal pumps in fission reactor systems and (vi) the fusion reactor blanket system. The discussion of the details of relevant information in quantitive terms is however at times postponed to the appropriate point in later Chapters to derive the benefit of direct comparison.

2.2 THERMOELECTRIC PROPERTIES OF MATERIALS AND THEIR MEASUREMENT

The thermoelectric phenomena were all discovered in the last century starting with the Seebeck effect in 1828. Yet, only in the last three decades have the thermoelectric properties of materials been investigated in detail. Experiments at the initial stage were mainly done to establish the basic physical behaviour of thermoelectricity in various materials, mostly in their solid state. Very recently such experimental measurement of thermoelectric properties of metals and semimetals has assumed importance in connection with the verification of the theoretical model advanced by Ziman (1961, 1967) based on electron-phonon interaction in solids and extended to liquid metals (Cusack 1963). The absolute scale of thermoelectricity was first constructed by the Borelius group in 1932 with the measurement of thermoelectric property of Pb. The fact that thermoelectricity disappears at superconducting temperature in the absence of any magnetic field has been used. Pb has been chosen as the reference

material because it could be easily produced and purified and has low thermoelectric power, insensitive to small amounts of chemical impurities that still remain, at low temperatures. Later Christian et al (1958) extended and modified the scale up to 300°K. As Pb is not a good reference material at higher temperature, Cusack and Kendall (1958) constructed tables for the absolute thermopower of Cu, Ag, Pt, Pd, Mo and W from the Borelius/Christian data and the Thomson effect (heat absorption or release due to current flow along temperature gradients) measurement data of Lander (1948). The scale range is up to the corresponding melting point of the element, 2400°K being the highest. However, inconsistencies have been detected, particularly near room temperature and above. Huebener (1966) reported absolute thermopower value of Pt at 500°K as -9.20 μVK^{-1} which is about 8% less than 9.89 μVK^{-1} value of Cusack and Kendall and in general discrepancies as great as 10% exist between individual measurements. Laubitz (1969) examined the relative thermopower of noble metals and has constructed an absolute thermopower table by correspondence and averaging and this is quoted in Smithels and Kaye/Laby. Even the universally accepted low temperature absolute thermopower scale of Pb has recently been challenged by Roberts (1977). Using direct measurement of Thomson heat with better instrumentation he has deduced a new scale above 20°K with a variation of as much as 0.3 μVK^{-1} in the extrapolated part of the scale of Christian et al. It would affect the analysis of thermopower of materials of less than 3 μVK^{-1} above 40°K significantly.

Under this uncertainty, the measurement of thermopowers of liquid metals is further complicated by the necessity of the choice of a counter-electrode which does not contaminate the liquid metal. The earlier experimental measurements are mostly unreliable, the counter-electrode not being chosen properly, and the first valuable set of

measurements in liquid metals is of Bradley (1962) using W counter-electrodes. Marwaha and Cusack (1966) report measurements with Cu and Pt counter-electrodes, the counter-electrode and the reactive liquid metal having been separated by a thin W disc. A small amount of impurity significantly alters the thermopower data and is evident from the measurements of Fielder (1967) in Hg alloys and of Ioannides et al (1975) in Li. The effect of pressure on absolute thermopower of liquid metals is given by Crisp et al (1970) but the effect of magnetic field on thermopower of liquid metals remains obscure at room temperature and above and reliable literature has yet to be found. In contrast, the effect of magnetic field on thermopower at low temperatures, in the range of temperature 20^{o}–100^{o}K where the subtle effects of phonon drag and Umklapp processes dominate over the diffusion process giving 'giant thermopower', has been investigated - this being important in the context of fundamental studies but not for the investigations reported in this thesis.

Obviously there is a need for the measurement of the thermopowers of the materials to be used in TEMHD; the combination of the liner material and the liquid metal and the impurity (e.g. induced by various transmutations) level in the liquid metal is important rather than the thermopower data of pure experimental grade elements. Such measurements and measurement details are reported in Chapter 3 and are compared with the data available in the literature.

2.3 FULLY DEVELOPED ISOTHERMAL MAGNETOHYDRODYNAMIC DUCT FLOW

The essence of liquid metal magnetohydrodynamics is that the liquid metal is contained in a solid walled duct. The solid-liquid interface therefore exerts a considerable influence on the flow as compared to the astrophysical events. Also in the range of technical interest, the ratio of the induced magnetic field to the applied magnetic field defined as the magnetic Reynolds number R_m in analogy

with the Reynolds number Re in ordinary hydrodynamics, is much less than unity; therefore the effects of the induced magnetic field can be ignored.

Though in practice bends, expansions and interconnection of ducts would occur, yet it is important to analyse the steady uniform flow. Fully developed magnetohydrodynamic duct flow started with the Hartmann study of the steady flow of mercury in a rectangular cross-sectional straight duct with a duct width much greater than the height in a steady uniform transverse magnetic field. The inertia-less flow is governed by the Hartmann number M, the square root of the ratio of electromagnetic force to the viscous force. At large values of M, the parabolic velocity profile in the absence of the magnetic field changes to a flattened uniform core flow and Hartmann boundary layers of thickness $\frac{L_o}{M}$, where L_o is the characteristic dimension of the duct, at the duct walls perpendicular to the magnetic field direction. Shercliff (1953) solved the corresponding problem for nonconducting walls but with an arbitrary aspect ratio and showed that in addition to the Hartmann layers there are boundary layers at the pair of walls parallel to the magnetic field of thickness $\frac{L_o}{\sqrt{M}}$. It is now known that in general at high values of M, depending on the magnetic field direction and the solid duct wall-liquid metal interface discontinuity (in geometry or in electrical conductance), the flow through a duct consists of 'core' flows separated or surrounded by boundary layers. Kulikovskii (1968) has identified the various 'core' regions in the flow depending on what boundary conditions the magnetic flux lines see at the two ends. Hunt and Shercliff (1971) have given extensive examples of the adjoining layers to the 'core' flow regions. These layers are very varied depending on whether there is a significant normal component of the magnetic field (B_n) or not and are considerably governed by the duct wall conductivity. Layers with significant normal component of the magnetic field B_n, i.e. the Hartmann layers, always adjoin solid walls

and are of thickness $O(\frac{L_o}{M})$ based on magnetic and viscous force balance. The layers parallel to the field and the flow may adjoin walls but also appear as free shear layers at duct wall discontinuities. In general, the thickness of these layers are of $O(\frac{L_o}{\sqrt{M}})$. The shear layers demonstrate the propagation of strong influence along field lines from constraints at the boundary (Lehnert 1955, Alty 1966, Malcolm 1968). When the wall is so nearly parallel to the field and B_n is small, a more complicated shear layer occurs. These layers have not been investigated except in the case of a nonconducting circular cross-sectional straight duct where the field and the wall are tangential for an infinitesimal space. Then a layer of thickness $\frac{L_o}{M^{\frac{1}{3}}}$ occurs as Roberts (1967) has shown and probably appears over a length of $O(\frac{L_o}{M^{\frac{1}{4}}})$. The boundary and the shear layers are thicker than the Hartmann layer, yet they are thin compared to the duct dimension at large M. Skewed Hartmann flow has been considered by Alty (1966) and it has been shown that the field component transverse to the long walls decides the skew Hartmann number. In a circular cross-sectional straight duct the Hartmann layer thickness varies as $\frac{L_o}{M\cos\theta}$ where θ is the polar angle (Shercliff 1956).

The electric current paths for these layers are in a plane perpendicular to the direction of fluid flow. The relative distribution of the current across the core in the return path through the fluid and the duct wall is decided by the fluid to wall conductance ratio

$$c = \frac{\text{conductance of the fluid}}{\text{duct wall conductance}} = \frac{\sigma L_o}{\sigma_w t_w}$$

where σ = conductivity of the fluid

σ_w = conductivity of duct wall

and t_w = thickness of the duct wall

If $c = \infty$ then the Hartmann layers in the fluid are the only way of return path for current and the high resistivity of the Hartmann layer

restricts the core current. The core current will be appreciably greater with $c << 1$ and the pressure gradient necessary to offset the magnetic drag will be much greater. Precisely what is important is the relative conductance of the duct wall and that of the boundary layers i.e. whether $c \gtrless M$. Hoffman and Carlson (1971) has compared the effect of transverse magnetic field on pressure losses in flows in rectangular channels with ideally conducting and non-conducting walls. For $M > 10$, the ideally conducting channel has been shown to give a pressure loss $\sim O(M^2)$. For the non-conducting wall channel the pressure loss due to the formation of Hartmann layers was shown to be $\sim O(M)$; however the latter trend is true for values of M two orders of magnitude greater than that in the case of ideally conducting channel. There is no analysis available for the rectangular cross-sectional duct with arbitrary wall conductivity in general, though particular solutions are available. Chang and Lundgren (1961) have analysed the case of ideally conducting walls. Hunt (1965) showed that the core does not always have the maximum velocity. In the case of conducting walls, the velocity at the walls parallel to the field is greater than the core velocity but is of the same order. However, in the case of mixed (a pair conducting and the other insulating) walls it has been shown that velocity at the sidewall, $c = \infty$, parallel to the field, boundary layers can be M times the core velocity at large value of M when the walls perpendicular to the field are ideally conducting. Such high velocities also occur in the M-shaped profile of Alty (1966) where the transverse magnetic field is oriented at an angle ($> 45^{o}$) to the sidewalls. These results have been experimentally verified (Gel'fgat et al 1971). Thus the slim duct has relatively higher flow rate. An analytical solution of flow in a circular cross-sectional straight tube with arbitrary c value is given by Ihara, Tajima and Matsushima (1967) in the form of a trigonometrical series whose coefficients satisfy an infinite set of linear algebraic

equations and the velocity structure is not easily identified. Gold (1967) also has considered the problem and a solution has been found in series form of the conductance parameter which is however not suitable in the intermediate range of the parameter. The approximate solution of Chang and Lundgren (1961) gives a monotonically flat velocity distribution across the duct cross section which has been refuted by Gnatyuk and Paramonova (1971) by experimental measurements in ducts with conducting walls. All the above cases assume strictly isothermal flow.

The magnetohydrodynamic flow can be either pressure driven as in the case of Alty (1966, 1971) or electrically driven (Moffatt 1964). In the ideal case of isothermal flow with uniform fluid properties, a uniqueness theorem for the flow solution exists given either pressure gradient or volume flow and the values of either the potential or the current in the external connections to the duct (Hunt 1967) but may not be valid in non-isothermal environment.

2.4 NONUNIFORM, SECONDARY AND TURBULENT FLOW IN MAGNETOHYDRODYNAMICS

It is inevitable that except in very special circumstances, the MHD flow in general would be nonuniform and certain conditions must be satisfied to retain the simplicity of analysis in section 2.3. The MHD flow has to accelerate to the steady value and the analysis during this building up process is fairly complicated.

Even when stationary flow has developed, in most cases the duct cross-sectional area and the field strength would vary, at least for some regions along the flow circuit. Entry to the duct and into the magnetic field and exit represent such cases. Gradients in the flow direction now create inertia forces and their relative importance is measured by the interaction parameter N, the ratio of the electromagnetic force to the inertia force. N is evaluated with current produced by the motion induced e.m.f. and is equal to M^2/Re but when

the current density is otherwise restricted N may not be a proper choice of guiding parameter. In the nonuniform field (Holroyd 1975) and variable area cross-sectional duct (Walker and Ludford 1975) there appears a possibility of current path adjustment through regimes of lower magnetic field or larger duct cross-sectional area. Hunt and Leibovitch (1967) have shown that in a uniform field, the layer thickness at regions where the slope of the duct wall changes abruptly is of the order of $O(\frac{L_o}{N^{\frac{1}{3}}})$ instead of $\frac{L_o}{M^{\frac{1}{2}}}$ for $Re^2 >> M$ but for sufficiently high values of M, the layer thickness again is $O(\frac{L_o}{M^{\frac{1}{2}}})$. The studies of Walker and Ludford on flows along ducts of varying cross-section in uniform fields revealed that disturbances can propagate both upstream and downstream into the uniform sections of the pipe. For the entry problem Shercliff (1962) has shown that for $N < 2$ the fluid is forced towards the sides parallel to the field with fractional velocity changes of the order of N times the mean velocity and lasts over a length of few pipe diameters. Holroyd (1975) considered the inertia-less flow to find that in the mixed conductivity wall rectangular duct the flow is affected by the conductance of the wall lengthwise and in the case of circular cross-sectional duct the pressure drop and the disturbance increase with wall conductance and rate of change of the magnetic field.

Turbulence in MHD. Early measurements of Hartmann and of Murgatroyd in straight ducts (see Cowling 1976 for easy ref.) show that if a gradual increase in the magnetic field is applied to a turbulent flow, the pressure drop for a given flow rate at first decreases, reaches a minimum and then begins to increase monotonically. The reduction in the pressure drop has been explained by the inhibition of turbulence by the magnetic field which dominates over the Hartmann effect over a range beyond which the Hartmann effect dominates. Branover (1967)

on the basis of collated experimental data in nonconducting ducts arrived at a criterion $Re/M <$ (130-215) for the magnetic field to suppress turbulence. No corresponding relation is available for a duct of arbitrary wall conductivity. The occurrence of large velocity shear layers (Lehnert 1955, Alty 1966) and boundary layers (Hunt 1965) raise the question of stability of such flows. Instabilities in the form of standing waves have been detected by Malcolm (1970). The inhibitive effect of the magnetic field in general gives the turbulence a two dimensional structure perpendicular to the magnetic field direction, which is important to note.

Rotational MHD flow Corresponding to the Taylor problem in ordinary hydrodynamics, there exists a class of flows different from those considered above, and the hydromagnetic case is extensively discussed by Chandrasekhar (1961). Heiser and Shercliff (1965) have demonstrated that in a radial magnetic field uniform movement of the nonconducting inner cylinder imparts to the fluid a rigid body rotation except in boundary layers where the no slip condition prevails. This is a case of forced vortex creation in the presence of magnetic field. Parallel to these problems, there are investigations where the flow is either pressure or electrically driven and the walls of the curved channel are stationary. The pressure driven case in an axial magnetic field has been considered by Chandrasekhar et al (1961) and the electrically driven case by Baylis (1966). The centrifugal force associated with the nonuniform curved flow gives rise to secondary circulation in a plane perpendicular to the primary flow and its importance is governed by the Dean number based on Reynolds number, the radius of curvature and the height of the duct. Baylis's experiment was conducted in closed annular channels of rectangular cross-section with the curved walls electrically conducting and the horizontal walls nonconducting for various aspect ratio of the channel section in a vertical magnetic

field. The flow was driven by radial current and uniform axial magnetic field. Measurement of the velocity profile was done by potential measurements at the top insulating boundary. Baylis was interested in the transition from laminar to dominant secondary flow regime at a Dean number now a function of M. No internal measurements were done and M was usually 16 and a maximum of 129. Even at M as low as 3.5, Baylis's results give good support to the Hunt and Stewartson (1965) theory in the case of straight duct, though the experimental values of the parameter proportional to (current/flow) were always higher. Though, in this thesis rotating containers will not be considered, it is interesting to note that the Taylor-Proudman theorem promotes two dimensional flows perpendicular to the rotation axis. Thus aligned rotation would promote two dimensional motion in the hydromagnetic case in the plane perpendicular to the magnetic field.

When the fluid is highly electrically conducting, disturbances can propagate in the form of Alfvén waves (Alfvén 1950) under the influence of a magnetic field. However, with R_m low and Hg as the liquid metal such disturbance can be ignored (Braginskii 1959).

When open surfaces exist, surface waves and disturbances are possible but Lehnert (1952) has shown that magnetic field in general can completely suppress such disturbances.

2.5 HEAT TRANSFER IN MAGNETOHYDRODYNAMICS

The effect of a magnetic field on heat transfer in liquid metals is judged by the effect of the field on thermal convection against a background of high molecular thermal conductivity. Most widely investigated is the classical Bénard problem - a shallow horizontal layer of fluid heated from below - modified by the magnetic field. The vertical magnetic field significantly delays the convective mechanism of heat transfer by increasing the critical value of the

nondimensional parameter - the Rayleigh number, a measure of the ratio of buoyancy force and viscous force. The convective cell dimensions decrease with increasing M. Theory asserts that for fluids with large magnetic Prandtl number overstability cannot occur and instability sets in as cellular convection (Chandrasekhar 1961). A horizontal magnetic field elongates the cells along the field for the whole length of the vessel (Lehnert and Little 1957).

The parallel set of problems is the Batchelor (1954) slot problem where the temperature difference is applied laterally between two parallel vertical sides of a box containing the fluid. Cowling and Singh (1963) have considered the effect of a transverse horizontal magnetic field on the buoyancy-induced circulation. The effect of a vertical magnetic field has not been considered. The nonmagnetic case in the laminar boundary layer regime has been treated by Elder (1965) and numerical computation reported by Davis and Thomas (1969). The aspect ratio(width/height) of the slot considered is however restricted to low values for moderate and large Prandtl (Pr) number. Temperature oscillations at the free top surface reported in high aspect ratio rectangular boats and low Pr number fluids (Hurle, Jakeman and Johnson 1974) raises an important question since as remarked earlier for magnetic Prandtl number > 1 overstability is ruled out in the Bénard problem. A theoretical explanation has been modelled by Gill (1974) but does not explain the experimental results completely. Thermocapillary motion is admissible.

In the absence of a magnetic field forced convective heat transfer in curved channel with a square cross-section has been considered by Mori et al (1971) and heat transfer in the radial direction for turbulent flow of mercury in annuli by Dwyer et al (1977). In a transverse magnetic field, with laminar Hartmann flow, the only mechanism influencing heat transfer is the flattening of the velocity

profile. Thus with the increase in M the heat transfer in general should increase (This excludes fully developed heat transfer across channels). However, in turbulent flow conditions, a major contribution to the variation in heat transfer is the result of the turbulence damping effect. If the flow is turbulent in the absence of the magnetic field and the magnetic field is strong enough to suppress the turbulent eddies, the heat transfer will be considerably reduced in the magnetic case. In weak magnetic fields the reduction of heat transfer would not be so pronounced. A magnetic field parallel to the flow only affects heat transfer in the turbulent case by damping eddies. The transverse magnetic field case has been verified by Gardner et al (1966). In the case of a circular cross-sectional pipe subjected to an uniform heat flux at the wall the influence of transverse field resulted in a reduction in heat transfer of 70%. The influence on the temperature profile was to lower the centre line temperature and is dependent on the angular orientation of the transverse field (Gardner and Lykoudis 1971). No account is available of heat transfer in channels with circumferentially-specified nonuniform heat transfer in transverse or parallel magnetic fields.

2.6 THERMOELECTRICALLY DRIVEN LIQUID METAL PUMPS FOR FISSION REACTORS

After starting the experimental investigation on TEMHD in 1976, it became apparent that the concept of thermoelectromagnetic pumping of coolants in nuclear fission reactors had already been considered. The fundamental difference with the system considered in this thesis is that the coolant fluid in the fission reactors is either Na or Na-K eutectic with very low insignificant values of thermoelectric power; therefore in these systems in fission reactors the fluid plays a passive role thermoelectrically. Basic magnetic field is also to be provided in such devices. Significant thermoelectric current has

to be produced by using semiconducting or metal alloys as elements in the thermoelectric circuit. The use of such elements in Fusion reactors may not be suitable unless they can sustain neutron radiation. In view of the ideas of TEMHD pumping presented in this thesis being parallel to these ideas and partly because these reports may not be readily available to refer to, a brief description of each of the systems considered in fission reactors is given below.

The use of liquid metal and integral pumping system has generally been considered from the point of view of self circulation for heat transfer, compactness of the devices and shielding space utilisation. The first of such ideas seems to be that of Murgatroyd (1951). Simplified versions of his schemes are shown in figure 2.1a, b. In figure 2.1a, the hot fluid is in tube 1 and the cold fluid in tube 2. Thermoelectric elements t_1 t_2 are mounted in the insulating block I filling and joining the recess at the sides of the tubes 1 and 2 at mid length between the hot and cold reservoirs. Solid copper leads connected to the thermoelectric elements are bent in opposite directions at the two ends into the central region of tube 1 and 2 respectively. The thermoelectric current path is completed through the thermoelectric elements, copper lead, hot fluid, wall of tube 1, cold fluid, copper lead back to the thermoelectric elements. In figure 2.1b, an annular section is mechanically formed between parts 1 and 2, the thermoelements, so that a radial flow of thermoelectric current is possible due to hot fluid flow in the central pipe and cooling at the outer rim. No theoretical analysis or experimental results are provided.

Luebke and Vandenberg (1953) report on a compact fission reactor power plant with combination heat exchanger and thermoelectric pump. A cross-section of the tube matrix carrying hot sodium and cooling water as given in their scheme is shown in figure 2.2. All the space between the tubes is filled with copper apart from the half rings of

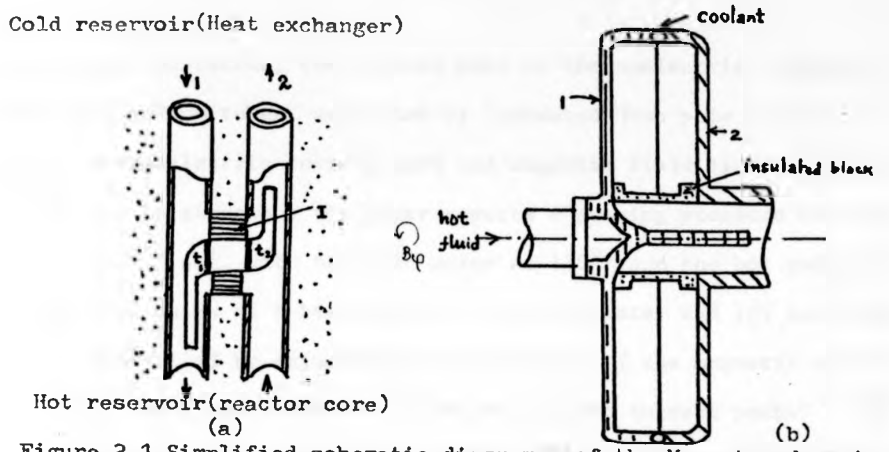

Figure 2.1 Simplified schematic diagrams of the Murgatroyd system of thermoelectric pump.

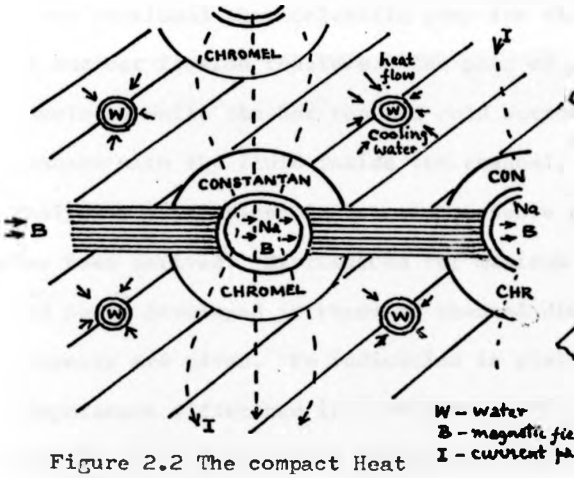

Figure 2.2 The compact Heat exchanger circulation system of Luebke and Vandenberg.

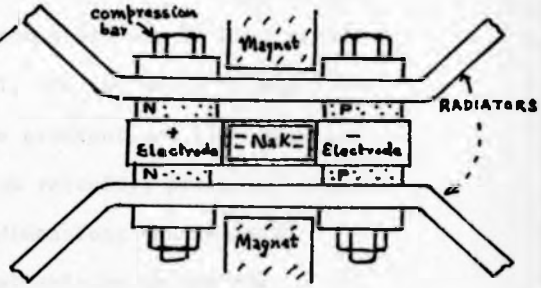

Figure 2.3 Thermoelectric pump fo SNAP 10A (Perlow and Davis)

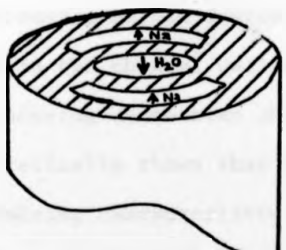

Figure 2.4 Basic form of ducting in de Cachard and Caunes petite thermopompe

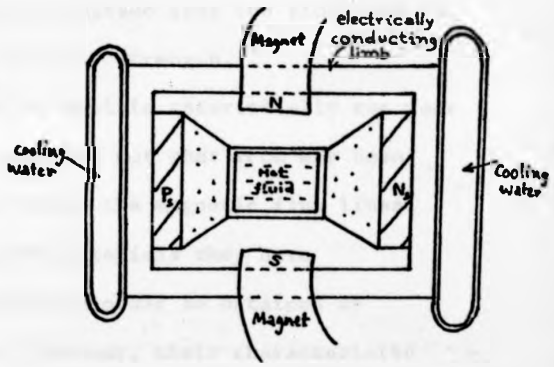

Figure 2.5 The thermoelectromagnetic pump of Makarov and Cherkasskii.

chromel and constantan, the matched pair of thermoelectric elements, around the sodium tubes, separated by laminated iron pole pieces. Typical thermoelectric current path and magnetic field lines are shown. No analysis is given but the paper reports a pumping pressure calculation of 14.5 p.s.i. with the cold water at 135°F and the hot sodium at 850°F in 707 pairs of tubes of about 1 inch diameter and 105 inch long. Flow is controlled by adjusting the reluctance of the magnetic circuit or by inserting resistance in the thermoelectric current path.

Rex (1961) was the first to report a theoretical analysis of a rectangular cross sectional thermcelectric pump for the coolant sodium circulation in nuclear fission reactors. The pair of sidewalls are electrically insulated while the hot top and cold bottom walls are in electrical contact with the fluid inside the channel. On the basis of slug flow analysis, a relationship between pressure gradient and flow velocity has been derived. Expressions for maximum velocity, pressure gradient and power developed in terms of channel dimensions and material property are given. No indication is available as to how the temperature difference is maintained. His experimental result of flow rate at 500°C temperature differnce of 30 litres/min falls much short of his analytical prediction of 12 litres/min for a temperature difference of 100°C. However, Rex duly realised that the flow rate is inversely proportional to the magnetic field strength.

Osterle and Angrist (1964) tried to explain theoretically the poor performance of the device of Rex by pointing out that iron has been used in the channel wall which would divert the magnetic flux lines. By choosing constantan and semiconductor materials they have theoretically shown that better performance could be obtained by optimising characteristic parameters. However, their characteristic optimum resulted in unrealistic channel dimensions.

The thermoelectric pump for circulating Na-K in the SNAP-10A

nuclear system is described by Perlow and Davis (1965). The arrangement shown in figure 2.3, uses thermoelectric elements made of PbTe powder compacts between two end layers of iron powder to give good electrical contact. No analysis is available but the performance figure of hot (1010^{o}F) Na-K flow rate 14 gallons/min at a net pressure of 1.22 psi is quoted.

A French thermosiphon device for liquid sodium in nuclear or irradiating combustion heating systems as reported by M de Cachard and Caunes (1969) includes a small thermoelectric pump. The fluid in the split halves of an annular channel (figure 2.4) is driven by the radial thermoelectric current across the field of permanent magnets located by the side of the pipe. The inner central tube carried the cooling water. Neither any theoretical analysis nor any experimental result is given.

Makarov and Cherkasskii (1969) report a design of thermoelectric pump using the hot fluid channel of rectangular cross-section as the hot junction of a thermocouple whose elements are semiconductor materials. The elements are placed on either side of the hot fluid channel having good electrical contact with the channel walls (figure 2.5). On the basis of an equivalent circuit analysis, a theoretical design is given to obtain the best performance characteristic (pressure-consumption) by optimising channel dimensions with given material property. Fluid dynamics of the system is restricted to a slug flow model; at low values of the magnetic field in such systems this model may not be accurate. Calculations using Te-Bi thermoelements with a temperature difference between the hot and the cold junction of 100^{o}C, the magnetic field of 0.384 Tesla, channel size 1.5 cm. square shows a developed electromagnetic force of 1.4 x 10^{5} $N/_{m}3$. The efficiency of the device is low, 1.4%.

All the above devices use the fluid only as the source of heat

at the hot junction of thermocouple and to provide the necessary electrical contact. Permanent magnets or magnetic devices are essential for providing the magnetic field. Poor performance figures for these devices even with the best thermoelectric material must be the reason for no attempt so far being made to analyse the detailed fluid dynamics or heat flow in such flows. The fluid has effectively zero thermoelectric power and does not participate in generating thermoelectric current itself; it is therefore less interesting in character.

2.7 FUSION REACTOR BLANKET

It is important to consider the various possible geometries of a thermonuclear reactor and its magnetic system for investigating the possible TEMHD effect. Various possible system geometries are available in Kammash (1975) and Post (1976). In the introduction it has been remarked that the magnetically confined TOKAMAK device using D-T fuel and the Li blanket is the most pertinent case for possible early applicability of TEMHD. Details of TOKAMAK systems are given by Artsimovich (1972). Since then modifications have been considered. However, the basic structure as shown in figure 2.6 is that of plasma confined within an evacuated metal liner in the form of a torus. The exciting coils on the iron core indirectly produces the B_φ magnetic flux but a very strong B_θ flux is produced by coils around the surface of the channel to eliminate the main magnetohydrodynamic instabilities and to confine the plasma away from material wall ($B_\varphi < 0{\cdot}1B_\theta$). The main magnetic field configuration is shown in figure 2.7. Additional coils are necessary to eliminate the applied field components that give uncontrollable plasma displacement:- they are (i) conductor strips inside the metal liner maintained to generate a time variable field and (ii) coils outside the liner to produce a quasisteady transverse vertical field to control the position of the plasma loop. The relative oscillation of B_θ is 0.5 to 1%. The concept of a diverter

at the hot junction of thermocouple and to provide the necessary electrical contact. Permanent magnets or magnetic devices are essential for providing the magnetic field. Poor performance figures for these devices even with the best thermoelectric material must be the reason for no attempt so far being made to analyse the detailed fluid dynamics or heat flow in such flows. The fluid has effectively zero thermoelectric power and does not participate in generating thermoelectric current itself; it is therefore less interesting in character.

2.7 FUSION REACTOR BLANKET

It is important to consider the various possible geometries of a thermonuclear reactor and its magnetic system for investigating the possible TEMHD effect. Various possible system geometries are available in Kammash (1975) and Post (1976). In the introduction it has been remarked that the magnetically confined TOKAMAK device using D-T fuel and the Li blanket is the most pertinent case for possible early applicability of TEMHD. Details of TOKAMAK systems are given by Artsimovich (1972). Since then modifications have been considered. However, the basic structure as shown in figure 2.6 is that of plasma confined within an evacuated metal liner in the form of a torus. The exciting coils on the iron core indirectly produces the B_φ magnetic flux but a very strong B_θ flux is produced by coils around the surface of the channel to eliminate the main magnetohydrodynamic instabilities and to confine the plasma away from material wall ($B_\varphi < 0.1 B_\theta$). The main magnetic field configuration is shown in figure 2.7. Additional coils are necessary to eliminate the applied field components that give uncontrollable plasma displacement:- they are (i) conductor strips inside the metal liner maintained to generate a time variable field and (ii) coils outside the liner to produce a quasisteady transverse vertical field to control the position of the plasma loop. The relative oscillation of B_θ is 0.5 to 1%. The concept of a diverter

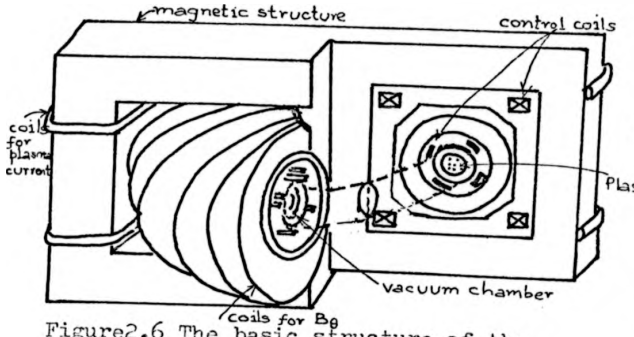

Figure2.6 The basic structure of the TOKAMAK Fusion reactor.

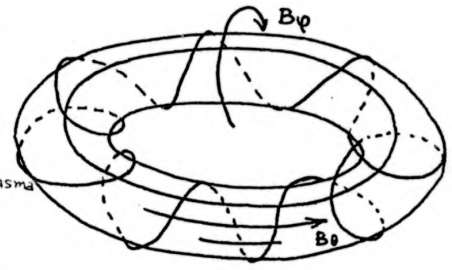

Figure 2.7 The helical magnetic field line around the TOKAMAK torus.

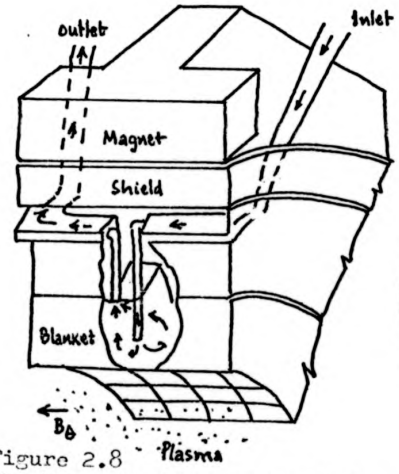

Figure 2.8 The U.K. AEA lithium blanket system

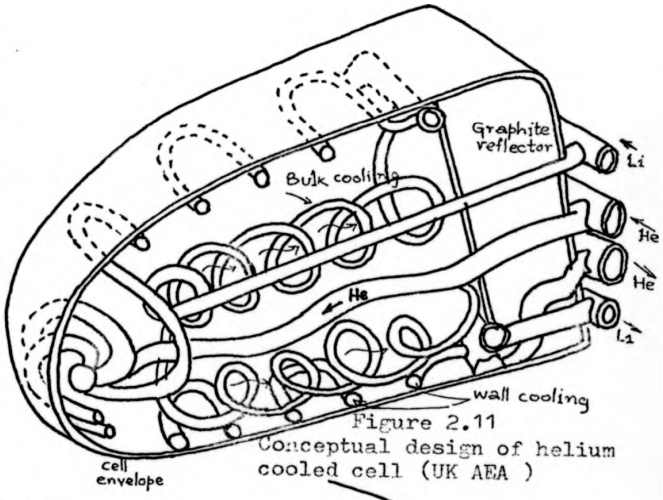

Figure 2.11 Conceptual design of helium cooled cell (UK AEA)

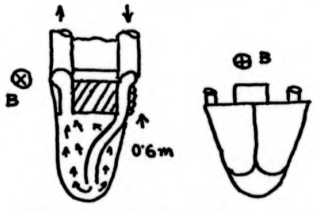

Figure 2.9 First wall element of lithium blanket design(UK AEA).

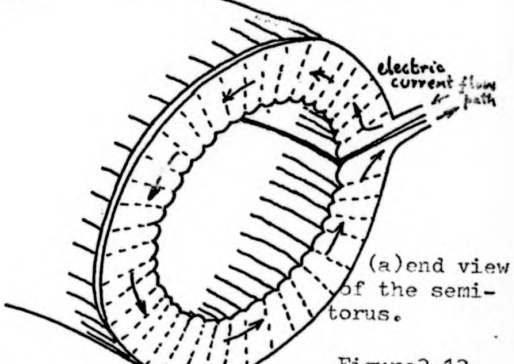

(a)end view of the semi-torus.

Figure2.12 The 'Racetrack' blanket cell of Fraas.

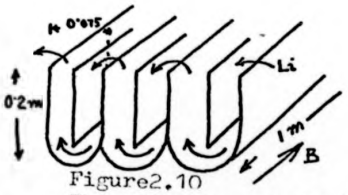

Figure2.10 The slim channel design of the Wisconsin device.

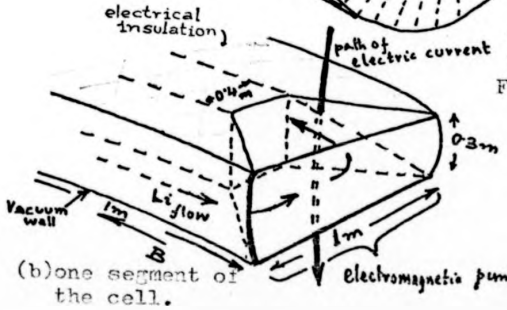

(b)one segment of the cell.

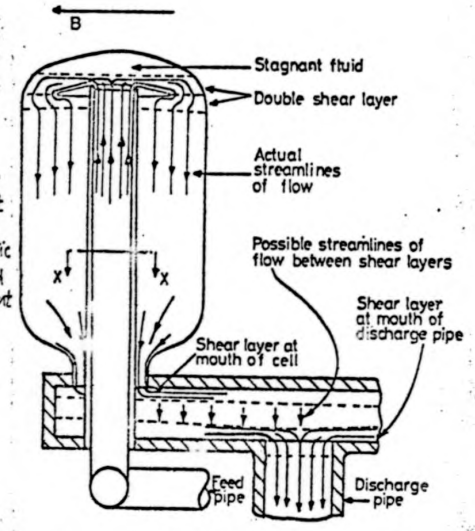

Figure 2·9 (redrawn)
First wall element of lithium blanket fluid flow characteristic shear layer and possible stagnant zones.

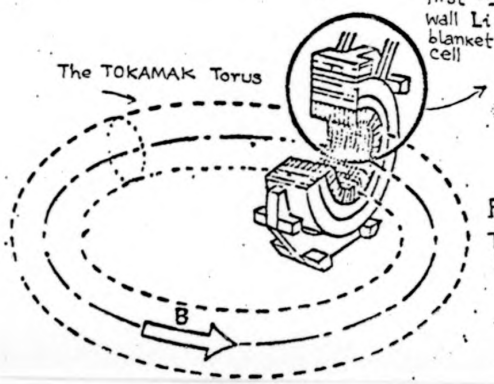

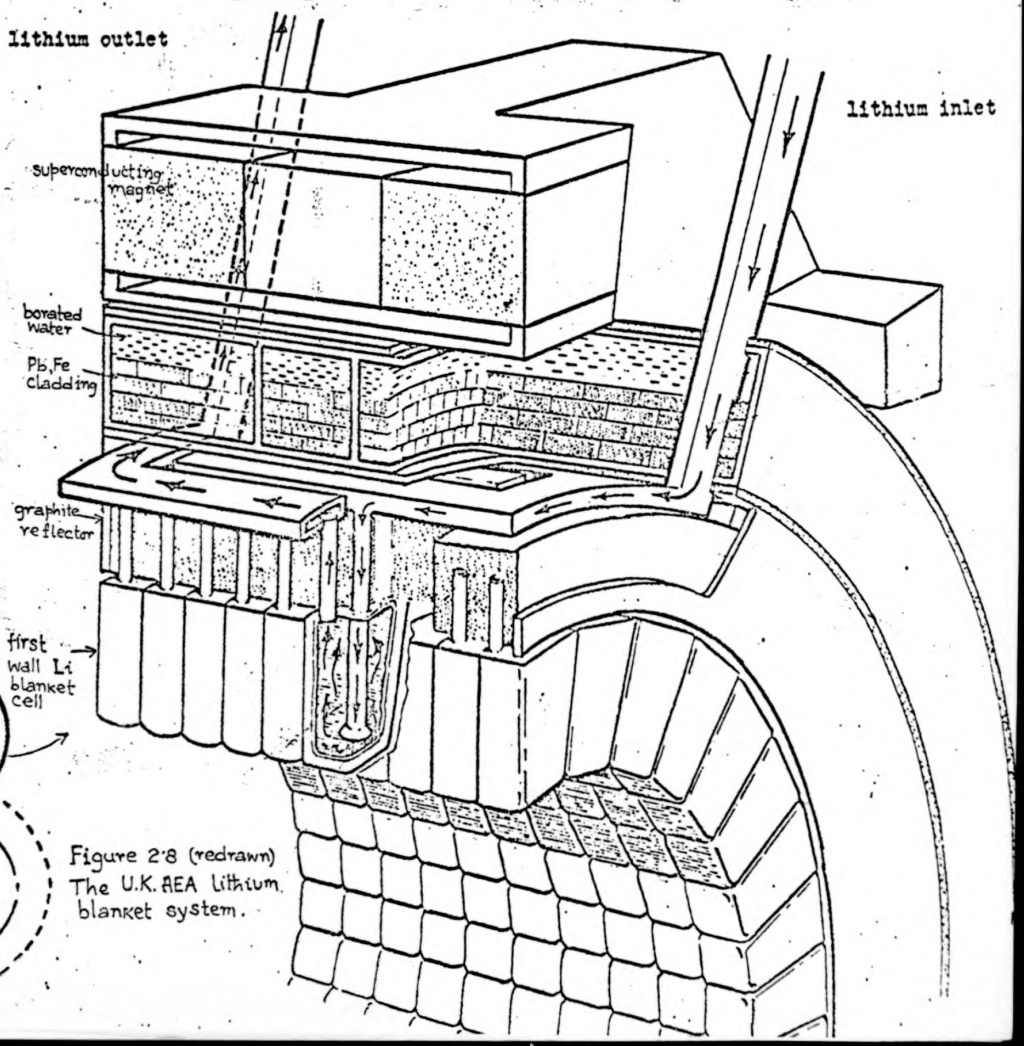

Figure 2·8 (redrawn)
The U.K. AEA lithium blanket system.

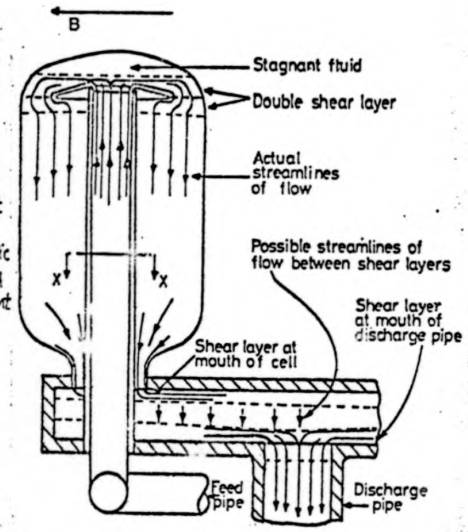

Figure 2·9 (redrawn)
First wall element of lithium blanket fluid flow characteristic shear layer and possible stagnant zones.

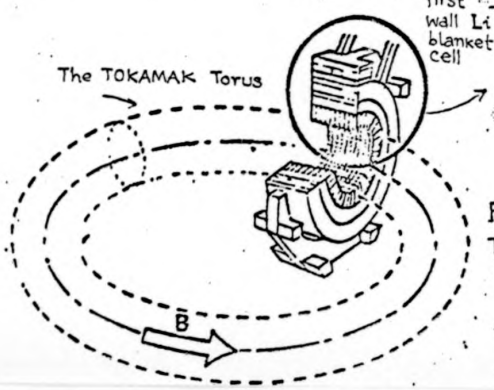

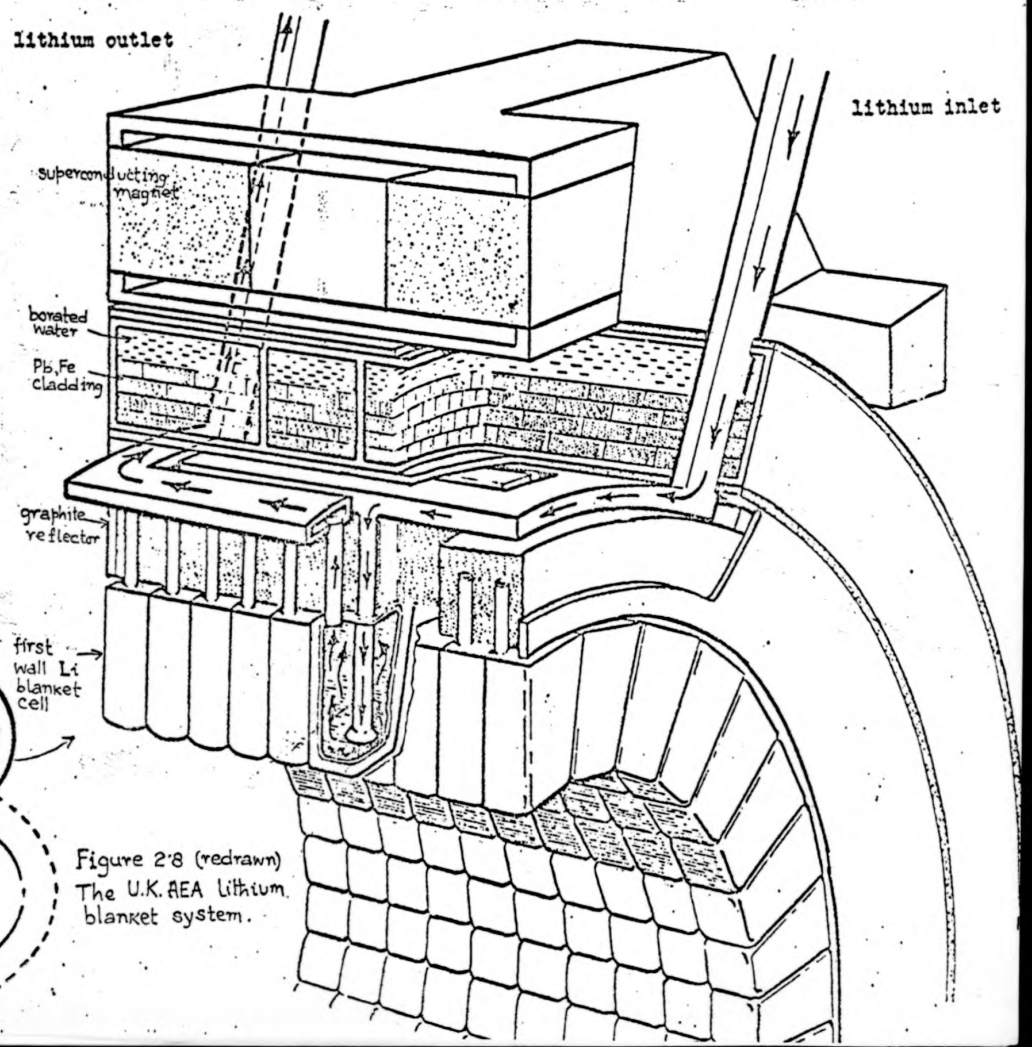

Figure 2·8 (redrawn)
The U.K. AEA lithium blanket system.

for diagnostic and purification purposes has an indirect effect but from the standpoint of stress considerations on the magnetic field coils the torus cross-section has changed to D shape rather than a symmetrical circular one.

Hoffman and Carlson (1971) were the first to consider the problem of lithium circulation in the blanket with calculations based on practical empirical formulae. Further details are available in Carlson (1974). However, details of hydromagnetic pressure drop and the associated stress limitations of the wall structure are provided by Hunt and Hancox (1971) and Hancox and Booth (1971). The conceptual design of the Li blanket cooling as proposed by the UK AEA is shown in figure 2.8. Essentially several modes of magnetohydrodynamic duct flow occur. The estimate of the pumping power is based on the magnetohydrodynamic flow in uniform ducts and field with a percentage addition due to pressure losses in bends and in nonuniform regions. Since insulators are incompatible with the hot Li and in the neutron radiation environment, metal walls are considered but to keep the magnetohydrodynamic pressure loss low only thin walls are used. Typical parameters of Hunt and Hancox (1971) calculation relevant to 5000 MW (thermal) TNR are B = 10 Tesla, plasma torus minor radius = 1.25 m, major radius = 5.6 m, first wall loading = 13 $\frac{MW}{m^2}$, M = 35000, N = 44000, Re = 28000, Rm = 0.07. The pumping power requirement even with the best duct shape (diamond) estimated is 10% of the reactor output (electrical), about six orders of magnitude higher compared to the pressure drop in the absence of the magnetic field. The corresponding wall stress is even more of severe limitation (Hancox et al 1971, Stanbridge et al 1974). Hunt and Holroyd (1977) have incorporated the results of magnetohydrodynamic flow in nonuniform magnetic fields and in expansions to predict higher pressure losses due to the flow of fluid in thin layers along characteristic surfaces (refer Kulikovskii

1973) in the nonuniform regions. However the first wall loading of 13 $MW/_m2$ is much higher than the typical recent design figure. The most important part of the problem, the flow in the immediate vicinity of the first wall and the heat transfer there has yet to be solved. Figure 2.9 shows the UK AEA design of the first wall elements for a 2500 MW(e) TNR with 4.3 $MW/_m2$ first wall loading and B_θ = 8.4 Tesla. However, no account of the heat transfer mechanism of the fluid flow is available and it is expected that the magnetic field would prevent the cool fluid from the duct reaching the inner surface of the front of the cell.

An alternative method of Li circulation proposed for the Wisconsin system (Culcinski & Conn 1974) corresponds to a 5000 MW (thermal) reactor with a maximum field B_θ = 8.66 Tesla but with a first wall loading of 1.25 $MW/_m2$ only. First wall cells are shown in figure 2.10 are shaped so as to ensure the minimum interaction of the liquid metal with the transverse magnetic field:- flow in slim rectangular channels with the long side parallel to the field. Pumping power,for the pressure drop, estimate reported is only 1.5% of the plant output. However, consideration has not been given to the reduced flow due to formation of thin layers near the first wall and the associated pressure drop.

Fujii-E and Suita (1974) have explored three possibilities for the blanket cooling system using Li, Na, K from the point of view of low operating pressure with given wall conductivity ratio values. The first of these is to apply an external electric potential across the channel to compensate for the e.m.f. due to magnetohydrodynamic interaction; this is really the introduction of a differential d.c. pumping device in the blanket. The second possibility is to use the liquid metal and an inert gas mixture as the working fluid to achieve a low working electrical conductivity. The third possibility is the

use of boiling two phase flow of the working fluid with heat transport in the form of latent heat of vaporization and simultaneous reduction in combined conductivity. In the first case it is difficult to introduce electrodes carrying large current into the blanket and the stress in the duct walls due to the interaction of the wall current with the magnetic field is not reduced. Not much is also known about nucleate boiling in magnetic fields and the recent accepted UK design corresponding somewhat to the second case of Fujii is shown in figure 2.11. The possibility of removing heat by means of sodium heat pipes has been considered by Carlson and Hoffman (1971) - though the capillary flow in magnetic fields is yet to be assessed properly.

The possibility of pumping the coolant Li by external current source in a 'race-track' shaped duct with the long axis parallel to B_θ (figure 2.12) is considered by Fraas (1972) for a 1000 MW (thermal) TNR with first wall loading of 1 $MW/_m2$ (figure 2.12). A one-sixth scale model experiment to test the feasibility of such a system is described in Young et al (1974). Though the pressure drop in the aligned field flow is one order of magnitude less than that in the transverse field flow, the pressure drop is much greater than expected. Also in the 90^o turn at the end, considerable pressure drop results at the high value of N considered.

It appears that the various proposals for reducing the pressure drop in the Li flow in the magnetic field are exhaustive but none of these consider the heat transfer and heat distribution in the blanket under the magnetic field constraint.

The Li blanket system is not exclusive to the TOKAMAK system but is also associated with other types of TNRs. Li blankets for mirror machines have been considered by Werner (1974). Also in inertial confinement systems Li blankets are used but there is no inherent magnetic field.

2.8 WORK AT WARWICK

A preliminary paper on TEMHD was presented at the second Bat -Sheva conference on MHD (Shercliff, Dutta Gupta and Alty (1978)). Details of TEMHD theory have been considered in a paper by Professor Shercliff published in the Journal of Fluid Mechanics (1979a). TEMHD-driven Hartmann flow and two-dimensional duct flows have been considered. The stirring of melts to give uniform composition has also been considered in detail. In a paper to the journal, Physics of Fluids (1979) Professor Shercliff (1979b) has considered thermoelectric magneto-hydrodynamics in closed containers with particular consideration of those having axisymmetry about the field direction and several solutions have been found for the case of a spherical container. The work reported in this thesis complements the work of Professor Shercliff.

CHAPTER 3

EQUATIONS, PRELIMINARY ANALYSIS AND EXPERIMENTAL SYSTEMS

3.1 Introduction

The basic equations of TEMHD and the boundary conditions under specific assumptions are generalised from the well-known equations of magnetohydrodynamics given in books, (e.g. Shercliff, 1964) in section 3.2. The order of magnitude of terms neglected is briefly described in section 3.3. Preliminary analysis of the Hartmann flow as modified in the TEMHD case is attempted in section 3.4. The next few sections are devoted to the description of the experimental devices - the experimental facility, apparatus and measuring instrumentation with calibration techniques.

3.2 The Equations of TEMHD

3.2.1 MHD equations

The basic equations of magnetohydrodynamics - the Maxwell equations, the Navier-Stokes equation and the continuity equation modified under magnetohydrodynamic assumptions are

$$\text{Curl } \underline{E} = \nabla \times \underline{E} = \frac{-\partial \underline{B}}{\partial t} \qquad (3.1)$$

$$\text{div } \underline{B} = \nabla \cdot \underline{B} = 0 \qquad (3.2)$$

$$\mu \underline{j} = \nabla \times \underline{B} = \text{curl } \underline{B} \qquad (3.3)$$

$$\rho \frac{D\underline{v}}{Dt} = \rho \left\{ \frac{\partial \underline{v}}{\partial t} + (\underline{V}.\nabla)\underline{V} \right\} = \rho \left\{ \frac{\partial \underline{v}}{\partial t} + (\underline{V}.\text{grad})\underline{V} \right. = -\nabla p + \underline{j}\times\underline{B} + \eta_v \nabla^2 \underline{V} + \underline{F} \qquad (3.4)$$

$$\text{and } \frac{D\rho}{Dt} = -\rho \text{ div } \underline{V} \qquad (3.5)$$

where $\underline{E}$ is the electric field, $\underline{B}$ the magnetic flux density = μ times the magnetic field with μ the permeability of the medium assumed same as the vacuum, ρ the density of the fluid, $\underline{v}$ the velocity, p the pressure, η_v the bulk viscosity of the fluid, $\underline{j}$ the current density and $\underline{F}$ is the body force, (e.g. gravitational) excluding $\underline{j}\times\underline{B}$

The inherent assumptions are (i) the velocities considered are much less than the speed of sound in the fluid, (ii) there are no

high frequency electromagnetic oscillations so that the 'displacement current can be ignored in (3.3), (iii) convection current is ignored though the charge concentration could be found from div $\underline{E}$, and (iv) the magnetic Reynolds number $R_m = \mu\sigma v L_o << 1$

Necessarily from (3.3), $\text{div } \underline{j} = 0$ with μ constant (3.6)

Though the density of the fluid varies with the temperature, the elementary assumption of incompressibility replaces (3.5) by

$$\text{div } \underline{V} = 0 \tag{3.7}$$

The variation of ρ is restricted to the buoyancy term (body force F in equation (3.4)), i.e. the Oberbeck-Boussinesq assumption is adopted.

$$\underline{F} = \rho(T_o)\beta \underline{g} \Delta T \tag{3.8}$$

$$\text{with } \rho(T_1) = \rho(T_o)\{1 - \beta\Delta T\} \tag{3.9}$$

where $\Delta T = T_1 - T_o$, T is the temperature, β is the expansion (volume) coefficient and g the acceleration due to gravity. However, the Ohm's law is modified by TEMHD and is considered in subsection 3.2.2.

3.2.2 Entropy balance in nonequilibrium systems

The entropy $S_\bullet$ in a volume element changes due to (i) flow of entropy into the volume and (ii) presence of entropy sources in the irreversible phenomena in the volume element itself. While (i) obeys the conservation laws of mass, momentum and energy, (ii) could be accounted for in a simple way, taking it as a sum of the product of flux $\underline{J}_i$ (time derivative of departure of state variables from equilibrium $\frac{dx_i}{dt}$) with affine force $\underline{X}_i$ (e.g. nonuniformity of the system or deviation from equilibrium $\frac{dS_\bullet}{dx_i}$) (de Groot and Mazur, 1951).

$$\text{i.e. } \frac{\partial S_\bullet}{\partial t} = \sum_i \left(\frac{\partial S_\bullet}{\partial x_i}\right) \cdot \frac{dx_i}{dt} = \sum_i \underline{X}_i \underline{J}_i$$

This relation is made useful with the assumption that within the restricted domain of the linear range, the phenomenological equation

$$\frac{dx_i}{dt} = \underline{J}_i = \sum_k L_{ik} \underline{X}_k = \sum_k L_{ik} \left(\frac{\partial S_\bullet}{\partial x_k}\right)$$

where L_{ik}'s are phenomenological coefficients, tensors for an anisotropic system, gives a simple relationship between flux and its affine force.

This is true for a large class of irreversible phenomena and for a wide range of experimental conditions. Fourier's law of heat conduction, Fick's law of diffusion and Ohm's law of electric conduction are all special cases of this. However, in general,certain cross-relations are possible as in Soret, thermoelectric,thermomagnetic, galvanomagnetic and electrokinetic effect and the constitutive relation

$$\underline{J}_i = \sum_k L_{ik}\underline{X}_k \qquad (3.10)$$

would allow values of k more than one.

Onsager's Reciprocity theorem (de Groot and Mazur, 1962),based on the concept of microscopic time reversibility reduces the number of independent coefficients L_{ik} by having

$$L_{ik}\ (\underline{B},\underline{\Omega}) = l_i l_k L_{ki}\ (-\underline{B},-\underline{\Omega})$$

where l_i, l_k are parity values + 1 or -1, $\underline{B}$ the magnetic field and $\underline{\Omega}$ the rotation. Woods (1975) does not consider rotation $\underline{\Omega}$ to affect the intrinsic state and considers

$$L_{ik}\ (\underline{B}) = l_i l_k L_{ki}\ (-\underline{B}) \text{ only.}$$

The condition for no current in a liquid metal system is that the (i) temperature T (ii) potential $\phi = \phi_e + \zeta_o$ (with ϕ_e the electrical potential and ζ_o the chemical potential) and (iii) magnetic flux linkage in the bulk of the fluid, are all constant throughout the system.

Therefore, consider first a stationary nonuniformly heated isotropic system in the absence of magnetic field where both the current density, $\underline{j}$, and the temperature gradient (grad T) are non-zero.

The amount of heat evolved per unit time per unit volume

$$Q = -\text{div } \underline{q} \text{ where } \underline{q} \text{ is the total energy flux} \qquad (3.11)$$

Rate of change of entropy in volume V

$$\frac{dS}{dt} = -\int \frac{\text{div } \underline{q}}{T} dV = \int \frac{\underline{E}}{T} . \underline{j} dV - \int \{ \frac{(\underline{q} - \phi \underline{j})}{T^2} . \text{grad } T \} dV$$

where $\underline{E} = -\text{grad } \phi$ and $\text{div} \underline{j} = 0$ have been used (with $\frac{\partial B}{\partial t} = 0$).

Comparison with equation (3.10) shows that the current density, $\underline{j}$, and the purely thermal energy flux $(\underline{q} - \phi \underline{j})$ have affine force fields $\frac{\underline{E}}{T}$ and $\frac{-\text{grad } T}{T^2}$ respectively.

It can be easily shown that

$$\underline{j} = \sigma(\underline{E} - \alpha \text{ grad } T) \qquad (3.12)$$

and

$$\underline{q} = (\phi + \alpha T)\underline{j} - \kappa \text{ grad } T \qquad (3.13)$$

with $L_{11} = \sigma T$, $L_{12} = L_{21} = \sigma \alpha T^2$, $L_{22} + \frac{L_{12} L_{21}}{L_{11}} = \kappa T^2$

where σ and κ are the isothermal electrical and thermal (at zero current) conductivity respectively and α is the absolute thermoelectric power of the medium. In the case when the medium is anisotropic, the coefficients are tensors of rank two.

In a stationary medium of uniform composition when the electric field is irrotational (i.e. $\frac{\partial B}{\partial t} = 0$) no current flow takes place whatever the T distribution. Therefore α must be a function of T alone, giving (α grad T) irrotational or (grad α) x (grad T) zero. In such a case (α grad T) can be replaced by grad ϕ_α where ϕ_α is a function of T only. Then (3.12) can be written as

$$\frac{\underline{j}}{\sigma} = -\text{grad } \phi - \text{grad } \phi_\alpha = -\text{grad } \phi^+ \qquad (3.14)$$

When the composition of the stationary medium varies, α grad T can become rotational as grad α need no longer be parallel to grad T. A special case is when T varies along the interface of two dissimilar metal systems, each having its own definite composition. Only at the interface grad α is not parallel to grad T, α varying across the interface and T along the interface. Therefore, as long as the composition of the liquid remains the same, irrespective of the T distribution

inside, the thermoelectric potential difference is determined by the temperature distribution along the interface with the dissimilar metal liner only.

For two different metal systems, a and b, connected as shown in Figure 3.1, with the interfaces S_1 and S_2 maintained at T_1 and T_2 respectively and S_{b_1} S_{b_2} at a common temperature, $\underline{j} = 0$:

$$\text{Seebeck e.m.f.} = \phi_{\alpha_{b_1 b_2}} = -\int_{S_{b_2}}^{S_{b_1}} \underline{E}.d\underline{s} = -\int_{S_{b_1}}^{S_{b_2}} \alpha \,\text{grad}\, T \, d\underline{s}$$

$$= -\int_{T_1}^{T_2} \alpha_a dT - \int_{T_2}^{T_1} \alpha_b dT = \int_{T_1}^{T_2} (\alpha_b - \alpha_a) dT \qquad (3.15)$$

From (3.11) and 3.13)

$$Q = -\text{div}\, \underline{q} = \text{div}\, (\kappa \,\text{grad}\, T) + \frac{\underline{j}\underline{j}}{\sigma} - T\underline{j}.\text{grad}\, \alpha \qquad (3.16)$$

The first two terms are easily recognised as the heat conduction and the joule heat term respectively.

The third term

$$-T\underline{j}.(\text{grad}\, \alpha) = -T\underline{j}.\left(\frac{\partial \alpha}{\partial T}\right)\text{grad}\, T = -\left(T\frac{\partial \alpha}{\partial T}\right)\underline{j}.\text{grad}\, T \qquad (3.17)$$

is the heat rate absorbed or evolved along the current path according to whether $T\frac{\partial \alpha}{\partial T}$ is positive or negative. This is the "Thomson heat".

At the junctions S_1 or S_2 the normal components of $\underline{q}$ are the same, giving amount of heat rate per unit area and time generated or absorbed at the interface

$$= \left[-\kappa \frac{\partial T}{\partial n}\right]_a^b = -j_n T(\alpha_b - \alpha_a) \equiv -jT(\alpha_b - \alpha_a) \qquad (3.18)$$

where n is the normal to the interface and $j_n \equiv j$, is the Peltier heat.

For isotropic stationary liquid metal systems in the presence of a weak magnetic field, it can be shown that (3.12) and (3.13) are replaced by

$$\underline{E} = \frac{\underline{j}}{\sigma} + \alpha \,\text{grad}\, T + R_H \frac{\underline{B} \times \underline{j}}{\mu} + N_H \frac{\underline{B} \times \text{grad}\, T}{\mu} \qquad (3.19)$$

$$\underline{q} - \phi \underline{j} = \alpha T \underline{j} - \kappa \,\text{grad}\, T + N_H T \frac{\underline{B} \times \underline{j}}{\mu} + L_H \frac{\underline{B} \times \text{grad}\, T}{\mu} \qquad (3.20)$$

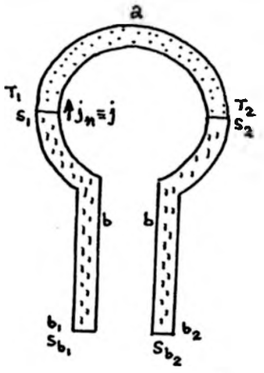

Figure 3.1
A simple thermoelectric circuit constructed from the two metal elements a and b. Ends b_1 and b_2 are maintained at the same temperature.

Figure 3.2 The co-ordinate systems

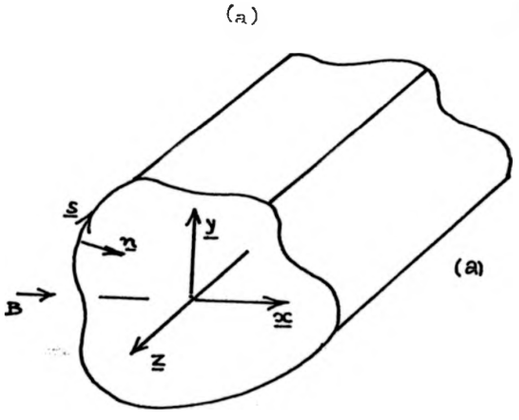

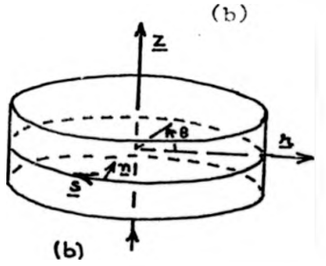

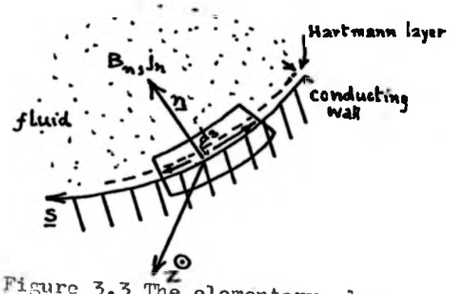

Figure 3.3 The elementary loop around a small segment of the solid-liquid interface.

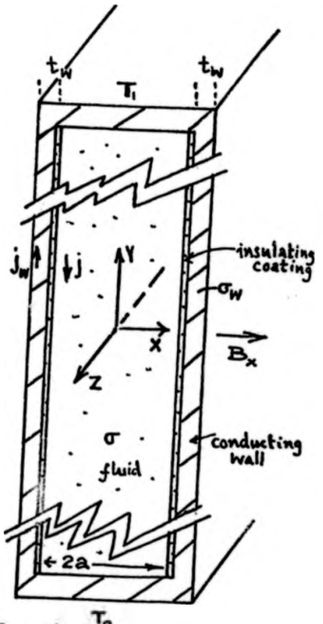

Figure 3.4 The simple configuration of the large aspect ratio channel for the preliminary TEMHD analysis.

For the analysis that follows in later chapters, it is tacitly assumed that R_H, the Hall coefficient, N_H the Nernst coefficient and L_H, the Ettinghausen coefficient are much smaller than α and κ so that the simple relationships of (3.12) and (3.13) are retained. Ion slip has been ignored as well. Also assumed inherently is that σ, α and κ are all scalar.

The relationship (3.12) can easily be extended to moving liquid systems, nonuniformly heated in a magnetic field $\underline{B}$ as

$$\underline{E} + \underline{V} \times \underline{B} = \frac{\underline{j}}{\sigma} + \alpha \text{ grad } T$$

$$\text{or} \quad \frac{\underline{j}}{\sigma} = \underline{E} - \alpha \text{ grad } T + \underline{V} \times \underline{B} \qquad (3.21)$$

$$= -\text{grad } \phi^{+} + \underline{V} \times \underline{B} \qquad (3.22)$$

This is the TEMHD counterpart of Ohm's law in magnetohydrodynamics.

The entropy equation is modified as

$$\rho T \frac{Ds_e}{Dt} = Q + Q_V + Q_N \qquad (3.23)$$

where Q_V = viscous energy dissipation (Chandrasekhar, 1961)

and Q_N = heat generation by nuclear reaction, per unit volume and time.

In liquid metal

$\rho T ds_e \underset{\sim}{=} \rho C_V dT$ where C_V is the volumetric heat capacity $\underset{\sim}{=} C_p$

Then

$$\rho C_V \frac{DT}{Dt} = Q + Q_V + Q_N \qquad (3.24)$$

3.2.3 The nondimensional parameters

Let the characteristic length be L_o, the characteristic velocity V - a measure of the mean velocity of flow - and the uniform steady magnetic flux density be B. Let the physical properties of the fluid at $T_o^{\circ}K$ be given by σ - the electrical conductivity, η_v - the dynamic viscosity, κ - the thermal conductivity and ρ - the density. Then, as defined in Chapter 2

Hartmann number $M = \left(\sqrt{\frac{\sigma}{\eta_v}}\right) BL_o$, Reynolds number $Re = \frac{\rho V L_o}{\eta_v} = \frac{VL_o}{\nu}$

Interaction parameter $N = \frac{\sigma B^2 L_o}{\rho V} = \frac{M^2}{Re}$, Magnetic Reynolds number

$$R_m = \frac{VL_o}{\frac{1}{\mu\sigma}} = \mu\sigma V L_o$$

Fluid to Wall conductivity ratio $C = \frac{L_o \sigma}{t_w \alpha_w}$ Aspect Ratio $L^* = \frac{L_b}{L_h}$

ratio of characteristic breadth to height

Rayleigh number $Ra = \frac{g\beta(\Delta T) L_o^3}{\chi\nu}$ Dean number $= (\sqrt{\frac{L_o}{R}}) Re$

Prandtl number $P_r = \frac{\nu}{\chi}$ Peclet number $= \frac{VL_o}{\chi}$ (3.25)

where β, g, ν, $\chi (= \frac{\kappa}{\rho C_p})$, $\eta = \frac{1}{\mu\sigma}$ are the coefficient of thermal volume expansion, the acceleration due to gravity, the kinematic viscosity (momentum diffusivity), the thermometric diffusity and the magnetic diffusivity respectively. R is the radius of curvature for Walls in curved channels, t_w and σ_w are the thickness and electrical conductivity of duct wall respectively.

3.2.4 The co-ordinate system

Although in some cases, as in the planar nonuniform magnetic field system with $R_m << 1$, it is advantageous to consider the co-ordinate system described by the orthogonal curvilinear co-ordinates along the constant vector and scalar potentials (Holroyd 1975; Kulikovskii, 1968), the conventional Cartesian and polar co-ordinate systems are adequate for the analysis of the systems considered in this thesis.

For the straight channels, x (= r cos θ) is taken as the direction of the impressed horizontal uniform steady magnetic field, y (= r sin θ) the direction of applied temperature gradient and z the direction of flow. In the case of the annular channel in a vertical magnetic field, z is taken along the field direction, which is the axis of symmetry; with a radial temperature gradient the flow is in the azimuthal (θ) direction. The solid-liquid interface at the channel wall is described by the peripheral co-ordinate s (clockwise) and the normal to the interface by the co-ordinate n (Figure 3.2 a, b).

3.2.5 The boundary conditions

Most of the boundary conditions as in magnetohydrodynamic duct flow with $R_m << 1$ (Hunt and Shercliff, 1971) and in ordinary heat transfer problems hold in the TEMHD case.

At a solid-liquid interface, the velocity is continuous. More specifically at a stationary wall $V_n = 0$. At the free fluid surface the viscous shear stress and the normal gradient of tangential velocity are zero.

With div $\underline{B} = 0$, $[\underline{B}.\underline{n}] = 0$, the square bracket meaning the change across the interface.

The current content of Hartmann layers is discussed in detail in Shercliff (1976) for a non-isothermal, non uniform fluid system. The relevant TEMHD correspondence is that in the Hartmann layers adjoining electrically non-conducting stationary walls, following Hide and Roberts (1962), $j_n = \pm \sqrt{\sigma\eta_v}\ (\text{curl}\ \underline{v})_n$ (3.25)

Also, at a thermally insulated wall

$$\frac{\partial T}{\partial n} = 0 \qquad (3.27)$$

The important difference in the TEMHD case is that along the conducting wall interface with the fluid, $\Delta\phi^+$, the potential difference is not necessarily zero. To simplify matters, let only homogeneous fluid systems be considered, so that $\Delta(\phi^+-\phi)$, thermoelectric potentials appear only through boundary conditions at the interface of the fluid and the dissimilar metal duct wall of the non-isothermal system. Let the fluid move over a stationary conducting wall in the presence of a magnetic field having a component B_n, as shown in Figure 3.3. Equation (3.21) may be integrated around the narrow loop surrounding an elementary length ds of the interface. Viscosity requires the velocity to be strictly zero at the interface, but when the Hartmann number M based on B_n is large, the Hartmann layer is so thin that it may

be taken to lie wholly within the loop, so that non-zero tangential velocity persist virtually up to the wall. Let v_z be the velocity normal to $\underline{s}$ and $\underline{n}$. Neglecting the contribution due to $\underline{E}$ (a second order small quantity)

$$\frac{j_{sw}}{\sigma_w} - \frac{j_s}{\sigma} + \frac{\partial}{\partial s}(\rho_c j_n) + v_z B_n = \alpha_{wf}\frac{\partial T}{\partial S} = \alpha\frac{\partial T}{\partial S} \qquad (3.28)$$

where suffixes s and n denote the peripheral and normal components in the plane of Figure 3.3, ρ_c is the contact resistance per unit area of the interface and $\alpha = \alpha_{wf} = \alpha_f - \alpha_w$, α_f and α_w being the absolute thermoelectric power of the fluid and the wall material respectively. It is tacitly assumed that there is no temperature gradient in the tangential direction z. Assuming $\rho_c = 0$,

$$\frac{j_{sw}}{\sigma_w} - \frac{j_s}{\sigma} + v_z B_n = \alpha\frac{\partial T}{\partial S} \qquad (3.29)$$

Equation (3.28) is given in Shercliff (1979a) and (3.29) in Shercliff, Dutta Gupta and Ality (1978).

The boundary condition for heat transfer at the interface of a conducting wall is altered to modify temperature gradients normal to the interface. Ignoring thermal contact resistance, across the Hartmann layers along the interface

$$\int \frac{j_{sw}^2}{\sigma_w} dn + - \kappa_w \frac{\partial T_w}{\partial n} + \alpha_w T j_n = \int \frac{j_s^2}{\sigma} dn - \kappa\frac{\partial T}{\partial n} + \alpha T j_n + \rho_c j_n^2 + \int \eta_v \left(\frac{\partial v_z}{\partial n}\right)^2 dn \qquad (3.30)$$

It is seen that the joule and viscous dissipation along with the Peltier heat absorption or generation would modify the ordinary heat transfer normal temperature gradient relationship of

$$\kappa_w \frac{\partial T_w}{\partial n} = \kappa \frac{\partial T}{\partial n} \qquad (3.31)$$

3.2.6 Order of magnitude of TEMHD effects with lithium

Consider Li and Pt or Pd in Table 1 in the Appendix as a suitable liquid metal-solid combination to demonstrate how significant TEMHD effects can be:

$$\alpha \simeq O(50\ \mu v/^{o}_{K})$$

With a temperature gradient of $\frac{\partial T}{\partial S} = 2000\ ^{o}K/m$ and a transverse magnetic field of 1 Tesla, for free flow without pressure gradient e.g. in an endless channel in uniform B, and $\underline{E} = 0$

$$|\underline{V}| \sim \frac{\alpha}{B} \frac{\partial T}{\partial S} \sim 0.10\ m/sec$$

For 10 Tesla $|\underline{V}| \sim 0.01$ m/sec

Clearly the magnitude is a significant value.

With V = 0, i.e. the flow blocked and $\underline{E} = 0$, and assuming perfect wall conductivity, $|\underline{j}| \sim 0.22 \times 10^{6} \frac{ampere}{m^{2}}$

Therefore, $\frac{\partial p}{\partial z} \sim 0.22 \times 10^{6}\ N/m^{3}$ for B = 1 Tesla

or $2.2 \times 10^{6}\ N/m^{3}$ for B = 10 Tesla.

For a meter length $\Delta p \sim 0.22 \times 10^{6}\ N/m^{2}$ ($\sim$ 32 psi) for B = 1 Tesla

$\sim 2.2 \times 10^{6}\ N/m^{2}$ ($\sim$ 320 psi) for B = 10 Tesla.

Order of magnitude of heat conduction per square meter

$$\kappa \frac{\partial T}{\partial S} \sim 0.10\ Mw/m^{2}$$

Order of magnitude of joule heating per unit volume in the fluid when there i no flow

$\frac{|\underline{j}|^{2}}{\sigma} \sim 0.022\ Mw/m^{2}$, an order of magnitude less than $\kappa \frac{\partial T}{\partial S}$.

Order of magnitude of Peltier heat absorption with $|V| = 0$

$\alpha T|\underline{j}| \sim 0.015\ Mw/m^{2}$ with $T \sim 1350^{o}$ K, a rather high value choice in practical terms.

Order of magnitude of Thomson's heat rate with V = 0

$|\underline{j}|T \frac{\partial \alpha}{\partial T} \frac{\partial T}{\partial S} \sim 0.009\ Mw/m^{2}$ with $T \sim 1350^{o}$, $\frac{\partial \alpha}{\partial T} \simeq 16 \times 10^{-9}\ \mu V/^{o}K^{2}$

When the flow is not blocked, j, and consequently the Peltier and Thomson heat, would be still smaller.

It is therefore reasonable to ignore the Peltier and Thomson heat rate and even the joule heating in comparison with heat conduction.

With good wetting, ρ_c should be very small, so that joule heating in contact resistance is negligibly small, with $\eta_v = 4.5 \times 10^{-4} \frac{Kg}{m\,sec}$ - viscous dissipation $\simeq \eta(\frac{\partial v}{\partial o})^2 \simeq \frac{8w}{m^2}$.

Therefore, considering the relative order of magnitude, equations (3.24) and (3.30) may be simplified to

$$\rho c_v \frac{DT}{Dt} = \text{div (K grad T)} + \frac{j.j}{\sigma} \tag{3.31}$$

and

$$K_w \frac{\partial T_w}{\partial n} = K \frac{\partial T}{\partial n} \tag{3.32}$$

As a consequence, apart from affecting heat transport by convection, the effect of TEMHD effect on heat transfer is ignored and the mutual coupling of the temperature and magneto-hydrodynamic field is greatly simplified.

Next consider the buoyancy force in relation to TEMHD force when there is no flow.

Buoyancy force per unit volume with adverse temperature gradient $\simeq \rho g \beta \Delta T \simeq 6.6\ N/m^3$ with $\Delta T \simeq 1000^o$ K, a high value.

Corresponding TEMHD force per unit volume

$\simeq jB \simeq 2.2\ N/m^3$ at B = 10 Tesla.

It is therefore necessary to consider a stably stratified fluid as otherwise buoyancy force effect would be important, if not dominant, in relation to TEMHD effect. This buoyancy effect is measured either in terms of Ra or $(Ra/Pr) = Gr$.

3.3 Some Preliminary Analysis

3.3.1 Modified Hartmann problem

Consider a simple problem of TEMHD in a slim (x direction) but infinitely long (y direction) rectangular channel, as shown in Figure 3.4. Basically it is a channel with conducting walls, but the side walls are coated, to justify the assumptions involved, with thermally and electrically insulating material at the solid-liquid interface. The magnetic field B_x is perpendicular to the sidewalls, while the top wall and the bottom walls are maintained at T_1° K and T_2° K respectively. Let $T_1 > T_2$, so that the fluid is stably stratified. The conducting sidewalls have thickness t_w, conductivity σ_w and the channel bore width is 2a. Ignoring variations of σ, η_v and ρ from (3.4) for fully developed flow in the z direction

$$\eta_v \frac{d^2 v_z}{dx^2} = j_y B_x + \frac{dp}{dz}$$

or

$$\eta_v \frac{d^2 v}{dx^2} = jB + \frac{dp}{dz} \quad ; \quad v \equiv v_z \quad j_y \equiv j \tag{3.33}$$

In the fluid

$$j = \sigma\left(B\, v - \frac{\alpha \Delta T}{h} - \frac{jw}{\sigma_w}\right) \tag{3.34}$$

where h is the height of the channel >> 2a and $\Delta T = T_1 - T_2$.

From current continuity

$$2t_w j_w = \int_{-a}^{a} j\,dx \tag{3.35}$$

From (3.33), (3.34) and (3.35)

$$v = \frac{M}{M + C \tanh M}\left\{\frac{\alpha \Delta T}{Bh} - \frac{1 + C}{\sigma B^2}\frac{dp}{dz}\right\}\left(1 - \frac{\cosh \frac{Mx}{a}}{\cosh M}\right) \tag{3.36a}$$

where $c = \frac{a\sigma}{t_w \sigma_w}$ and $M = Ba\sqrt{\frac{\sigma}{\eta_v}}$

The mean velocity is given by

$$V = \frac{M - \tanh M}{M + C \tanh M}\left\{\frac{\alpha \Delta T}{Bh} - \frac{1 + c}{\sigma B^2}\frac{dp}{dz}\right\} \tag{3.36b}$$

and $j = -\frac{1}{B}\frac{dp}{dz} - \frac{\sigma BVM}{M-\tanh M}\frac{\cosh Mx/a}{\cosh M}$

$$= \frac{\sigma B}{1+c}\left(\frac{M + c\tanh M}{M - \tanh M}V - \frac{\alpha\Delta T}{Bh}\right) - \frac{\sigma BVM}{M-\tanh M}\frac{\cosh Mx/a}{\cosh M} \qquad (3.37)$$

Compare this with the solution given by Professor Shercliff in (Shercliff, Dutta Gupta and Alty, 1978) and (Shercliff, 1979a) for the case where the insulating layers from the inside surface of the side walls are removed in Figure 3.4. Now it is necessary to assume $\frac{dT}{dy}$ constant to keep the problem simple. Following Professor Shercliff's analysis

From (3.22) $\quad j = \sigma Bv - \frac{d\phi^+}{dy} = \sigma Bv + j_s$ say $\qquad (3.38)$

From (3.4) $\quad \eta\frac{d^2v}{dx^2} - \sigma B^2 v = Bj_s + \frac{dp}{dz} \qquad (3.39)$

Therefore $v = -\frac{1}{\sigma B^2}\left(Bj_s + \frac{dp}{dz}\left(1 - \frac{\cosh Mx/a}{\cosh M}\right)\right)$ with

$$V = -\frac{1}{\sigma B^2}\left(Bj_s + \frac{dp}{dz}\right)\left(1 - \frac{\tanh M}{M}\right) \qquad (3.40a,b)$$

From (3.29) with $v = 0$ at the wall

$$\frac{j_w}{\sigma_w} - \frac{j_s}{\sigma} = \alpha\frac{dT}{dy} \qquad (3.41)$$

Current conservation gives

$$\sigma BV + j_s = \frac{-t_w}{a} j_w \qquad (3.42)$$

From (3.40b), (3.41) and (3.42)

$$V = \frac{M-\tanh M}{M + C\tanh M}\left\{\frac{\alpha}{B}\frac{dT}{dy} - \frac{1+c}{\sigma B^2}\frac{dp}{dz}\right\} \qquad (3.43a)$$

The analysis can be extended to show that

$$v = \frac{M}{M + c\tanh M}\left\{\frac{\alpha}{B}\frac{dT}{dy} - \frac{1+c}{\sigma B^2}\frac{dp}{dz}\right\}\left(1 - \frac{\cosh Mx/a}{\cosh M}\right) \qquad (3.43b)$$

Thus two cases have identical velocity profiles though basically the structures of the channels are different. In Professor Shercliff's case, heating should be done in such a way that $\frac{dT}{dy}$ remains constant y-wise but no such restriction is necessary in the insulated sidewall case.

and $j = -\frac{1}{B}\frac{dp}{dz} - \frac{\sigma BVM}{M-\tanh M}\frac{\cosh Mx/a}{\cosh M}$

$$= \frac{\sigma B}{1+c}\left(\frac{M + c\tanh M}{M - \tanh M}V - \frac{\alpha\Delta T}{Bh}\right) - \frac{\sigma BVM}{M-\tanh M}\frac{\cosh Mx/a}{\cosh M} \qquad (3.37)$$

Compare this with the solution given by Professor Shercliff in (Shercliff, Dutta Gupta and Alty, 1978) and (Shercliff, 1979a) for the case where the insulating layers from the inside surface of the side walls are removed in Figure 3.4. Now it is necessary to assume $\frac{dT}{dy}$ constant to keep the problem simple. Following Professor Shercliff's analysis

From (3.22) $\quad j = \sigma Bv - \frac{d\phi^+}{dy} = \sigma Bv + j_s$ say $\qquad (3.38)$

From (3.4) $\quad \eta_v \frac{d^2v}{dx^2} - \sigma B^2 v = Bj_s + \frac{dp}{dz} \qquad (3.39)$

Therefore $v = -\frac{1}{\sigma B^2}(Bj_s + \frac{dp}{dz}(1 - \frac{\cosh Mx/a}{\cosh M})$ with

$$V = -\frac{1}{\sigma B^2}(Bj_s + \frac{dp}{dz})\left(1 - \frac{\tanh M}{M}\right) \qquad (3.40a,b)$$

From (3.29) with $v = 0$ at the wall

$$\frac{j_w}{\sigma_w} - \frac{j_s}{\sigma} = \alpha\frac{dT}{dy} \qquad (3.41)$$

Current conservation gives

$$\sigma BV + j_s = \frac{-t_w}{a} j_w \qquad (3.42)$$

From (3.40b), (3.41) and (3.42)

$$V = \frac{M-\tanh M}{M + C\tanh M}\left\{\frac{\alpha}{B}\frac{dT}{dy} - \frac{1+c}{\sigma B^2}\frac{dp}{dz}\right\} \qquad (3.43a)$$

The analysis can be extended to show that

$$v = \frac{M}{M + c\tanh M}\left\{\frac{\alpha}{B}\frac{dT}{dy} - \frac{1+c}{\sigma B^2}\frac{dp}{dz}\right\}\left(1 - \frac{\cosh Mx/a}{\cosh M}\right) \qquad (3.43b)$$

Thus two cases have identical velocity profiles though basically the structures of the channels are different. In Professor Shercliff's case, heating should be done in such a way that $\frac{dT}{dy}$ remains constant y-wise but no such restriction is necessary in the insulated sidewall case.

When the fluid is prevented from flowing

$$\frac{dp}{dz} = \frac{\sigma B\alpha}{1 + c} \frac{dT}{dy} = \frac{\sigma B\alpha}{1 + c} \frac{\Delta T}{h} \qquad (3.44)$$

which gives a new method of measuring α in a transverse magnetic field by noting the pressure gradient developed, increasing directly proportional to B.

When $\frac{dp}{dz} = 0$ $\quad V = a\alpha \frac{\sqrt{\sigma}}{\sqrt{\eta_v}} \frac{dT}{dy} F(M)$ with $F(M) = \frac{M - \tanh M}{M(M + c \tanh M)}$ (3.45)

The variation of the function F(M) with M and C is given by Shercliff (1979) and is shown in Figure 3.5. It may be noted that at low M (weak B) the mean velocity V is directly proportional to M but after a critical value of M depending on C, the mean velocity has an inverse relationship with M (strong B). It is explained from the point of view that, while the driving force is proportional to B, the restraining viscous force is independent of B at weak B, whereas the drag is proportional to B^2 at strong B (viscous and magnetic force balance).

For high Hartmann number M

$$V \to \frac{a\alpha \left(\sqrt{\frac{\sigma}{\eta_v}}\right)}{M + c} \frac{dT}{dy} \qquad (3.46)$$

restricted by the conductance of the side wall and the Hartmann layers in the fluid. As $C \to 0$, the maximum V is attained, for a given M.

It is important to note in (3.46) that the condition $C \to 0$ is superfluous in the case where M is very large. Thus, in magnetically confined reactors with $M \gtrsim 10^4$, c of the order of 10 or 100 has very little effect. A better conducting wall gives more TEMHD flow, which contrasts with reduced flow in magnetohydrodynamics for a given $\frac{dp}{dz}$ and M.

Consider next the temperature distribution in the fluid of the channel of Figure 3.4. Assume no variation of T in the z direction. Therefore, in the steady situation there is no heat convection.

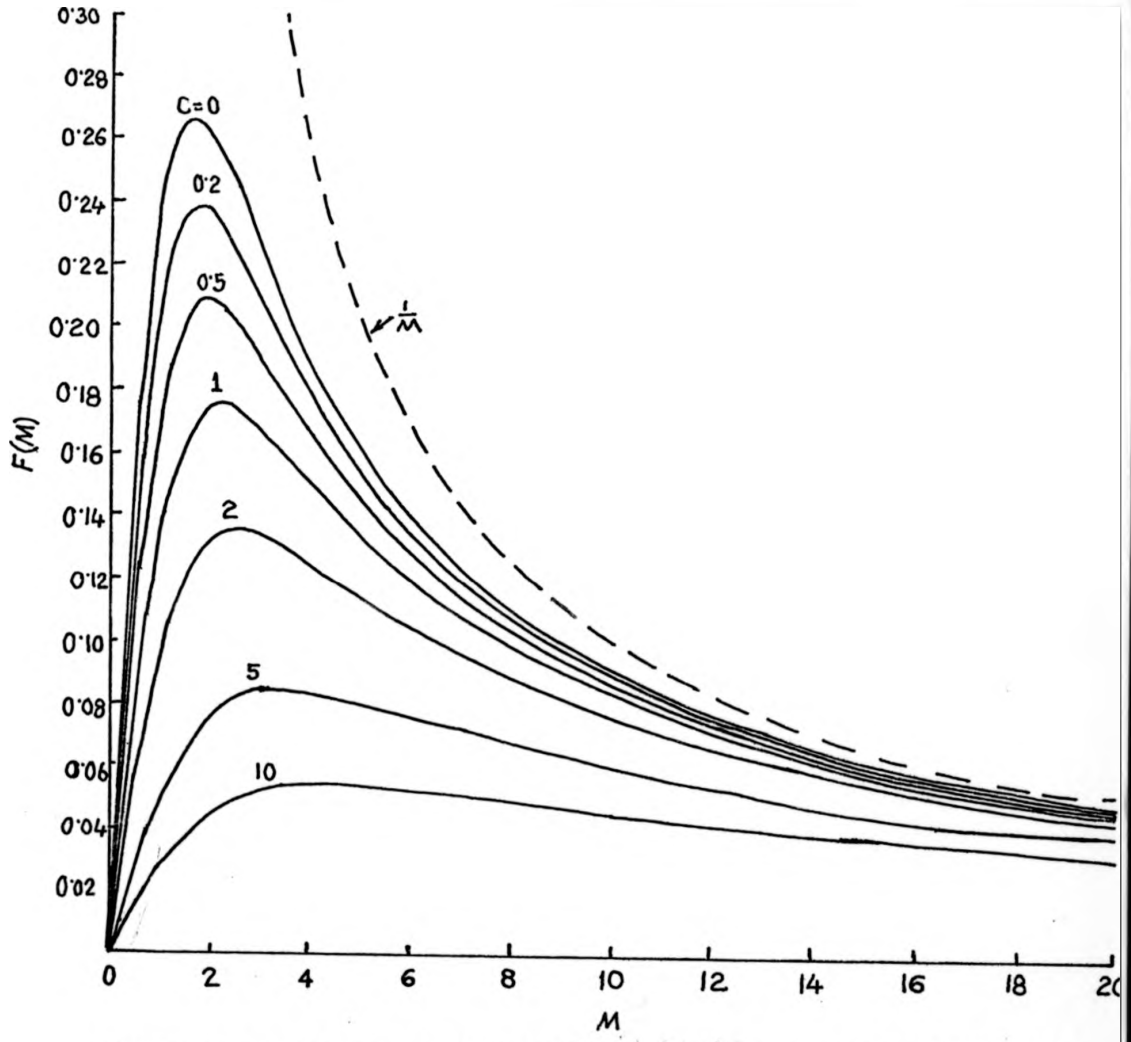

Figure 3.5 The function F(M).Variation with c and M (Shercliff 1979a).

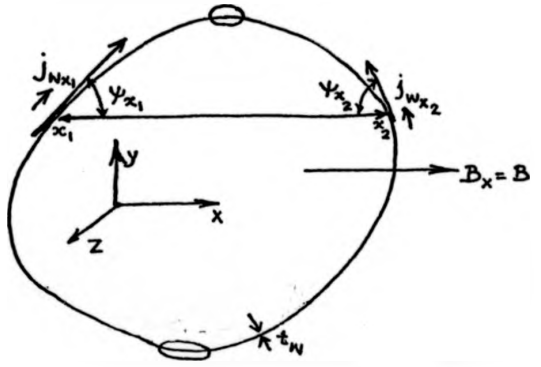

Figure 3.6 The conducting wall duct for two-dimensional MHD flow analysis.

Equation (3.24) gives with $Q_N = 0$

$$-K\left(\frac{\partial^2 T}{\partial y^2} + \frac{\partial^2 T}{\partial x^2}\right) = \frac{|j|^2}{\sigma} + \eta_v\left(\frac{\partial v}{\partial x}\right)^2 - jT\frac{\partial \alpha}{\partial T}\left(\frac{\partial T}{\partial y}\right) \qquad (3.47)$$

$$= \frac{\sigma B^2}{(1+c)^2}\left\{\frac{M + c\tanh M}{M - \tanh M} V - \frac{\alpha \Delta T}{hB}\right\}^2 - \frac{\sigma B^2}{1+c}\left(\frac{M + c\tanh M}{M - \tanh M} V - \frac{\alpha \Delta T}{hB}\right).$$

$$\frac{VM\cosh Mx/a}{(M-\tanh M)\cosh M}$$

$$+\frac{\sigma B^2 V^2 M^2}{(M-\tanh M)^2}\frac{\cosh 2Mx/a}{\cosh 2M}$$

$$-\left(\frac{\partial \alpha}{\partial T}\right)\left[\left\{\frac{M + c\tanh M}{M - \tanh M} V - \frac{\alpha \Delta T}{hB}\right\}\frac{\sigma B}{1+c} - \frac{\sigma BVM}{M - \tanh M}\frac{\cosh Mx/a}{\cosh M}\right] T\frac{\partial T}{\partial y}$$

In the case $V = 0$ and $\frac{\partial \alpha}{\partial T} = 0$

$$T = \left(\frac{T_1 + T_2}{2} - \frac{\Delta T}{h} y\right) + \frac{\sigma \alpha^2 (\Delta T)^2}{K(1+c)^2 h^2}\left(y^2 - \frac{h^2}{4}\right) \qquad (3.48)$$

3.3.2 Two dimensional TEMHD duct flow in transverse magnetic field

It has been remarked earlier that a transverse magnetic field helps the laminarisation of the fluid flow and the flow configuration tends to be two dimensional. Consider a fully developed flow in a conducting wall duct whose cross-section is shown in Figure 3.6 and extends in the z direction under the influence of an imposed uniform steady transverse magnetic field $B_x = B$ in the x direction. Following the analysis of Professor Shercliff (1979a), it is assumed that the conducting wall thickness t_w is uniform and thin, and that the fluid is in good electrical contact with the duct wall all along the interface, so that the contact resistance is negligible and the problem is greatly simplified. Since the flow is fully developed, there is no variation of flow parameters in the z direction except that of pressure p. A fully developed flow also implies that there is

Equation (3.24) gives with $Q_N = 0$

$$-K\left(\frac{\partial^2 T}{\partial y^2} + \frac{\partial^2 T}{\partial x^2}\right) = \frac{|j|^2}{\sigma} + \eta_v\left(\frac{\partial v}{\partial x}\right)^2 - jT\frac{\partial \alpha}{\partial T}\left(\frac{\partial T}{\partial y}\right) \qquad (3.47)$$

$$= \frac{\sigma B^2}{(1+c)^2}\left\{\frac{M + c\tanh M}{M - \tanh M} V - \frac{\alpha \Delta T}{hB}\right\}^2 - \frac{\sigma B^2}{1+c}\left(\frac{M + c\tanh M}{M - \tanh M} V - \frac{\alpha \Delta T}{hB}\right).$$

$$\frac{VM\cosh Mx/a}{(M-\tanh M)\cosh M}$$

$$+ \frac{\sigma B^2 V^2 M^2}{(M-\tanh M)^2}\frac{\cosh^2 Mx/a}{\cosh^2 M}$$

$$-\left(\frac{\partial \alpha}{\partial T}\right)\left[\left\{\frac{M + c\tanh M}{M - \tanh M} V - \frac{\alpha \Delta T}{hB}\right\}\frac{\sigma B}{1+c} - \frac{\sigma BVM}{M - \tanh M}\frac{\cosh Mx/a}{\cosh M}\right] T\frac{\partial T}{\partial y}$$

In/case $V = 0$ and $\frac{\partial \alpha}{\partial T} = 0$ /the

$$T = \left(\frac{T_1 + T_2}{2} - \frac{\Delta T}{h} y\right) + \frac{\sigma \alpha^2 (\Delta T)^2}{K(1+c)^2 h^2}\left(y^2 - \frac{h^2}{4}\right) \qquad (3.48)$$

3.3.2 Two dimensional TEMHD duct flow in transverse magnetic field

It has been remarked earlier that a transverse magnetic field helps the laminarisation of the fluid flow and the flow configuration tends to be two dimensional. Consider a fully developed flow in a conducting wall duct whose cross-section is shown in Figure 3.6 and extends in the z direction under the influence of an imposed uniform steady transverse magnetic field $B_x = B$ in the x direction. Following the analysis of Professor Shercliff (1979a), it is assumed that the conducting wall thickness t_w is uniform and thin, and that the fluid is in good electrical contact with the duct wall all along the interface, so that the contact resistance is negligible and the problem is greatly simplified. Since the flow is fully developed, there is no variation of flow parameters in the z direction except that of pressure p. A fully developed flow also implies that there is

no heat convection in the z direction, and the wall peripheral temperature distribution is also the same in the z direction; $\underline{j}$ has no component j_z. Since the flow is laminar, except in the boundary layers of thickness $O(\frac{1}{\sqrt{M}})$ and probably $O(\frac{1}{M^{\frac{2}{3}}})$, the inviscid inertialess steady flow gives from (3.4)

$$-\text{grad}\, p + \underline{j} \times \underline{B} = 0 \quad \text{or} \quad -\frac{dp}{dz} - j_y B = 0 \tag{3.49}$$

with $\frac{dp}{dz}$ = constant, j_y = constant (3.50)

$\text{div}\underline{j} = 0$ gives $j_x = j_x(y)$, a function of y alone (3.51)

From (3.14) $$\sigma B \frac{\partial v}{\partial x} = -\frac{dj_x}{dy} = \sigma B \frac{v_{x_2}(y) - v_{x_2}(y)}{x_2(y) - x_1(y)} \tag{3.52}$$

Since the wall thickness t_w is very small, wall peripheral current density may be taken as the tangential component j_w. Current conservation in the y direction gives

$$t_w (j_{w_{x_1}} + j_{w_{x_2}}) + j_y (x_2 - x_1) = 0 \tag{3.53}$$

Also $$t_w \frac{dj_{w_{x_1}}}{dy} = j_x + j_y \cot \psi_{x_1}$$

and $$t_w \frac{dj_{w_{x_2}}}{dy} = j_x + j_y \cot \psi_{x_2} \tag{3.54}$$

Boundary condition (3.29) gives with $v_z = v$

$$\frac{j_{x_1}}{\sigma_w} + \frac{1}{\sigma}(j_x \cos\psi_{x_1} + j_y \sin\psi_{x_2}) + v_{x_1} B \sin\psi_{x_1} = \frac{\alpha(T_{x_1})\, dT_{x_1}}{dy} \tag{3.55}$$

$$\frac{j_{x_2}}{\sigma_w} + \frac{1}{\sigma}(-j_x \cos\psi_{x_2} + j_y \sin\psi_{x_2}) + v_{x_2} B \sin\psi_{x_2} = \alpha(T_{x_2}) \frac{dT_{x_2}}{dy} \tag{3.56}$$

From (3.52) and (3.55), (3.56)

$$\frac{1}{\sigma_w}\left\{\frac{j_{x_2}}{\sin\psi_{x_2}} - \frac{j_{x_1}}{\sin\psi_{x_1}}\right\} - \frac{d}{dy}\left(\frac{j_x}{\sigma}(x_2 - x_1)\right) = \alpha(T_{x_2})\frac{dT_{x_2}}{dy} - \alpha(T_{x_1})\frac{dT_{x_1}}{dy} \tag{3.57}$$

These results are used in Chapter 4.

For the analysis of Chapter 6 it is more convenient to have the imposed uniform steady vertical magnetic field B in the z direction. Then the curl of grad p = $\underline{j} \times \underline{B}$ gives

$$(\underline{B}.\nabla)\ \underline{j} = 0 \text{ or } B\frac{dj}{dz} = 0 \text{ or } \frac{dj}{dz} = 0 \qquad (3.58)$$

Therefore $\underline{j}$ is independent of z.

Since div $\underline{j} = 0$, there exists a stream function $H(r,\theta)$ such that

$$j_r = \frac{\partial H}{r\partial\theta} \quad \text{and} \quad j_\theta = \frac{-\partial H}{\partial r} \qquad (3.59)$$

From (3.14) and (3.59)

$$\sigma B\frac{\partial v_r}{\partial z} = \frac{\partial j_z}{r\partial\theta}, \quad \sigma B\frac{\partial v_\theta}{\partial z} = -\frac{\partial j_z}{\partial r} \qquad (3.60)$$

Also div $\underline{v} = 0$ gives

$$\begin{aligned}\frac{\partial v_z}{\partial z} &= -\frac{\partial v_r}{\partial r} - \frac{v_r}{r} - \frac{\partial v_\theta}{r\partial\theta} \\ &= -\frac{1}{r}\frac{\partial}{\partial r}(rv_r) - \frac{\partial v_\theta}{r\partial\theta} \qquad (3.61)\\ &= 0\end{aligned}$$

Therefore v_z is independent of z. Also v_r and v_θ can be expressed as

$$v_r = \frac{z}{\sigma B}\frac{\partial j_z}{r\partial\theta} = \frac{\partial\psi}{r\partial\theta}$$

$$v_\theta = \frac{-z}{\sigma B}\frac{\partial j_z}{\partial r} = -\frac{\partial\psi}{\partial r}$$

From (3.14)

$$j_r = -B\frac{\partial\psi}{\partial r} - \frac{\partial\phi^+}{\partial r} = -\frac{\partial}{\partial r}(B\psi + \phi^+)$$

$$j_\theta = -B\frac{\partial\psi}{r\partial\theta} - \frac{\partial\phi^+}{r\partial\theta} = -\frac{\partial}{r\partial\theta}(B\psi + \phi^+)$$

3.4 The Experimental System

3.4.1 The choice of the fluid and the duct wall metal

The choice of the fluid and the duct wall material for TEMHD essentially requires that the solid-liquid combination should have significant thermoelectric power and should not react chemically at temperatures at which it would be worked. It must have very small contact resistance. Keeping in mind the application in the TNR, Li and Nb would be an ideal choice. However, Hg was chosen as the working fluid for the laboratory experiments in TEMHD for the following reasons:-

(i) it is a liquid metal with its working range around room temperature so that cooling could be carried out by circulating water at room temperature (22% Na + 78% K eutectic solution is an exception m.p. -11° C)

(ii) Hg has been most extensively used for magnetohydrodynamic and heat transfer experiments; its properties are well established so that comparison of corresponding experiments could be done

(iii) the thermoelectric power α of Hg at 300° K is approximately $-5\ \mu V/^{\circ}K$. The magnitude of $\alpha_{Hg} < \alpha_{Li}$, but even with values of α_{Hg} TEMHD effects should be demonstrable. Hg is one of the elements with large α variation with temperature T. This fact does not fit into the simple theory of Ziman and the study of the thermoelectric property of Hg itself constitutes an interesting problem

(iv) there is no risk of fire or explosion as with Na or Li, and this permits open access

(v) Hg forms an amalgam with copper, which was chosen as the liner material, giving very low contact resistance.

Necessarily the choice was finally clinched because of the ready availability of the requisite amount of Hg and Cu in stock. The choice of Cu is also relevant from the point of view that Cu is one of the standard reference materials for thermoelectric power measurement around and above room temperature with

$$\alpha_{Cu} = 0.05 + 5.45 \times 10^{-3}\ T \quad \mu V/^{\circ}K \text{ for } 300 < T < 1300^{\circ}\ K$$

In contrast to the present day idea (ref. Hunt and Hancox, 1971) about Li coolant circulation ducts where low conductance walls are preferred, it is essential to have fairly large wall conductance, even with thin walls, for significant TEMHD effects, except in the special case when the motion induced e.m.f. just balances the Seebeck e.m.f. (ref. section 3.3). Cu has an electrical conducitivity approximately 60 times that of Hg.

Furthermore, stainless steel is not a good choice as Hg does not ordinarily wet it, giving considerable thermal and electrical contact resistance.

Though least hazardous amongst the liquid metals, Hg is toxic. Having had to heat it made it worse; even though the MHD laboratory has been designed to exhaust the vapour, medical checks on mercury absorption frequently indicated overdose exposure to Hg, resulting in interruption of experimental runs. The choice of Cu-Hg, both opaque substances, obviously ruled out the possibility of fluid-dynamic flow visualisation and optical measurement techniques in the interior of the fluid. In Chapter 6, experiments are described where an open surface is retained to make measurements at the surface as well as in the interior of the fluid, rather than rest icting measurements to the boundaries. Having an open surface of Hg in contact with Cu, copper being soluble in Hg to the extent of 0.003% by weight, resulted in contamination of Hg by oxide formation of Cu and Hg. The use of PVC tubes in the connecting circuits also affected the contamination of Hg and cleaning of Hg had to be carried out regularly.

In no way, however, did the choice of the Hg-Cu combination undermine the related study of Li-Nb systems, and the greater TEMHD effects in Li-Nb system should be predictable by simply scaling up the results of the Hg-Cu system.

3.4.2 The electromagnets and flux density measurements

For the TEMHD experiments with straight ducts, it is theoretically possible to maintain a stabilizing temperature gradient by heating the duct at the top and cooling it from the bottom so that convection due to buoyancy forces is avoided. Thus the thermo-electric current is in the vertical direction. Necessarily, the

corresponding transverse magnetic field for producing TEMHD effects has to be horizontal in such a case. The horizontal magnetic field was obtained in the iron cored 'Lintott' electromagnet 'I" originally used by Hunt (1967). The pole face area measures 1.524 x 0.229 m^2 (60" x 9") and the air gap between the pole pieces is 7.62 cm (3"). The pole faces have 2 mm deep dents 1.3 cm (½") in height at each vertical edge to accommodate stainless steel supporting plates for the electromagnet coils in flush with the pole faces in the central region. This effectively reduces the uniform zone in the air gap. The hollow copper coils of the magnet are energised by a 60 volt 1000 ampere d.c. generator whose output can be controlled by the exciter resistance adjustment. The coils are water cooled at the rate of 15 litres per minute. A pressure switch at the water inlet to the coils sets off an alarm in case the water flow rate drops below this rate. The tendency of the pole faces to move towards each other at higher exciting currents is prevented by adjustable height brass spacers, 2.54 cm diameter at the centre and 3.75 cm at the base, positioned over flat plates at the horizontal edge of the pole faces. The flux density in the air gap has been calibrated with a Cambridge fluxmeter with search coils and also by Hall effect magnetometers (HIRST GMI gaussmeter, HIRST II fluxmaster FM 7OA). Apart from the calibration checks with the stabilized permanent magnets, one of the Hall probe magnetometers (HIRST GMI gaussmeter) has been precalibrated in the range 0-2 Tesla by fixing the Hall probe on the pole face of the NMR magnet (Department of Physics, University of Warwick), and measuring its flux density. The comparison of the flux density is made with the calculated value arrived at through the measured resonant spectral frequency of ^2D lines (6.5366 m/Hz at 1 Tesla) of samples in a

Varian probe assembly accommodated in the air gap of the magnet to give high resolution nuclear magnetic resonance spectral analysis. A check with the NMR magnet gaussmeter was also made. The accuracy of the calibration was restricted by the smallest division that can be read on the Hall probe magnetometer scale, but this error is less than ½% at 1.2 Tesla. For the 'Lintott' electromagnet 'I', air gap flux density was calibrated by measuring the potential difference across a 1000 ampere 125 mV shunt connected in series with the magnet coil by a Weston millivoltmeter, and measuring the flux density. The calibrated $B\text{-}I_{exc}$ curve is shown in Figure 3.7a. The measurements were carried out for increasing and decreasing magnet coil current, and also by reversing the direction of the magnet current. No measurable hysterisis effect was observed, and the calibration agreed with that of Hunt (1967). At the final stage of experimentation, the bus bars (10 x 0.6 cm^2) had to be disconnected frequently so as to allow the MAGLEV group to use the d.c. power supply, and the air gap flux density was measured directly by the Hall effect magnetometers, though calibration was also checked.

Measurements revealed that the air gap flux density is uniform within ½% in the control space 1.15 x 0.18 m^2 over the pole face at 1.2 Tesla. The TEMHD section(i.e. where TEMHD interaction was effective) was restricted to 0.5 m,and with the entry length in PVC connecting tubes, the total length in the magnet was 0.9 m . The PVC connecting tubes were led out of the magnet air gap space vertically, and the plot of flux density variation with height from the horizontal centre line of the magnet pole face according to measurements is shown in Figure 3.8a.

Though the 'Lintott' electromagnet 'I' could be excited to 1.3 Tesla, the time stability requirement restricted the use of

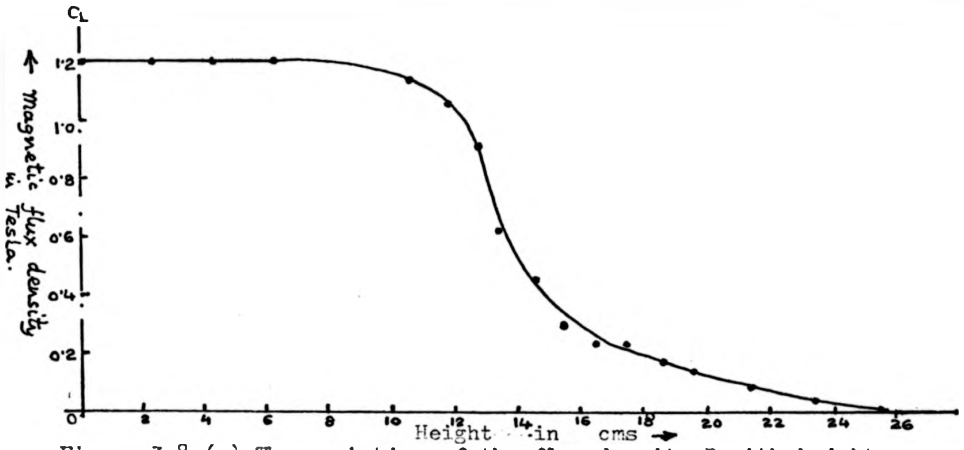

Figure 3.8 (a) The variation of the flux density B with height measured from the horizontal centre line of the Lintott electromagnet I air-gap

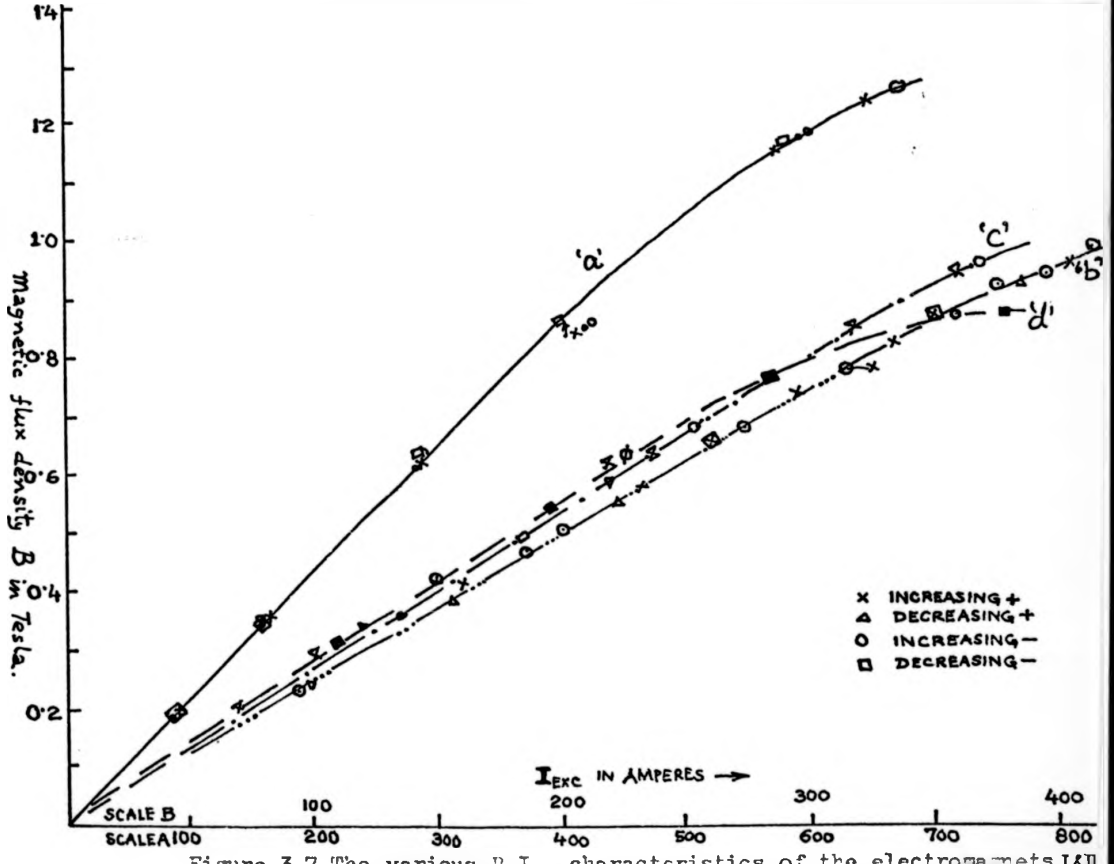

Figure 3.7 The various B-I_{exc} characteristics of the electromagnets I&II

(a) SCALE A (b)(c), (d) SCALE B.

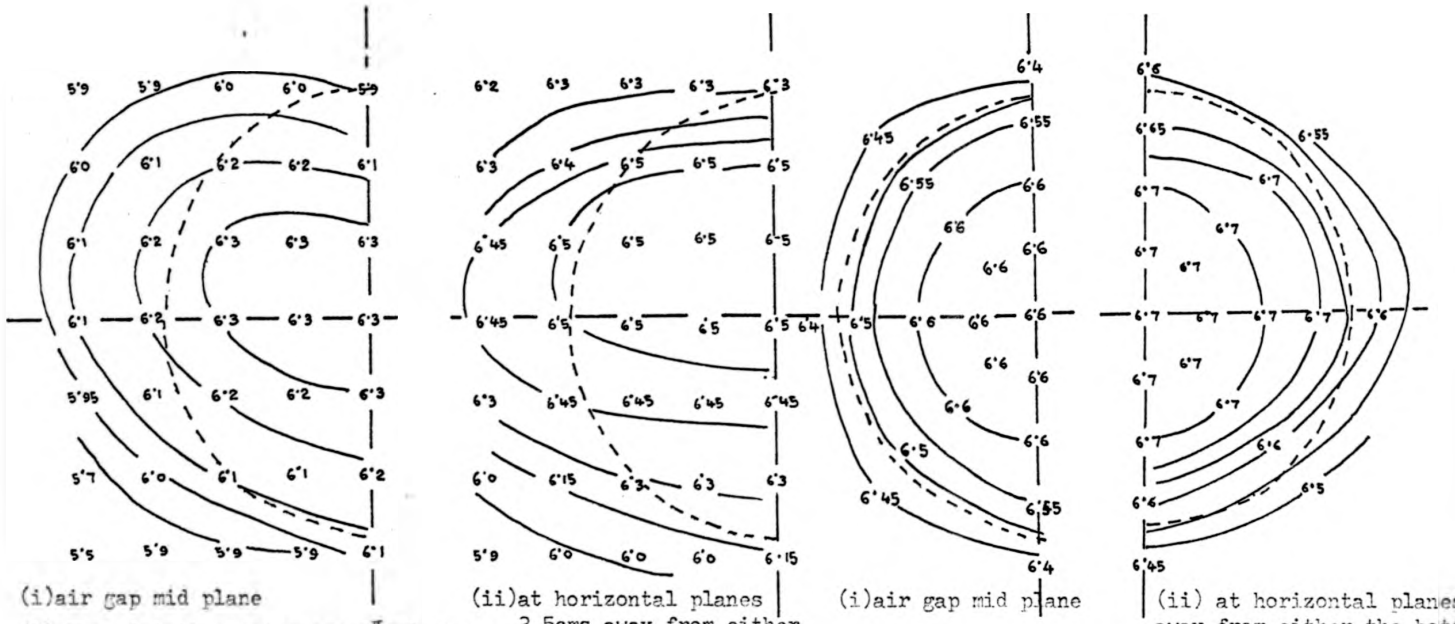

(i)air gap mid plane

(b) The Lintott electromagnet II poleface only.

(ii)at horizontal planes 2.5cms away from either the bottom or top pole face

(i)air gap mid plane

(ii) at horizontal planes 2.5 cms away from either the bottom or top pole face.

(c)With the addition of the circular plates, attached to the Lintott electromagnet II pole faces.

Figure 3.8(b),(c)The plots of B_z in KiloGauss in horizontal planes in the air gap of the Lintott electromagnet II without and with the extra pole face attachment. (Length scale 1: 2).

flux density to a maximum of 1.25 Tesla and a minimum of 0.01 Tesla over 0.5 hour periods. Over a period of 5 to 10 minutes, 1.3 Tesla could be maintained. The residual flux density is very small and never exceeded 0.001 Tesla.

For the TEMHD experiment in annular ducts, the choice was between two alternatives: (a) vertical stabilizing temperature gradient with corresponding radial (essentially non-uniform) magnetic field and (b) radial (in horizontal planes) temperature gradient giving buoyancy driven convection with a vertical uniform magnetic field. It is also possible to conceive an arrangement with an azimuthal circular magnetic field. Practical consideration, as described in Chapter 6, led to the choice of system (b). The Lintott electromagnet II, originally used by Fussey (1969) to provide a horizontal magnetic field, was adopted for the purpose by turning it through 90° to give a vertical field. The support structure (Figure 3.9) was designed to carry the 2-Ton. load, with the provision of adjustment to keep the pole faces exactly horizontal at eye level for convenience of visual observation. The pole faces measure 30.5 x 15.25 cm^2 (12" x 6") and the air gap between the pole faces 15 cm ($\sim$ 6"). The electromagnet has two hollow copper coils, each coil having 4 pancake sections. The coils are water-cooled, a minimum flow rate of 10 litres per minute is monitored by a pressure switch. The temperature of the outlet water is monitored by 8 thermocouples and a high temperature switch set at 70° C trips an indicator light and sets off an alarm bell. Relay contacts are available for automatic tripping of the generator, but have not been used. The electromagnet was excited by the 60 volts d.c. generator. Since the other generator (80 volts, 500 amp) originally associated with the magnet has not been installed, the maximum flux density obtainable was $\sim$ 0.9 Tesla instead of 1.1 Tesla. The use of the 80 volts d.c. generator was not considered

advantageous as it was self-excited only in the range of 400 to 500 amperes, while TEMHD effects were more easily obtained at lower field strengths. The calibration of a B-I_{exc} curve on similar lines to those described for the 'Lintott' electromagnet I is shown in Figure 3.7b, magnet current being measured across a 500 ampere 100 mV/(0·2 mΩ) shunt in series with the magnet coil. Even with the bevelled edges around the nominal pole face area of 0 (30 x 15 cm^2) the uniformity of the flux density as measured at the midplane between the pole faces and at other parallel planes varied as much as 8%. Two mild steel circular plates of 23 cm diameter and 0.5 cm thickness were used in the central region to improve the uniformity of the vertical magnetic field. The field maps of B_z for the magnet and with the additional mild steel plates at three different horizontal planes are shown in Figure 3.8b, c. The uniformity improved to a variation of maximum 1% of B_z. With the attached steel plates at 0.66 Tesla, the magnetic field in the θ and the radial direction was less than 0.5% and 1% of B_z respectively. The calibration of the magnetisation characteristic with the circular plates is shown in Figure 3.7c.

To observe the effect of slightly inclined magnetic field with respect to the vertical, two tapered mild steel plates with a slope of 0.04 and thickness at the centre of 0.6 cm were used. The B-I_{exc} calibration curve is shown in Figure 3.7d.

To protect the aluminium guard plates of the magnet coil from spilled mercury, the upper surface of the aluminium plate was coated with gloss paint. The space between the central slot in the guard plate and the pole face was filled with plasticine and a ring of plasticine around the outer periphery of the guard plate was erected to arrest any spilled mercury.

advantageous as it was self-excited only in the range of 400 to 500 amperes, while TEMHD effects were more easily obtained at lower field strengths. The calibration of a B-I_{exc} curve on similar lines to those described for the 'Lintott' electromagnet I is shown in Figure 3.7b, magnet current being measured across a 500 ampere 100 mV/(0.2 mΩ) shunt in series with the magnet coil. Even with the bevelled edges around the nominal pole face area of 0 (30 x 15 cm^2) the uniformity of the flux density as measured at the midplane between the pole faces and at other parallel planes varied as much as 8%. Two mild steel circular plates of 23 cm diameter and 0.5 cm thickness were used in the central region to improve the uniformity of the vertical magnetic field. The field maps of B_z for the magnet and with the additional mild steel plates at three different horizontal planes are shown in Figure 3.8b, c. The uniformity improved to a variation of maximum 1% of B_z. With the attached steel plates at 0.66 Tesla, the magnetic field in the θ and the radial direction was less than 0.5% and 1% of B_z respectively. The calibration of the magnetisation characteristic with the circular plates is shown in Figure 3.7c.

To observe the effect of slightly inclined magnetic field with respect to the vertical, two tapered mild steel plates with a slope of 0.04 and thickness at the centre of 0.6 cm were used. The B-I_{exc} calibration curve is shown in Figure 3.7d.

To protect the aluminium guard plates of the magnet coil from spilled mercury, the upper surface of the aluminium plate was coated with gloss paint. The space between the central slot in the guard plate and the pole face was filled with plasticine and a ring of plasticine around the outer periphery of the guard plate was erected to arrest any spilled mercury.

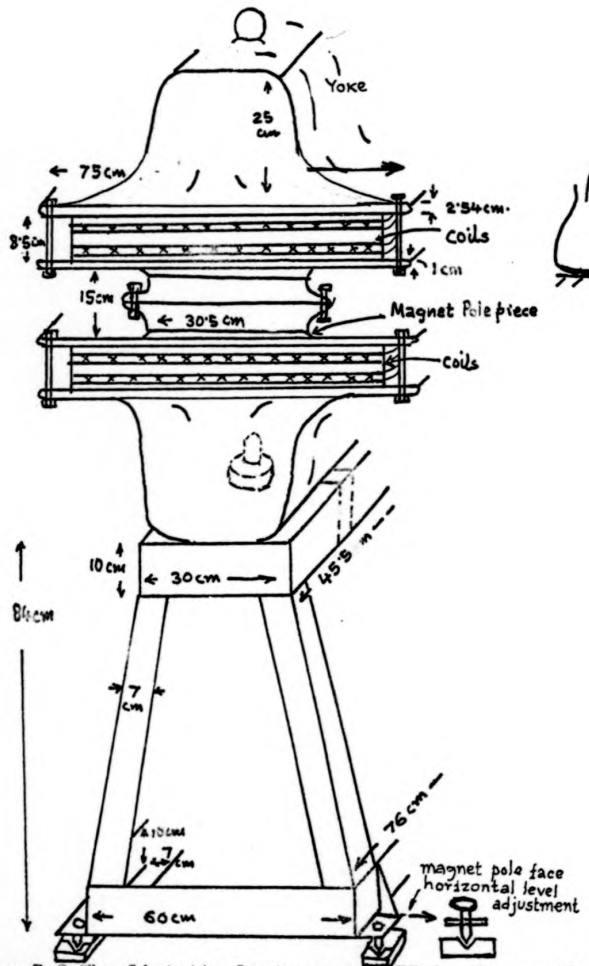

Figure3.9 The Lintott electromagnet II in the vertical field position,on the fabricated support structure.

Not to scale

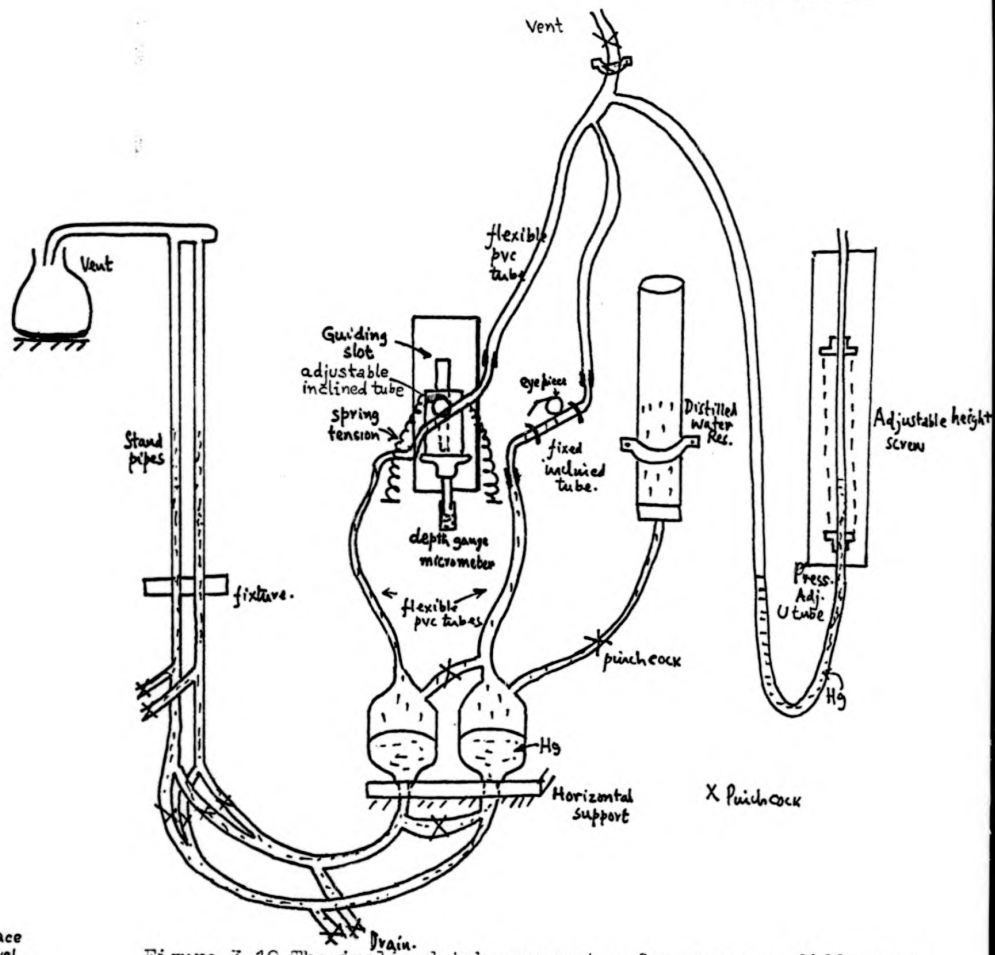

Figure 3.10 The inclined tube manometer for pressure difference measurements.

3.4.3 Pressure measurement

The static pressure difference at two tapping points along the length of the TEMHD duct was measured to find how a significant thermoelectically driven current could be generated and whether the pressure difference generated agreed well with theory. Conversely, the static pressure difference measured at known values of the magnetic field and the temperature distribution gives a new method of thermopower measurement,provided the electrical conductivity of the materials are known.

The pressure was measured by a device which is basically a Shercliff (1955) design of inclined tube air over liquid over mercury manometer capable of measuring 0.025 mm of Hg. The arrangement of the measuring device is shown in Figure 3.10. From the tappings through 6.25 mm internal diameter PVC tubes, Hg is allowed to stand in vertical 6 mm diameter(outer diameter)glass tubes with a free surface to show any pressure difference if great enough. The standpipes are also connected (pinchcocks to isolate) to the two limbs of the manometer. Each of the menisci was arranged to be in an inclined (1 in 4) uniform 1.5 mm bore glass capillary tube by adjusting the level of the U tube containing Hg partially to pressurise the menisci and by the vertical movement of one of the inclined tubes. The moveable inclined tube was fixed on a spring loaded block in a guiding slot and its position was measured by a 'Tessa' depth micrometer. The micrometer is first adjusted for zero pressure difference reading by opening the pinchcock X_m joining the Hg reservoirs. For pressure difference measurement pinchcock X_m is closed and the menisci in the inclined tubes brought back to reference datum points, by adjusting the position of the pressurising U tube and the micrometer screw. Even with Hg heated in the copper pipe in the thermoelectromagneto-hydrostatic case, the

arrangement worked satisfactorily even though the zero position drifted and had to be checked frequently. However, as explained in Chapter 4, adjustments had to be made for measuring TEMHD pressure differences when the fluid was allowed to circulate in a closed loop, resulting in the temperature rise of the total Hg volume in the loop. Air bleeds allowed the gas bubbles to escape which sometimes accumulated, and the drain and filling pipe facilitated emptying and filling liquid out of and into the system respectively. Checks for electrical isolation when the pinchcocks are closed were made. Parallel scratches on the front and the back of eye pieces over the two inclined tubes permitted avoiding parallax error in observing the location of the magnified meniscus. The smallest head measured was 0(1 mm) and the error in the measurement did not exceed ± 1% of 1 mm. The pressure difference measured was often greater than 2.5 cm, the total travel of the micrometer screw, and in that event the difference in height of the menisci in the standpipes was read directly.

A capacitance transducer type micromanometer (Furness Control) was also used for comparison, but measurements by this meter were not very reliable, being susceptible to ambient temperature changes.

3.4.4 Potential measurement

The basic electrical potential measurement and standardisation of other potential measurement devices were made with a Pye Vernier Potentiometer (7568/1963). The least count is 1 μV (range selector 0.1) with an absolute accuracy of the readings ± 0.004% or ± 1 μV, whichever is greater. Thus potential measurements of the potential probes at the electrodes of flowmeters, shunts, and thermocouples were accurately measured nearest to a μV in the steady state, and even could be extended to read fractions of a μV by observing the

Scalamp galvanometer deflection used as null detector. However, when the potential difference to be measured is not steady and when continuous potential measurement is necessary, the potentiometer device is not convenient unless the galvanometer oscillations are recorded by UV recorders. When the potential readings are not steady and when continuous measurement is essential, a digital voltmeter (Advance Instrument DVM) with a least count of 10 μV was used, and its calibration checked by the potentiometer at steady signal level. A Hewlett Packard d.c. differential voltmeter 3420A, capable of measuring 0.1 μV, was also used, but its readings were prone to drift and hence were unreliable. At the initial stages of the TEMHD experimentation, it was necessary to employ signal (d.c.) amplification and filtering to make measurements possible, but the perennial problem of drift, introduced by the d.c. amplifier, could not be eliminated. Later, with higher signals generated in carefully controlled and higher temperature operation of the TEMHD rigs, preamplification of the signals was not necessary, and signals could be recorded on a Hewlett Packard X-Y plotter with an input range of 40 μV/cm. For viewing the waveform and measuring the frequency of fluctuation a Tektronix double beam oscilloscope (model 565) was used. In addition, Solartron DVM s reading 0.1 mV were also used.

3.4.5 Time interval measurement

To measure rotational velocity, an electronic timing device started and stopped by mechanically made electrical contact was used, but recording the number of revolutions by stopwatch, though tedious, was found to be reliable. The time measurement was in the range of a minute and the error in time measurement would not exceed 1% as evident from the scatter of repeated readings. A more sophisticated version of time measurement by photoelectric cells and optical triggering of the electronic counter was not felt necessary for time intervals in the range of a minute.

3.4.6 Temperature measurement

Temperature measurements in liquid metal MHD flow, that have been reported in the literature, are relatively few compared with the pressure and velocity measurements since most of the experimental investigations were concerned with isothermal flows. Hydromagnetic Bénard problem is an exception, and in Plasma Hydromagnetics temperature (T) measurement is very important since the plasma electrical conductivity is very much dependent on T. In TEMHD, T measurement is of vital importance. The basic requirements in the adoption of the temperature measurement system are that (i) the system should permit the use of very thin probes for internal T measurement in the fluid so as to affect the fluid circulation by blockage or by exciting disturbance as little as possible; (ii) the measuring probe should be unaffected in the magnetic field and stable operation in a Hg environment should be possible; (iii) the measuring system should preferably have a linear temperature scale and a fast response time. The temperature range to be covered is considered as 0° C to 200° C, with a possibility of reaching 300° C compatible with operation with Hg. Two basic systems were used: (a) the thermocouple and (b) the thermistor.

3.4.6.1 Thermocouples

The availability of a temperature measuring device by Comark Electronics Ltd. (Rustington/Littlehampton, Sussex) Type 166C (BS1827) was taken advantage of in the initial stages of experimentation when the temperature measurements were restricted to the copper surface. The 'Comark' device gives a temperature range of -120° C to $+1100^{\circ}$ C, 0° to 1100° C in steps of 100° C and 0° to -120° C with a least count of 1° C. Facility for calibration with potentiometers is available and the error is restricted to 1%. However, the measuring device is powered by

4 Mallory RM-12R batteries, and care had to be taken that the failure of the cells did not introduce error. The temperature measuring probe is a 1.5 mm diameter stainless steel sheathed Chromel (Ni-Cr)-Alumel(NiAl) or T_1-T_2 alloy thermocouple junction. While there was no problem in measuring the temperature at the cold end, the probe,when inserted under the heater coil, frequently developed electrical faults. Further, though copper has a sufficiently high thermal conductivity (380 watts/m ^{o}K) and the temperature drop across the thin copper wall is negligible, the temperature measurement at the copper-fluid interface is more relevant. A Chromel-Alumel junction when exposed is almost immediately attacked by Hg and therefore the probe junction had to be protected. A very thin coating of tensol cement (I.C.I.) is found reasonably good for the purpose, but a coating of boron nitride, applied as suspension in water and then dried, was also used so that the thermal contact resistance thus introduced is assuringly small. Coating with Araldite leaves a much bigger blob and is unsuitable. Apart from the original probe, various thermocouple probes were made of 0.315 mm (0.0124"), T_1/T_2 bare wires insulated with PVC sleeves. Later, the bare wire size was changed to 0.09 mm (0.0036") to save space. Much time has been spent on spot-welding the thin wires on to a changeover section for strength in the long leads to be connected to the meter away from the magnetic field and in insulating them with very thin PVC, vulcanised and ceramic rubber sleeves. While initial attempts at coating the 0.09 mm wires with fine sprays of lacquer and PTFE (Emraleen 823, Acheson Colloids) were disastrous, resulting in blobs and dash appearance, very diligently and patiently the technique of uniform coating had to be mastered. The electrical insulation between such coated wires was checked before making the thermocouple junction

at the end. As long as stainless steel sheaths were used, both the wires of the pair had to be insulated. Very fine bore silica tubes with outer diameters of 1, 1.5 and 2 mm were used where only one wire had to be insulated. Double barrel, flame-drawn glass capillaries of overall maximum width 0.75 mm were also made to avoid individually coating or insulating the bare wires otherwise. The silica glass probes gave excellent performance, apart from the fact that they were very fragile and much time was spent on making glass insulated probes because of breakage. With both silica and stainless steel tubes, care had to be taken while inserting insulated wires into them so that scraping of the insulation at the point of entry did not result in a short circuit. The alloy T_2 is magnetic, and the effect of magnetic field on temperature measurement was ascertained by measuring temperatures in the absence of and in magnetic fields as high as 1.2 Tesla. The change is less than $\frac{1}{2}^{o}$ C in the range of temperature 0^{o} to 100^{o} C. No corresponding data is available in the literature, but extrapolation from lower temperature data of Chiang (1974) corroborates such observation.

At the final stages of the experimentation, the best choice of Copper-Constantan (Type T) thermocouple wires 0.2 mm diameter, p.t.f.e. coated with a close linear response of 40 $\mu V/^{o}K$ in the temperature range of 0^{o} C to 300^{o} C was made. This very much facilitated the making of thermocouple probes. Cu-Constantan is fairly stable in a mercury environment and thus the junction tips could be left bare without any coating. This led to their use as potential probes for velocity measurements as will be explained in the next section; it so works out that a new method of simultaneous local temperature and velocity measurements can be done without having to pass controlling current in the mesuring device from external sources as in the case of thermistors and in thermoanemometry.

at the end. As long as stainless steel sheaths were used, both the wires of the pair had to be insulated. Very fine bore silica tubes with outer diameters of 1, 1.5 and 2 mm were used where only one wire had to be insulated. Double barrel, flame-drawn glass capillaries of overall maximum width 0.75 mm were also made to avoid individually coating or insulating the bare wires otherwise. The silica glass probes gave excellent performance, apart from the fact that they were very fragile and much time was spent on making glass insulated probes because of breakage. With both silica and stainless steel tubes, care had to be taken while inserting insulated wires into them so that scraping of the insulation at the point of entry did not result in a short circuit. The alloy T_2 is magnetic, and the effect of magnetic field on temperature measurement was ascertained by measuring temperatures in the absence of and in magnetic fields as high as 1.2 Tesla. The change is less than $\frac{1}{2}^{o}$ C in the range of temperature 0^{o} to 100^{o} C. No corresponding data is available in the literature, but extrapolation from lower temperature data of Chiang (1974) corroborates such observation.

At the final stages of the experimentation, the best choice of Copper-Constantan (Type T) thermocouple wires 0.2 mm diameter, p.t.f.e. coated with a close linear response of 40 $\mu V/^{o}K$ in the temperature range of 0^{o} C to 300^{o} C was made. This very much facilitated the making of thermocouple probes. Cu-Constantan is fairly stable in a mercury environment and thus the junction tips could be left bare without any coating. This led to their use as potential probes for velocity measurements as will be explained in the next section; it so works out that a new method of simultaneous local temperature and velocity measurements can be done without having to pass controlling current in the mesuring device from external sources as in the case of thermistors and in thermoanemometry.

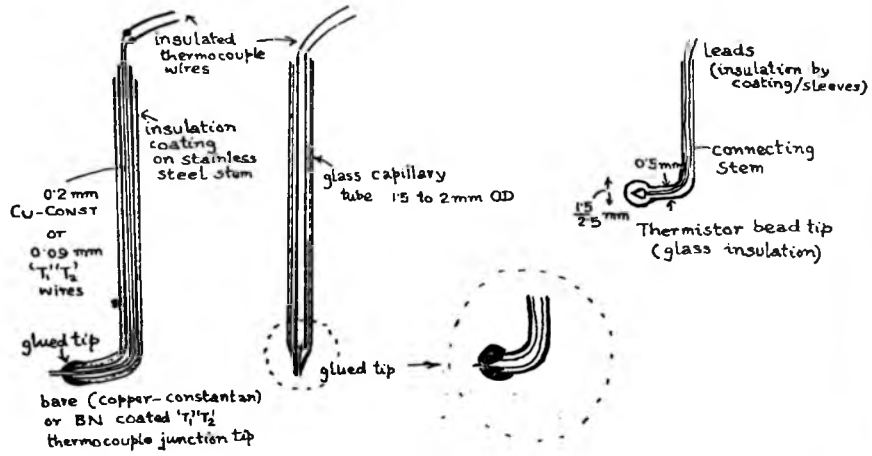

Figure 3.11 The temperature measuring probes. (not to scale)

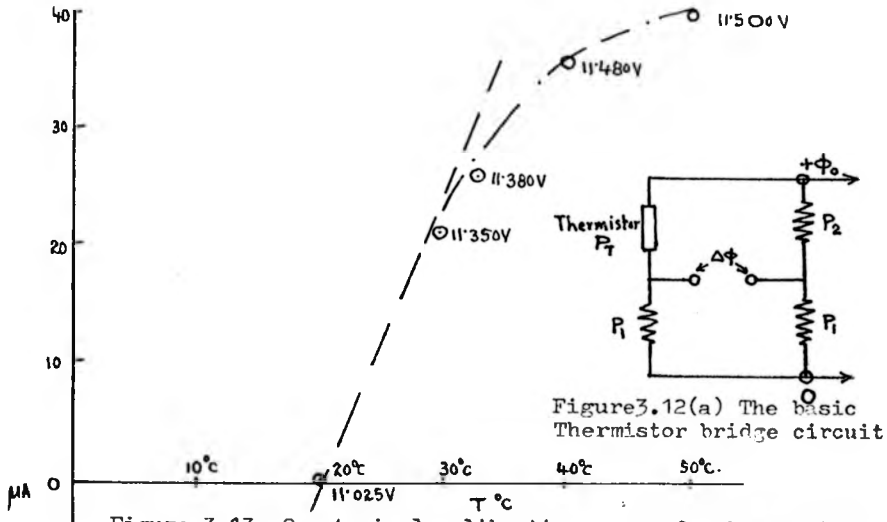

Figure3.12(a) The basic Thermistor bridge circuit.

Figure 3.13 One typical calibration curve for temperature measurement with Thermistors using the circuit of figure 3.12b

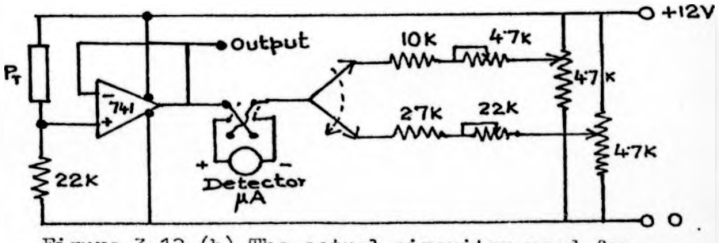

Figure 3.12 (b) The actual circuitry used for temperature measurements with Thermistors.

The copper constantan thermocouples, though insulated, were flexible and had to be encased in 1 mm glass tubes or 2 mm stainless steel tubes to provide rigidity. The shape of the probe and its traversing mechanism is described in section 3.48. The copper constantan thermocouple output was measured by the Pye Vernier Potentiometer for calibration by comparing measurements done with a Hg-inglass thermometer. The calibration agrees with BS 4938/1974 for type T thermocouples, and is linear within a tolerance of 8.0% in 0.-100° C range, 7.0% in the range 0-200° C and 4.5% in the range 0-300° C. The effect of magnetic field on the thermocouple output is similar to that in the case of Chromel Alumel and should not show error of more than ¼° C.

3.4.6.2 Thermistors

Thermistors are used to measure temperature based on the principle that the resistance change of the thermistor in one arm of a resistance bridge is detected by the bridge unbalance voltage. The measuring system therefore requires external power input into the system. Bead thermistors with tip diameter 1.5 mm and 2.5 mm with thinner stem size from R.S. Components were considered for T measurement basically in the range of 0 to 100° C, but extendable up to + 300° C. The choice of this system is motivated by the combined T and speed measurements of Fowlis (1970) in nonmagnetic heated annuli. The analysis put forward by Fowlis requires elaborate numerical calculation in a computer to evaluate the temperature of the environment from the bridge unbalance voltage. The following analysis developed in this thesis enables one to calculate T directly from bridge parameters without computer analysis, and the resultsobtained by this method agree with the numerical results of Fowlis(1970) given in Table I.

The nonlinear variation of the resistance of the thermistor with temperature T in ^{o}K is given by

$$P_T = P_o \exp \left[\gamma\left(\frac{1}{T} - \frac{1}{T_o}\right)\right] \qquad (3.63)$$

where P_T and P_o are the resistances of the thermistor at T and T_o respectively, T_o corresponding to either 20^{o} C (type 151-029) or 25^{o} C (type 151-142) the specification temperature and γ aconstant. When the thermistor is heated by the bridge arm current I in P_T and cooled by its environment at T_f in the steady state

$$T = T_f + \frac{I^2 P_T}{K} \qquad (3.64)$$

where K is a specific parameter of the thermistor and can be interpreted as the power necessary to raise the thermistor temperature above the fluid environment temperature by 1^{o} K. K is a function of the fluid property as well, but for the type of application considered here it can be taken to depend predominantly on the fluid speed. In the stationary fluid, K is a constant for a given fluid. Consider now the bridge unbalance voltage $\Delta\phi$ shown in Figure 3.12a.

$$\frac{\Delta\phi}{\phi_o} = \frac{P_2}{P_1 + P_2} - \frac{P_T}{P_T + P_1} \qquad (3.65)$$

From (3.63) and (3.65)

$$P_T = P_1 \left\{ \frac{\frac{P_2}{P_1 + P_2} - \Delta\phi/\phi_o}{\frac{P_1}{P_1 + P_2} + \frac{\Delta\phi}{\phi_o}} \right\} \qquad (3.66)$$

From (3.64) and (3.66)

$$T = T_f + \phi_o^2/KP_1 \left(\frac{P_2}{P_1 + P_2} - \frac{\Delta\phi}{\phi_o}\right)\left(\frac{P_1}{P_1 + P_2} + \frac{\Delta\phi}{\phi_o}\right) \qquad (3.67)$$

with a choice of $P_1 = P_2 = P_o = P$ and ignoring higher order of $\frac{\Delta\phi}{\phi_o}$,

$$T = T_f + \frac{\phi_o^2}{4KP} - \frac{(\Delta\phi)^2}{KP}$$

and $$T = T_o \left\{1 + \frac{4T_o}{\gamma} \frac{\Delta\phi}{\phi_o}\right\} \qquad (3.68)$$

From (3.68) the calibration for $\phi_o < 2T_o \frac{\sqrt{KP}}{\sqrt{\gamma}}$

$$\Delta\phi = \frac{\gamma\phi_o^3}{16KPT_o^2} - \frac{\gamma\phi_o}{4T_o^2} (T_o - T_f) \qquad (3.69)$$

Results based on equation (3.69) agree with the tabulated numerical evaluation in Table I of Fowlis (1970) for $\phi_o < 15$ volts. During the TEMHD experimentation, the thermistor bridge output circuit was modified by the inclusion of an operational amplifier working in the voltage follower mode to eliminate any error in the unbalance voltage/current detection system by loading the bridge circuit. The modified circuit is shown in Figure 3.12b, and combines range changeover facility, zero setting adjustment for ambient temperature and indicator meter full scale deflection adjustment (sensitivity) control. The measured bead characteristics for calibration are given in the Appendix I . One typical calibration curve is shown in Figure 3.13 with zero setting for the ambient temperature at 20° C with an average voltage sensitivity of -22 mV/$^{\circ}$C over its linear range of temperature scale $\sim$ 0-40° C. The beads are sealed in a glass casing, but the leads are not insulated and hence the same problem of electrically insulating the leads as in the case of thermocouples had to be solved. The beads are magnetic and are attracted towards the pole face. Thus extra rigid mounting devices were necessary. Though magnetic, the calibration of the thermistors is not significantly affected (< 1.5%) by the magnetic field. The unbalance current was measured with a microammeter with an accuracy of 1 % and the output voltage of the voltage follower by a voltmeter with an ohms/volt sensitivity of 2KΩ/volt. F.S.D.

Comparatively, the thermocouple system was found to be better suited to the TEMHD experiments described in this thesis and the thermistor T measuring system was only used in the annular channel to confirm T measurement by thermocouple devices that seemed different from the expected values at the initial stages of experimentation. The thermocouple T measurement system is superior in the sense that no external current supply and hence heat dissipation by the measuring system is involved, and the linearity range of the temperature scale is not prone to adjustment as in the case of thermistors. Thermistor calibration is additionally affected by fluid movement.

The coolant water at the inlet and outlet port at the cooling jacket were measured by thermocouples and Hg-in-glass thermometers to estimate how much heat was lost through the thermal lagging and hence the effectiveness of the heat transfer device in the TEMHD section of the channel.

3.4.7 Velocity measurement

The essential presence of the magnetic field in MHD flow permits one to introduce more novelty into the velocity measurement of conducting fluids as compared to that in ordinary hydrodynamics. This however does not imply that velocity measurement is a simple task; rather it is the most difficult measurement in MHD. Velocity measurement in TEMHD is no exception. Various systems of velocity measurement have been investigated for application to the TEMHD experiments described in this thesis, and are detailed in the following subsections to provide a guideline for selection and further development of velocity measuring systems in TEMHD. These various systems have been used in the experimental TEMHD investigation to confirm the

accuracy of measurement and compare one system of velocity measurement with the other.

3.4.7.1 Mean velocity or total flow measurement

Flow meters.- The constructional details of the flowmeter used is shown in Figure 3.14a,b,c. A Swift-Levick permanent magnet with a gap flux density of 0.3 Tesla is used. The design is similar to that of Hunt, but with different physical dimensions. The entry cross-sectional radius of 1.25 cm is matched to the slit in the measuring section of half height of 1 mm by carefully tapering the intermediate section. The two halves of the pvc assembly were glued and kept in position with brass bolts. The stainless steel connectors at the inlet and the outlet were fixed to the PVC material by brass screws and any leakage of Hg was stopped by fitting O rings between the connector pipes and the slots in the PVC material. Each of the electrodes is a 1.5 mm hole in the PVC material matched to a step of 2.5 mm bore into which stainless tubes are press fitted with glue, so that Hg stands into these tubes; to provide electrical connections, leads are brazed on to the stainless steel tubes. The stainless steel tubes are also connected to PVC tubes to work as bleeds, which were very helpful in eliminating gas bubbles that collected occasionally at the electrodes, resulting in the loss of electrical continuity. The flowmeter was calibrated by similar procedure to that of Shercliff (1955) and Hunt (1967), but with a makeshift arrangement of the collecting tank. A stopwatch was used for counting time for a given volume flow to measure the flowrate at a specific open position of the flow regulating value. The discharge collection in the measuring tank II was started by switching the flow from an initial collector I and stopped by diverting the flow back to

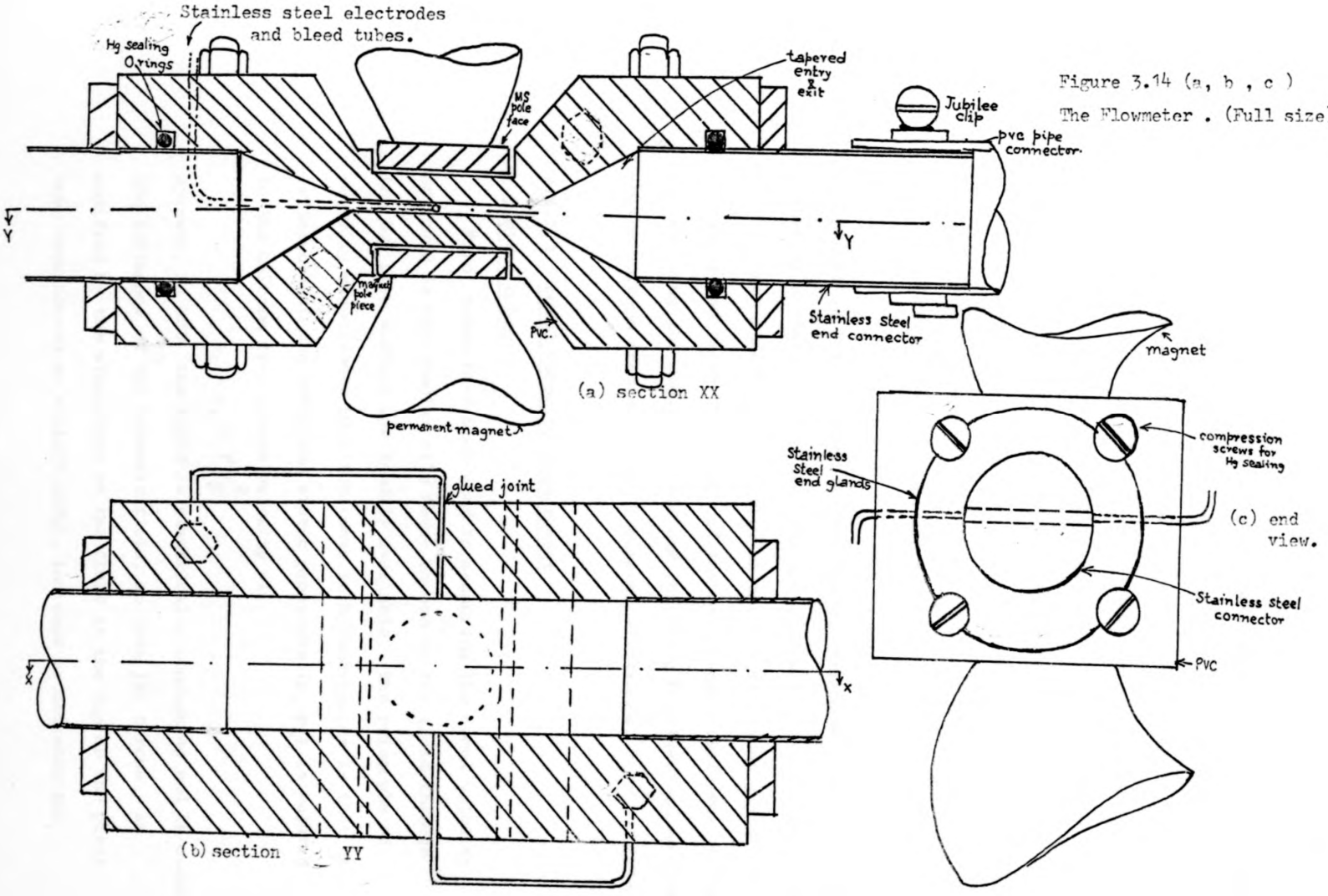

Figure 3.14 (a, b , c)
The Flowmeter . (Full size).

the collector I. The flow loop is shown schematically in Figure 3.14d. The discharge volume was weighed as well as measured by a calibrated burette. The flowmeter electrode potential was measured by the 'Advanced Instrument' DVM and also checked by the 'Pye' potentiometer. The calibration data is given in the Appendix I and the mean calibration constant is given by 6.25 cc/sec/mV with a variation of 1% over the measured range and an estimated maximum error of 1%.

The flowmeter was used to measure the flowrate generated by the TEMHD effect in the straight channel experiments. The flowmeter was placed as far as possible from the electromagnet and additionally screening by mild steel plates was made,which was felt necessary at the highest magnetic flux density of the electromagnet gap of 1.2 Tesla and above.The effect of the main magnet field was checked by reversing the magnetic field and observing that there was no change in the voltage reading at the flowmeter electrodes.

3.4.7.2 Local velocity measurement

(a) Pitot tubes

Pitot tubes have been used in measuring the local velocity of fluid in the annular ri-g where access to the fluid through the top free surface was readily available. The principle of velocity measurement by pitot tubes in hydrodynamics is that the difference of the total and static pressures (p_t,p_s) is related to the uniform free stream velocity v by

$$p_t - p_s = \rho \frac{v^2}{2}$$

However, in MHD, the fluid is electrically conducting and is under the influence of the magnetic field, so that $\underline{j} \times \underline{B}$ forces , as modified by the stagnation of the fluid at the tip of the pitot tube (considered as a bluff body), increase or decrease the

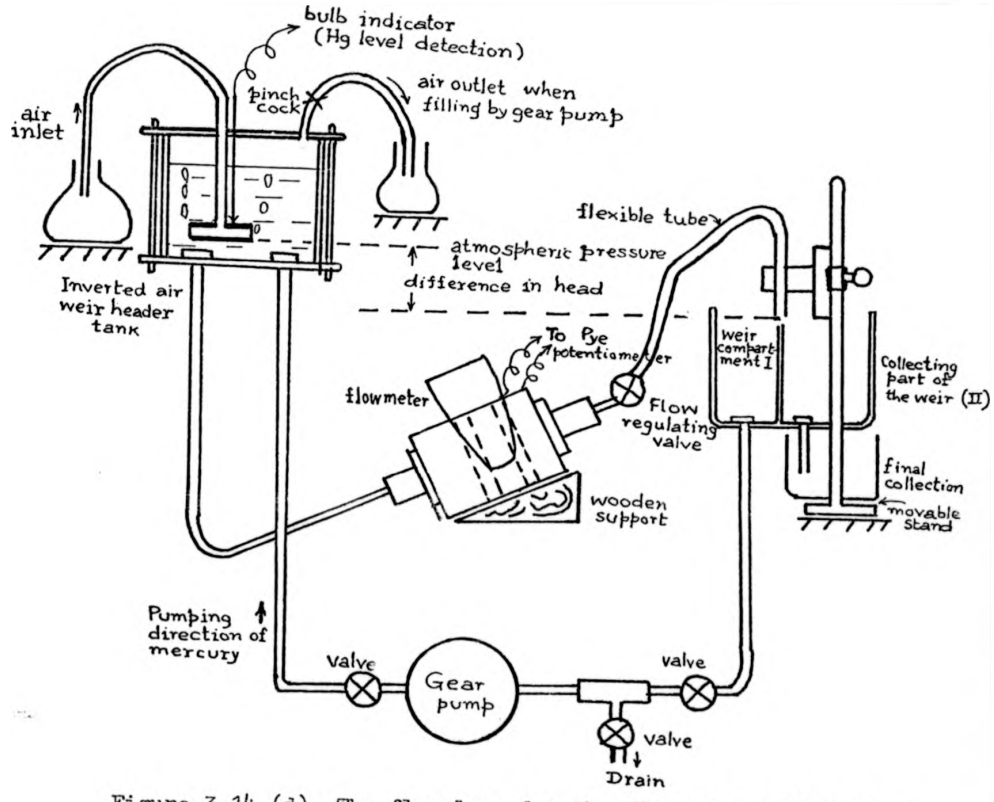

Figure 3.14 (d). The flow loop for the Flowmeter calibration.
(not to scale)

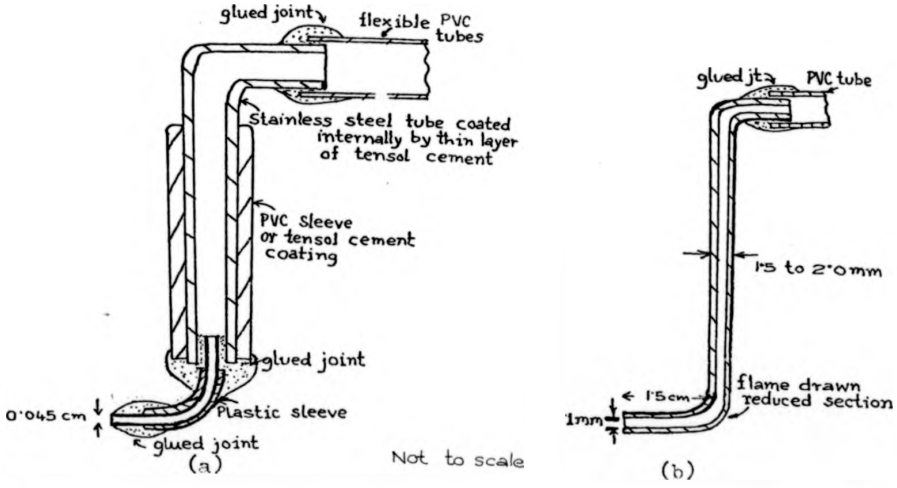

Figure 3.15 (a) The Stainless steel pitot tube.
(b) The glass capillary pitot tube.

apparent pressure difference measured by the pitot tube. The MHD error, a function of the interaction parameter N, thus introduced could be made zero for a specific measurement by choosing the appropriate tube wall conductivity and the tip dimension but not for all measurements,as shown by Hunt (1967), and the choice is also difficult to make in practive. Considering the further uncertainty introduced by the TEMHD error, the use of conducting wall pitot tubes in electrical contact with the fluid was rejected. Hunt (1967) estimated the error for $N \ll 1$, $\Delta p = -\frac{1}{2}\rho v^2 \frac{N}{\pi}$ which is < 5% for $N \leq 0.15$. Hunt's estimate of the error could be extended to the cylindrical geometry as follows for the pitot tube electrically insulated from the fluid.

Let the free stream condition be such that

$$\underline{v} = (o, v_\theta, o), \quad \underline{E} = (-\text{grad}\,\phi^+, o, o), \quad \underline{B} = (o, o, B)$$

a weak applied field and $\underline{j} = (\sigma B v_\theta - \text{grad}\phi^+, o, o)$.

At the tube walls $\underline{v} = o$ and $\underline{n}.\underline{j} = 0$

Since $R_m \ll 1$ $\quad \underline{B} \equiv (o, o, B)$

Consistent with the boundary conditions and div $\underline{v} = 0$, neglecting buoyancy effect, the perturbed velocities U_r, U_z for a symmetric probe tip w.r.t r and z, are zero. Neglecting the viscous term with Re > 1,integration of the θ component of equation (3.4) for $F = 0$ and $\frac{\partial}{\partial t} = 0$ gives

$$p_t - p_s = \rho\frac{v_\theta^2}{2} + \sigma B r \int_o^\theta \{-\text{grad}\phi^+ + B(v_\theta + u_\theta)\}\, d\theta$$

where $\theta = 0$ is the position of the probe tip and $\theta = \theta$ far away from it and u_θ is the perturbation introduced in velocity v_θ in the free stream.

In a uniform core flow without pressure gradient in the free stream

$$-\text{grad}\phi^+ + B v_\theta = 0$$

and the MHD error term $\Delta p = \sigma B^2 r \int_o^\theta U_\theta d\theta \simeq N \frac{\rho v_\theta^2}{2}$ using potential flow approximation of $U_\theta = \frac{(R/2)^2 v_\theta}{(R/2 + r\theta)^2}$

In the experiments for the measurable velocity range $N \ll 1$ and the correction factor is insignificant compared to the error in pressure measurement in the actual system. The constructional details of the pitot tubes are shown in Figure 3.15. The basic defect of the design is that the streamwise length of the tube could not be matched with the curvature at every radial position without making a probe for each radial position; a mean curvature was all that could be implemented. Though the contact resistance of stainless steel is great enough, the inside and outside walls of the stainless steel tube was coated with 'Tensol' cement (I.C.I.). The inside wall coating required very patient filling with the cement fluid and quick blowing with the air line. The inclined tube Hg manometer was no longer useful for the order of velocity magnitudes measured, and distilled water over Hg was used to amplify the pressure measurement in the manometer.

In the absence of buoyancy-induced vorticity, the static pressure measurements from the tappings at the bottom boundary also provided a measure of the average v_θ over the vertical height and the radial spacing through the relationship

$$\frac{\Delta p_s}{\Delta r} = \frac{\rho \bar{v}_\theta^2}{\bar{r}}$$

The response time of the pitot tube was very slow, and though reproducible readings could be obtained by carefully and patiently removing accumulated gas bubbles, probably made worse because of Hg being sucked up in the PVC tubes from the lower level in the channel, the pitot tube method of velocity measurement in TEMHD-driven Hg is not very effective at high magnetic field.

(b) Visual measurement system

The open horizontal Hg surface available in the annular channel experiment provided the opportunity to visualise the surface

movement of the TEMHD-driven Hg. The formation of an oxide layer and deposit of contaminants from within the interior on the free surface of Hg, with their dominating surface tension that masks the free surface movement, make the free top annular channel no better than one with rigid top surface, not necessarily horizontal. Arrangements were made for operation in a N_2 atmosphere which gave improved performance in keeping the free surface clean for 15 to 20 minutes. The disadvantage was that the free access to the Hg surface was lost by having a gas tight enclosure around the channel. In actual practice, N_2 was flushed out of a liquid N_2 reservoir through pipes leading in and out of the enclosure on the top of free surface of Hg and the N_2 flow rate affected the temperature profile and introduced secondary flow. Regular cleaning of the mercury surface, keeping the free surface of Hg covered with a thin layer (1.5 to 3 mm) of either distilled water or dilute nitric acid plus distilled water permitted the discarding of the N_2 enclosure. Surface rotation rates could then be measured very consistently with tracer particles (white sand, glass beads, plastic capsules, paper clips and even patches of scum) positioned at a fixed radial location by timing the number of revolutions per minute by stopwatch. However, as is explained in Chapter 6, not all TEMHD driven flows in the annular channel are amenable to such measurement due to shear and secondary flow. The concept of using tracer particles to measure surface velocity was extended to the use of free floats to confirm at the initial stages of experimentation whether the bulk of the fluid was moving or there was only surface wave-like circulation. A number of floats were designed and made, using heavier metals than Hg such as Pt and W. Even with the density of such materials, about 1.5/1.6 times that of Hg, the fine coating of insulation on the surface made these

floats remain virtually on the top of the Hg surface. Indeed, so great was the meniscus effect that to insert Pt and W in Hg, they had to be pushed under the Hg surface. With great care a few free floats could be operated stably with depth of penetration as much as 1.5 to 2.5 cm. The 5 and 6 cm depth operations were invariably plagued with instability, hydrodynamic as well as that due to shear at the Hartmann layer, which was thicker than it should be. The buoyancy-induced secondary flows at low azimuthal rotation rate could also be measured by observing the displacement in the radial direction with time of the free float or the tracer particle.

The primary interest in the velocity measurement being that of azimuthal motion due to TEMHD effects in the annulus experiment , floats constrained at a particular radial location,by fixing its position along a radial arm pivoted at the annulus central axis, were developed. The possibility of exploring the nature of fluid vorticity along the magnetic field as well was arranged with the provision of a cross arm paddle at the bottom end of the float. The principle of this method of vorticity detection is similar in principle to that of Heiser and Shercliff (1965), but the design details differ to suit the TEMHD environment. The depth of the float and the paddle below the mercury surface could be adjusted by putting counterweights on the detachable head (a flat platform) at the top of the float spindle. The float spindle was kept vertical with the help of two small brass bearings vertically aligned with a spacing of 1 cm between them. This arrangement worked much better than the 1 cm long sleeve bearing originally made because of lower contact friction. Initially two horizontal thin tufnol discs,separated vertically by 0.9 cm but attached to one another, were centrally pivoted to act together as a balanced

radial arm. Later the discs were cut in the form of a cross-arm arrangement. Brass bearings located at 2.3, 3.0, 3.75, 4.45 and 5.2 cm radial distances permitted the location of the float at these positions. In addition, measurements could be done at 2.5, 2.75, 3.2, 3.65, 4.0, 5.0, 6.3 and 7.1 cm radial positions with other cross-arms. Thus the float spindle was free to spin about its own axis while the pivoted cross-arm rotated around the central pivot due to the azimuthal drag on the float by the fluid circulation. Painting the top of the spindle head black and white as well as having a pointer indicator permitted the observation of the state of paddle alignment to reveal the fluid vorticity in the vertical direction. The system gives a very steady balanced operation with very little friction and rotation rates as low as 1 rev/120 seconds could be measured, beyond which error due to friction was introduced. (The author is greatly indebted to Mr. A.E. Webb for perfect workmanship in making the tiny bearings, pivots and the cross-arms in the final form which replaced the original ones made by the author, even though the original ones also worked). The design of the bearings needs a special mention. Ideally jewel bearings should be used, but these experimental facilities are not considered as permanent fixtures, and therefore brass bearings were adopted. The central pivot is conically shaped with the vertex semiangle of 60° while the matching part of the bearing had a corresponding slope of 75°. The tufnol cross-arm provides the essential electrical isolation of the system from the Cu-Hg thermocouple circuit. In addition, the floats are also coated with insulation. The float spindle diameter ranged from 0.05 cm to 0.09 cm. This is the minimum that could be used while retaining its straight shape and

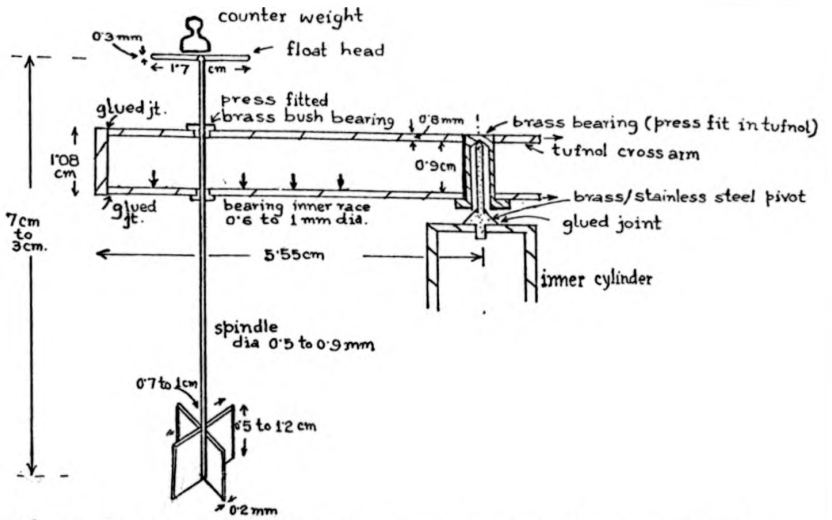

Figure 3.16 The Paddle type of float, constrained at a fixed radial location w.r.t. the central axis, on the pivoted cross arm. Only one set of brass bush bearings for the float spindle is shown for clarity, other positions are marked ↓

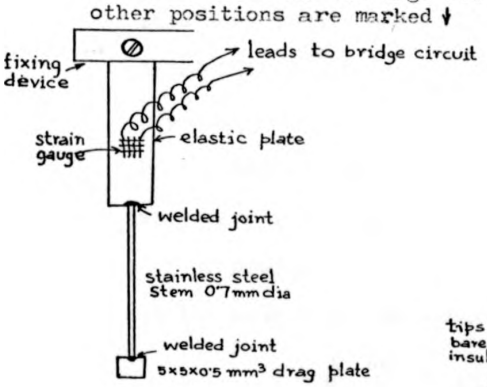

Figure 3.17 The hinged drag plate velocity measuring probe.

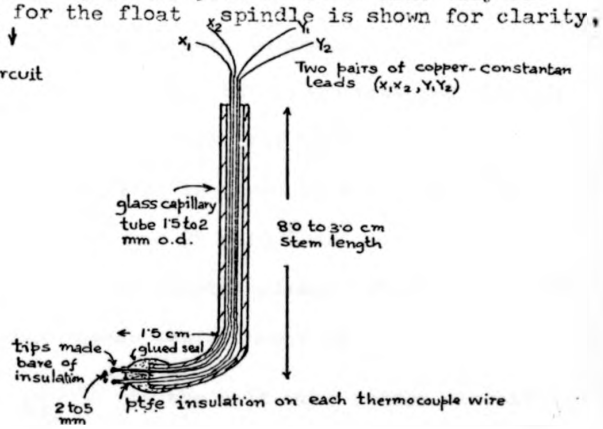

Figure 3.18 The thermoelectric potential probe. Potentiometer connection to the pair of terminals (i) X_1X_2 (ii) Y_1Y_2 (iii) either X_1Y_1 or X_2Y_2.

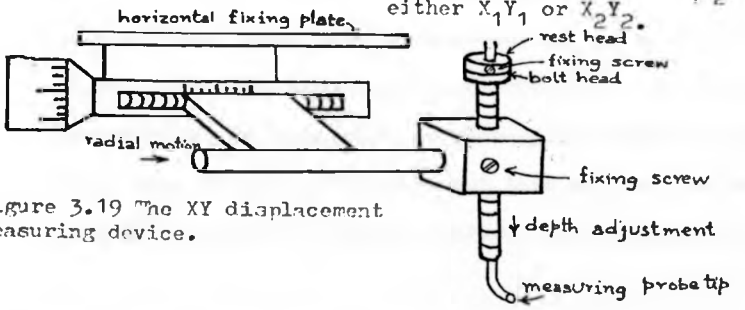

Figure 3.19 The XY displacement measuring device.

stiffness. The error introduced due to drag on the projected area of the stem would therefore be present to this extent.

Drag plate hinged via an elastic element

Three dimensional fluid velocity measurement in a small enclosure where MHD effects of the welding metal pool were simulated has been reported by Kublanov and Erokhin (1974). Motivated by the principle of their measurement technique, a drag plate type of velocity measuring device (Figure 3.17) was made. The drag plate measured 5 x 5 x 0.5 mm^3. Through a rigid stem the plate was linked to an elastic element, a thin foil of brass 0.025 cm thick, 3.5 x 0.9 cm^2 face area. The elastic element was rigidly fixed at the other end and on its both faces a PS-3 Polyester gauge type P strain gauge / with a nominal resistance of 120 Ω, gauge factor k = 1.89, size 3 mm x 2 mm was bonded. The strain gauges formed a half-wave circuit to compensate the thermal strains and their response due to strain measured through a bridge circuit similar to the one used for thermistors. The hydrodynamic drag on the flat plate is given by $F = 1.28\ \rho\frac{V^2}{2} A$ where $\rho = 13.6 \times 10^3$ for Hg and $A = 25 \times 10^{-6}$ in^2.

F produces a strain ε in the elastic element which is related to the change in the strain gauge resistance P by

$$\varepsilon = \frac{1}{k}\frac{\delta P}{P} \quad \left(= \frac{2}{k\phi_o}\Delta\phi \text{ in the half-wave bridge circuit}\right)$$

The brass foil, however, did not produce enough deflection due to the low thrust on the drag plate at about 5 cm/sec fluid velocity and, though some measurement of the signal could be demonstrated. the magnitude of the signal was extremely low and sensitivity was very poor. A glass plate type of elastic element would have functioned better, but this was not pursued. It is not known what elastic elements Kublanov and Erokhin used.

Potential probes

In MHD with fluid flow in a transverse magnetic field, potential probes not only give the potential distribution in the flow but also provide information about the fluid velocity. In fact, in a current-free zone of uniform flow in a transverse magnetic field velocity should be measurable very accurately. The two-electrode potential difference sensor then has a simple linear relationship of velocity versus potential difference, instantaneous response and this type of probe can be constructed in very small sizes and therefore causes less disturbance to the flow by probe insertion.

Consider for $R_m \ll 1$, a steady flow in uniform field. Taking divergence of (3.22) and using div $\underline{j} = 0$

$$\nabla^2\phi^+ = B.(\nabla X \underline{V}) \qquad (3.70)$$

In a fully developed flow in the θ direction in an applied field (o,o,B) under the assumption of an isothermal environment from (3.70)

$$Bv_\theta = \frac{\partial\phi}{\partial r} + \frac{A_1}{r}$$

where A_1 depends on j_r and variations with respect to z are suppressed.

For a small variation in r, $\frac{\partial\phi}{\partial r} \simeq \frac{\delta\phi}{\delta r}$

Further, if $j_r = 0$, i.e. in the core, $\overline{v}_\theta = \frac{1}{B}\frac{\delta\phi}{\delta r}$

In the presence of j_r, error would be introduced in the velocity measurement by the potential probe. In particular, in measuring velocity profiles in the Hartmann layer by potential probes, $\underline{j}$ measurement also has to be done, and this is very difficult to do.

Next consider the presence of velocity fluctuations in the (o,o,B) field. The fluctuating components (ϕ^f, u, $\underline{j}^f$) are given by

$$\frac{\partial \phi^f}{\partial r} = BU_\theta - \frac{j_r^f}{\sigma}$$

$$\frac{\partial \phi^f}{r\partial \theta} = BU_r - \frac{j\theta^f}{\sigma}$$

$$\frac{\partial \phi^f}{\partial z} = - \frac{jz^f}{\sigma}$$

The root mean square of velocity fluctuation $\overline{U}_\theta^2$ and $\overline{U}_r^2$ can then be found only if mean fluctuation $\overline{jf}^2$ components and the average values of the correlation of velocity and current fluctuations $\overline{U_r j_\theta}^f$, $\overline{U_\theta j_r}^f$ are known. During such velocity fluctuations, curl $\underline{E}$ cannot be set to zero in the equation

$$\frac{\partial b^f}{\partial t} = \text{curl } (\underline{V} \times \underline{B}) + \frac{1}{R_m} v^2 b^f$$

unless the Lundquist Number = $NR_m << 1$.

In the above treatment, isothermal conditions have been imposed to avoid thermal e.m.f's in the probes of different material from that of the fluid. This problem has been circumvented by drawing Hg up the pitot tubes to a point of isothermal environment from where lead connection to the potentiometer is taken. However, in such a case the probe is as big as the pitot tube and the error due to the finite size of the probe has to be considered. If the flow in the free stream is uniform, $\frac{\partial \phi}{\partial z} = 0$ and $\frac{\partial \phi}{\partial r}$ is uniform, a symmetric probe about $z = 0$, $v = 0$ would give the error $\Delta_e \phi = 0$. In a non-uniform free stream flow, $\frac{\partial \phi}{\partial r} = v_\theta(r)$; then the error is of order $O\left[R_1 B \frac{\partial v_\theta}{\partial r}\right]$.

Apart from the Hg-potential probe, ordinary potential probes are useless in TEMHD environment if they are not supplemented by temperature measurements at the exact spots.

Thermoelectric potential probes

A novel method of simultaneous temperature and velocity measurement has been developed which would be of great use in TEMHD experimentation. Basically it is a potential probe, but the

probe itself is made of thermoelectric materials in matched pairs. Thus each probe tip is the junction of the thermocouple that measures the temperature at that point when the potential difference appearing across the twin leads of the thermocouple is measured (Fig. 3.18). The information about the velocity is obtained by measuring the potential difference between two wires of the same type of the two distinct thermocouple pairs whose tips are separated by a small spacing Δr. A further check could be made by measuring the potential difference between the other two similar wires, but essentially no further new information is obtained. It is no longer necessary to measure potentials from Hg led away into isothermal environment to avoid thermal e.m.f. and therefore the basic small size of the probes can be retained. This new type of probe is much more convenient and simple compared to their counterparts, the hot wire anemometer probe and the thermistor probe, in that the thermoelectric probe is a passive device and therefore responds to temperature and its fluctuation. Similarly the velocity and the superimposed temperature fluctuations due to thermoelectric e.m.f. variation is recorded by the similar type of wire potential probe between two thermocouples without any external current flow in the device. In uniform core flow, without any current, such measurement produces very accurate results, provided that the fluid thermoelectric power is accurately known.

Consider the twin thermoelectric probes T_{p1} and T_{p2} with their tips in the plane $z = c$ and at radial locations r and $r + dr$ respectively in the annular channel TEMHD experiment where $\underline{B} \equiv (o,o,B)$. T_{p1} measures temperature T_1 and T_{p_2}, T_2.

The thermoelectric potential probe output

$$= \alpha_{M-Hg}(T_{av})(T_1 - T_2) + Bv_\theta \Delta r$$

where M refers to the element of the thermocouple wire used as the potential probe. The instantaneous response is only limited by the thermal inertia of the tiny probe. The constructional details are similar to that of potential probes and is shown in Figure 3.18.

Other methods of velocity measurement not pursued in this thesis

The thermistor probe developed for temperature measurement could be used for velocity measurement as well by calibrating k with respect to the speed of the fluid. The variation is non-linear and the effectiveness of velocity measurement relies on the temperature sensitivity being higher at low heating rate, whereas velocity sensitivity is highest at higher heating rate. The calibration of such probes in nonisothermal and fluctuating environments proved to be difficult, and in view of the satisfactory operation of the thermoelectric potential probe, the thermistor probe was not developed further. A very important method of velocity and temperature measurement is hot wire anemometry, working either in the constant current mode or the constant temperature mode. The calibration of such probes in its most useful form is given by (Malcolm, 1968).

$$\Delta\phi_c(Pe') = \pi K_f L(T-T_f) \frac{(P + P_e')^2}{P} \{\Delta\phi^{-2}(0) - \Delta\phi^{-2}(Pe')\}$$

where L is the length of the sensor, k_f the thermal conductivity of the fluid and Pe' is the Péclet number, $\Delta\Phi$ the sensor output. In the presence of both temperature and velocity fluctuation, the calibration is difficult since basically it is like the thermistor measuring device and at no finite control current the sensor works exactly cold. With accurate determination of the temperature and velocity coefficients at at least three temperature levels, individual measurement of T and V is theoretically possible,

but in practice it does not seem simple at all, and therefore was excluded from consideration.

Niblett (1958) used the radioactive isotope of Hg as a tracer particle within the fluid, but the effectiveness of the detection system is dubious; Niblett's results do not lead to any definite conclusive interpretation. Yet another method of velocity measurement would be provided by viscometers as used by Donnelly (1958). Very little is known about ultrasonic measurements in MHD.

3.4.8 Probe traversing mechanism

The presence of the heater coil and the cooling water jacket did not permit the positioning of the probe assembly straight into the TEMHD section as is done in MHD experiments (Holroyd, 1975) for the straight duct TEMHD experiments for internal measurements. As described later in Chapter 4, the probe assembly was inserted from one longitudinal end of the TEMHD section, and could be controlled to give measurements at continuously variable axial and azimuthal positions, but for only 5 fixed radial positions. For the square cross-sectional straight duct TEMHD experiments, the probes were inserted through a central insulated section of the duct, symmetrically positioned between two identical halves of TEMHD affected sections of the duct. In the annular duct experiment, a basic X-Y positioning device, X along r, Y along θ direction (Figure 3.19) with a controlling accuracy of radial position up to 0.025 mm and depth up to 0.625 mm was used. The system being symmetric with respect to the azimuthal direction, the validity of the symmetry was checked by manually positioning the X-Y displacement measuring device to other θ orientations.

However, the availability of very little clearance for adjusting the height of the probe between the free Hg surface and the pole face required that there should be modification of the probe depth fixing device with different stem lengths.

3.4.9 Thermoelectric property measurement

The magnitude of the TEMHD effect that can be generated very much depends on the thermoelectric property of the material used. Thus it is necessary to know the thermoelectric power of the materials to evaluate theoretically the TEMHD generated pressure difference or fluid velocity for comparison with the experimental results. Measurement of thermoelectric property of Hg has been reported by Bradley (1962), Marwaha (1967) and Ioannides *et al.* (1975). Earlier measurements are also available in the International Critical Tables, Kaye/Laby and Handbooks of Physics and Smithels (1974). Though the literature values of α_{Hg} differ from one another, at the early stages of TEMHD experimentation only very little TEMHD effect could be generated. Though great care was taken to minimise contact resistance by amalgamating copper with Hg and removing dissolved gas in Hg, the magnitude of the TEMHD effect remained 60% of the theoretically predicted values calculated with the α_{Hg} data from literature. It transpired that these experimentally observed results were poor because of the Hg being contaminated, having been taken from a previously used stock. It was therefore decided to experimentally measure the thermoelectric e.m.f. of the Cu-Hg combination being used by the conventional thermopower measurement. Basically, the conventional methods of thermopower measurement are of three categories: (i) Seebeck e.m.f. measurement, (ii) Peltier heat measurement, (iii) Thomson heat measurement. While only

category (iii) permits the evaluation of absolute thermopower of an element, categories (ii) and (iii) necessarily involve accurate calorimetric measurement and therefore are left out. Basic arrangements for such measurements are shown in Figures 3.20a,b for reference and these methods are adopted at very low temperatures near 4^{o} K with advantage. The more direct method of thermopower measurement by category (i), the Seebeck e.m.f. measurement, was adopted for convenience. The principle of such measurement is based on the equation (3.15)

$$\Delta\phi_{\substack{\alpha \\ Cu-Hg}} = \int_{T_1}^{T_2} (\alpha_{Hg} - \alpha_{Cu})dT$$

Even in this method, two ways of control are possible depending upon whether T_1 is fixed and T_2 only increased, or T_1 and T_2 both increase simultaneously, such that T_1-T_2 is very small, giving the so-called 'Integral' and the 'Differential' type of measurements respectively. Data processing in the differential mode of measurement is easier, but requires a temperature controlled chamber for the whole assembly and very small temperature difference measurement and low potential difference measurement. Thus the final choice was that of maintaining T_1 at 0^{o} C, the temperature of melting ice, and increasing T_2 by a small, electrical heater coil supplied from a d.c. source. The experimental devices used are shown in Figure 3.21a,b. Originally the Cu-Hg thermocouple assembly was made by drawing in Hg samples into the capillary glass tube by suction with the help of a vacuum pump and making epoxy sealed joints at both ends with copper strip samples taken from the pipes used in the TEMHD ducts used for the experiments. Leads to the potentiometer were taken from brazed joints at copper pipes, into which ambient temperature water ran to provide a common temperature. The

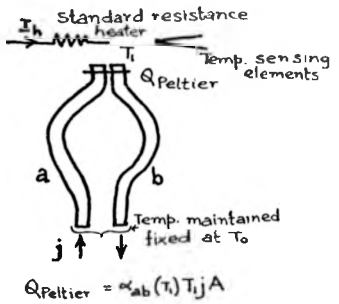

Figure 3.20(a) The basic arrangement of determining α by the Peltier heat $Q_{Peltier}$ measurement.

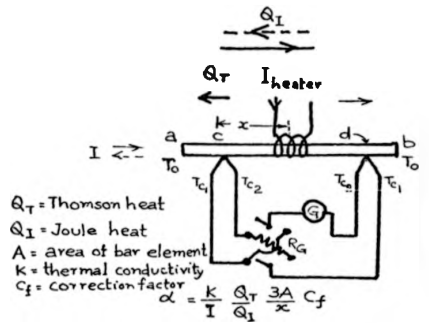

Figure 3.20(b) The basic arrangement of determining α by Thomson heat measurement.

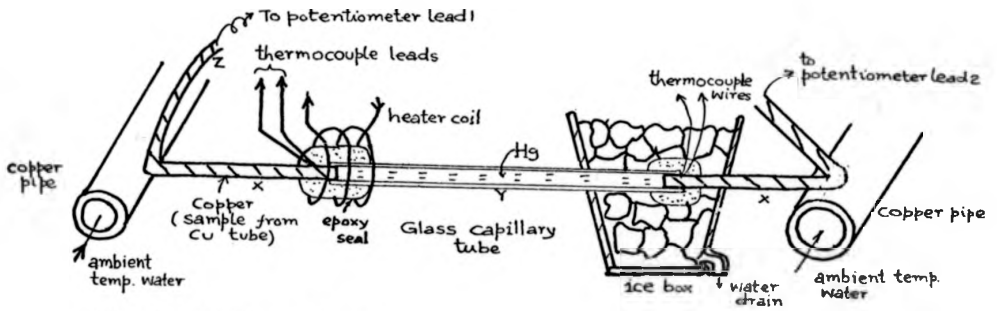

(a) The initial set up

Figure 3.21 (a,b) The experimental set up for the conventional Seebeck e.m.f. measurement by the Integral method.

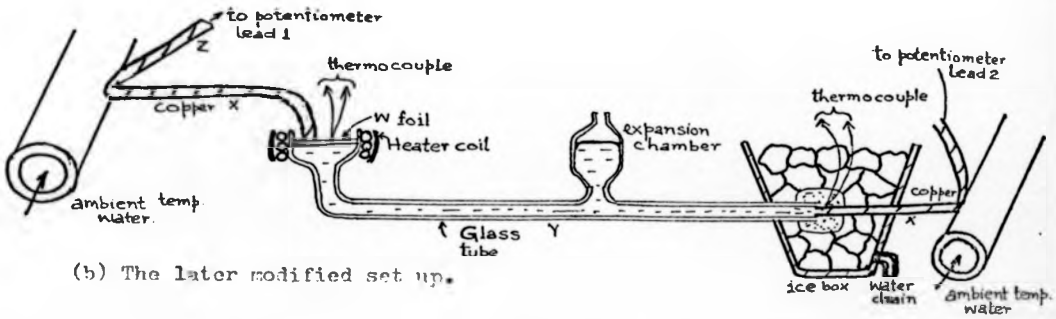

(b) The later modified set up.

capillary glass tubes were selected for such assemblies from the point of view of heat conduction, and possible movement of Hg being restricted by the narrow cross-section. The making of the epoxy seals needed considerable skill to ensure low thermal resistance, good mechanical strength and no gas void trapping. A number of such assemblies operated satisfactorily up to a temperature T_1 of 150° C, but at temperatures higher than this the epoxy seals were broken due to pressure of expansion of Hg and this could be detected immediately by the absence of continuity of the electrical circuit. The modified version of the assembly is shown in Figure 3.21b where an expansion space is provided at the central section of the capillary tube and the heated end joint was replaced by a free float of tungsten foil on the surface of Hg. Heater coils are shown in position. The thermocouples were brazed to the copper strip nearest to the end that made the Cu-Hg thermocouple joint. The glass capillary containing Hg and the copper strips were kept in a horizontal position in the gap between the pole pieces of the 'Lintott' II electromagnet which provided the transverse vertical magnetic field when thermopower was measured in the presence of magnetic field.

Out of repeated measurements on a number of samples, three representative classes of characteristics evolved and these experimental results of Seebeck e.m.f. *versus* temperature T_1 are shown in Figure 3.22 for (a) the contaminated Hg initially used, (b) distilled Hg (Harrison Clark Ltd.) and (c) Hg treated chemically and cleaned in the laboratory. Clearly the contaminants present were responsible for the 25% to 30% lower value of α_{Cu-Hg} compared to α_{Cu-Hg} for the pure metals. Chemical and X-ray fluorescence methods of tests carried out indicated the

TABLE II Thermopower measurement Cu-Hg thermocouple $T_2 = 0^{\circ}C$

Temperature	Sample I		Sample II		Sample III Clean			
	E.m.f. in μV							
T_1 °C	B ≃ 0	B 0.1 T	B = 0	B = 0.5 T	B = 0 T	Processed B ≃ 0	Processed B = 0.11 T	B = $\frac{0.55}{0.88}$ T
20			100	90-120	100	100	90-120	90-130
21	80	69-90						
25	90	70-100						
30	110	90-120	140	130-150	150	150	140-160	140-170
35	130	100-130						
40	150	130-160	185	170-190	200	200	180-200	180-210
45	170	160-200						
50	200	180-210	230	220-230	260	250	240-260	240-260
55	220	210-240						
60	240	220-250	290	280-300	330	320	310-330	310-340
65	260	230-260						
70	280	260-280	350	340-370	400	390	380-400	380-410
75	310	300-340						
80	330	300-340	410	410-450	480	470	460-470	460-480
85	360	330-370						
90	400	380-410	475	500-520	560	550	530-560	540-570
95	420	390-430						
100	440	410-440	560	590-610	640	630	630-650	630-660

(continued)

TABLE II (continued)

105	470	430–460						
110	510	460–490	600	660–680	720	700	690–720	690–730
115	530	490–530						
120	570	520–560	700	740–760	800	780	780–810	790–820
125	600	570–620						
130	640	580–630	790	820–840	890	870	870–900	880–910
135	670	620–660						
140	700	660–700	880	910–930	980	960	950–970	960–990
145	730	690–730						
150	770	730–770	975	1000–1010	1090	1070	1050–1080	
155	800	790–810						
160	840	820–850	1060	1100–1130	1190	1170		
165	880	880–910						
170	920	920–940	1155	1200–1230	1300	1270		
175	970	970–990						
180	1020	1000–1020		1320–1350	1450			
185	1050	1060–1090						
190	1100	1110–1150			1560			
200					1700			

TABLE II (continued)

105	470	430–460						
110	510	460–490	600	660–680	720	700	690–720	690–730
115	530	490–530						
120	570	520–560	700	740–760	800	780	780–810	790–820
125	600	570–620						
130	640	580–630	790	820–840	890	870	870–900	880–910
135	670	620–660						
140	700	660–700	880	910–930	980	960	950–970	960–990
145	730	690–730						
150	770	730–770	975	1000–1010	1090	1070	1050–1080	
155	800	790–810						
160	840	820–850	1060	1100–1130	1190	1170		
165	880	880–910						
170	920	920–940	1155	1200–1230	1300	1270		
175	970	970–990						
180	1020	1000–1020		1320–1350	1450			
185	1050	1060–1090						
190	1100	1110–1150			1560			
200					1700			

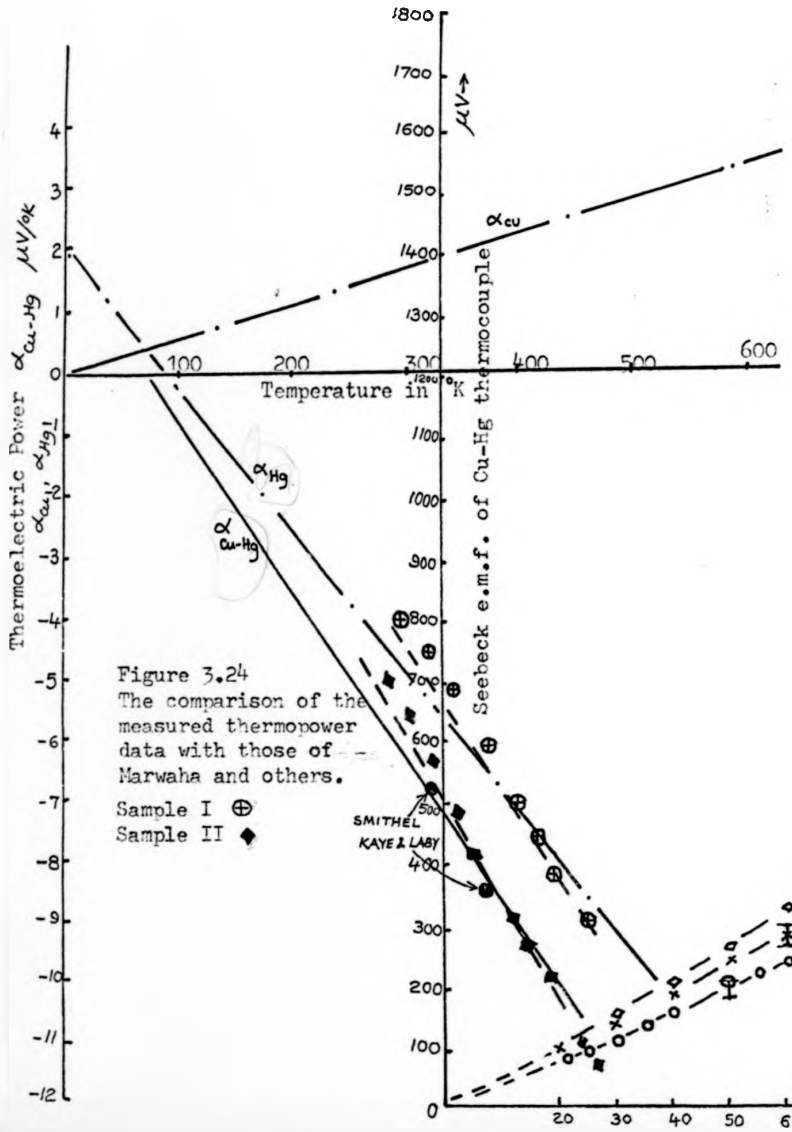

Figure 3.24
The comparison of the measured thermopower data with those of Marwaha and others.
Sample I ⊕
Sample II ◆

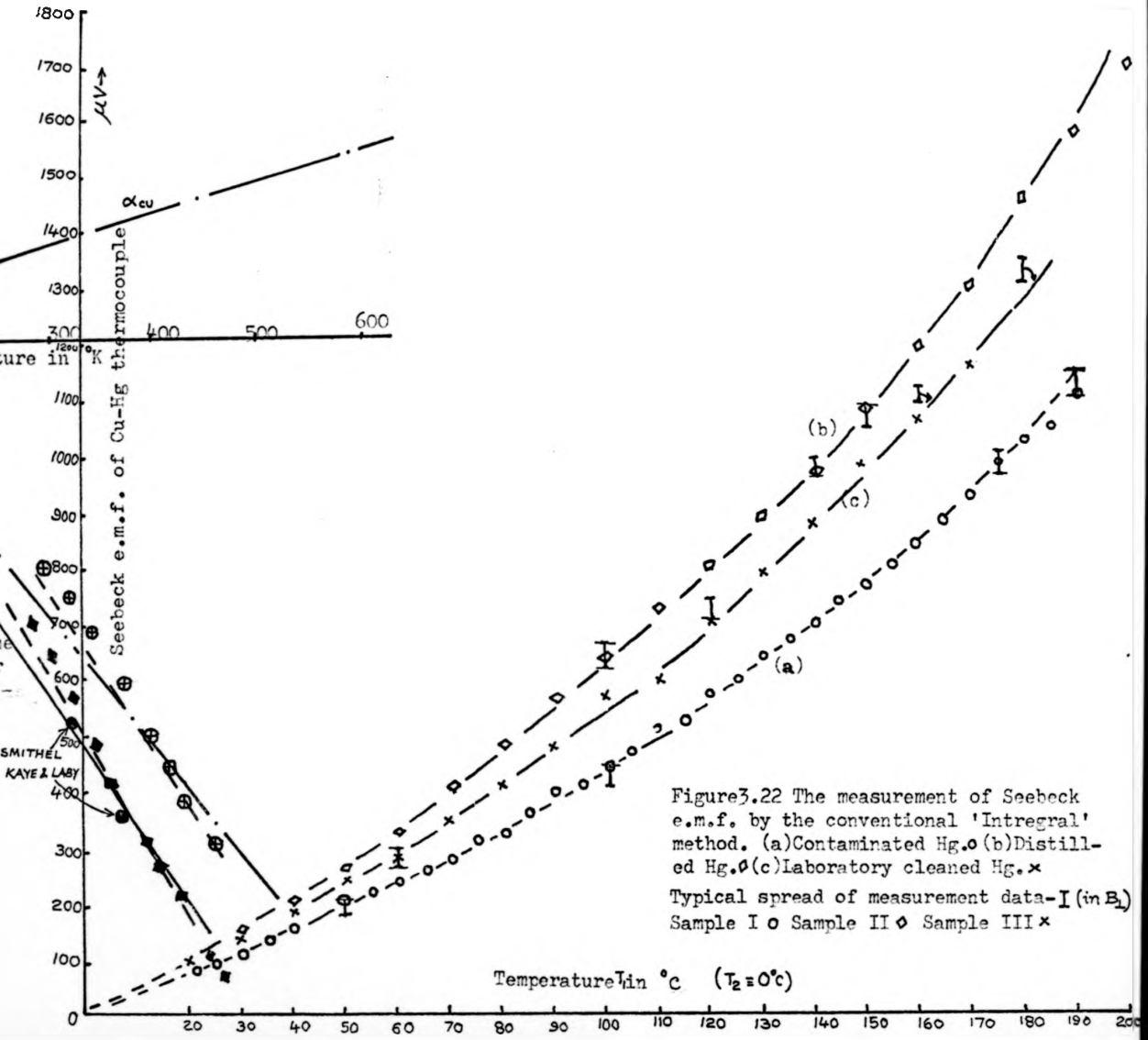

Figure3.22 The measurement of Seebeck e.m.f. by the conventional 'Intregral' method. (a)Contaminated Hg.o (b)Distilled Hg.◊ (c)Laboratory cleaned Hg.×
Typical spread of measurement data-I (in B_1)
Sample I o Sample II ◊ Sample III ×

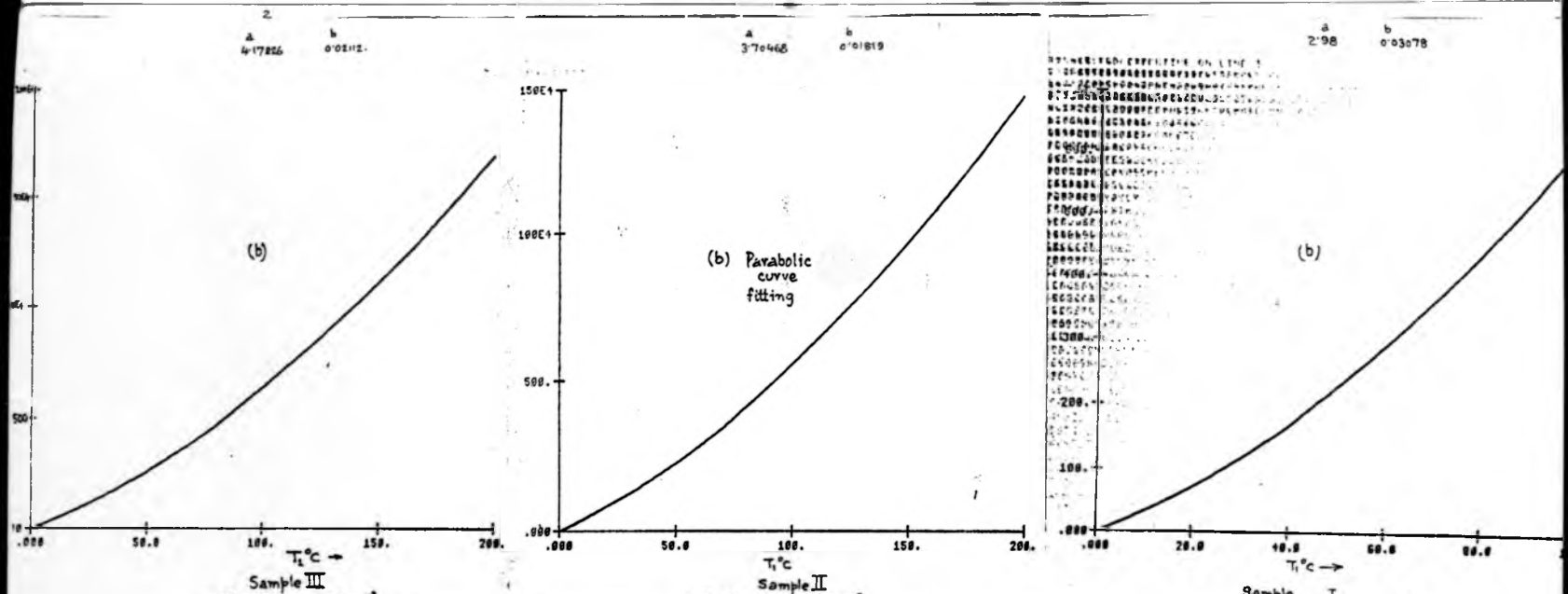

Figure 3.23 Seebeck e.m.f. measurement data processing in the digital computer. $\alpha_{Cu-Hg} = \alpha_1 + \alpha_2 T°K$ $T°K = T°C + 273$

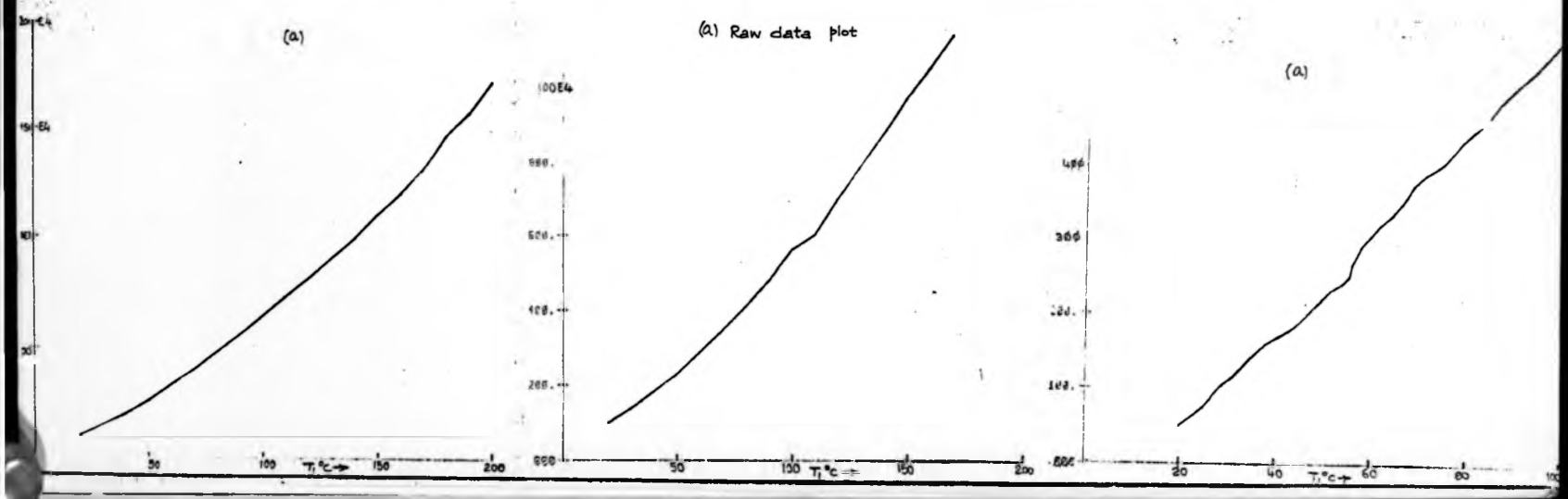

presence of metallic impurities of Sn, Cu, Zn, Cd, Pb and Ag. The experimental data of English (1893) and Fielder (1967) confirm that on the average 1% by atomic weight presence of Bi, Sn, Pb, Zn, Au. Cu reduce the thermopower of Hg by 15% whereas 1% atomic weight of Li, Ga, K, Na, In and Tl increase the thermopower of Hg by 15%. Unfortunately, quantitative assessment of the impurities present in p.p.m. could not be carried out. Data processing for the evaluation of α_{Cu-Hg} is based on the fact that from Ziman's theory the diffusion thermopower $\alpha_d = -\frac{\pi^2 K_B^2}{3/e/\epsilon_F} T\zeta \simeq A_1 T$, the dominant term at room temperature and above, and the phonon drag thermopower $\alpha_p = -\frac{Cg}{3/e/n_o} \simeq A_2 T^3$ at low temperature give $\alpha = \alpha_d + \alpha_p = A_1 T + A_o$ at room temperature and above. (K_B, Boltzmann constant, $|e|$ electronic charge, ϵ_F Ferni energy, Cg lattice specific heat, n_o electron density and $\zeta = \epsilon_F \left(\frac{d\hbar\sigma}{d\epsilon}\right)_{\epsilon = \epsilon_F}$). Therefore the raw data of Seebeck e.m.f. is fitted to the $\Delta\phi_\alpha = aT + bT^2$ relationship to evaluate a, b constants, and from there the constants A_o and A_1. The computer fitted curves for the experimental data in Table II are shown in Figure 3.23. The thermopower relationship of α_{Cu-Hg} with temperature T is shown in Figure 3.24 and for comparison Marwaha (1967) and Ioannides *et al.* (1975) data are also shown. A second method of α evaluation from the raw Seebeck data that has been employed is by the graphical evaluation of the gradient of the Seebeck e.m.f. *versus* T plot; these calculated values are plotted as discrete points in Figure 3.24. While the experimentally determined α_{Hg-Cu} *versus* T curve for clean Hg matches the data of Marwaha (1967) and Ioannides *et al.* (1975) in the working range of temperature 273° K to 473° K, the fitted α_{Hg-Cu} curve shows more temperature dependence of α. The values of α_{Hg-Cu} from

the gradient of Seebeck e.m.f. versus T curve shows not only a higher temperature dependence but also a higher power of T variation which raises doubts about the validity of the $\alpha = a + bT$ relationship. Bradley (1962) also has observed such increases, but has later dismissed such effects by attributing them to be caused by the volume expansion of Hg. The Seebeck e.m.f. measurement has been repeated for the Cu-Hg samples in a transverse magnetic field $B_{\perp}$. While the average value of the Seebeck e.m.f. did not differ significantly from the measurements in the absence of the field (variation $\simeq$ 2% on the average), the presence of $B_{\perp} \geq 0.05$ Tesla caused fluctuations in ϕ_{α} values with respect to time to the tune of 20 to 40 μV. Since quantum oscillations of thermopower in single crystals, in magnetic field (Trodahl (1969)) is expected at low temperatures only, being blurred out at higher temperatures, no conclusive reason could be arrived at for such fluctuations in α values. In Figure 3.22 the magnitude of such fluctuation in α values is shown by the bar height. No comparison of such data could be made in the absence of α_{Cu-Hg} data in a transverse magnetic field in the literature. The thermopower evaluation of α_{Cu-Hg} in this thesis does not include any correction due to volume expansion of Hg and its electrokinetic phenomenon.

3.4.9.1 Mercury handling and cleaning

Mercury was filled into the experimental channels under gravity and by suction of a vacuum pump. The connecting tubes were of flexible PVC, tufnol, copper and stainless steel. Glued or plastic band joints were used at the connecting points inside the magnet and jubilee clips outside the magnet. The mercury channels were housed in stainless steel or PVC trays to arrest Hg in case it leaked through the joints. Hydraulic pumping of Hg

was done by a Watson-Marlow orbital lobe flow inducer and a stainless steel gear pump. Mercury was drained out of the channel at the lowest point. Pinchcocks and valves were used to stop and regulate the flow of mercury. Spilled mercury was collected in a Hg trap by suction through the Edwards vacuum pump. Continuous PVC matting with a slope of 1 in 24 on the MHD laboratory floor facilitated the free movement of spilled Hg into a collecting trough. The toxic vapour of Hg was removed by approximately 2/3 air change per minute by a 100 cubic metre per minute capacity fan running at 910 r.p.m. However, the operation of the fan interfered with the experimental measurements due to vibration, and it had to be put off during experimental runs. The heating of Hg caused excessive toxic vapour and its level was monitored by a Hendrey type E 3472 mercury vapour concentration detector in µgramme per cubic metre. Medical checks for Hg absorption were frequently carried out, and experimental runs had to be suspended whenever overdose exposure was detected.

The cleaning procedure for contaminated Hg in the laboratory was as follows. The solid scum that floated on the Hg surface,after bubbling air through the bulk of Hg, was first removed with a wiper. This always quickened the cleaning through the next few steps. Hg was then filtered through very fine pores to remove the last traces of filterable material and the fine droplets of Hg were allowed to trickle through a column of dilute NaOH. The Hg collected from the bottom of the column after repeated runs was washed in a column of distilled water. It was then trickled in fine droplets through a dilute HNO_3 column, starting with a 15% solution and then down to 5%.

Finally, copious wash in distilled water followed by three hours of exposure to vacuum gave consistent values of thermopower as reported in section 3.4.9, Figure 3'24b. Skimming the scum, keeping the free surface of Hg under a thin layer of distilled water or very dilute HNO_3 acid in the annular rig experiment prolonged the duration of experimental runs without having to clean the Hg to a fortnight. By that time leaks developed, and the rigs had to be emptied for repair,and the Hg was treated at the same time.

CHAPTER 4

THERMOELECTRIC MAGNETOHYDRODYNAMICS IN CIRCULAR CROSS SECTIONAL STRAIGHT DUCTS

4.1 Introduction

The choice of the uniform, circular cross-sectional straight duct for the first of the set of experimental investigation of TEMHD was guided by two reasons:- (i) the circular cross-sectional duct is the most commonly formed and widely used one in plumbing and heat exchangers, (ii) the axial symmetry, the absence of discontinuity or sharp corners along the periphery admits analytical solutions in the exact form.

The subsections are organised in the following order. In section 4.2 a simple analysis of a stationary system with sinusoidal variation of temperature around the circumference of the duct but uniform along the length is given. The result of this analysis was first reported in the research report (Dutta Gupta, 1977) which provided a new method of measuring thermoelectric power in a transverse magnetic field. In section 4.3, general analytical treatment is presented following the analysis of Shercliff (1979a). In section 4.4 an order of magnitude calculation of temporal effect is considered. The experimental device is described in 4.5 and the experimental results are presented and discussed in section 4.6.

4.2 A Simple Analytical Model

Consider a horizontal uniform duct of circular cross-section in a uniform steady horizontal transverse magnetic field in the x direction, $\underline{B} = (B, o, 0)$. The duct is heated and cooled along the circumference in such a way that the temperature distribution along the circumference is sinusoidal (first harmonic) with the

CHAPTER 4

THERMOELECTRIC MAGNETOHYDRODYNAMICS IN CIRCULAR CROSS SECTIONAL STRAIGHT DUCTS

4.1 Introduction

The choice of the uniform, circular cross-sectional straight duct for the first of the set of experimental investigation of TEMHD was guided by two reasons:- (i) the circular cross-sectional duct is the most commonly formed and widely used one in plumbing and heat exchangers, (ii) the axial symmetry, the absence of discontinuity or sharp corners along the periphery admits analytical solutions in the exact form.

The subsections are organised in the following order. In section 4.2 a simple analysis of a stationary system with sinusoidal variation of temperature around the circumference of the duct but uniform along the length is given. The result of this analysis was first reported in the research report (Dutta Gupta, 1977) which provided a new method of measuring thermoelectric power in a transverse magnetic field. In section 4.3, general analytical treatment is presented following the analysis of Shercliff (1979a). In section 4.4 an order of magnitude calculation of temporal effect is considered. The experimental device is described in 4.5 and the experimental results are presented and discussed in section 4.6.

4.2 A Simple Analytical Model

Consider a horizontal uniform duct of circular cross-section in a uniform steady horizontal transverse magnetic field in the x direction, $\underline{B} = (B, o, 0)$. The duct is heated and cooled along the circumference in such a way that the temperature distribution along the circumference is sinusoidal (first harmonic) with the

maximum and minimum temperature at the top and the bottom respectively so that a stable thermal stratification exists. The temperature distribution along the circumference is assumed the same along the length L of the duct in the axial direction z. Let the outer radius be R_2 and the inner radius R_1. The thickness of the duct wall is $t_w = R_2 - R_1$. The duct wall has a thermal conductivity K_w and an electrical conductivity σ_w. The fluid thermal conductivity is K and the electrical conductivity is σ, both assumed constant.

4.2.1 Thermal analysis

By proposition $\frac{\partial T}{\partial z} = 0$, where T is the temperature in the stationary system, not affected by the fully developed flow along the axial direction.

If the joule heating, Peltier and Thomson heat are ignored,

$$\frac{1}{r}\frac{\partial}{\partial r}\left(r\frac{\partial T}{\partial r}\right) + \frac{1}{r^2}\frac{\partial^2 T}{\partial \theta^2} = 0 \qquad (4.1)$$

The general solution of the two dimensional Laplace equation by the method of separation of variables is

$$T = a_o + c_o \ln r + \sum_{n=1}^{\infty} r^n (a_n \cos n\theta + c_n \sin n\theta) + \sum_{n=1}^{\infty} r^{-n} (f_n \cos n\theta + g_n \sin n\theta) \qquad (4.2)$$

where the physical condition that T is a single valued function of θ is used.

Let the temperature distribution at $r = R_2$ be given by

$$T = T_m \sin\theta \qquad (4.3)$$

Then (4.2) simplifies to

$$\begin{aligned} T &= \left(a_{w1} r + \frac{g_w}{r}\right)\sin\theta \qquad && R_1 \le r \le R_2 \\ &= a_1 r \sin\theta && 0 \le r \le R_1 \end{aligned} \qquad (4.4)$$

Applying the simple boundary condition from (3.31)

$$\lim_{r \to R_1^+} T = \lim_{r \to R_1^-} T \qquad (4.5)$$

and $K_w \left(\frac{\partial T}{\partial r} \right)_w \Big|_{R_1^+} = K \left(\frac{\partial T}{\partial r} \right) \Big|_{R_1^-}$

$$T = \frac{R_2 T_m}{R_1^2 (K_w - K) + R_2^2 (K_w + K)} \left\{ (K_w + K) r + \frac{R_1^2}{r} (K_w - K_1) \right\} \sin\theta \quad , R_1 \leq r \leq R_2$$

$$= \frac{2 K_w R_2 T_m}{R_1^2 (K_w - K) + R_2^2 (K_w + K)} \left\{ r \sin\theta \right\} \quad , 0 \leq r \leq R_1 \qquad (4.6)$$

In the absence of joule, Peltier and Thomson heat the fluid is therefore thermally stably stratified, the same temperature at a given horizontal level. This ideal case avoids the thermal instability that might arise due to local adverse temperature gradient.

In practice it is more appropriate to consider the interface temperature at the top and the bottom as T_1 and T_2 ^{o}K respectively.

Then $T = T_{av} + T_m \frac{r}{R_1} \sin\theta \qquad 0 \leq r \leq R_1 \qquad (4.7)$

where $T_{av} = \frac{T_1 + T_2}{2}$ and $T_m = \frac{T_1 - T_2}{2}$

4.2.2 The thermoelectric circuit analysis

First suppose the fluid is so constrained that there is no flow of the fluid.

Since the fluid does not move, there is no $\underline{V} \times \underline{B}$ e.m.f.

By symmetry, $j_x = 0$

Therefore the electrical circuit is as shown in Figure 4.1.

Assume no contact resistance at the interface.

For the elemental circuit shown in Figure 4.1, the Seebeck e.m.f. $= 2\alpha_{av} T_m \sin\theta$ with $\alpha = \alpha_1 + \alpha_2 T$, $\alpha_{av} = \alpha_1 + \alpha_2 T_{av}$

Applying the current conservation at the interface and the voltage balance in the elementary circuit

$$j_y = \frac{\sigma}{R_1} \left(1 + \frac{\sigma R_1}{t_w \sigma_w} \right)^{-1} \alpha_{av} T_m \qquad (4.8)$$

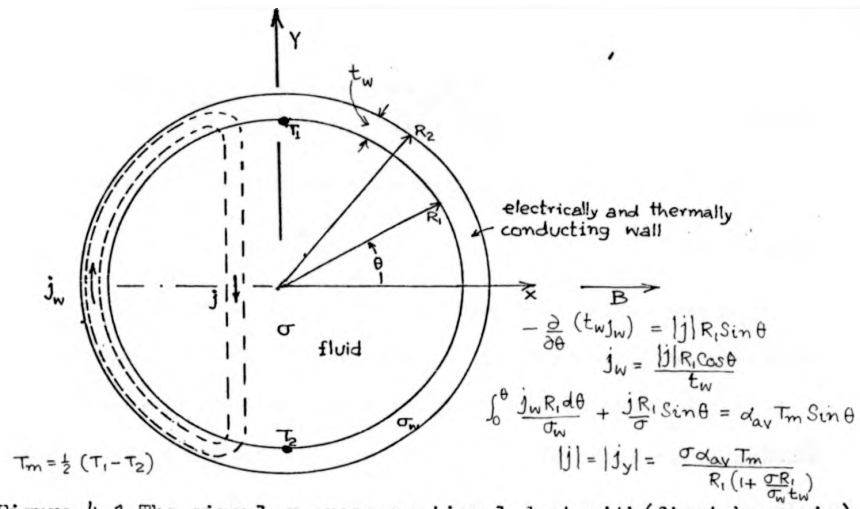

Figure 4.1 The circular cross-sectional duct with(first harmonic) sinusoidal temperature variation around the periphery.The elemental current path is shown for the simple analysis of section 4.2 .

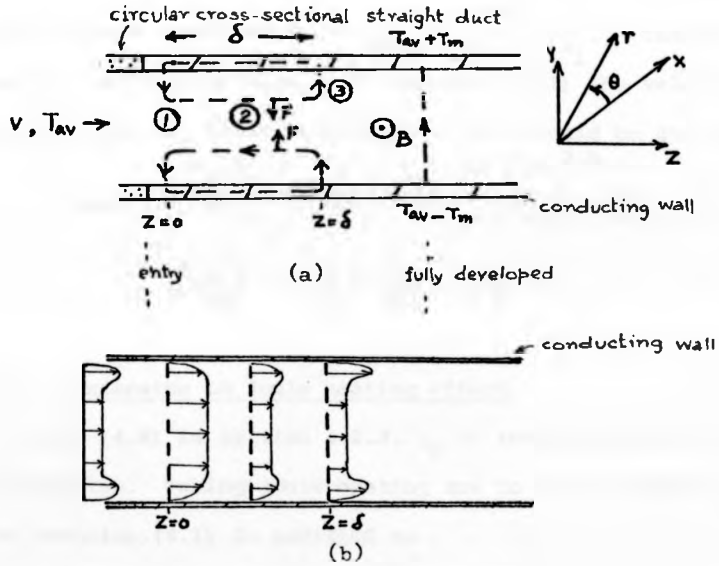

Figure 4.2 (a) The simplified TEMHD entry problem. (b) The corresponding expected velocity profile in the vertical plane YZ.

From (3.4) $$\frac{\partial p}{\partial z} = j_y B = \frac{\sigma \alpha_{av} T_m B}{(1 + c) R_1} \qquad (4.9)$$

Therefore, for an effective length L

$$\Delta p = \frac{\sigma \alpha_{av} T_m B L}{(1 + c) R_1} \qquad (4.10)$$

This gives a new method of thermoelectric power α_{av} measurement for fluids of known σ by measuring the pressure difference created across a length L due to TEMHD effect in a transverse magnetic field B in a circular cross-sectional duct of inner radius R_1, the temperature varying sinusoidally around the interface; c is the fluid/wall conductance ratio. For a given T_m, Δp varies linearly with B and inversely with (1 + c) and R_1. For a fixed temperature T_2 and increasing T_1, Δp has a parabolic variation with T_1 or T_m, if conductivity variation with T is ignored and α is assumed linear in T. With the flow blocked, the effect of B on thermoelectric current is to give a basic pressure gradient $\partial p/\partial z_{TEMHD} = \frac{\sigma \alpha T_m B}{(1 + c) R_1}$. Therefore, from the analysis of Chang and Lundgren (1961) the velocity in the core when the fluid is allowed to flow would be given by

$$v_{core} = \left\{ \frac{\alpha_{av} T_m}{B R_1} - \frac{c + 1}{\sigma B^2} \frac{\partial p}{\partial z} \right\} \frac{(1 - Y^2/R_1^2)^{\frac{1}{2}}}{(1 - Y^2/R_1^2)^{\frac{1}{2}} + \frac{c}{M}}$$

$$\rightarrow \left\{ \frac{\alpha_{av} T_m}{B R_1} - \frac{c + 1}{\sigma B^2} \frac{\partial p}{\partial z} \right\} \text{ as } \frac{c}{M} \rightarrow 0$$

4.2.3 Extension to joule heating effect

From (4.8) in section 4.2.2, j_y is independent of r, θ, z co-ordinates. Taking joule heating due to this constant j_y into consideration, (4.1) is modified to

$$K \left\{ \frac{1}{r} \left(r \frac{\partial T}{\partial r} \right) + \frac{1}{r^2} \frac{\partial^2 T}{\partial \theta^2} \right\} + \frac{j_y^2}{\sigma} = 0 \qquad (4.11)$$

The corresponding temperature distribution in the fluid with the interface temperature still maintained sinusoidal with respect to θ, with an amplitude T_m over air average value T_{av} is given by

$$T = T_{av} + \frac{T_m r}{R_1} \sin\theta + (R_1^2 - r^2) \frac{j_y^2}{4K\sigma}, \quad 0 \leq r \leq R_1 \qquad (4.12)$$

It would be appreciated from (4.12) that though the joule heating is much smaller than the heat conduction rate, yet it introduces local adverse temperature gradient in the central zone.

The Peltier heat and the Thomson heat would further increase the adverse temperature gradient.

4.2.4 Offset sinusoidal temperature distribution

Consider next the sinusoidal circumferential temperature distribution to be such that the maximum and minimum temperatures T_1 and T_2 respectively do not correspond to the top and bottom temperatures. Suppose the temperatures T_1 and T_2 lie at the end of a diameter at θ' from the horizontal diameter in the anti-clockwise direction. In such a case, the fluid is not thermally stably stratified and secondary flow due to buoyancy force would be initiated in planes z = constant. The transverse magnetic field, however, restricts such secondary circulation. When the secondary circulation can be ignored, with no flow,

$$j_x = \frac{\sigma}{(1 + c)R_1} \alpha_{av} T_m \cos\theta' \qquad (4.13)$$

$$j_y = \frac{\sigma}{(1 + c)R_1} \alpha_{av} T_m \sin\theta' \qquad (4.14)$$

Equation (4.10) now corresponds to

$$\Delta p = \frac{\sigma BL}{(1 + c)R_1} \alpha_{av} T_m \sin\theta' \qquad (4.15)$$

4.3 General Two Dimensional TEMHD Analysis

In section 4.2 a very restricted problem had been considered with the circumferential interface temperature distribution strictly sinusoidal and there being no fluid flow; this may be termed as a TEMH-static problem. In general, the interface temperature distribution can be an arbitrary function of θ though uniform along z. Fourier representation of a general T(θ) around the interface may be given by

$$T = T_{av} + \sum_n T_{cn} \cos n\theta + \sum T_{sn} \sin n\theta \qquad (4.16)$$

$$n = 1, 2....$$

where θ is measured anticlockwise from the horizontal diameter.

Professor Shercliff has given the analysis for TEMHD flow in a circular duct whose wall thickness t_w is much less than the duct cross-sectional radius R_1, when the Hartmann number M is much greater than $C = \frac{R_1\sigma}{t_w\sigma_w}$, ignoring any secondary flow due to buoyancy effects. Essentially the analysis is as follows for inviscid inertialess flow.

From (4.16), (3.57), (3.53) and (3.54) with $y = R_1 \cos\theta$ and $x_2 - x_1 = 2R_1 \cos\theta$

$$\frac{R_1}{2\sigma_w}(j_{w_{x_2}} - j_{w_{x_1}}) - R_1 \frac{d}{d\theta}\left(j_x \frac{\cos\theta}{\sigma} + \sum_n n\alpha_{av} T_{cn} \sin n\theta\right) = 0 \qquad (4.17)$$

$$t_w(j_{w_{x_2}} + j_{w_{x_1}}) + j_y(2R_1 \cos\theta) = 0 \qquad (4.18)$$

and $$t_w \frac{dj}{d\theta}_{w_{x_2}} = R_1(j_x \cos\theta + j_y \sin\theta) \qquad (4.19)$$

From (4.17), (4.18) and (4.19)

$$\frac{d^2}{d\theta^2}(j_x \cos\theta) - c\, j_x \cos\theta = \alpha_{av} \sum_n \frac{n^2\sigma}{R_1} T_{cn} \cos n\theta \qquad (4.20)$$

The solution of (4.20) is

$$j_x \cos\theta = g_1 \exp\sqrt{c}\theta + g_2 \exp(-\sqrt{c}\theta) - \sum_n \frac{\sigma}{R_1} \frac{\alpha_{av} T_{cn} \cos n\theta}{\frac{c}{n^2} + 1} \qquad (4.21)$$

For finite j_X at $\theta = \pm\pi/2$, g_1 and g_2 must be zero giving

$$j_X = \sum_n \frac{n^2 \sigma \alpha_{av} T_{cn} \cos n\theta}{R_1 (c + n^2) \cos\theta} \quad , \ n \text{ odd only.} \tag{4.22}$$

Thus $j_X = 0$ only if $T_{cn} = 0$. In such a case from (3.52)

$$V = \text{constant, independent of } x$$

From (3.55) and (3.56) , $T_{cn} = 0$

$$BV(y) = \sum_n \frac{n \alpha_{av} T_{sn} \cos n\theta}{R_1 \cos\theta} + \frac{j_y}{\sigma}(1 + c) \tag{4.23}$$

Integrating over the tranverse cross-section for the mean velocity V

$$\pi R_1^2 V = \int_0^{\pi} \sum_n \frac{n \alpha_{av} T_{sn} \cos n\theta . 2R_1^2 \cos^2\theta d\theta}{BR_1 \cos\theta} + \int_0^{\pi} \frac{j_y (1 + c)}{B\sigma} . 2R_1^2 \cos^2\theta d\theta \tag{4.24}$$

giving $V = \frac{\alpha_{av} T_{s1}}{BR_1} - \frac{1 + c}{\sigma B^2} \frac{dp}{dz}$ where (3.49) has been used.

Thus the mean velocity depends only on the first harmonic amplitude T_{s1}. When the flow is blocked

$\frac{dp}{dz} = \frac{\sigma \alpha_{av} T_{s1} B}{R_1 (1 + c)}$ which confirms (4.9). It is to be noted that the present analysis is based on high Hartmann number, but (4.9) is not so restricted, and therefore the $\frac{dp}{dz}$ expression holds for any value of M.

From (4.24) it can be seen that only the first harmonic of temperature distribution $T_{s1} \sin\theta$ contributes to the mean velocity V. The TEMH-static pressure gradient similarly depends on the first harmonic of the circumferential temperature distribution.

Returning to equation (4.22)

if (a) $T_{cn} = 0$ for all $n = 1, 2, \ldots\ldots$, $j_X = 0$

if (b) $T_{c1} \neq 0$, $T_{cn} = 0$ $(n > 1)$ } $j_X = \frac{\sigma \alpha_{av} T_{c1}}{R_1 (1 + c)}$ = constant, independent of x and y

if (c) $T_{cn} \neq 0$ $n > 1$

$$j_x = \sum_n \frac{n^2 \sigma \alpha_{av} T_{cn} \cos n\theta}{R_1 (c + n^2) \cos\theta} \quad , n \text{ odd only.}$$

giving $\frac{dj_x}{dy} \neq 0$

Under such cases $\frac{\partial v}{\partial x} \neq 0$ and a vorticity component perpendicular to the magnetic field would persist.

The simple theoretical model adopted here does not reveal immediately that there would be a vorticity component $\frac{\partial v}{\partial x}$ due to T_{sn}, $n > 1$. In addition, even with a two-dimensional temperature distribution, buoyancy-driven vorticity along z direction would occur. These vorticity components would never be completely suppressed even in a very strong magnetic field. For a weak magnetic field, stronger vorticity might lead to TEMHD turbulence. As long as the interface temperature gradient is maintained, this TEMHD turbulence would persist. In practice, however, the interface temperature distribution would fall due to increased heat transfer by turbulence (even for a low Prandtl number fluid). This might lead to oscillatory instability with temperature fluctuation in the fluid as well as in the liner material.

Consider a special case of temperature distribution of

$T = T_{av} + T_{c1} \cos\theta + T_{S1} \sin\theta = T_{av} + T_m \sin(\theta + \theta")$, along the periphery.

where $T_m = \sqrt{\frac{1}{T_{c1}^2 + T_{S1}^2}}$, $\tan\theta" = T_{c1}/T_{c2}$

then $j_x = \frac{\sigma \alpha_{av} T_{c1}}{R_1 (1 + c)} = \frac{\sigma \alpha_{av} T_m \sin\theta"}{R_1 (1 + c)}$

$$j_y = \frac{\sigma \alpha_{av} T_{S1}}{R_1 (1 + c)} = \frac{\sigma \alpha_{av} T_m \cos\theta"}{R_1 (1 + c)} \qquad (4.25)$$

are both independent of x and y if T_{c1} and T_{S1} are constant; v is therefore independent of x and is given by

$$v = \frac{\alpha_{av} T_m \cos\theta"}{R_1 B} - \frac{1 + c}{\sigma B^2} \frac{dp}{dz} \qquad (4.26)$$

(4.26) is the same as that of Professor Shercliff's derivation (1979a)

since $\theta' = \pi/2 - \theta''$ for $V = 0$

$$\frac{dp}{dz} = \frac{\sigma B}{R_1(1 + c)} \alpha_{av} T_m \sin\theta'$$

which confirms (4.15). There is no TEMHD generated vorticity but buoyancy driven vorticity is present.

4.4. Temporal and Entry Effects

The starting process, entry effects and axially non-uniform flows are very difficult to analyse, and even more difficult to devise simple experiments to verify the analytical models. In this section, a modest effort has been made to analyse some simple cases.

4.4.1 Transient time to steady pressure difference

Consider an extension of the problem considered in section 4.2 to find how much time is taken to build up the final steady state pressure gradient due to TEMHD effect against gravity force ρg with v spatially uniform at any time.

$$\rho\frac{dv}{dt} = \frac{\alpha T \sigma B}{R_1(1 + c)} - \frac{\rho g}{L} \int v dt - \sigma B^2 v/(1+c) \quad (4.27)$$

with $V = 0$ at $t = 0$

Case a

$$\frac{\sigma B^2}{2\rho(1+c)} >> \sqrt{g/L} \quad \text{then } v \simeq \frac{\alpha T}{BR_1} \{e^{-\varepsilon_1 t} - e^{-(\sigma B^2/\rho)t/(1+c)}\} \quad (4.28)$$

where $\varepsilon_1 = -\frac{\sigma B^2}{(1+c)2\rho} + \sqrt{\left(\frac{\sigma B^2}{(1+c)2\rho}\right)^2 - g/L}$. It is interesting to note that the maximum velocity during the build-up is $\frac{\alpha T}{BR_1}$

Since the final pressure gradient is given by (4-9), the time t_f for attaining this value is

$$t_f \simeq 2\left\{\frac{1}{1+c}\cdot\frac{L\sigma B^2}{\rho g}\right\} \qquad (4.29)$$

$\frac{2L\sigma B^2}{\rho g}$ may be taken as the characteristic time in which the pressure difference is steadily and uniformly built up. It is independent of the thermoelectric power α and temperature T and the wall conductance ratio c.

With Hg-Cu system with B = 1.3 Tesla and L $\simeq$ 1m

$$\frac{2L\sigma B^2}{\rho g} \simeq 25 \text{ seconds.}$$

Case b

$$\frac{\sigma B^2}{2\rho(1+c)} \ll \sqrt{\frac{g}{L}}, \quad v \simeq A_2\, e^{-\varepsilon_2 t}\, \sin(\sqrt{\frac{g}{L}})t \qquad (4.30)$$

where $\varepsilon_2 = \frac{\sigma B^2}{2\rho(1+c)}$ and A_2 depends on α, T_m, g and L.

It can be shown that the steady pressure difference is attained through an overshoot and pressure head oscillations could be generated. The characteristic time of demonstrating the pressure difference, though small is much quicker than 2 secs. The same conclusion may be drawn when $\frac{\sigma B^2}{(1+c)2\rho} = \sqrt{\frac{g}{L}}$

$$\text{giving } v \simeq A_3\, t\, e^{\left(\frac{-\sigma B^2}{2\rho(1+c)}t\right)} \qquad (4.31)$$

where A_3 depends on α, T_m, B and R_1

4.4.2 Thermal entry problem

Consider next the problem of entry into the TEMHD section. The problem is simplified by having the fluid flow fully developed in the homogeneous magnetic field in a straight channel before it enters the TEMHD section. Thus at the entry the velocity profile is that of the ordinary MHD pressure driven flow, and the temperature profile is assumed to be flat at T_{av} (isothermal). The implication of temperature profile being flat is that joule heating and viscous dissipation is ignored. There is no change in the cross-sectional area of flow at entry. If the heating and the

cooling reservoirs that maintain the temperature around the circumference sinusoidal and along the length of the TEMHD section constant were of infinite capacity, the steep temperature gradient $\frac{\partial T}{\partial y}\,|r = R$ would quickly establish a constant vertical temperature gradient in the fluid similar to the stationary fluid situation. Assume the entry length small in view of high thermal conductivity and, in any case, there is no longitudinal temperature variation along the wall. However, such infinite heat capacity reservoirs are met only in ideal situations, and in practice the temperature of the pipe wall would change over a characteristic length δ at entry. Ignoring the joule, Thomson and Peltier heat as well as viscous dissipation energy, equation (3.26) gives

$$\rho c_p V \frac{\partial T}{\partial z} = K \left(\frac{\partial^2 T}{\partial r^2} + \frac{1}{r} \frac{\partial T}{\partial r} + \frac{1}{r^2} \frac{\partial^2 T}{\partial \theta^2} + \frac{\partial^2 T}{\partial z^2} \right) \qquad (4.32)$$

Ignoring $\frac{\partial^2 T}{\partial x^2}$,

$$\rho c_p V \frac{\partial T}{\partial z} = K \left(\frac{\partial^2 T}{\partial y^2} + \frac{\partial^2 T}{\partial z^2} \right) \qquad (4.33)$$

with the boundary conditions

$$\frac{\partial T}{\partial z} = 0 \quad \text{at } z = 0,\ y = 0; \quad z = \delta \text{ for all } y$$

$$\frac{\partial T}{\partial z} = \text{finite at } z = 0,\ y \neq 0$$

and $$\frac{\partial T}{\partial y} = \frac{T_m}{R} \quad \text{at } z = \delta$$

A solution of (4.33) which satisfies all the above boundary conditions is difficult to obtain.

For a slug flow velocity $= \frac{\alpha T_m}{RB}$, an estimate of δ from (4.33) is given by

$$\delta \simeq O\left(\frac{\rho c_p V R^2}{K}\right) \simeq \frac{\rho c_p \alpha T_m R}{KB} \qquad (4.34)$$

This can be interpreted as the length over which conductive diffusion of heat must take place to compensate for the heat transported away by the fluid. With boundary layer of the velocity profile, $\delta < \frac{\rho C_p \alpha T_m R}{\kappa B}$

In the region of length δ, therefore, there is a longitudinal temperature variation with extremum at the top and the bottom of the horizontal TEMHD pipe, while at the central section there is no such longitudinal temperature variation. This is a special case, $T = T_{av}$, of the more general class of entry temperature profiles. The corresponding thermoelectric current circulation path is shown in Figure 4.2. The entry region can then be subdivided into three distinct regions: (i) where the fluid is retarded at entry near the top and the bottom boundary, and thereby increases the core flow, (ii) where the longitudinal current loop interacting with the imposed magnetic field results in creating electromagnetic vortex force. Effectively such vorticity slows down the flow in the centre of the pipe and speeds up near the top and bottom boundary wall, (iii) where the fluid is accelerated at the top and bottom boundary walls and the core flow indirectly retarded. The top and the bottom regions exactly correspond to the singular regions of Roberts (1967) where the field lines are momentarily tangential to the duct wall. Measurements of Guatynk and Paramnova (1971) indicate a 15% velocity overshoot in these regions for magneto-hydrodynamic flow in highly conducting wall circular pipe. Thus it would be expected to have a M shape velocity profile across the vertical plane, whereas across the horizontal plane the velocity profile would be flat with drooping ends. The effect of joule heating and viscous dissipation do not contribute to the electromagnetically generated vorticity, but would cause secondary circulation through thermal instability.

In the fully developed TEMHD flow for circumferential sinusoidal temperature variation without any longitudinal temperature gradient, there is no net heat extraction by the fluid. Such heat extraction is permitted in the fully developed TEMHD flow with circumferential heat flux prescribed and allowing for a constant longitudinal gradient of temperature. The velocity and temperature distribution are solutions of

$$\rho v \frac{\partial v}{\partial z} = - \partial p/\partial z + \rho \nu \left(\frac{\partial^2 v}{\partial r^2} + \frac{1}{r} \frac{\partial v}{\partial r} + \frac{1}{r^2} \frac{\partial^2 v}{\partial \theta^2} - \frac{v}{r^2} + \frac{\partial^2 v}{\partial z^2} \right) + (\underline{j} \underline{X} \underline{B})_z$$

$$\underline{j} = \sigma \quad (-\text{grad } \phi^+ + \underline{V} \underline{X} \underline{B})$$

and $$\rho c_p \nu \frac{\partial T}{\partial z} = K\left(\frac{\partial^2 T}{\partial r^2} + \frac{1}{r} \frac{\partial T}{\partial r} + \frac{1}{r^2} \frac{\partial^2 T}{\partial r^2} + \frac{\partial^2 T}{\partial z^2} \right)$$

with the boundary conditions

$$v(r,\theta,o) = V \frac{\sin\theta}{\sin\theta + c/M} \left(1 - e^{-M \cos\theta \sqrt{1-r/R}}\right)$$

$$T(r,\theta,o) = T_{av}$$

$$T(r,\theta,z_\infty) = \left(\frac{\partial T}{\partial z} \right)_c z \frac{r \sin\theta}{R}$$

$$\left. \frac{\partial T}{\partial r} (r,\theta,z) \right|_{r = R} = \frac{q(o) + q \sin\theta}{2\pi RK}$$

where q is the heat input per unit time per unit length in the flow direction z. The heat extraction rate is $\rho c_p \nu \, \partial T/\partial z$. The analysis of this problem is beyond the scope of this thesis.

4.5 Constructional Details and the Experimental Layout

The choice of the basic size of the circular cross-sectional duct with sinusoidal peripheral temperature distribution for TEMHD experiments in straight channels was guided by the fact, that it should conform to measurable TEMHD effect within the restriction posed by the air gap space of 7.6 x 15 cm^2. A steep gradient T_m/R directly increases the TEMHD effect, but with too

small a peripheral space it becomes, in practice, impossible to design heating and cooling systems to produce the required circumferential sinusoidal temperature distribution to any great accuracy. With smaller surface area available, the amount of thermal power that can be injected into the system and withdrawn from it is also restricted, giving a lower value of T_m.

The circular cross-sectional ducts were made of commercial copper pipes instead of making them out of solid copper blocks, as it was thought that the wastage of material in making such would outweigh the benefit of accuracy by avoiding porosity and impurity level. The commercial pipes tend to have their surface contaminated with carbon compounds mainly due to lubricants used during extruding. It is therefore necessary to scrape the copper surface at the inside. For reasonable cleaning convenience, the length of the TEMHD section was restricted to 0.5 metre instead of using the total length of the magnet gap, 1.5 metres, which would have given higher total Δp, though $\partial p/\partial z$ essentially remains the same. In practice, the scraping of the inner copper surface of the commercial pipes used proved to be essential for good thermal and electrical contact of copper and mercury at the interface.

For practical convenience, cooling was provided by running tap water in a jacket over the surface to be cooled instead of using thermoelectric cooling elements. Though,initially, heating was considered by using steam in a similar jacket as that of the cooling water, it was given up in favour of electrical heating. The sinusoidal heating distribution design and the mode of control of power input thus became considerably simplified.

The first of the two circular cross-sectional straight ducts was made of 2.55 cm outer diameter copper pipe with a wall thickness of 1.2 mm. The constructional details are shown in Figure 4.3. The effective length of the 0.50 m long copper pipe contributing to the TEMHD effect was 0.45 m, 2.5 cm length on either end being used up by connector lengths. These projections of the connectors into the copper pipe made seats for two 'O' rings on each to prevent any leakage of mercury. 'Tufnol' connectors specially made for this purpose were used rather than the stainless steel ones to avoid the complications of longitudinal heat transfer through stainless steel and the associated TEMHD effect in the Hg-Cu-stainless steel environment in the entry region. The pressure tappings were taken out from the 'Tufnol' connectors at either end to the vertical standpipes and the inclined tube manometer. The 'Tufnol' connectors led to the weir type of mercury reservoir, through lengths of flexible PVC tubes, 0.625 cm internal diameter. The 'Tufnol' connectors were turned to provide a tapered section to match the smooth transition from a cross-sectional area of $\frac{\pi}{4}(0.625)^2$ cm^2 to $\pi(1.15)^2$ cm^2. Glued joints at the pressure tapping proved leakfree, but the joints at the PVC tubes leading to the Hg reservoir posed leakage problems, probably due to cracking of glued seals under the stress of sheer weight of Hg. For flexibility of dismanting, steel jubilee clips were used; although the jubilee clips are magnetic, they were too far away from either end of the TEMHD section to appreciably alter the magnetic field homogeneity at the TEMHD section. However, for the final assembly, connector joints were made of special nylon gripping bands, and thus any possibility of field distortion was eliminated.

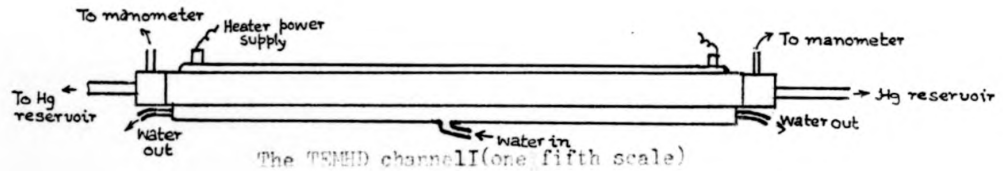

The TEMHD channelI(one fifth scale)

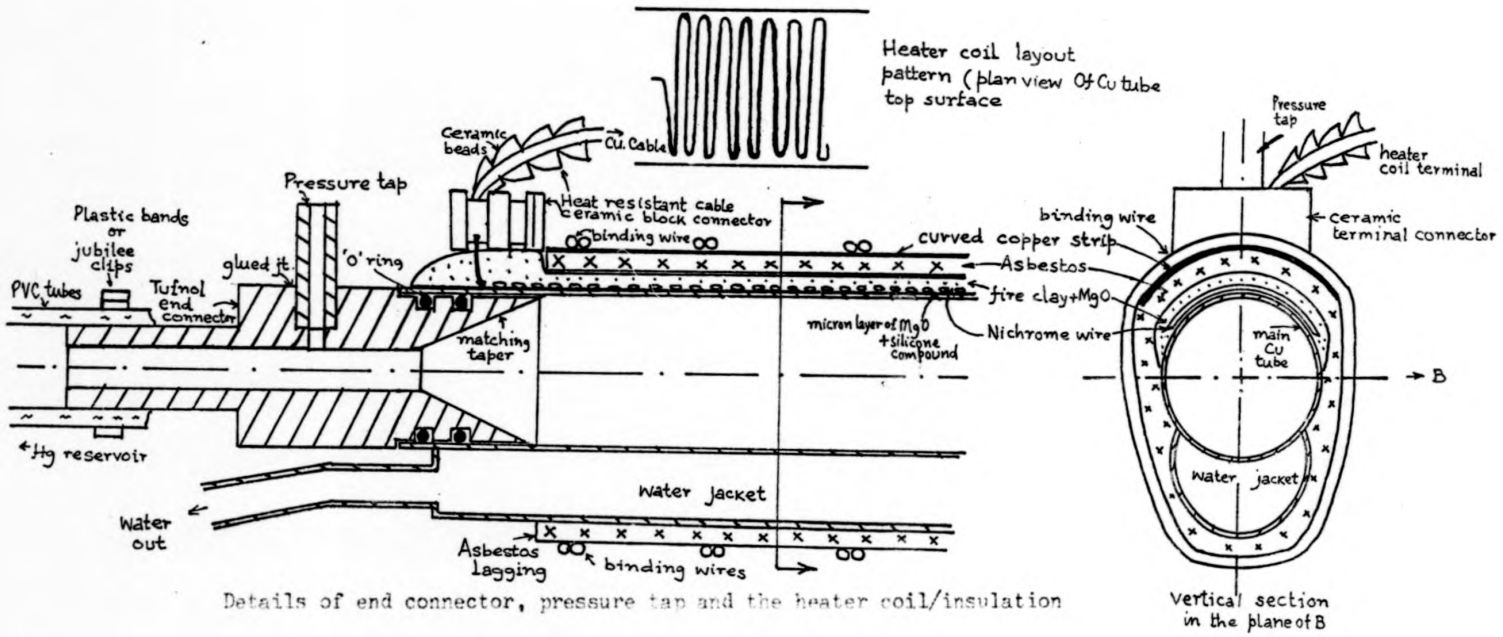

Details of end connector, pressure tap and the heater coil/insulation

Figure 4.3 The constructional details of the circular cross-sectional channel I for TEMHD experiments.

The water jacket was made on the main copper tube itself by brazing on it a longitudinally straight slotted, three-quarters of circumferential arc length, of a 2.1 cm outer diameter copper pipe. After brazing, the water jacket covered 29% of the circumferential surface of the main copper tube over a length span of 49 cm. The cooling water was taken from the tap. The tap water temperature varied from day to day, but during the experimental runs it was checked that the temperature variation of the tap water did not exceed $\frac{1}{2}^{o}$ C at the worst and $\frac{1}{4}^{o}$ C usually by monitoring the water temperature with a thermocouple. The cooling water was made to enter the water jacket at the entry port located at midlength, and the water was let out through two symmetrically located outlet ports at the two ends of the water jacket. A high rate of flow of water up to 20 litres/minute could be maintained. The proportion of the peripheral length in the jacket and the approximate parabolic velocity profile of water flow in the horizontal plane contributed in a sinusoidal circumferential cooling. A more precise control of temperature distribution would only have been possible by controlling the temperature of water flow in each of the channels of an array of cooling water tubes distributed over the main copper pipe periphery. The flow rate of the cooling water was measured by GEC-Elliott Rotameters (2000 metric 3SE) and also by timing a given discharge volume. The outlet water temperature was monitored by a thermocouple as well as by a Hg-inglass thermometer to estimate the effective heat transfer in the TEMHD device.

The heater coil was initially made of a single length of 26 SWG Nickel-Chromium wire from the Scientific Wire Co., in the shape of zig-zag coil across the central axis; the heater

coil occupied 27% of the circumferential length of the main copper pipe for a length of 48.5 cm. Insulating the heater coils electrically from the copper pipe while retaining good thermal contact with it provided a good exercise in looking for suitable materials and in efficiently using them.

The first choice was mica. The problem with it was to keep the mica strips in shape over the curved surface of the copper pipe to give compact contact without fracturing the brittle mica into flakes or powder. With heat applied to the coil, the mica tended to bulge out; because of this, and that due to magnetic force on the current carrying heater coil, the whole assembly was held in position with asbestos cover pressed down by a matched curved copper pipe length. With asbestos lagging all around retained in position by binding wires, the heat transfer in the TEMHD section could be much improved. However, even then occasional hot spots developed at places in the mica, and invariably they occurred near the grooves on the main copper pipe for the thermocouple probe.

Mica insulation was given up in favour of MgO. Applying MgO powder on the copper surface is difficult. The MgO powder was mixed with water to give a colloidal solution which, when run down the copper surface, left a very fine micron coating of the powder. Alternatively, a thin paste of MgO fire clay was made with a little addition of water, and then brushed on to the copper surface to give a coating of less than 0.1 mm. The MgO when treated with water resulted in magnesium hydroxide, and the wet compound was not a good electrical insulator. Moisture has to be removed by heating, and then the cement like, very brittle structure, that remained provided good electrical insulation. The non-availability of BN in sufficient quantity

prevented the use of BN instead of MgO. The bare heater coils laid on such a foundation were packed up with more MgO and finally fire clay and asbestos were used to provide thermal lagging to the ambient atmosphere. The fire clay, when set, provided rigidity to the coil structure and held it to the copper surface. Application of heat led to cracks appearing in the fire clay assembly and often deteriorated to the point when the heater coil separated from the copper surface. The binding wires were therefore essential to stop such development. Though it seems elementary, great care was necessary to avoid entrapped voids in such an assembly. Encasing the heater coil in MgO and fire clay prevented any oxidation of the Nichrome wire, particularly when red hot, as was always the problem when mica insulation was used. Later silicone compounds in the form of paste were available which provided a very good thermal contact with uniform wetting. MgO powder could then be sprayed on such a coating. Nichrome coils , interleaved with fibre glass to prevent electrical failure between consecutive turns of the heater coil,were then laid and finally encased with fire clay, overall asbestos lagging and kept in position by the binding wires. This final arrangement of heater assembly worked perfectly well.

The whole assembly was made to stand horizontally on tufnol blocks on wooden supports inside a PVC tray positioned in the airgap of Lintott electromagnet I. The supporting grooves on the tufnol blocks permitted the orientation of the heat transfer axis away from the vertical axis.

The second circular cross-sectional straight TEMHD channel was primarily built with the idea of internal measurements to be carried out with reasonable sensitivity and accuracy. It also

provided an opportunity of verifying the effect of wall to fluid conductance ratio of the TEMHD duct. A 5.25 cm O.D. commercial copper pipe with a wall thickness of 0.125 cm, a representative size of tube that might be used in TNR's, was chosen for this purpose. The bigger size of the TEMHD section permitted the insertion of internal probe assembly of a given size and rigidity with relatively less blockage and error. The relative error in the accuracy of the positioning device also was smaller. The total length of the copper pipe was 67 cm, so that with 8.5 cm lengths at either end being used up in accommodating the tufnol connectors and the 'O' rings, a net length of 50 cm of TEMHD section remained. The constructional details are shown in Figure 44 .

It was impossible to locate a probe insertion system like Hunt's (1967) or Holroyd's (1975) through the circumferential surface due to the heater coils, water jacket and the lagging; the air gap space restriction prevented the insertion of probes from the sides. The entry and exit connectors for the Hg loop were therefore modified to have right angle bends leaving the straight horizontal end free for probe insertion from the end. Only thermocouple potential probes have been used for the purpose. Five pairs of copper-constantan 0.2 mm diameter (ptfe insulation) thermocouple wires were led into the main copper tube along the central axis through a rigid 3 mm O.D., (bore 2 mm diameter) stainless steel tube. At the end of the stainless steel encasing tube, a stiff nylon T piece was press-fitted with a brass sleeve having a slot and integral pin type fixture to ensure rigid rotational coupling. The tips of the thermocouple probes were made bare at the end of the miniature holes in the T-piece arm to provide measurement of temperature and potential at 5 equally spaced radial positions at a given angle θ. The total length of the two arms of the T piece exactly corresponded to the

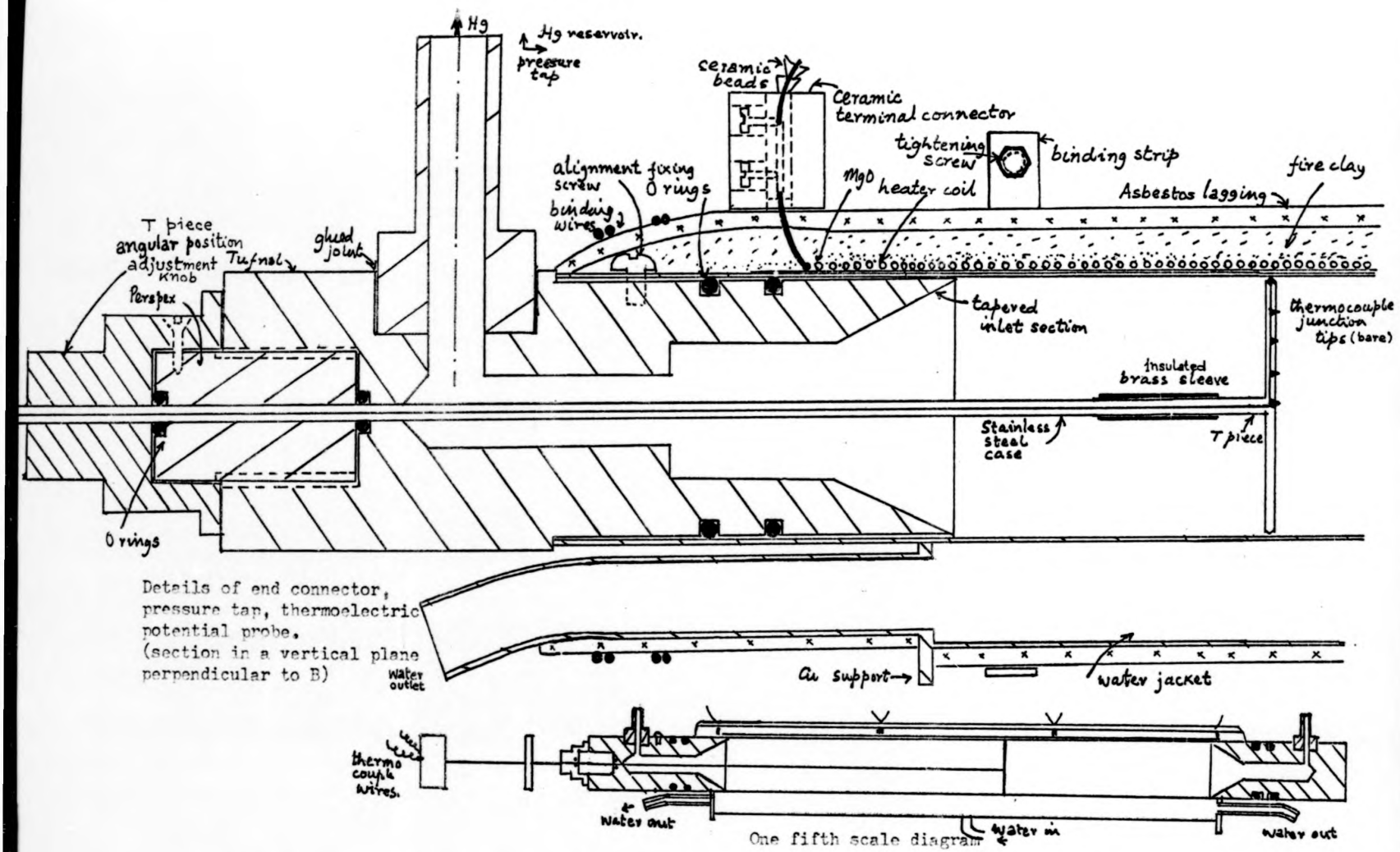

Figure 4.4 The constructional details of the circular cross-sectional straight channel II for TEMHD experiments.

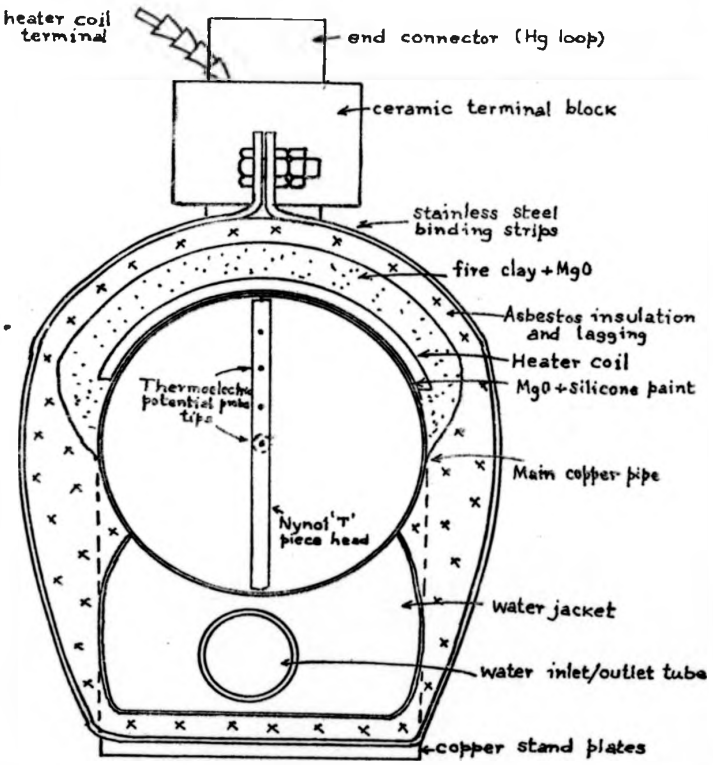

Figure 4.4 continued. Vertical section in the plane of the magnetic field..

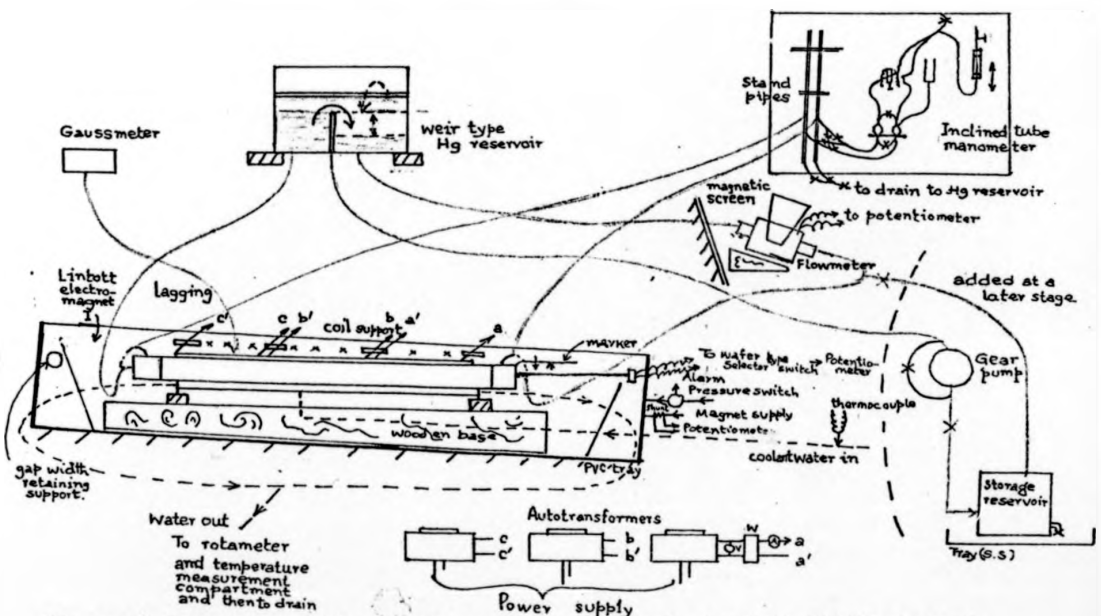

Figure 4.5 Layout of the circular cross-sectional straight TEMHD channel experiment(Not to scale).

inner diameter of the copper pipe so that the end tips just scratched around the inner copper face of the main tube. The five radially spaced thermocouple probe tips were all on one arm to provide information on one radial line orientation at a time. Initially it was thought that three more different radial locations could be achieved on the second arm of the T piece, but in practice only 10 thermocouple wires could be squeezed through the stainless steel tube. The thermocouple wires in the 2 mm internal diameter hole of the T piece were held fixed by glue. The stainless steel and the brass sleeve were encased in a thin PVC sleeve glued at the ends to prevent contact with mercury. The end seal is shown in Figure 4.4. The 'O' rings on the stainless steel tube permit the rotation of the T piece arm as well as the change of its location along the axial length. The angular orientation could be read from a graduated knob fixed to the outer exposed end of the stainless steel tube and the axial position of the T piece determined by the linear displacement of the knob position from the end face of the tufnol connector. The total length of the stainless steel tube was 62 cm, but a maximum of 35 cm in the TEMHD section could be reached from one end with ease. The flattening of the stainless steel tube in fixing the indicator knobs made it difficult to move through the close tolerance for the remaining few centimetres. The five pairs of thermocouple wires were numbered and led out to wafer selector switches to make it possible to collect, by measurement with the potentiometer or the DVM, temperature data from the corresponding thermocouple pair as well as the potential difference data between two similar material thermocouple wires from two different thermocouple junctions.

The minor points of difference in constructional details for the second channel from the first are (a) the water jacket

was made from a 1.5 mm copper sheet,bent in the form of a channel and brazed on to the main pipe. The ends of the water jacket were made of 3 mm copper plates projecting out of the jacket to act as the stands for the TEMHD channel. The size of the overall assembly,and particularly the water inlet and outlet port projections, did not permit the orientation of the heating-cooling maxima axis more than a few degrees away from the vertical as was possible with the smaller TEMHD channel. The heating maxima axis orientation away from vertical therefore was not experimentally investigated in the case of the second TEMHD channel. (b) The heater coils were made in three symmetrical sections along the length of the TEMHD section, using high surface loading (4-6 watts/cm^2, 1300^{o} C) Kanthal electrical resistance wires from Bulten-Kanthal AB, Hallstahammar,Sweden, with 0.511 mm diameter and resistivity of 139 $\mu\Omega$-cm at 20^{o} C. A maximum of 3000 watts could be applied in such a coil arrangement with an overall strip length 5 x 50 cm^2. (c) The binding wires for retaining coils in shape and position were replaced by six 1 cm wide, 2 mm thick stainless steel straps in the form of O clamps at the central section, and two sets of binding wires at the ends. (d) A higher cooling water flow rate, 25/30 litres/min could be maintained. The maximum temperature rise was 1.5^{o} C giving a maximum axial temperature variation of 6^{o} C/m, 0.15% of the corresponding vertical temperature gradient. The channel was supported by wooden blocks in a horizontal position and a plastic tray collected any leakage of mercury at the bottom.

The heating current was controlled by auto-transformers from the a.c. mains. The possible adverse effect of a.c. heating current was checked to be insignificant by observing the response

and cleaning procedure, but even then the reproducible steady readings required a waiting period of 4 weeks. Once properly amalgamated, the steady experimental results could be reproduced within the measuring accuracy of ± 1% even after 18 months. Emptying the Hg out of the channels and subsequent refilling again required a settling time of about a week.

(ii) The static pressure rise is critically affected by dissolved gases in Hg, and in particular contamination from grease. Even small traces of selective metallic impurity in Hg could cause increase or decrease in the magnitude of the pressure rise. Cleanliness of the experimental device and extreme care in filling up Hg in the channel is therefore strongly recommended for very accurate measurements in such experimentation.

(iii) Though copper and mercury are very good thermal conductors (380 and 8 watts/$m^{o}K$ respectively), there was a steep temperature drop from the red hot electric heater coil to the copper surface. Good thermal contact between the heater coil and the copper surface was therefore essential to achieve any significant level of temperature gradient in the TEMHD system

(iv) Any misalignment of the heating axis away from the vertical axis (gravity) and the transverse horizontal magnetic field used in these experiments affected the measurements. In addition, it is recommended to eliminate buoyancy effects, and therefore indirectly minimise the volume expansion of Hg in the connecting loop (external to the TEMHD section) by contriving a vertically down and then up U turn sections of the flexible PVC connecting loop next to either end of the TEMHD section, as has been done during this experimentation. Though an inclination of the longitudinal axis of the channel to the horizontal plane is recommended in isothermal MHD experiments

of the system with the heater current switched off and also by comparing the heating with a d.c. system. The heater coils were connected to heat resistant fibre glass insulating material covered copper cables via ceramic connector blocks.

The mercury loop was similar to that described in the flow meter calibration experiment with weir type of mercury reservoir. By changing the total volume of mercury in the flow loop, TEMHD flow could be investigated at different head difference levels over the weir. The flow meter in the loop recorded the average volume flow rate. When the static pressure difference was measured, the mercury volume in the loop was reduced so that the difference in head across the weir did not cause flow over the weir.

4.6 The Experiments and the Experimental Results

4.6.7 The static pressure measurement

Static pressure rise determination was the first experimental measurement to test the hypothesis that significantly discernible effect could be generated in practice by the interaction of the thermoelectric current at the non-isothermal solid-liquid interface with the magnetic field. As with any new field of investigation, a lot had to be learnt with time and experience. The difficulties faced during the initial stages of experimentation are detailed in Research Reports I and II (Dutta Gupta, 1977, 1978). The following points are summarised for recording guidelines in such experimentation:-

(i) Good amalgamation at the copper-mercury interface is essential. A settling time of several weeks was necessary before steady and reproducible results were achieved. The settling process of amalgamation could be expedited by repeated scraping

and cleaning procedure, but even then the reproducible steady readings required a waiting period of 4 weeks. Once properly amalgamated, the steady experimental results could be reproduced within the measuring accuracy of ± 1% even after 18 months. Emptying the Hg out of the channels and subsequent refilling again required a settling time of about a week.

(ii) The static pressure rise is critically affected by dissolved gases in Hg, and in particular contamination from grease. Even small traces of selective metallic impurity in Hg could cause increase or decrease in the magnitude of the pressure rise. Cleanliness of the experimental device and extreme care in filling up Hg in the channel is therefore strongly recommended for very accurate measurements in such experimentation.

(iii) Though copper and mercury are very good thermal conductors (380 and 8 watts/m^{o}K respectively), there was a steep temperature drop from the red hot electric heater coil to the copper surface. Good thermal contact between the heater coil and the copper surface was therefore essential to achieve any significant level of temperature gradient in the TEMHD system

(iv) Any misalignment of the heating axis away from the vertical axis (gravity) and the transverse horizontal magnetic field used in these experiments affected the measurements. In addition, it is recommended to eliminate buoyancy effects, and therefore indirectly minimise the volume expansion of Hg in the connecting loop (external to the TEMHD section) by contriving a vertically down and then up U turn sections of the flexible PVC connecting loop next to either end of the TEMHD section, as has been done during this experimentation. Though an inclination of the longitudinal axis of the channel to the horizontal plane is recommended in isothermal MHD experiments

to facilitate the removal of entrapped voids and gas, the channel axis was made exactly horizontal to avoid convection induced by buoyancy.

A pressure difference of 1 mm head of Hg could be increased to 5 cm of head of Hg for the same power input, channel dimensions and the magnetic field as the techniques improved. The chronological details are left out and measurement data where nonreproducibility still remained are discarded. Only the reproducible steady measurement data, some of them with a standing of 2 years, are included in the following section.

Channel I

In Figure 4.6a to g the variation of the pressure difference, Δp, measured in cms of Hg, generated by TEMHD effect in the 2.55 cm O.D. channel with the variation of the strength of the horizontal magnetic field for heating currents 2 to 5 amps in steps of 0.5 amps is shown. The heating axis was vertical and the longitudinal axis of the TEMHD section horizontal. The Hg used for this set of measurements was from the previously used stock corresponding to the conventional thermopower measurement of Sample I.

The experimental points show a definite linear relationship with the magnetic field, B, for a given heater current, though a slight departure from linearity could possibly be detected at higher B. The Δp measurements include measurement with B in the normal as well as in the reverse direction by changing the supply generator exciter polarity. The reversal of Δp by an identical magnitude when the direction of B is changed, keeping the magnitude the same for a given heating condition, could so well be verified that it provided great confidence in such TEMHD effects not being spurious thermal expansions, even when

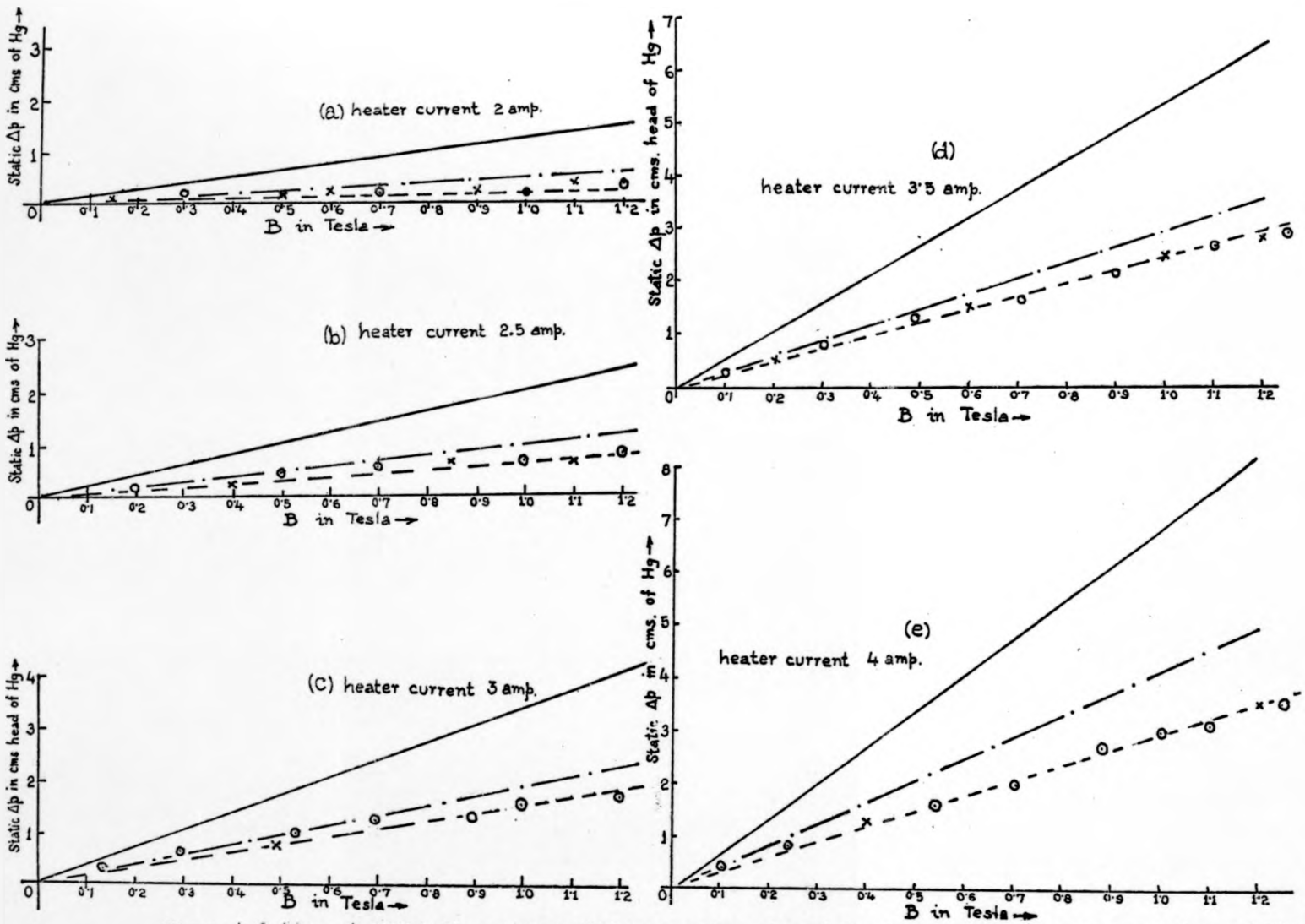

Figure 4.6 (a to e) TEMHstatic pressure difference across channel I , in cms head of Hg. Theoretical trend line with pure grade $\alpha_{Cu\text{-}Hg}$ data, —— trend line with measured(conventional)-·-data (sample I); --- experimental trend line. $\alpha_{theoretical}$

o B normal direction x B reverse direction.

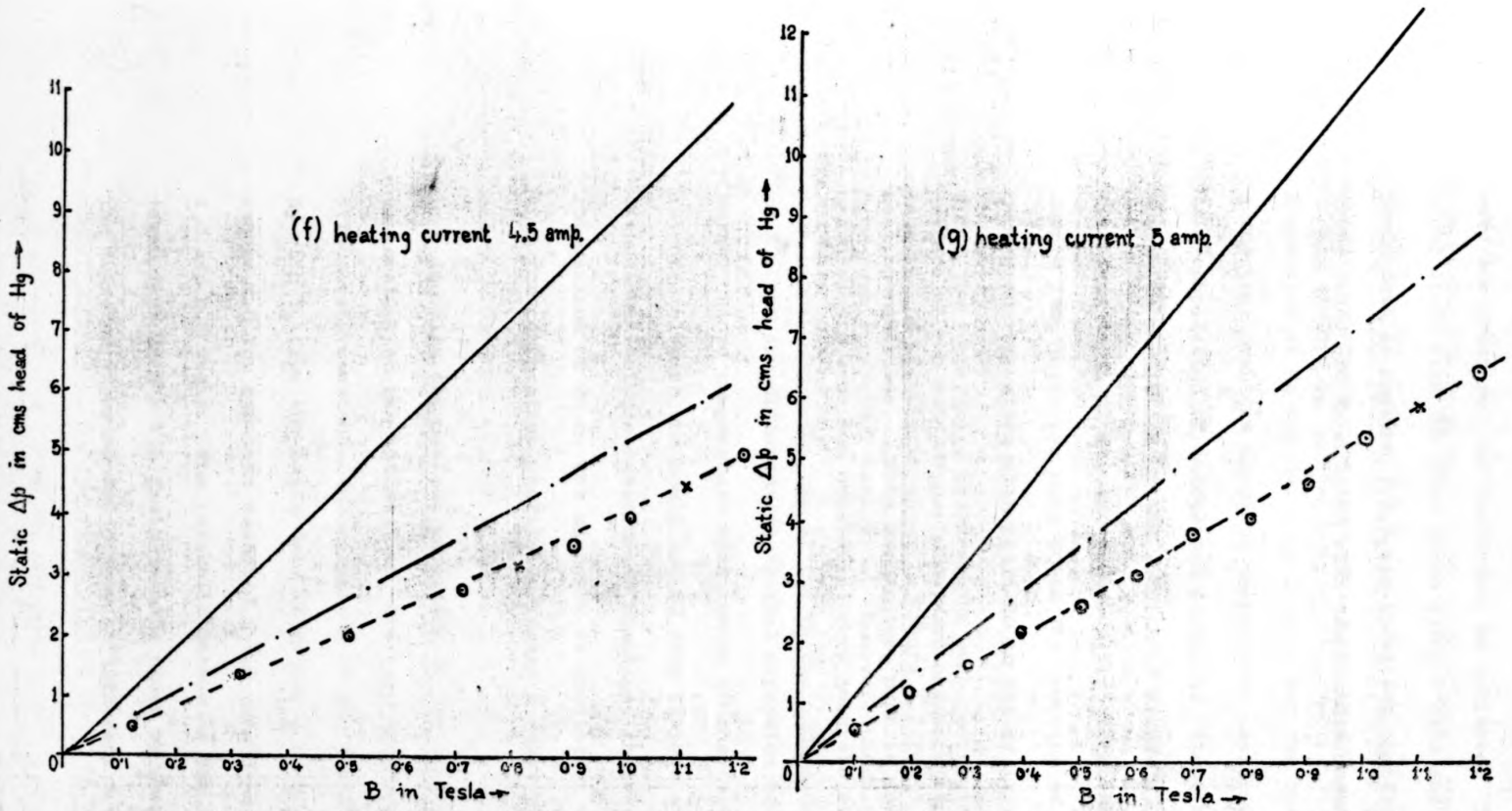

Figure 4.6 continued. (f to g) TEM static pressure difference across channel I in cms head of Hg. Theoretical trend line with pure grade α_{Al} data, ——, trend line with measured (conventional) —·—·— data (sample I), - - - experimental trend line For clarity only a few points are shown. Experimental points with B normal direction ○ reverse direction ×. For operating conditions refer to Table III

very low pressure rise could only be achieved. The theoretical trend lines with the pure grade Hg-Cu α data and the measured Hg-Cu data in section 3.4.9 are shown for comparison. These trend lines are calculated with temperature dependent physical properties of Hg and Cu. In fact, c for the channel is not a constant over the range of temperature variation. Table III is a compilation of calculated parameter values at the operating conditions of the results of Figure 4.6a to g. As seen from these plots, the lower values of the measured α of sample I Hg justifies only 80 to 75% lowering of Δp from the pure grade Δp values with still 20 to 25% of it unaccounted for. The temperature measurements were restricted to the outer surface of the main copper pipe, and one such representative temperature profile is shown in Figure 4.7 for 5 amperes heating condition. This temperature profile reveals departure from pure sinusoidal variation. However, these temperature measurements were not considered very accurate since an error of 1 mm in positioning the tip of the thermocouple made an angular error of 5^{o}, and any differential thermal expansion could make it worse. Since temperature measurement at the Cu-Hg interface is more relevant and could not be done in this smaller channel without appreciable interfering blockage, the explanation for the maximum of 20 to 25% mismatch is consistent with the fact that the temperature profile indicates a lower $T_m = T_1 - T_2$ and T_{av}.

Ignoring the maximum variation of the cooling water temperature at the outlet (1.5^{o} C), i.e. treating T_2 as effectively constant, the variation of the pressure difference Δp with T_1 from the basic data of Figure 4.6 is shown in Figure 4.8 for constant magnetic field strengths of B = 1.2, 1.0 and 0.5 Tesla. The parabolic nature of the experimental trend line at B = 1.2 Tesla is made clear by drawing rays to the measured experimental points at different T_1.

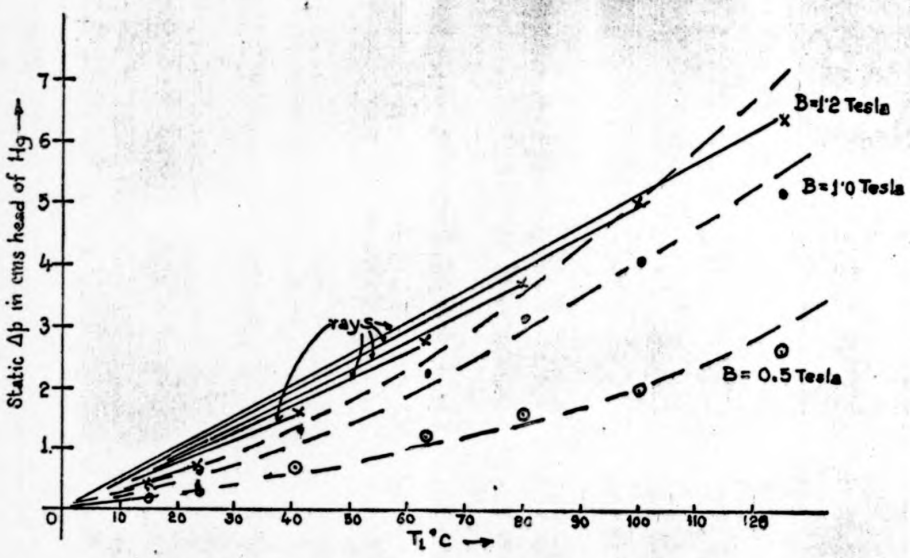

Figure 4.8 TEMHstatic pressure difference versus T_1°C with T_2° effectively constant (maximum variation 1½° C), Channel I

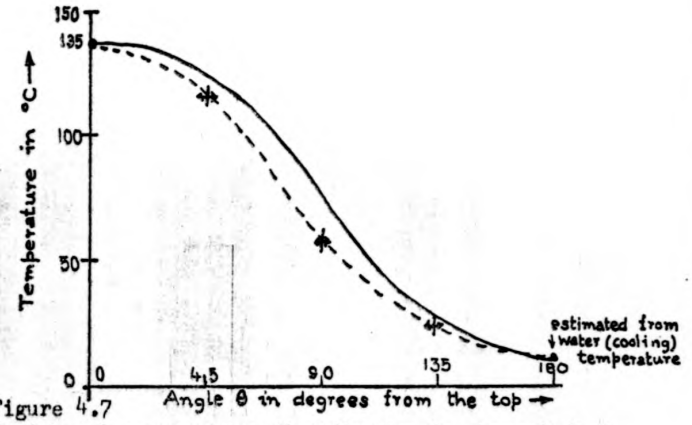

Figure 4.7
Peripheral temperature distribution in channel I at 5 ampere heating current. Sinusoidal variation from T_1 to T_2, ——— , experimental distribution ----

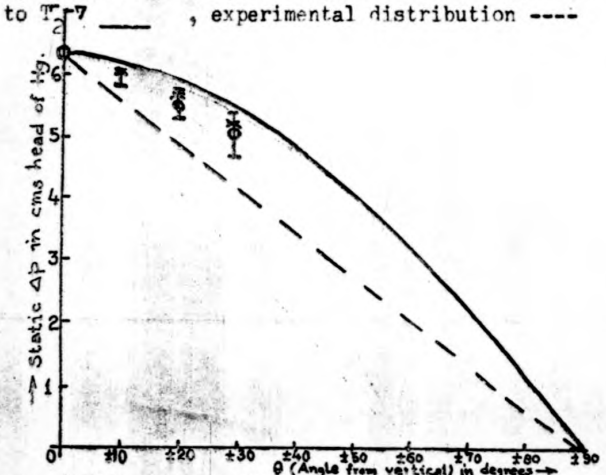

Figure 4.9 Variation of TEMHstatic pressure difference with the inclination of the externally impressed temperatur gradient axis away from the vertical (5 amp heating 1.2Tesl Channel I.

TABLE III Experimental operating condition data for Channel I and comparison of measured α values of contaminated Hg with the pure grade value

Heater voltage volts	Heater current amps	Wattage	T_1 °C	T_2 °C	ΔT	T_{av}	T_m	C	$\Delta h=\frac{\sigma\alpha T_m}{(1+c)R_1}\frac{BL}{\rho g}$	α pure grade	$\alpha_{m/s}$
210	5.0	1050 (1050)	135°C	10½°C	125°C	72½°C	62½	0.225	11.45B	7.99	5.2
186	4.5	835 (837)	110°C	10°C	100°C	60°C	50	0.214	9.09B	7.633	4.5
168	4.0	670 (672)	90°C	10°C	80°C	50°C	40	0.206	7.1B	7.345	4.3
144	3.5	500 (504)	72°C	9½°C	62°C	40½°C	31	0.2	5.35B	7.058	3.9
120	3.0	360 (360)	50°C	9½°C	41°C	29½°C	20½	0.1925	3.43B	6.75	3.8
93	2.5	230 (232.5)	33°C	9°C	24°C	21½°C	12	0.187	1.96B	6.5	3.25
72	2.0	140 (144)	24°C	9°C	15°C	16½°C	7½	0.1844	1.21B	6.393	3.0

Figure 4.9 shows the effect of shifting the heating axis away from the vertical, the longitudinal axis of the channel still being horizontal. Although the total overall dimension of the main copper pipe and the water jacket should have permitted a full orientation through 90°, the tap connectors, lagging material and the binding wire on it limited the effective orientation of the heating axis away from the vertical to 30° only (60° to 120° from the horizontal plane). A check was made with the heating from the bottom and cooling from the top. The reversal of Δp, though not by an identical magnitude for a given magnitude and direction of imposed B, confirmed the TEMHD effect. However, significant drifts in Δp were observed in such a situation, and it was not pursued further due to the complexity generated by convection (Bénard effect).

From the flow rate of water at 9 litres/min and the cooling water temperature rise an estimate of 90% heat transfer through the TEMHD section can be inferred, but the accuracy of this estimation is limited by the resolution of the temperature measuring scale of the thermometer. From Table III it could also be inferred that the temperature gradient was roughly proportional to the wattage input.

Channel II

The availability of the internal temperature measurement system in Channel II and its satisfactory performance greatly facilitated resolving the discrepancy between the theoretically predicted Δp values and the experimental results obtained in Channel I. In addition, the Hg from the distilled stack was used, having appreciated the lower thermopower value of sample I from the conventional thermopower measurement reported in section 3.4.9. The bigger dimension of the channel increased

the space resolution accuracy but at the same time excluded the possibility of experimenting with the heating axis oriented at an angle to the vertical. The heater coil power rating could be increased,but the corresponding temperature gradient was much lower than that of Channel I. The internal measurement in Hg provided further new information - temperature oscillations in Hg - though Hg was supposed to be stably thermally stratified with the sinusoidal circumferential temperature variation.

For the Δp measurements in Channel II, the heating currents in the three identical heater coils were adjusted by controlling the voltage by three separate autotransformers and monitored by ammeter-voltmeter and wattmeter measurement. The Δp measurements for various heating currents, i.e. differing levels of T_{av} and T_m, against various imposed magnetic flux density are shown in Figure 4.10. For clarity, only a few representative experimental points are shown against a background of the trend lines calculated with the pure grade α_{Cu-Hg} value. Table IV gives the corresponding operating point data and the relevant calculations based on temperature dependent pure grade Cu and Hg data. The correspondence is so close that it justifies confidence in explaining the mismatch between the theoretical and experimental Δp values in Channel I due to (i) lower α_{Cu-Hg} of sample I, (ii) uncertainty in the temperature measuring system with the then mode of thermocouple junction location. Figure 4.11 shows the measured Δp in cms of head of Hg at constant B of 1.0 Tesla and 0.5 Tesla for various T_1 values with the cooling water temperature (T_2) variation ignored ($\sim 2^{\circ}$ C except ◀ for which $\Delta T_2 = 5^{\circ}$ C). The parabolic nature of Δp variation with T_1 can easily be recognised. The Δp measurements of various values of B have been utilised in computing the average thermoelectric

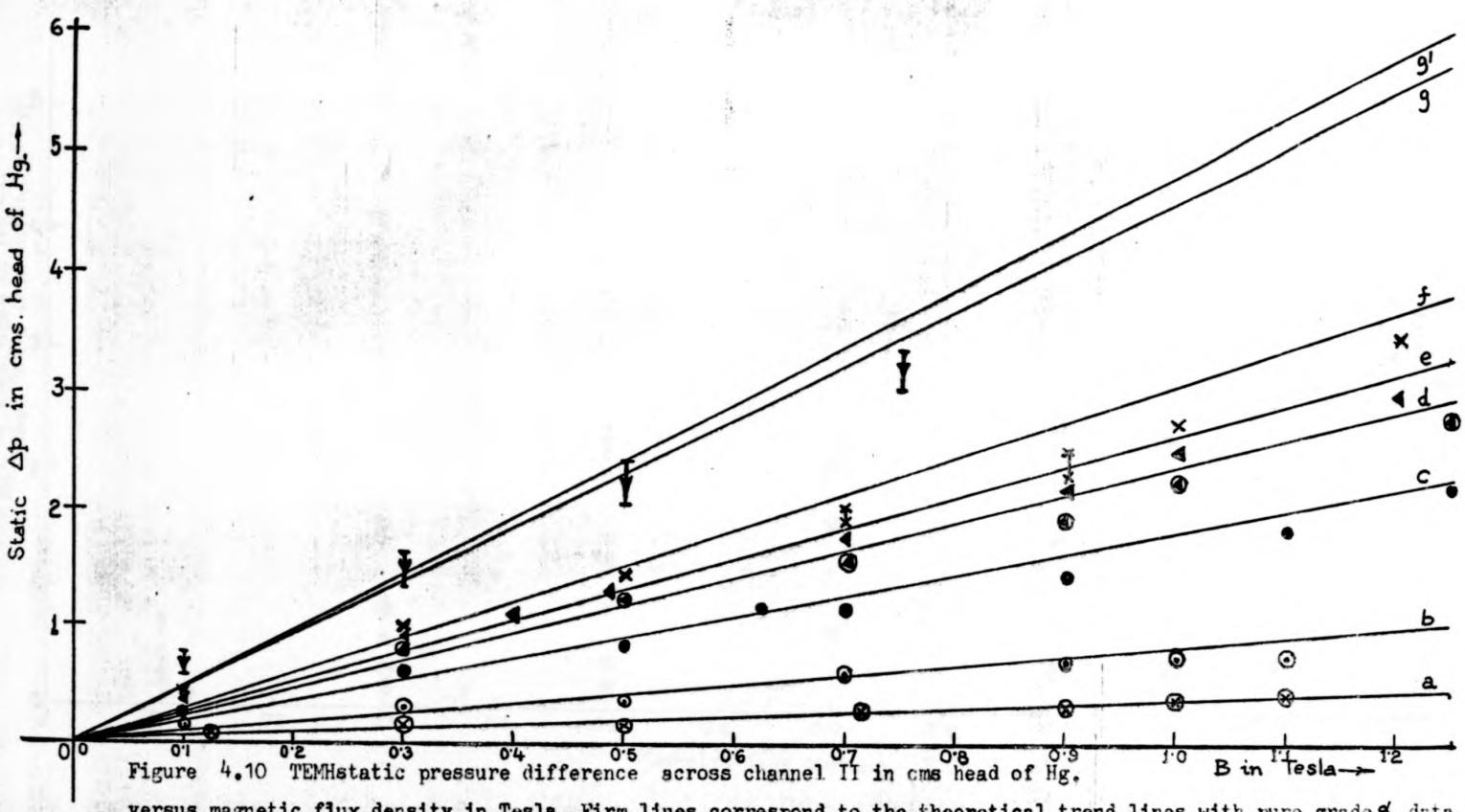

Figure 4.10 TEMHstatic pressure difference across channel II in cms head of Hg. versus magnetic flux density in Tesla. Firm lines correspond to the theoretical trend lines with pure grade α_{Au} data . Key to the symbols : (a) ⊗ heater current 1.1amp (b) ⊙ heater current 2 amp (c) ● heater current 3 amp (d) ◐ heater current 3.2 amp (e) ◀ heater current 3.5 amp (f) × heater current 4 amp (g and g′) ⚜ heater current 5 amperes. For complete operating conditions refer to Table IV.

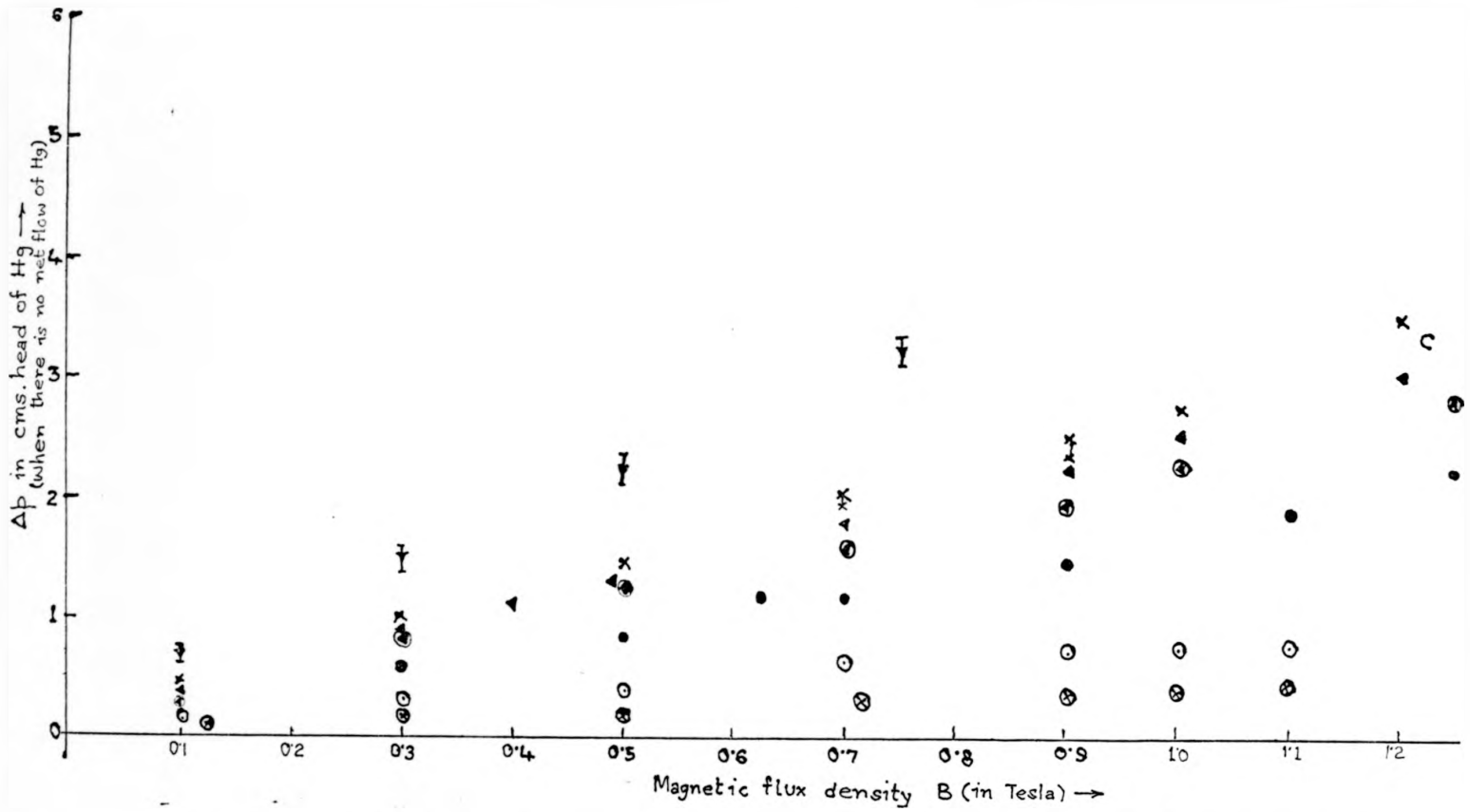

Figure 4·10a Δp vs B experimental points for a number of fixed thermal transport conditions in the circular cross-sectional straight channel II when V=0. For keys to the experimental points refer to that in figure 4.10

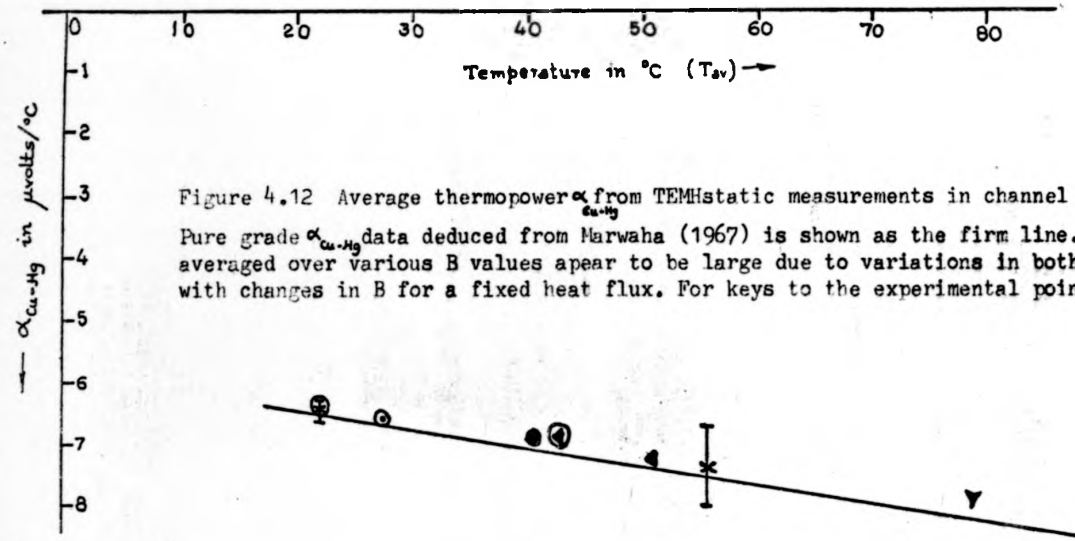

Figure 4.12 Average thermopower α_{Cu-Hg} from TEMHstatic measurements in channel II versus $T_{avarage}$. Pure grade α_{Cu-Hg} data deduced from Marwaha (1967) is shown as the firm line. The spread of data averaged over various B values apear to be large due to variations in both T_{av} and T_m values with changes in B for a fixed heat flux. For keys to the experimental points refer to figure 4.10

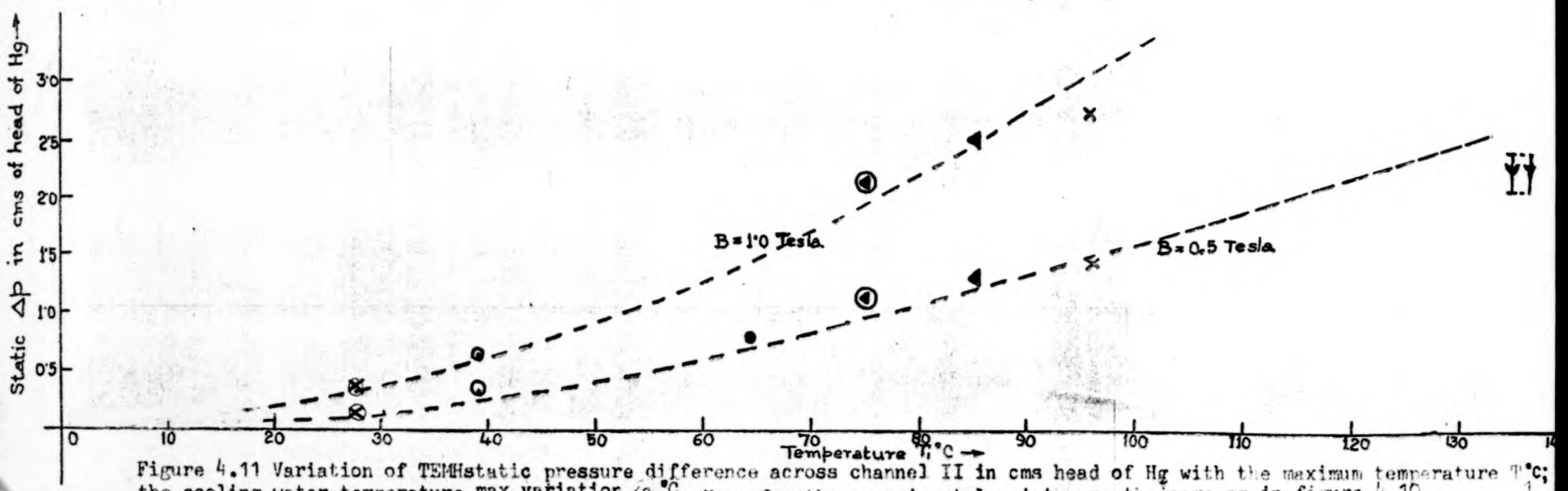

Figure 4.11 Variation of TEMHstatic pressure difference across channel II in cms head of Hg with the maximum temperature T °C; the cooling water temperature max. variation <2 °C. Keys for the experimental points are the same as in figure 4.10

TABLE IV Experimental operating conditions for Channel II with the corresponding theroetical parameter calculations

Heater current	Supply voltage	B = 0 T_1	T_2	ΔT °C	B ≥ 0.3 Tesla T_1	T_2	ΔT	T_{av} °C	T_m	C	α_{Cu-Hg} $\mu V/K$	$\Delta h = \frac{\sigma \alpha T_m L}{(1+c) R_1 \rho g} B$
3 x 0.75	3 x 31	18°	11°	7	-	-	-	-	-	-	-	-(in cm of Hg)
3 x 1.1	3 x 40	32	19.5	13	27.5	16.25	11.25	22 (21.85)	5.5 (5.62)	0.405	6.54	0.392 B
3 x 2	3 x 65/70	47	17.5	29.5	39	16	23	27.5	11.5	0.412	6.698	0.833 B
3 x 3	3 x 110	81.5	18	61	65.5	16	48.5	40.25	24.25	0.43	7.06	1.810 B
3 x 3.2	3 x 115/118+	83.5	14	69.5	74.5	11.5	63	43	31.5	0.435	7.144	2.366 B
3 x 3.5	3 x 130	104.5	19	85.5	85	16.5	68.5	51	34.25	0.447	7.374	2.62 B
3 x 4	3 x 145/150	123	19.5	104.5	96	16	80	56	40	0.456	7.517	3.09 B
3 x 5	3 x 188/189	186/189	20	166/169	135/139	18	117/121	76.5/78.5	58.5/60.5	0.495/0.499	8.008/8.165	4.61/4.84 B

power α_{Cu-Hg} for the range of T_{av} values in the TEMHD experiments of Table IV and are shown as experimental points against the pure grade α_{Cu-Hg} line in Figure 4.12. Two typical spreads of the average $\alpha(T)$ values are shown by bars. The apparently large spread in case X and the possibility of higher $\alpha_{measured}$ than the pure grade α is probably due to the changing temperature levels T_1 and T_2 (especially that of T_1) as the magnetic field is changed from one level to the other as reported in the next paragraph.

The temperature profile along the circumference was extensively obtained to verify how accurately sinusoidal the profile is and to evaluate its harmonic contents. Later, the temperature distributions in the entire region of Hg in the TEMHD section were extensively obtained at various heating current levels and at different magnetic field intensities, to understand the nature of temperature fluctuations that were observed in such measurements.

The interesting outcome of these measurements are (i) remarkably identical temperature distribution was obtained for cross-sections at various axial positions in the central 25 cms of the channel, where measurements could be conducted for a given value of B and thermal energy transport (heating and cooling flux). This confirms the longitudinal parametric invariance. (ii) For the same thermal energy input and the cooling water flow rate and temperature, changes in the magnetic field intensity B resulted in the change of both T_1 and T_2 at the Cu-Hg interface at a cross-section corresponding to fixed axial position. The internal temperature distribution in Hg also changed. A set of isotherm diagrams for a heater current value of 3 x 1.1 amperes is shown in

Figure 4.13 and the peripheral temperature distribution in Figure 4.14. It can be seen from these diagrams that the maximum temperature T_1 and, to a lesser extent, T_2 have been decreased by an increase of B by 0.12 Tesla from the residual flux level. This is contrary to what one usually expects due to inhibition of convection by B, and the mechanism of such a fall in T_1 is explained later. A maximum fall in these temperatures is reached at B $\sim$ 0.2/0.3 Tesla. Further increase of B from 0.3 Tesla to 1.1 Tesla shows no more variation in the very steady characteristic pattern of peripheral T distribution obtained at B = 0.3 Tesla. The circumferential temperature profile also changes shape to a more closely sinusoidal variation in the range of B 0.3 to 1.1 Tesla as compared to those at lower B values.

(iii) The internal T distribution differs greatly from the ideal case of horizontal isotherms, and in particular the departure from the ideal case at the central region at all magnetic flux levels is easily recognisable. Though the peripheral T profile remains unchanged in the range of B 0.3 to 1.1 Tesla, the isotherm profiles are more distorted with the increase of B in this range. While the vertical gradient of temperature along the circumference does not depart appreciably from a linear law, and cannot at least be noticed in the scale length used in the plots, the temperature variation along the vertical diameter at any axial position in the central 25 cm of the TEMHD section shown in Figure 4.15 for different values of B but a fixed heater current of 3 x 1.1 amperes and cooling water temperature of 16° C and fixed flow rate of 9 litres/min, tells a different story. While the temperature gradient at B = 0 is more reminiscent of the profile in the presence of joule heating, at higher B invariably a steeper temperature gradient develops. Also noticeable in Figure 4.15 is that the application of the external magnetic field transforms the

Figure 4.13 and the peripheral temperature distribution in Figure 4.14. It can be seen from these diagrams that the maximum temperature T_1 and, to a lesser extent, T_2 have been decreased by an increase of B by 0.12 Tesla from the residual flux level. This is contrary to what one usually expects due to inhibition of convection by B, and the mechanism of such a fall in T_1 is explained later. A maximum fall in these temperatures is reached at B $\simeq$ 0.2/0.3 Tesla. Further increase of B from 0.3 Tesla to 1.1 Tesla shows no more variation in the very steady characteristic pattern of peripheral T distribution obtained at B = 0.3 Tesla. The circumferential temperature profile also changes shape to a more closely sinusoidal variation in the range of B 0.3 to 1.1 Tesla as compared to those at lower B values.

(iii) The internal T distribution differs greatly from the ideal case of horizontal isotherms, and in particular the departure from the ideal case at the central region at all magnetic flux levels is easily recognisable. Though the peripheral T profile remains unchanged in the range of B 0.3 to 1.1 Tesla, the isotherm profiles are more distorted with the increase of B in this range. While the vertical gradient of temperature along the circumference does not depart appreciably from a linear law, and cannot at least be noticed in the scale length used in the plots, the temperature variation along the vertical diameter at any axial position in the central 25 cm of the TEMHD section shown in Figure 4.15 for different values of B but a fixed heater current of 3 x 1.1 amperes and cooling water temperature of 16° C and fixed flow rate of 9 litres/min, tells a different story. While the temperature gradient at B = 0 is more reminiscent of the profile in the presence of joule heating, at higher B invariably a steeper temperature gradient develops. Also noticeable in Figure 4.15 is that the application of the external magnetic field transforms the

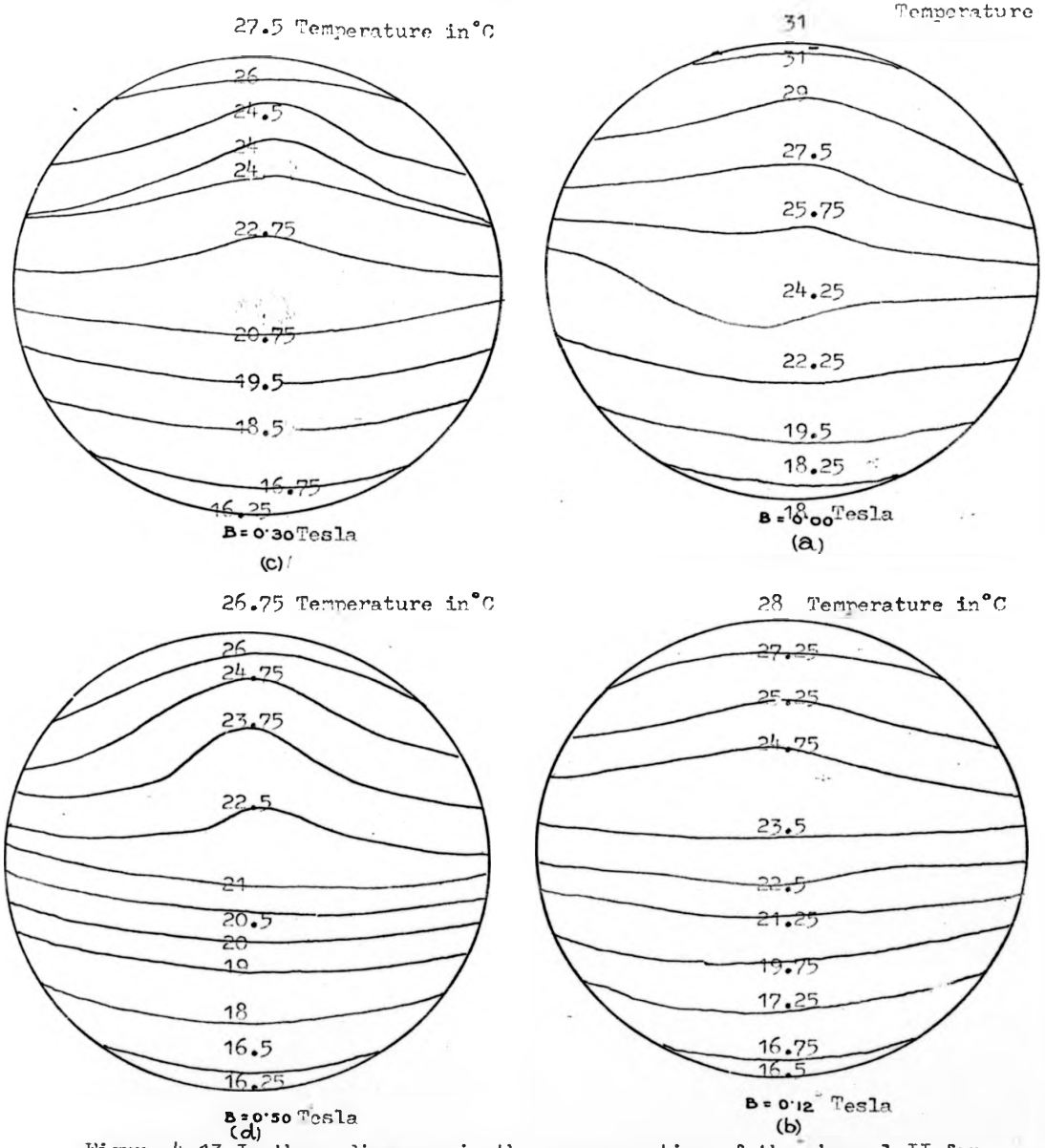

Figure 4.13 Isotherm diagrams in the cross-section of the channel II for a fixed heating current of 3 x 1.1 amperes (cooling water temperature change < 1°C)

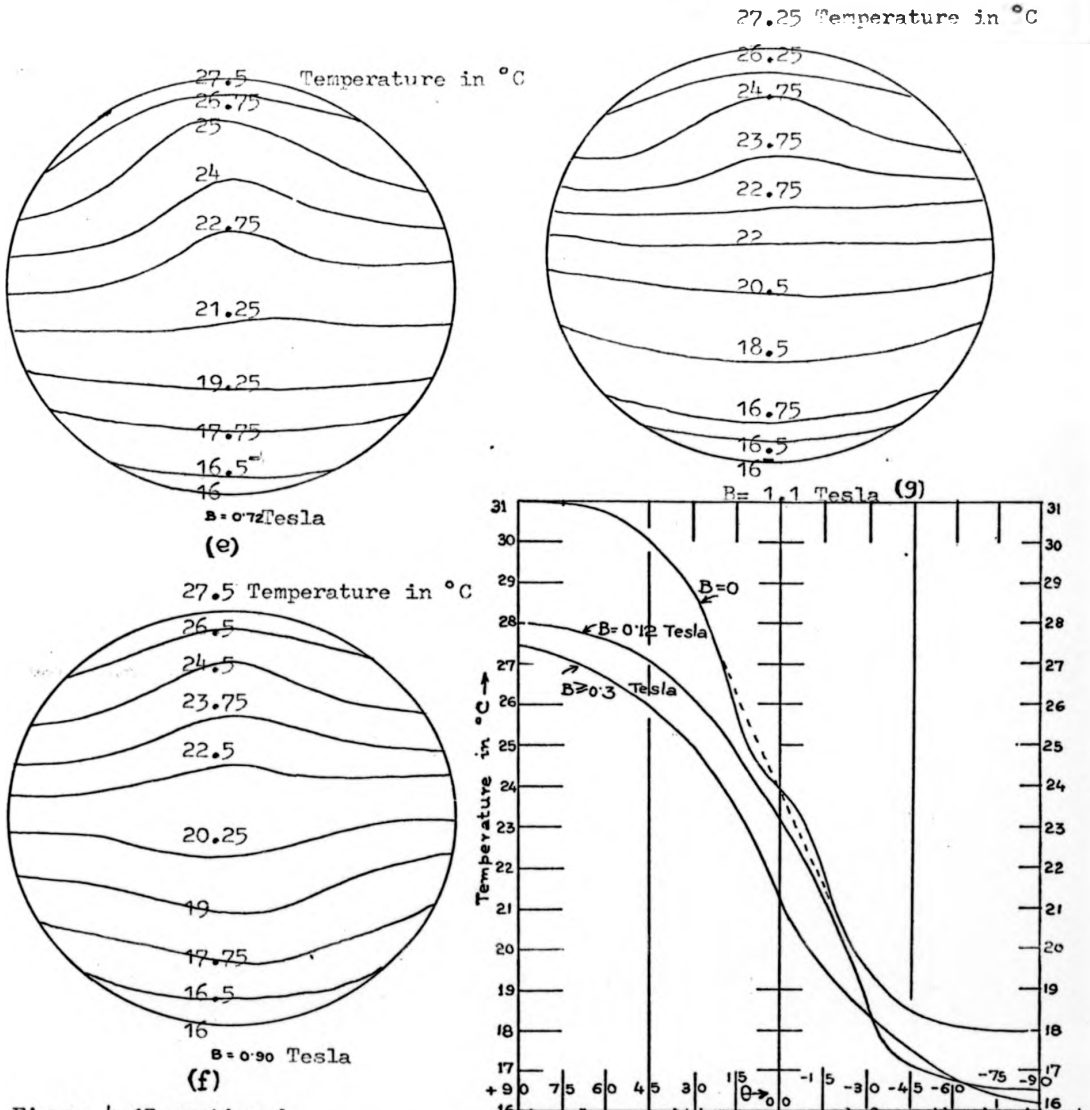

Figure 4.13 continued

Isotherm diagrams in the cross-section of the channel II for a fixed heating current of 3x 1.1 amperes. (cooling water temperature change $< \frac{1}{2}°C$)

Angular position measured from the horizontal line ($\parallel$ to B_1) in midplane. → (θ in degrees)

Figure 4.14

Peripheral temperature distribution at the solid-liquid interface in channel II for heater current 3x 1.1 amp.

one-sided nature of the temperature distribution with respect to the linear gradient line at B = 0 to a two-sided one at higher B.

To confirm this fall in the magnitude of T_1 and T_2 with the increase in the magnetic field, this experiment was repeated to determine the peripheral T profile at other heating currents and one such set is shown in Figure 4.16 for a heater current of 3 x 3 amperes. This trend agrees with the temperature profile measured at other heater currents of 3 x (0.5, 1.1, 3.2, 3.5, 4 and 5 amperes) apart from the persistent dip at the topmost temperature which was not characteristic of any other measurements. No explanation could be put forward for this particular snag on this set of data, though at one time it was thought that the cooler (R/2,θ vertical) region in Hg could be explained in terms of such a dip. (Peltier heat absorption, though small, could be a reasonable guess). However, since this is not representative of T profiles for other measurements, it was not pursued. A very careful measurement of circumferential T profile measurement at 3 x 3.2 amperes heating current at B = 0.5 Tesla,conducted at $\frac{\pi}{16}$ radian intervals is shown in Figure 4.17, and the Fourier analysis results by computer in Table V.

During the measurement of the temperature distribution in Hg, temperature oscillations at particular regions in Hg were observed. While at 3 x 0.5 ampere heater current such temperature oscillations were not at all present, there were indications that very feeble oscillations started at 3 x 1.1 ampere heating condition. The magnitude of the temperature oscillation could be measured from the 3 x 2 ampere current operation, and upwards with the magnitude of oscillation increasing with the heater current. Contrary to the belief that a transverse magnetic field inhibits convective motion, it was observed that the temperature

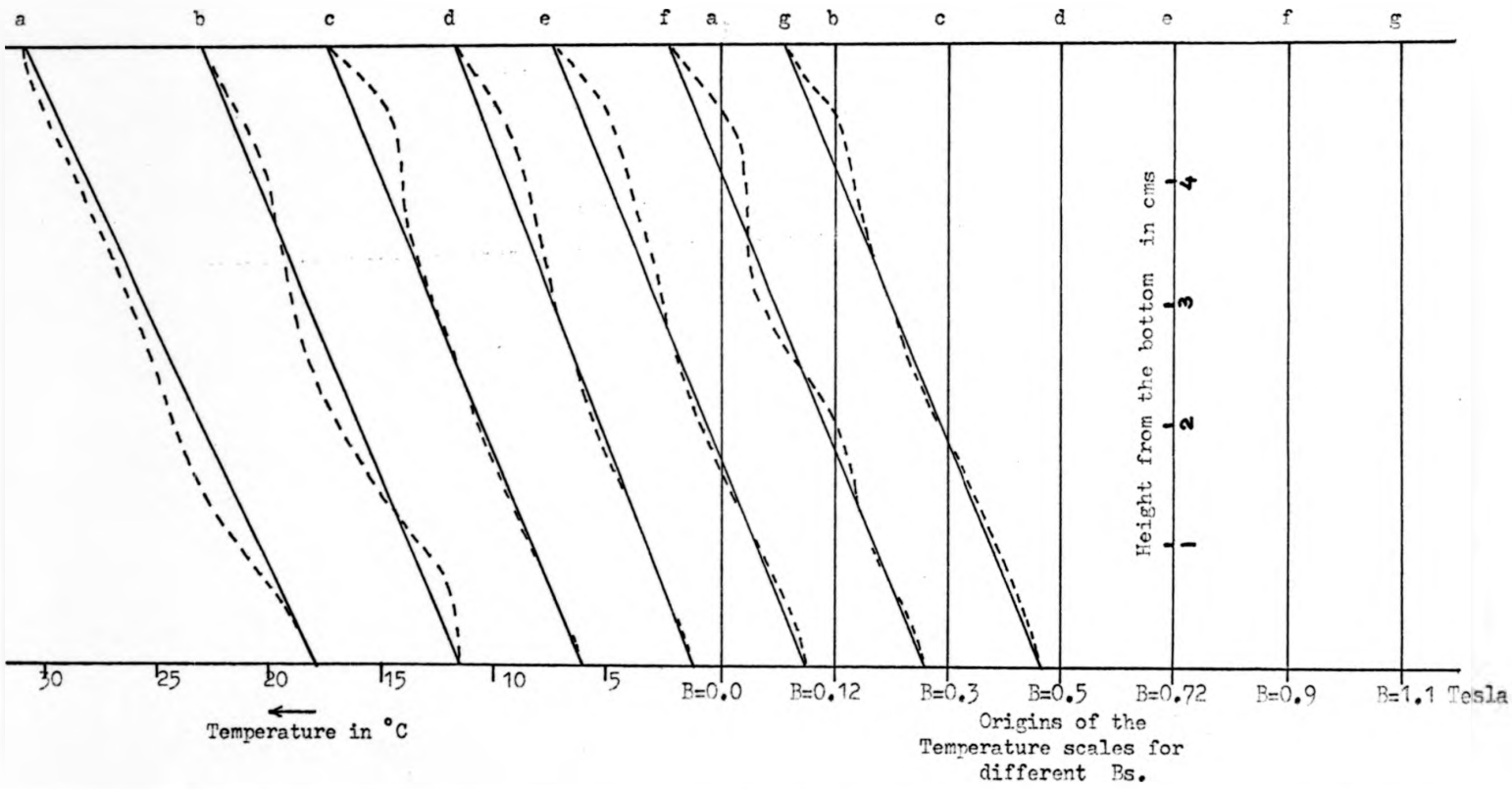

Figure 4.15 Temperature variation along the vertical diameter in channel II for a fixed heating current of 3x 1.1 amp. (cooling water temperature variation $<\frac{1}{2}$°C)

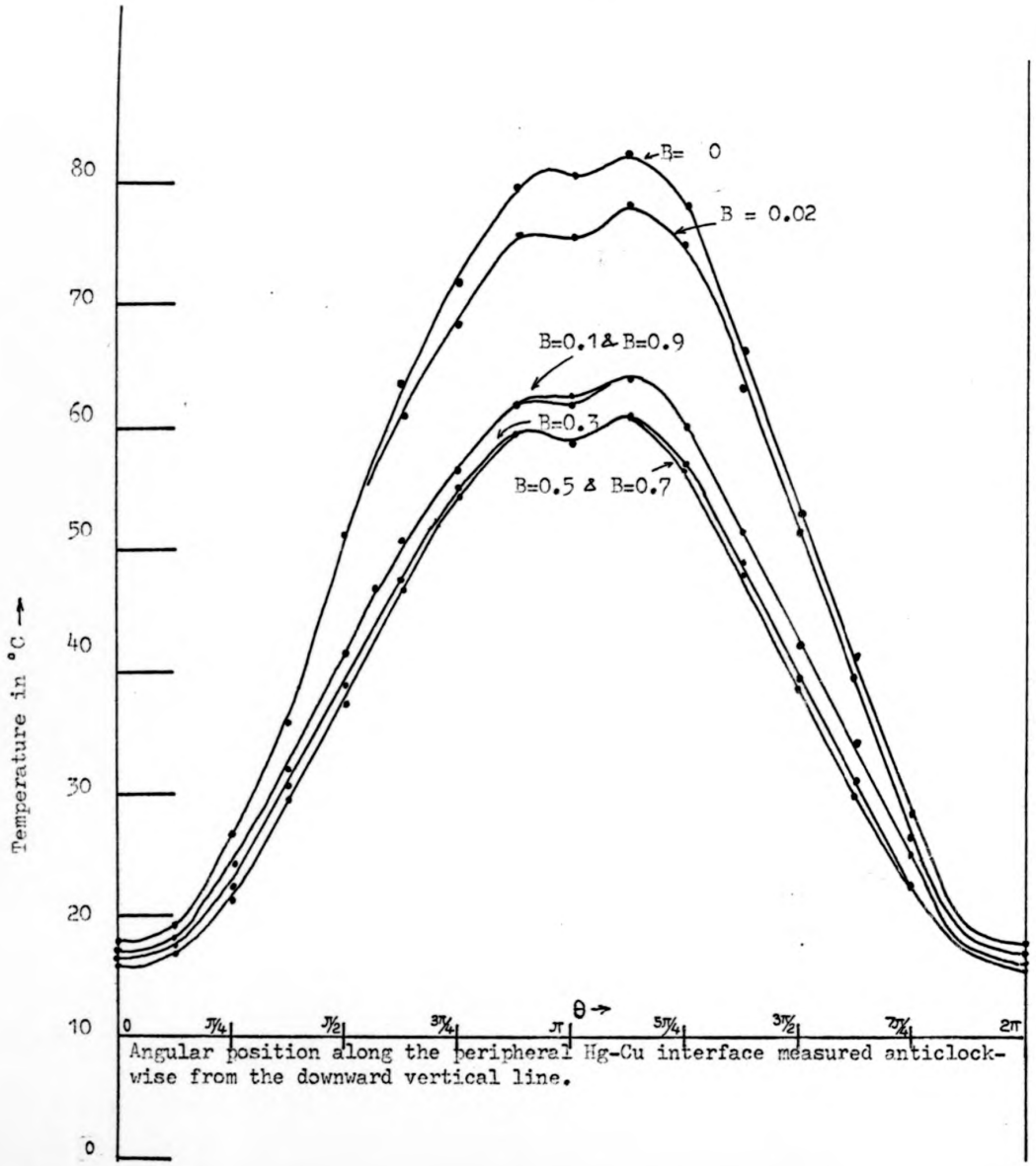

Figure 4.16 Peripheral temperature distribution in channel II for a fixed heater current of 3 x 3 amperes and the cooling water temperature of 16 ° C at various magnetic flux density.B. (in Tesla)

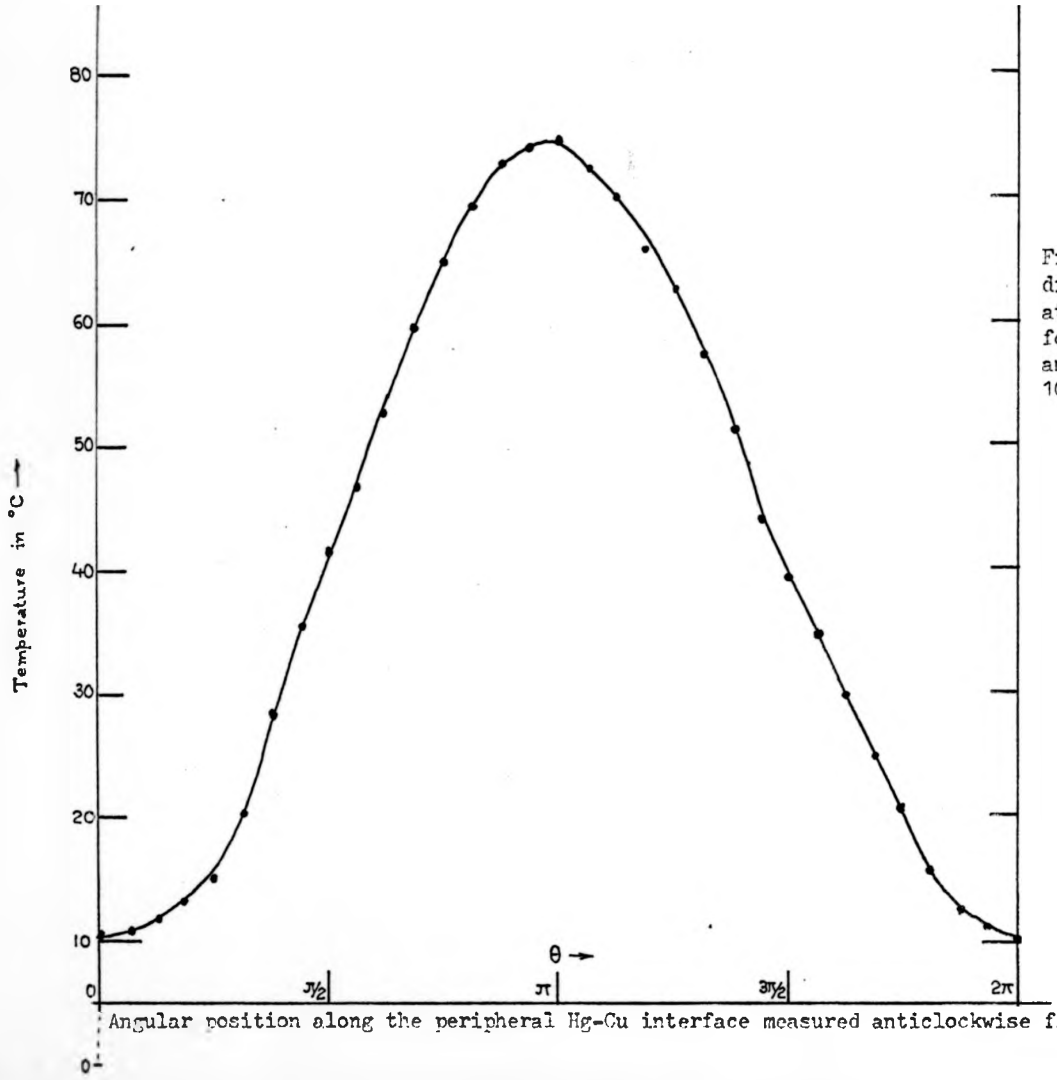

Figure 4.17 Peripheral temperature distribution in channel II (measured at closer intervals than in fig 4.16) for B= 0.5 Tesla, Heater current 3x3½ amperes, cooling water temperature 10.75°C.

(Fourier Analysis of this waveform - discrete experimental points- is to be found in Table V.)

TABLE V Results of the Fourier analysis of the wave form in Figure 4.17 as done by computer

$$F(X) = \frac{A_o}{2} + \sum_{n=1}^{7} \{A_n \cos nx + B_n \sin nx\} \quad \text{in } ^{\circ}C$$

n = 0	A = 82.0897	B = 0
1	-3.16169	-31.1618
2	-1.07564	9.504437 E-02
3	0.398629	1.00120
4	0.610280	0.641057
5	0.759792	0.698573
6	-0.170599	0.914689
7	0.263953	0.622449

The corresponding typical error in Table IV in not considering the harmonic content for 3 x 3.2 ampere heating and at B = 0.5 is 4.59% in T_{av} and 0.57% in T_m.

oscillations increased with the magnetic field to 1.25° C in the 3 x 2 ampere operation at B = 0.1 Tesla, but reduced to $\frac{1}{2}^{\circ}$ C at B > 0.3 Tesla, and small fluctuations persisted even at the highest B of 1.2 Tesla. The maximum temperature fluctuations were confined to the two regions $(\pm R/2, \theta_{vertical})$, but at higher heater current operation reached the periphery as well. Typical magnitudes are shown in Table VI for 3 x 3.5 and 3 x 4 ampere operations. At 3 x 5 amperes operation, the fluctuations increased so much that it became impossible to measure with consistency. A typical record of the temperature oscillations at 3 x 3 ampere heating condition at $(R/2, \pi/2)$ and $(R/2, \frac{5\pi}{4})$ are shown in Figure 4.19a,c. From the period of oscillations (varying from 6 seconds to 12 seconds) in the fluctuating zone, an estimate of the fluid fluctuation velocity is possible. For the 3 x 3.2 ampere heating conditions and the XY plotter trace of Figure 4.19a, the maximum fluctuating speed is of the order of 0.75/0.4 mm/sec.

The temporal analysis in section 4.5 indicated starting transients in the form of longitudinal oscillations for smaller B values. After sufficient lapse of time and with molecular heat conduction dominating, there should be no T fluctuation, at least in the central section, due to such oscillations. The potential measuring system was incapable of measuring any fluid movement $\parallel$ to B and $\perp$ to B in the vertical direction. However, since the measurements at different axial positions show remarkably identical measurements of the average and oscillation amplitude of T and ϕ^{+}, (cf. Figure 4.19a,b), it implies that oscillations caused by fluid motion in the horizontal planes containing B or in vertical planes perpendicular to B are highly

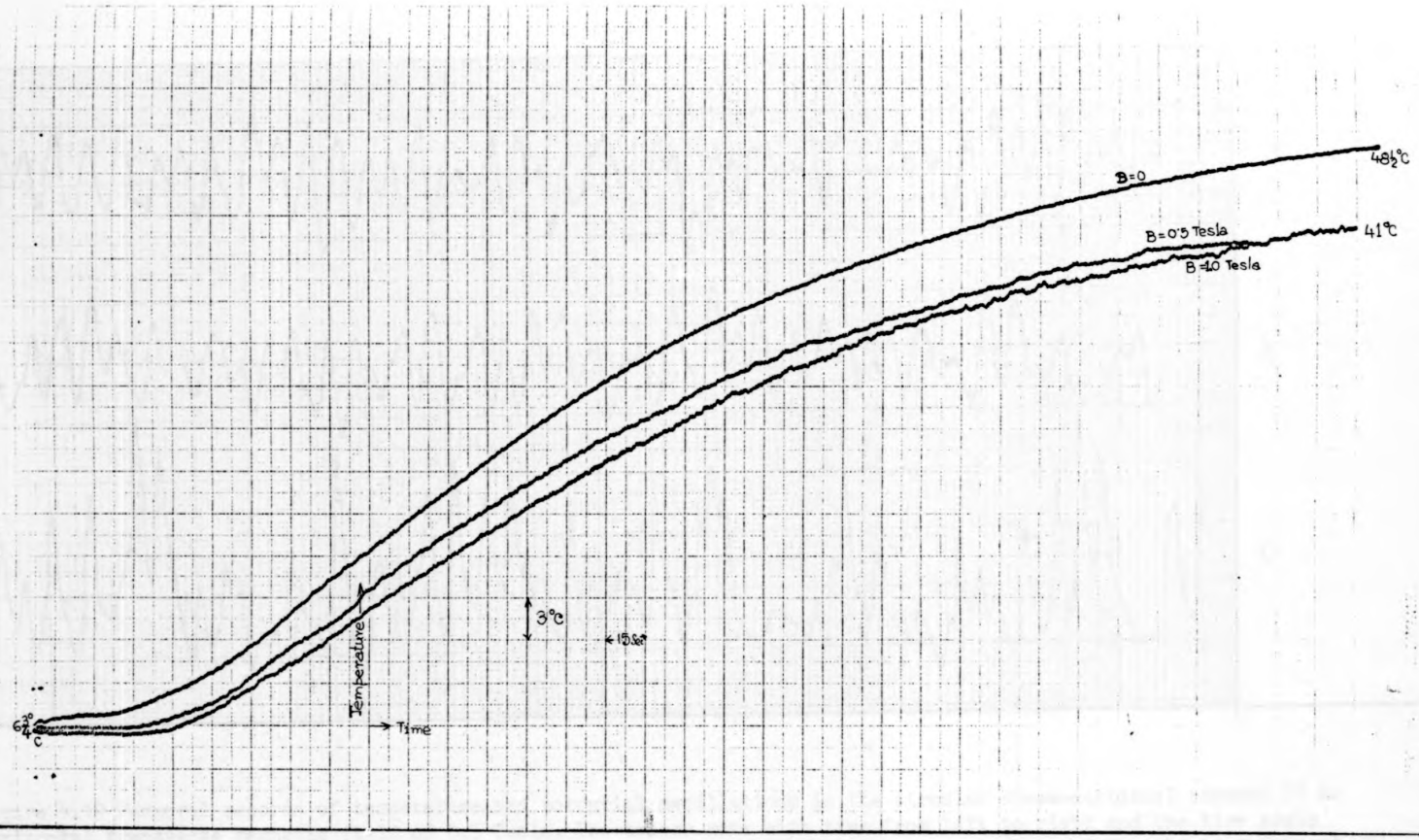

Figure 4.18 The time record of temperature build up in the circular cross-sectional straight channel II in various steady values of the horizontal transverse magnetic field .Heater current raised suddenly from zero value to 3x3.2 amperes.

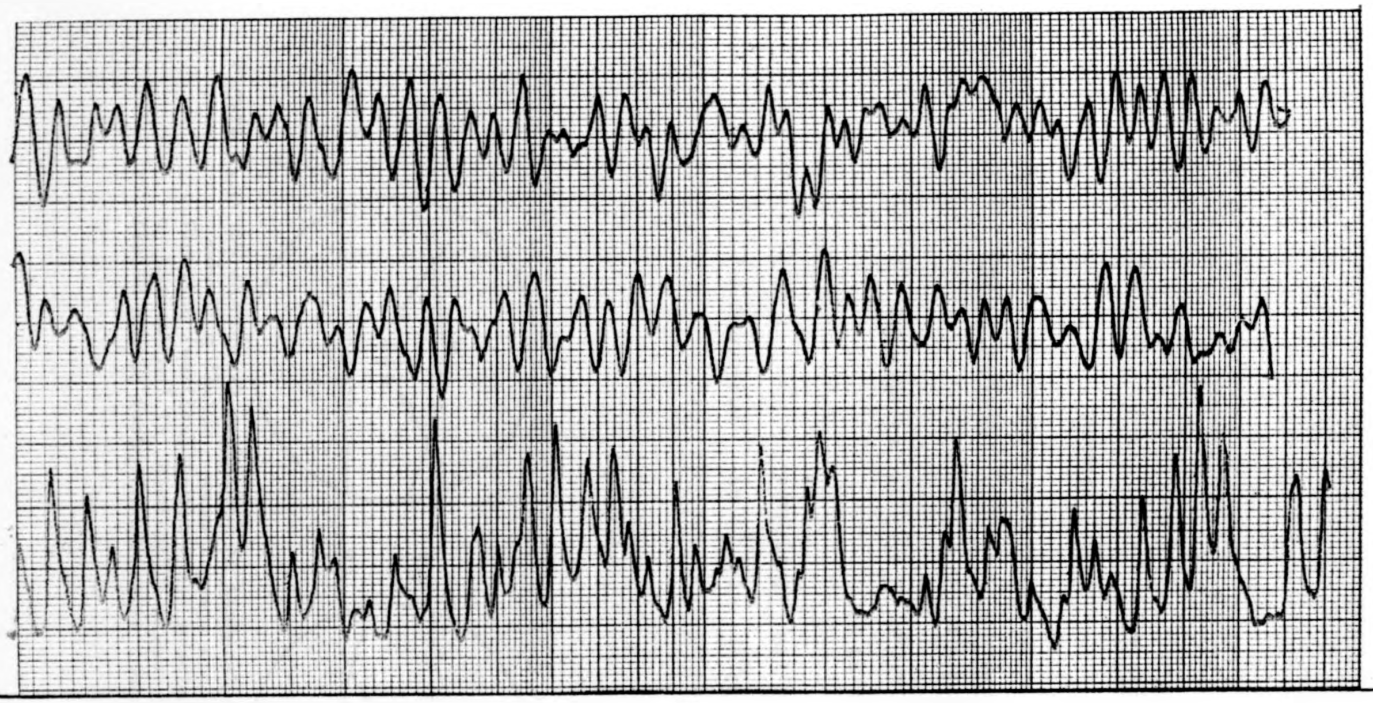

Figure 4.19 Temporal records of temperature and potential oscillations in the circular cross-sectional channel II in horizontal transverse magnetic field of 0.5 Tesla. The traces move with time from left to right and the time scale (horizontal X direction) is 8 sec/ cm. The Y axis scale is 60 μvolts /cm. Operating condition; 3x3amp heating current. (a) Temperature oscillation at $(R/2, \pi/2)$ (b) Potential oscillation across vertical radius from centre point to $(R/2, \pi/2)$ (c) Temperature oscillation at $(R/2, 5\pi/4)$. Angles measured from the horizontal magnetic field direction (anticlockwise).

TABLE VI Amplitude of temperature oscillations in Channel II

Heater current		Temperature oscillations (P-P)				
		B = 0.02	B = 0.1	B = 0.3	B = 0.5-0.7 Tesla	
3 x 3.5 amperes	at $(\frac{R}{2},\theta_v)$	2°/3° C (2 to 3)	2½° C	<1°C for B ≥ 0.3 Tesla		
	at the periphery	nil	nil	nil		
3 x 4 amperes	at $(\frac{R}{2},\theta_v)$	5°C	3°C	3°C	1°C	<1°C for B ≥ 0.9 Tesla
	at the periphery		1.25° C, <0.25° C for B ≥ 0.3 Tesla			

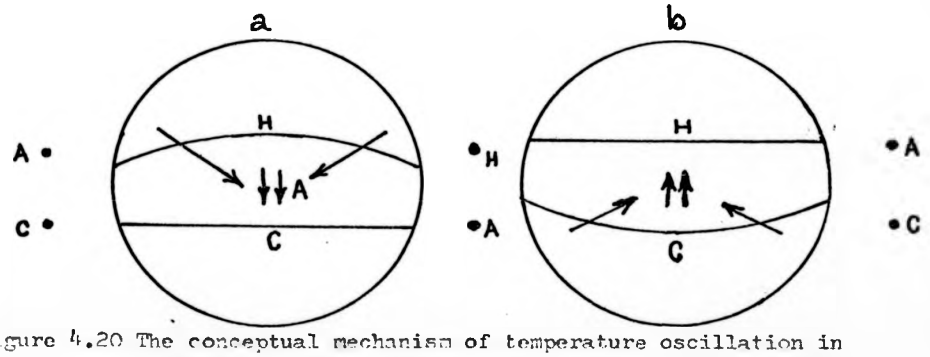

Figure 4.20 The conceptual mechanism of temperature oscillation in conducting fluids with a basic stable thermal stratification (vertical temperature gradient also constant by assumption) in horizontal steady uniform magnetic fields due to isotherm curvature instability.

improbable. The only distinct possibility is therefore of fluid circulation in vertical planes perpendicular to the longitudinal axis and containing B. The correspondence of the measured temperature fluctuations and the thermally induced ϕ^+ fluctuations, though not measured simultaneously(phase lag!) confirm such juxtaposition.

Consider the possibility of temperature fluctuation in Hg in the TEMHD channel under such a situation. Any curvature of the isotherms,in the vertical plane XY, containing B and perpendicular to the longitudinal axis, away from the horizontal line causes a variation of T(X,Y) with both X and Y. This induces baroclinic instability. In Figure 4.20, an arbitrary curvature of isotherm 1 is considered for fixing ideas at time t = O. H corresponds to hot, A to an average temperature and C to the cold regions of the fluid. Baroclinic instability causes flow from the sides in H to the central hump in A pushing the fluid in the central region of A down,as shown by arrows. This in turn alters the isotherm 2 correspondingly, as shown in Figure 4.20b. Reversed curvature causes similar instability, now at isotherm 2,with the result that the fluid A is pushed upwards. In the absence of any $B_{horizontal}$ in the plane XY, such vertical movements of the fluid and the corresponding T fluctuations are greatly reduced in magnitude, due to/absence (the small fluctuations exist due to the) of magnetic drag, but possibly / fluid viscosity. With a horizontal B in the plane XY, the magnetic field inhibits such movement so that if the magnetic field B > a critical value of B, B_{cr} depending on $\frac{\partial T(X,Y)}{\partial Y}$, it can hold back any buoyancy driven fluctuations and the curvature of the isotherm increases. This can be visualised in the isotherm diagrams of Figure 4.13 c,d,e,f,g for B $\geq$ O.3 Tesla. At any lower value of B,$< B_{cr}$, the

magnetic field inhibits any brisk movement until the buoyancy force is strong enough to burst through the critical limit. Following the burst of flow, the isotherms straighten out, reducing the buoyancy force,and the fluid movement is limited by the magnetic field ready for the next burst. This periodic relaxation or the possibility of an overstability,as explained in the twin curvature isotherm, explains the possible T fluctuations. The relaxation time is clearly a function of B, $\frac{\partial T(X,Y)}{\partial Y}$ and the process is possible only in low Pr number fluids. This is in contrast with the Bénard problem in Hydromagnetics, as discussed by Chandrasekhar (1961). At $B < B_{cr}$ the fluctuations cause the average temperature measurements to show a flat isotherm profile for B < 0.3 Tesla in Figure 4.13b. At a higher rate of heating, i.e. higher $\frac{\partial T(X,Y)}{\partial Y}$, $B_{critical}$ is correspondingly increased as can be seen from the isotherm diagrams of 3 x 32ampere heating in Figure 4.21 for B = 0, 0.5 and 1.2 Tesla (B_{cr}> 0.5 Tesla).

With this physical picture of the mechanism of temperature fluctuations, it is now possible to visualise the drop in temperatures T_1 and T_2. The fluid fluctuating movement (bursts of flow gives greater mixing) increases the heat transfer effectively over that of molecular heat conduction, reducing the temperature gradient for the same amount of net heat energy transport. In fact, beyond $B_{critical}$, i.e. $B > B_{cr}$, the temperature T_1 rises, as can be seen in Figure 4.16 for B = 1.2 Tesla. It is therefore certain that the application of an inhibiting magnetic field to stop temperature oscillations during crystal growth in melts by the Czochralsky and the zone refining techniques would produce more adverse effect than in the absence of B, unless B is sufficiently greater than B_{cr}.

Isotherms not numbered

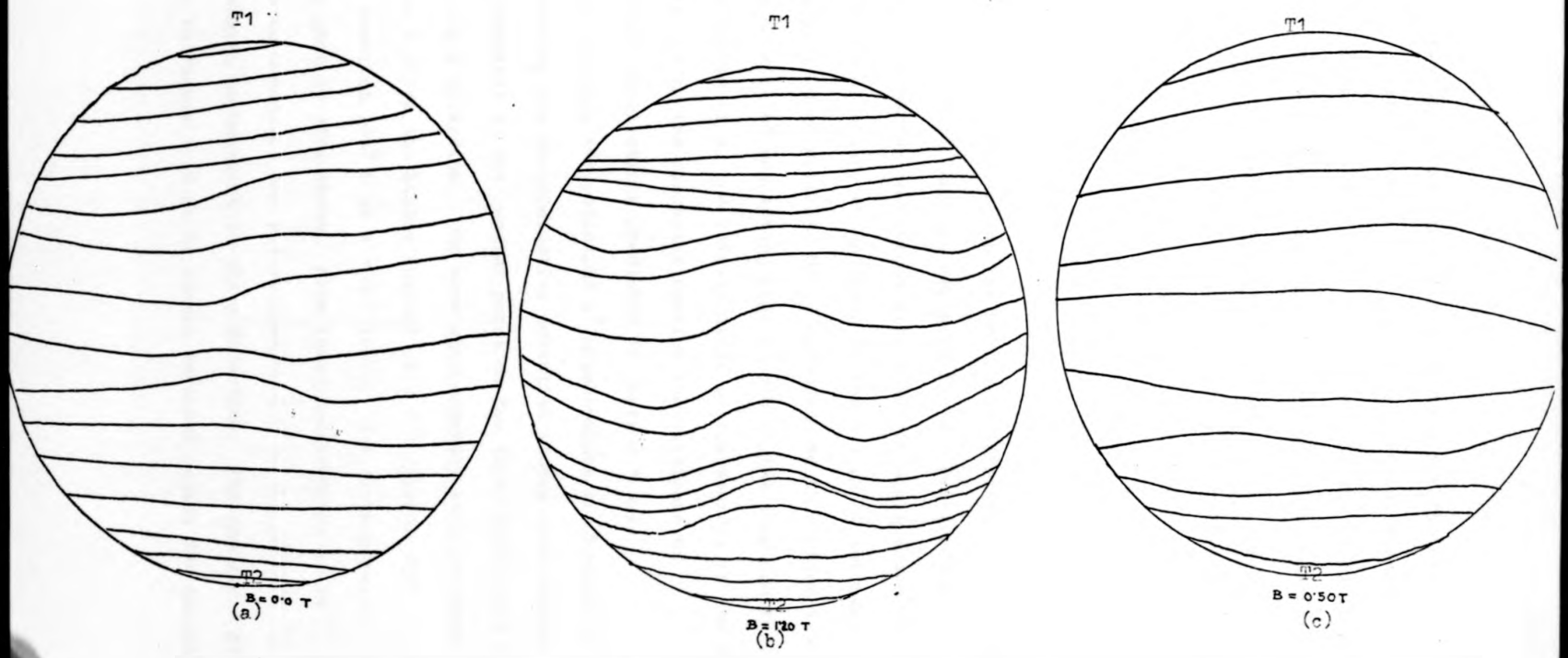

Figure 4.21 The patterns of isotherm diagrams in the circular cross-sectional straight channel II in the plane of the magnetic field for (a) B=0 (b) B=1.2 Tesla (c) B=0.5 Tesla. Heating current 3x3amperes .

The curves of temperature rise with time for the central point of the vertical cross-section in the absence of and at various magnetic flux densities, as recorded by the XY plotter in conjunction with the measurement data taken by the potentiometer, and DVM are shown in Figure 4.18 for heater currents of of 3 x 3.2 amperes and cooling water at $7/6\frac{1}{2}^{o}$ C. The characteristic time of build-up of the final mean temperature for any value of B is, however, not much dependent on B magnitude. For the 3 x 3.2 ampere heating condition shown in Figure 4.18, this characteristic time is 4 minutes.

The time for building up the pressure difference is dependent on the heating level and the magnetic field. For the 3 x 3 ampere steady heating conditions with a sudden application of 1.2 Tesla, the final steady state value is reached in 20 seconds corresponding to an estimate of 12 seconds made in section 4.4.1 with the associated connecting pipe length in the loop ignored. At lower values of B, the initial drift of the menisci in the Hg reservoir and in the manometer confirm the existence of longitudinal oscillations predicted in section 4.4.1.

Next consider the potential ϕ^{+} measurements in Channel II as measured by the thermoelectric potential probes with respect to the potential at the central point on the axis, still with no flow in the z direction. One such equipotential plot is shown in Figure 4.22 for the heater current of 3 x 3 amperes and cooling water at $10\frac{1}{4}^{o}$ C at B = 0.5 Tesla. The corresponding isotherm plot is also shown. From these measurements it is possible to construct the ϕ distribution due to the current (j) flow assuming no movement in the z direction. The resultant plot is shown in Figure 4.23 as $\Delta\phi$ across vertical chords for angular

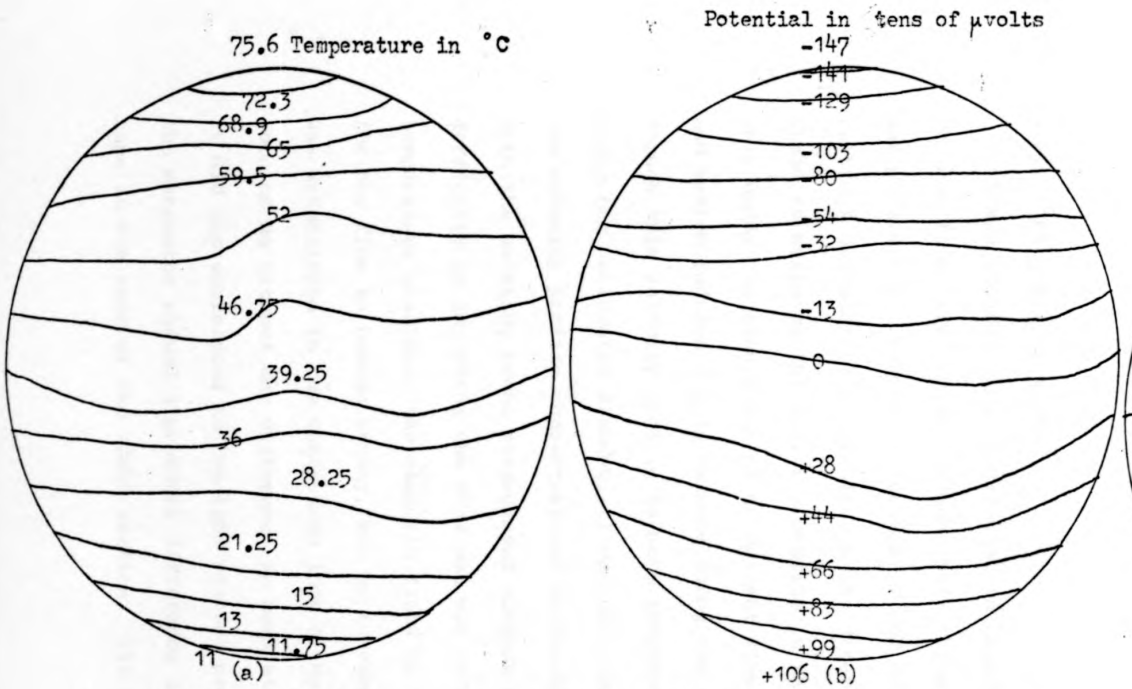

Figure 4.22 The (a) isotherm and equipotential (ϕ^{+}) plots in channel II vertical cross-section in the plane of the magnetic field direction. Heater current 3 x 3 amperes. Magnetic flux density 0.5 Tesla. Measurements with Cu-Const. thermoelectric potential probes.

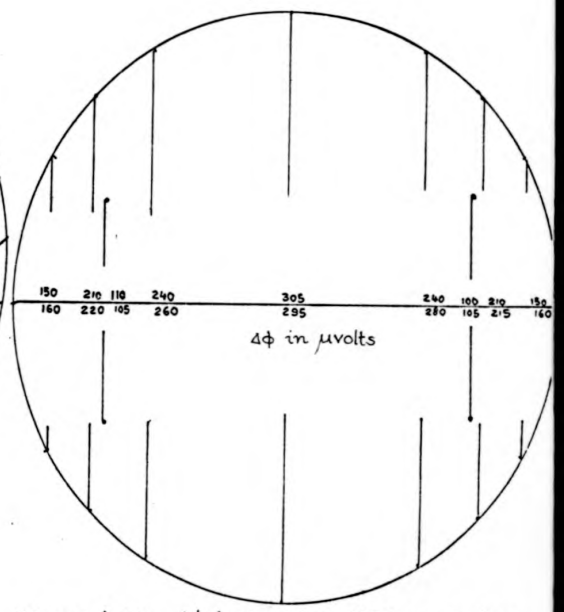

Figure 4.23 $\Delta\phi$ (potential difference due to current flow) across vertical chords at (R ; $\pi/2$, $\pi/3$, $\pi/4$, $\pi/6$, 0, $5\pi/6$, $3\pi/4$, $2\pi/3$,) and at ($3R/4$; $\pi/6$, $5\pi/6$) corresponding to data in figure 4.22

positions of (R; 0, $\pi/6$, $\pi/4$, $\pi/3$, $\pi/2$, $\frac{2\pi}{3}$, $\frac{3\pi}{4}$, $\frac{5\pi}{6}$, π) and ($\frac{1}{4}$R, $\pi/4$), θ being measured from the horizontal line along B. With no circulation in the z direction

$j_y = \frac{\Delta\phi}{l}\sigma$ shows a remarkably uniform j_y for values of X = R/2, R/$\sqrt{2}$, $\frac{\sqrt{3}R}{2}$ and 0 (cf. Table VII).

From the corresponding Δp measurement

$$j_y = \frac{\sigma\alpha T_m}{(1 + c)R} = 6370 \text{ amperes/m}^2$$

A non-dimensional plot of $(\partial p/\partial x)/\frac{\alpha\sigma T_m}{R}$ vs. M is shown in Figure 4.24 to demonstrate the effect of c.

4.6.2 Flow measurements

TEMHD induced flow measurement in Channel I was restricted to mean flow velocity measurement only, while in Channel II it was possible to measure temperature T and potential ϕ^+ along the vertical diameter perpendicular to the direction of the magnetic field to evaluate the velocity profile in the vertical direction only under the assumption of no current flow at thermo e.m.f. and motion induced e.m.f. balance along the vertical direction. Though this velocity profile is more interesting than the one along the horizontal diameter, it was not possible to measure the velocity profile characteristic in the horizontal direction with the existing probe arrangement without modification. The difficulty in adjusting the flow was not in controlling the temperature gradient, the magnetic field or the waiting period for the flow to become steady, but an inherent pressure gradient was established in the connecting loop of Hg. Even with a closed loop of Hg without any difference in head at the weir reservoir, it did not correspond to the flow without pressure gradient, and the manometer showed a pressure difference across the two pressure taps at the ends of the TEMHD section. (It is more because of

TABLE VII j_y evaluation from ϕ^+, T measurements, 3 x 3.2 ampere operation at B = 0.5 Tesla

n = 0, 1

Radial position	Angular position	1 cm	$\Delta\phi$ μv min/max	j_y amp/m^2
R	0	0	0	indeterminate
R	$\pm \pi/6$	2.515	150/160	6090/6500
$\frac{3R}{4}$	$\pm \pi/6$	1.87	$\frac{100}{105}$	5465/5740
R	$\pm \pi/4$	3.556	$\frac{210}{215}$	6035/6179
R	$\pm \pi/3$	4.35	240,280	5640,6580
R	$\pm \pi/2$	5.03	305,295	6200,6000
R	$\pm 2\pi/3$	4.35	240,260	5640,6180
R	$\pm 3\pi/4$	3.556	210,220	6035,6325
3R/4	$\pm 5\pi/6$	1.87	110,105	6010,5760
R	$\pm 5\pi/6$	2.515	150,160	6090,6500
R	π	0	0	indeterminate

$$j_y = \frac{\sigma\alpha T_m}{(1 + c)R}$$

$$= \frac{1.022 \times 7.144 \times 31.5}{1.435 \times 2.515} \times 10^2$$

$$= 6370 \frac{\text{ampere}}{m^2}$$

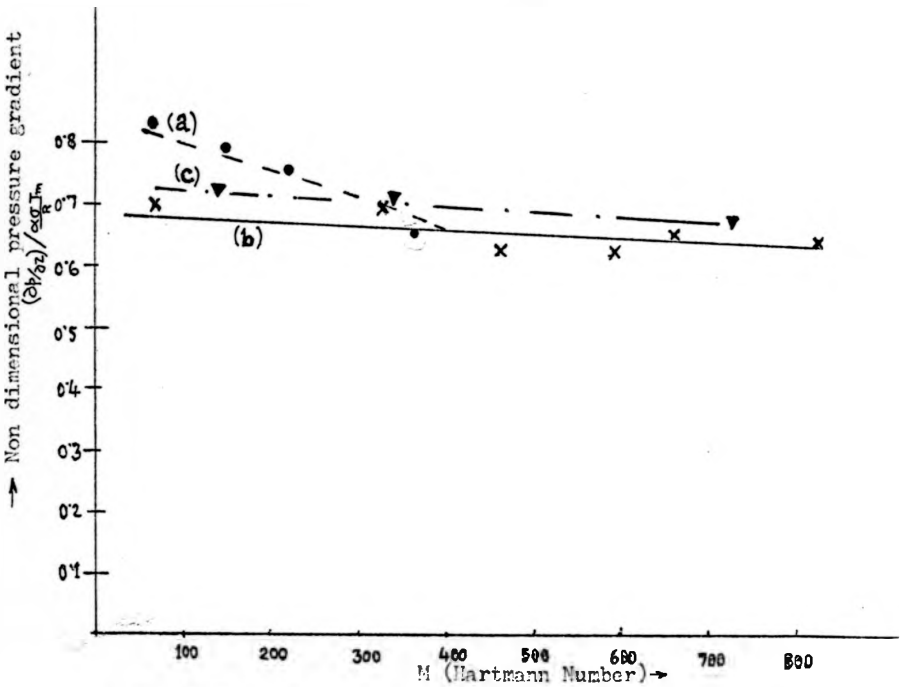

Figure 4.24 The non-dimensional pressure gradient plot against Hartmann number based on channel radius .(a) Channel I,3.5amp heating current (b) Channel II, 3x 3.2 amp heatung current (c) Channel II , 3 x 1.1 amp heating current.

(Circular cross-sectional straight ducts)

this reason that the TEMHD experiments in the annular channel with endless flow entirely inside uniform B were conducted, though it so happened that these experiments unfolded further interesting aspects of TEMHD as reported in Chapter 6). The positioning of the pressure taps were very critical during the fluid flow in the z direction as compared to their insignificance during the static (no flow) Δp measurements. Since it was not possible to locate the pressure taps exactly at the ends of the TEMHD section, the pressure measurements at these taps are only apparent pressure heads and the pressure difference so measured was always less than the true value. From the theoretical expected value and the measurements, an estimate of this error is possible. In the following paragraph,flow measurement results during steady state only are presented.

Figure 4.25a shows the mean flow rate, V, as measured by the flow meter in mm/sec against the pressure head (in cms of Hg) measured at the pressure taps due to a head difference in Hg at the weir reservoir for Channel II (3 x 3.2 ampere heating, B = 1.25 Tesla). Figure 4.25b shows the corresponding mean flow rate in cms/sec against the pressure head in cms of Hg in Channel I for 5 amperes heating condition and B = 1.2 Tesla. The theoretical curves are shown as continuous lines,while for Channel I the theoretical curve corresponding to the measured α_{Cu-Hg} value of sample I (ref. section 3.4.9) is shown chain-dotted. Figure 4.26 shows the mean flow rate in mm/sec in Channel II for the 3 x 3.2 ampere heating condition, with the weir reservoir completely filled up, against the variation of Hartmann number based on the TEMHD duct inner radius. The raw data of the flow meter measurements as well as the corrected flow rate corresponding to the pressure difference measured at the manometer from the

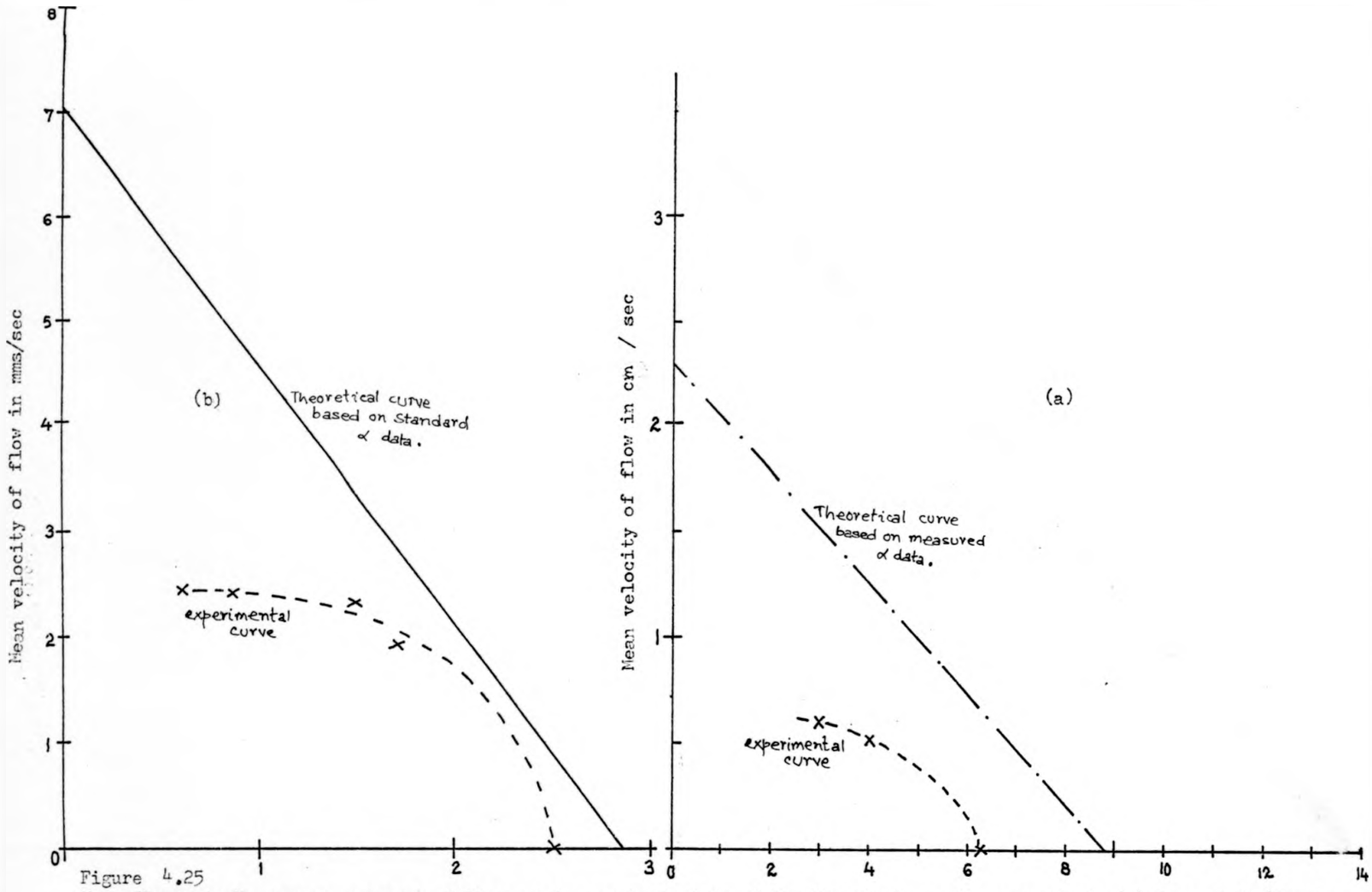

Figure 4.25
Mean flow rate V versus pressure difference in cms head of Hg at the Hg weir type of reservoir in (a) Channel I (Heating current 5 amp., B=1.2 Tesla) and (b) Channel II (Heating current 3 x 3.2 amp., B = 1.25 Tesla

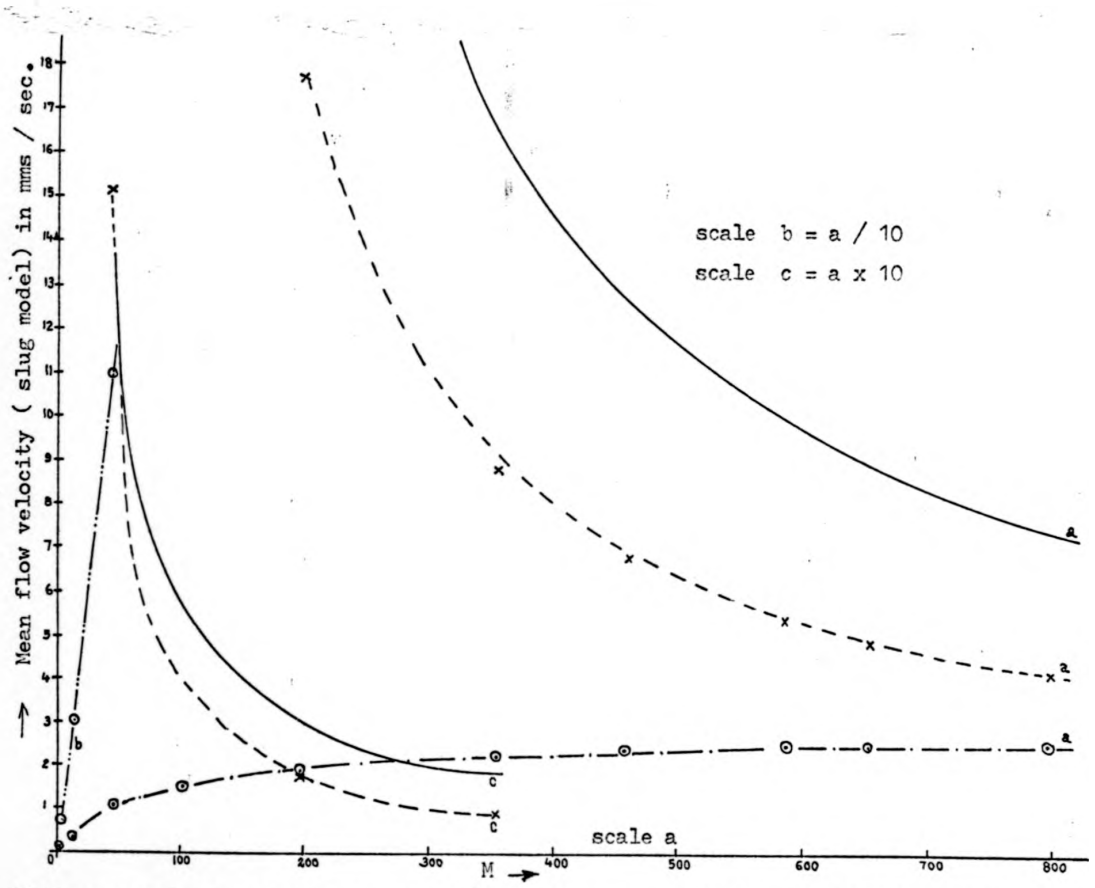

Figure 4.26 Mean velocity of flow, in channel II (circular cross-sectional straight duct), variation with Hartmann number based on channel radius . —— Theoretical profile. ═:═ Trend lines through experimental points without correction for pressure difference at the pressure taps across the TEMHD section. —x—x— Experimental trend line when corrected for the pressure difference measured across the TEMHD channel pressure taps. (Heater current 3 x 3.2 amp., No pressure difference at the weir type mercury reservoir.

pressure taps are shown. The theoretical curve is shown by the continuous line and it is to be noted that three scale lengths along the ordinate have been used in Figure 4.26. The effect of pressure difference between the ends of the TEMHD sections and the exact locations of the pressure taps (including right angle bends in between) is clearly observable. At very low values of B corresponding to the residual flux density of the magnet and the lowest stable flux density level, there is a velocity jump which could not be determined in detail because of the instability of the magnetic field in this range. Figure 4.27 shows the velocity profile along the vertical diameter of Channel II for the 3 x 3.2 ampere heating condition under the assumption of no current flow in the vertical direction, evaluated from T and ϕ^+ measurements. In fact, the assumption is not valid since there was a pressure gradient, but even with a uniform j_y this velocity profile should be representative of such flow with higher velocity at the hot end.

The starting process of the TEMHD flow has not been studied due to its complexity. The steady flow and temperature conditions (apart from temperature oscillations and secondary flow fluctuations) are attained in 20 to 25 seconds. The temperature of the Hg in the connecting loop and in the weir reservoir (in the flow experiment) rises and, in the steadying time of 20 to 25 seconds, reaches the corresponding T_{av} value very consistently. At lower flow rate, the time required for steady flow is greater than at higher flow rate.

No serious effort was made to study the heat convection by TEMHD flow in detail, but that it is possible has been demonstrated by detecting rise in cooling water temperature (at steady flow) at the weir reservoir of mercury.

Figure 4.27 Velocity profile , along the vertical diameter in channel II, evaluated from the T and ϕ^+ measurements at 3 x 3.2 amperes heating current under the assumption of $j_y = 0$.

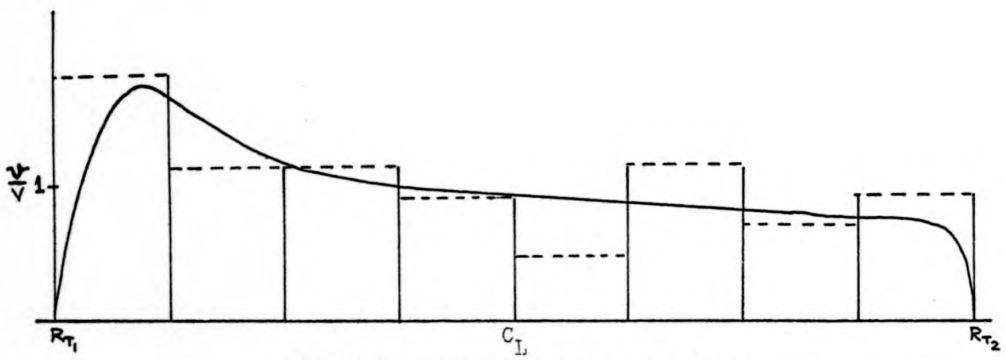

Radial distance along the vertical diameter
of Channel II
(each vertical line corresponds to the
location of the tip of thermoelectric
potential probe)

CHAPTER 5

THERMOELECTRIC MAGNETOHYDRODYNAMICS IN RECTANGULAR CROSS-SECTIONAL DUCT

5.1 Introduction

The rectangular cross-sectional duct is next to the circular cross-sectional duct in order of importance to be found in practical installations. The basic configuration of the TEMHD device considered here is that of a uniform rectangular cross-sectional duct whose longitudinal axis is horizontal, placed in a uniform, steady, transverse, horizontal magnetic field. The heating is done from the top and cooling from the bottom to ensure that the fluid in the duct is thermally stably stratified. Thus the complexity introduced by buoyancy effects when the fluid is heated from below (Bénard problem) is avoided. It has already been observed during the preliminary analysis of an infinitely long channel in section 3.2 that,for the configuration adopted, the top and bottom walls are necessarily conducting both thermally and electrically at the solid/fluid interface; the side walls may be either in thermal and electrical contact with the fluid at the interface or isolated by having a coating of insulation. It is to be noted here that while in practice all thermal insulators are also necessarily electrical insulators, it is possible to insulate electrically with reasonable thermal conduction across the insulation layer. The case of stainless steel is dubious as it is affected by its wetting property, and both thermal and electrical contact resistances vary widely.

The theoretical analysis of TEMHD in a rectangular cross-sectional duct of the configuration given above is presented in sections 5.2 and 5.3. The experimental device is described in section 5.4 and the experimental results are presented and discussed in section 5.5.

5.2 Theoretical Analysis: Stationary System

Assume that the walls of the rectangular duct are thin (t_w) compared to the dimensions of the duct cross-section (L), particularly at the top and the bottom boundaries where heating and cooling are done by devices external to the channel. The temperature drops across the thicknesses of these walls can therefore be ignored, and the top interface can be taken to be at the uniform temperature T_1 and the bottom interface at T_2 with $T_1 > T_2$. Though thin, the electrical potential drop across/top and bottom walls is neglected for convenience of analysis. Also neglected are thermal and electrical contact resistances at the top and the bottom interfaces.

5.2.1 Conducting sidewalls with insulated interface

Consider the case of the rectangular cross-sectional duct with its conducting side walls separated from the fluid with a thin layer of insulation, thermal and electrical. When the fluid is stationary, i.e. when the fluid flow in the z direction is blocked, the configuration shown in Figure 5.1 is just like two short-circuited conventional thermocouples on either side of the vertical central axial plane, apart from the fact that the element in one leg of the thermocouple is a fluid. Thus the shape of the fluid element is that of the duct (possibly deformed by the heating and cooling), but material displacement of the fluid in the z direction is allowed. If the TEMHD section is long compared to its end sections (non-TEMHD), $j_y = j$ is constant (from grad p = $\underline{j}\times\underline{B}$).

From equation 3.16 the equation of heat transfer is given by

$$Tj\left(\frac{\partial\alpha}{\partial Y}\right)_T + \left(T\frac{\partial\alpha}{\partial T}\right) j\frac{dT}{dY} - j^2/\sigma - \frac{d}{dY}\left(K\frac{dT}{dY}\right) = 0 \quad (5.1)$$

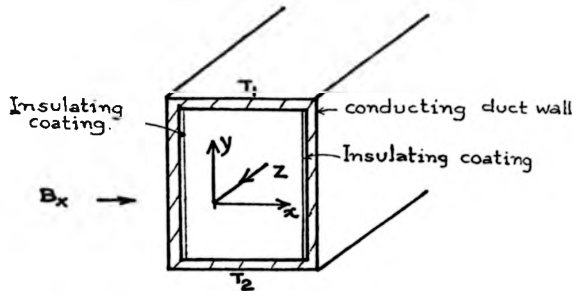

Figure 5.1 The rectangular cross-sectional duct with conducting horizontal wall to fluid interface but insulated interface at the vertical sidewalls in a transverse horizontal magnetic field.

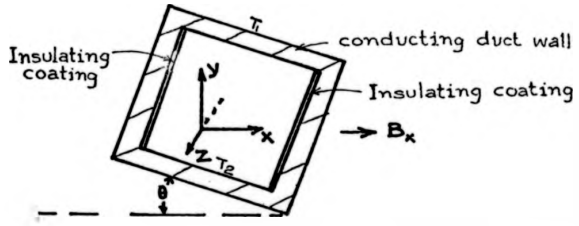

Figure 5.3 The rectangular channel with conducting solid-liquid interface at one pair of parallel walls and insulating interface at the other, positioned with the sidewalls inclined at an angle θ to the vertical in a transverse horizontal magnetic field B_x.

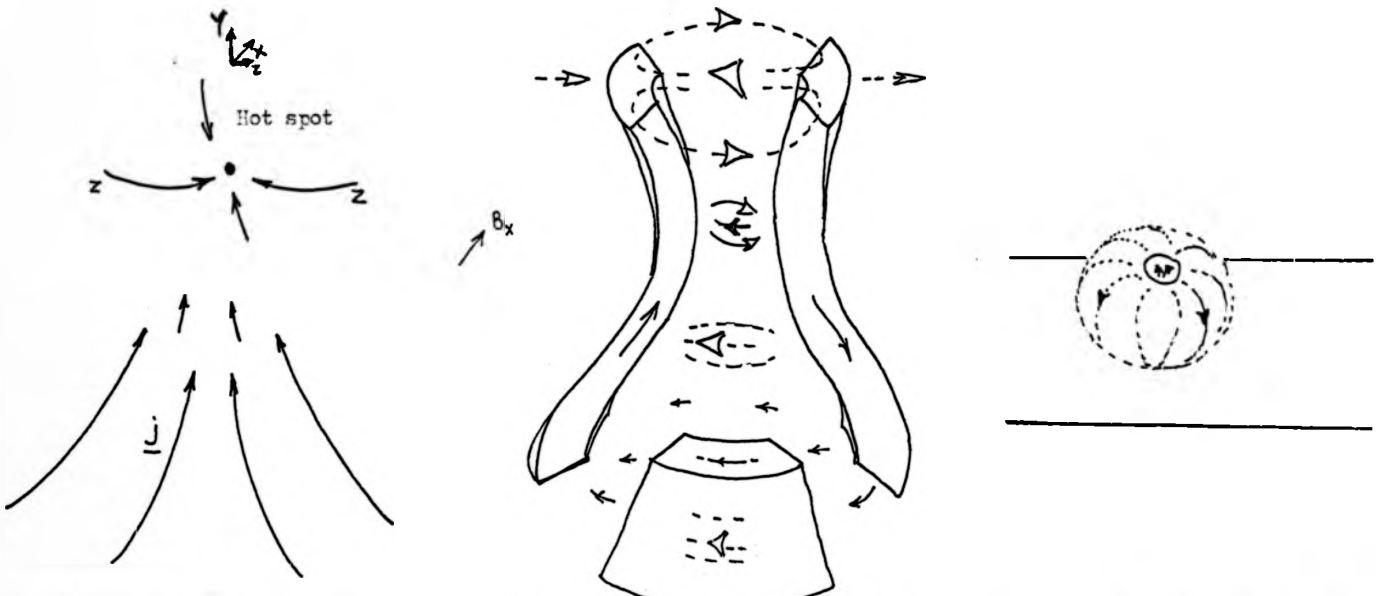

(a) Current flow pattern due to a hot spot at the top conducting wall of the rectangular cross-sectional straight duct

(c)Conceptual diagram of the fluid vorticity due to hot spotin the top wall- effect of increased B_x

(b) Fluid vorticity due to B_x and the thermoelectric current caused by the hot spot.

Figure 5.2 Effect of local perturbation in temperature in an otherwise isothermal horizontal wall of the rectangular cross-sectional straight duct in transverse horizontal magnetic field. ZZ axis of the channel in the longitudinal direction.

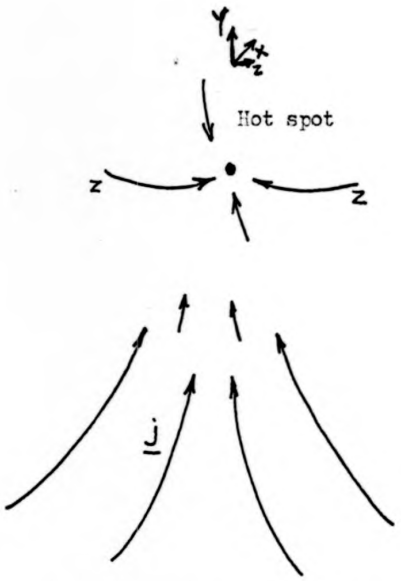

(a) Current flow pattern due to a hot spot at the top conducting wall of the rectangular cross-sectional straight duct

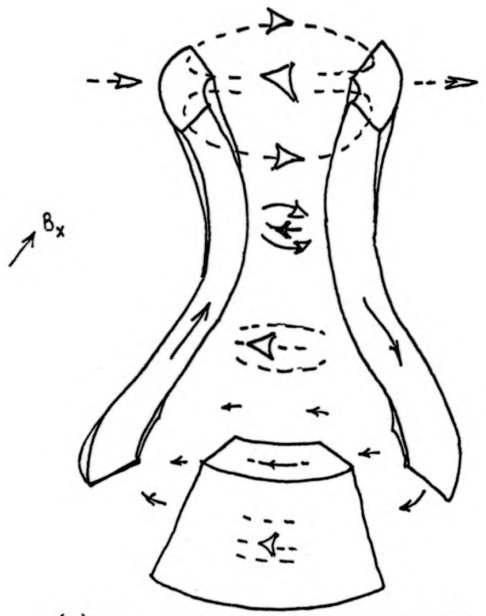

(c)Conceptual diagram of the fluid vorticity due to hot spotin the top wall- effect of increased B_x

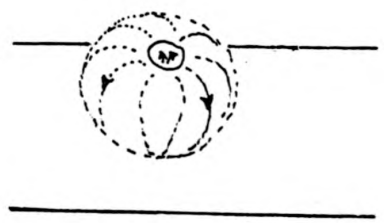

(b) Fluid vorticity due to B_x and the thermoelectric current caused by the hot spot.

Figure 5.2 Effect of local perturbation in temperature in an otherwise isothermal horizontal wall of the rectangular cross-sectional straight duct in transverse horizontal magnetic field. ZZ axis of the channel in the longitudinal direction.

Consider the fluid to be isotropic, homogeneous, with average values of the fluid physical properties

$$K \equiv \langle K \rangle_{av}, \sigma \equiv \langle \sigma \rangle_{av}, \langle T\frac{\partial \alpha}{dT} \rangle = \langle T\frac{\partial \alpha}{dT} \rangle_{av}$$

$$K \frac{d^2T}{dY^2} - \langle T\frac{\partial \alpha}{\partial T} \rangle j \frac{dT}{dY} + j^2/\sigma = 0 \qquad (5.2)$$

Solving for T

$$T = A_1 e^{\langle T\frac{\partial \alpha}{\partial T} \rangle j \frac{Y}{K}} + A_2 + \frac{jY}{\sigma \langle T\frac{\partial \alpha}{\partial T} \rangle} \qquad (5.3)$$

With boundary conditions $T = T_1 \quad Y = +L_y$

$$T = T_2 \quad Y = -L_y$$

evaluating A_1 and A_2

$$T = T_{av} = \{T_m - \frac{jL_y}{\sigma \langle T\frac{\partial \alpha}{\partial T} \rangle}\} \{1 + \frac{e^{-\langle T\frac{\partial \alpha}{\partial T} \rangle \frac{jL_y}{K}} + e^{\langle T\frac{\partial \alpha}{\partial T} \rangle \frac{jY}{K}}}{\sinh \langle T\frac{\partial \alpha}{\partial T} \rangle \frac{jL_y}{K}}\} + \frac{jY}{\sigma \langle T\frac{\partial \alpha}{\partial T} \rangle} \qquad (5.4)$$

where $T_{av} = (T_1 + T_2)/2$ and $2T_m = T_i - T_2$.

As a check with both $\langle T\frac{\partial \alpha}{\partial T} \rangle \to 0$, $\langle j \rangle \to 0$, using L'Hospital's rule

$$T = T_{av} + T_m \frac{Y}{L_y} \qquad (5.5)$$

which gives the linear temperature profile in ordinary heat transfer problem without thermoelectric effect.

With $\langle T\frac{\partial \alpha}{\partial T} \rangle$ small and expanding exponential functions in powers of $\langle T\frac{\partial \alpha}{\partial T} \rangle$

$$(\text{grad } T)_Y = \frac{dT}{dY} = \frac{T_m}{L_y} + \langle T\frac{\partial \alpha}{\partial T} \rangle \frac{jT_m}{KL_y} Y - \frac{j^2 Y}{\sigma K} \qquad (5.6)$$

Therefore the heat conduction rate (with time), with $A = L_x L_z$

$$= -KA\frac{dT}{dY} = -KA\frac{T_m}{L_y} + \langle T\frac{\partial \alpha}{\partial T} \rangle \frac{T_m}{L_y} jAY - \frac{j^2 A^2 2L_y}{\sigma A} \frac{Y}{2L_y} =$$

$$-KA\frac{T_m}{L_y} + \langle T\frac{\partial \alpha}{\partial T} \rangle T_m (jA) \frac{Y}{L_y} - \tfrac{1}{2}(jA)^2 \frac{2L_y}{\sigma A} \cdot \frac{Y}{L_y} \qquad (5.7)$$

which shows that the heat conduction across the horizontal cross-section passes through both the upper and lower boundaries in the same direction in the absence of j. With $j \neq 0$, half the total joule heat generated by the current flow in the interior of

the thermoelectric elements travel to each face $Y = \pm L_y$ in opposite directions. Similarly each half of the total Thomson heat $\frac{1}{2}\langle T\frac{\partial\alpha}{\partial T}\rangle (2T_m)(jA)$ in an element travels to $Y = \pm L_y$ in the opposite sense to that of the joule heat if $\langle T \frac{\partial\alpha}{\partial T}\rangle$ for the element as well as the direction of jA are positive.

The time rate of the total energy input at $Y = L_y$ at T_1 from (3.13)

$$q_i = \overline{KA}\,\frac{T_m}{L_y} - \langle T\frac{\partial\bar{\alpha}}{\partial T}\rangle |(jA)|\,T_m - \tfrac{1}{2}(jA)^2\,\bar{P} + (\bar{\alpha}(T_1)T_1 + \phi)|(jA)| \qquad (5.8)$$

while the time rate of the total energy rejected at $Y = -L_y$ at T_2 is given by

$$q_o = \overline{KA}\,\frac{T_m}{L_y} + \langle T\frac{\partial\alpha}{\partial T}\rangle |(jA)\,|T_m + \tfrac{1}{2}(jA)^2\bar{P} + (\bar{\alpha}(T_2)T_2 + \phi)|\,(jA)|\,(5.9)$$

where $\bar{\alpha} = \alpha_{Cu} \sim \alpha_{Hg}$, $\overline{KA} = K_wA_w + A_fK_f$, $\bar{P} = 2L_y\{\frac{1}{\sigma_wA_w} + \frac{1}{\sigma_fA_w}\}$ $A_w = t_wL_z$, $A_f = 2L_xL_z$, $jA = j_fA_f = j_wA_w$, suffixes f and w referring to the wall and the fluid respectively. For simplicity ϕ is taken to be the same at $Y = \pm L_y$.

Therefore the time rate of energy input into the system

$$q_i - q_o = \{T_1\bar{\alpha}(T_1) - T_2\bar{\alpha}(T_2)\}(jA) - (jA)^2\bar{P} - \langle T\frac{\partial\bar{\alpha}}{\partial T}\rangle |(jA)|\,(2T_m) \qquad (5.10)$$

In the stationary system, no energy is extracted from the system, therefore

$$A_fj_f = A_wj_w = Aj = \frac{T_1\alpha(T_1) - T_2\alpha(T_2) - \langle T\frac{\partial\bar{\alpha}}{\partial T}\rangle 2T_m}{\bar{P}}$$

$$= \frac{2T_m}{\bar{P}}\{\bar{\alpha}(T_{av})\} = \frac{2T_m\,\bar{\alpha}(T_{av})}{2L_y\{\frac{1}{\sigma_wA_w} + \frac{1}{\sigma_fA_f}\}} \qquad (5.11)$$

where a linear relationship $\alpha(T_1) = \alpha_o + (\frac{\partial\alpha}{\partial T})_oT$ is assumed.

This is consistent with j_f determined from the Kirchhoff's law for the electric circuit

$$j_f = \frac{\int_{T_2}^{T_1} \bar{\alpha} dT}{A_f \bar{P}} = \frac{2T_m \bar{\alpha}(T_{av})}{A_f \{\frac{1}{\sigma_w A_w} + \frac{1}{\sigma_f A_f}\} 2L_y} = \frac{\sigma_f \alpha T_m}{(1 + c) L_y} \qquad (5.12)$$

where $c = \frac{\sigma_f L_x}{\sigma_w t_w}$ and $\bar{\alpha}$ is replaced by the unambiguous symbol α.

(5.12) has a similar form to that in the circular cross-sectional duct with sinusoidal peripheral heating.

A simpler case of heat transfer is given by equation (5.2) with $< T\frac{\partial \alpha}{\partial T} > = 0$, which with boundary conditions $T = T_1$ at $Y = L_y$ and $T = T_2$ at $Y = -L_y$ results in the temperature distribution

$$T = T_{av} + \frac{T_m}{L_y} Y + (L_y^2 - Y^2) \frac{j^2}{2K\sigma} \qquad (5.13)$$

It should be appreciated that the temperature variations with Y in (5.4) and (5.3) are not linear, and adverse temperature gradient can be generated if in (5.4)

$$\frac{T_m}{L_y} + < T\frac{\partial \alpha}{\partial T} > \frac{jT_m}{KL_y} Y - \frac{j^2 Y}{\sigma K} < 0 \qquad (5.14a)$$

or in (5.13)

$$\frac{T_m}{L} - \frac{j^2 Y}{\sigma K} < 0 \qquad (5.14b)$$

With the maximum value of $Y = L_y$, (5.14b) gives the condition for adverse temperature gradient as

$$\alpha \geq (1 + c) \sqrt{\frac{K_f}{\sigma_f T_m}} \qquad (5.15)$$

It is interesting to note that the condition (5.15) is independent of L_y.

Consider the generation of maximum j_f with the constraint $(A_w + A_f)$ fixed, and for the minimum total energy rate input at $Y = L_y$ at T_1. With ϕ the electrochemical potential and the Thomson coefficient $< T\frac{\partial \alpha}{\partial T} >$ neglected, from (5.12) and (5.8)

$$j = \frac{\sigma \alpha T_m}{L_y (1 + c)}$$

$$q_i = \frac{\overline{KAT}_m}{L_y} - (jA)^2 \frac{\overline{P}}{2} + \alpha T_1 (jA)$$

$$= \frac{T_m}{L_y} \left\{ K_w A_w + K_f A_f + \frac{\sigma_f \alpha^2 A_f T_{av}}{1 + c} \right\}$$

Minimisation of the function

$$\textcircled{H} = \left\{ q_i / (A_f + A_w) \right\} / j_f = \frac{\alpha T_{av} F}{1 + F} + \frac{(K_w + K_f F)(1 + \sigma_f F/\sigma_w)}{\sigma_f \alpha (1 + F)}$$

where $F = A_f/A_w$, w.r.t F for maximum current with minimum of heating gives

$$F = A_f/A_w = \left\{ (1 - \frac{K_w}{K_f})(1 - \frac{\sigma_w}{\sigma_f}) - \alpha^2 \frac{\sigma_w}{K_f} T_{av} \right\}^{\frac{1}{2}} - 1 \quad (5.16)$$

which also gives the ratio of (t_w/L_x). Since $(A_f + A_w)$ is fixed, both A_f and A_w are determined.

Next consider the question of thermal instability with the top and bottom surfaces maintained at the uniform temperature T_1 and T_2 respectively. A similar problem in gas without thermo-electric current has been considered by Wright (1963) and Kulikovskii and Regirer (1965) for infinitely wide channels. The fluid physical properties considered in equation (5.2) are the averaged values, i.e.

$$\sigma = \frac{1}{2L_y} \int_{L_y}^{L_y} \sigma(Y) dy$$

which is equal to $\sigma(T_{av})$ if the temperature distribution were linear and $\sigma(T)$ were a linear function of T. Consider the local perturbation of temperature in the bulk of the fluid so that $\sigma(y)$ is also perturbed. Depending on the nature of $\sigma(T)$ variation with T, the liberation of joule heat is modified and, in some cases, may lead to thermal instability. The general three dimensional perturbation analysis is difficult, but the analysis of the simple case of two dimensional perturbation is included here for having a feel of the problem. The two dimensional channel is considered infinitely wide, $L_x \to \infty$, and any variation of

parameters with x is excluded. Ignoring the Thomson heat from (5.2) in the stationary fluid

$$K\frac{d^2T_o}{dY^2} + j_o^2/\sigma = 0 \quad , \quad T_o(\pm L_y) = T_{av} \pm T_m \qquad (5.17)$$

with $j_o = \frac{\sigma\alpha T_m}{(1+c)L_y}$, suffix o refers to unperturbed values.

With a local perturbation in temperature T, (no variation along x)

$$\rho c_v \frac{\partial T}{\partial t} = K\left(\frac{\partial^2 T}{\partial y^2} + \frac{\partial^2 T}{\partial z^2}\right) + 2\frac{\partial \phi}{\partial y} j_o + j_o^2 \frac{T}{\sigma^2}\frac{d\sigma}{dT} \qquad (5.18a)$$

where variation in K is ignored, $\sigma = \sigma(T_o(Y))$, $\frac{d\sigma}{dT} = \left(\frac{d\sigma}{dT}\right)_{T = T_o(Y)}$ and ϕ is the perturbed electrical potential.

Corresponding to div $\underline{j} = 0$

$$\frac{\partial}{\partial z}\left(\sigma\frac{\partial \phi}{\partial z}\right) + \frac{\partial}{\partial y}\left(\sigma\frac{\partial \phi}{\partial y} + j_o \frac{T}{\sigma}\frac{d\sigma}{dT}\right) = 0 \qquad (5.18b)$$

With T_1 and T_2 fixed and uniform, the boundary conditions for (5.17) and (5.18) are

$$T(\pm L_y) = 0, \quad \phi(\pm L_y) = 0$$

Equations (5.17) and (5.18) can be nondimensionalised by having

$$\overline{T} = \frac{T}{T_c} , \ \overline{t} = \frac{tK}{\rho c_v L_y^2} , \ \overline{Y} = \frac{Y}{L_y} , \ \overline{Z} = \frac{Z}{L_y} , \ \frac{\overline{j_o^2}}{\sigma} = \frac{j_o^2 L_y^2}{K\sigma T_c}$$

where T_c is some characteristic temperature, and then dropping the bars into

$$\frac{\partial T}{\partial t} = \frac{\partial^2 T}{\partial z^2} + \frac{\partial^2 T}{\partial y^2} + 2\frac{\partial \phi}{\partial y} j_o + \frac{j_o^2}{\sigma^2} T \frac{d\sigma}{dT}$$

and $$\frac{\partial}{\partial z}\left(\sigma\frac{\partial \phi}{\partial z}\right) + \frac{\partial}{\partial y}\left(\sigma\frac{\partial \phi}{\partial y} + j_o \frac{T}{\sigma}\frac{d\sigma}{dT}\right) = 0 \qquad (5.19)$$

with boundary conditions $T(\pm 1) = 0$, $\phi(\pm 1) = 0$ (5.20)

Particular solutions of the system (5.19), (5.20), consistent with the two dimensional analysis, of the form

$$T = \textcircled{T}(Y)\, e^{i\mu z - \lambda t}$$

$$\phi = \textcircled{\phi}(Y)\, e^{i\mu z - \lambda t}$$

give $\textcircled{T}'' + \left(\frac{T_o'''}{T_o'} - \mu^2 + \lambda\right)\textcircled{T} + 2j_o\textcircled{\phi}' = 0$ (5.21)

and $\left(\frac{j_o\textcircled{\phi}'}{T_o''}\right)' - \mu^2\frac{j_o\textcircled{\phi}}{T_o''} + \left(\textcircled{T}\frac{T_o'''}{T_o'T_o''}\right)' = 0, \ \textcircled{T}(\pm 1) = \textcircled{\phi}(\pm 1) = 0$ (5.22)

where the prime ' indicates ordinary differentiation w.r.t Y, i.e. $\frac{d}{dY}$.

Consider the case of large wavelength only, so that $\mu \to 0$.

Then, $\textcircled{T}'' + \left(\lambda + \frac{T_o'''}{T_o'}\right)\textcircled{T} + 2j_o\textcircled{\phi}' = 0$ (5.23)

$\left(\frac{j_o\textcircled{\phi}'}{T_o''}\right)' + \left(\textcircled{T}\frac{T_o'''}{T_o'T_o''}\right)' = 0, \ \textcircled{T}(\pm 1) = \textcircled{\phi}(\pm 1) = 0$ (5.24)

Therefore

$$\textcircled{T}'' + \left(\lambda - \frac{T_o'''}{T_o'}\right)\textcircled{T} + \frac{2T_o''}{T_o'(1) - T_o'(-1)}\int_{-1}^{1}\frac{T_o'''}{T_o'}\textcircled{T}\,dY = 0, \ \textcircled{T}(\pm 1) = 0 \quad (5.25)$$

This equation (5.25) is the same as that of equation (13), (14) in Kulikovskii and Regirer (1965), and therefore the conclusions therein are valid here as well. The conclusions are as follows:-

(i) For all odd solutions of $\textcircled{T}$, the perturbations decay exponentially with time.

(ii) For even solutions of $\textcircled{T}$, for $\sigma(T) = \sigma_o e^{\varepsilon T}$, the system is stable for $\varepsilon < 0$; the system is stable also for $\varepsilon > 0$ if $T_o(0) < T_{o_{critical}}(0)$, but unstable if $T_o(0) > T_{o_{critical}}(0)$ where $T_{o_{critical}}(0)$ corresponds to the solution of (5.25) when λ is in transition through 0. Since $\varepsilon < 0$ for liquid metals, the system would be stable for large wavelength perturbations in general.

Next consider an altogether different situation, that of a local perturbation in temperature at the top and bottom interfaces, otherwise maintained at uniform T_1 and T_2 respectively. For fixing ideas, consider a hot spot $T(x, L_y, z)$ at the top interface. The thermoelectric current flow due to such perturbation is shown in Figure 5.2a. The buoyancy driven vortex is toroidal around the hot spot if it is a sufficient distance away from the side walls

(Figure 5.2b). The vorticity induced by the electromagnetic force ($\underline{j}X\underline{B}$) has its axis oriented preferentially either in the direction of the magnetic field B or in the direction transverse both to B and the longitudinal channel axis (L_z), but not along L_z. A conceptual diagram of such $\underline{j}X\underline{B}$ induced vorticity is shown in Figure 5.2c. At strong B, the overall vortex shrinks in the z direction

The practical possibility of a situation where $(\Delta T)_y$ is uniform but T_1 and T_2 are linear functions of x needs mention. At critical values of $\frac{\partial(T_1,T_2)}{\partial x}$, shear layers in both central horizontal and vertical planes containing L_z could be generated. This problem is considered in detail in Chapter 6.

The pressure difference across the TEMHD section, when the flow in the z direction is blocked, is given by equation (3.1) with V = O if

$$\frac{\partial p}{\partial z} = \underline{j}_f X \underline{B}$$

From (5.12)
$$\frac{\partial p}{\partial z} = \frac{\sigma_f \alpha T_m B}{(1 + c)L_y} \tag{5.26}$$

therefore
$$\Delta p = \frac{\sigma_f \alpha T_m B}{(1 + c)L_y} L_z \tag{5.27}$$

The corresponding difference in head of Hg is given by

$$\Delta h = \frac{\sigma_f \alpha T_m B L_z}{(1 + c)L_y \rho_{Hg} g} \tag{5.28}$$

where g is the acceleration due to gravity. It is interesting to note that the expression is similar to that in the case of a circular cross-sectional tube with a sinusoidal circumferential temperature distribution.

Still considering the basic stationary system, i.e. the flow in the z direction blocked, if the channel is so oriented that the top and the bottom interfaces (A,A) (Figure 5.3) are inclined at θ (measured anticlockwise) to the horizontal plane, buoyancy driven longitudinal vortices do appear above the critical value of the

parameter $\mathcal{N} = \dfrac{g\beta\left(\frac{\partial T}{\partial y}, \frac{\partial T}{\partial x}\right) L_y^4}{\nu K M^2}$ / with $\left(\frac{\partial T}{\partial y}, \frac{\partial T}{\partial x}\right)$ a function of $\frac{\partial T}{\partial y}$ and $\frac{\partial T}{\partial x}$. In the case where the temperatures T_1 and T_2 at AA are maintained

$$\Delta p = \frac{\sigma_f \alpha T_m B \sin\theta}{(1 + c) L_y} \qquad (5.29)$$

but for finite capacity external heating and cooling devices at AA, Δp would be reduced for $\mathcal{N} < \mathcal{N}_{critical}$.

5.2.2 Conducting sidewalls with electrical contact with the fluid at the interface

From the preliminary analysis of the TEMHD channel in section 3.3, it is clear that as long as $\frac{dT}{dy}$ remains constant, i.e. T is a linear function of y alone, the analysis of rectangular TEMHD ducts makes no distinction between the case of conducting side walls, whether in electrical contact or not, with the fluid at the interface. Thus with $\frac{dT}{dy}$ constant, the analysis of (5.21) is valid here. However, when $\frac{dT}{dy}$ is not constant, as it would not be when there is significant level of j_{fy}, j_x will no longer be zero and j_{fy} independent of x. The fluid will therefore circulate with the vortex axis along B, even though net flow in the z direction may be blocked in the external connecting loop of the fluid. The probable neutral shear layer is now in the central section of the horizontal plane containing L_z.

5.3 TEMHD Analysis (Fluid Moving)

5.3.1 Sidewall interface insulated

Consider the configuration described in section 5.2.1, but now the flow in the z direction being allowed with blocks in the circulating loop connected at the ends of the TEMHD section removed. The top (heated uniformly at T_1) and bottom (at T_2) perfectly conducting walls are strictly horizontal and parallel

to the external magnetic field $B_x = B$ to avoid the possibility of M shaped velocity profile of Alty (1966). There is no exact solution for the corresponding ordinary MHD problem, but a solution based on boundary layer analysis at large values of M has been worked out by Hunt and Stewartson (1965) and Chiang and Lundgren (1967). Such analysis relies on the fact that there is a predominantly uniform core flow flanked by thin boundary layers on the walls and the complex flow near the corners is ignored. In the theoretical analysis that follows, TEMHD flow has been treated as electrically driven (due to a potential source equivalent to the thermoelectric e.m.f. applied across the channel height perpendicular to B) ordinary MHD flow. Thus the analysis closely follows the ordinary MHD analysis of Hunt and Stewartson (1965); however, the details of the mathematical steps are provided to arrive at the result. Consider the fully developed TEMHD flow with no variation of flow parameters w.r.t z except that of pressure p (refer to Figure 5.1).

Therefore div $\underline{j} = 0$ gives $\frac{\partial j_x}{\partial x} + \partial j_y/\partial y = 0$, so that a stream function H(x,y) exists such that

$$j_y = \frac{\partial H}{\partial x} = \sigma(-\frac{\partial \phi}{\partial y} - vB) \tag{5.30}$$

$$j_x = \frac{\partial H}{\partial y} = \sigma(-\frac{\partial \phi}{\partial x}) \tag{5.31}$$

where $\sigma = \sigma(x,y) \equiv \sigma(y)$ here, but for simplicity only the average value of σ is considered. $v \equiv v_z$, ϕ is the electrical potential.

From equation (3.1), since the flow is fully developed

$$0 = -\partial p/\partial z + j_y B + \eta_v(\frac{\partial^2 v}{\partial x^2} + \frac{\partial^2 v}{\partial y^2})$$

$$= -\partial p/\partial z + B\frac{\partial H}{\partial x} + \eta_v(\frac{\partial^2 v}{\partial x^2} + \frac{\partial^2 v}{\partial y^2}) \tag{5.32}$$

where η_v is also considered as the average value for simplicity.

From (5.30) and (5.31)

$$\frac{1}{\sigma}\left(\frac{\partial^2 H}{\partial x^2} + \frac{\partial^2 H}{\partial y^2}\right) + B\frac{\partial v}{\partial x} = 0 \qquad (5.33)$$

The corresponding boundary conditions for (5.32) and (5.33) are

$$v = 0 \quad y = \pm L_y,\ x = \pm L_x$$

$$\partial H/\partial y = 0 \qquad y = \pm L_y,\ x = \pm L_x \qquad (5.34)$$

Therefore at $x = \pm L_x$, H is independent of y so that if $H = H_1$ at $x = L_x$ and $H = H_2$ at $x = -L_x$ from (5.30)

$$\frac{I}{L_z} = \int_{-L_x}^{L_x} j_y\Big|_{y=L_y} dx = H_1 - H_2 \qquad (5.35)$$

where I is the total current crossing the solid/liquid interface at the top wall and L_z is the length of the channel.

The equations (5.32) and (5.33) are nondimensionalised by having

$$\bar{y} = \frac{y}{L_x},\ \bar{x} = \frac{x}{L_x},\ M = L_x B\left(\frac{\sigma}{\eta_v}\right)^{\frac{1}{2}},\ -\frac{\partial p}{\partial z} + \frac{B}{2L_x}(H_1 - H_2) = \bar{p}$$

$$\bar{v} = \frac{\eta v}{L_x^2 \bar{p}} \quad \text{and} \quad \bar{H} = \frac{H - \frac{1}{2}(H_1 + H_2) - \frac{1}{2}(H_1 - H_2)\bar{x}}{L_x \bar{p}\left(\frac{\sigma}{\eta_v}\right)^{\frac{1}{2}}} \qquad (5.36)$$

and then dropping the bars

$$\frac{\partial^2 v}{\partial x^2} + \frac{\partial^2 v}{\partial y^2} + M\frac{\partial H}{\partial x} = -1$$

$$\frac{\partial^2 H}{\partial x^2} + \frac{\partial^2 H}{\partial y^2} + M\frac{\partial v}{\partial x} = 0 \qquad (5.37)$$

with boundary conditions $v = 0$, $H = 0$ at $x = \pm 1$

and $v = 0$, $\partial H/\partial y = 0$ at $y = \pm L_y/L_x$

(a) Core flow: pertinent solutions of v and H are of order $\frac{1}{M}$

$v = \frac{ay + b}{M}$ with $H = -x/M$ satisfies equation (5.37) but not the boundary conditions. (5.38)

Therefore there must be boundary layers at the walls to satisfy the boundary conditions.

(b) Hartmann boundary layers: these layers are of the order $O(\frac{1}{M})$ near $x = \pm 1$. Let $v = \frac{ay + b}{M} + v_h$

$$H = -x/M + H_h$$

Then since $\partial/\partial x >> \partial/\partial y$ from (5.37)

$$\frac{\partial^2 v_h}{\partial x^2} + M\frac{\partial H_h}{\partial x} = 0$$

$$\frac{\partial^2 H_h}{\partial x^2} + M\frac{\partial v_h}{\partial x} = 0$$

with boundary conditions $H_h = \frac{1}{M}$, $v_h = \frac{-(ay + b)}{M}$ at $x = 1$ while both $\to 0$ immediately away from $x = 1$.

Then $a = 0$ and $b = 1$

and $v_h = -\frac{1}{M} e^{-M(1-x)}$, $H_h = \frac{1}{M} e^{-M(1-x)}$ (5.39)

Similarly at $x = -1$,

$$v_h = -\frac{1}{M} e^{M(-1+x)}, \quad H_h = -\frac{1}{M} e^{M(-1+x)}$$

(c) Conducting wall boundary layers: For all walls nonconducting, Shercliff (1953) has shown that for finite L_y the Hartmann solution is valid except at the top and bottom walls (Figure 5.1) where there is a boundary layer of thickness $O(\frac{1}{\sqrt{M}})$. It is assumed that such boundary layers do occur here as well, so that v and H change across these layers from the core value to satisfy the boundary conditions at these walls. Assume therefore thin boundary layers so that $\frac{\partial}{\partial y} >> \partial/\partial x$

Let $v = \frac{1}{M} + v_b$ (since $a = 0$ and $b = 1$)

$$H = \frac{-x}{M} + H_b$$

In the boundary layer at $y = + L_y/L_x$, v_b and H_b satisfy

$$\frac{\partial^2 v_b}{\partial y^2} + M\frac{\partial H_b}{\partial x} = 0 \qquad (5.40)$$

and

$$\frac{\partial^2 H_b}{\partial y^2} + M\frac{\partial v_b}{\partial x} + 0$$

(b) Hartmann boundary layers: these layers are of the order $O(\frac{1}{M})$ near $x = \pm 1$. Let $v = \frac{ay + b}{M} + v_h$

$$H = -x/M + H_h$$

Then since $\partial/\partial x >> \partial/\partial y$ from (5.37)

$$\frac{\partial^2 v_h}{\partial x^2} + M\frac{\partial H_h}{\partial x} = 0$$

$$\frac{\partial^2 H_h}{\partial x^2} + M\frac{\partial v_h}{\partial x} = 0$$

with boundary conditions $H_h = \frac{1}{M}$, $v_h = \frac{-(ay + b)}{M}$ at $x = 1$ while both $\to 0$ immediately away from $x = 1$.

Then $a = 0$ and $b = 1$

and $$v_h = -\frac{1}{M} e^{-M(1-x)}, \quad H_h = \frac{1}{M} e^{-M(1-x)} \tag{5.39}$$

Similarly at $x = -1$,

$$v_h = -\frac{1}{M} e^{M(-1+x)}, \quad H_h = -\frac{1}{M} e^{M(-1+x)}$$

(c) Conducting wall boundary layers: For all walls nonconducting, Shercliff (1953) has shown that for finite L_y the Hartmann solution is valid except at the top and bottom walls (Figure 5.1) where there is a boundary layer of thickness $O(\frac{1}{\sqrt{M}})$. It is assumed that such boundary layers do occur here as well, so that v and H change across these layers from the core value to satisfy the boundary conditions at these walls. Assume therefore thin boundary layers so that $\frac{\partial}{\partial y} >> \partial/\partial x$

Let $v = \frac{1}{M} + v_b$ (since $a = 0$ and $b = 1$)

$$H = \frac{-x}{M} + H_b$$

In the boundary layer at $y = + L_y/L_x$, v_b and H_b satisfy

$$\frac{\partial^2 v_b}{\partial y^2} + M\frac{\partial H_b}{\partial x} = 0 \tag{5.40}$$

and

$$\frac{\partial^2 H_b}{\partial y^2} + M\frac{\partial v_b}{\partial x} + 0$$

and the boundary conditions are $\frac{\partial H_b}{\partial y} = 0$, $v_b = -\frac{1}{M}$ at $y = \frac{L_y}{L_x}$, $|x| \leq 1$

Away from $y = \frac{L_y}{L_x}$, $H_b \to 0$, $v_b \to 0$

and $H_b + v_b \to 0$ at $x \to 1$ and $v_b - H_b \to 0$ at $x \to -1$

Let H_b at $y = +L_y/L_x$ be given by $H_b = \frac{H(x)}{M}$ (Note this $H(x)$ is different from $H(x,y)$, H etc.)

Also let $X = v_b + H_b$, then

$$v_b = \tfrac{1}{2}\{X(x) + X(-x)\}$$

$$H_b = \tfrac{1}{2}\{X(x) - X(-x)\}$$

From (5.40)

$$\frac{\partial^2 X}{\partial y^2} + M\frac{\partial X}{\partial x} = 0$$

with boundary conditions $X = \frac{H(x) - 1}{M}$, $\frac{\partial}{\partial y}\{X(x) - X(-x)\} = 0$ at $y = \frac{L_y}{L_x}$.

Away from $y = \frac{L_y}{L_x}$ $X \to 0$, and $X = 0$ at $x = 1$.

Introduce a new co-ordinate transform $Y = \frac{L_y}{L_x} - y$

Then $$\frac{\partial^2 X}{\partial Y^2} + M\frac{\partial X}{\partial x} = 0 \qquad (5.41)$$

$$X = \frac{H(x)-1}{M}, \ \frac{\partial}{\partial Y}\{X(x)-X(-x)\} = 0 \quad \text{at } Y = 0$$

$$Y \to \infty \Big\}, \ X \to 0; \quad X = 0 \text{ at } x = 1$$
$$\frac{\partial X}{\partial Y} \to 0$$

Multiply (5.41) by sinfY and integrate w.r.t Y from 0 to ∞

$$\int_0^\infty (\sin fY)\frac{\partial^2 X}{\partial Y^2}\,dY + M\int_0^\infty (\sin fY)\,\frac{\partial X}{\partial x}\,dY = 0 \qquad (5.42)$$

Integrate by parts

$$\int_0^\infty (\sin fY)\frac{\partial^2 X}{\partial Y^2}\,dY = (\sin fY)\,\frac{\partial X}{\partial Y}\Big|_0^\infty - f\int_0^\infty (\cos fY)\,\frac{\partial X}{\partial Y}\,dY$$

$$= -f\,(\cos fY)\,X\Big|_0^\infty - f^2\int_0^\infty (\sin fY)\,X\,dY$$

$$= +\frac{H(x)-1}{M}\,f - f^2\int_0^\infty X \sin fY\,dY \qquad (5.43)$$

From (5.42) and (5.43) with $\bar{X}(f,x) = \int_0^\infty X \sin fY\,dY$

$$M\frac{\partial}{\partial x}\bar{X}(f,x) - f^2\bar{X}(f,x) + \frac{H(x)-1}{M}\,f = 0$$

Integrating between 1 to x and having X = 0 at x = 1

$$\bar{X}(f,x)\ e^{-f^2/M^x} = \frac{f}{M}\int_x^1 \left(\frac{H(\zeta)-1}{M}\right) e^{-f^2/M^\zeta}\, d\zeta$$

Inverse transform gives

$$X = \frac{2}{\pi}\int_0^\infty \bar{X}(f,x)\sin fY\, df = \frac{2}{\pi}\int_0^\infty \int_x^1 \frac{f}{M}\left\{\frac{H(\zeta)-1}{M}\right\}\sin fY\ e^{\left(-\frac{f^2}{M}\zeta + f^2/M^x\right)} d\zeta df$$

$$= \frac{1}{\pi}\int_x^1 \frac{H(\zeta)-1}{M}\, d\zeta \int_0^\infty \frac{2f}{M} e^{-\frac{1}{M}f^2/M)(\zeta-x)} \sin fY df$$

Integrating by parts the inner integral

$$= \frac{Y}{\pi}\int_x^1 \frac{H(\zeta)-1}{M}\, d\zeta \int_0^\infty \frac{e^{-\frac{1}{M}f^2/M)(\zeta-x)}}{(\zeta-x)} \cos fY df$$

$$= \frac{Y}{\pi}\int_x^1 \frac{H(\zeta)-1}{M}\cdot\frac{1}{(\zeta-x)}\cdot\tfrac{1}{2}\cdot\left(\frac{\pi}{\frac{\zeta-x}{M}}\right)^{\frac{1}{2}} e^{-\frac{Y^2M}{4(\zeta-x)}}\, d\zeta$$

$$= \frac{Y}{2\sqrt{M\pi}}\int_x^1 \frac{H(\zeta)-1}{(\zeta-x)^{3/2}}\ e^{-Y^2M/4(\zeta-x)}\, d\zeta \qquad (5.44a)$$

$$= +\frac{2}{\sqrt{\pi}}\int_\infty^{\frac{Y\sqrt{M}}{\sqrt{1-x}}} \frac{e^{-\zeta^2}}{M} d\zeta + \frac{Y}{2\sqrt{M\pi}}\int_x^1 \frac{H(\zeta)}{(\zeta-x)^{3/2}} e^{\frac{-Y^2M}{4(\zeta-x)}}\, d\zeta \qquad (5.44b)$$

Reverting back to $Y = L_y/L_x - y$

$$X = \frac{(-1)}{M}\operatorname{erfc}\frac{(L_y/L_x-y)\sqrt{M}}{2\sqrt{1-x}} + \frac{(L_y/L_x-y)}{2\sqrt{M\pi}}\int_x^1 \frac{H(\zeta)}{(\zeta-x)^{3/2}} e^{-M\left(\frac{L_y}{L_x}-y\right)^2/4(\zeta-x)}\, d\zeta \qquad (5.44c)$$

Differentiating x w.r.t y and having $\frac{\partial}{\partial y}\{X(x)-X(-x)\} = 0$

at $y = L_y/L_x$, i.e. $Y = 0$

$$\int_x^1 \frac{H'(\zeta)\,d\zeta}{(\zeta-x)^{\frac{1}{2}}} = \int_{-1}^x \frac{H'(\zeta)\,d\zeta}{(x-\zeta)^{\frac{1}{2}}} \qquad (5.45)$$

In the interval

(i) 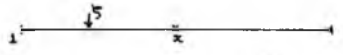

(ii) 

Figure 5.4

Interval of integration

(i) $(1,x)$, $(\zeta-x)$ is +ve; so is $(x-\zeta)$ in the interval (ii) so that the integrands can be replaced by the modulus

therefore $$\int_{x}^{1} \frac{H'(\zeta)}{|\zeta-x|^{\frac{1}{2}}}\, d\zeta - \int_{-1}^{x} \frac{H'(\zeta)}{|x-\zeta|^{\frac{1}{2}}}\, d\zeta = 0$$

therefore $$\int_{x}^{1} \frac{H'(\zeta)}{|\zeta-x|^{\frac{1}{2}}} \operatorname{sgn}(x-\zeta)\, d\zeta + \int_{-1}^{x} \frac{H'(\zeta)}{|x-\zeta|^{\frac{1}{2}}} \operatorname{sgn}(x-\zeta)\, d\zeta = 0$$

or $$\int_{-1}^{1} \frac{H'(\zeta)}{|x-\zeta|^{\frac{1}{2}}} \operatorname{sgn}(x-\zeta)\, d\zeta = 0 \qquad (5.46)$$

This can be transformed into a standard integral equation with the substitution

$$x = \frac{1+X}{2} \text{ and } Y = \frac{1+\zeta}{2}$$

ao that

$$\int_{0}^{1} \frac{H'(Y)}{|X-Y|^{\frac{1}{2}}} \operatorname{sgn}(X-Y)\, dY = 0 \qquad (5.47)$$

whose solution is $H'(X) = A_1 X^{-\frac{1}{4}}(1-X)^{-\frac{1}{4}}$

substituting back

$$H'(x) = A_2(1-x^2)^{-\frac{1}{4}} \qquad (5.48a)$$

The solution, however, is non-unique. Evaluating the constant by integrating both sides w.r.t X between the limits +1 and -1

$$A_2 = \frac{2\sqrt{2\pi}}{(\Gamma\frac{1}{4})^2}$$

therefore $$H'(x) = \frac{2\sqrt{2\pi}}{(\Gamma\frac{1}{4})^2}(1-x^2)^{-\frac{1}{4}} \qquad (5.48b)$$

It is important to note that the characteristic thickness of the boundary layer as seen from equation (5.44a) is $O(\frac{1}{\sqrt{M}})$, the same as that of all nonconducting wall case of Shercliff (1953).

Ignoring the complex flow at the corners and the overlapping Hartmann and boundary layers, the velocity flux can be calculated from (a), (b) and (c)

(a) $$\int_{D} v\,dx\,dy = \frac{4L_y/L_x}{M}$$

$\int_{D} v\,dx\,dy \equiv \int dx \int v\,dy$ = total flux in (a) (symmetry condition used implicitly)

$$\text{(b)}\quad \int_{b_D} v_h\,dxdy = \int_{-L_y/L_x}^{+L_y/L_x} 2dy \int_{-1}^{1} \left\{-\frac{1}{M} e^{M(-1+x)}\right\} dx = \frac{-4L_y/L_x}{M^2} \qquad (5.49)$$

(c) v_b is even in x and H_b is odd in x and independent of x; therefore X can be used straightway in the evaluation of velocity flux in place of v_b. Since the boundary layer is of characteristic length $O(\frac{1}{\sqrt{M}})$, it is appropriate to consider $\bar{Y} = Y\sqrt{M}$ so that

$$\int_{c_D} v_b\,dxdy = -2\int_{-1}^{1} dx \int_{o}^{\infty} \frac{d\bar{Y}}{\sqrt{M}}\, X = 2\int_{-1}^{1} \frac{dx}{M\sqrt{M\pi}} \int_{x}^{1} \left\{\frac{H(\zeta)-1}{(\zeta-x)^{1/2}}\right\} d\zeta \int_{o}^{\infty} \frac{2\bar{Y}d\bar{Y}}{4(\zeta-x)}\, e^{-\bar{Y}^{-2}/4(\zeta-x)}$$

(from 5.44a)

$$= -2\int_{-1}^{1} \frac{dx}{M\sqrt{M\pi}} \int_{x}^{1} \left(\frac{1-H(\zeta)}{(\zeta-x)^{1/2}}\right) d\zeta = -2\int_{-1}^{1} \frac{dx}{M\sqrt{M\pi}} \left\{\overline{1-H(\zeta)}\;\; 2(\zeta-x)^{1/2}\Big|_{x}^{1} + 2\int_{x}^{1} H'(\zeta)(\zeta-x)^{1/2}\, d\zeta\right\}$$

(integration by parts)

$$= -2\int_{-1}^{1} \frac{dx}{M\sqrt{M\pi}} \frac{2\sqrt{2\pi}}{(\Gamma\tfrac{1}{4})^2} (1-x^2)^{-3/4} \int_{x}^{1} 2(\zeta-x)^{1/2}\, d\zeta \qquad \text{(from 5.48)}$$

$$= -\frac{(2)^3\sqrt{2\pi}}{M\sqrt{M\pi}(\Gamma\tfrac{1}{4})^2} \cdot \frac{2}{3}\left(2(\Gamma\tfrac{1}{4})^{3/4}\Gamma\tfrac{1}{4}\right)$$

$$= -\frac{8\sqrt{2}}{M^{3/2}} \frac{\Gamma\tfrac{3}{4}}{\Gamma\tfrac{1}{4}} = -\frac{3.625}{M^{3/2}} \qquad (5.50)$$

Combining (5.49) and (5.50)

$$\int_{abc_D} v\,dxdy = \frac{4L_y}{M}\left\{1 - \frac{1}{M} - \frac{0.956}{\sqrt{M}}\right\} \text{ neglecting terms } O(\frac{1}{M^n}),$$

$n > 1$ for complex regions of flow. (5.51)

This only differs slightly from that of all nonconducting walls of Shercliff (1953)

$$\int_{D} v\,dxdy = 4\frac{L_Y/L_x}{\sqrt{M}}\left\{1 - \frac{1}{M} - \frac{0.852}{\sqrt{M}}\right\}$$

However, having an all nonconducting duct is of no use in TEMHD. Integrating (5.30) the potential drop across the fluid is given by

$$\frac{2L_y}{2L_x\sigma}\ \frac{I}{L_z} + \frac{B\ \int^* v\,dx\,dy}{2L_x} \qquad (5.52)$$

where * means dimensional v, x, y are used.

The conducting sidewalls and the thermoelectric e.m.f. may be replaced by the Thévenin's equivalent

$$2\alpha T_m - \frac{2L_y\ I}{2t_w\sigma_w L_z} \qquad (5.53)$$

From (5.36) the dimensional volume flow rate (time)

$$\int_D^* v\,dx\,dy = \left(\frac{BI}{2L_xL_z} - \frac{\partial p}{\partial z}\right)\frac{4L_x^{\,3}L_y}{\eta M}\left\{1 - \frac{1}{M} - \frac{0.956\ L_x}{L_y\sqrt{M}}\right\} \qquad (5.54)$$

$$\text{where } I = \frac{2\alpha T_m - \frac{B}{2L_x}\int_D^* v\,dx\,dy}{\frac{2L_y}{2L_xL_z\sigma} + \frac{2L_y}{2t_w\sigma_w L_z}} \qquad \text{(from (5.52) and (5.53))} \qquad (5.55)$$

$$\text{that is } \langle j_y\rangle = \frac{\sigma\alpha T_m - \frac{B}{2L_x}\int_D^* v\,dx\,dy}{L_y(1+c)}$$

It is to be noted here that only average values of σ and η_v have been used in the above analysis. As long as the fluid is uniformly stratified and there is no variation in σ and η_v with x, the flow should not be affected to a great extent. The type of velocity profile in such flows with fluid property variation with temperature is an intriguing one. From the experimental results of the circular cross-sectional duct, it is expected that the velocity profile along B would be flat, while in the direction transverse to B, it is an asymmetrical M shape with higher velocity near T_1.

The mean velocity $V = \frac{1}{4L_xL_y}\int_D^* v\,dx\,dy$ can be obtained from (5.54) and (5.55)

$$\text{as } V\left\{1 + \frac{M}{1+c}\left(1 - \frac{1}{M} - \frac{0.956L_x}{L_y\sqrt{M}}\right)\right\} = \left(\frac{\alpha T_m}{L_yB} - \frac{1+c}{\sigma B^2}\frac{\partial p}{\partial z}\right)\left(1 - \frac{1}{M} - \frac{0.956L_x}{L_y\sqrt{M}}\right)\frac{M}{1+c} \qquad (5.56)$$

If M >> 1 and c,

$$V = \frac{\alpha T_m}{L_y B} - \frac{1 + c}{\sigma B^2} \frac{\partial p}{\partial z}$$

which has a striking similarity with the V in case of circular cross-sectional duct with sinusoidal circumferential heating, the temperature gradient T_m/L_y being replaced by T_m/R.

5.3.2 All wall interfaces electrically conducting

The problem of rectangular cross-sectional duct flow in ordinary MHD with the walls parallel to B perfectly conducting and those transverse to B of finite conductivity and having electrical contact with the fluid has not yet been solved. Chang and Lundgren (1961) have solved the extreme case when all the walls are perfectly conducting, and Hunt (1965) that with walls parallel to B of finite conductivity and perfectly conducting walls transverse to B. In the case when all the walls are perfectly conducting, i.e. C = O, there should be an exact balance between $\frac{\partial}{\partial s} \phi^+$ and Bv along the interface at walls transverse to B for $\partial p/\partial z$ = O. With a linear variation of T along y, a slug flow model would be quite appropriate. Consider the perfectly conducting rectangular duct with symmetrical temperature distribution in a horizontal transverse magnetic field $B_x = B$ (Figure 5.5a). Let the total potential be ϕ^+ (including thermo-electric e.m.f., $\int_y \alpha dT$, a function of y, the height, only.)

Then in the fluid, from the equation of inertialess steady motion

$$\partial p/\partial z = - \sigma B(Bv - \partial\phi^+/\partial y) + \eta \nabla^2 v$$

and from div $\underline{j}$ = O,

$$\nabla^2 \phi^+ = B \partial v/\partial y$$

Substitute $\phi = \phi^+ - \int_y \alpha dT$ (= O at the walls). Then, provided

$$\frac{d}{dy} \left(\int_y \alpha dT\right) = \text{constant}$$

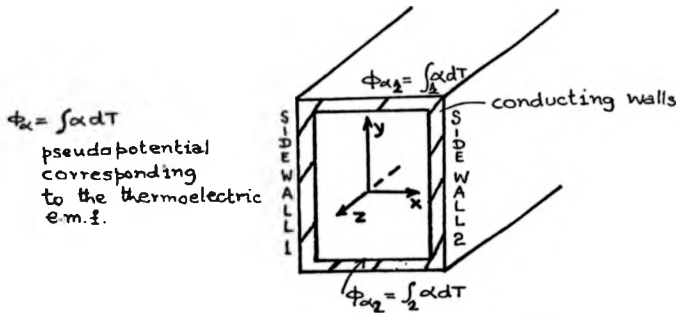

Figure 5.5(a) The rectangular cross-sectional straight duct with all solid-liquid interfaces electrically and thermally conducting. The temperature distribution along the vertical sidewalls assumed perfectly symmetrical and to be linear in the vertical direction so that ϕ_α is the same at the corresponding opposite points at the side walls.

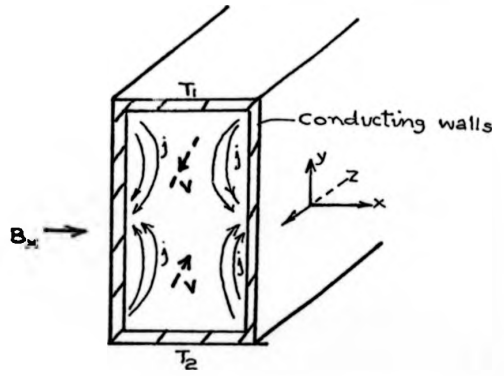

Figure 5.5 (b) Fluid vorticity induced by nonuniform $\partial T/\partial y$ on the sidewalls with conducting solid-liquid interface.

$$\partial p/\partial z - \sigma B \frac{d(\int \alpha dT)}{dy} = -\sigma B(Bv - \frac{\partial \phi}{\partial y}) + \eta \nabla^2 v$$

and $\nabla^2 \phi = B\, \partial v/\partial y$

and the boundary conditions are $v = \phi = 0$ at the walls.

This shows that the TEMHD flow is the same as ordinary MHD flow (with potential ϕ) under an axial pressure gradient $\partial p/\partial z - \sigma B \frac{d}{dy} (\int \alpha dT)$ provided $\int \alpha dT$ is independent of x and only a linear function of y. Following Chang and Lundgren (1961) for the case of all perfectly conducting walls, the governing equations are identical with (5.37) in section 5.3.1, i.e.

$$\frac{\partial^2 v}{\partial x^2} + \frac{\partial^2 v}{\partial y^2} + M \frac{\partial H}{\partial x} = 1$$

and $$\frac{\partial^2 H}{\partial x^2} + \frac{\partial^2 H}{\partial y^2} + M \frac{\partial v}{\partial x} = 0$$

but now the boundary conditions are

$$v = 0 \text{ on all walls}$$

and $$\frac{\partial H}{\partial y} = 0 \quad \text{on } y = \pm \frac{L_y}{L_x} \quad \text{and } \frac{\partial H}{\partial x} = 0 \text{ on } x = \pm 1$$

The volume flow (time) rate (compare Chang and Lundgren, 1961)

$$= \frac{L_x^2}{\eta_v} \left(\frac{\sigma \alpha T_m B}{L_y} - \frac{\partial p}{\partial z}\right) 8 L_x L_y \sum_{n=0}^{\infty} \frac{1}{(n+\frac{1}{2})^2 \pi^2 \{(n+\frac{1}{2})^2 \pi^2 + M^2\}} \cdot$$

$$\left[1 - \frac{(n+\frac{1}{2})\pi \cosh 2 f_n \frac{L_y}{L_x} - \cos 2 f_n \frac{L_y}{L_x}}{\frac{L_y}{L_x}\{(n+\frac{1}{2})^2 \pi^2 + M^2\}\{f_n \sinh 2 f_n \frac{L_y}{L_x} - g_n \sin 2 g_n \frac{L_y}{L_x}\}}\right]$$

with

$$f_n = \left\{\frac{(n+\frac{1}{2})\pi}{2}\right\}^{\frac{1}{2}} \left\{(n+\frac{1}{2})\pi + ((n+\tfrac{1}{2})^2 \pi^2 + M^2)^{\frac{1}{2}}\right\}^{\frac{1}{2}}$$

and

$$g_n = \left\{(n+\tfrac{1}{2})\frac{\pi}{2}\right\}^{\frac{1}{2}} \left\{-(n+\tfrac{1}{2})\pi + ((n+\tfrac{1}{2})^2 \pi^2 + M^2)^{\frac{1}{2}}\right\}^{\frac{1}{2}}$$

$$\sim L_x L_y \left\{\frac{\alpha T_m}{L_y B} - \frac{1}{\sigma B^2} \frac{\partial p}{\partial z}\right\} \left(1 - \frac{1}{M} - \frac{2.40}{\frac{L_y}{L_x} M^{3/2}}\right)$$

therefore

$$v \to \left\{\frac{\alpha T_m}{L_y B} - \frac{1}{\sigma B^2} \frac{\partial p}{\partial z}\right\} \quad \text{as } M \to \infty \qquad (5.57)$$

Since the analysis of the conducting interface at the side wall of the channel in section 3.3 shows identical result with that of an insulated interface of the conducting side walls, as long as $\frac{dT}{dy}$ = constant for the rectangular duct with side walls of arbitrary conductivity and in electrical contact with the fluid (the top and bottom walls being perfectly conducting and α linear in T), V is given by

$$V \sim \{ \frac{\alpha T_m}{L_y B} - \frac{1}{\sigma B^2} \frac{\partial p}{\partial z} \} \text{ as } M \to \infty$$

The advantage of this configuration during experimentation is that there is less problem of accurate alignment of the top and bottom walls with the magnetic field to avoid shear layers as in the case of insulated interface side walls. The disadvantage is that $\frac{dT}{dy}$ is not strictly constant if further control to maintain it constant is not introduced, and therefore secondary circulation at the side walls cannot be avoided (Figure 5.5b).

5.3.3 A critical review of the uniqueness of the solutions

In the absence of an exact method of solution, boundary layer analysis is applied to some of the MHD problems. Hunt (1969) proposed a theorem to establish the uniqueness of fully developed isothermal conducting fluid flow in uniform B with uniform fluid properties. The theorem states that the specification of (i) either $\frac{\partial p}{\partial z}$ or the volume flow rate $\int v dx dy$ and (ii) either the electric current leaving/entering the duct at connecting points on the duct walls to external electric circuits or the electric potential at these points, uniquely determines the fully developed flow. The proof of the theorem is based on an energy balance and the positive definiteness of the irreversible heat dissipation (entropy process). In the case of TEMHD fully developed flow,

the flow can be initiated without literally having an external electrical connection, and the energy input is basically thermal. Even if the thermoelectric current flowing in the duct itself or the thermoelectric potential in the duct wall interfaces were specified, treating the interfaces as the connecting points to the external circuit, yet there would remain the possibility of the heating conditions giving buoyancy induced secondary flow to upset the uniqueness of the solution based on specifications (i) and (ii) only.

Consider a TEMHD (nonisothermal) fully developed flow in the z direction (the y axis being vertical in opposite direction to $\underline{g}$, the gravity vector) such that

$$\frac{\partial}{\partial t}(\underline{V}, \underline{B}, \phi^{+}, \underline{j}, T) = 0 \quad \text{and} \quad \frac{\partial}{\partial z}(\underline{V}, \underline{B}, \phi^{+}, \underline{j}, T) = 0 \tag{5.58}$$

and $\underline{V} = 0$ all along the boundaries of the duct, the symbols having the usual meaning. The fluid properties σ, η_v are considered to have average values to avoid further complexity and the variation of density ρ is confined to the buoyancy term only (Oberbeck-Boussinesq assumption). From equation (3.1) and the conditions (5.58)

$$\rho(\underline{V}.\nabla)\underline{V} = -\nabla p + \underline{j}X\underline{B} + \eta_v\nabla^2\underline{V} + \frac{\partial T}{\partial y}\underline{g} \tag{5.59}$$

therefore $\frac{\partial}{\partial z}\{\rho(\underline{V}.\nabla)\underline{V} - \underline{j}X\underline{B} - \eta_v\nabla^2\underline{V} - \rho\beta\frac{\partial T}{\partial y}\underline{g}\} = -\frac{\partial}{\partial z}(\nabla p) = 0$

Therefore $p = -(\Delta p)z + f(x,y)$ with (Δp) a constant.

From equation (3.1) with $\nabla^2 = \partial^2/\partial x^2 + \partial^2/\partial y^2$, $F(x,y) = f(x,y) + |\underline{B}|^2/2\mu$, a scalar function

and $\underline{X}.\nabla = X_x\frac{\partial}{\partial x} + X_y\partial/\partial y$,

$$\rho(\underline{V}.\nabla)v_x = -\frac{\partial F}{\partial x} + \frac{(\underline{B}.\nabla)B_x}{\mu} + \eta_v\nabla^2 v_x \tag{5.60}$$

$$\rho(\underline{V}.\nabla)v_y = -\frac{\partial F}{\partial y} + \frac{(\underline{B}.\nabla)B_y}{\mu} + \eta_v\nabla^2 v_y - \rho\beta\frac{\partial T}{\partial y}\underline{g} \tag{5.61}$$

$$\rho(\underline{V}.\nabla)v_z = (\Delta p) + \frac{(\underline{B}.\nabla)B_z}{\mu} + \eta\nabla^2 v_z \qquad (5.62)$$

From (3.22) i.e.

$$\underline{j} = \sigma(-\text{grad}\ \phi^+ + \underline{V}\times\underline{B}) \text{ and } \nabla.\underline{B} = 0$$

$$(\underline{V}.\nabla)\underline{B} = (B.\nabla)\underline{V} + \frac{1}{\mu\sigma}\nabla^2\underline{B} \qquad (5.63)$$

with $\frac{\partial\phi^+}{\partial z} = 0$, on the boundaries $(\nabla\times\underline{B})_z = j_z = \sigma\frac{\partial\phi^+}{\partial z} = 0$

Since div $\underline{B}$ = 0 = div $\underline{V}$ and because $\left.\begin{matrix} B_z\frac{\partial}{\partial z} \\ v_z\frac{\partial}{\partial z}\end{matrix}\right\}$ does not contribute to $\underline{B}.\nabla$ and $\underline{V}.\nabla$ from equations (5.60), (5.61), it can be inferred that v_x, v_y, B_x and B_y are independent of v_z and B_z. Therefore, setting $v_z = B_z = 0$, ignoring their effect on F, in (5.60), (5.61) and (5.62), (5.63), the set of equations can be written in the compact form

$$\rho(\underline{V}.\nabla)\underline{V} = -\nabla F + \frac{(\underline{B}.\nabla)\underline{B}}{\mu} + \eta\nabla^2\underline{V} - \rho\beta\frac{\partial T}{\partial y}\underline{g} \qquad (5.64)$$

$$\text{and}\quad -\nabla\times(\underline{V}\times\underline{B}) = \nabla^2\underline{B}/\mu\sigma \qquad (5.65)$$

with $\underline{B} = (B_x, B_y, 0)$, $\underline{V} = (v_x, v_y, 0)$ and ∇, ∇^2 referring to the two dimensional operators. Scalar multiplication of (5.64) by $\underline{V}$ and (5.65) by $\frac{\underline{B}}{\mu}$ and addition of the two equations integrated over the duct cross-section gives

$$\rho\int_D \underline{V}\left[(\underline{V}.\nabla)\underline{V}\right]dxdy = \int_D \{-(\underline{V}.\nabla)F + \frac{\underline{V}.(\underline{B}.\nabla)\underline{B}}{\mu} + \frac{\underline{B}.\nabla\times(\underline{V}\times\underline{B})}{\mu} + \eta\underline{V}.\nabla^2\underline{V}$$

$$+ \frac{\underline{B}.\nabla^2\underline{B}}{\mu^2\sigma} - \rho\beta\frac{\partial T}{\partial y}\underline{V}.\underline{g}\ \}\,dxdy \qquad (5.66)$$

Using the boundary conditions, $\underline{V}$ = 0 and the divergence equations div $\underline{j}$ = div $\underline{B}$ = div $\underline{v}$ = 0

$$\int_D \underline{V}.((\underline{V}.\nabla)\underline{V})dxdy = \int_D \nabla.(\frac{\underline{V}.|\underline{V}|^2}{2})dxdy = 0$$

$$\int_D (\underline{V}.\nabla)F\,dxdy = \int_D \nabla.(\underline{V}F)\,dxdy = 0$$

$$\int_D (\underline{V}.\nabla^2\underline{V})\,dxdy = -\int_D |\underline{w}|^2\,dxdy \qquad \text{with } \underline{w} = \nabla\times\underline{V}$$

$$\int_D \frac{\underline{B}.\nabla^2\underline{B}}{\mu^2\sigma}\,dxdy = -\int_D \frac{(\nabla\times\underline{B})^2}{\mu^2\sigma}\,dxdy = -\frac{1}{\sigma}\int_D |\underline{j}|^2 dxdy$$

$$\int_D \underline{B}.(\nabla X(\underline{V}X\underline{B}))\ dxdy = -\int_D \underline{V}.((\underline{B}.\nabla)\underline{B})\ dxdy$$

Therefore, from (5.66)

$$0 = \eta\int_D |\underline{w}|^2\ dxdy + \frac{1}{\sigma}\int_D |\underline{j}|^2\ dxdy + \int_D \rho\beta\frac{\partial T}{\partial y}\underline{V}.\underline{g}\ dxdy \qquad (5.67)$$

The expression on the right hand side is no longer, as compared with Hunt, 1967, positive definite because of the last term being negative for adverse temperature gradient. Therefore, in general,

$$\underline{w} \neq \underline{j} \neq 0$$

Therefore $v_x \neq v_y \neq 0$ in general, and secondary flow is possible. With this condition, the preliminary theorem of Hunt (1969) is invalidated, leading to the breakdown of arguments in the uniqueness theorem, i.e. the flow is not purely longitudinal.

The physical interpretation of the above conclusion is that, even though energy input may be specified, if certain temperature conditions are being maintained (adverse vertical (y) or horizontal (x) temperature gradients), then the release of energy by the buoyancy forces can provide fluid vorticity and joule dissipation. The same is true of energy release by centrifugal forces in curved ducts (refer Chapter 6) or when the coriolis force acts on the fluid. However, at very strong magnetic fields, the secondary flows are suppressed and the uniqueness theorem of longitudinal motion holds again. The temperature oscillations, fluid vorticity as experienced during experimental runs in TEMHD fully developed flows with constant energy input confirm such statement. The basic point that is being emphasised is that for the uniqueness of the TEMHD flow (including secondary flow) it is not sufficient to specity ϕ^+ or I due to thermal effects over and above Δp and/or volume flow rate only, but a complete specification of T around the duct boundary is essential.

5.3.4 Comments on further analysis

(a) Starting process and thermal oscillations

The starting process can be analysed in a simple way similar to that followed in the case of circular cross-sectional duct in section 4.4. During the starting process, the steady state flow would therefore be asymptotically approached at magnetic field strengths > B_{cr}; B_{cr} is independent of the temperature difference, but is governed by the flow circuit inertial parameters. At $B < B_{cr}$, the flow would pulsate in the z direction and would continue to do so until a time when the external connecting loop parameters damp out such pulsation.

It is obvious from the analysis and the discussion of section 4.6.1 that any adverse vertical or lateral temperature gradient would cause thermal oscillations in the fluid due to fluid vorticity induced by baroclinic instability in the magnetic field of $B < B_{cr}$, B_{cr} being a function of the parameter $(Ra)/(Pr).M^2$.

(b) Entry problem

The solution to the TEMHD problem in the case of rectangular cross-sectional duct can also be approached in the same way as that discussed for the circular cross-sectional duct in section 4.4, resulting in M shaped velocity profiles with asymmetry.

(c) Flow with B inclined to the side walls

The TEMHD flow in a rectangular cross-sectional duct with the side walls insulated from the fluid at the interface and a magnetic field inclined to side walls at an angle ($>< 45^{o}$) could easily be inferred from the analysis of Alty (1966).

(d) Combined free and forced convective flow

The real practical problem of combined free and forced convections TEMHD flow requires special mention in connection with heat transfer studies in nuclear reactor cooling circuits. The free and forced convective ordinary MHD flow in a horizontal channel has been analysed by Gupta (1969). The characteristic temperature in such a flow is given by

$T = Az + T(x,y)$.

It is shown that for positive $\partial T/\partial z$, i.e. A positive, flow instability (separation) can occur at the channel top wall for $\frac{(Ra)/(Pr)}{Re} > \frac{2M^4}{(M \coth\frac{M}{2} - 2)^2}$ where Ra is based on $A = \partial T/\partial z$. For A negative, instability at a much reduced scale occurs at the bottom wall at the same critical value of $\frac{Ra Pr}{Re}$. It can then easily be shown from physical considerations that in the corresponding TEMHD flow, such instability would be promoted at certain regions and suppressed at others along the channel length. The velocity profile is necessarily asymmetrical and depends on the sign as well as the magnitude of $(Ra)/Re Pr$. A detailed analysis of such a problem is beyond the scope of this thesis.

5.4 The Experimental Device

5.4.1 Introduction

The rectangular duct experiment was planned at a stage when the experimental results of the circular cross-sectional Channel I were available, but the reason for the discrepancy of the experimental results with the theoretically predicted ones were not fully understood. To avoid every possible mode of experimental uncertainty, care was taken in designing the experimental device. Also, distilled Hg was used for the first

time in these experiments as against the Hg from the previously used stock utilised in the circular cross-sectional TEMHD channel I. Though the rectangular cross-sectional duct experiment went a long way towards confirming the understanding of TEMHD flow, the overall significance of it was a shade irrelevant when the experimental results of the circular cross-sectional TEMHD Channel II were available. The scope of the experimental programme with the rectangular cross-sectional duct was also otherwise curtailed by preferring the use of the limited time available in the more interesting study of the TEMHD flow in annular channels of rectangular cross-section (Chapter 6).

5.4.2 Device constructional details and probing mechanism

The basic structure of the channel was made from a rectangular cross-sectional (nominal size 3.81 x 3.09 cm^2, inner bore 2.7 x 2.46 cm^2) copper pipe obtained from Coventry Metal Bars Ltd. The wall thickness of the sidewall was 0.55 cm and the other pair of walls, 0.32 cm thick, were used as the top (heating) and bottom (cooling) boundaries. The total TEMHD section of 31 cm length (effective length 30 cm) was made up of two symmetrical sections of copper pipe, each 15 cm long, with a central insulating gland (Tufnol) 1 cm long separating them. The central insulating gland was designed to accommodate probes for internal measurements. The water jacket was likewise built on each Cu section by brazing at the bottom wall a cutaway half-section of the same size Cu tube and closing up the ends by brazing Cu end plates. The water inlet port was at the middle of each section and the outlets at the ends, symmetrically located at the bottom of the water jackets. The sidewalls of

the main copper pipe (TEMHD section) were insulated from the fluid by glueing thin strips (0.5 mm thick) of tufnol (Bakelite) to eliminate any possibility of current eddies and the associated fluid vorticity due to temperature gradient being nonuniform. It was initially planned that the insulating strips and the glue would be later scrapped for experimenting on rectangular cross-sectional duct with wall to fluid electrical contact at all the interfaces, (The insulated case had to be done first for glueing is ineffective with the copper surface already amalgamated) but was not pursued. The final cross-sectional dimensions were: inner bore, L_y = 2.46 cm, L_x = 2.485 cm; outer size, L_y = 3.10 cm, L_x = 3.785 cm, with a maximum tolerance of 0.005 cm, i.e. 0.2%. The TEMHD channel therefore effectively had a square cross-section. Extreme care and skill were necessary during the process of glueing and placing the Bakelite strips to maintain parallelism within such tolerance. Two symmetrical heater coils were made of 26 swg Nichrome wire wound in a zig-zag fashion and embedded in MgO insulation applied on the top wall outside surface and covering up with fire clay and asbestos,in somewhat similar way to that done in the case of circular cross-sectional duct.

The end sections of the overall assembly were made of blocks of Tufnol into which connector round tubes were fixed by sealing with 'O' rings and glueing. The sealing of Hg at the rectangular peripheries at the end flanges and at the central gland were made of vulcanised rubber gasket which proved very satisfactory even with heat applied very close to it. A partial blown-up perspective view of the assembly is shown in Figure 5.6. Two temperature probes made of Chromel-Alumel insulated by vulcanised rubber sleeves and encased in stainless steel tubes

Figure 5.6 The perspective view of the experimental, rectangular cross-sectional straight duct.

(Heater Coils and the insulation not shown)

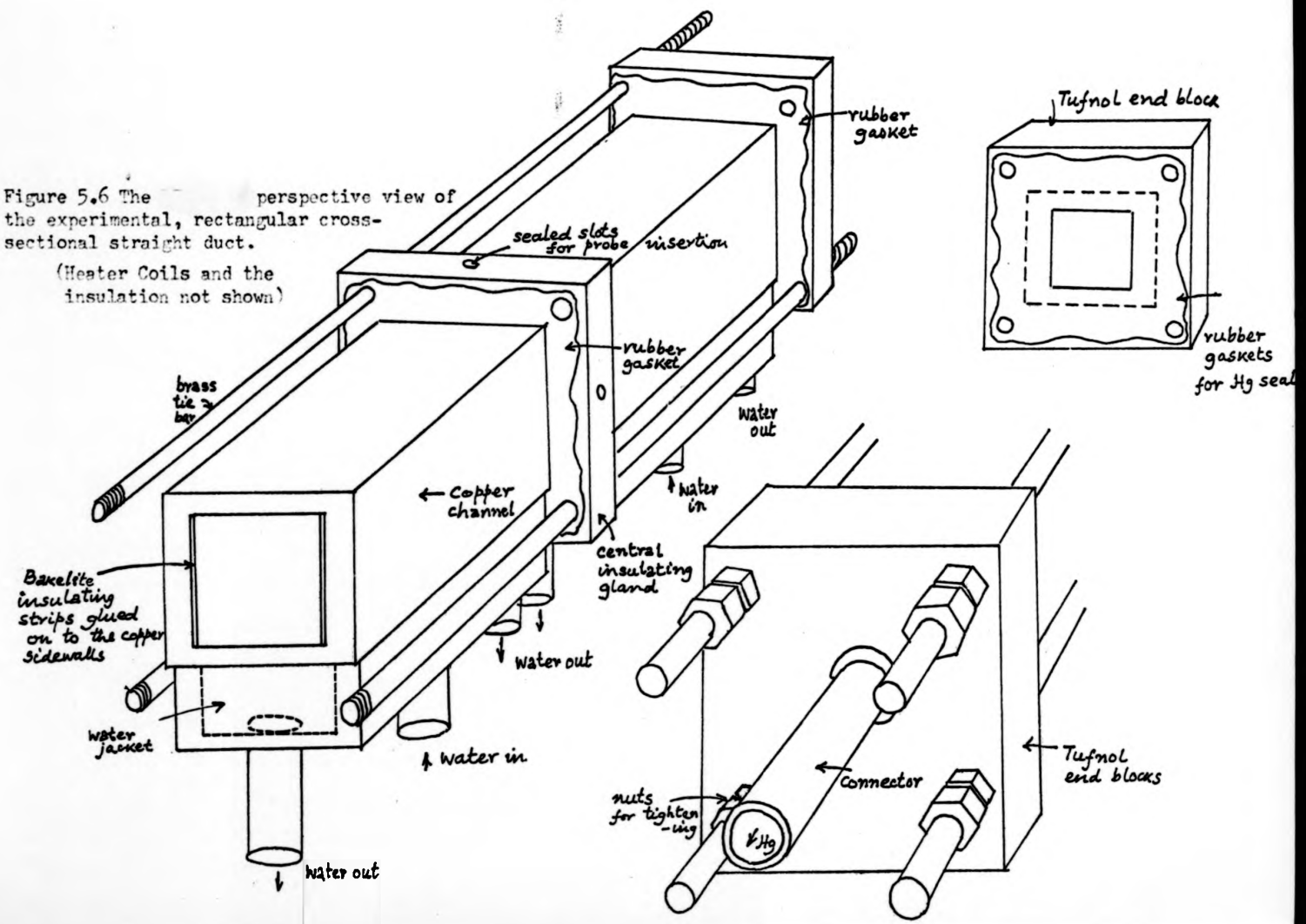

insulated at the outer surface (ptfe insulated Cu-Constantan was not available at that time) were inserted through the central gland. The tips of the TE probes were located at central points in horizontal planes of the top and the bottom walls of one of the TEMHD half sections, making sure that the tips scratch the Cu surface and are mutually aligned parallel to the sidewalls. Though initially glass capillary tubes were used, the process of alignment invariably resulted in their breakage so that,finally,stainless steel casing was used, with the associated problem of having insulation on it as well. Pressure taps were correspondingly located at the central gland and at the end flanges. A flexible positioning device of probes with rotary traversing mechanism could not be perfected and was finally left out because of Hg sealing problems while inserting it through the central insulating gland. Sectional views of the TEMHD rectangular channel are shown in Figure 5.7.

5.5 Experiments, Experimental Results and Discussion

The rectangular cross-sectional TEMHD channel was placed in the air gap of the Lintott electromagnet I in a true horizontal alignment over wooden supports in a PVC tray. The Hg loop was similar to that for the circular cross-sectional duct experiment. PVC tubes were used for the Hg loop as well as for cooling water, and care was taken to ensure the symmetry of connecting loops.

5.5.1 Static pressure difference measurement

The static pressure difference across the TEMHD section was measured with the inclined tube manometer, when the level of Hg in the weir reservoir was so adjusted that there is no flow over

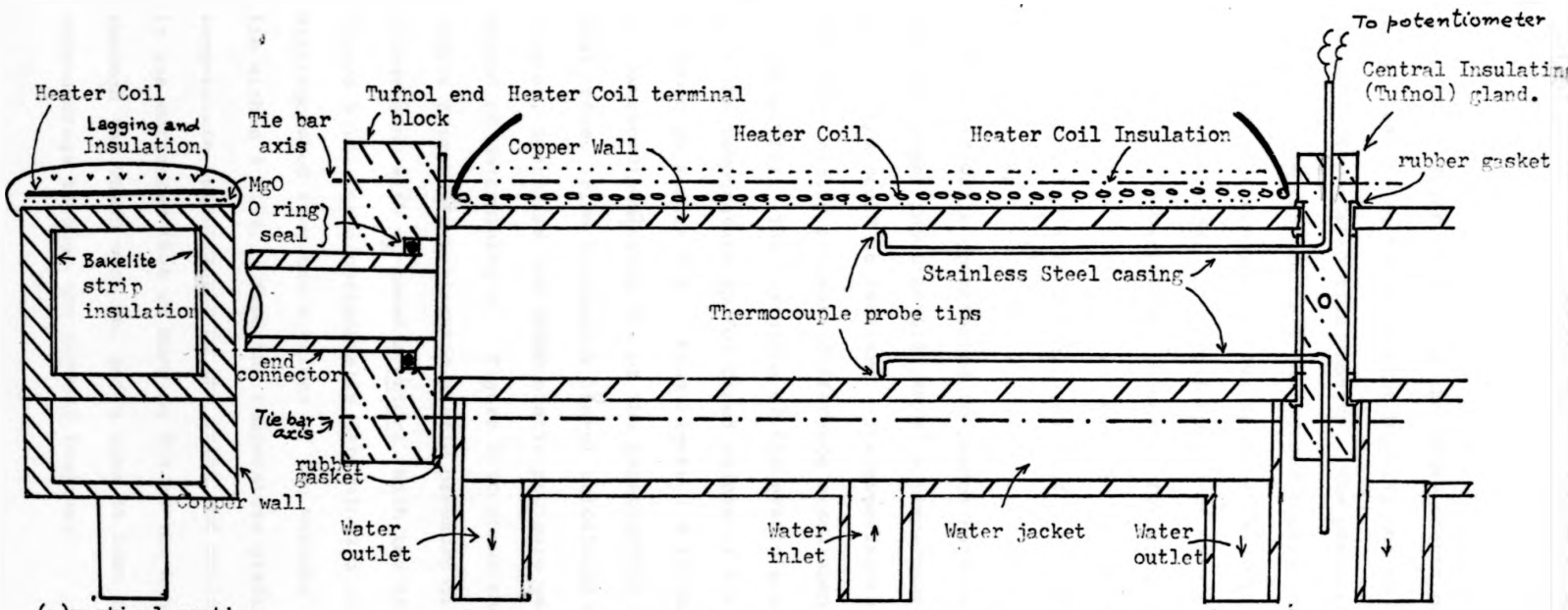

(a) vertical section in the plane of B

(b) vertical section in a plane perpendicular to B (Only a little more than half the total length is shown)

Figure 5.7 Sectional views of the rectangular cross-sectional straight duct for TEMHD experiment.
(Full Scale Diagram)

the weir. Figure 5.8 shows the TEMH - static pressure difference in mms head of Hg for different heating and cooling conditions against the magnetic flux density. The pressure difference readings were reproducible and agreed consistently when the direction of the magnetic flux density was reversed, by having the same magnitude. A typical spread of data for curve f is shown as ± 1.5% variation. However, for smaller pressure difference it is ± 3%. It is to be noted that thicker side walls have contributed a very small value of c = 0.040 ± 0.001, so that effectively $\Delta p \simeq \frac{\sigma_f \alpha T_m}{L_y} BL_z$ with an error of only 3.85%. The thicker sidewalls contributed to predominant heat conduction so that for power input of 6.35 KW/m^2 a temperature gradient of only 609.75 $^{o}K/m$ could be realised. The experimental conditions for the TEMH - static pressure difference measurements are summarised in Table VIII. The variation of the static pressure difference with the temperature T_i, for fixed values of B = 1T and 0.5 Tesla, is shown in Figure 5.9. From Figure 5.8 it can be said that the extraordinarily good fit of the experimental data with the theoretical lines (firm continuous lines) calculated with the pure grade α value, justifies the TEMHD static pressure measurement as another method of determining α. Figure 5.10 shows the calculated α values from the experimental static pressure difference measurement with σ_f known a priori. With the scale used in Figure 5.10, the experimentally determined α values can not be distinguished from the α values of the Marwaha (1967) data, but lie within ± 1.5%. From the temperature gradient and the temperature measurements of the inlet and outlet cooling water, it was estimated that as much as 95% of the heat was conducted through the TEMHD section, and a bare 5% lost to the ambient surroundings through the thermal lagging.

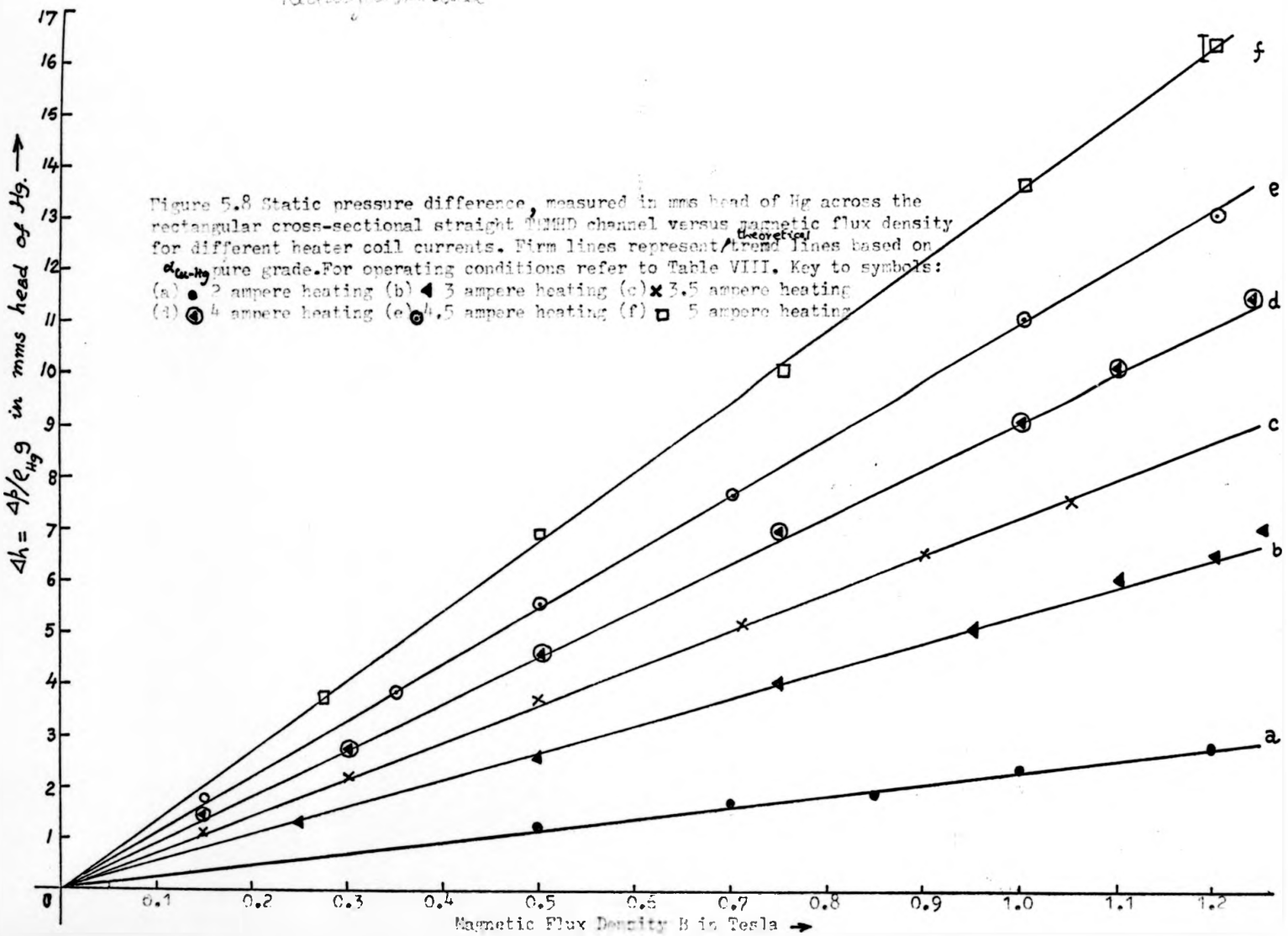

Figure 5.8 Static pressure difference, measured in mms head of Hg across the rectangular cross-sectional straight MHD channel versus magnetic flux density for different heater coil currents. Firm lines represent theoretical trend lines based on σ_{Lm-Hg} pure grade. For operating conditions refer to Table VIII. Key to symbols: (a) ● 2 ampere heating (b) ◀ 3 ampere heating (c) × 3.5 ampere heating (d) ◀ 4 ampere heating (e) ⊙ 4.5 ampere heating (f) □ 5 ampere heating

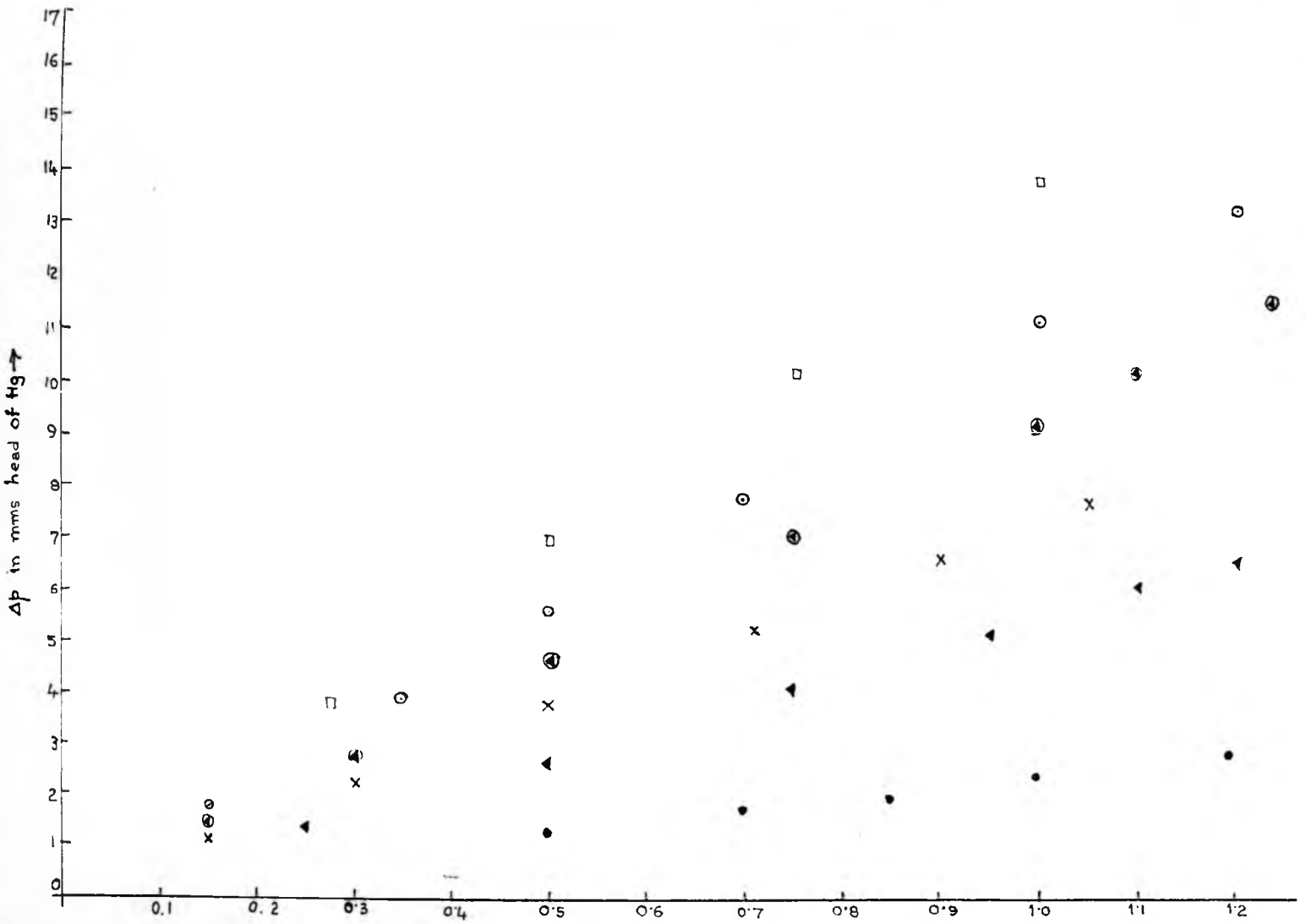

Figure 5.8 a. Δp vs B in the rectangular cross-sectional straight channel when v=0. For Keys to experimental points see fig 5.8

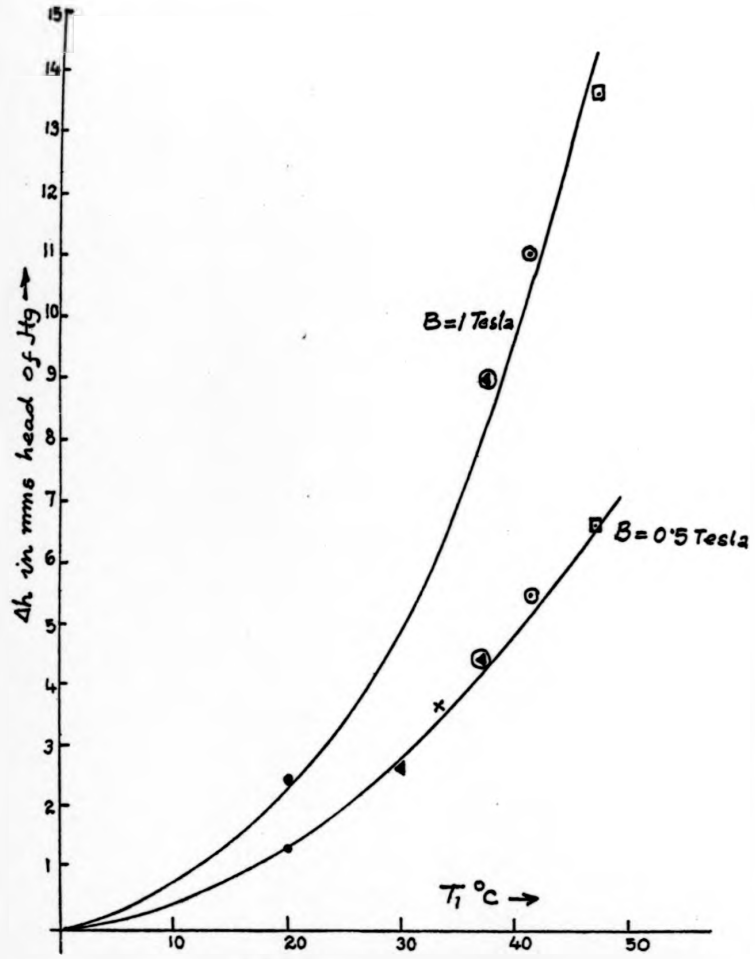

Figure 5.9 TEMHstatic pressure difference acrossthe rectangular cross-sectional straight channel vs T_1 for B= 0.5 and 1.0 Tesla. Key to symbols refer to figure 5.8

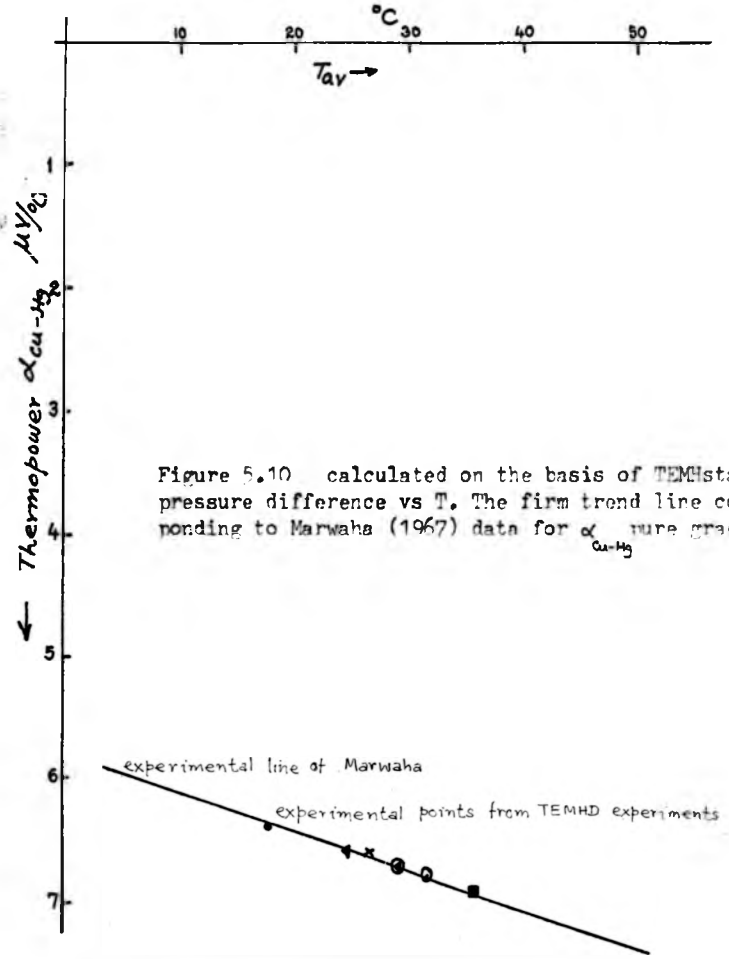

Figure 5.10 calculated on the basis of TEMHstatic pressure difference vs T. The firm trend line corresponding to Marwaha (1967) data for α_{Cu-Hg} pure grade.

Table VIII Experiment operating conditions in the rectangular cross-sectional duct experiment and evaluation of α to compare with α pure grade

Heater coil Voltage	Current	T_1	T_2	ΔT	T_m	T_{av}	c	σ	Trend line $\Delta h = \frac{\sigma\alpha T_m B \times 0.3}{\rho_{Hg} g(1+c) L_y}$	$\alpha_{pure\ grade}$	$\alpha_{expt_{av}}$
		^oC									
95	2	20	16	4	2	18	0.0391	1.046	0.2335 B	6.423	6.43
135/140	3	30	21	9	4.5	25.5	0.0401	1.039	0.5387 B	6.64	6.6
160	3.5	33	21	12	6	27	0.0402	1.038	0.7218 B	6.8.	6.6
180	4	37	22	15	7.5	29.5	0.0406	1.035	0.9095 B	6.756	6.75
205	4.5	41	23	18	9	32	0.0409	1.033	1.1003 B	6.825	6.8
230	5	47	25	22	11	36	0.0414	1.029	1.3623 B	6.945	6.9

The most surprising observation was that of temperature oscillations at both the top and bottom interface, since this experiment was the first time that the internal temperature measurements were conducted. The temperature oscillations persisted even in a magnetic flux density as high as 1.2 Tesla. A time record of temperature oscillations T_1 and T_2, 2 to 3° C oscillating magnitude, is shown in Figures 5.11a,b for the 3 ampere heating condition at B = 1 Tesla. The fluctuations are more random than those observed later in the TEMHD Channel II experiments, but definitely indications are there of a faster oscillating mode over that of a slow periodic change. The magnitude of B also affected the magnitudes of T_1 and T_2 as compared with those in the absence of the magnetic field, in somewhat irregular fashion, in most cases a drop in T_1 and T_2 by 1 to 2° C. Accurate determination of such changes was made impossible in the presence of an over-riding temperature fluctuation of the same/greater magnitude.

The duration of the settling process during the pressure difference build-up with a step change in B, after steady heating conditions have been attained, is of the same order as in the case of the circular cross-sectional duct, varying between 15 to 20 seconds. With the flow along the connecting loop blocked, the temperature of Hg on either side of the weir in the reservoir remained at ambient temperature- it implies that fluid vorticity does not extend beyond the TEMHD interaction zone, i.e. where grad T and B are present, at least to a great extent.

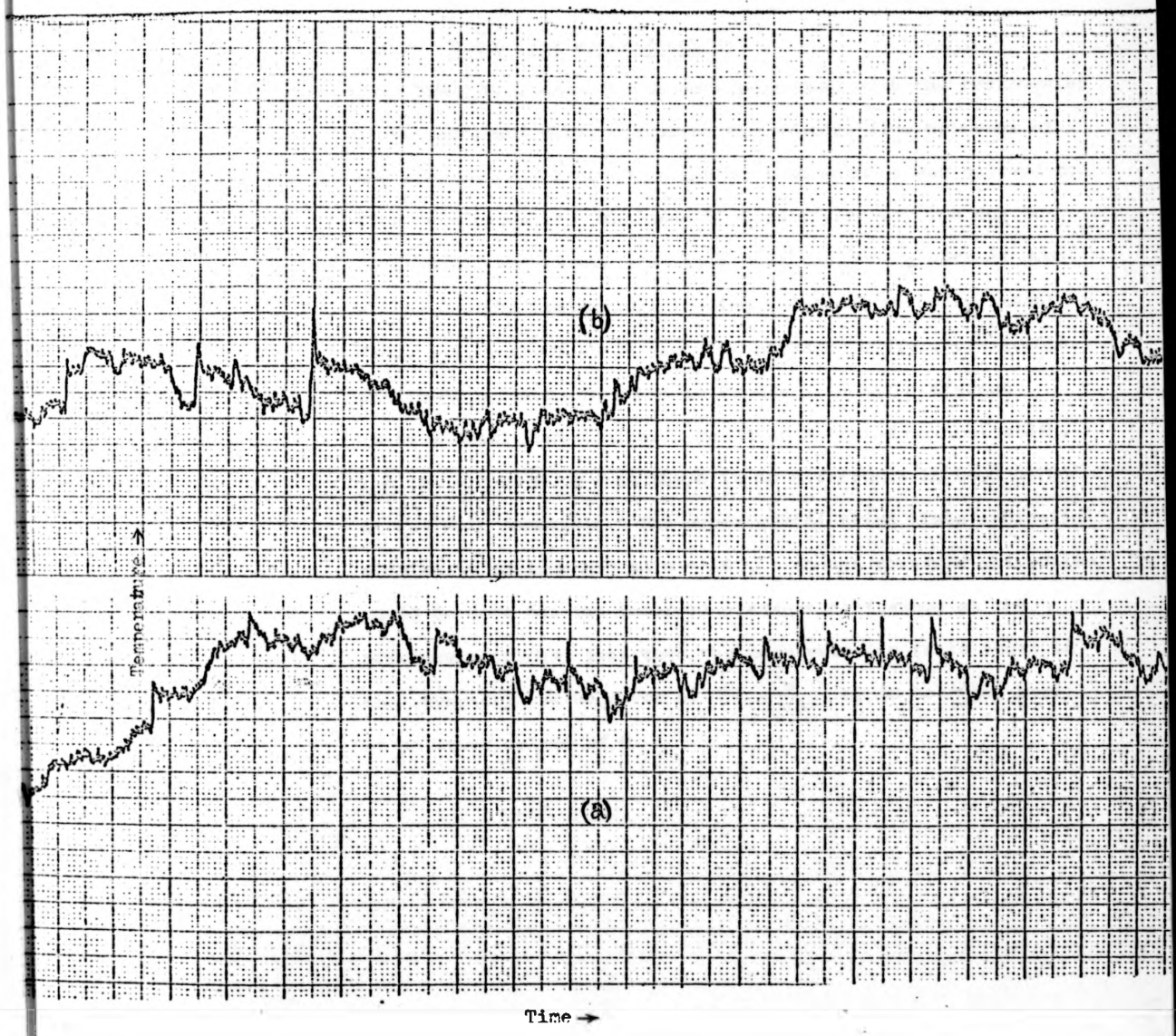

Figure 5.11 Temperature fluctuation with time in the rectangular cross-sectional straight channel under the influence of the transverse magnetic field. The traces progress from left to right with time with horizontal time scale of 15 sec / cm . The vertical scale corresponds to 1°C / cm.

(a) Fluctuations in T_1, top wall solid-liquid interface temperature and
(b) Fluctuations in T_2, Bottom wall solid-liquid interface temperature.

$T_1 > T_2$

Operating condition 3amp heating current
B= 1.0 Tesla.

5.5.2 TEMHD flow experiments

TEMHD flow experiments were performed with the rectangular cross-sectional duct, measuring the average flow by means of the flow meter connected in the Hg loop when Hg was allowed to flow over the weir. The mean flow rate was very low due to very small temperature gradients that could be generated even at the maximum heater coil loading. The raw velocity (mean) data, i.e. without correction for pressure differences across the TEMHD section, is shown in Figure 5.12 for different heating conditions against M based on half the channel width, i.e. L_x = 1.2425 cm when there is no difference in head of Hg at the weir reservoir. The experimental trend lines indicate a velocity maximum around M = 160. Though pressure correction could be done for the observed pressure difference at the pressure tappings, even then the mean velocity falls short of the asymptotic value given by $V = \frac{\alpha T_m}{L_y(B)}$ by 30 to 50%, more so at lower values of M.

Figure 5.12 Plot of mean velocity (without pressure drop correction) in the rectangular cross-sectional straight channel in mm/sec against M based on half width of the channel L = 1.2425 cm.

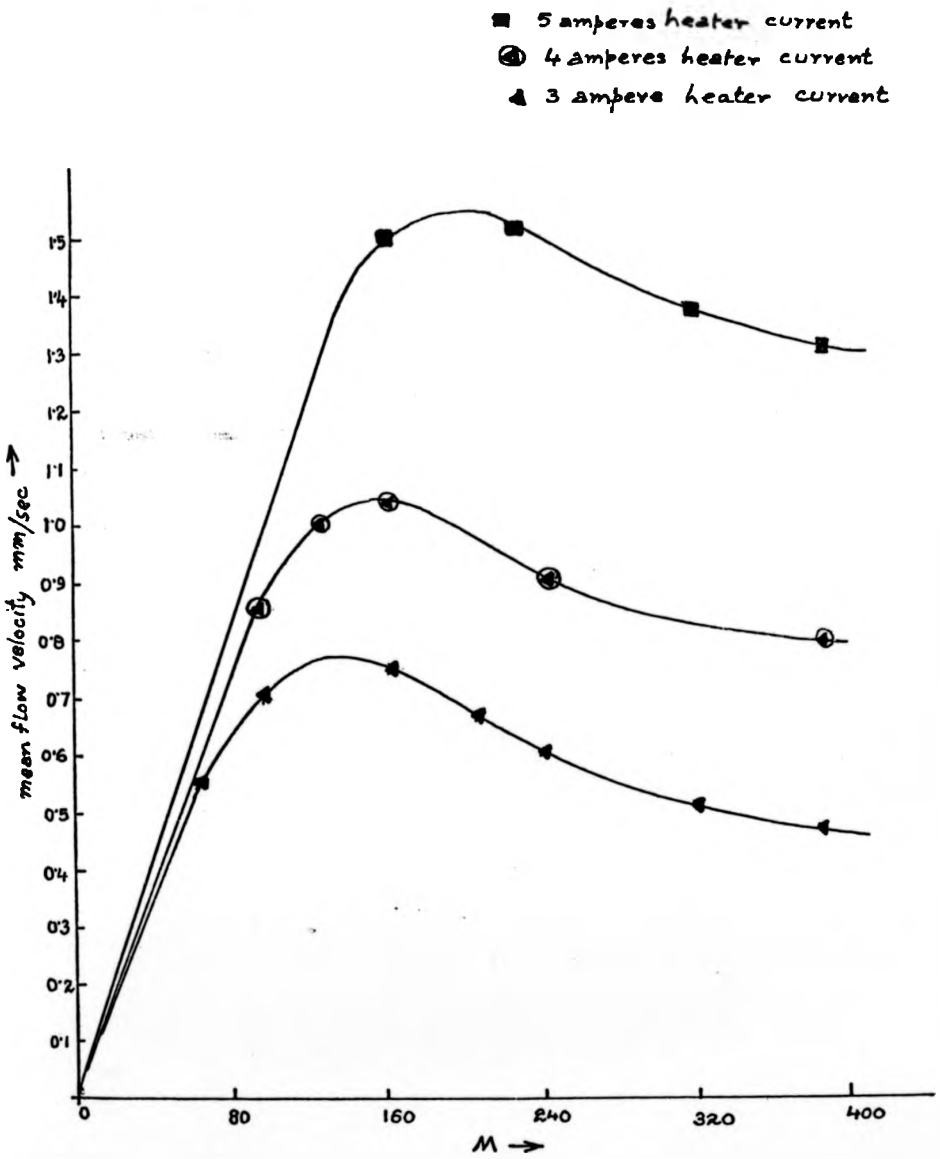

CHAPTER 6

THERMOELECTRIC MAGNETOHYDRODYNAMICS IN ANNULAR CHANNELS OF RECTANGULAR CROSS-SECTION

6.1 Introduction

The possibility of attaining fully developed flow and the elimination of pressure gradients due to fluid entry in and exit out of magnetic field region, where non-linear effects predominate (changing cross-section, bends and non-uniform magnetic field) leads to the consideration of fluid flow in an endless channel totally inside the uniform region of the magnet air gap. The channel therefore is in the form of a torus compatible with the requirements of symmetry. Its cross-section in general would be any closed contour, but for obvious reasons of simplicity the cross-sectional shape considered in this chapter is rectangular. The possible combinations of orientations of the thermoelectric current and the magnetic field B that induce fluid flow are (B_r, j_θ or j_z; B_θ, j_z or j_r; B_z, j_r or j_θ) where the z axis is taken along the vertical, opposite to the gravity vector and r, θ in accordance with the convention detailed in Chapter 3. When rotation of the fluid in horizontal planes in azimuthal direction is considered, the choice is then restricted to either (i)(B_r,j_z) with a horizontal radial magnetic field B_r or (ii) (B_z,j_r) with a vertical axial magnetic field B_z. For maximum TEMHD interaction, the thermoelectric current has to be generated by heating and cooling (i) the horizontal top and bottom walls or (ii) the vertical side walls. Theoretically it is possible to maintain the advantage of stable thermal stratification of the fluid in case (i). Since this would just be an extension of the straight TEMHD channel configuration of rectangular cross-section considered in

Chapter 5 and because case (ii) would be (a) more interesting with the possibility of investigating the associated buoyancy induced vorticity in the presence of magnetic field (this particular orientation of the heat flow and magnetic field directions surprisingly has not received any attention in the literature), (b) practically convenient for the experimental set-up (why it is so is made clear later) and, for reasons of brevity, only the configuration of uniform axial vertical magnetic field with radial thermoelectric current and heat transfer will be considered in this thesis. The basic structure is that of an annular cylinder shown in Figure 6.1. The theoretical analysis for different boundary conditions (all rigid walls ; top surface left free; insulating or electrically conducting contact at the fluid to wall interface along the top and bottom boundaries) is presented in section 6.2. In section 6.3, the experimental details (constructional features, experimental and diagnostic techniques) are described. The experimental results are presented in section 6.4, and these results and their implications critically discussed therein.

6.2 Theoretical Analysis

The following steady state equations of TEMHD in the cylindrical polar co-ordinates (ref. Figure 6.1) are easily obtained from equations (3.1) - (3.9), (3.16) to suit the annular channel configuration in general, with axial symmetry along the azimuthal direction (i.e. $\frac{\partial}{\partial\theta} = 0$), and an imposed steady uniform vertical (axial) magnetic field $\underline{B} = (0,0,B)$:

$$v_r\frac{\partial v_r}{\partial r} + v_z\frac{\partial v_r}{\partial z} - \frac{v_\theta^2}{r} - \frac{1}{\mu\rho}\{B_r\frac{\partial B_r}{\partial r} + B_z\frac{\partial}{\partial z}B_r - \frac{B_\theta^2}{r}\} = -\frac{\partial}{\partial r}(\frac{p}{\rho} + \frac{|\underline{B}|^2}{2\mu} + \Phi) + \nu(\frac{\partial^2 v_r}{\partial r^2} + \frac{1}{r}\frac{\partial v_r}{\partial r} + \frac{\partial^2 v_r}{\partial z^2} - \frac{v_r}{r^2}) \quad (6.1)$$

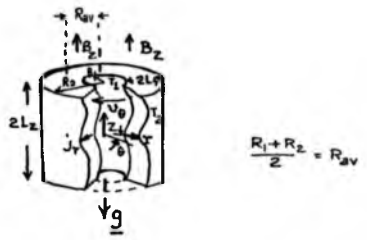

Figure 6.1 The basic annular channel configuration of section6.2 and the co-ordinate system.

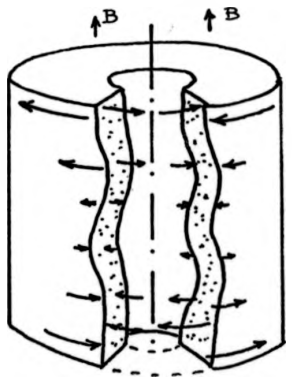

Figure 6.2 Conceptual diagram of the shear flow of the fluid due to longitudinal temperature variation (along the curved side walls parallel to B) in the annular channel.

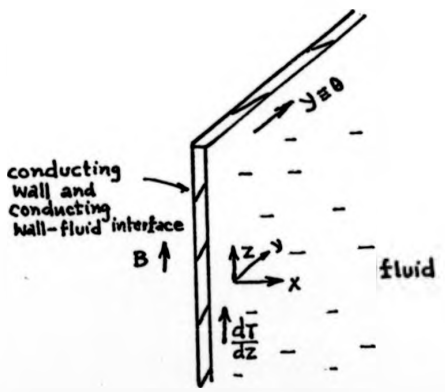

Figure 6.3 The simple configuration for TEMHD flow analysis with $\partial T/\partial z$ parallel to B.

$$v_r \frac{\partial v_\theta}{\partial r} + v_z \frac{\partial v_\theta}{\partial z} + \frac{v_\theta v_r}{r} - \frac{1}{\mu\rho}\left\{ B_r \frac{\partial}{\partial r} B_\theta + B_z \frac{\partial}{\partial z} B_\theta + \frac{B_\theta B_r}{r} \right\} =$$

$$\nu\left(\frac{\partial^2 v_\theta}{\partial r^2} + \frac{1}{r}\frac{\partial v_\theta}{\partial r} - \frac{v_\theta}{r^2} + \frac{\partial^2 v_\theta}{\partial z^2}\right) \tag{6.2}$$

$$v_r \frac{\partial v_z}{\partial r} + v_z \frac{\partial v_z}{\partial z} - \frac{1}{\mu\rho}\left\{ B_r \frac{\partial}{\partial r} B_z + B_z \frac{\partial}{\partial z} B_z \right\} = -\frac{\partial}{\partial z}\left(\frac{p}{\rho} + \frac{|B|^2}{2\mu} + \Phi\right) +$$

$$\nu\left(\frac{\partial^2 v_z}{\partial r^2} + \frac{1}{r}\frac{\partial v_z}{\partial r} + \frac{\partial^2 v_z}{\partial z^2}\right) + g\beta(T-T_o) \tag{6.3}$$

$$v_r \frac{\partial B_r}{\partial r} + v_z \frac{\partial B_r}{\partial z} - B_r \frac{\partial v_r}{\partial r} - B_z \frac{\partial v_r}{\partial z} = \frac{1}{\mu\sigma}\left(\frac{\partial^2 B_r}{\partial r^2} + \frac{1}{r}\frac{\partial B_r}{\partial r} - \frac{B_r}{r^2} + \frac{\partial^2 B_r}{\partial z^2}\right) \tag{6.4}$$

$$v_r \frac{\partial B_\theta}{\partial r} + v_z \frac{\partial B_\theta}{\partial z} - B_r \frac{\partial v_\theta}{\partial r} - B_z \frac{\partial v_\theta}{\partial z} + \frac{1}{r}(v_\theta B_r - B_\theta v_r) =$$

$$\frac{1}{\mu\sigma}\left(\frac{\partial^2 B_\theta}{\partial r^2} + \frac{1}{r}\frac{\partial B_\theta}{\partial r} - \frac{B_\theta}{r^2} + \frac{\partial^2 B_\theta}{\partial z^2}\right) \tag{6.5}$$

$$v_r \frac{\partial B_z}{\partial r} + v_z \frac{\partial B_z}{\partial z} - B_r \frac{\partial v_z}{\partial r} - B_z \frac{\partial v_z}{\partial z} = \frac{1}{\mu\sigma}\left(\frac{\partial^2 B_z}{\partial r^2} + \frac{1}{r}\frac{\partial B_z}{\partial z} + \frac{\partial^2 B_z}{\partial z^2}\right) \tag{6.6}$$

$$\frac{\partial v_r}{\partial r} + \frac{v_r}{r} + \frac{\partial v_z}{\partial z} = 0 \tag{6.7}$$

$$\frac{\partial B_r}{\partial r} + \frac{B_r}{r} + \frac{\partial B_z}{\partial z} = 0 \tag{6.8}$$

$$\mu j_r = \mu\sigma\left(-\frac{\partial \phi^+}{\partial r} + v_\theta B_z - v_z B_\theta\right) = -\frac{\partial B_\theta}{\partial z} \tag{6.9}$$

$$\mu j_\theta = \mu\sigma(v_z B_r - v_r B_z) = \frac{\partial B_r}{\partial z} - \left(\frac{\partial B_z}{\partial r}\right) \tag{6.10}$$

$$\mu j_z = \mu\sigma\left(-\frac{\partial \phi^+}{\partial z} + v_r B_\theta - v_\theta B_r\right) = \left(\frac{\partial B_\theta}{\partial r} + \frac{B_\theta}{r}\right) \equiv \frac{1}{r}\frac{\partial}{\partial r}(rB_\theta) \tag{6.11}$$

$$v_r \frac{\partial T}{\partial r} + v_z \frac{\partial T}{\partial z} = \frac{K}{c_p \varrho}\left(\frac{\partial^2 T}{\partial r^2} + \frac{1}{r}\frac{\partial T}{\partial r} + \frac{\partial^2 T}{\partial z^2}\right) + \frac{q_g}{c_p \varrho} \tag{6.12}$$

Φ being a potential function (for example, gravitation potential) of external forces, and q_g is the internal generation of heat per unit volume and time.

6.2.1 Four rigid conducting walls; electrical contact at the wall-fluid interfaces of the perfectly conducting vertical curved sidewalls but insulated interfaces at the horizontal top and bottom plane walls (abv. INTB by the nature of connection between two vertical walls)

The configuration prescribed in the section title (INTB) does resemble that adopted by Baylis(1966) in his experiments with the exception that the system considered here is not isothermal. From another angle, the INTB configuration is an extension of the 'Corbino Disc type of Thermocouple' to that of two such identical units being connected back to back (physical, electrical and thermal contact) and in having one element of the thermocouple in the fluid state. It is easy to recognise the influence of the curvature specified by R_{av} ($= \frac{R_1 + R_2}{2}$), aspect ratio L_r/L_z, $2T_m = T_2 - T_1$, or more specifically, T_m/L_x on the type of solution of the governing equations (6.1) to (6.12).

Case (a) Narrow channel, negligible curvature, low temperature gradient

$L_r/L_z \ll 1$, $L_x/R_{av} \ll 1$ and $\frac{g\beta \frac{T_m}{L_r} L_z^4}{\frac{K}{\rho c_p} \nu}$, $\frac{g\beta \frac{T_m}{L_r} L_z^4}{\nu^2 M^2} \ll 1$ (ref. page 159)

This is the simplest case when secondary flow due to buoyancy and centrifugal forces can be ignored ($v_r = v_z = 0$), and j_r can be taken as independent of z. Also $j_\theta = j_z = 0$ and $B_r = 0$, $B_z = B$. From (6.2) and (6.9)

$$\rho\nu\left(\frac{\partial^2 v_0}{\partial r^2} + \frac{1}{r}\frac{\partial v_0}{\partial r} - \frac{v_0}{r^2}\right) = -\frac{B}{\mu}\frac{\partial B_0}{\partial z} = j_r B = \frac{2IB}{2\pi(2L_z)r} \qquad (6.13)$$

with I being the total current in each of the horizontal walls of thickness t_w with the relevant boundary condition $v_\theta = 0$ at $r = R_1, R_2$.

$$v_\theta = \frac{IB}{4\pi L_z \eta_v}\left\{ r\ln r - \frac{R_2^2 \ln R_2 - R_1^2 \ln R_1}{R_2^2 - R_1^2}\, r + \frac{1}{r}\,\frac{R_1^2 R_2^2}{R_2^2 - R_1^2}\,\ln\frac{R_2}{R_1}\right\} \quad (6.14)$$

From Kirchhoff's voltage law around the one half symmetrical circuit, ignoring contact potential and integrating equation (6.9) from $r = R_1$ to R_2 with v_θ from (6.14) and $v_z = 0$

$$2\alpha T_m - \frac{I \ln R_2/R_1}{2\pi t_w \sigma_w} = \frac{I \ln \frac{R_2}{R_1}}{2\pi L_z \sigma} - \frac{IB^2}{4\pi L_z \eta_v}\left\{ \frac{R_1^2 R_2^2 \ln(\frac{R_2}{R_1})^2}{R_2^2 - R_1^2} - \frac{R_2^2 - R_1^2}{4} \right\} \quad (6.15)$$

$$\text{therefore } j_r = \frac{2\alpha T_m \sigma}{r(\ln \frac{R_2}{R_1})\left\{1 + c - \frac{\sigma B^2}{2\eta_v}\left(\frac{R_1^2 R_2^2}{R_2^2 - R_1^2}\ln\frac{R_2}{R_1} - \frac{R_2^2 - R_1^2}{\ln R_2/R_1}\right)\right\}} \quad (6.16)$$

For $B = 0$ and the radial difference $R_2 - R_1 = 2L_r \ll R_{av}\left(=\frac{R_1 + R_2}{2}\right)$, so that $\frac{(2L_r)^2}{R_1}$ and higher orders of $\frac{L_r}{R_1}$ can be neglected

$j_r \to \frac{\alpha T_m \sigma}{L_r(1 + c)}$, which is the same as that of a rectangular cross-sectional straight duct.

The mean velocity $V = \frac{1}{R_2 - R_1}\int v\,dr$ is given by (from (6.14) and (6.16))

$$|V| = \frac{\sigma \alpha T_m B}{(R_2 - R_1)\eta_v}\,\frac{\left\{\frac{R_1^2 R_2^2}{R_2^2 - R_1^2}\ln\frac{R_2}{R_1} - \frac{R_2^2 - R_1^2}{\ln R_2/R_1}\right\}}{\left\{1 + c - \frac{\sigma B^2}{2\eta_v}\left(\frac{R_1^2 R_2^2}{R_2^2 - R_1^2}\ln\frac{R_2}{R_1} - \frac{R_2^2 - R_1^2}{\ln \frac{R_2}{R_1}}\right)\right\}},$$

$$c = \frac{L_z \sigma}{t_w \sigma_w} \quad (6.17)$$

Again in the limit $R_2 - R_1 = 2L_r \ll R_{av}$, higher powers of $\frac{L_r}{R_1}$ neglected and $M \to \infty$

$|V| \to \frac{\alpha T_m}{L_r B}$ which agrees with the mean velocity $\frac{\alpha T_m}{L_r B}$ in the rectangular cross-sectional duct with $\frac{\partial p}{r\partial\theta} = 0$ and $M \to \infty$ (M based on L_z).

The velocity profile, however, is given by the form of the expression in the curly bracket in (6.14) and tends to $A_1\zeta(\zeta-1)$, the velocity profile of Poiseuille flow between parallel planes when $2L_r \ll R_{av}$, $\zeta = \frac{r-R_1}{R_2-R_1}$ and terms of order $(\frac{2L_r}{R_1})^2$ are neglected so that $A_1 = (2L_r)^2/R_1$.

From (6.14) it can be inferred that in an electrically driven flow, as long as control is by current I, if I is kept constant, the velocity magnitude (mean as well as maximum amplitude) increases with increased B, the velocity profile remaining unaltered. However, when j_r is controlled by the thermoelectric e.m.f. αT_m, V departs from linear variation, and in the extreme limit of $M \to \infty$ is inversely proportional to B.

From (6.17) with $L_r/R_1 \ll 1$ but for moderate M, based on L_z

$$|V| = \frac{\alpha T_m}{L_r B} \{1 + \frac{8(1+c)L_r^2}{15M^2(\frac{L_r}{L_z})^2 R_1^2}\}^{-1} \sim \frac{\alpha T_m}{L_r B} \{1 - \frac{8(1+c)L_r^2}{15M^2(\frac{L_r}{L_z})^2 R_1^2} + O(\frac{1}{M^4})\} \tag{6.18}$$

If M is based on L_r

$$|V| \sim \frac{\alpha T_m}{L_r B} \{1 - \frac{8(1+c)L_r^2}{15M^2 R_1^2} + O(\frac{1}{M^4})\}$$

Case (b) Wide channel, low temperature gradient

Consider the case where the temperature gradient is still small so that the buoyancy term in (6.3) can be ignored. Equation (6.1) through (6.11) is then obviously satisfed by the stationary ($\frac{\partial}{\partial t} = 0$) solution $v_r = v_z = 0$, $B_r = 0$, $v_\theta = v_\theta(r,z)$ $B_\theta = B_\theta(r,z)$, $B_z = B$.

From (6.2), (6.5), (6.9) and (6.11)

$$\frac{\partial^2 v_\theta}{\partial r^2} + \frac{1}{r}\frac{\partial v_\theta}{\partial r} - \frac{v_\theta}{r^2} + \frac{\partial^2 v_\theta}{\partial z^2} + \frac{1}{\eta\mu} B \frac{\partial B_\theta}{\partial z} = 0 \tag{6.19}$$

$$\partial^2 B_\theta/\partial r^2 + \frac{1}{r}\frac{\partial B_\theta}{\partial r} - B_\theta/r^2 + \frac{\partial^2 B_\theta}{\partial z^2} + \mu\sigma B \frac{\partial v_\theta}{\partial z} = 0 \qquad (6.20)$$

$$-\frac{\partial B_\theta}{\partial z} = \mu\sigma(-\frac{\partial \phi^+}{\partial r} + B v_\theta) \qquad (6.21)$$

$$\frac{1}{r}\frac{\partial}{\partial r}(rB_\theta) = \mu\sigma(-\frac{\partial \phi^+}{\partial z}) \qquad (6.22)$$

The boundary conditions are $z = \pm L_z$, $r = R_1, R_2$ $\}$ $v = 0$, $\frac{\partial}{\partial r}(rB_\theta) = 0$

From $\frac{\partial}{\partial r}(rB_\theta) = 0$ at $z = \pm L_z$ let $B_\theta = \frac{\mu H_2}{2\pi r}$ at $z = L_z$ and $= \frac{\mu H_1}{2\pi r}$ at $z = -L_z$ with H_1 and H_2 constants, so that the total radial current $2I$ (at any r fixed)

$$2\pi r \int_{-L_z}^{L_z} j_r dz = \int_{-L_z}^{L_z} 2\pi r \left(-\frac{\partial B_\theta}{\mu \partial z}\right) dz = H_2 - H_1 = 2I$$

The following nondimensional parameters with bars are considered

$$\bar{B}_\theta = \frac{B_\theta - \frac{\mu(H_1 + H_2)}{4\pi r}}{\frac{2\mu I}{4\pi L_z}} \qquad \bar{v}_\theta = \frac{v_\theta}{\frac{2I}{4\pi L_z \sqrt{\sigma\eta}}} \qquad \bar{\phi}^+ = \frac{\phi^+}{2I/4\pi L_z \sigma}, \quad \bar{r} = \frac{r}{L_z}, \quad \bar{z} = \frac{z}{L_z}$$

Dropping the bars, equation (6.19) to (6.22) become

$$\frac{\partial^2 v_\theta}{\partial z^2} + \frac{\partial^2 v_\theta}{\partial r^2} + \frac{1}{r}\frac{\partial v_\theta}{\partial r} - \frac{v_\theta}{r^2} + M\frac{\partial B_\theta}{\partial z} = 0 \qquad (6.23)$$

$$\frac{\partial^2 B_\theta}{\partial z^2} + \frac{\partial^2 B_\theta}{\partial r^2} + \frac{1}{r}\frac{\partial B_\theta}{\partial r} - B_\theta/r^2 + \frac{M\partial v_\theta}{\partial z} = 0 \qquad (6.24)$$

$$-\frac{\partial \phi^+}{\partial r} + M v_\theta = -\frac{\partial B_\theta}{\partial z} \qquad (6.25)$$

$$-\frac{\partial \phi^+}{\partial z} = \frac{1}{r}\frac{\partial}{\partial r}(rB_\theta) \quad \text{where } M = \frac{\sqrt{\sigma}}{\sqrt{\eta}} BL_z \qquad (6.26)$$

with boundary conditions $v = 0$ at $z = \pm 1$, $r = \frac{R_1}{L_z}$, $r_2 = \frac{R_2}{L_z}$

and $B_\theta = \pm(\frac{1}{r/L_z})$ at $z = \pm 1$; $\frac{\partial}{\partial r}(rB_\theta) = 0$ at $r = \frac{R_1, R_2}{L_z} = r_1, r_2$.

Since $v = 0$ at $r = r_1$, r_2 and also on $z = \pm 1$, it would have been customary to apply successively Hankel transform and cosine transform for v_θ (even in z) and sine transform to B_θ (odd in z) in (6.23) and (6.24).

$$\bar{v}_\theta = \pi \int_{-1}^{1} \int_{r_1}^{r_2} rB_1(p_s r) v_\theta \cos(\pi n z)\, dr\, dz$$

$$\bar{B} = \pi \int_{-1}^{1} \int_{r_1}^{r_2} rB_1(p_s r) B_\theta \sin(\pi n z)\, dr\, dz$$

with $n = 2K + 1$, K integer and $B_1(p_s r) = J_1(p_s r)Y_1(p_s r_i) -$

$$Y_1(p_s r)J_1(p_s r_1)$$

J and Y being Bessel's functions of first order, of first and second kind respectively; p_s is the root of $B_1(p_s r_2) = 0$;

and then taking the inverse transform

$$v_\theta = \pi \sum_{K=1}^{\infty} \sum_{s=1}^{\infty} B_1(p_s r) \frac{p_s^2 J_1^2(p_s r_2)\bar{v}_\theta}{J_1^2(p_s r_1) - J_1^2(p_s r_2)} \cos(n\pi z)$$

$$B_\theta = \pi \sum_{K=1}^{\infty} \sum_{s=1}^{\infty} B_1(p_s r) \frac{p_s^2 J_1^2(p_s r_2)\bar{B}_\theta}{J_1^2(p_2 r_1) - J_1^2(p_s r_2)} \sin(n\pi z)$$

However, the boundary conditions of B_θ on $r = r_1, r_2$ cannot be satisfied in this way. Turning to (6.23) and (6.25)

$$\frac{\partial^2 v_\theta}{\partial z^2} + \frac{\partial^2 v_\theta}{\partial r^2} + \frac{1}{r}\frac{\partial v_\theta}{\partial r} - (M^2 + \frac{1}{r^2})v_\theta = -\frac{\partial \phi^+}{\partial r} \qquad (6.27)$$

If $v_\theta \equiv v_\theta(z)v_\theta(r)$ and $\phi^+ \equiv v_\theta(z)\phi^+(r)$, a separable solution is possible of the form

$$v_\theta = \cos(n\pi z)\; A_1\left\{\begin{matrix} J_1 \\ \text{or} \\ K_1 \end{matrix}\right.\left(\sqrt{n^2 - M^2}\, r\right) + A_2\left\{\begin{matrix} Y_1 \\ \text{or} \\ I_1 \end{matrix}\right.\left(\sqrt{M^2 - n^2}\, r\right) + \text{P.I.}\}$$

J_1/K_1, Y_1/I_1 depending on $n \gtrless M$.

$n = \frac{2K + 1}{2}$, K integer.

However, if v_θ, Φ^+ are independent of z, then a solution can be obtained for the equation (6.27) in terms of Bessel's functions or modified Bessel's functions.

$$v_\theta = A_1 K_1(Mr) + A_2 I_1(Mr) + \text{P.I.} \left\{\frac{-M\frac{\partial \phi^+}{\partial r}}{\partial^2/\partial r^2 + \frac{1}{r}\partial/\partial r - 1/r^2 - M^2}\right\}$$

In view of the problems in fitting boundary conditions to the solution of (6.23)-(6.26), consider a boundary layer analysis with a basic core flow flanked by thin Hartmann layers on the

horizontal walls and boundary layers ($O(\frac{1}{\sqrt{M}})$) on the curved side walls. Neglect secondary flow due to the curvature of the side walls and due to buoyancy; these assumptions are justified if (Chandrasekhar S. 1961)

$$\frac{L_r Re}{R_{av} M^2} << 1 \text{ and } \frac{g\beta\frac{\partial T}{\partial r} L_z^4}{\frac{K}{c_p \rho}\nu} \text{ and } \frac{g\beta\frac{\partial T}{\partial r} L_z^4}{\nu^2 M^2} << 1$$

Addition and subtraction of (6.23) and (6.24) give

$$\frac{\partial^2 x}{\partial z^2} + \frac{\partial^2 x}{\partial r^2} + \frac{1}{r}\frac{\partial x}{\partial r} + M\frac{\partial x}{\partial z} - \frac{x}{r^2} = 0$$

$$\frac{\partial^2 y}{\partial z^2} + \frac{\partial^2 y}{\partial r} + \frac{1}{r}\frac{\partial y}{\partial r} - \frac{y}{r^2} - M\frac{\partial y}{\partial z} = 0$$

with $x = v_\theta + B_\theta$ and $y = v_\theta - B_\theta$.

In the Hartmann layers since $\frac{\partial}{\partial z} >> \frac{\partial}{\partial r}$

$$\frac{\partial^2 x}{\partial z^2} + M\frac{\partial x}{\partial z} = 0$$

$$\partial^2 Y/\partial z^2 - M\frac{\partial y}{\partial z} = 0$$

with the boundary condition $x = \frac{1}{r}$ at $z = 1$ and $y = \frac{1}{r}$ at $z = 1$.

Also $x_{\text{Hartmann layer}} - X_{\text{core}} \to 0$ away from $z = 1$

$y_{\text{Hartmann layer}} - Y_{\text{core}} \to 0$ away from $z = -1$.

A consistent solution is given by

(i) In the core $v_\theta = \frac{1}{r}$, $B_\theta = 0$

(ii) In the Hartmann layer $v_\theta = \frac{1}{r}\{1-e^{-M(1-z)}\}$, $B_\theta = \frac{1}{r}e^{-M(1-z)}$.

For the boundary layers on the side (curved walls)

$$\frac{\partial}{\partial r} >> \partial/\partial z \text{ gives}$$

$$\frac{\partial^2 x}{\partial r^2} + \frac{1}{r}\frac{\partial x}{\partial r} - \frac{x}{r^2} + M\frac{\partial x}{\partial z} = 0$$

which is still difficult to solve. Further neglect of terms of order $\frac{L_z\sqrt{M}}{R_{av}}$, $(\frac{L_z}{R_{av}})^2$ with respect to terms of order M gives

$$\frac{\partial^2 x}{\partial r^2} + M\frac{\partial x}{\partial z} = 0$$

which is the same that has been solved in section 5·3 but the boundary conditions on B_θ in the present case contain an additional factor of $\frac{1}{r_1}$ or $\frac{1}{r_2}$ each assumed constant depending on which boundary layer at $r = r_1$ or $r = r_2$ is being considered.

Therefore $|V|$ is given by

$$V = \frac{-2I \ln\frac{R_2}{R_1}}{8\pi L_z\sqrt{\sigma\eta_v}}\left\{1 - \frac{0.956\{\frac{1}{R_1} + \frac{1}{R_2}\}L_z}{\sqrt{M}\ln\frac{R_2}{R_1}} - \frac{1}{M} + \text{terms of higher order of product of } (\frac{1}{R_1}, \frac{1}{R_2}, \frac{1}{M})\right\} \quad (6.28)$$

Integrating (6.25) over the volume from $z = 1$ to $z = -1$ and $r = r_1$ to r_2 and dimensionalising

$$\Delta\phi = \frac{B\int_D v\,dr\,dz}{2L_z} - \frac{2I\ln R_2/R_1}{4\pi L_z\sigma} = \frac{-IB\ln R_2/R_1}{2\pi\sqrt{\sigma\eta_v}}\{1 - \frac{1}{M} - \frac{0.956(\frac{1}{R_1} + \frac{1}{R_2})L_z}{\sqrt{M}\ln\frac{R_2}{R_1}} + O(\frac{1}{M R_1 R_2})\} - \frac{I\ln\frac{R_2}{R_1}}{2\pi L_z\sigma} \quad (6.29)$$

and by Kirchhoff's law of the electrical circuit

$$\equiv 2\alpha T_m - \frac{I\ln R_2/R_1}{2\pi t_w\sigma_w} \quad (6.30)$$

$$\therefore\ I = \frac{2\alpha T_m}{\frac{\ln R_2/R_1}{2\pi L_z\sigma}\{1 + c + B\sqrt{\frac{\sigma}{\eta_v}}L_z(1 - \frac{1}{M} - \frac{0.956(\frac{1}{R_1} + \frac{1}{R_2})L_z}{\sqrt{M}\ln R_2/R_1} + \text{terms of higher order of } \frac{1}{R_1 R_2 M})\}} \quad (6.31)$$

This checks with $I = \dfrac{2\alpha T_m}{\frac{\ln\frac{R_2}{R_1}}{2\pi L_z\sigma}(1 + c)}$ in the absence of a magnetic field.

$$\frac{\partial^2 x}{\partial r^2} + M \frac{\partial x}{\partial z} = 0$$

which is the same that has been solved in section 5·3 but the boundary conditions on B_θ in the present case contain an additional factor of $\frac{1}{r_1}$ or $\frac{1}{r_2}$ each assumed constant depending on which boundary layer at $r = r_1$ or $r = r_2$ is being considered.

Therefore $|V|$ is given by

$$V = \frac{-2I \ln\frac{R_2}{R_1}}{8\pi L_r \sqrt{\sigma\eta_\nu}} \left\{ 1 - \frac{0.956\{ \frac{1}{R_1} + \frac{1}{R_2} \} L_z}{\sqrt{M} \ln \frac{R_2}{R_1}} - \frac{1}{M} + \text{terms of higher order of product of } (\frac{1}{R_1}, \frac{1}{R_2}, \frac{1}{M}) \right\} \quad (6.28)$$

Integrating (6.25) over the volume from $z = 1$ to $z = -1$ and $r = r_1$ to r_2 and dimensionalising

$$\Delta\phi = \frac{B \int_D v dr dz}{2L_z} - \frac{2I \ln R_2/R_1}{4\pi L_z \sigma} = \frac{-IB \ln R_2/R_1}{2\pi\sqrt{\sigma\eta_\nu}} \{1 - \frac{i}{M} - \frac{0.956(\frac{1}{R_1} + \frac{1}{R_2})L_z}{\sqrt{M} \ln \frac{R_2}{R_1}} + O(\frac{1}{MR_1R_2})\} - \frac{I \ln \frac{R_2}{R_1}}{2\pi L_z \sigma} \quad (6.29)$$

and by Kirchhoff's law of the electrical circuit

$$\equiv 2\alpha T_m - \frac{I \ln R_2/R_1}{2\pi t_w \sigma_w} \quad (6.30)$$

$$\therefore \quad I = \frac{2\alpha T_m}{\frac{\ln R_2/R_1}{2\pi L_z \sigma} \{1 + c + B\sqrt{\frac{\sigma}{\eta_\nu}} L_z (1 - \frac{1}{M} - \frac{0.956(\frac{1}{R_1} + \frac{1}{R_2})L_z}{\sqrt{M} \ln R_2/R_1} + \text{terms of higher order of } \frac{1}{R_1 R_2 M})\}} \quad (6.31)$$

This checks with $I = \frac{2\alpha T_m}{\frac{\ln\frac{R_2}{R_1}}{2\pi L_z \sigma}(1 + c)}$ in the absence of a magnetic field.

From (6.31) and (6.28), the mean flow rate is given by

$$|V| = \frac{\alpha T_m}{L_r B}\left\{1 + \frac{1+c}{M}\left(1 - \frac{1}{M} - \frac{0.956\left(\frac{1}{R_1}+\frac{1}{R_2}\right)L_z}{\sqrt{M}\,\ln R_2/R_1} + \text{higher order terms in } \frac{1}{R_1 R_2 M}\right)^{-1}\right\}^{-1} \tag{6.32}$$

$$\equiv \frac{\alpha T_m}{L_r B}\left\{1 - \frac{1+c}{M} + \frac{0.956\left(\frac{1}{R_1}+\frac{1}{R_2}\right)L_z(1+c)}{M^{3/2}\ln R_2/R_1} + o\left(\frac{1}{M}\right)\right\} \simeq \frac{\alpha T_m}{L_r B}$$

for $M \gg 1,\ c,\ \frac{L_z}{R}$.

The fact that $|V| \to \infty$ for $B \to 0$ in (6.32) is fallacious since the analysis does not hold for small B. In fact, when T_{av} and T_m are maintained constant and independent of z, $V \propto B$ for weak magnetic field strength. The basic physical concept is that of j_r $(\propto \frac{1}{r})$ being uniform with respect to height L_z in the core for small B; current flow in the core diminishes with stronger B and is confined to the Hartmann layers. The increased resistance in the fluid circuit reduces I and hence j_r = constant (independent of B) in the Hartmann layer; the force balance is therefore between $\underline{j}\times\underline{B} \simeq O(B)$ and viscous $\eta_v \frac{\partial^2 v}{\partial z} \simeq O(B^2 v)$; $V \simeq O(B^{-1})$. This is in contrast to the case where the effective control is by I. As long as I is constant, $|V|$ is independent of B for a wide channel ($L_r \gg L_z$).

The other extreme case of ($L_r \ll L_z$) similarly gives for constant T_{av}, T_m, $|V| = O(B)$ for small B and $|V| = O(B^0)$ for large B. For constant I, $|V| = O(B)$ for small B, $|V| = O(B^0)$ for large B but with large curvature $|V| \sim O(B)$ for all B.

In the absence of buoyancy induced convection and secondary flow due to curvature, i.e. $v_r = v_z = 0$, ignoring viscous dissipation and $\frac{\partial^2 T}{\partial z^2}$, the energy equation is

$$K\left(\frac{\partial^2 T}{\partial r^2} + \frac{1}{r}\frac{\partial T}{\partial r}\right) + \frac{I^2}{\sigma(2\pi L_z)^2 r^2} = 0$$

whose solution corresponding to boundary conditions of $T = T_2$ at $r = R_2$ and $T = T_1$ at $r = R_1$ is

$$T = T_{av} + \frac{T_m \ln \frac{r^2}{R_1 R_2}}{\ln R_2/R_1} + \frac{I^2}{2K\sigma(2\pi L_z)^2}(\ln \frac{r}{R_1})(\ln \frac{R_2}{r}) \qquad (6.33)$$

The third term in the R.H.S. of (6.33) is insignificant for large B. At small B, buoyancy-induced convection dominates.

Buoyancy induced secondary flow estimates

Consider the buoyancy-induced convection in the absence of any thermoelectric current. Take $v_\theta = 0$. The symmetry of the configuration permits the neglect of $\frac{\partial}{\partial\theta}$ terms. Take the origin at the centre of the rectangular cross-section of the channel (xz plane $x \equiv r$), z vertical; under the assumptions of $R_{av} >> 1$, $R_m << 1$, $\underline{B} = (0,0,B)$, the steady inertialess flow equations are from (3.1)

$$0 = -\frac{\partial(p + \rho g z)}{\partial x} + \eta_v\left(\frac{\partial^2}{\partial x^2} + \frac{\partial^2}{\partial z^2}\right) v_x - \sigma B^2 v_x \qquad (6.34)$$

$$0 = -\frac{\partial(p + \rho g z)}{\partial z} + \eta_v\left(\frac{\partial^2}{\partial x^2} + \frac{\partial^2}{\partial z^2}\right) v_z + g\rho\beta(T - T_{av}) \qquad (6.35)$$

$$v_x \frac{\partial T}{\partial x} + v_z \frac{\partial T}{\partial z} = \frac{K}{C_p \rho}\left(\frac{\partial^2}{\partial x^2} + \partial^2/\partial z^2\right) T \qquad (6.36)$$

Eliminating $p + \rho g z$ between (6.34) and (6.35)

$$\left(\frac{\partial^2}{\partial x^2} + \partial^2/\partial z^2\right)(\omega)_{y=0} - \frac{\sigma B^2}{\eta_v}\frac{\partial v_x}{\partial z} = \frac{g\beta\frac{\partial}{\partial x}(T - T_{av})}{\nu} \qquad (6.37)$$

where ω_y is the y = 0 component of vorticity $\frac{\partial v_x}{\partial z} - \frac{\partial v_z}{\partial x}$.

The equations (6.36) and (6.37) can be nondimensionalised with respect to x and z by dividing them by L_z.

The trivial solution of (6.36) is $T = T_{av} + T_m x$

In the event of $v_z << v_x$ and $\frac{\partial}{\partial z} >> \frac{\partial}{\partial x}$ which is valid for core flow with $L_z < L_x$, (6.37) becomes

$$\frac{\partial^3 v_x}{\partial z^3} - M^2 \frac{\partial v_x}{\partial z} = \frac{g\beta}{\nu} \frac{T_m}{L_x} (L_z)^3 \qquad (6.38)$$

The solution of (6.38) with the boundary condition $v_x = 0$ at $z = \pm 1$ (rigid walls) and at $z = 0$ (by symmetry) is

$$v_x = \frac{g\beta \frac{T_m}{L_x} (L_z)^3}{\nu M^2} \left(\frac{\sinh Mz}{\sinh M} - z\right) \qquad (6.39)$$

At high Hartmann number M

$v_{x_{max}} \to \frac{g\beta \frac{T_m}{L_x} (L_z)^3}{\nu M^2}$ and therefore the buoyancy induced vorticity decreases as $\frac{1}{M^2}$ as expected, and is independent of viscosity. At low values of M, if terms up to the order of M^2 only are retained, (6.39) leads to

$v_x \to \frac{g\beta T_m}{6\nu L_x} (L_z)^3 (z^3 - z)$ which is the exact solution of

$$\frac{\partial^3 v}{\partial z^3} = \frac{g\beta T_m}{\nu L_x} (L_z)^3$$

The ratio of magnetic damping to viscous damping of the peak vorticity due to buoyancy is therefore given by $\frac{1}{0.064\ M^2}$ so that, for effective magnetic damping $M > 4$. The temperature field away from the curved walls is given by $T = T_{av} + x \frac{T_m}{L_x} + \text{Ⓗ}(z)$ where T_m/L_x is a constant, the solution satisfies

$$v_x \frac{\partial T}{\partial x} = \frac{K}{C_p \rho} \frac{\partial^2 T}{\partial z^2}$$

Ⓗ (z) is given by

$$\text{Ⓗ}(z) = \frac{C_p \rho}{K} \frac{g\beta \left(\frac{T_m}{L_x}\right)^2 (L_z)^3}{\nu M^2} \left[\frac{\sinh Mz}{M^2 \sinh M} - \frac{z^3}{3} + z\left(\frac{1}{2} - \frac{\coth M}{M}\right)\right]$$

An order of magnitude comparison of TEMHD rotational speed and buoyancy induced circulation can be made, ignoring the interaction of v_θ and v_r as follows :

Hg $\beta \sim 1.8 \times 10^{-4}$ $\alpha \sim 10^{-5}$ V/°K $\nu \sim 1.11 \times 10^{-7}$

$g \sim 9.98$ $c \to 0$ $L_z \sim 1$ cm

B small

$$V_{r_{max}} = 10^{-4} \frac{T_m}{L_r} \text{ m/sec}$$

B high ~ 1 Tesla

$$V_{r_{max}} = 2.4 \times 10^{-7} \frac{T_m}{L_r} \text{ m/sec}$$

B $\sim$ 0.01 Tesla

$$V_{\theta_{max}} = 0.6 \frac{T_m}{L_r} \text{ m/sec (viscous force balance)} \qquad L_r \sim 10 \text{ cm}$$

$$= 10^{-3} \frac{T_m}{L_r} \text{ m/sec (magnetic drag balance)}$$

$V_\theta \sim 10^{-5} \frac{T_m}{L_r}$ m/sec (6.40)

The buoyancy-induced circulation is therefore much weaker than the TEMHD circulation (V_θ at least an order of magnitude higher, at the worst, than V_r). For Li the ratio V_r/V_θ is still smaller. It is to be noted that V_z has been ignored in the above analysis which considers V_z to be confined in thin boundary layers along the vertical rigid side walls (cf. $\frac{\partial V_x}{\partial x} + \frac{\partial V_z}{\partial z} = 0$).

In the presence of thermoelectric potentials along the radial direction, ignoring V_z and higher order terms in V_z and V_r, the equations of core flow are given by

$$-\frac{\rho V_\theta^2}{r} = -\frac{\partial}{\partial r}(p + g\rho z) + \eta\{\frac{\partial^2}{\partial r^2} + \frac{1}{r}\frac{\partial}{\partial r} - \frac{1}{r^2} + \partial^2/\partial z^2\} V_r - \sigma V_r B^2 \quad (6.41)$$

$$\rho\{V_r \frac{\partial V_\theta}{\partial r} + \frac{V_r V_\theta}{r}\} = \eta\{\frac{\partial^2}{\partial r^2} + \frac{1}{r}\frac{\partial}{\partial r} - \frac{1}{r^2} + \partial^2/\partial z^2\} V_\theta - \sigma B^2 V_\theta + \frac{2\sigma\alpha T_m B}{r\left(\ln \frac{R_2}{R_1}\right)(1 + c + M - 1 - O(\sqrt{M}))} \quad (6.42)$$

$$0 = -\partial/\partial z(p + g\rho z) + \rho\beta g(T - T_{av}) \quad (6.43)$$

Eliminating $(p + \rho gz)$ terms between (6.41) and (6.43),

$$-\frac{\partial}{\partial z}\left(\frac{v_\theta^2}{r}\right) = \nu\left\{\frac{\partial^2}{\partial r^2} + \frac{1}{r}\frac{\partial}{\partial r} - \frac{1}{r^2} + \frac{\partial}{\partial z^2}\right\}\frac{\partial v_r}{\partial z} - \sigma B^2\frac{\partial v_r}{\partial z} - g\beta\frac{\partial(T-T_{av})}{\partial r} \qquad (6.44)$$

In (6.44) the dominating extra terms compared to those in (6.37) are $-\frac{\partial}{\partial z}\left(\frac{v_\theta^2}{r}\right)$ and $-\frac{\nu}{r^2}\frac{\partial v_r}{\partial z}$. They are in such a direction as to oppose the buoyancy induced circulation due to the term $g\beta\frac{\partial}{\partial r}(T-T_{av})$ in one vertical half space. Physically they represent the vorticity driving force due to rotation and curvature. Therefore the symmetry of v_r about the central horizontal plane is lost and in general v_r would be reduced in magnitude compared to that of v_r in the absence of v_θ.

In arriving at the linear solution of the temperature distribtuion from (6.36) as $T = T_{av} + T_m x$, the effects of curvature and buoyancy-induced circulation w have been ignored, and it is tacitly assumed that the sidewalls are maintained at temperatures T_1 and T_2. The effect of curvature imparts a logarithmic variation of T with r, and in practice it is difficult to maintain isothermal sidewall interfaces when the buoyancy-induced fluid circulation is present. It is therefore more appropriate to consider a vertical temperature gradient along the sidewalls ($\frac{\partial T}{\partial z}$ positive and constant), i.e.

$$T_{w_{1,2}} = T_{1,2} + Az \qquad (6.45)$$

The solution of the problem is difficult, but some physical insight can be obtained by superposing the solution due to longitudinal temperature variation at the sidewalls, i.e. $T_w = Az$, on the solution for the isothermal sidewall case.

This TEMHD problem is entirely different in character to those considered so far in generating maximum TEMHD interaction. The temperature gradient (along the direction $\underline{B}$ = (O,O,B) in this case) at the solid liquid interface circulates thermoelectric current across a boundary layer (assumed thin) in the fluid where no $\frac{\partial \Phi}{\partial z}$ exists otherwise because of insulated interfaces at the top and bottom walls. j_r in the top half space is in the opposite directions to that in the bottom half. Assume j_r is confined in the thin boundary layer of thickness t_f in the fluid parallel to B and the sidewalls. The fluid in the boundary layer therefore has $v_\theta \equiv v_y$ in opposite directions in the top and bottom half spaces. This results in the possibility of rotational shear flow at the central horizontal plane. This type of shear layer would also occur in the case of a straight TEMHD channel of rectangular cross-section, but in such a case the driving mechanism is due to the temperature distribution along the nonisothermal sidewalls not being linear.

Consistent with the nature of the problem, in the present case the condition that the sidewalls are perfectly conducting is replaced by that of the thin conducting wall of thickness t_w and finite conductivity σ_w. From the continuity of current flow

$$j_{fx} = -\frac{\partial}{\partial z}(j_{wz})\,t_w \qquad (6.46)$$

and the Kirchhoff's voltage law gives

$$\int_0^z \int_0^z \left(\frac{j_{fx}\,dz}{t_f}\right)\frac{dz}{\sigma_f} = \int_0^z \frac{j_{wz}}{\sigma_w}\,dz - \int_0^z A\alpha\,dz \qquad (6.47)$$

The mean value of T (i.e. T at z = O) may be taken as=O without loss of generality in equation (6.45)

From (6.47) $\frac{j_{wz}}{\sigma_w}\ \frac{1+c}{c} = A\alpha$ where $c = \frac{\sigma_f t_f}{\sigma_w t_w}$ (6.48)

Assuming a linear temperature variation of α with T and therefore also with z, i.e.

$$\alpha = \alpha_1 + \alpha_2 ZA$$

$$|j_{fx}| = \frac{\sigma_f t_f}{1+c}\ \alpha_2 A \tag{6.49}$$

The viscous force balance gives

$$|v_y| \equiv |v_\theta| = \frac{\alpha_2 A^2}{1+c}\ \frac{M^2}{B}\left(\frac{L_r}{L_z}\right)^2\ \nu^{3/2}\ \frac{L_r (R_{1'2})^{3/4}}{L_z^{9/4}} \tag{6.50}$$

where $M = (\sqrt{\frac{\sigma}{\eta}})\ BL_z$, $L_r \equiv L_x$, $t_f = L_r/\left(\frac{L_z}{R_{1'2}}\right)^{1/4}\left(\frac{L_z \nu_\theta \rho}{\eta}\right)^{1/2}$ the boundary layer thickness of the 'Dean' problem.

$|v_\theta|$ in such a case increases with $B^{2/5}$.

The flow configuration due to linear longitudinal (z)-temperature variation at the second side wall is similar to that at the first side wall velocity magnitude modified by the curvature ratio, but the respective flows are in opposite θ= y directions for the same z. Each of the top and bottom vertical half spaces is occupied by the fluid rotating in opposite directions at their respective side walls, while at a given side wall the v_θ direction changes from the top half to the bottom half. The physical situation is shown in Figure 6.2. Thus there exist a shear layer at the horizontal midplane and a weaker shear layer at the curved vertical surface at $r = R_s$, R_s depending on $1/R_1$ and $1/R_2$.

For $\Lambda > \frac{\partial T}{\partial x}$, the combined radial and longitudinal temperature gradient in the INTB (6.21) configuration leads to TEMHD flow whose profile is antisymmetrical about the horizontal midplane as well as about the curved vertical midplane. In each vertical half space, the TEMHD flow can be compared with the

combined Couette (counter rotating co-axial concentric cylinder case) and uniform azimuthal pressure gradient flow in a uniform axial field (ref. Chandrasekhar, 1961). It would be very interesting to solve such a problem in view of indications of the way the fluid behaves, as observed during experimentation, but further analysis is beyond the scope of this thesis.

An analogy can be drawn with the case of an infinitely long (y, z directed) thin plate of thickness t_w in $\underline{B} = (0,0,B)$ with longitudinal, ~~continu-~~ soidal temperature gradient $\frac{dT}{dz}$ (Shercliff, 1978) as shown in Figure 6.3. Taking advantage of the stream function H such that $j_x = -\frac{\partial H}{\partial z}$, $j_z = \frac{\partial H}{\partial x}$ from (3.1), and taking the curl of (3.22), neglecting $\partial/\partial z$ w.r.t $\partial/\partial x$, $v = v_\theta \equiv v_y$.

$$\frac{\partial^2 H}{\partial x^2} + \sigma B \frac{\partial v}{\partial z} = 0 \tag{6.51}$$

$$\eta_v \frac{\partial^2 v}{\partial x^2} + B \frac{\partial H}{\partial z} = 0 \tag{6.52}$$

a consistent solution with boundary conditions $v = 0$ at $x = 0$ and $x \to \infty$ gives

$$v = V e^{-\sqrt{M/2}(x/L_z)} \sin(\sqrt{M/2}\, x/L_z) \sin(z/L_z) \tag{6.53}$$

$$H = -\sqrt{\sigma\eta_v}\, V\, e^{-\sqrt{M/2}(x/L_z)} \cos(\sqrt{M/2}\, x/L_z) \cos(z/L_z) \tag{6.54}$$

Using (3.29)

$$\alpha\frac{\partial T}{\partial z} = \frac{V}{L_z}(\sqrt{\frac{\eta}{\sigma}}) e^{-\sqrt{M/2}x} \cos\frac{z}{L_z} \frac{1}{\sqrt{c^2 + M + \sqrt{2M}c}} \cos(\frac{\sqrt{M/2}x}{L_z} - \tan^{-1}\frac{\sqrt{M/2}}{c + \sqrt{\frac{M}{2}}}) \tag{6.55}$$

At $x = 0$

$$V = \frac{\alpha L_z \frac{\partial T}{\partial z} \sqrt{\sigma/\eta_v}}{(\cos\frac{z}{L_z})(c + \sqrt{\frac{M}{2}})} \sim O(B^{-\frac{1}{2}}) \tag{6.56}$$

These are then shearing toroidal (θ) boundary layer flows.

Further consideration of the effect of longitudinal temperature gradient along the side walls is provided in the next

section for the problem with conducting solid-liquid interfaces at the top and the bottom rigid walls.

No direct consideration has so far been given to the presence of j_θ. Order of magnitude calculation shows $j_\theta \sim$ Order $(\sigma_f V_r B)$, $j_{\theta_{max}} \sim (0.24 \frac{T_m}{L_r}$ amp/m^2 at B = 1 Tesla, which is small compared to j_r.

6.2.2 Conducting wall-fluid interface at top and bottom rigid walls (CTB)

It has been pointed out that for the TEMHD flow described in Chapter 5, the configuration - whether the sidewall to fluid interface is insulated or not - does not matter much ($\frac{\partial T}{\partial y}$ = constant). However, in the annular channel configuration, with heating/cooling and magnetic field orientation the same as that adopted in (6.2.1) the all-conducting wall to liquid interface case is basically different from the case considered in 6.2.1. The radial temperature gradients along the top and bottom horizontal planes exert definite influence on the magnitude and the shape of the velocity profile of v_θ in the CTB case compared to the Hartmann layer controlled flow in the INTB case; narrow width channel cases are, however, still the same.

When buoyancy- and curvature-induced secondary flow can be ignored, the temperature distribution is given by 6.33, i.e.

$$T = T_{av} + \frac{T_m \ln(r^2/R_1R_2)}{\ln(R_2/R_1)} + \frac{I^2}{2K\sigma(2\pi L_z)^2} \ln\frac{r}{R_1} \ln\frac{R_2}{r} \quad (6.57)$$

with viscous dissipation also neglected.

If $I \to 0$ motion induced e.m.f. in the fluid and the thermoelectric e.m.f. balance at the horizontal wall interface gives

$$v_\theta B = \frac{2\alpha T_m}{r \ln(R_2/R_1)} \quad (6.58)$$

With $\alpha = \alpha_1 + \alpha_2 T$

$$v_\theta = \frac{2T_m}{Br \ln R_2/R_1}\left\{\alpha_{av} + \alpha_2 \frac{T_m \ln(r^2/R_1R_2)}{\ln R_2/R_1}\right\},\ \alpha_{av} = \alpha_1 + \alpha_2 T_{av} \tag{6.59}$$

However, this solution cannot satisfy the no-slip boundary conditions at all the walls, and hence boundary layers occur at all the walls.

When the lateral (radial) temperature gradient is high and the strength of the magnetic field is low, v_θ is high; the secondary flow induced by rotational fluid flow is in the opposite direction to that of buoyancy induced secondary flow at one of the horizontal walls ($T_1 < T_2$ → bottom wall; $T_1 > T_2$ → top wall) and therefore strong boundary layers occur at the curved vertical sidewalls; and the boundary layers at the horizontal walls, except near the curved sidewalls, become insignificant. There is thus a large temperature gradient near each curved wall along the radial direction. In effect then, the bulk rotation of the fluid is controlled by two co-axial boundary layers rotating in the same sense due to TEMHD forces at the overlapping horizontal and vertical boundary layers. At very high values of the lateral gradient of temperature, the single cell buoyancy circulation breaks up into multicellular toroidal vortices in the boundary layers along the curved side walls. The buoyancy induced circulation also raises the possibility of adverse vertical temperature gradients at the horizontal walls and the associated marginal convective instability. The temperature distribution, controlled by buoyancy effect, in the bulk of the fluid away from the curved walls when $R_{av} \to \infty$ is given by

$$T = T_{av} + x\frac{T_m}{L_x} + \frac{C_p\rho}{K}\,\frac{g\beta\left(\frac{T_m}{L_x}\right)^2 (L_z)^3}{\nu M^2}\left\{\frac{\sinh MZ}{M^2 \sinh M} - \frac{z^3}{3} + \left(\frac{1}{6} - \frac{1}{M^2}\right)Z\right\} \tag{6.60}$$

In the presence of a longitudinal temperature gradient of the form $T = Az$ along the vertical curved sidewalls, there is in this case (CTB) the possibility of j_z aligning totally along B, entering or leaving the bulk of the fluid at the horizontal walls. Therefore the possibility of shear flow as discussed in section 6.2.1 does not arise in the case of CTB configuration.

6.2.3 Top surface free; solid-liquid interface at bottom rigid wall insulating (FTINB)

As explained later, this configuration has practical advantages during experimentation. Loosely speaking it is half the symmetrical configuration of section 6.2.1 (INTB). However, the presence of the free surface permits the top surface level to be non-planar, non-horizontal and surface waves may occur. Also to be noted is the fact that the interaction of buoyancy and the TEMHD circulation makes INTB configuration asymmetric about the horizontal midplane. At high values of M, i.e. in strong magnetic fields, the solution of the FTINB corresponds asymptotically to the bottom half space INTB configuration solution with both v_θ and v_r becoming small.

Assuming the top free surface to be horizontal, the buoyancy driven circulation is such that the flow of the fluid towards the cold vertical sidewall boundary layer is mostly restricted to the top layer of the fluid. The solution of the simplified vorticity equation (6.38) corresponding to a stress-free top surface ($\frac{\partial v}{\partial z} = 0$ at $z = L_z$) and the net flow in the meridional plane zero, with no slip at the bottom boundary ($v = 0$ at $z = 0$) is given by

$$v_x = \frac{g\beta \frac{T_m}{L_x} (L_z)^3}{\nu M^2} \left[z + \frac{\sinh Mz \left(M + (\sinh M)\frac{M^2}{2} - 1\right)}{M(\sinh M - M\cosh M)} + \frac{\left(1 + (\cosh M)\frac{M^2}{2} - 1\right)(1 - \cosh Mz)}{M(\sinh M - M\cosh M)} \right] \qquad (6.61)$$

Using this value of v_x, a corresponding expression for T in the cove can be obtained which shows a vertical stable thermal stratification of the fluid compared to the strong lateral temperature gradient at the sidewall boundary layers.

Rotation of the fluid in the isothermal condition imparts on the bulk of the fluid a radial outward force; when the top surface is free, the height of the fluid layer varies with the radial distance to balance the hydrostatic pressure. In the case of solid body rotation, the free surface is known to be a paraboloid of revolution with the concave surface facing upwards. When a lateral temperature gradient is present, the buoyancy induced circulation creates a sink at the top surface of the cold sidewall boundary layer. In analogy with the bath tub exit flow configuration, such flow is characterised by a spiralling motion downwards, resulting in the free surface of the fluid being a surface of revolution, the profile generatrix having a curvature convex facing upwards. Since v_r is at least one order of magnitude smaller than v_θ from (6.1), a very approximate relationship given by

$$-\partial p/\partial r + \eta_v\left(\frac{\partial^2 v_r}{\partial z^2} - \frac{v_r}{r^2}\right) + \frac{\rho v_\theta^2}{r} = 0 \qquad (6.62)$$

may be considered. Since the static pressure p is given by $\rho g L_z(r)$, $L_z(r)$ is predominantly influenced by the radial dependence of v_θ. For $v_\theta(r) \sim \frac{A}{r}$, $L_z(r)$ has a predominant term $\frac{A}{r^2}$, which is convex facing upwards. The free surface profile is further complicated by the meniscus effect. The combined effect of all the forces is difficult to evaluate analytically, more so at the boundary layers near the sidewalls.

The free surface at the top of the liquid column permits non-vanishing shear stress due to variation of surface tension. The variation in the radial direction only is considered, and it is assumed to originate from temperature variation. This is a very simplified model of an otherwise complex problem with the curvature of the surface due to meniscus effect at the sidewall and the variation of surface tension due to surface active material concentration gradient. The semi-rigid oxides at the free surface makes it more complex. The simplified core flow problem as stated above can be solved within the limitations of (6.38) by changing the boundary conditions to $v_r = v_x$ at $z = 0$, $\eta_v \frac{\partial v_x}{\partial z} = \frac{\partial \sigma_s}{\partial x} \left(\equiv \frac{d_{\sigma s}}{dT}\right)$ at $z = 1$, where σ_s is the surface tension, assumed as a linear function of temperature T, and the net flow across any vertical plane $r = x = R$ as zero. The solution is given by

$$v_x = \frac{g\beta \frac{T_m}{T_x} (L_z)^3}{\nu M^2} \left[Z + \sinh Mz \left\{ \frac{\frac{1}{\eta_v} \frac{d\sigma_s}{dT} (\sinh M - M)}{M(\sinh M - M \cosh M)} + \frac{M + \frac{\overline{M^2}}{2} - 1 \sinh M}{M(\sinh M - M \cosh M)} \right\} \right.$$

$$+ (1 - \cosh M) \left\{ \frac{1 + \frac{\overline{M^2}}{2} - 1 \cosh M}{M(\sinh M - M \cosh M)} \right.$$

$$\left. \left. - \frac{\frac{1}{\eta_v} \frac{d\sigma_s}{dT} (1 - \cosh M)}{M(\sinh M - M \cosh M)} \right\} \right] \qquad (6.63)$$

It is known that liquid in motionless rigid containers with a free surface would be prone to oscillations (sloshing problem: Moiseev and Petrov, 1966), and there exist natural frequencies $f_n^{(i)}$ for containers of given shape and size. The problem can be specified in terms of the velocity potential Ψ^* and the elevation of the free surface ζ^* above the equilibrium state Σ given by

$$\Psi^* (x,y,z,t) = (x,y,z) \cos f_n t$$

$$\zeta^* (x,y,t) = (x,y) \sin f_n t$$

with $\Delta\Psi = 0$ in the volume interior, $\frac{\partial \Psi}{\partial n} = 0$ on the rigid boundaries (n,direction of normal to the boundary) and $\frac{\partial \Psi}{\partial n} = \lambda\zeta$ on the surface Σ. The eigen value λ is related to the natural frequency by the relation $\lambda = \frac{fn^2}{g}$ where g is the gravitational acceleration. One can construct a variational formulation of the problem and solve it by the Ritz method (Moiseev and Petrov, 1966) in the case of annular cylindrical geometry (axis vertical) to give

$$\lambda_m^{(i)} = K_m^{(i)} \tanh K_m^{(i)} L_z \qquad (6.64)$$

where $K_m^{(i)}$ is the m^{th} root of

$$J_n'(K) Y_n'(\frac{R_2}{R_1} K) - Y_n'(K) J_n'(\frac{R_2}{R_1} K) = 0,$$

J and Y being Bessel's function of first and second kind.

Such oscillations are modified by the surface tension and damped by the viscous shear. The axial vertical magnetic field does not affect such oscillations directly, but damps them indirectly by vorticity control and TEMHD induced rotational shear.

The longitudinal temperature gradient along the vertical curved surface results in the same sort of situation as discussed in section 6.2.1 for the INTB case, the horizontal plane across which shearing of v_θ takes place, being at the mid-height of the mercury column for a linear temperature gradient along z.

6.2.4 Free top surface and conducting liquid-solid interface at rigid bottom wall (FTCB)

The main difference in FTCB case compared with the other configurations (INTB, CTB, FTINB) discussed above, arises when there is a longitudinal temperature gradient ($\frac{\partial T}{\partial z}$) along the curved sidewalls. At each sidewall the thermoelectric current flow path from the hot-top end to the base horizontal wall permits shearless v_θ along the vertical direction apart from that in the Hartmann layer at the bottom wall.

When the buoyancy effect is not negligible, the buoyancy-induced circulation causes a vertical temperature gradient; it can be shown by the following analysis that adverse temperature gradients would be present just above the base conducting wall due to the difference in thermal conduction in the solid and the liquid and the buoyancy-induced convection of heat in the opposite direction. Ignore the effect of j^2/σ which contributes an additional difference factor.

In the solid $$K\left(\frac{d^2T_s}{dz^2}\right) = 0$$

and in the liquid

$$\rho C_p v_x \frac{\partial T_L}{\partial x} = K\left(\frac{d^2T_L}{dz^2}\right)$$

where $\frac{\partial^2 T}{\partial x^2} = 0$ at the central part of the annulus (radial direction; v_z in the central part of the annulus (radial direction) $\to 0$ and $\frac{dT_L}{dz}$ is finite, giving $V_z \frac{\partial T_L}{\partial z}$ a lower order of magnitude than $v_x \frac{\partial T_L}{\partial x}$. A crude estimate of the adverse temperature gradient is therefore given by

$$\frac{\partial (T_s - T_L)}{\partial z} = \int_0^{z = z^*} \frac{T_m}{L_r} \frac{\rho C_p}{K} v_x \, dz \qquad (6.65)$$

where v_x is given by (6.63) and z* corresponds to z for v_x maximum as given as $z = \frac{\ln M}{M}$ for large values of M.

6.2.5 Shallow channels

For the sake of completeness, it is to be mentioned that when the height $2L_z$ of the channel << $2L_r$ and the curvature effect is negligible, the azimuthal velocity in the absence of secondary flow is given by

$$v_\theta = \frac{2\alpha T_m}{B(1 + c\,\frac{\tanh M}{M})\,\ln\frac{R_2}{R_1}} \cdot \frac{1}{r}\left\{1 - \frac{\cosh(Mz/L_z)}{\cosh M}\right\} \qquad (6.66)$$

where $c = \frac{\sigma_f L_r}{\sigma_w t_w}$, $L_r = \frac{R_2 - R_1}{2}$ and $2L_z$ is the height of the channel.

6.2.6 Instabilities

While rigorous perturbation analysis for the flow and thermal instability in annular channel TEMHD (basic state itself being not amenable to exact analysis) is beyond the scope of this thesis, a few exploratory physical arguments are developed in the following paragraphs.

(i) It has been already remarked in Chapter 2 that,by virtue of the Proudman-Taylor theorem, the rotation of the fluid imparts on the fluid a two-dimensional structure; it follows therefore that rotation stabilizes the flow instability caused by adverse temperature gradients (Chandrasekhar, 1961). However, in the case of lateral heating, the density variation is no longer restrained along $\underline{\Omega}$ (rotation, z direction) and $\underline{\Omega}\times\nabla(\rho)$ is not equal to zero. Thus even if the body forces, $\underline{F}$, were irrotational, i.e. curl $\underline{F}$ = O, then Kelvin's theorem (which states that circulation Γ of the fluid round a closed loop moving with the fluid is constant) fails (Shercliff, 1964), because $\underline{F}$ x grad ρ does not vanish. Thus vorticity would persist, the motion being no longer constrained by rotation to be the same in all planes normal to the rotational axis. In the presence of rotation, the buoyancy-induced vorticity equation is given by

$$2(\underline{\Omega}\cdot\nabla)(\rho\underline{v}) = g\underline{x}(\nabla\rho) \qquad (6.67)$$

A careful consideration of (6.67) by Hide (1971) revealed that even when $\nabla\rho \neq 0$, steady flows can exhibit certain two dimensional features.

From (6.67) $2\Omega \frac{\partial}{\partial z}(\rho v_x, \rho v_y, \rho v_z) = (-g\frac{\partial \rho}{\partial y}, \frac{\partial \rho}{\partial x}, 0)$

$\therefore 2\Omega \frac{\partial}{\partial z}(v_y/v_x) = (v_x \frac{\partial \rho}{\partial x} + v_y \frac{\partial \rho}{\partial y}) g/\rho v_x^2$

In the isotropic limit and steady motion (Hide, 1971)

$$v_x \frac{\partial \rho}{\partial x} + v_y \frac{\partial \rho}{\partial y} + v_z \, \partial\rho/\partial z = 0$$

gives

$$\frac{\partial}{\partial z}(v_y/v_x) = (-g/\rho)\frac{\partial \rho}{\partial z} \frac{v_z}{2\Omega v_x^2} \qquad (6.68)$$

Therefore, as long as the R.H.S. of (6.68) is << 1, the horizontal flow pattern changes very slowly with z, even though large gradients of flow speed in z direction may possibly exist.

The effect of axial magnetic field in the TEMHD annular flow is to be evaluated from the standpoint that high magnetic field is associated with low rotational speed; very high magnetic field therefore imparts a two-dimensional pattern due to its own influence. As the magnetic field, B, is reduced from a large value, the effective state passes through an intermediate regime to that corresponding to high rotational speed when two-dimensional pattern(under conditions following (6.68)) again prevails. Finally, at very low value of B, the stabilizing effect of both B and Ω is lost.

(ii) TEMHD circulation of fluid in annular channels is more akin to azimuthal pressure gradient driven flow; therefore the stability is decided by $Re\frac{L_r}{R_1}$ where $R_e = \frac{VL_r}{\nu}$. Since for practical devices $R_{av} >> 1$ and longitudinal temperature gradients would give rotational shear, it is worth considering the stability criterion given by the Taylor number, $\mathcal{T}$, as

modified by Chandrasekhar (1961) in the axial magnetic case with small radius ratio R_2/R_1 and $R_{av} \ll 1$.

For viscous fluid and the pertinent case of conducting sidewalls $\mathcal{T}_{av}$ must exceed 451.27 M^2 for instability (cf.

$$\frac{d}{dr}(rv_\theta^2)_{r=R} = -D^2 \frac{B^2}{\mu\rho} \nu\sigma\mu \ , \ D = f(L_r, L_z).$$

$\mathcal{T}_{av}$ is given by $\frac{1}{2}(1 + \frac{\Omega_2}{\Omega_1}) \frac{4\Omega_1 (\frac{R_1}{R_2})^2 \left\{1 - (\frac{\Omega_2}{\Omega_1})(\frac{R_2}{R_1})^2\right\}}{\nu^2} \frac{}{1 - (\frac{R_1}{R_2})^2} (2L_r)^2$ (6.69)

where Ω_2 is the rotational speed as $v \to R_2$

Ω_1 is the rotational speed as $v \to R_2$ and $R_2 - R_1 = 2L_r$.

The expression in (6.69) can be approximated by

$$\frac{2(2L_r)^2}{\nu^2} \frac{v_\theta}{r} \frac{d}{dr} (v_\theta r)$$

Therefore, the marginally stable velocity profile of v_θ is given by

$$\left|\frac{2(2L_r)^2}{\nu^2} \frac{v_\theta}{r} \frac{d}{dr} (v_\theta r)\right| = 451.27 M^2$$

Therefore

$$\left|\frac{(v_\theta r)}{r^2} \frac{d}{dr} (v_\theta r)\right| = K_1 M^2 \text{ where } K_1 = \frac{451.27 \ \nu^2}{2(2L_r)^2}$$

which when integrated gives

$$v_\theta = \sqrt{\frac{2}{3} K_1 M^2}\ r^{\frac{1}{2}} \left(1 - \frac{R_1}{r}\right)^{\frac{1}{2}} \text{ at } r \to R_1 \qquad (6.70)$$

and $$v_\theta = \sqrt{\frac{2}{3} K_1 M^2}\ r^{\frac{1}{2}} \left(\frac{R_2}{r} - 1\right)^{\frac{1}{2}} \text{ at } r \to R_2$$

(iii) Since the average velocity $V \propto \frac{1}{M}$, it is to be concluded that TEMHD flow at high Hartmann number M is stabilized by the magnetic field. However, the strong velocity gradients in the boundary layers at the sidewalls of thickness $L_r/\sqrt{M}$ requires an independent assessment of the stability problem which is, to some extent, covered by (6.70), but a fuller treatment is beyond the scope of this thesis.

With $u_\theta \equiv u_\theta(r)$ and $\frac{\partial u_\theta}{\partial r} >> \frac{\partial u_\theta}{\partial z}$, a two-dimensional flow pattern is inherently assumed; the most unstable disturbances are then those whose wave number vector $\underline{K}$ are parallel to the basic flow direction ($R_{av} >> 1$). The vorticity of these disturbances is in the z direction, and therefore $\underline{B} = B_z$ has no effect on the stability of such flow (Hunt, 1966). Since two-dimensional disturbances are unaffected by B, and points of inflexion may occur on the velocity profile, two-dimensional disturbances could be destabilizing.

In 6.2.1 it has been shown that the presence of longitudinal temperature gradients along the vertical sidewall ($\frac{\partial T}{\partial z}$) causes vertical shear of v_θ about the horizontal midplane and $\frac{\partial u_\theta}{\partial r} >> \frac{\partial u_\theta}{\partial z}$ may no longer hold. A conceptual three-dimensional disturbance still constrained to propagate in the basic flow direction but with amplitude varying in the z direction given by $\underline{u} = \left[u_r(r,z) \exp i(m\theta - \omega t),\ u_\theta(r,z) \exp i(m\theta - \omega t),\ 0\right]$, may be superimposed on the basic flow $\underline{v} = (0, v_\theta(r,z), 0)$ to explore the effect of such situations. The necessary, though not sufficient, condition for the disturbance not to amplify is given by curl $\underline{j} = 0$. Since curl $\underline{j} = \{ B\frac{\partial u_\theta(r,z)}{\partial z} \exp i(m\theta-\omega t),\ B\frac{\partial u_\theta}{\partial z}(r,z) \exp i(m\theta-\omega t, 0) \}$ where div $\underline{u} = 0$ has been used, $\underline{j}$ could interact with B to help the disturbance grow.

A similar situation arises in the study of electrically driven flow (Malcolm, 1968) where damping of such disturbances by the $\underline{j}\times\underline{B}$ force at some places but amplification at other regions have been postulated. Therefore, whether the disturbance grows, alternates or remains stationary is dependent on the rate of energy transfer into the disturbance by inertial stress $\rho u_r u_\theta$, thermal convection in relation to thermal conduction, viscous and joule heat dissipation.

(iv) The presence of rotation, magnetic field and density gradients permit inertial and hydromagnetic plane waves of the form $\exp i(\underline{K}.\underline{r}-wt)$ in the fluid associated with the angular frequency w governed by $\underline{\Omega},\underline{K},\frac{\underline{B}}{\sqrt{\rho\mu}}.\underline{K}$ and $\underline{G}$, $\underline{K}$ where $\underline{G} = (0,0,(\frac{g}{\rho}\cdot\frac{\partial\rho_o}{\partial z})^{\frac{1}{2}})$, $(\frac{g}{\rho}-\frac{\partial\rho_o}{\partial z})^{\frac{1}{2}}$ being the Brunt-Väisälä frequency of the adversely stratified thermal systems. Usually, the Lundquist number is far too low for significant 'Alfven' wave or its variants to be present. The free surface at the top of the fluid column allows surface waves controlled by the gravity factor g and the surface tension σ_s, what are known as gravity waves and capillary waves. The study of such waves would constitute an altogether different facet of the TEMHD problem and is therefore left out. It is only worth noting that, even with uniform density, the uniform rotation of a fluid in a spatial nonuniform $B_\theta(r)$ causes non-axisymmetrical unstable disturbances of the type $f(r)\exp i(m\theta + nz - wt)$, m and n real, to propagate in the direction or against the direction of basic rotation (Acheson, 1972). When $|\frac{mB_\theta}{r}| < |nB_z|$ the waves propagate in the direction of basic rotation; when $|\frac{mB_\theta}{r}| > |nB_z|$ the drift of the waves is against the basic rotation, a result which has been so characteristic of the rotating annulus problem and has a bearing in explaining the westward drift of the geomagnetic field. The basic condition for the generation of these unstable modes is that $\frac{v_\theta^2}{r^2}$ increases with radius anywhere in the interval $R_1 \leq r \leq R_2$. In the presence of adverse density gradients, such propagation occurs if

$$\frac{r}{\mu\rho_o}\left(\frac{B_\theta^2}{r^2}\right)' - \frac{\rho_o' g}{\rho_o}\left(1 + \frac{m^2}{r^2 n^2}\right) > 0$$

where the prime indicates gradient in the r direction with $\rho_o = \rho_o(r)$ and $B_\theta \equiv B_\theta(r)$.

(v) Thermal oscillations in stably stratified fluid of low Pr number as observed in the straight channel TEMHD experiments has been explained from the point of view of relaxation of isotherms in Chapters 4 and 5. In the case of the annular channel geometry, the lateral heating, even though in the central region of the channel, causes a stable thermal stratification at low rotation rates or in the case of very low magnetic fields, yet the buoyancy effect can always promote thermal instability. In general the basic temperature distribution is given by $T = Ax + T(z)$, $x \equiv r$, $R_{av} >> 1$. In the case of a conducting solid-liquid interface at the bottom wall, it has been shown in 6.2.4 that adverse temperature gradients can exist. The buoyancy-induced circulation in the INTB case gives $\frac{\partial T(z)}{\partial z} \geq 0$, but, with a free surface at the top, $\frac{\partial T(z)}{\partial z}$ may be either > 0 or < 0, depending on the heat transfer to the ambient surroundings (convection and radiation). In general $\partial T/\partial z > 0$ is considered as stabilizing. In contrast to the mode of instability that occurs in conducting fluids in magnetic fields due to adverse temperature gradients ($\partial T/\partial z < 0$), where instability usually occurs as aperiodic or marginal forms, and overstability (periodic growth) is ruled out for ($K/c_p\rho < \frac{1}{\mu\sigma}$) (Chandrasekhar, 1961), in the case of lateral heating the most unstable mode of disturbance, whether a longitudinal roll (aligned with the basic convective flow) or a transverse roll (normal to the basic connective flow) is critically dependent on the Pr number. In fact a lateral temperature gradient can substantially alter the mode of instabilities in the conventional Rayleigh-Bénard configuration of fluid with an adverse temperature gradient. For low values of (Ra_r/Pr) marginally stable disturbances dominate, whereas for large values of (Ra_r/Pr) oscillatory instabilities occur (Ra_r based on $\partial T/\partial r$). A physical concept of the

situation may be drawn from energy concepts of the interaction of $\rho v_r v_\theta$, $v_r T$, $\eta \nabla^2 v$, $K\nabla^2 T$, $v_z T$ and j^2/σ. While $\eta \nabla^2 v$, $K\nabla^2 T$ and j^2/σ exert a stabilizing effect, $v_r T$ and $v_z T$ are destabilizing and $\rho v_r v_\theta$ could be stabilizing or destabilizing. In the case of an adverse temperature gradient ($\frac{\partial T}{\partial z} < 0$), overstability cannot occur unless sufficiently strong stabilizing (restoring) force is available in the form of rotation or magnetic field. In the case of lateral heating, viscous and joule dissipation may be enough to excite overstable instabilities, more so with rotation and strong magnetic field, if instabilities do occur at all. This is intimately connected with the cell structure (rolls) of motion that is preferred in the thermal configuration adopted. Detailed analytical treatment is beyond the scope of this thesis.

6.3 Design of the Channel and its Constructional Details

6.3.1 Design consideration

The TEMHD experiments in the annular channel, as already has been remarked, were motivated by the possibility of measuring v without any pressure gradient in the flow direction. For the convenience of experimentation, the configuration adopted was that of lateral heating on the curved walls with uniform B_z, while the top and bottom surfaces were left free from heating or cooling arrangements, so that measuring devices could be freely inserted through those surfaces. The initial design considered was that of INTB configuration because it was thought that it would provide the maximum flexibility in obtaining other configurations, for example by removing the top wall or by removing the insulation coating from the inner surface of the top and bottom horizontal walls. It is necessary to insulate the copper surface and conduct the insulated interface experiments first

because once the copper surface is amalgamated with mercury it is very difficult to insulate its surface. The basic considerations were the choice of

(i) channel height and gap width; the maximum radial dimension and the height were necessarily constrained by the Lintott electromagnet pole face dimension (air gap separation) of 15 cm. A long and narrow channel (z axis long) is more suitable for theoretical analysis, but a wide channel is more convenient in devising probing instruments which are not necessarily delicately thin. Having decided to utilise the maximum of 7.5 cm for the outer radius, consideration was given to optimising the thermo-electric circuit and hence arriving at the other dimensions of the channel. A radial arm thermocouple differs in design from the straight arm one due to the thermal and electrical resistances having logarithmic variation in radius ratio rather than the dependence on the difference of the radii. Since both the solid and the fluid elements have the same radius ratio, the thermoelectric ciruit is optimised for c = 1, giving the ratio of tw/L_z. However, c/M is the effective parameter in the presence of B, and hence such consideration loses its significance. In the case where the height of the annular channel is fixed ($2L_z$) and so is the total volume 2W, a rough calculation shows that an optimum radius ratio exists for minimum heat input for a ΔT_{fixed}. Consider a thermoelectric current I due to hot and cold junctions being maintained at T_2 and T_1 respectively at radial positions $r = R_2$ and $r = R_1$. Ignoring axial heat transfer, convection and curvature, the heat conduction equation from (3.16) is given by

$$\frac{\partial^2 T}{\partial x^2} - \frac{\alpha I T_1 \delta(x,1)}{KW} - \frac{I^2 \ln x}{2\pi L_z \sigma KW} = 0$$

where $x = R_2/R_1$ and $\delta(x,1)$ is a Dirac δ function having a value 1 at $x = 1$ and zero elsewhere. The solution

$$T = \frac{\alpha I T_1 x}{KW} - \frac{I^2}{2\pi L_2 \sigma KW}\left\{\frac{x^2}{2}(\ln x - 1.5)\right\} + T_2$$

is consistent with the physical consideration at the limit $x \to 1$ and $x \to 0$.
As x varies, the temperature difference is a minimum for a given I, when $I = \frac{\sigma\alpha T_1(2\pi L_2)}{x\{\ln x - 1.5\}}$.
The singular conditions are $x = 0$ (which does not correspond to an annular geometry) and $\ln x - 1.5 = 0$, giving a radius ratio of $\frac{R_2}{R_1} = 4.5$. This calculation was carried out independently, but later a similar calculation in a slightly different configuration by Landecker (1977) was noticed. The optimum (thermoelectric) radius ratio gives the annular gap width $\simeq$ 5 cm with $R_2 \sim$ 7cm
A point in favour of such wide gap was the flexibility of inserting a copper pipe of intermediate radius to provide two narrow gap channels.

(ii) Inner cylinder hot or cold.

The inner cylinder cold corresponds to better operation of the radial arm thermocouple, and it is easier to construct a cooling system at the central zone rather than at the periphery of the outer radius of the channel. The buoyancy induced flow therefore is in the opposite direction to that due to centrifugal force of rotation in the bottom horizontal boundary layer, but in the same direction in the top horizontal boundary layer (when there is a top cover (solid wall)). This configuration also corresponds to the situation where convective instability could be generated in the TEMHD rotational flow in the annulus (c.f. Busse, 1970 - thermal rotating system). Heating of the outer surface is also advantageous from the point of view of larger surface area and space for installing heater coils so that high level of heat generation can be maintained.

(iii) The heating and the cooling system.

In the TEMHD channel with the inner sidewall cold configuration, the inner hollow cylinder that forms the sidewall at $r = R_1$ could conveniently be utilised in forming the cooling water jacket. Initially it was thought that cooling water would be let in from the bottom and let out at the top, but since in that case the top connection to the water outlet port would occupyspace at the top and obstruct clear view of the top surface, the following configuration was adopted. A third hollow cylinder of radius $< R_1$ placed co-axially within the TEMHD channel was considered to guide the cooling water, let in at the bottom central port, up to the top of the cylinder (height $2L_z$) (ref. to figures in 6.3.2). Through the clearance at the top between the inner-most water pipe and the inner bore of the cylindrical surface at $r = R_1$, the cooling water would then flow down the annular space between these cylindrical surfaces. It would then be let out through a port located at the sidewall of the bottom of the extended cylindrical surface at $r = R_1$ below the lower horizontal wall of the TEMHD channel. Thus the extended cylindrical bottom at $r = R_1$ houses both the inlet and outlet ports of the cooling water and is conveniently used to support the annular channel on the magnet pole face. This also provided space for leading out the tap connections from the static pressure taps at the lower horizontal wall of the TEMHD channel. The heating of the outer periphery by steam was considered, but since then a steam jacket had to be built at the outer periphery, electrical heating by wrapping heater coils on the outer copper surface was only considered.

6.3.2 Constructional details

For the obvious reason of wastage of material milling out an annular channel out of a solid block of copper was not considered and instead the annular channel was fabricated out of commercial copper pipes and sheet metal. Even with so much consideration given to attain flexibility with one channel only, eventually a number of them were built due to various reasons. First, since a 15 cm diameter (or with dimensions near about that range) for the outer sidewall of the channel was not immediately available, a 30 cm long piece was ordered. It took an unusually long time(more than four months) and the uncertainty of obtaining one such prompted the fabrication of a cylinder out of 3 mm thick copper sheet metal. The 3 mm copper sheet metal (47 cm long) was rolled into cylindrical shape in the sheet metal rolling machine having retained the appropriate peripheral length. The ends of the copper sheet along the straight line generatrix of the right circular cylinder with a bevelled gap in between them were brazed, using 'Easiflow silver brazing alloy' and 'grade 2 Easiflow', available in stock from Johnson Matthey Metals Ltd., while holding the curved sheet metal very carefully around wooden formers from the inside and jubilee clips from outside. The cylindrical pipe so formed was then reamed and polished to give a very smooth surface and symmetry about the axis. Before using the brazing material, it was checked that Hg did not attack the material; however, it proved wrong later on as the test was done only at room temperature and a different situation developed at the higher temperature of the outer channel wall. The impurities,particularly Ag, Cd and Zn in Hg samples from the annular channel experimental rig, even when distilled Hg was used to start with, as observed in the X-ray fluorescence and

chemical tests mentioned in Chapter 3 could be traced to originate from the brazing alloy going into solution in Hg when the composition of such alloys and the p.p.m. content of other elements were obtained from Johnson Matthey Metals Ltd. Brazing alloys suitable for much higher temperature operation, free from Cd and Zn content, are catalogued in the appendix. This information and the realisation of the problem in using the relatively lower melting point silver alloys as the brazing material came at a much later stage of experimentation and higher melting point alloys could not be used.

10 cm length of the fabricated 15.37 diameter cylinder was used for making the outer sidewall of the channel. The inner sidewall of the channel was made out of a 5.4 cm diameter copper pipe with 15 cm length of it used so that it just fitted between the pole faces of the electromagnet (Lintott II) and thus acted as a spacer restraining any tendency of the pole pieces to come closer to each other when energised. Originally, out of the 15 cm of length, 2.5 cm at the top was retained for fixing the cooling water outlet port and 2.5 cm at the bottom for the cooling water inlet port. Later, due to change in the cooling water flow arrangement, the 2.5 cm of length at the top end proved superfluous. The cooling water jacket was formed within the 5.4 cm diameter copper pipe . The constructional feature was such as to lead water in through a 90° bent connector into a 1.25 cm diameter copper pipe fixed co-axially at the central zone of the 5.4 cm diameter pipe (ref. Figure 6.5). The idea of using helical vanes to make the water spiral down the annular gap between the 1.25 cm and 5.4 cm diameter pipes was given up when it was felt that such an arrangement is not essential for attaining uniform cooling. The water inlet and

outlet pipes were aligned with each other at the bottom 2.5 cm region. The ends of the 5.4 cm pipe were blocked by brazing matched circular shaped flat brass plates and then machined to give true flat surfaces at either end.

The bottom wall of the channel was formed by brazing a 3 mm thick copper plate, 15.37 cm in diameter, with a matching 5.4 cm diameter hole drilled at the centre, on to the 5.4 cm pipe at 2.5 cm from the end and to the 15.37 cm diameter pipe at the end of its length. The bevelling and steps made in the copper flat plate before brazing are shown in Figure 6.4. At the time of brazing, the job was held accurately so that the base of the 5.4 cm diameter cylinder was exactly parallel to the flat plate at a distance of 2.5 cm from the base. The cylindrical surfaces were then reamed and polished. Next araldite was applied to the copper flat plate surface (at the channel inside face) that formed the horizontal plane bottom wall of the channel and a 3 mm thick 'Tufnol' matched annular ring type disc (5.4 cm inner diameter and 14.8 cm outer diameter) was fixed. While fixing the insulating disc, araldite was allowed to set under pressure by using equal heights of compression blocks held by C clamps to make the insulator face accurately parallel to the copper baseplate. After the araldite had set and the insulating disc was held firmly fixed, five 1 mm diameter pressure taps were drilled at equal spacings along a radius, the two extreme locations being such that the periphery of the holes drilled just touched the sidewalls of the channel. The tap hole size was increased at the Cu plate end to 3 mm to fix Cu tube connectors which then were connected to flexible PVC tubes to the inclined tube manometer. Originally in the design insulating connectors were used to isolate electrical connection locally between the Hg in the pressure tap hole and the copper base plate. In practice it proved very difficult to fit such insulating connectors in the narrow space

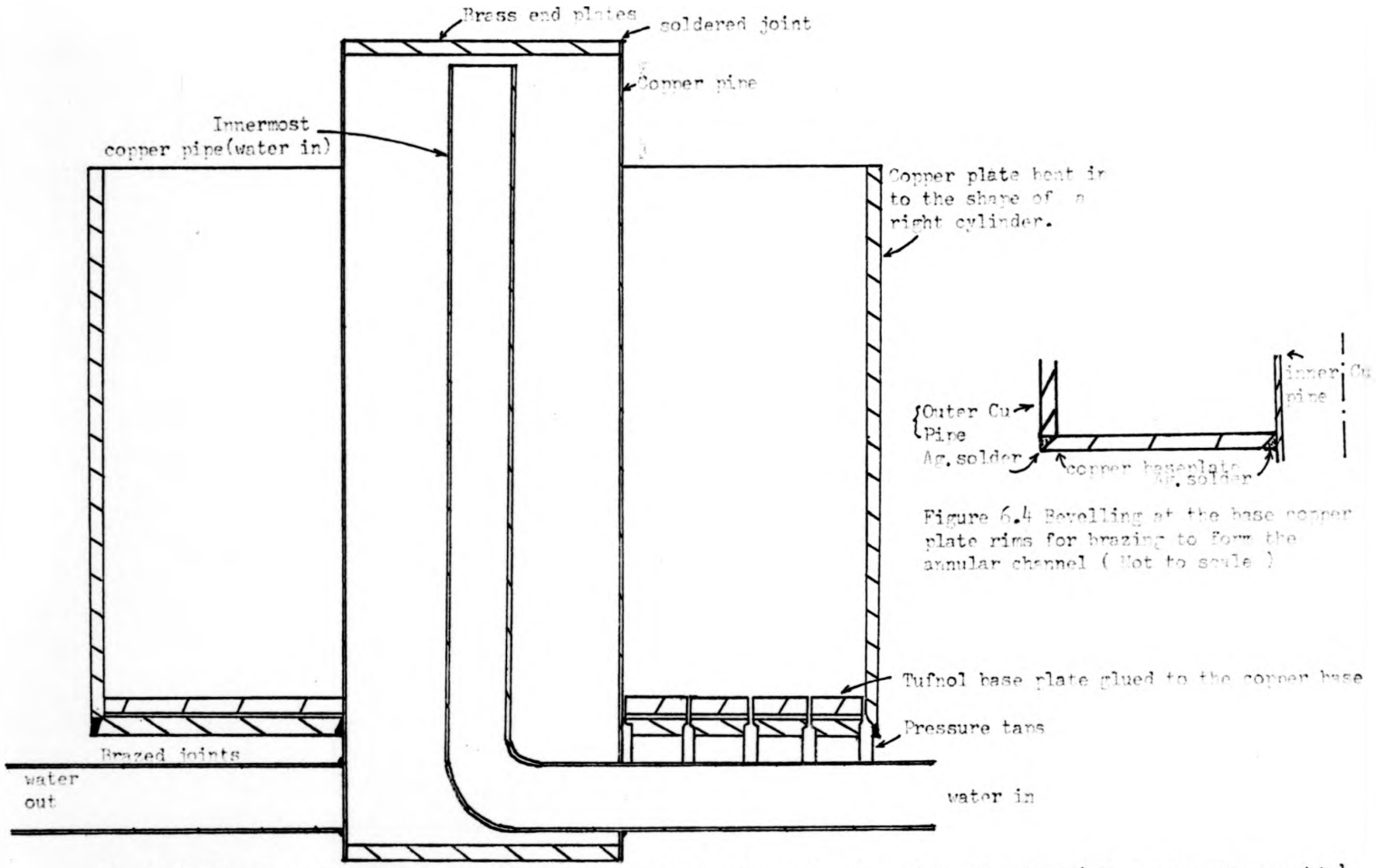

Figure 6.4 Bevelling at the base copper plate rims for brazing to form the annular channel (Not to scale)

Figure 6.5 The Mark I annular channel{vertical section (Full scale diagram) through the radial line containing pressure taps} with insulated solid-liquid interface at the bottom wall.

below the Cu base plate of the channel. The implications of such construction are discussed later in section 6.4. The final dimensions of the channel, shown in Figure 6.5, are all within the maximum tolerance of 0.01 cm. A cut-away sectional view is shown in Figure 6.6.

The top end Cu plate was made in an identical manner to that of the lower end plate, but there was uncertainty about the mode of fixing it on to the channel. The choice was between (i) a flexible joint with 'O' rings at the sidewalls of the channel and (ii) a fixed brazed joint (good electrical continuity and possibly less of a Hg leakage problem) at the sidewalls with a small aperture for cleaning and insertion of measuring probes. The practical difficulty in fixing the 'O' rings (refer to Chapter 7 for details of such sealing arrangements) led to the only other alternative of having brazed fixtures. However, the better and easier way of checking the amalgamation was without fixing the top end plate, and filling up of the channel with Hg. In hurried enthusiasm to observe whether TEMHD rotation is indeed possible or not, the assembly, without top, was installed in the Lintott electromagnet II air gap with the side-walls heated and cooled as stipulated in the design. The succcess in establishing TEMHD rotation in this configuration and the realisation of the fact that TEMHD rotation can be observed directly by actually seeing the rotation of Hg and that there are obvious major advantages of leaving the top surface free for diagnostic purpose as against minor disadvantages in doing so, gave the idea to proceed with experimentation on the FTINB configuration of the TEMHD channel. Since no dramatically new and interesting results were expected from the INTB configuration with rigid boundaries at the top, experiments on the INTB channel were dropped, and hence the top end plate was not

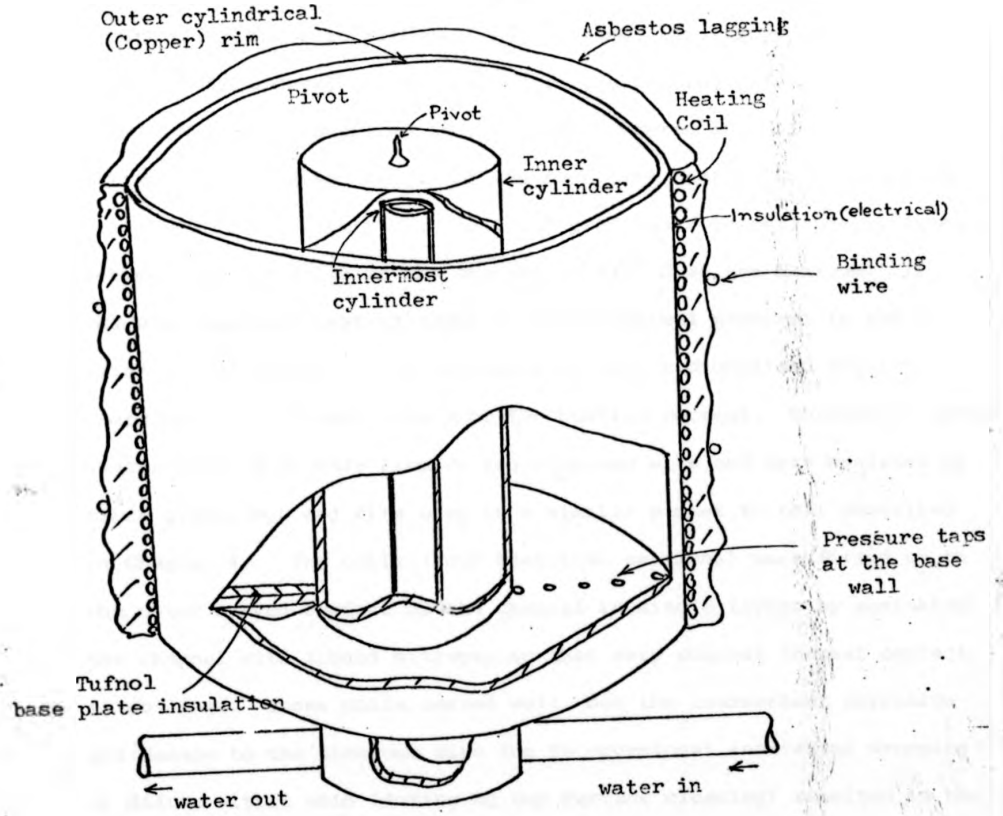

Figure 6.6 The cutaway view of the annular channel, Mark II

brazed into position. (Oddly enough, it served only as a hotplate over the gas burner where,apart from technical activities, tea was also made!).

The heating was initially done by a 4.5 m long, one continuous piece 'Heat by the Yard' fibre glass insulated wire mesh type of nichrome ribbon (Electrothermal Engineering, Ltd.) wrapped round the outer curved sidewall of the channel. The heating rate was fixed from a nomograph, supplied by the manufacturers, against supply voltage for the given length of the tape. The heating rate within the specified voltage limit was small and produced a temperature difference between the sidewalls of the channel $\Delta T \simeq 4^{\circ}/5^{\circ}$ C at the maximum. It was also realised that in order to avoid thermal gradient in the axial (z) direction, it is necessary to have sectionalised coils energised at different levels of the heating current. Therefore, later, heater coils were made from 26 swg nichrome wire and were insulated by fibre glass, MgO and fire clay in a similar manner to that described in Chapter 4. The coils (four identical sections) were fitted on to the outer curved surface of the channel in single layers by shrinking the channel with liquid nitrogen so that very compact thermal contact is obtained. These coils served well, but the inadvertent corrosion and damage to the nichrome wire due to occasional accidental dropping or dilute nitric acid (during Hg top surface cleaning) resulted in the damage to the coils and,due to the stress of shrink-fitting, repair of the coils was almost impossible. KANTHAL resistance wire was also then available, and four identical sections of 25 turn coils insulated by fibre glass, MgO and fire clay as before were made, but fitted on to the channel without shrinkage of the channel, so that the coils could be removed for repair. The thermal bonding was ensured by silicone paste. The overall thermal lagging was provided by asbestos over the coil assembly. With the free surface at the top,heat transfer to the

ambient surroundings could not be controlled as efficiently as in the case of totally enclosed lagging system of the straight channels (Chapters 4 and 5). The maximum heat transfer to the cooling water was only 75 to 85% as compared to 90 to 95% in the straight channel experiments.

The nonuniform amalgamation at the brazed end of the cylinder and the rest of its copper surface, the appearance of a regular pattern of 2-3 mm etch marks on the amalgamated surface, the arrival of the 15 cm diameter copper pipe and the necessity of altering the central cylinder height to permit an unobstructed view of the entire annular top surface of Hg and to provide space for the central pivot for the rotating radial arm of the float(with paddle,velocity-vorticity measuring device)led to the construction of the second channel (Mark II). The constructional details of Mark II are similar to that of Mark I, and the final dimensions of the channel are shown in Figure 6.7. The main changes in the Mark II model as compared to Mark I are (i) the sidewall ends at the top were flush (i.e. the inner and outer cylinders ended at the same height) with each other in the same horizontal plane, (ii) a conical pivot at the central axis on horizontal top surface end of the inner cylinder, (iii) a reduction in the diameter of the inner cylinder to 3.2 cm so that the radius ratio is 4.5, (iv) reduction in the height of the channel to 7.5 cm to provide more space for the inclined mirror at the top and for measuring probes, (v) a rubber padded support at the bottom of the 3.2 cm cylinder to eliminate vibration.

Professor Shercliff suggested the idea of obtaining composite velocity profiles that might lead to a sharp shear layer in a channel of mixed electrical interfacial contact (partly

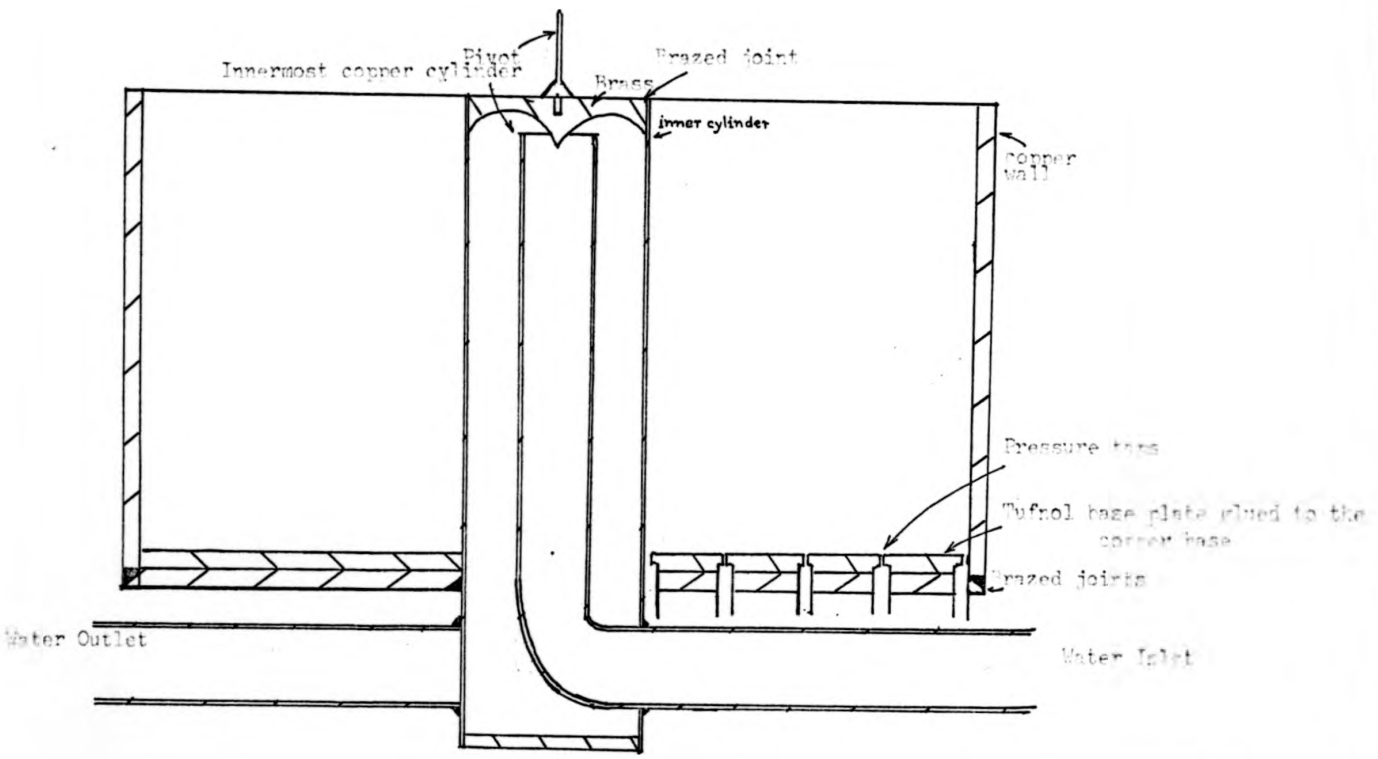

Figure 6.7 The Mark II annular channel (vertical section (Full scale diagram), through radial line of pressure taps) with insulated solid-liquid interface at the bottom wall.

conducting and partly non-conducting) at the bottom wall. It is possible by controlling the heating distribution (like concentrated heating at the bottom edge of the outer sidewall) to adjust the temperature/gradient variation directly proportional to the radial distance (by the funnelling out of the heat flux towards the cold sidewall w.r.t height) so that solid body rotation of the fluid could be generated over the conducting interface part of the base wall, whereas over the rest of the insulating interface portion of the base wall the ordinary free vortex flow could be maintained (Figure 6.8a). It is possible in such a case to generate a shear layer at the sharp transition boundary of electrical interfacial contact at the bottom wall. Stripping of the bottom interface insulation in either of Mark I and II models of the channel proved very difficult without damage to the perfect dimensional features of the assembly, and therefore a third channel was built (Mark III). It also provided the opportunity of further investigations on the FTINB configuration of the channel. For the Mark III model, the conducting part at the base wall interface was chosen as the outer half; the inner zone of the base wall top interface was insulated by applying a uniform coating 0.2 mm thick of PVC paint by holding the brush fixed and rotating the channel base by fixing the channel on the chuck of a lathe. After the paint had set and dried, the boundary edges were made sharp for accuracy and the rest of the bare copper surface cleaned. No effort was given to eliminate the small step difference in the horizontal level of the bare copper and the insulated surface. Checks on the electrical insulation were made to ensure its uniformity and perfection. The other differences of Mark III model (Figure 6.8b) from that of Mark II were (i) no pressure taps at the base

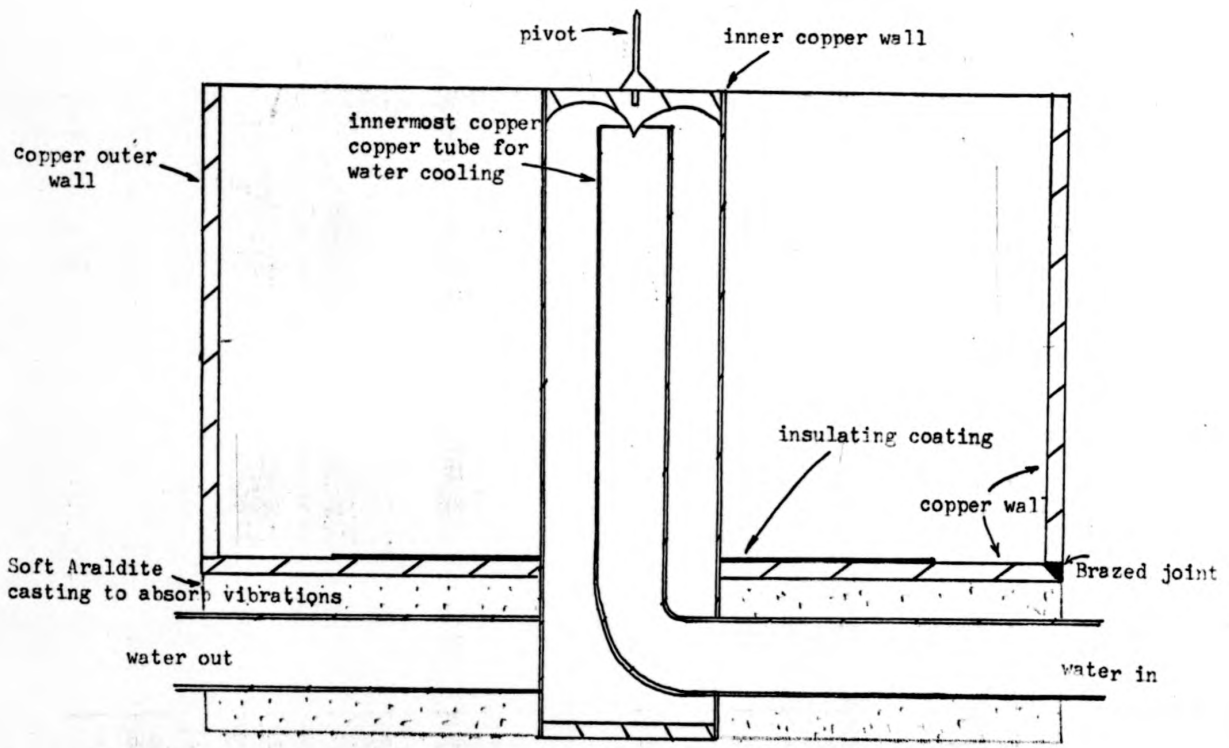

Figure 6.8 (b) The Mark III annular channel with partly conducting and partly insulated sol.-liq. interface at the bottom wall . (Full scale diagram)

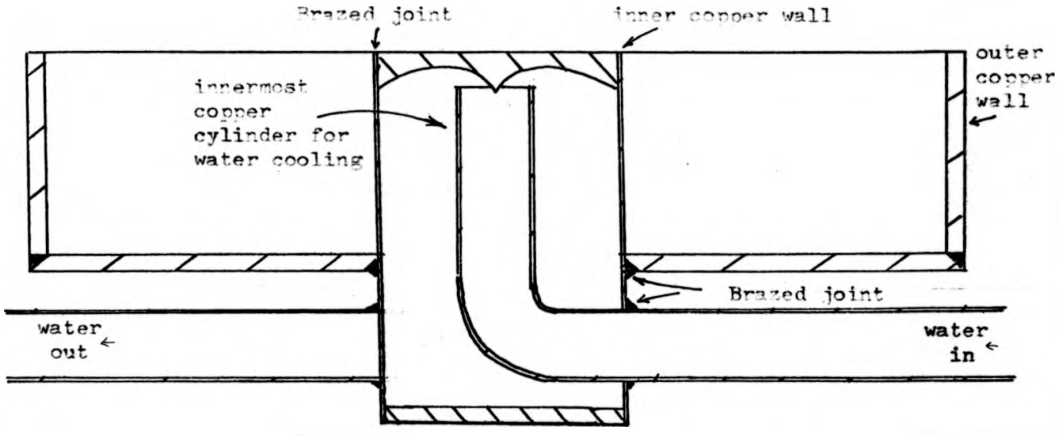

Figure 6.9 The Mark IV annular channel with conducting solid-liquid interface at the bottom wall. (Full scale diagram)

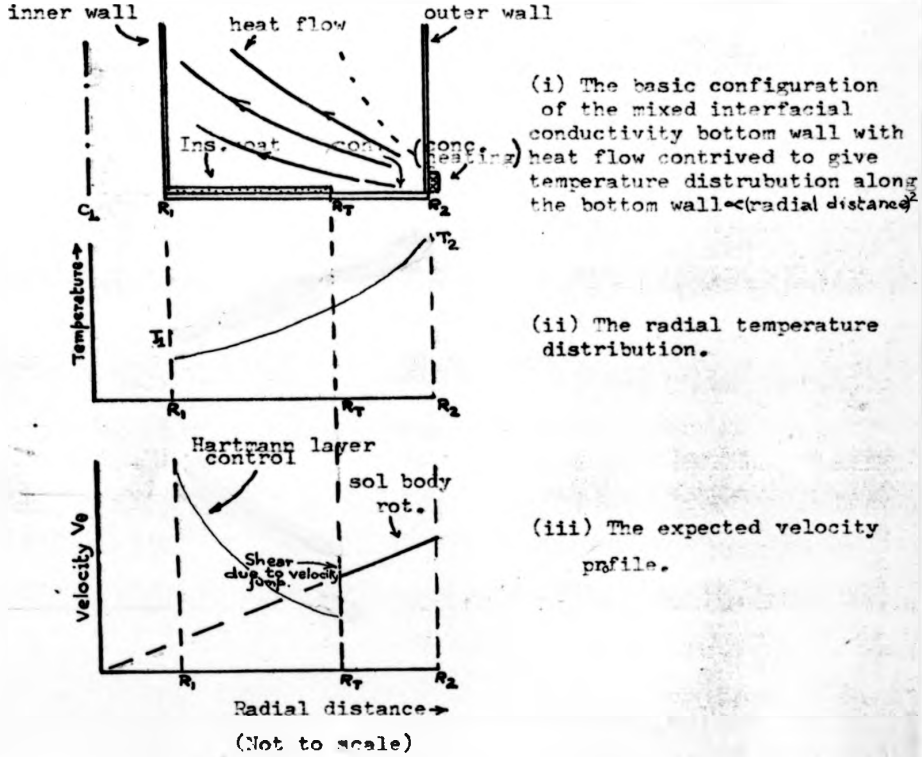

Figure 6.8 (a) The schematic diagram showing the physical configuration to generate TEMHD shear layer and the expected velocity profile.

wall, (ii) the channel base below the lower end horizontal copper plate was encased by casting heat resistant soft glue to eliminate vibration being transmitted to the channel and to distribute the total weight of the channel over a wider area. The PVC insulation stayed in position for nearly six months, after which slow creeping of mercury beneath the outer radial edge of the coating made it separate from the base copper plate. This was very much in contrast to the Mark I and II model where the insulation and the fixing device stayed perfect for all the time. The heating was done by a concentrated KANTHAL wire coil of 20 turns located at the lower edge of the outer side-wall.

The last (Mark IV) model channel was built out of the left over short length of the 15 cm diameter copper pipe with a totally conducting interface at the base wall. This provided a very clear view of the TEMHD rotation without the inclined mirror at the top. No static pressure taps were provided at the base. The central pivot was also not provided in this shallow channel. The inner sidewall of the channel was made out of a 4 cm diameter copper cylinder. The soft resin casting at the bottom of the channel,as in Mark III model, was not considered as a great advantage, and was not made for the Mark IV model. The heating was provided by two identical sections of single layer 22 turn KANTHAL wire heater coils, mounted on the outer sidewall of the channel as in the other models. The final dimensions of the Mark IV model are shown in Figure 6.9.

6.4 Experimental Results and Discussion

In demonstrating TEMHD rotation in the annular channel Mark I, the initial problems of nonuniform amalgamation, low thermopower of Hg (sample I) and the top surface of Hg behaving like a rigid surface due to scum, resulted in doubts being raised at to whether TEMHD forces.were significant enough to drive the fluid motion. The first demonstration of the TEMHD rotation was realised by the way of a casual observation at the end of a frustrating day's work. The magnetic field was switched off first on that occasion rather than the heater supply. Very feeble ripples on the Hg surface seemed to move in the azimuthal direction as seen through the inclined mirror. Even with the overheated 'Heat by the Yard' heating tape used initially, the ripples could at best be described as surface waves. Though later, with better experimental techniques, it was possible to show that vortex patterns and wavelike motion do exist, the conviction that the moving surface ripples were really the indication of steady circulation of the bulk of the fluid masked by the rigid contamination layer on the top of the Hg, and not surface waves or transient phenomena,proved to be true. Cleaning the mercury and maintaining the mercury surface free of rigid contamination stretching from one vertical sidewall to the other made the demonstration of TEMHD rotation quite easy; yet the peculiar aspects of the fluid velocity and vorticity, secondary flow and thermal oscillations required an extensive investigation of the velocity and temperature variation in the interior of the bulk of the fluid in the presence of magnetic fields of various strengths, including zero magnetic field strength.

6.4.1 Measurements on Mark I channel

One of the first reproducible results of TEMHD rotation in the Mark I channel is shown in Figure 6.10. The data for this plot were taken for a fixed heating level (1.67 amperes at 220 volts), and cooling water at 10° C and measuring the fluid velocity near the top surface and at the surface at mid-radius (r = 5.1 cm) with shallow free floats and tracer particles. The time for 20 revolutions was noted by stop-watch for various steady values of the magnetic field strength in either direction. Though the curve of Figure 6.10 resembles the shape of the theoretical curve (ref. Figure 3.5) for the mean velocity it was necessary to find the velocity profile as a function of the radial co-ordinate. It is interesting to note that even with the aspect ratio of $\frac{L_z}{L_r} = 2$ (9.6 cm of height of Hg and 4.8 cm of width) and uniform surface heating, the isotherms departed from the vertical even at high magnetic fields. The application of the magnetic field raised the temperature of the outer wall in contrast with observation in the case of straight TEMHD channels. The increase in the wall temperature is normally expected due to the suppression of buoyancy induced convection by the magnetic field. When Hg from the Mark I channel was emptied out for checking the uniformity of amalgamation, the brazed joint region appeared smooth, but a regular 2-3 mm array of etched pattern was noticeable on the rest of the copper surface. Though steady stationary vortices scouring such a regular pattern were highly improbable, the possibility could not be summarily discounted until it was found out that in the Mark II channel no such pattern was discernible. The pattern on Mark I channel was then considered to be caused by nonuniform amalgamation of the stretched grain boundaries during the rolling process of the straight copper sheet metal into the curved form. A photograph of the pattern is shown in Plates P.3 and 4

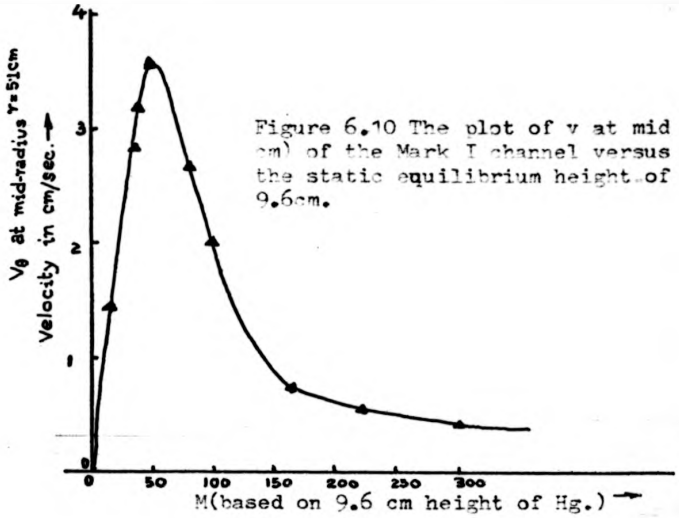

Figure 6.10 The plot of v at mid radius(r=5.1 cm) of the Mark I channel versus M based on the static equilibrium height of the Hg column 9.6cm.

Figure 6.11 The radial profiles of V_θ in Mark II channel.Height of Hg column 7.25 cm. Heating current 1.7 amp at 230 volts in the 'Heat by the Yard' coil.

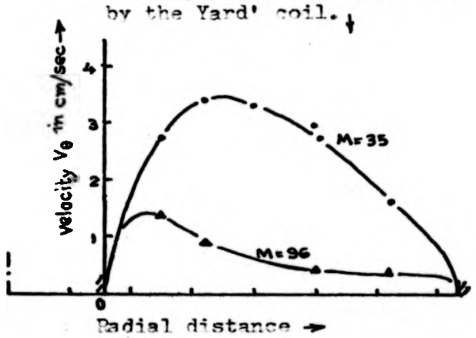

.Figure6.13(a) The velocity profile of V_θ across the height of the 7.25 cm of Hg column. Conditions similar to that in figure 6.11

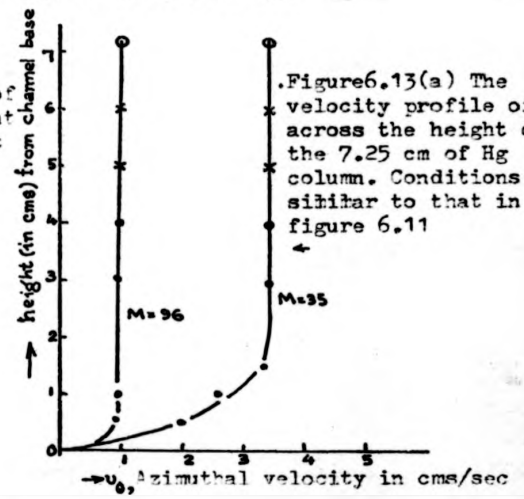

Figure6.13(b) Variation of v_θ measured at r=3.3 cm at a depth of 3.5 cm from the free Hg surface in the Mark II channel with M (based on 7.25cm of Hg)

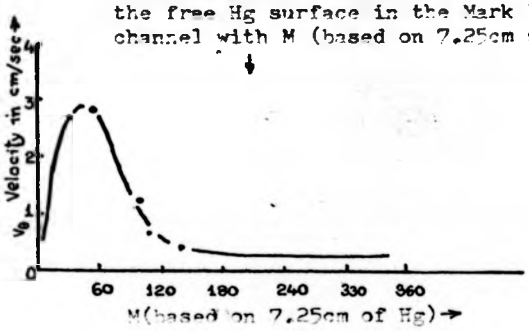

Figure 6.13(c)Variation of v_θ (measured at r=3.3cm at a depth of 3.5 cm for fixed M=42.5, based on Hg column height 7.25cm at equilibrium(static)) against outer wall temperature in °C.Cooling water temperature 10°C

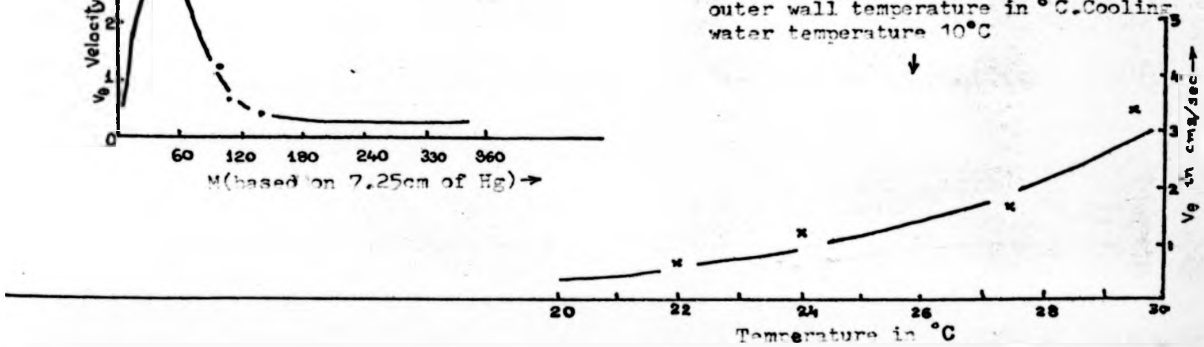

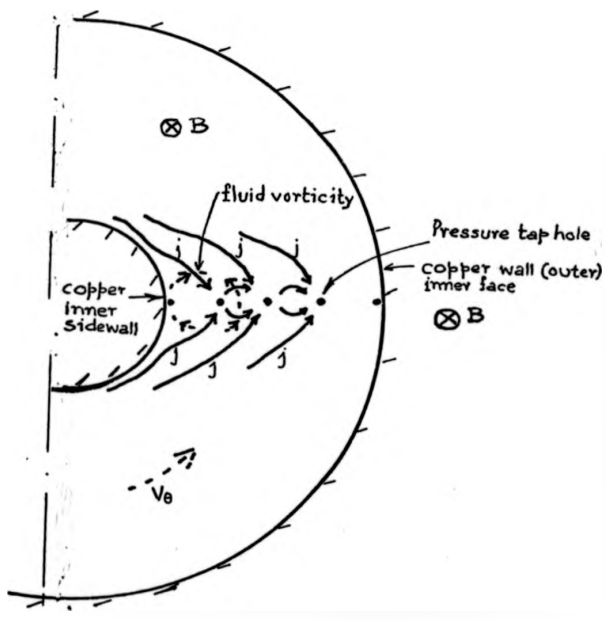

Figure 6.12 Schematic diagram of the distortion of the radial thermoelectric current in the presence of strong axial magnetic field and the associated fluid vorticity at the regions of the static pressure taps at the bottom wall in the Mark II annular channel.

6.4.2 Measurements on Mark II channel

The azimuthal velocity v_θ measurements were carried out on the Mark II channel, using the paddle type pivoted vorticity/velocity measuring probe (ref. 3.47 2b), pitot tubes and thermoelectric potential probes. Below the threshold value of magnetic field strength of B = 0.1 Tesla, the thermoelectric potential probe resulted in errors more than 5%, whereas the pitot tube measurements were in general more effective in the range of B = 0.01 Tesla to B = 0.2 Tesla. The measurement of v_θ with the pivoted paddle type probe was satisfactory down to the angular speed of 1 revolution in 2 minutes; for lower speeds the lag between the paddle type pivoted probe&tracer particles on the surface could be distinguished. This is probably when the drag at the pivot due to friction became relatively important. Since the interest is primarily on the velocity profile, the measurement data are presented for the corroborating measurements by the above methods and are not shown for individual types of measurement system. The profiles of v_θ with radial distance as measured on the Mark II channel with the height of Hg column 7.25 cm at depths of 3 and 4 cm below the free surface for 1.7 amperes of heating current at 230 volts in the 'Heat by the Yard' heating tape are shown in Figure 6.11. The velocity profile in the core region agrees with the theoretical characteristic of free vortex. However, at lower magnetic fields below 0.02 Tesla, there was evidence of departure from free vortex mode to that of forced vortex mode as revealed by the vorticity probe near the inner radius. At B around 0.02 Tesla the fluid circulation,even very close to the inner radius, was so fast that it seemed the no-slip condition does not hold.

A very peculiar thing was observable only at higher magnetic fields greater than 0.2 Tesla in that v_θ was not uniform with respect to θ and an abrupt effective blocking of flow existed at the radial line containing the static pressure taps at the bottom wall.On holding the vorticity probe stationary w.r.t θ at this particular region very slow rotary oscillations (period of order of 12 seconds) of 20 to 30 degrees in amplitude could be demonstrated. Figure 6.12 shows the possible mode of the distortion of j_r due to electrical contact at the pressure taps and the resulting vorticity. In obtaining the velocity profiles, the pressure taps were blocked with 'tensol' cement. A very convenient static pressure measurement was missed thereby.

While the measurements of v_θ at the depths of 3 and 4 cm below the free Hg surface were identical, to investigate how far below the free surface v_θ remains constant, measurement of at other depths was made at the fixed radial position of r = 3.2 cm and heater current of 1.7 amperes for Hartmann number M values of 35 and 96. The velocity profiles w.r.t the depth suggest (Figure 6.13a) the velocity boundary layer thickness to be much greater than the Harmann layer thickness. However, the effect of increasing the value of M definitely shows the decrease in the thickness of the velocity boundary layer. Figure 6.13b shows the variation of v_θ at r = 2.3 cm at a depth of 3.5 cm, with M based on mercury column static equilibrium height of 7.25 cm. Figure 6.13c shows the variation of v_θ for a fixed value of Hartmann number M = 42.5 at the fixed radial distance of r = 3.2 cm and at a depth of 3.5 cm from the free surface for different heater currents measured in terms of the outer wall temperature in ^{o} C for a fixed cooling water temperature at 10^{o} C.

Initially the temperature measurements were conducted with a fixed heater current in the absence of the magnetic field.

However, with such measured values of ΔT_r, the balance between $\alpha\Delta T_r$ and $B\int v_\theta dr$ could not be obtained. This led to the measurement of ΔT_r in the presence of corresponding magnetic fields. With the same heater current the hot wall temperature increased with the increase of magnetic field. Reversing the magnetic field to an identical value resulted in the same temperature distribution. It is therefore essential to associate temperature distribution measurement with the corresponding level magnetic field strength. Temperature distribution measurements were carried out in detail only for the large temperature gradients generated when the 'Heat by the Yard' heating tape was replaced by the four identical Nichrome/Kanthal coil sections mounted in a single layer. The effect of magnetic field strength variation on the temperature distribution in the meridional cross-section is shown in Figure 6.14a (i), (ii) and (iii) for uniformly distributed heating by passing 1 ampere current through each of the four sections of the heater coil for B = 0, B = 0.045 and B = 0.9 Tesla. The isotherms for B = 0 and B = 0.045 Tesla are drawn through the mean values of the fluctuating temperature at the point of measurement. In Figure 6.14a (i), corresponding to B = 0, a predominant thermally stable stratification exists in the core and there are two boundary layers at the vertical sidewalls with intense temperature gradients at the two opposite corners. This type of isotherm contour agrees with the experimental results of Elder (1965) and numerical solution of Valh Davis and Thomas (1969). Temperature oscillations at a point 3 mm away from the inner sidewall at a depth of 3.5 cm below the free surface as measured by the copper constantan thermocouple and recorded by the Hewlett Packard XY plotter is shown in Figure 6.14b. The effect of TEMHD rotation and the

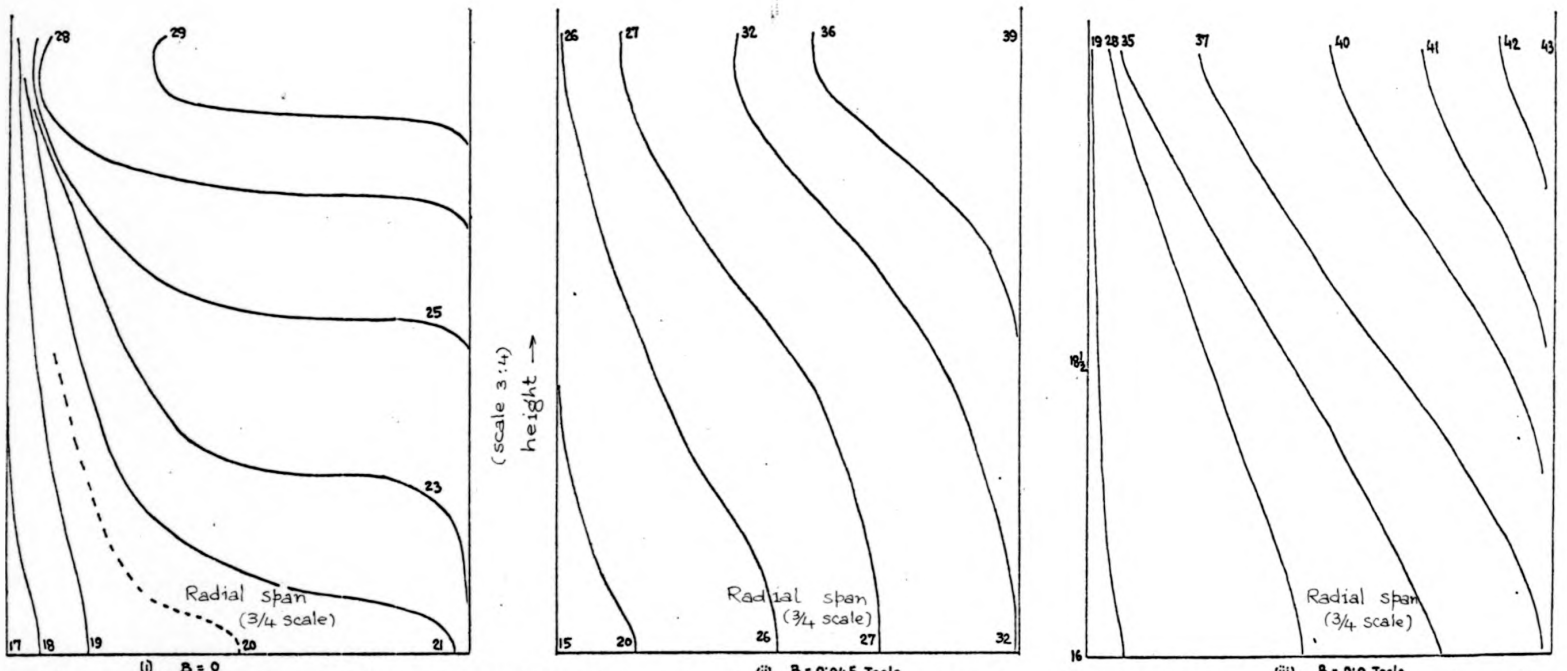

(i) B = 0 (ii) B = 0·045 Tesla (iii) B = 0·9 Tesla

Figure 6.14(a) Isotherm plots in the meridional cross-section in the MarkII annular channel with distributed heating (1amp.4KL wire

Figure 6.14(b) Steady state temperature oscillations in Mark II channel 3mms away from the inner wall at a depth of 3.5 cms with 1 amp. distributed heating in the four sections of the Kanthal wire.The trace moves with time from left to right.Time scale 15sec per cm, Amplitude scale 1°C per cm

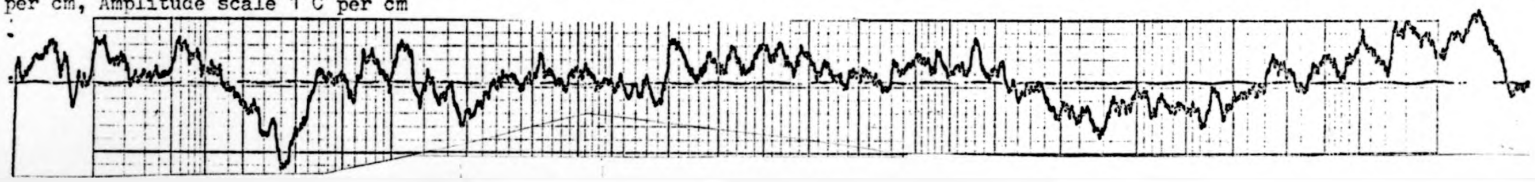

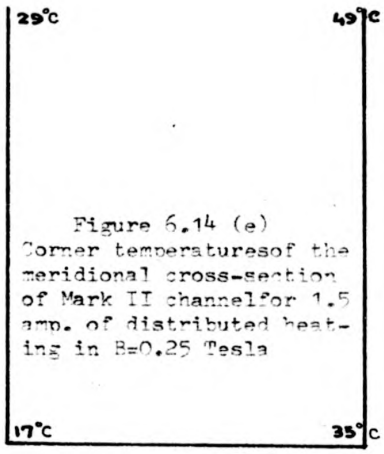

Figure 6.14 (e)
Corner temperaturesof the meridional cross-section of Mark II channelfor 1.5 amp. of distributed heating in B=0.25 Tesla

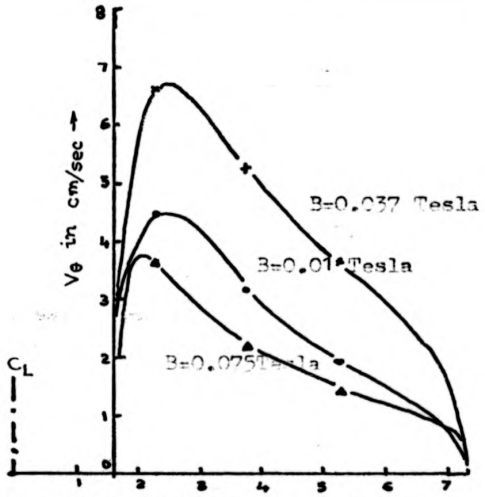

Figure 6.14(c)Radial profiles of V_θ at 1 amp. of distributed heating in the Mark II channel (Kanthal wire of 4 sections for heater coil)

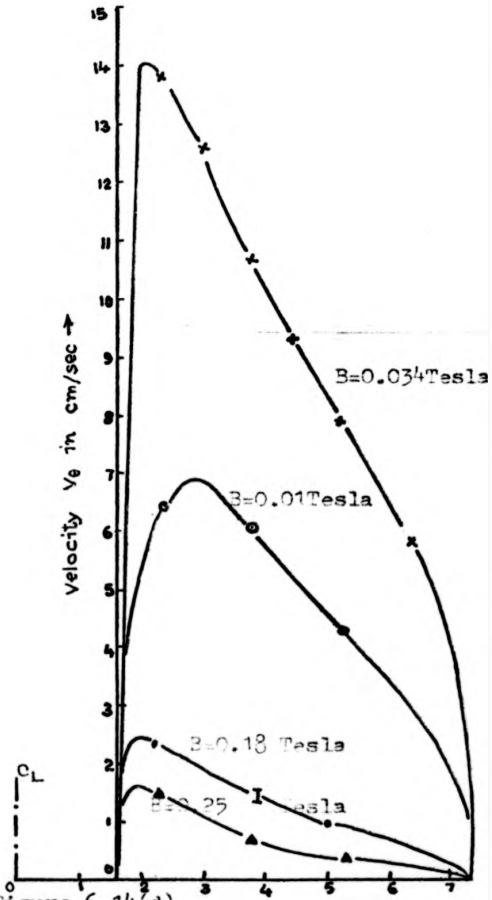

Figure 6.14(d)
Radial profiles of V_θ at 1.5 amp. of distributed heating in Mark II channel (Kanthal wire heating)

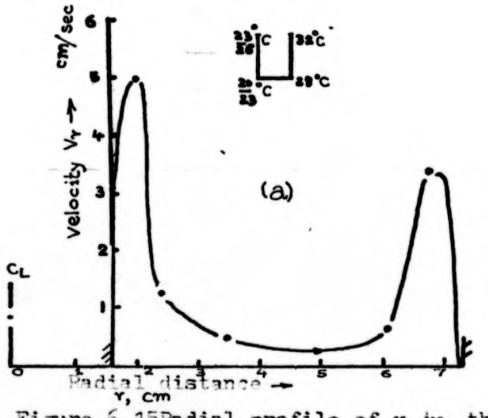

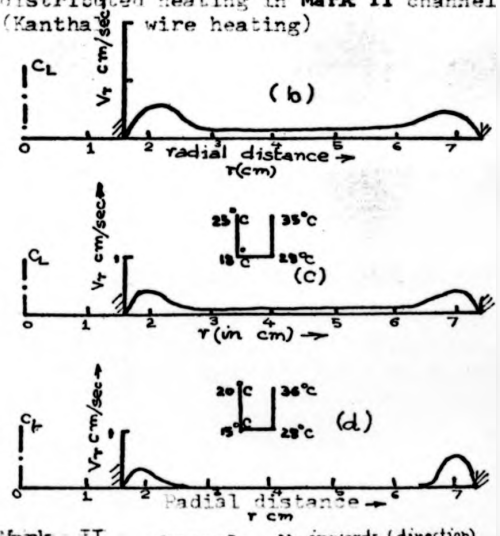

Figure 6.15Radial profile of v_r in the Mark II channel v_r inwards (direction)
(a)B=0 (b) B= 0.02 Tesla (c) B=0.1 Tesla (d) B=0.35Tesla

magnetic field is to straighten out the isotherms more in the vertical direction and suppress the temperature oscillations. For the heating condition under consideration, even at B = 0.9 Tesla, the isotherms are not entirely vertical,as can be seen in Figure 6.14a (iii),and the heat flow is in an inclined direction to the horizontal and vertical temperature gradients that are maintained at the sidewalls. There is uncertainty of the order of $\frac{1}{2}^{o}$ C in the reproduction of the free surface temperature which is ignored in the plot. It is assumed that such variation resulted from the changes in heat loss from the free Hg surface. The velocity v_θ profile measurements across the radial distance with uniform distributions of heater current of 1 and 1.5 amperes at 75 volts and 110 volts respectively are shown in Figures 6.14c and d. The corresponding temperature at the four corners of the meridional cross-section of the channel for the 1.5 amperes heating at B = 0.2 Tesla is shown in Figure 6.14e. The measurement of secondary flow velocity v_r by free floats and thermoelectric potential probes was restricted to being very close to the free surface of Hg down to a depth of 5 mm only. By maintaining the free surface clean, such v_r measurement was independent of this depth variation. The profiles of v_r against radial distance for B = 0, B = 0.02, B = 0.01 and B = 0.35 Tesla and shown in Figure 6.15 for a fixed heating condition, the appropriate corner temperatures have been shown also as insets. v_r at the central zone is two orders of magnitude smaller than the theoretical values calculated with the shallow layer approximation. In the boundary layer v_r measurement with thermo-electric potential probes (used as potential probes for this purpose) shows a fluctuation in magnitude to the extent of 25% of the maximum amplitude, with a characteristic time period of

6 to 12 seconds even at B = 0.35 Tesla, around a distance 5 mm away from the sidewalls.

The variation of v_θ with B for a fixed heating coil (Nichrome/Kanthal) current, giving a larger temperature gradient than that shown in Figure 6.13b, is shown in Figure 6.16 for the fixed radial position of r = 3.75 cm and at a depth of 3.5 cm from the Hg free surface.

Figure 6.17 shows the shape of the mercury surface at M = 64 for the uniformly distributed heater current of 1.5 amperes in each of the heater coil sections. The measurement of the level of Hg surface was made with a level detector fixed on the XY displacement measuring device with the directions of X and Y aligned radially and vertically respectively. The horizontal level was checked on the Hg surface in the absence of heating, cooling and the magnetic field. The error in measurement of height does not exceed 7.5% in the central radial span, though meniscus problem makes such measurements tedious. It may be noted that with good amalgamation Hg does completely wet the copper sidewalls,and the contact angle changes direction with respect to that of unwetted copper. The bathtub like profile of the Hg surface near the inner wall confirms the downwelling of the fluid there, whereas surface tension probably plays a more important role at the outer wall. This surface profile checks with the static pressure measurements at the bottom wall pressure taps by the inclined tube manometer.

A good deal of time was devoted to maintaining uniform temperature at the outer wall to within 1° C by distributing non-uniform current in the four sections of the heater coil, but it was impossible to maintain such uniformity at a once-for-all fixed nonuniform heating current distribution at all values of

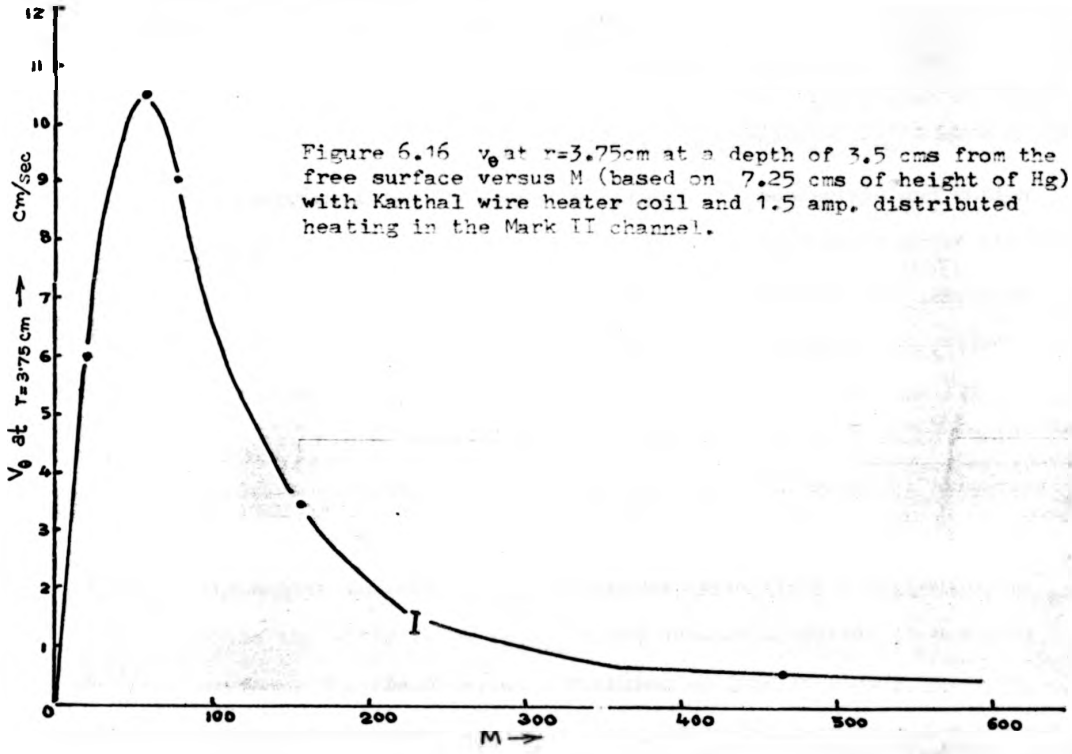

Figure 6.16 v_θ at r=3.75cm at a depth of 3.5 cms from the free surface versus M (based on 7.25 cms of height of Hg) with Kanthal wire heater coil and 1.5 amp. distributed heating in the Mark II channel.

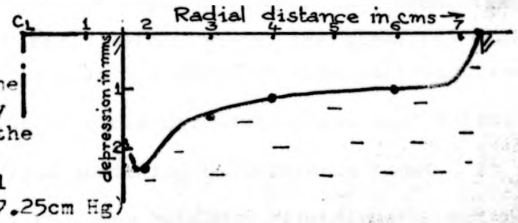

Figure 6.17 The shape of the free surface of Hg shown by the measure of depth from the highest meniscus level at M=64 in the Mark II channel (I_{ht}=1.5 amp, KL 4sections, 7.25cm Hg)

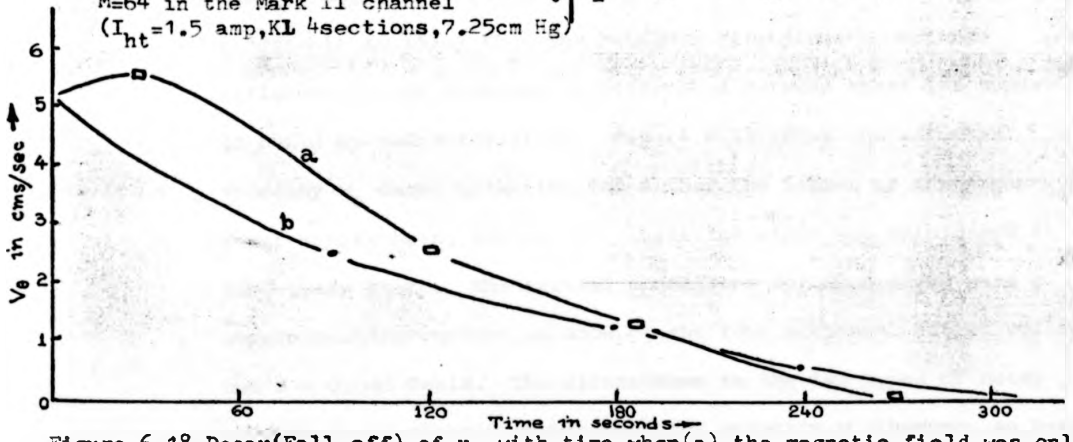

Figure 6.18 Decay(Fall off) of v_θ with time when(a) the magnetic field was only switched off from steady state (b) the heater supply only was switched off in the Mark II channel. Initial steady state B=0.045 Tesla and 1 amp. of distributed heating in the four sections of the Kanthal heater wire.

the magnetic field. The velocity profile for such a case at high values of M ($\sim$ > 150) agrees with the free vortex flow characteristic and the balance between thermoelectric and motion induced e.m.f. can be readily verified. A feedback type of heater coil power supply control system in more than four coil sections would be ideal for maintaining the sidewall temperature uniform at all magnetic field strengths, but in the limited time for experimentation such detailed arrangement was not pursued. Only a restricted effort was made in measuring the transient processes like the building up time for v_θ into its steady state with either the heater current I_{heater} or the magnetic field B switching on, while the other (B or I_{heater}) had been held already in a steady state. The characteristic building up time to steady value of v_θ was of the order of 4-6 minutes counting time from the instant of I_{heater} switching on. In the case when time count was from the instant of magnetic field switching on, the steadying time was only marginally smaller than in the previous case, although invariably the first indication of fluid circulation was much quicker in the case of magnetic field switching on reference count. It seems reasonable to think that the buoyancy effect has a definite influence in the creating of difference between these two types of build up characteristics. Figure 6.18 shows the azimuthal velocity v_θ decay with time for either the heater or the magnet power supply being turned off, while the other was maintained at its steady state. The initial conditions for such plots were 1 ampere heating current in each of the four sectional heater coils and B = 0.045 Tesla. The differences in the two types of decay processes are clearly observable, the velocity v_θ having an overshoot (less than $v_{\theta_{max}}$ corresponding to the optimum magnetic field B $\sim$ 0.02 Tesla) in the case of magnetic field switching off; the effect of even momentary passage through the optimum B value is phenomenal.

6.4.3 Measurements on Mark III channel

As remarked earlier, Professor Shercliff suggested that it should be possible to demonstrate vertical shear layer at the changeover region with a mixed solid-liquid interface electrical conductivity at the bottom wall by maintaining a nonlogarithmic radial temperature profile on the conducting interface zone. The experimental results on the Mark III channel with insulated interface at the bottom horizontal wall from r = 1.59 cm to r = 5.3 and conducting interface from r = 5.3 cm to r = 7.3 cm demonstrate the presence of such a shear layer. Figure 6.19 shows the radial profile velocity v_θ for various magnetic field strengths, and for four different levels of heater current. The heating is generated by the concentrated heating at the outer wall lowermost region spanning 1.75 cm height. The measurements were made with 7.5 cm height of Hg column and at depths of 1, 2, 3, 4 cm from the static equilibrium free surface. The variation in the depths for these four measurements did not produce any significant difference and therefore,at least in the upper half of the mercury column,there was no significant horizontal shearing motion of v_θ. The fluid velocity very close to the outer wall was very difficult to measure, particularly for magnetic field strengths of the order of 0.02 to 0.04 Tesla, as the fluid moved with high velocity next to the wall as though it does not obey the no slip condition. The outermost radial position where measurements could be conducted within 5% (a rather high value because of high rotational speed of 1 rev/sec), reproducibility with the pivoted float was at 7.1 cm. In the plots,v_θ measured at this point is joined to zero value at 7.3 cm to correspond to the no slip condition, and does not represent actual measurement. However, for the 3 ampere heating case, a

Figure 6.19 The radial profile of v_θ for (a) 2 amperes and (b) 4 amperes of heating in the concentrated heater coil near the bottom of the outer periphery, in the Mark III channel for different B values in Tesla.

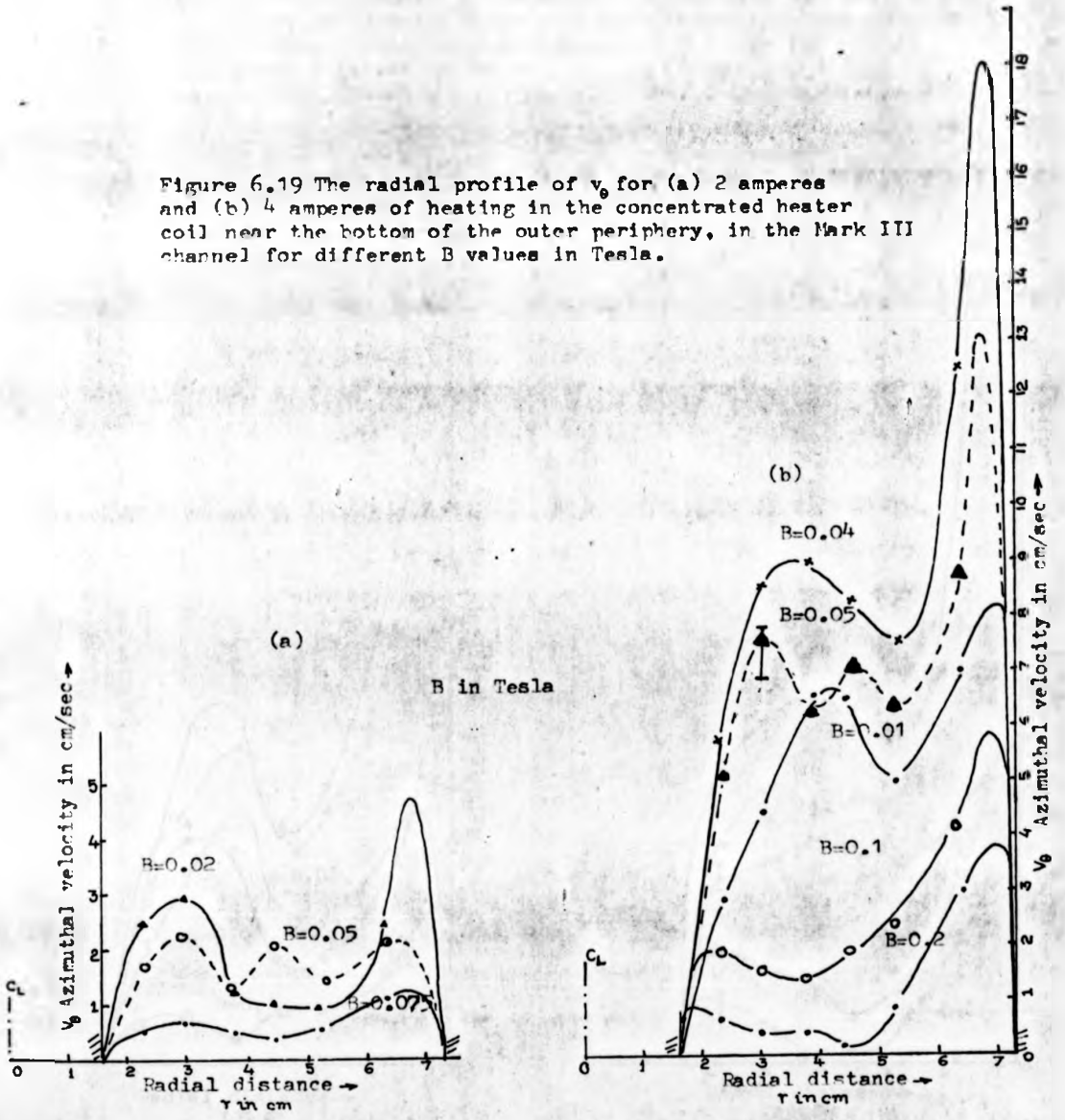

Figure 6.19 (continued) The radial profile of v_θ for (c) 3 amp and (d) 5 amp. of heating current in the concentrated heater coil near the bottom of the outer periphery, in the Mark III channel for different B values in Tesla.

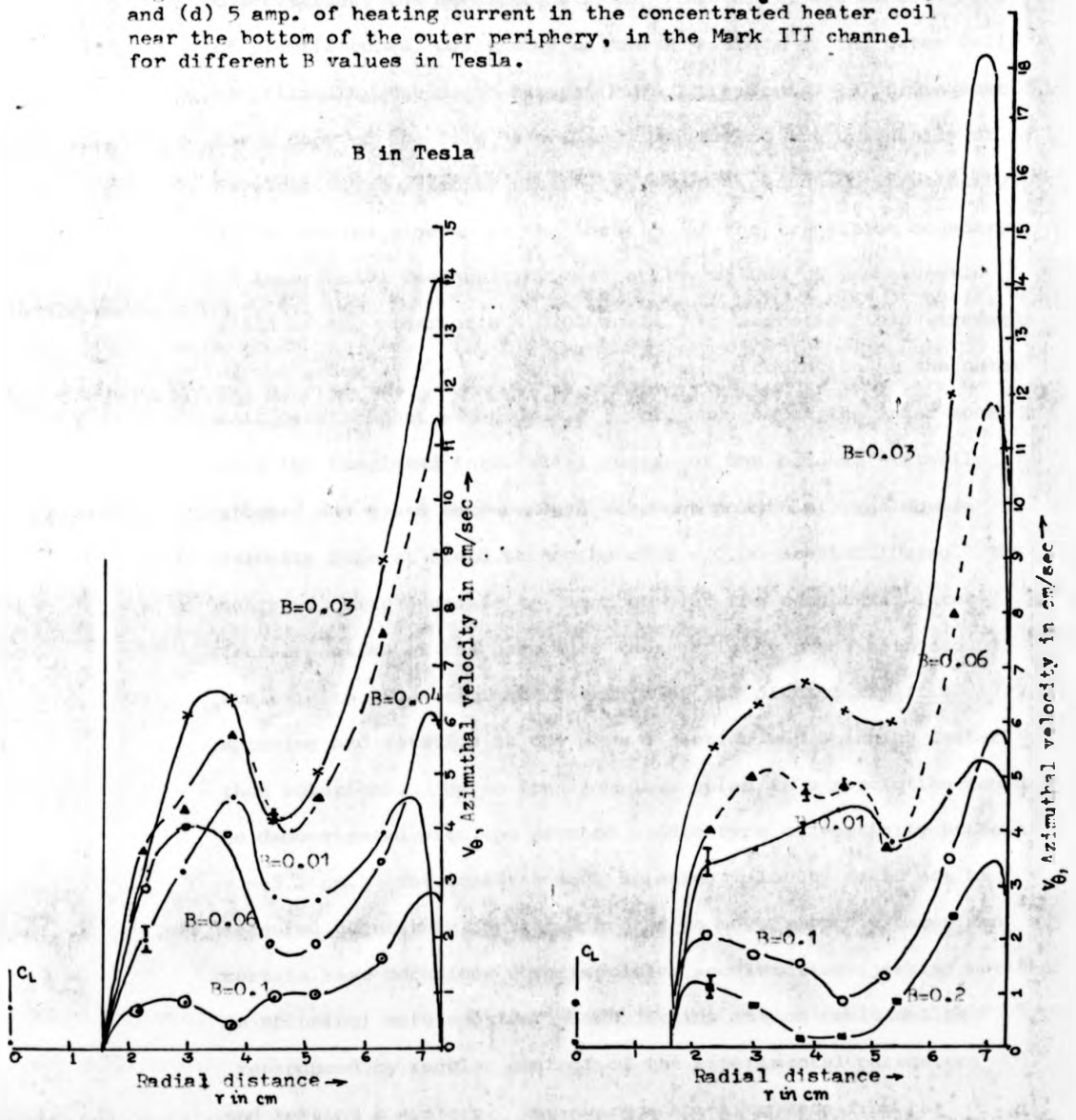

1 mm bit of plastic tube was used as a tracer particle and the corresponding velocity noted,though the tracer particle was touching the outer wall at the time and surely would have produced some drag on it. In order to record such experimental observations, the movement of 2 and 3 mm thick, 4/5 mm long bits of plastic tubes, positioned on the Hg surface at the outer wall, was filmed by the movie camera (P.B. Dutta Gupta, 1978b; request for a copy of the film on loan may be made to the University of Warwick). The velocity profile V_θ shows a reduction in velocity at the radial midspan at the location of the transition boundary of interfacial conducticity,even at low values of the magnetic field of the order of B = 0.02 Tesla. At magnetic field strengths of the order of B = 0.9 Tesla, the fluid circulation at the outer wall persisted at a measurable level, whereas in the inner zone over the insulated interfacial region of the base it virtually stopped and speed measurements were not possible. The double velocity dips at field strengths of B = 0.06 are intriguing. The sharp velocity increase in the zone over the conducting interfacial portion of the base made the vorticity probe spin around its axis in advance of the rotation of the pivoted arm (i.e. spinning and rotation in the same direction and spinning faster than rotation). Up to four complete spins in a revolution could be demonstrated with the pivoted paddle type of vorticity probe at r = 5.2 cm. The instantaneous spinning velocity could not be measured accurately, but it appeared to move smoothly except on certain rare occasions when impulsive acceleration (jerking motion in spinning) were spotted. Such jerking motion could not be reproduced by regular control of the experimental parameters and remains a mystery. The average spinning rate from the observation of the number of complete spins in a given time was

extremely sensitive to changes in temperature and the magnetic field. On the free surface of mercury very feeble vortex rolls could be observed,but they never formed sharp regular streets of vortex rows.

The temperature distributions in the meridional cross-section were measured according to a mesh grid location scheme,with radial intervals of 6.75 mm (starting from the outer wall) and vertical spacing of 1 cm (starting from the bottom wall). Measurement at the inner wall was also made so that two sets of temperature measurement at the inner wall was available with a horizontal spacing of 3 mm at the inner wall. Temperature measurement at the free surface of mercury was also made. The isotherm contours for two different levels of heating at different magnetic field strengths are shown in Figure 6.20. For lower magnetic field strengths, the isotherms are drawn through the mean value of the fluctuating temperature measured at the particular grid point. A characteristic time plot of the temperature fluctuation as measured by the copper-constantan thermocouple junction positioned at r = 1.89 cm at a depth of 3.5 from the static equilibrium free surface of Hg and recorded by the XY plotter is shown in Figure 6.21.

A characteristic sinusoidal temperature oscillation with a period of 20/25 seconds can be observed. Irregular spiky fluctuations that ride over the sinusoidal signal have a faster fluctuation frequency,and it is difficult to imagine such fast fluctuations originating from fluid turbulence. The maximum amplitude of temperature oscillation in Figure 6.21 is 4.5° C (peak to peak) which was also confirmed by direct temperature measurement by the 'Comark' instrument. At higher levels of heating, this amplitude of oscillation increased and oscillations of amplitude as great as 8° C could be demonstrated. Hg is a good

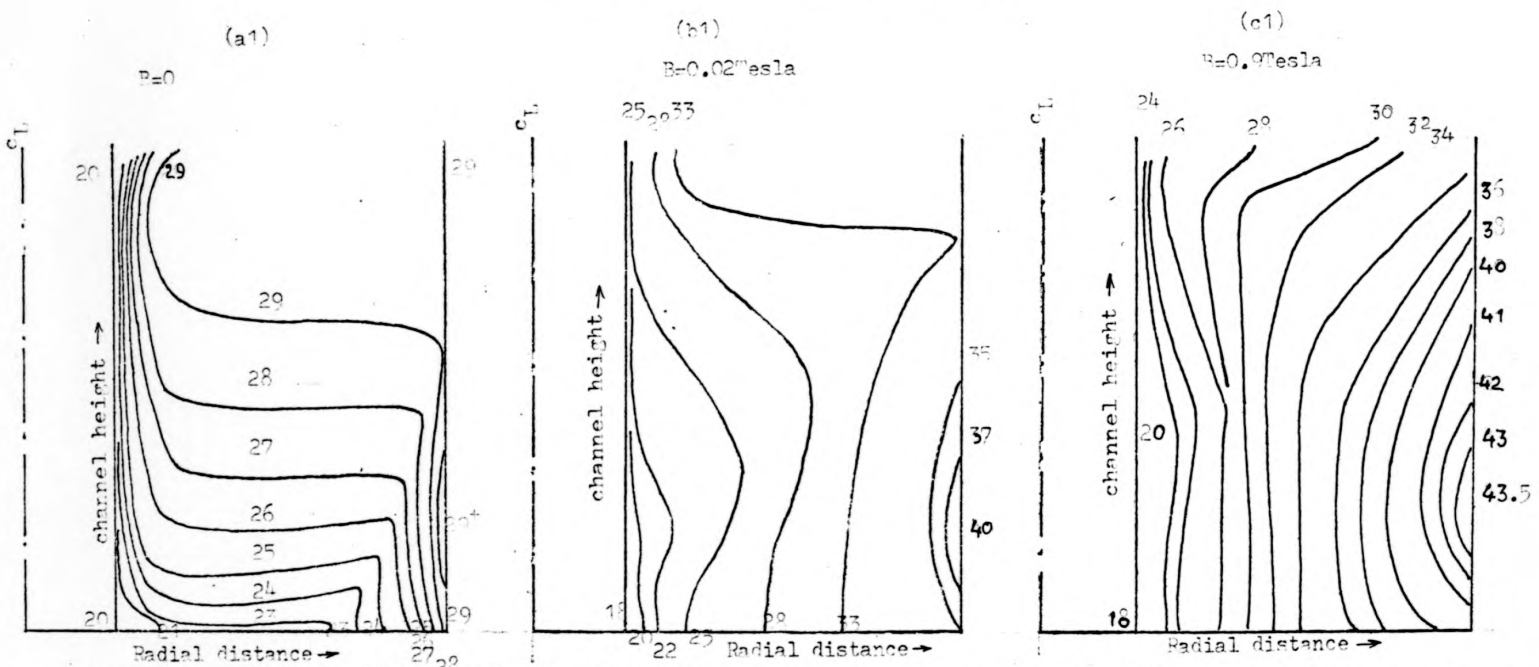

Figure 6.20 Isotherm (in °C) plots in the meridional planes (rectangular cross-sectional) in the Mark III annular channel with concentrated heating at the outer periphery bottom boundary and mixed interfacial conductivity at the bottom wall. Heating current 3 amp. at 72 volts. Cooling water flow rate 15 litres per minute.

(a1) B=0 (b1) B= 0.02 Tesla (c1) B=0.9 Tesla

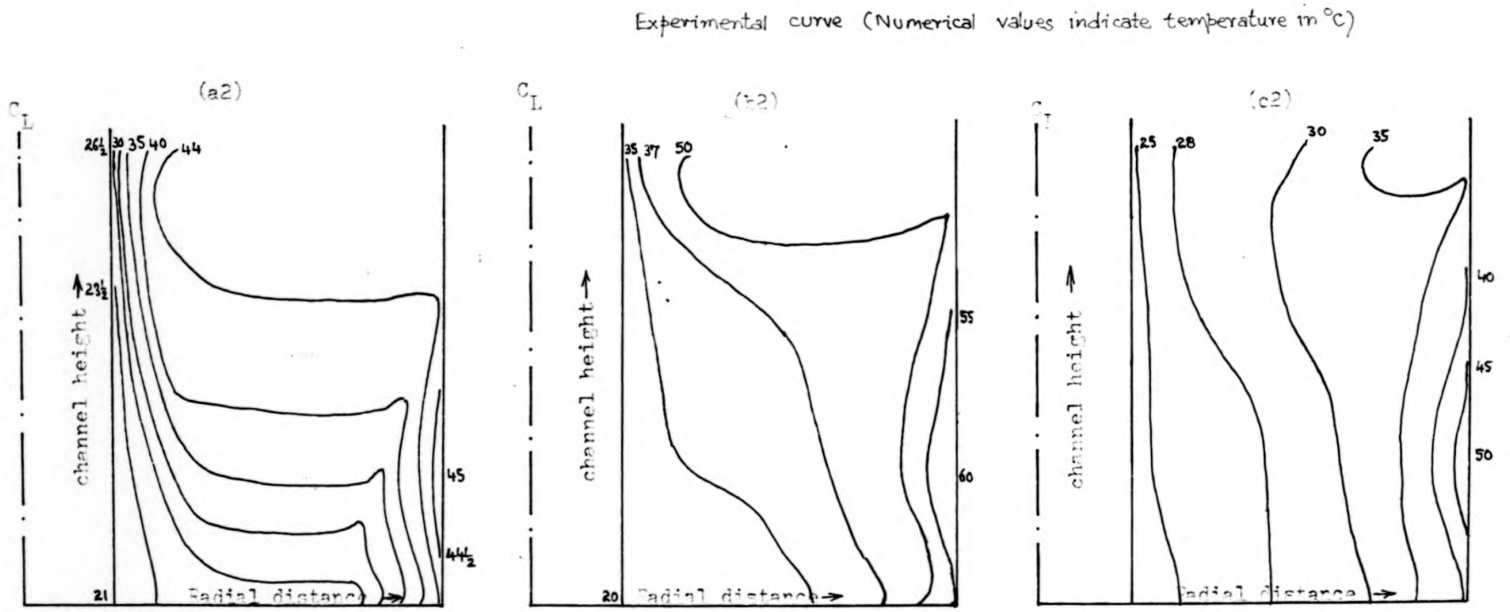

Figure 6.20 (continued) Isotherm plots in the meridional planes (rectangular cross-sectional) in the Mark III annular channel with concentrated heating at the outer periphery bottom boundary and mixed interfacial conductivity at the bottom wall. Heating current 5 amperes (a2) B=0 (b2) B=0.02 Tesla (c2) B=0.2 Tesla. Temperatures in °C

Mark III annular channel with partly conducting(O) and partly insulating (i) interface at the base wall .(Concentrated heating with 3 amperes flowing in the heater coil at channel bottom outer rim.)

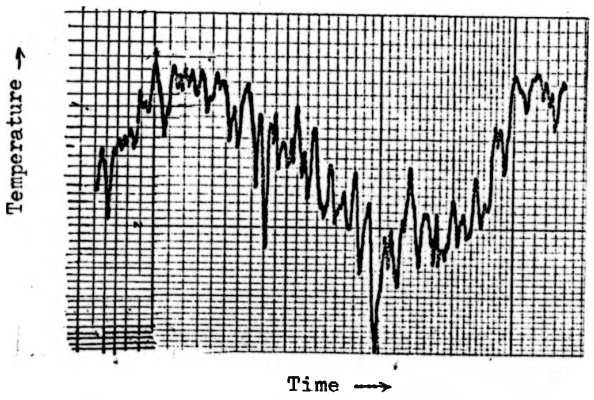

Figure 6.21 Record of temperature oscillation by the Hewlett-Packard XY plotter . Position of the copper-constantan thermocouple probe tip inside Hg at r= 1.89 cm and at a depth of 3.5 cms from the free surface of Hg. The trace moves with time from left to right . Horizontal time scale 8sec / cm and the vertical scale corresponds to 60 μV / cm which is approximately equivalent to 1.5 $^{\circ}$C / cm.

thermal conductor, yet the presence of such large amplitude temperature oscillations are indeed a measure of the influence of buoyancy.With the increase of magnetic field strength beyond 0.02 Tesla temperature oscillations were greatly suppressed.

For academic interest, it may be noted that the insulated coating on the copper base lasted properly for a period of six months only, after which it was observed that at the outer edges the layer of coating slowly started separating from the copper surface. Hg crept in and amalgamated the copper surface separated from the insulation coating. It was very interesting to note the symmetry in the separation process about the vertical axis. The experimental results presented in this subsection were therefore considered from the investigation during the period when the insulated coating was sticking securely to the copper base.

6.4.4 Experimental results on Mark IV channel

The shallow Mark IV channel with its totally conducting solid-liquid interface at the bottom wall permitted easy visual observation of the free mercury surface as well as detailed temperature distribution measurement at closer space intervals. The heater coil was comprised of two identical sections of 20 turn KANTHAL wire in single layer. The radial profiles of v_θ measured with tracer particles on the free surface and the paddle type floats at a depth of up to 1.5 cm from the free surface of Hg for heater currents of 1, 1.5, 2,25 and 3 amperes are shown in Figure 6.22 for various steady values of the magnetic field with heights of mercury column 3.0, 3.3 and 3.5 cm. At B = 0.005 Tesla, the velocity profile corresponds to the free vortex pattern, but at intermediate values of magnetic field around which $v_{\theta_{max}}$ w.r.t B occurs, v_θ profile shows a peculiar rigid body line motion. At

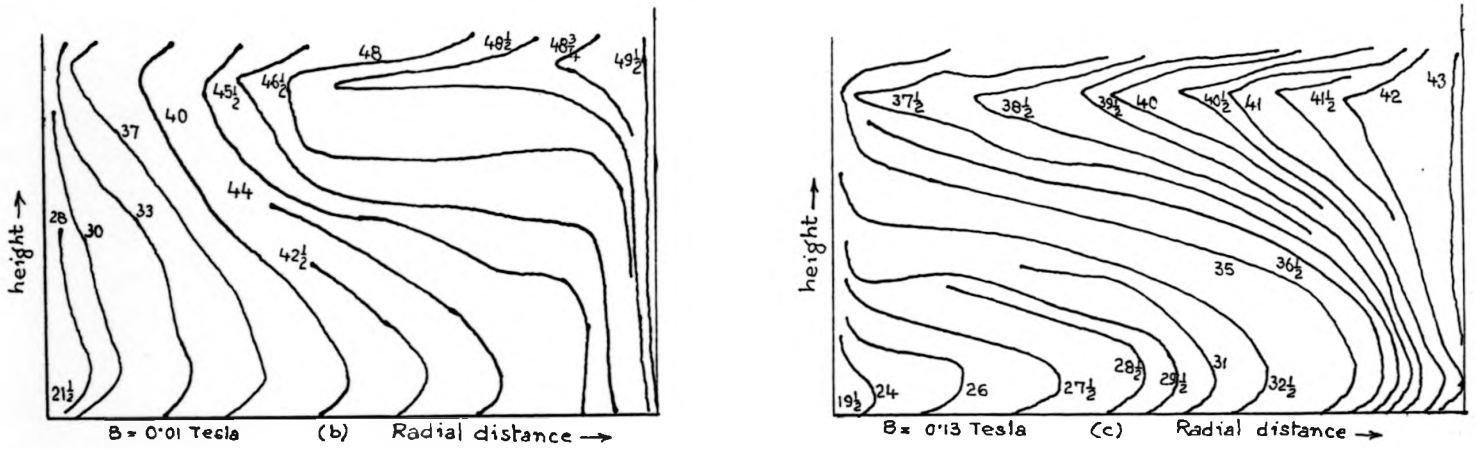

Figure 6.23 Detailed isotherm plots, in the meridional planes of the Mark IV annular channel with uniformly distributed heating at the outer periphery for 3.1 amperes heating current and (a) B = 0 (b) B = 0.01 Tesla (c) B = 0.13 Tesla (d) B = 0.45 Tesla (scale : Double Full Sc.)

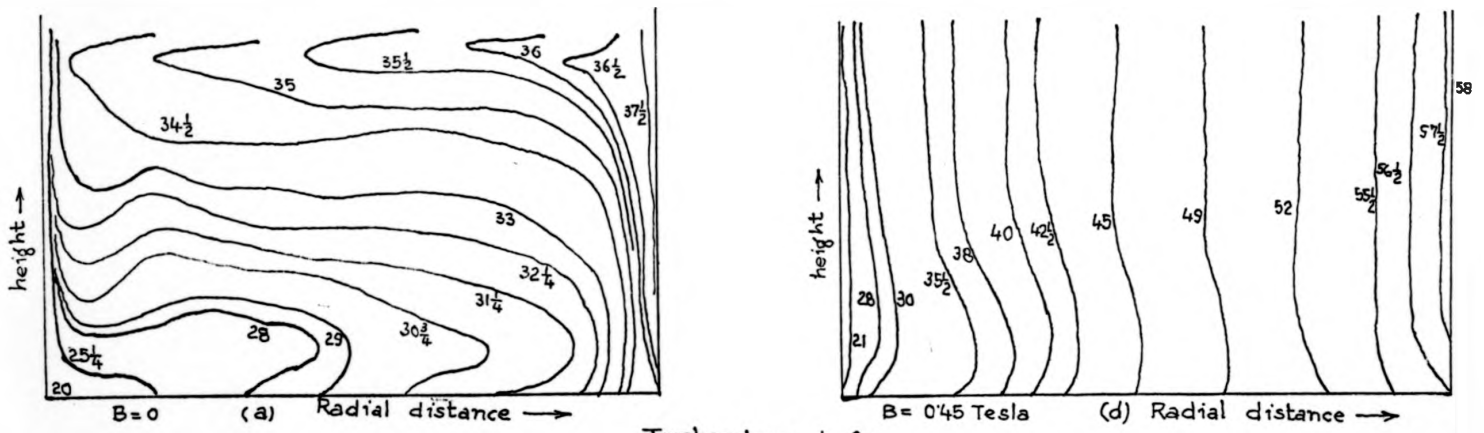

Temperatures in °C

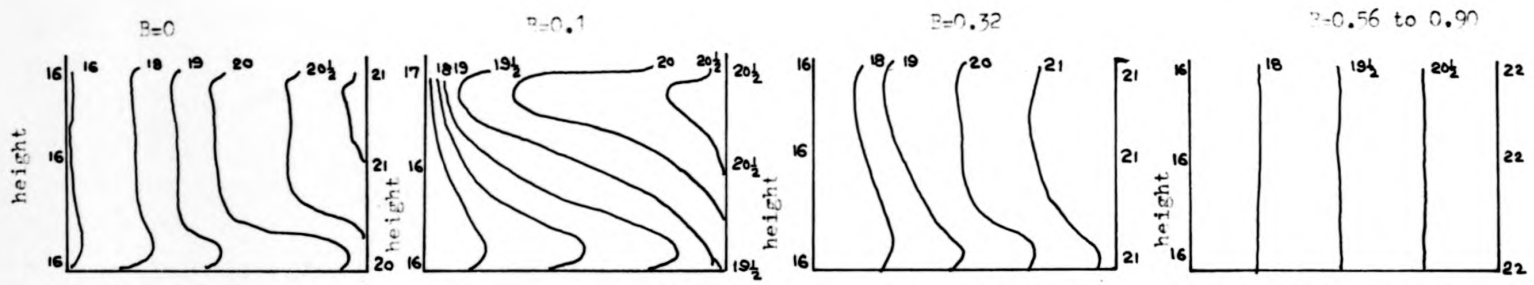

Figure 6.24a Isotherm plots in the meridional plane of the Mark IV channel for 1 amp. distributed heating current. T in °C , Full scale diagram, B in Tesla

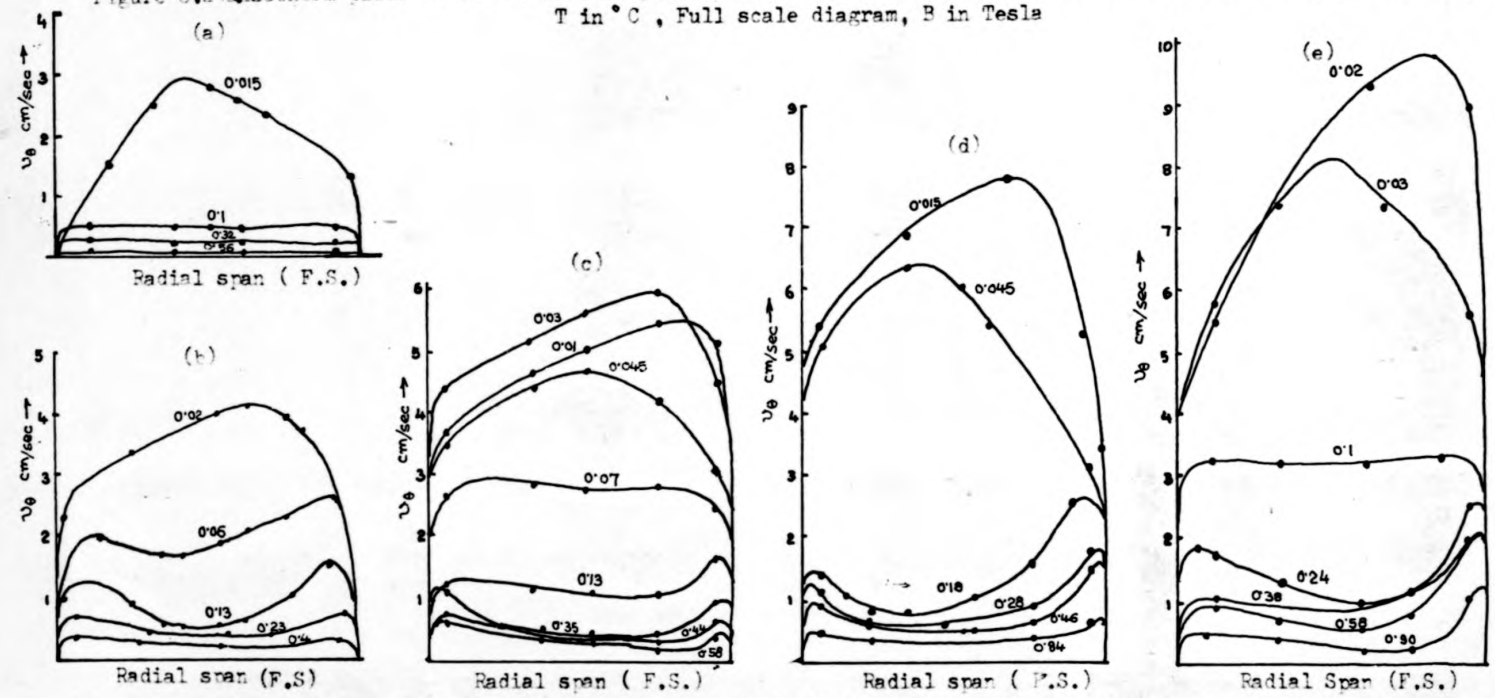

Figure 6.22 The radial profiles of v measured in the Mark IV annular channel at uniformly distributed heating current of (a) 1 amp. (b) 1.5 amp. (c) 2 amp. (d) 2.5 amp (e) 3 amp. The magnetic flux density in Tesla is marked along the curves.

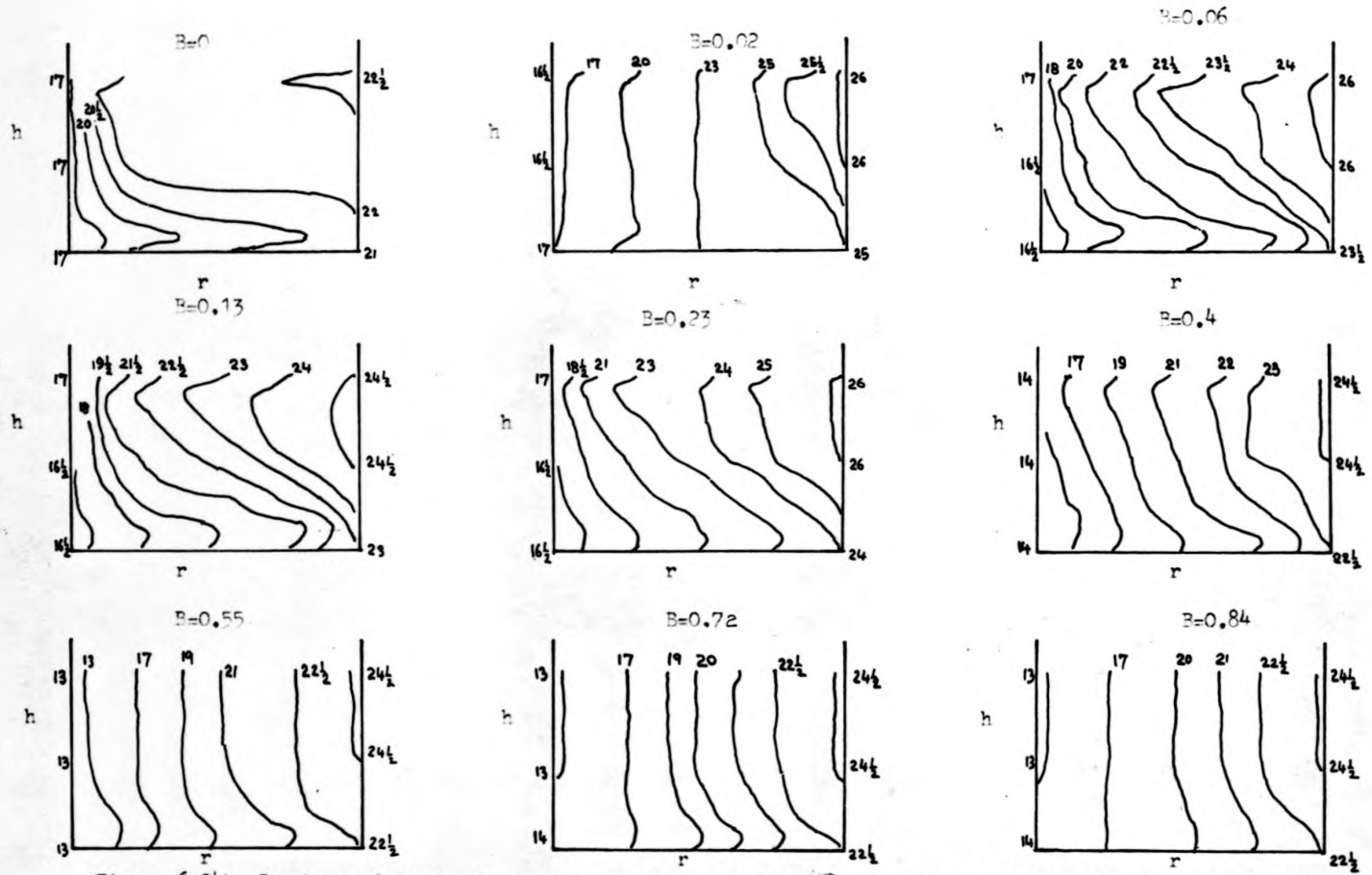

Figure 6.24b. Isotherm plots in the meridional plane of the Mark IV channel for 1.5 amp uniformly distributed heating current. T in °C, Full scale diagram , B in Tesla (r - Radial span, h- Height.)

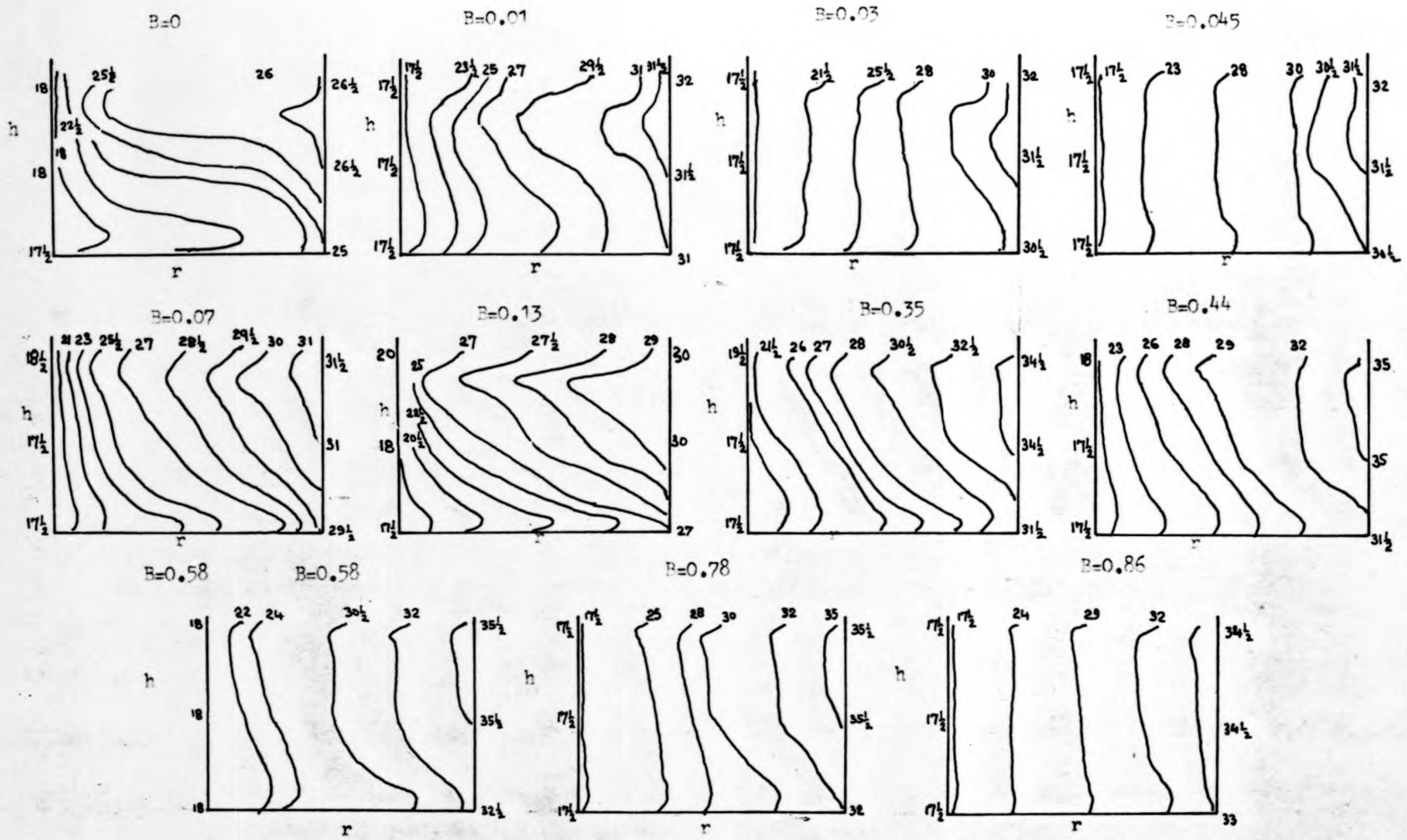

Figure 6.24c. Isotherm plots in the meridional plane of the Mark IV channel for 2 amp uniformly distributed heating current. T in °C, Full scale diagram , B in Tesla . (r - Radial span , h - height .)

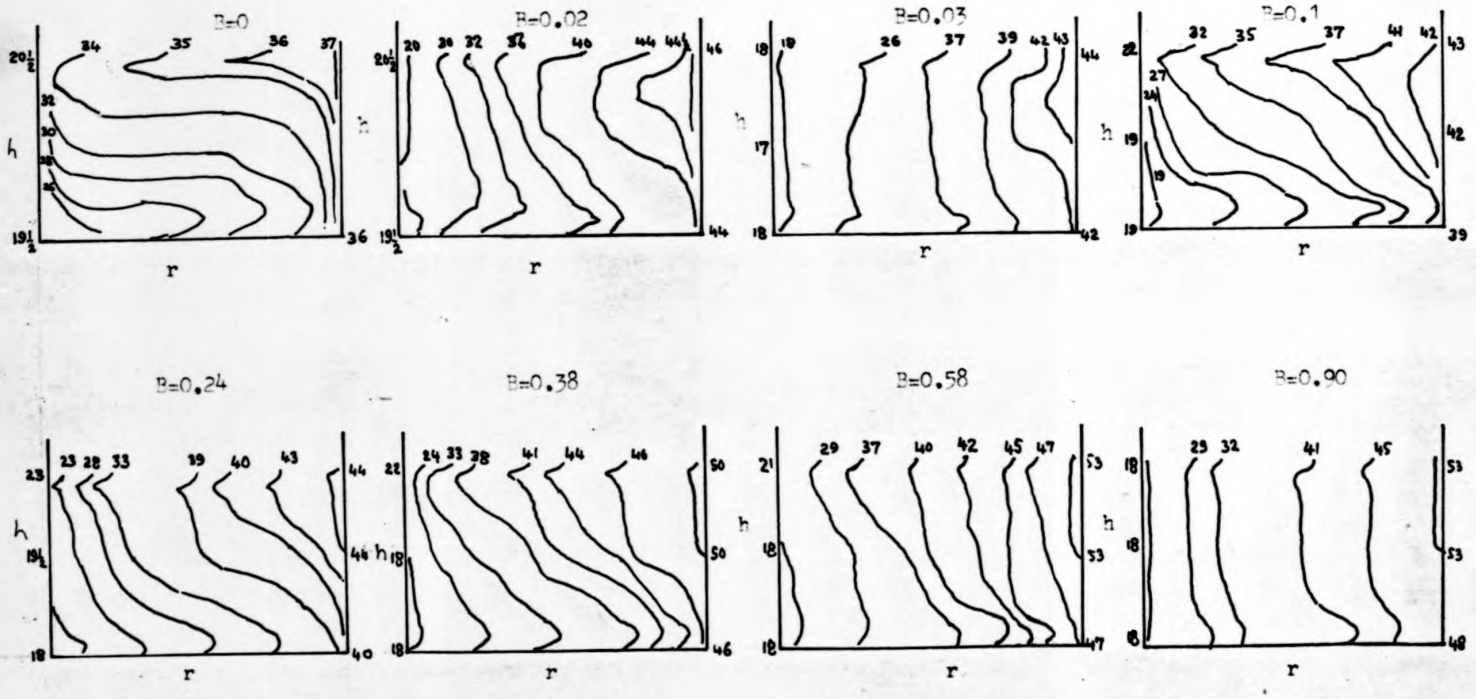

Figure 6.24d. Isotherm plots in the meridional plane of the Mark IV channel for 3 amp uniformly distributed heating current. T in °C, Full scale diagram , B in Tesla . (r- Radial span , h - Height .)

higher magnetic fields of 0.1 Tesla and above, the velocity profile changes over to a characteristic M profile with higher velocities at either sidewall. Considering the attempt to control the vertical temperature uniformity at the outer wall by altering I_{ht} in the upper section of the heater coil, the M shape profile could not be entirely due to the vertical temperature gradient aligned with the magnetic field.

The detailed investigation of the temperature distribution in the interior of the bulk of Hg was made at 6.25 cm radial intervals only, but in the vertical direction the measuring locations were at 0.125, 0.3, 0.5, 1, 1.5, 2, 2.5, 2.7, 2.8 and 3.0 cm away from the horizontal base wall. The isotherm profiles are shown in Figure 6.23 for heating at 3.1 amperes at different field strengths. Temperature fluctuations were observed at lower field strengths, and these could be suppressed by increasing the magnetic field. The isotherms at lower magnetic field strengths are drawn through the mean of the fluctuating temperature at the grid point of measurement and interpolating T in between grid points. The detailed close measurement above the conducting base revealed an adverse temperature gradient to exist in certain regions in a characteristic thickness layer of 0.3 to 0.5 cm up to $B \lesssim 0.1$ Tesla. This specific layer at only certain regions over the copper base is an indication of the difference in temperature levels at the bottom boundary in the fluid (buoyancy dominated at lower field strengths) and in the copper base (heat transfer mechanism by conduction; radiation ignored). The way in which TEMHD rotation and the magnetic field inhibit the buoyancy effect can be clearly observed from the isotherm plots. At $B \lesssim 0$, the buoyancy effect dominates, creating thermal stratification (horizontal isotherms) in the

core and vorticity in the sidewall boundary layers. At the optimum magnetic field, B $\simeq$ 0.04 Tesla, v_θ is maximum, and though B is not sufficiently strong to straighten the isotherms in the vertical direction, the high rotational speed does so (Taylor-Proudman effect). As the magnetic field is slightly increased from this optimum value, there is a sharp drop in the TEMHD rotation and the isotherms can be observed to conform back to the buoyancy-dominated pattern, though somewhat differently to that at B = 0. Further increase in the magnetic field steadily inhibits buoyancy-driven vorticity and the isotherms straighten out in the vertical direction. The complete set of isotherm plots for the various heating current operations corresponding to the radial profile plots of v_θ in Figure 6.21 are shown in Figure 6.24 in groups of identical heating conditions at different magnetic field strengths.

In order to obtain a clearer picture of the radial profile of temperature at the solid-liquid interface of the bottom wall, the experimental temperature plots are shown in Figure 6.25. Straight lines are superposed to emphasize the departure from linearity and one logarithmic curve is included to provide comparison with such a type of variation. In the central region, a straight line law is valid at zero and high values of the magnetic field B, whereas in the sidewall boundary layer the temperature variation is nonlinear. A very steep parabolic rise in temperature near the outer wall conforms to the experimentally measured increased v_θ in this region.

The temperature oscillations at some specified points on the mercury surface and in the interior of Hg column are shown in Figure 6.26 as recorded by the Hewlett Packard XY plotter with temperature sensing by the copper-constantan thermocouple at

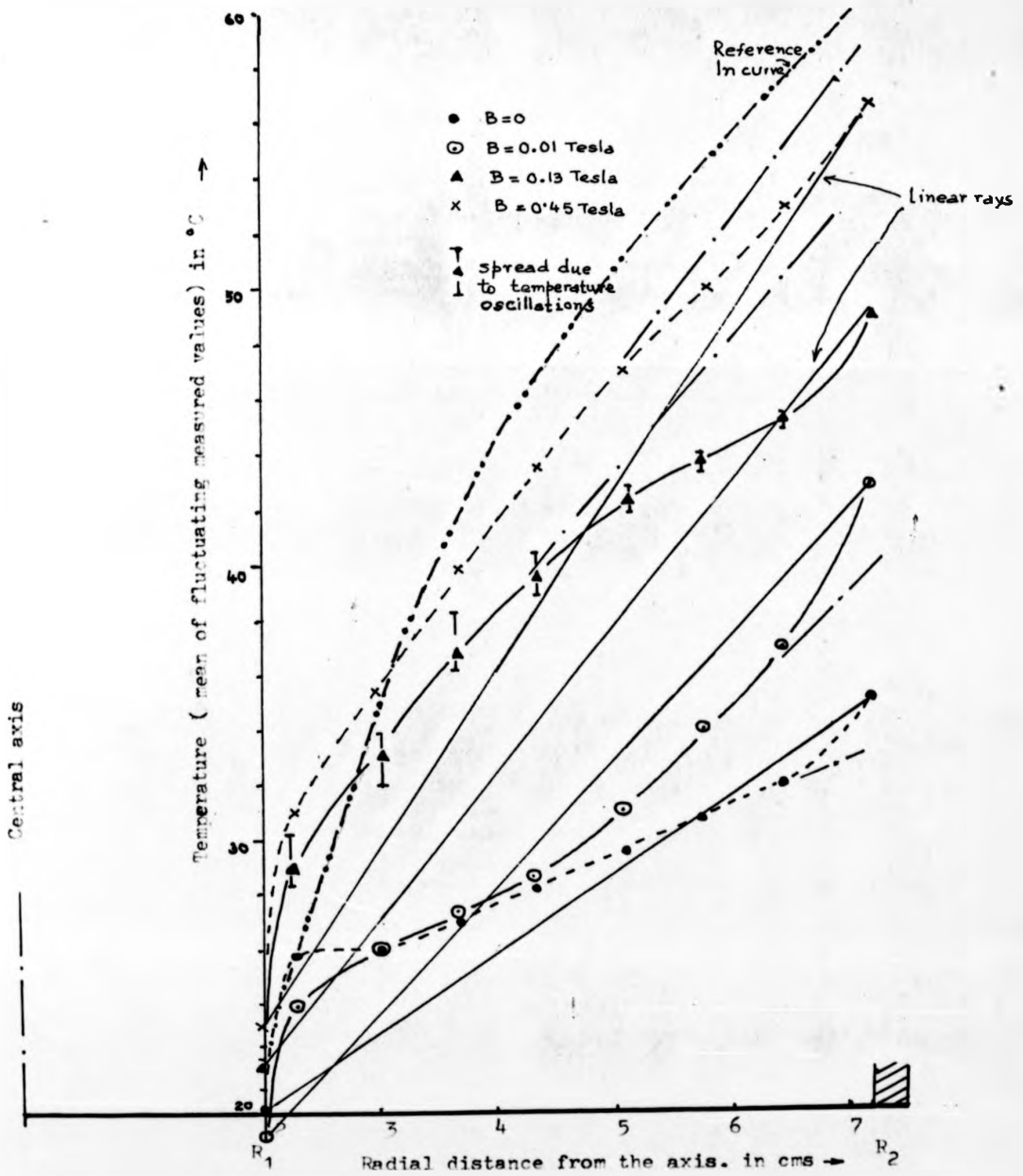

Figure 6.25 Temperature (in°C) profile along the radial span at the base ofthe Mark IV annular channel for 3.2 amperes of heater current (uniform vertical distribution) and at magnetic flux densities of 0.0.01,0.13 and 0.45 Tesla.

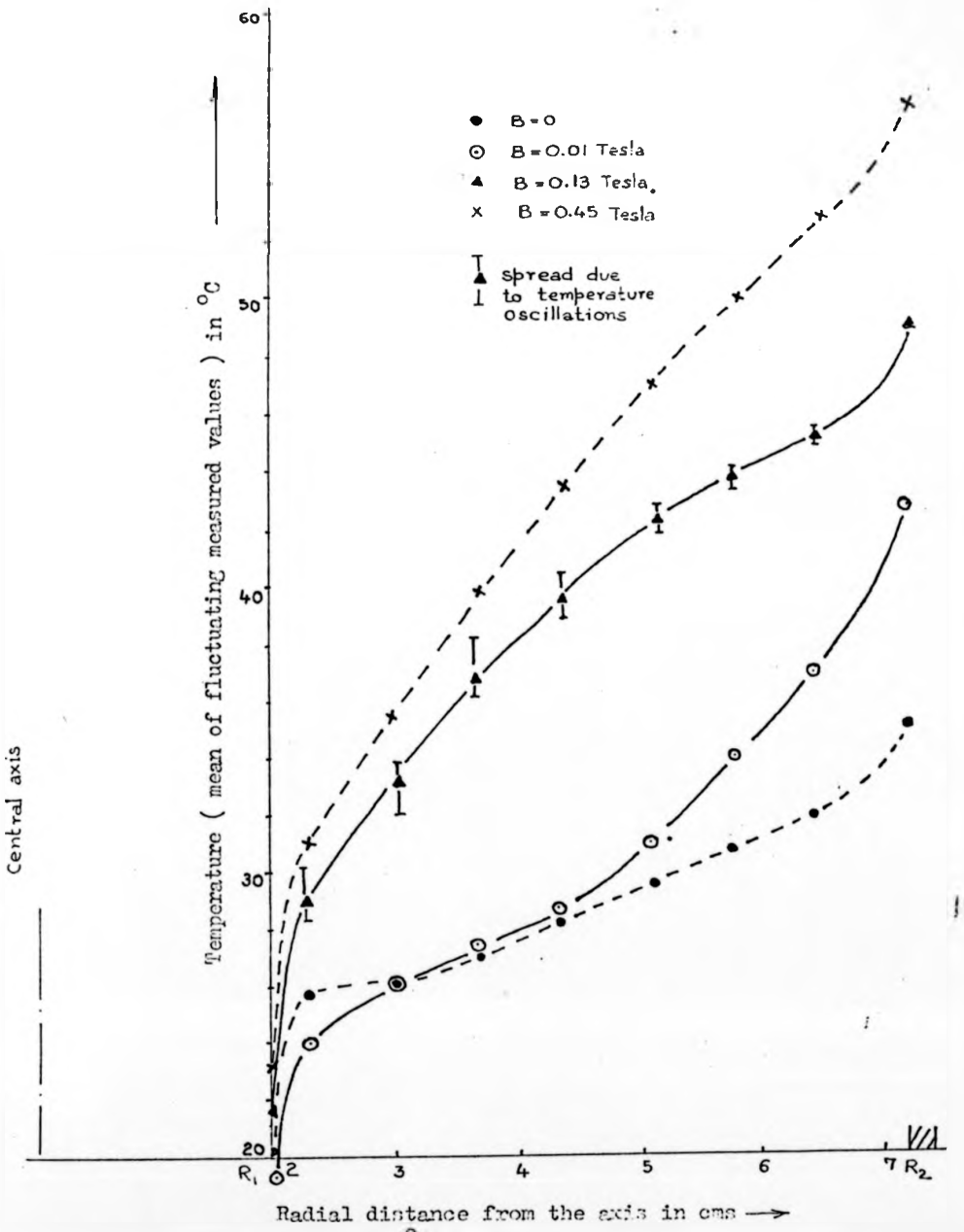

Figure 6.25 Temperature(in ^{0}C) profile along the radial span at the base of the MarkIV annular channel for 3.2 amperes of heater current (uniform vertical distribution) and at magnetic flux densities of 0 ,0.01,0.13and 0.45 Tesla.

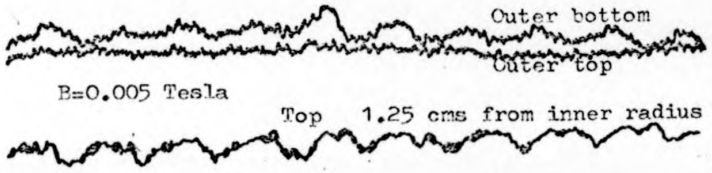

(a)

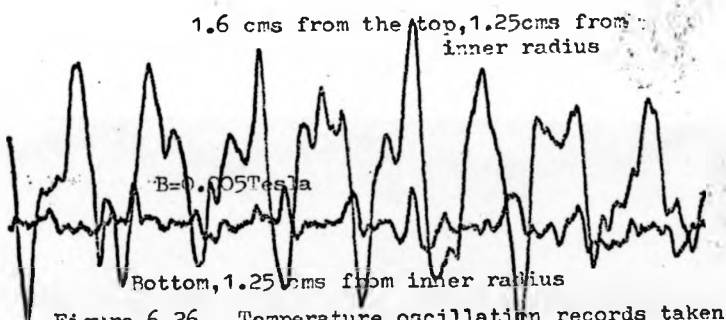

Figure 6.26 Temperature oscillation records taken with the Hewlett-Packard XY plotter in the Mark IV annular channel I_{ht}=3 amp at 150 volts. The trace proceeds with time from left to right at the speed of 4cc/cm. Amplitude scale 40μV/cm ≃1°C/cm

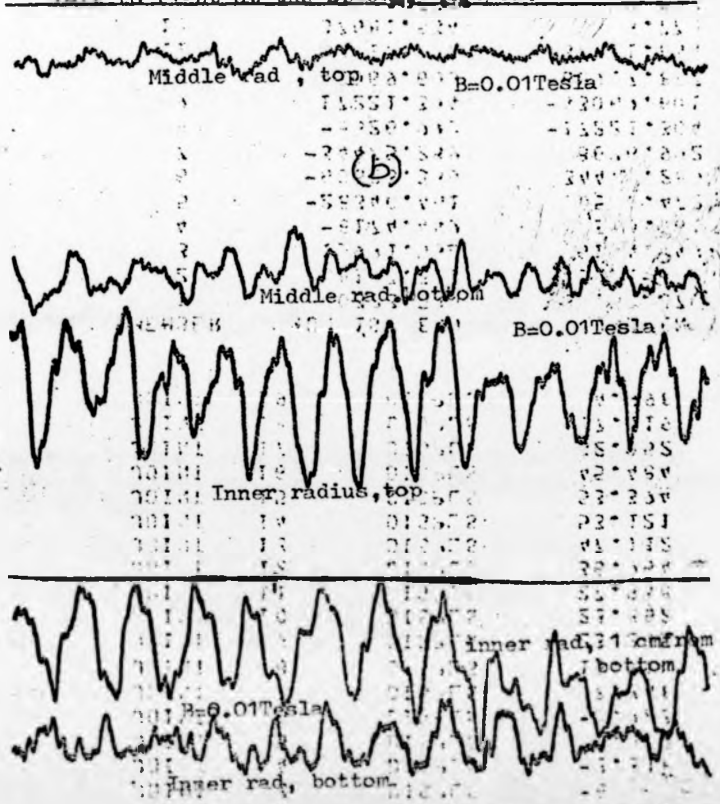

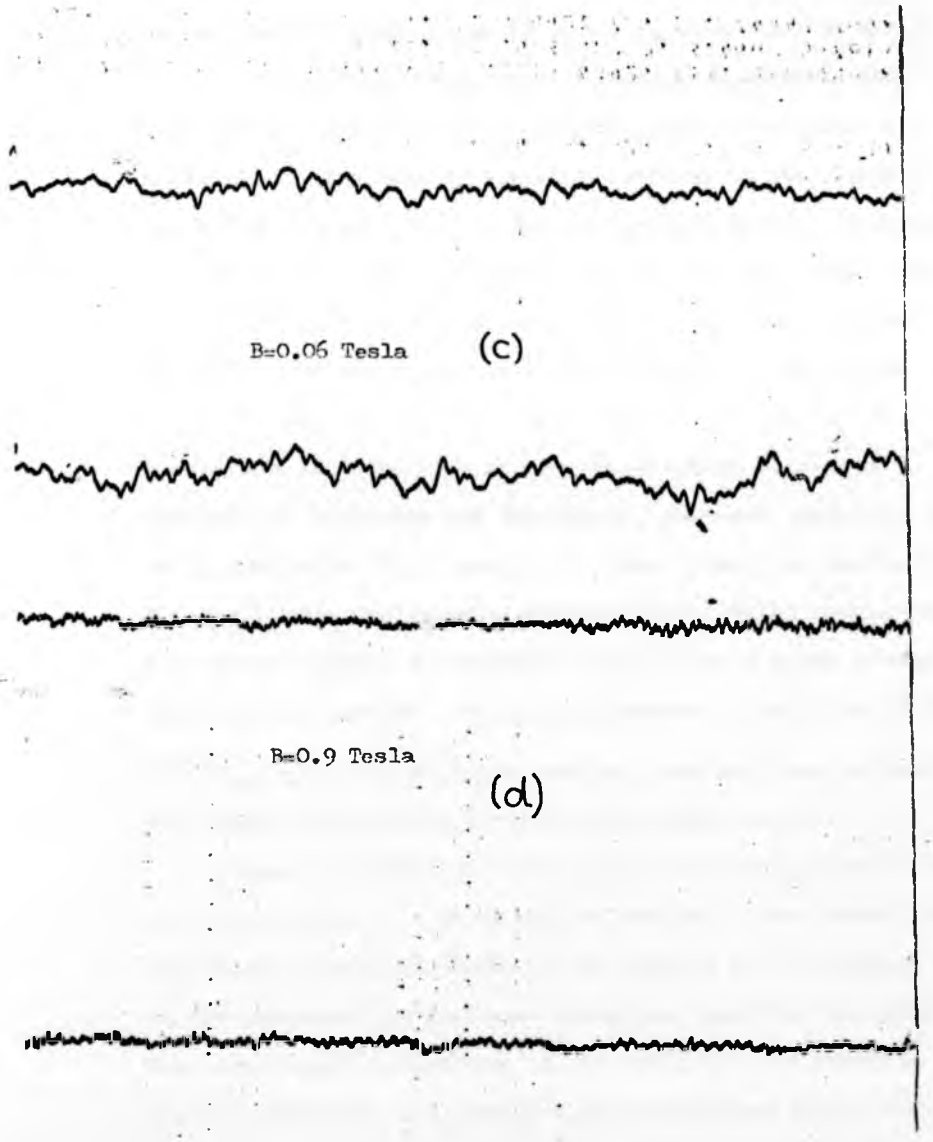

Figure 6.26 (continued) Typical records of temperaure oscillations in Hg. in the Mark IV annular channel at B=0.06 Tesla and B = o.9 Tesla For legends refer to Figure 6.26 (a)

B = 0.005 and B = 0.01 Tesla. Figure 6.27 shows the variation of the radial average value of v_θ = V, v_θ at r = 2.3 cm and v_θ at r = 4.45 cm with respect to the Hartmann number for the five different heating levels corresponding to the data of Figure 6.22. The mean v_θ variation conforms to the theoretically predicted, composite linear and inverse proportional variation, with a change-over region at M = 10 to 20 which is much closer to the theoretical value of M $\underset{\sim}{\sim}$ 2 for infinitely long (narrow) channels than those obtained at M = 160 and M = 300 for the straight TEMHD channels in Chapters 4 and 5, where the pressure gradient in the direction of flow could not be eliminated entirely nor accounted for accurately. However, there is a very subtle indication that there is a second transition region at M $\sim$ 50/100 when the buoyancy effects get inhibited completely. A plot of V against a logarithmic scale of M is shown in Figure 6.28 for this purpose. The slight increase in the value of M for $v_{\theta_{max}}$ w.r.t M with higher heating level may be attributed to the change in the fluid to wall conductivity ratio C.

Figure 6.29 shows the variation of the radial average value of v_θ and v_θ at r = 4.45 cm against mean ΔT_r; the cooling water temperature variation, being of the order of $\pm 1^{o}$ C between sets of data collected on different dates, may therefore be ignored. The variations of temperature at the outer wall for identical heating conditions are indicated by chain-dotted lines so that the effect of magnetic field on the outer wall temperature for a fixed heating level can be seen very clearly compared to the isolated temperature distribution plots in Figure 6.24. From the V data of Figure 6.29 and the corresponding cooling water temperature, the thermopower values are calculated with the help

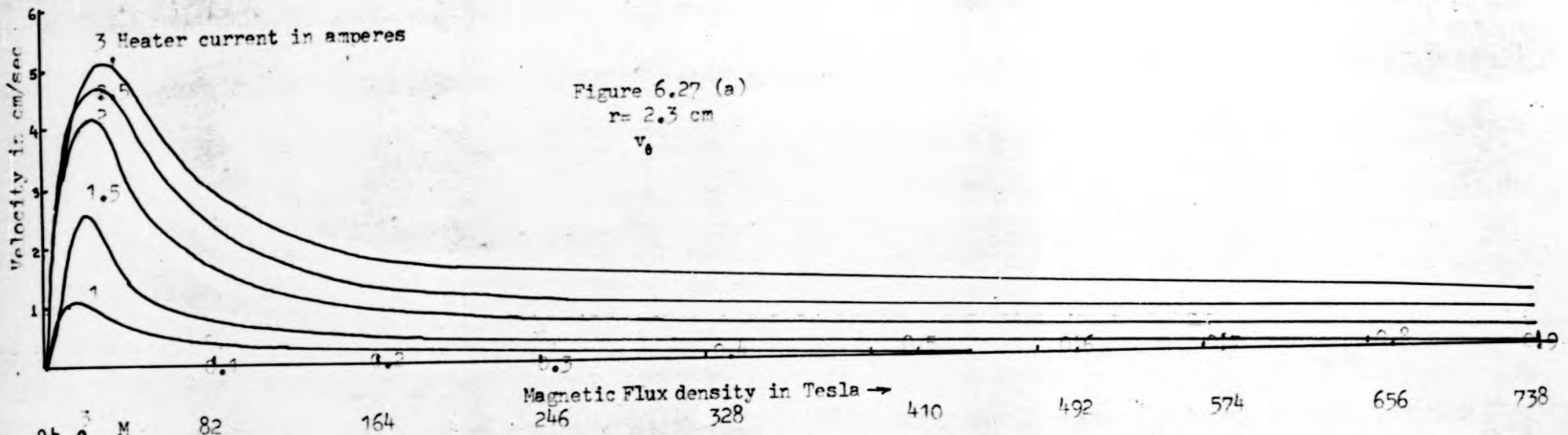

Figure 6.27 (a)
r= 2.3 cm
V_θ

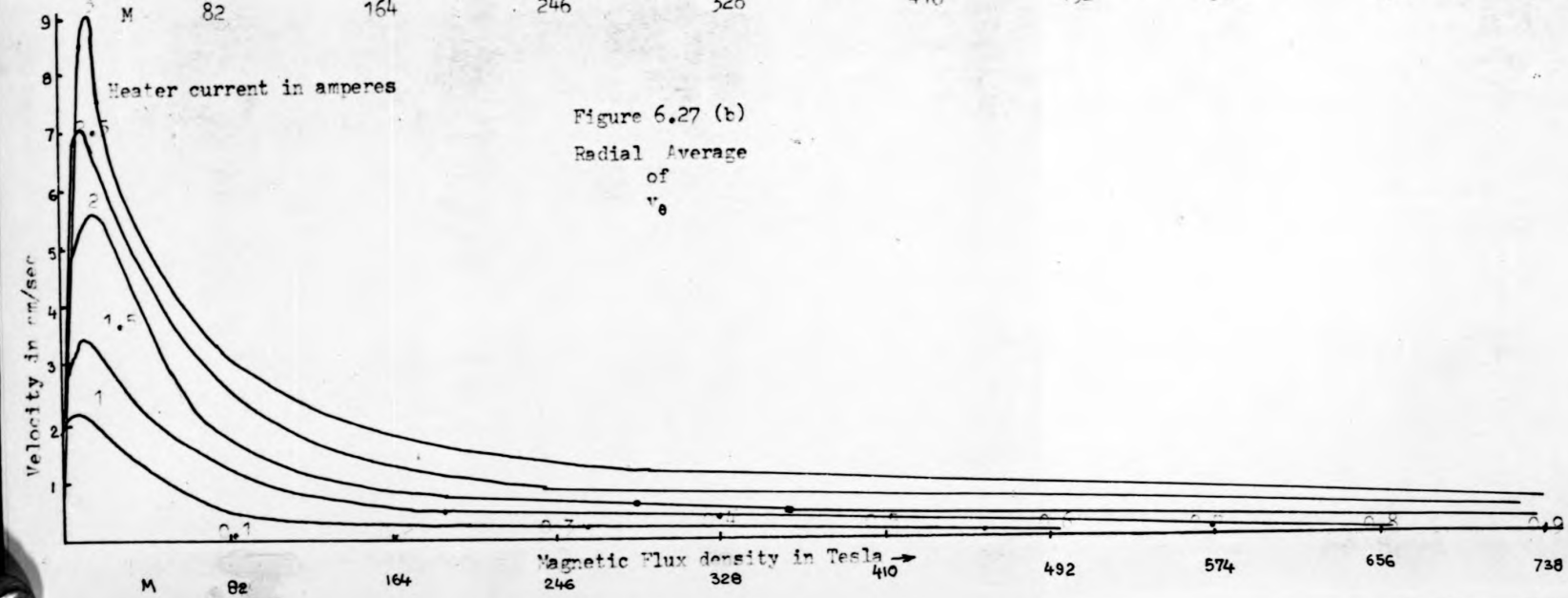

Figure 6.27 (b)
Radial Average
of
V_θ

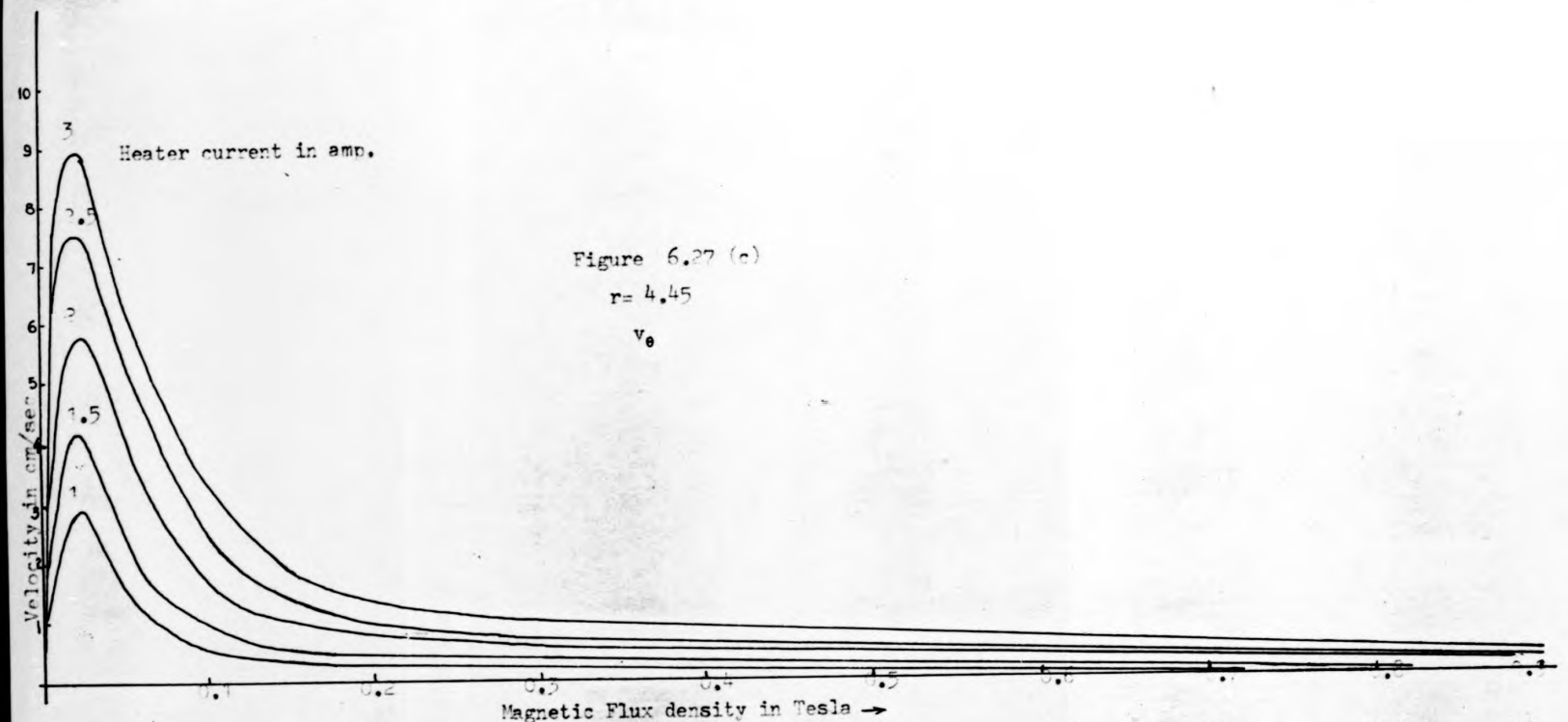

Figure 6.27 (c)

r= 4.45

v_θ

Figure 6.27 (a , b , c) Velocity plots against magnetic flux density B / Hartmann number (based on 3.15 cm- mean height) for the Mark IV annular channel at various values of steady heater current .

(a) v_θ measured at r=2.3cm (b) V, radial average of v_θ (c) v_θ measured at r= 4.45 cm

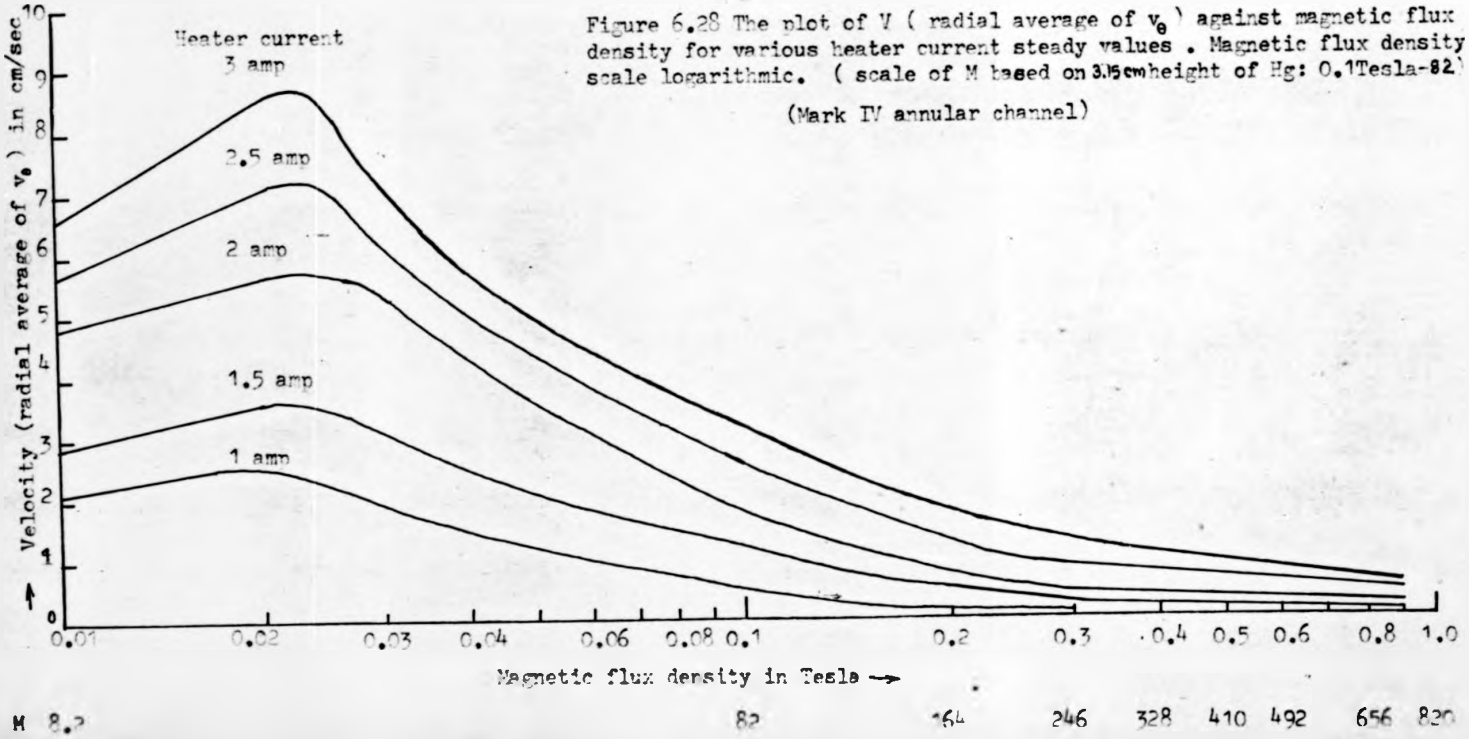

Figure 6.28 The plot of V (radial average of v_θ) against magnetic flux density for various heater current steady values . Magnetic flux density scale logarithmic. (scale of M based on 3.15 cm height of Hg: 0.1 Tesla-82)

(Mark IV annular channel)

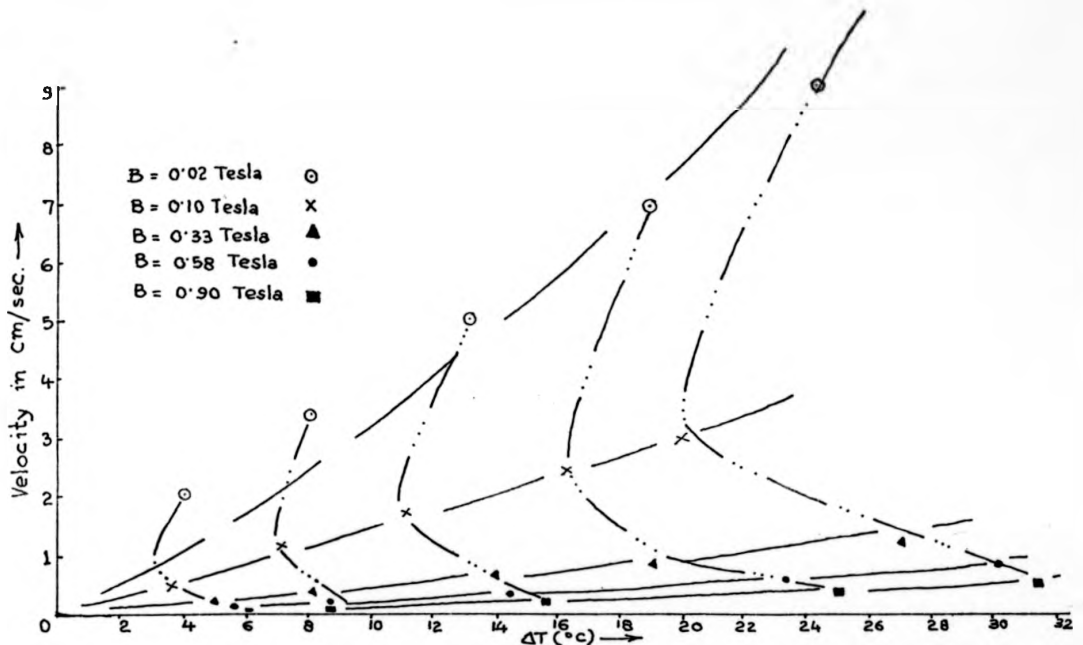

Figure 6.29 (a) The plot of the radial average value of v_θ against Temperature difference in the Mark IV annular channel . (Cooling water at 18°C).

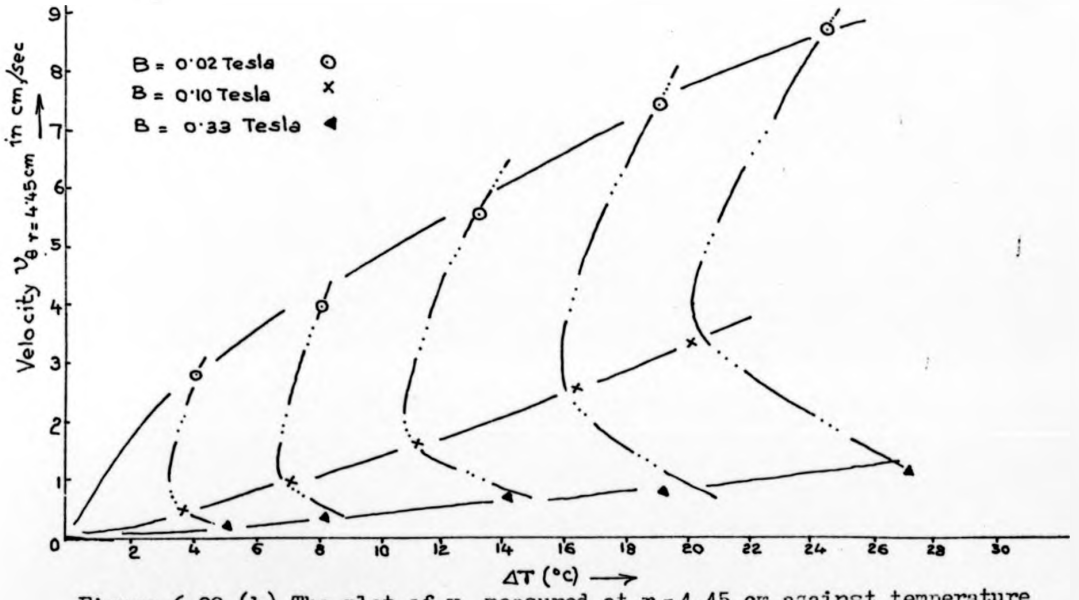

Figure 6.29 (b) The plot of v_θ measured at r = 4.45 cm against temperature difference in the Mark IV channel. (Cooling water at 18°C).

of the thermoelectric and motion-induced e.m.f. balance equation and plotted against the mean temperature in Figure 6.30 against the background of Marwaha's (1967) line of α_{Cu-Hg}.

The measurement of V_r proved very difficult and sometimes very confusing in the presence of magnetic field, as even reversal of the direction of V_r was observed occasionally. At B = 0.005 Tesla, the measured radial profile of V_r is shown in Figure 6.31. At higher magnetic field strengths, not only the magnitude of V_r decreased, but in short radial ranges fluctuations or even flow in the reverse direction (radially outwards) was also observed. These indicate the possible existence of shear between multiple rolls. The vorticity probe indeed exhibited up to 8 complete spins in a revolution around the channel in the azimuthal direction. These vorticity and wavelike motion at the Hg surface as well as in the bulk of Hg have a striking resemblance to the typical lower symmetric-wave-turbulent regimes of the differentially heated rotating annulus problem, where the Coriolis force has a dominating influence. This aspect of the investigation requires further detailed study and is not included in this thesis.

The concept of the second transition zone at B_{cr_2}, apart from that of B_{cr_1}, when V_θ maximum occurs, was very consistently revealed by measuring the total potential drop by the Pye potentiometer across the total radial span of the rotating column of Hg (the tips of the potential probe electrodes being maintained at the same horizontal level) in the magnetic field as a function of M. Each of the copper, constantan and the mercury electrode potential probes (if they may be called so with such a big separation in between electrodes, unsuitable for local measurements) showed exactly the same pattern of a hump and a dip

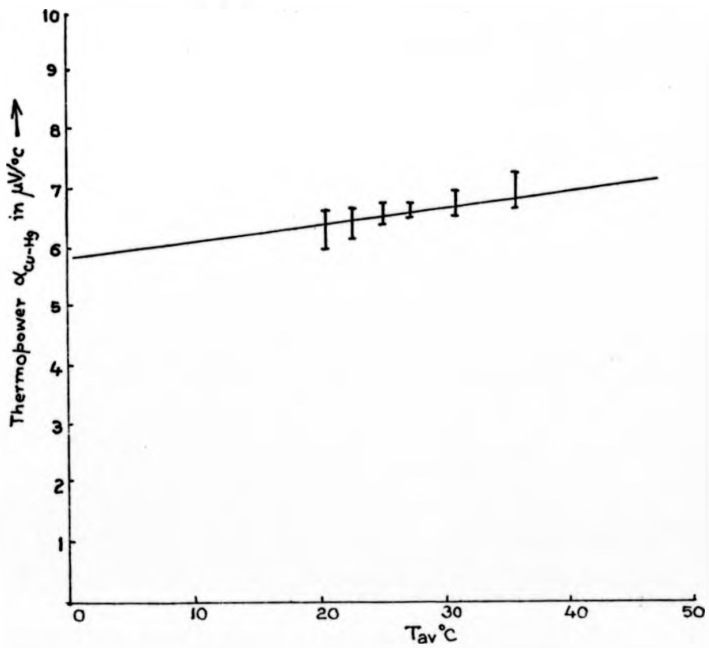

Figure 6.30 Plot of the thermopower α_{Cu-Hg} values calculated from the velocity measurement data of figure 6.29 (the spread in α for a given T_{av} with different B is shown by bar height) as a function of T_{av} in the Mark IV annular channel. The firm line corresponds to Marwaha data

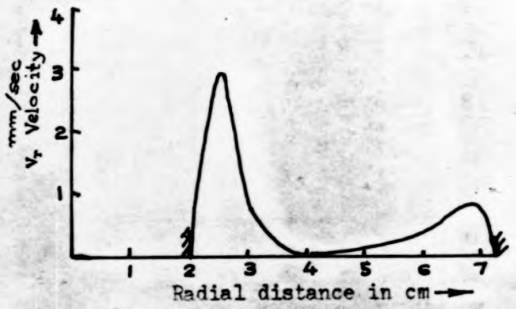

Figure 6.31 Radial profile of v_r at B=0.005 Tesla with 2amperes of distributed heating current in the Mark IV annular channel

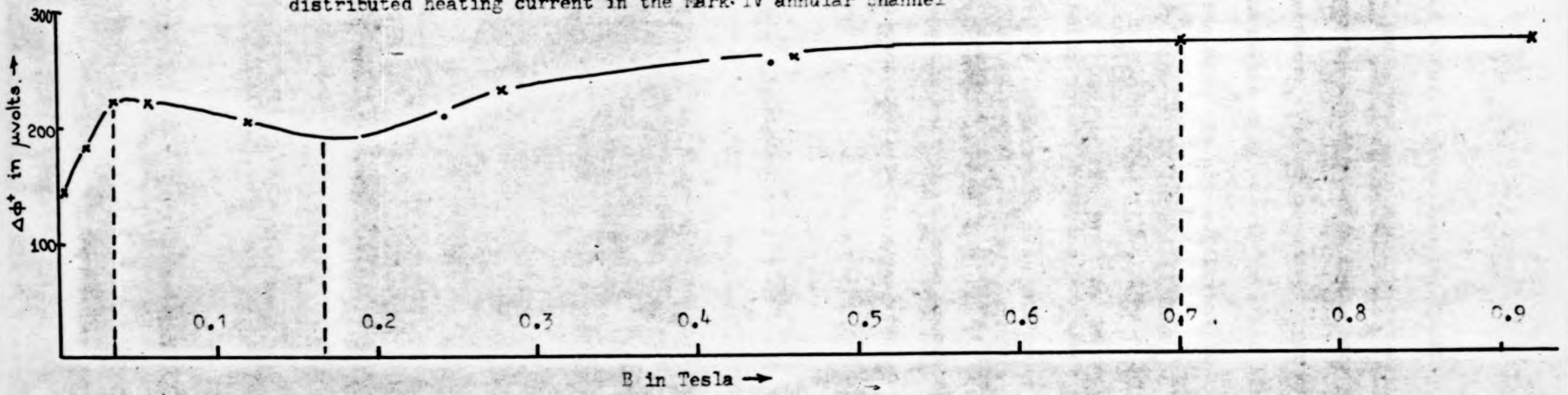

Figure 6.32 The variation of $\Delta\phi^+$, the potential difference measured across the total radial span of Hg (with Hg electrode potential probe) with the magnetic flux density in the Mark IV annular channel heated at the outer and cooled at the inner rim.

at the same two values of M for a given heating/cooling condition. Figure 6.32 shows one such measurement with the mercury electrodes. It may be inferred from these measurements that the formation of Hartmann type of boundary layer takes place at B_{cr_1} when the magnetic drag starts exerting its influence but the magnetic drag is not sufficient to inhibit buoyancy-driven secondary flow until increased to B_{cr_2}, depending on the heating/cooling condition.

The transients, building up and decaying processes have not been studied. Time plots of temperature rise and decay in two different steady magnetic field levels are, however, included in Figure 6.33 to demonstrate the fact that these processes involve very complex fluctuating characteristics.

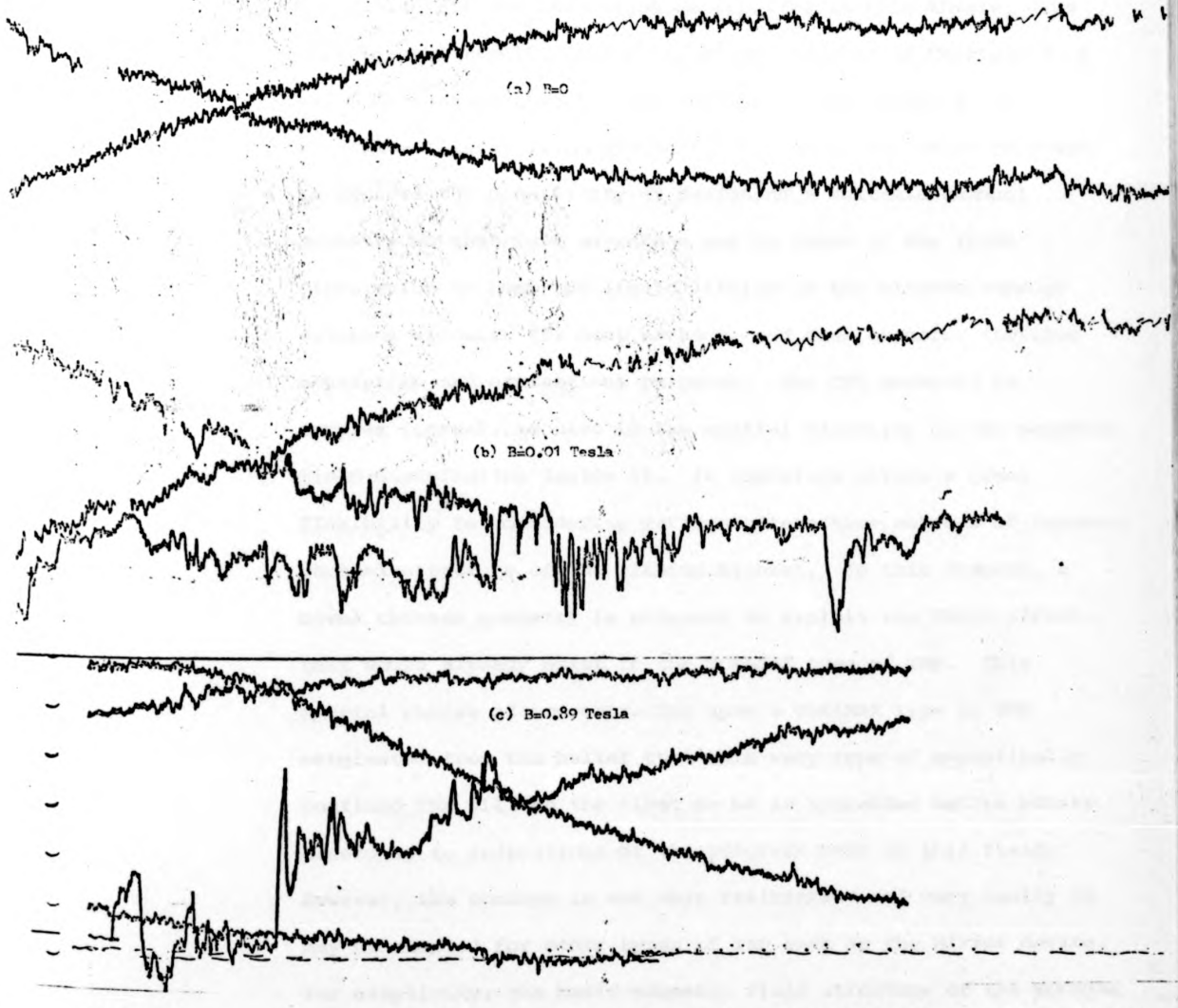

Figure 6.33 The temperature rise and fall traces with time , the temperature measured in Hg 6.25 mms from inner cylinder at the base wall, for magnetic flux density of (a) B=0 (b) B=0.01 Tesla and (c) B=0.89 Tesla in the Mark IV channel with 3.2 amperes of distributed heating current. The trace moves from left to right with time. scale 15 sec/cm ,6.25°C /cm

N.B. Xerox reduction 3:4

CHAPTER 7

THERMOELECTRIC MAGNETOHYDRODYNAMIC FORCED SWIRLING FLOW IN CHANNELS SPIRALLING IN THE FLOW DIRECTION

7.1 Introduction

Possible application of TEMHD circulation in the liquid lithium blanket of magnetically confined TNR's has been the prime motivation for the investigation reported in this thesis. The experimental results of investigation reported in Chapters 4, 5 and 6 do confirm that the idea of TEMHD circulation at a significant level is indeed feasible. It is therefore relevant to explore the possibility of designing a suitable channel geometry so that full advantage may be taken of the TEMHD circulation to pump the liquid lithium in the blanket through external circuits for heat exchange and mass transfer (tritium separation and extraction) purposes. The TNR geometry is complex (torus), so also is the spatial variation of the magnetic field distribution inside it. It therefore offers a great flexibility in considering various alternative schemes of internal channel structure of the lithium blanket. In this chapter, a novel channel geometry is proposed to exploit the TEMHD effect that would already exist in the TOKAMAK type of TNR. This special choice of concentrating upon a TOKAMAK type of TNR originated from the belief that this very type of magnetically confined TNR will be the first to be in operation before others according to indications of the progress made in this field. However, the concept is not very restricted, and very easily it may be adopted for other types of TNR such as the Mirror device. For simplicity, the basic magnetic field structure of the TOKAMAK type of TNR is supposed to consist of very strong toroidal plus a weak poloidal steady field. The quasi-steady poloidal fields

that control the overall plasma loop position and that generate helicity to prevent charged particle leakage to the wall are therefore ignored. The engineering constraints lie in the (i) desirability of modular construction for easy assembly and repair purposes, (ii) restricted space for the inlet-outlet ports for the lithium flow in and out of the blanket squeezed in between the superconducting magnet sections at the outer periphery of the blanket, (iii) temperature limitation at the first wall due to nonavailability of suitable material that would withstand high level of neutron and α-particle radiation and Bremsstrahlung, and (iv) desirability of compact, strong internal structure with the minimum of structural material that might absorb neutrons (irradiation and thermal stress).

Bearing such restictions in mind, the basic concept of the novel scheme of blanket structure that would pump liquid lithium TEMHD-ally at the expense of negligibly small amount of energy available in the blanket is presented in section 7.2. A simple analytical treatment is considered in section 7.3. In order to test the feasibility of such a scheme, a laboratory model was fabricated which is described in section 7.4. The limited experimental results that could be obtained on this device with Hg as the working fluid are put forward in section 7.5.

7.2 Basic Concept of the Spiral Channel

It is convenient to consider the radial, toroidal and poloidal co-ordinates (r, θ, φ) to describe the torus of a TOKAMAK as shown in Figure 7.1. Without committing a serious error, one may safely assume the first wall of the lithium blanket to be the hot region and the cold region to be very near the superconducting magnet site at the outer periphery of the blanket. Technically

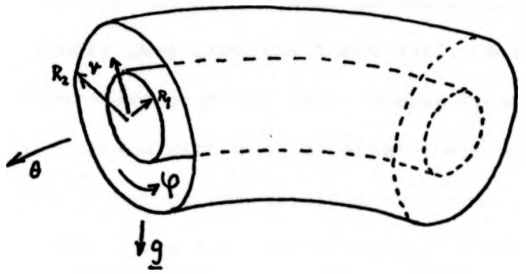

Figure 7.1 The Co-ordinate system suitable for the plain lithium blanket of the TOKAMAK type of TNR.

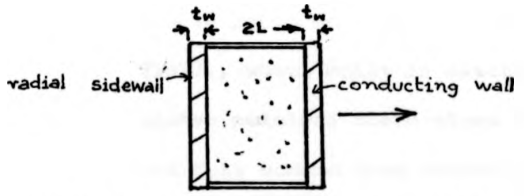

Figure 7.2 The channel cross-section

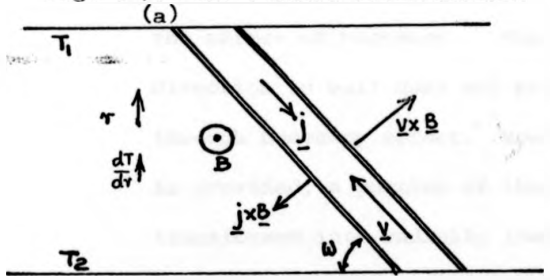

Figure 7.2 (b) The inclined channel configuration (linear approximation of the curved spiral channel). Inclination of the channel axis to the isotherms ω ; no pressure gradient in the flow direction assumed, and only slug flow is considered.

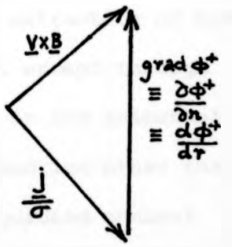

Figure 7.2(c)The vector diagram of the modified Ohm's law for the TEMHD analysis in the channel configuration of fig7.2b

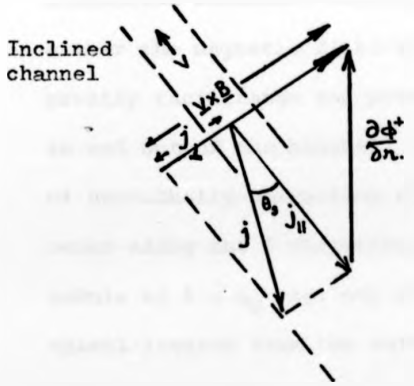

Figure 7.3 The vector diagram of the modified Ohm's law when
$j_{\parallel}$ component of $\underline{j}$ parallel to v
$j_{\perp}$ component of $\underline{j}$ perpendicular to v

speaking, the hot zone is in the interior of the lithium, slightly away from the first wall. A significant radial temperature gradient would therefore exist. TEMHD fluid circulation with such a radial temperature gradient is possible with either of the toroidal or poloidal field, with the current returning via toroidal partitioning walls. The toroidal field would circulate the fluid in the azimuthal direction φ whereas the poloidal field would induce circulation in the θ (toroidal) direction. With the choice of circulation in the θ direction, the scheme could well be like the 'Racetrack' structure of Fraas (1972), where built in electromagnetic pumps have been used. The weaker poloidal field gives a higher TEMHD circulation velocity, but this scheme does notbasically cater for the extraction of heat from near the first wall to the outer periphery, except through the effect of buoyancy. The TEMHD circulation in the azimuthal direction as well does not produce any heat convection other than through buoyancy effect. However, if a spiral guiding channel is provided, a portion of the momentum of rotation may be transformed into radially inwards or outwards velocity v_r. The resultant movement would therefore be along the guiding spiral and can be used either to make the fluid move towards the first wall or away from it. This reversing possibility with a mechanical structure without having to contrive the reversal of either the magnetic field or the temperature gradient direction greatly facilitates the process of combined pumping of the fluid in and out of the blanket. The scheme thus consists of modules of azimuthally spiralling channels in pairs placed next to each other along the θ direction. The first spiralling channel of a module at $\theta = L_\theta$ say, may be taken without loss of generality to spiral inwards from the outer periphery of the blanket for φ

anticlockwise up to the first wall, but not closed on the first wall to avoid blocked ends. This is the channel that guides the fluid towards the first wall by TEMHD circulation in the φ anticlockwise direction, but also could serve to guide the fluid away from the first wall for TEMHD circulation in the φ clockwise direction. The second spiralling channel of the module at $\theta = L_{2\theta}$ should then be spiralling outwards for φ anticlockwise sense, so that TEMHD fluid circulation in the anticlockwise sense propels the fluid away from the first wall. The second spiralling channel starts a little away from the first wall. The clearance between the first wall and the ends of the two spiralling channels of the module forms the transition region for the flow from one channel to the other via a θ directional motion. The TEMHD force due to the poloidal field may be so directed that the forcing of the fluid in the θ direction is in the correct sense from the first channel to the second in the transition region. Thus the spiralling movement and heat extraction at the first wall is guaranteed. The scheme is flexible in the choice of the channel cross-section, spiralling curvature, and even allows for change in channel cross-section along r, θ, φ directions (tapering). If a higher circulation speed is necessary, external pumping may be introduced, the pumping power requirement being less than that in the case of ordinary pumping only by the amount produced TEMHD-ally. The stress limitation on the duct walls is also relieved by this amount as well. The possibility of further reduction of such external pumping power may be attained by suitably combining the modules in such a way that 'flow coupler' action takes place in the adjoining two modules, while in the middle module external pumping in addition to the TEMHD pumping is employed. 'Flow couplers' utilise the magnetic drag component of the current

that would be otherwise wasted in the duct wall of the first channel, to drive the fluid in the second channel. The basic scheme described above inherently considers spiral channels that span the entire lithium blanket. An alternative approach would be to employ such pumping only near the first wall. The extremely intense temperature gradient that could be generated in this region would produce significant TEMHD induced circulation. It may be noted that in the non-TEMHD pumping schemes in the lithium blankets, lithium stagnates near the first wall, seriously reducing the effectiveness of heat extraction. The TEMHD circulation scheme is definitely advantageous in this respect, as maximum circulation at the first wall is guaranteed, if the geometry is right. The TEMHD scheme is not restricted to steady state operation only as TEMHD circulation during magnetic field rise and decay with time has been observed during experimentation. Some order of magnitude figures for TEMHD circulation with realistic temperature gradient and B values are given in section 3.2.6.

7.3 Theoretical Analysis

In this thesis a few illustrative cases under simplifying assumptions are presented for brevity rather than building an elaborate detailed coupled thermal and magnetohydrodynamic analysis of the flow in the spiral channel.

Consider first the linear version (curvature ignored) of the flow in an elemental length of the channel inclined at an angle α to the isotherms T_1 and T_2, $(T_2 > T_1)$ at the ends of the elemental length. Ignore the effect of gravity and buoyancy, and consider the cross-section rectangular and uniform (Figure 7.2a). The channel and the magnetic field configuration for the case of

no pressure gradient along the flow direction is shown in Figure 7.2b. The vector diagram according to the modified Ohm's law, including the thermoelectric potential (3.22) is shown in Figure 7.2c to correspond to grad ϕ^+ in the r direction and $\underline{j}$ along the channel length S (no pressure gradient along the flow). Two possibilities exist: (i) the inclined boundaries to the isotherms (at an angle Ψ) to be electrically insulating in which case current in the return path is entirely in the conducting wall (thickness, t_w) at the end side along r, (ii) both the inclined and sidewall boundaries are electrically conducting.

Consider case (i). Neglect the small temperature drop across the thin duct walls. In the wall

$$\frac{\underline{j}_w}{\sigma_w} = -\text{ grad } \phi_w^+ \equiv -\frac{\partial \phi_w}{\partial r}\,, \quad \underline{j}_w \text{ being the direction of r} \tag{7.1}$$

and in the fluid

$$\frac{\underline{j}}{\sigma} = \underline{v}\times\underline{B} - \text{grad } \phi^+ \tag{7.2}$$

From the continuity of current

$$j_w t_w = jL \sin \Psi \tag{7.3}$$

From the balance of components in the fluid along and perpendicular to r in a plane perpendicular to B, ignoring velocity profile variation across the channel,

$$\frac{\partial \phi^+}{\partial r} = Bv \cos \Psi + \frac{j}{\sigma} \sin \Psi \tag{7.4}$$

$$0 = Bv \sin \Psi - j/\sigma \cos \Psi \tag{7.5}$$

From (7.1) and (7.4), using relations (7.3) and (7.5) to eliminate j's

$$\frac{\partial}{\partial r}(\phi^+ - \phi_w^+) = Bv\cos \Psi + (1 + c)\frac{\sin^2 \Psi}{\cos \Psi} Bv$$

$$= \frac{Bv}{\cos\Psi}\{1 + c \sin^2 \Psi\} \quad \text{where } c = \frac{\sigma L}{\sigma_w t_w}\,, \tag{7.6}$$

Therefore

$$v = \frac{\cos \Psi}{1 + c \sin^2 \Psi} \frac{\alpha}{B} \frac{dT}{dr} \; ; \quad \frac{\partial}{\partial r}(\phi^+ - \phi_w^+) \text{ being taken as } \propto \frac{dT}{dr} \qquad (7.7)$$

Since v is a constant w.r.t. r for fixed Ψ (inclination) for a given B, $\propto \frac{dT}{dr}$ must be a constant. v is independent of sign changes of Ψ as long as the sign of $\frac{\alpha}{B} \frac{\partial T}{\partial r}$ is maintained and is zero for $\Psi = \pi/2$. $v = 0$ at $\Psi = \pi/2$ is not surprising if one traces back the build-up process. At $\Psi = \pi/2$, $\underline{j}$ is along r and also parallel to the channel length, and hence there is no component perpendicular to the magnetic field to cause a $\underline{j} \times \underline{B}$ force along the channel length; v therefore does not build up at all. v is maximum for $\Psi = 0$ which really corresponds to the configuration of Chapter 5.

Consider now that the pressure gradient along the channel is non-zero. To maintain simplicity consider $\partial p/\partial s$ constant. For steady state velocity v, the current density $\underline{j}$ in the fluid is no longer along the length of the channel. Let $j_\parallel$ be the component along the channel and $j_\perp$ perpendicular to it in a plane perpendicular to B. Then (refer to Figure 7.3)

$$\partial\phi^+/\partial r = Bv \cos\omega + \frac{j_\parallel}{\sigma} \sin\omega + \frac{j_\perp}{\sigma} \cos \Psi \qquad (7.8)$$

$$0 = Bv \sin\omega - \frac{j_\parallel}{\sigma} \cos\Psi + \frac{j_\perp}{\sigma} \sin\Psi \qquad (7.9)$$

$$\frac{-\partial\phi_w^+}{\partial r} = j_w/\sigma_w \qquad (7.10)$$

$$j_\perp B = \partial p/\partial s \quad \text{and} \quad j_w t_w = j_\parallel L \sin\Psi \qquad (7.11)$$

From (7.8) through (7.11) gives

$$v = \frac{\alpha}{B} \frac{\partial T}{\partial r} \frac{\cos\Psi}{1 + c \sin^2\Psi} - \frac{1 + c}{\sigma B^2} \partial p/\partial s \qquad (7.12)$$

This expression of velocity v in (7.12) shows that the TEMHD flow is characterised by an equivalent mechanical pressure gradient of $\sigma \alpha B \frac{dT}{dr} \frac{\cos\Psi}{(1 + c \sin^2\Psi)(1 + c)}$.

Consider now the problem from the heat flow point of view. Ignoring the generation of heat in the bulk of the fluid like that due to the dominant release of heat of nuclear reactions and the relatively insignificant joule heating, and also ignoring heat sources and sinks due to Peltier and Thomson effects from (3.24)

$$K \frac{d^2T}{dr^2} = \rho c_p v \sin W \frac{dT}{dr} \qquad (7.13)$$

where $K = K_f + \frac{t_w}{L} K_w$, the combined equivalent thermal conductivity, suffixes f and w being for the fluid and the wall respectively, ρ and c_p being the density and specific heatof the fluid, curvature is still ignored so that variations are taken directly as d/dr.

For q, the uniform time rate of heat flux and convection in the r direction per unit length along isotherms T_1 and T_2 at $r = R_1$ and $r = R_2$ respectively and perpendicular to B, integration of (7.13) w.r.t r gives

$$q = - LK \frac{dT}{dr} + \rho c_p Lv (\sin W) \, T \qquad (7.14)$$

$$T = T_1 + \frac{T_2 - T_1}{e^{\frac{\rho c_p v \sin W}{K} R_2} - e^{\frac{\rho c_p v \sin W}{K} R_1}} \left\{ e^{\frac{\rho c_p v \sin W}{K} r} - e^{\frac{\rho c_p v \sin W}{K} R_1} \right\} \qquad (7.15)$$

From (7.14) and (7.15) it is evident that T has an exponential variation w.r.t r and hence $\alpha \frac{dT}{dr}$ is not constant. Therefore $\partial p/\partial s$ is no longer constant and θ_s in Figure 7.3 must change with s. From (7.12) it may be inferred that $\partial p/\partial s$ variation with r to consist of a linear and an exponential term, for v and W constant.

To make $\partial p/\partial s$ constant, one may consider (i) the convective process much greater than the conductive heat transfer if $K \frac{dT}{dr} << \rho c_p v (\sin W).T$, (ii) variation of v by tapering of the

cross-section with respect to s and (iii) the effect of curvature in the variation of Ψ with s.

However, in case (i) for constant rate of heat transfer $dT/dr \simeq 0$ and the TEMHD process vanishes. The case of constant Ψ but variation of v by tapering of cross-section along s with dilation of spacing w.r.t r is illustrated with the channel formed by the equiangular or logarithmic spiral $r = e^{\mu\varphi}$ with $\Psi = \mu$, maintaining the sidewalls parallel to each other. Then $v \sim \frac{A}{r}$. Now, if the convective process dominates over the conductive process, $T \propto r$ and $\alpha\frac{dT}{dr}$ is indeed constant if α is constant. In general $\alpha = A_1 T + A_2$ where A's are constants. This gives a $\partial p/\partial s$ variation with r of the form $g_1 r + \frac{g_2}{r} + g_3$. When both conductive and convective processes are equally important, $T \propto r^2$ and the variation of $\partial p/\partial s \sim g_1 r^2 + \frac{g_2}{r} + g_3$. In actual practice, the effect of curvature cannot be ignored and the variation with φ must occur in a spiral channel. If the variation w.r.t φ is still ignored and the cross-section varied as r, the energy equation may still be maintained simply as

$$K\left(\frac{d^2T}{dr^2} + \frac{1}{r}\frac{dT}{dr}\right) = \rho c_p v \frac{dT}{dr} + f(r)$$

$$= \rho c_p \frac{g_1}{r}\frac{dT}{dr} + f(r) \qquad (7.16)$$

where the function f(r) is decided by the heat generation rate in the fluid and g_1 is a constant. The deposition of heat in the lithium in the TNR blanket would fall off logarithmically away from the first wall. Let, for convenience, f(r) be chosen as $\frac{Kg_2}{r^2}$; then for $K = \rho c_p g_1$ from (7.16)

$$T = -g_2 \log r + g_3 r + g_4 \text{ where g's are constants.}$$

From (7.12), with a choice of

$$-g_1/g_2 = \frac{\cos\Psi}{i + c\sin^2\Psi}\,\frac{\alpha}{B},$$

$\frac{\partial p}{\partial s}$ can be made equal to a constant $\frac{\sigma B \alpha \cos \Psi}{(1 + c)(1 + c \sin^2 \Psi)} g_3$. For configurations with $g_3 = 0$, this constant is zero.

This does suggest that two short spiral channels in two different θ planes, as shown in Figure 7.4(a) would literally be able to convert the TEMHD rotational motion into fluid pumping action in and out of the rest of the blanket space. This can be generalised into multiple segment arrangement with helically twisted transition zones at the first wall where fluid flow would change over from one spiral in θ_1 plane to the corresponding matched pair channel in the θ_2 plane (Figure 7.4(b)). The variation in the channel cross-section is not necessarily restricted in the φ direction only. Tapering may be introduced in the θ direction simply or in addition to the dilation in the φ direction. This would result in the partial derivatives of T w.r.t r, θ and φ in the energy equation, which makes it very complex.

Consider case (iii) with constant cross-section so that ν is constant. The basic inner spiral profile that would give $\frac{\partial p}{\partial s} = 0$ is given by

$$e^{rA_1} \frac{\alpha}{B} \frac{\cos \Psi}{1 + c \sin^2 \Psi} = A_2 \text{ where } A_1 \text{ and } A_2 \text{ are constants.}$$

The constant cross-sectional spiral channel can then be built up on this inner profile with uniform dilation in the φ direction as

$$r = \frac{2L\varphi}{2} + \ln \frac{A_2(1 + c \sin^2 \Psi)}{A_1} \frac{B}{\alpha} \qquad (7.17)$$

so that the spiral channel has, to the first approximation, parallel walls.

Consider next the effect of buoyancy in a plain lithium blanket without any vane structure between the first wall and outer wall of the torus (r, θ, φ) (Figure 7.1). Let the electrical conductivities and the absolute thermopowers of the fluid and the container material be taken as uniform and constant. Also let the Oberbeck-Boussinesq approximation be valid so that density variations are considered only in the body

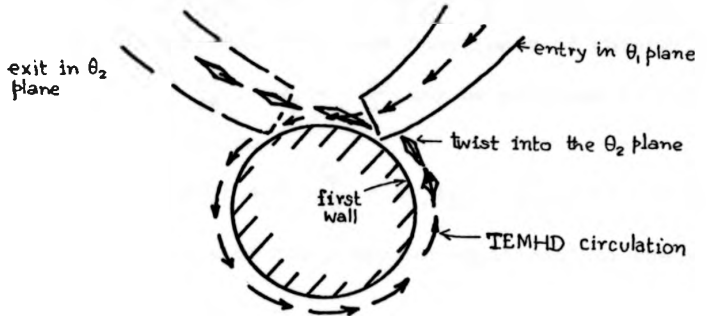

Figure 7.4(a) A simple fluid inlet and outlet device in the presence of TEMHD circulation in the annular horizontal torus.

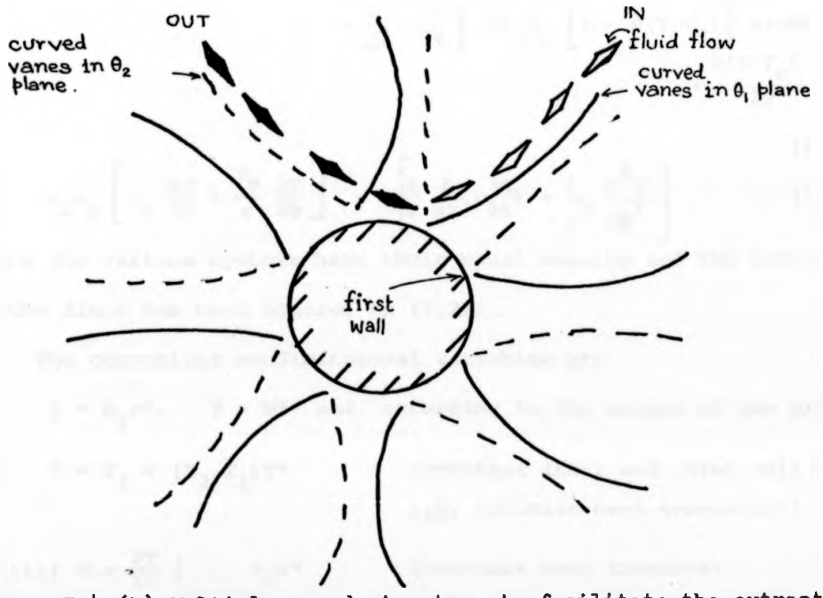

Figure 7.4 (b) Multiple vaned structure to facilitate the extraction of fluid momentum due to TEMHD circulation for pumping purpose.

Vanes in different θ planes are distinguished by firm and dashed lines. The twisting transition zones in between the θ planes are not shown.

force (buoyancy) term in the momentum equations. Ignoring the effect of the poloidal field, the steady ($\partial/\partial t = 0$) motion , due to the toroidal field B, and buoyancy may be taken to be two dimensional in the (r,φ) plane so that the concept of stream function Ψ of Chapter 3,

$$v_r = \frac{1}{r}\frac{\partial \Psi}{\partial \varphi}, \quad v_\varphi = -\frac{\partial \Psi}{\partial r} \text{ may be utilised in order to satisfy}$$

the conservation equation

$$\frac{1}{r}\frac{\partial}{\partial r}(rv_r) + \frac{1}{r}\frac{\partial v_\varphi}{\partial \varphi} = 0 \ , \left(\frac{\partial}{\partial \theta} = \frac{\partial}{\partial t} = \text{div } \rho = 0\right) \qquad (7.18)$$

The r and φ components of the momentum equations and the energy equation are given by

$$\rho_o\left[v_r\frac{\partial v_r}{\partial r} + \frac{v_\varphi}{r}\frac{\partial v_r}{\partial \varphi} - \frac{v_\varphi^2}{r}\right] = -\frac{\partial p}{\partial r} + \eta_v\left[\frac{\partial}{\partial r}\left(\frac{1}{r}\frac{\partial}{\partial r}(rv_r)\right) + \frac{1}{r^2}\frac{\partial^2 v_r}{\partial \varphi^2} - \frac{2}{r^2}\frac{v_\varphi}{\partial \varphi}\right]$$
$$+\rho_o g_o\left[1 - \beta(T-T_2)\right]\cos\varphi - \sigma v_r B^2 \qquad (7.19)$$

$$\rho_o\left[v_r\frac{\partial v_\varphi}{\partial r} + \frac{v_\varphi}{r}\frac{\partial v_\varphi}{\partial \varphi} + \frac{v_r v_\varphi}{r}\right] = -\frac{\partial p}{r\partial \varphi} + \eta_v\left[\frac{\partial}{\partial r}\left(\frac{1}{r}\frac{\partial}{\partial r}(rv_\varphi)\right) + \frac{1}{r^2}\frac{\partial^2 v_\varphi}{\partial \varphi^2}\right.$$
$$\left. + \frac{2}{r^2}\frac{\partial v_r}{\partial \varphi}\right] - \rho_o g_o\left[1 - \beta(T-T_2)\right]\sin\varphi + \frac{\alpha\sigma}{1+c}\cdot$$
$$\cdot\frac{\partial (T-T_o)}{\partial r}B - \sigma v_\varphi B^2 \qquad (7.20)$$

$$\text{and} \quad \rho_o c_p\left[v_r\frac{\partial T}{\partial r} + \frac{v_\varphi}{r}\frac{\partial T}{\partial \varphi}\right] = K\left[\frac{1}{r}\frac{\partial}{\partial r}\left(r\frac{\partial T}{\partial r}\right) + \frac{1}{r^2}\frac{\partial^2 T}{\partial \varphi^2}\right] \qquad (7.21)$$

where the various symbols have their usual meaning and the heat generation in the fluid has been ignored in (7.21).

The convenient nondimensional variables are

$r = R_2 r^*$, $\Psi = \nu\Psi^*$ and, according to the nature of the problem,

(i) $T = T_1 + (T_2 - T_1)T^*$ (constant inner and outer wall temperatures i.e. infinite heat capacities)

or (ii) $T = \left.\frac{\partial T}{\partial r}\right|_{r = R_2} R_2 T^*$ (constant heat transfer) (7.22)

Using the nondimensional variables of (7.22) in the vorticity equation, i.e. $\frac{1}{r}\frac{\partial}{\partial \varphi}$ (7.19) $- \frac{\partial}{\partial r}$ (7.20) and in (7.21), dropping the stars,

$$\nabla^4\psi = \frac{1}{r}\frac{\partial(\nabla^2\psi,\psi)}{\partial(r,\phi)} + Gr\left(\frac{\cos\phi}{r}\frac{\partial T}{\partial\phi} + \sin\phi\frac{\partial T}{\partial r}\right) + M^2\left(\frac{\partial^2\psi}{r^2\partial\phi^2} + \frac{\partial^2\psi}{\partial r^2}\right) - M^2\frac{\alpha(T_2-T_1)}{\nu B}\frac{\partial^2 T}{\partial r^2} \qquad (7.23)$$

$$\text{and} \quad \nabla^2 T = \frac{Pr}{r}\frac{\partial(T,\psi)}{\partial(r,\phi)} \qquad (7.24)$$

where $\nabla^2 \equiv \frac{\partial^2}{\partial r^2} + \frac{1}{r}\frac{\partial}{\partial r} + \frac{\partial^2}{r^2\partial\phi^2}$, $Gr = g_o\frac{\beta(T_2-T_1)R_2^3}{\nu^2}$ or $g_o\beta\left(\frac{\partial T}{\partial r}\right)_{r=R_2}\cdot\left(R_2^4/\nu^2\right)$

according to (i) or (ii) of (7.22), $Pr = \frac{\nu\rho_o c_p}{K}$, $M^2 = \frac{\sigma}{\rho_o\nu}R_2^2B^2$ and the Jacobian notation $\frac{\partial(X,Y)}{\partial(r,\phi)} \equiv (\partial X/\partial r)(\partial Y/\partial\phi) - (\partial X/\partial\phi)(\partial Y/\partial r)$ has been used to simplify the writing of the equations. The various terms in (7.23) can be identified as the viscous, inertial, buoyancy, magnetic drag (ordinary MHD) and TEMHD force induced vorticity. It may be noted that if the inner cylindrical wall of the torus is hot, (Gr) is negative. A new nondimensional parameter $\frac{\alpha(T_2-T_1)}{\nu B} \equiv D$ gives the comparison of thermoelectric e.m.f. and motion induced e.m.f.

Exact solutions of (7.23) and (7.24) are difficult, and numerical solutions only are possible. Even in the nonmagnetic case (Custer et al., 1977), the solution is sought in a double perturbation expansion in powers of Gr and Pr in the following form:-

$$\psi(r,\phi) = \sum_{n=0}^{\infty}\sum_{m=0}^{\infty} Pr^n Gr^m \psi_{nm}(r,\phi)$$

$$T(r,\phi) = \sum_{i=0}^{\infty}\sum_{j=0}^{\infty} Pr^i Gr^j T_{ij}(r,\phi) \qquad (7.25)$$

substitution of (7.25) in (7.23) and (7.24) with M = 0, equating coefficients of equal powers of Pr gives an infinite set of equations in Gr which are to be solved sequentially.

The series solution truncated to the second order in Gr is given by

$$T(r,\phi) = T_{oo}(r) + Gr\ Pr\ T_{11}(r)\ \cos\phi$$

$$\Psi(r,\phi) = Gr\Psi_{o1}(r)\ \sin\phi + Gr^2\Psi_{o2}(r)\ \sin 2\phi$$

where the functions $T_{mn}(r)$ and $\Psi_{mn}(r)$ are of the form $\gamma_{ij} \cdot r^i (\ln r)^j$ with i and j integers and γ_{ij} constants.

Figure (7.5) shows representative 'crescent' and 'kidney' shaped patterns of Ψ at $|Gr|$ values $\leq 10^2$ and $\geq 10^5$ (Custer et al, 1977). The corresponding isotherms show a distortion in axial symmetry at higher Gr values. The higher Gr value not only promotes multicellular vorticity, but shows chimney oscillations (with respect to space and time) at the vertical top region (Bishop and Carley, 1966: experiment with air).

For all practical purposes the basic motion in the nonmagnetic case may be taken as shown in Figure (7.6a). Then in the magnetic case, the overall solution may be tentatively obtained by superposing a uniform azimuthal velocity v_ϕ over the buoyancy driven flow. The fluid is then accelerated at the outer wall and decelerated at the inner wall for a half section ($o \leq \varphi \leq \pi$) and in the other half section ($\pi \leq \varphi \leq 2\pi$) the fluid is decelerated at the outer wall and accelerated at the inner wall (Figure 7.6b). This result is important from the point of view of mixing and convective heat extraction in the off period of the pulse type of operation of TOKAMAKS. The mean velocity in spiral channels would therefore be unaffected by buoyancy (if at all important) but the velocity profile will be affected to give it an unsymmetrical shape.

7.4 The Prototype Laboratory Model

A very brief description of the design and fabrication of a laboratory-scale prototype model of a double spiral module for

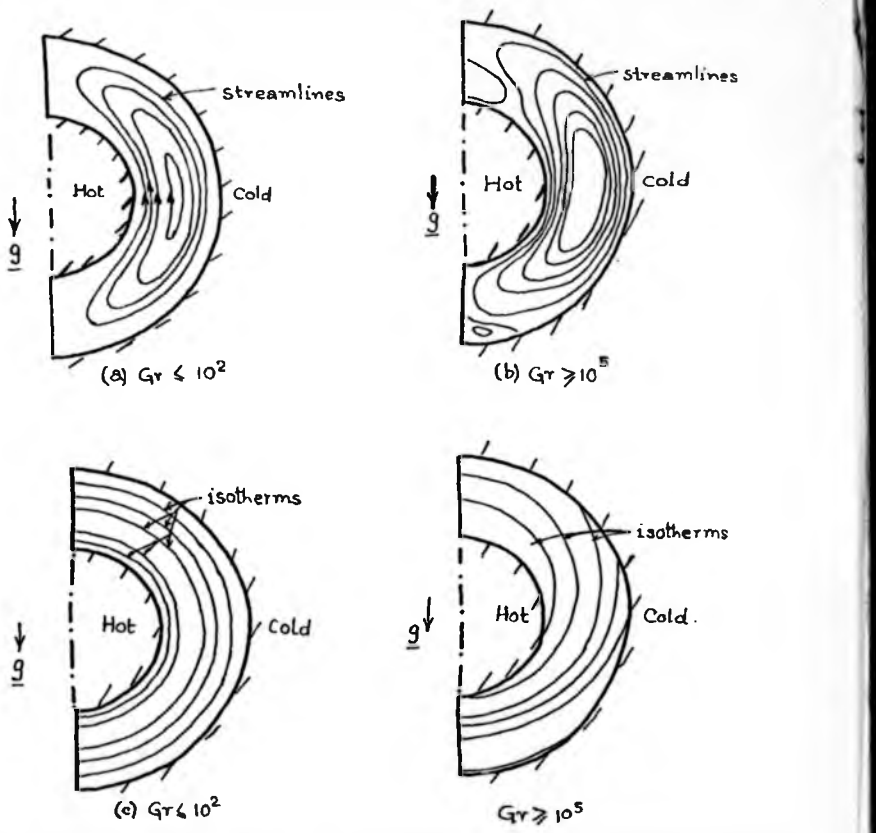

Figure 7.5 (a,b) The 'Crescent' and the 'Kidney' shaped buoyancy driven flow in a horizontal annulus with one curved surface heated and the other cooled (Custer et al 1977) (c,d) the corresponding isotherms.

Figure 7.6 Drawn below

(a)The simplified model of buoyancy driven flow in the horizontal annulus.
(b)Superimposed motions of TEMHD rotation and buoyancy driven flow in heated and cooled horizontal annulus in a transverse magnetic field.

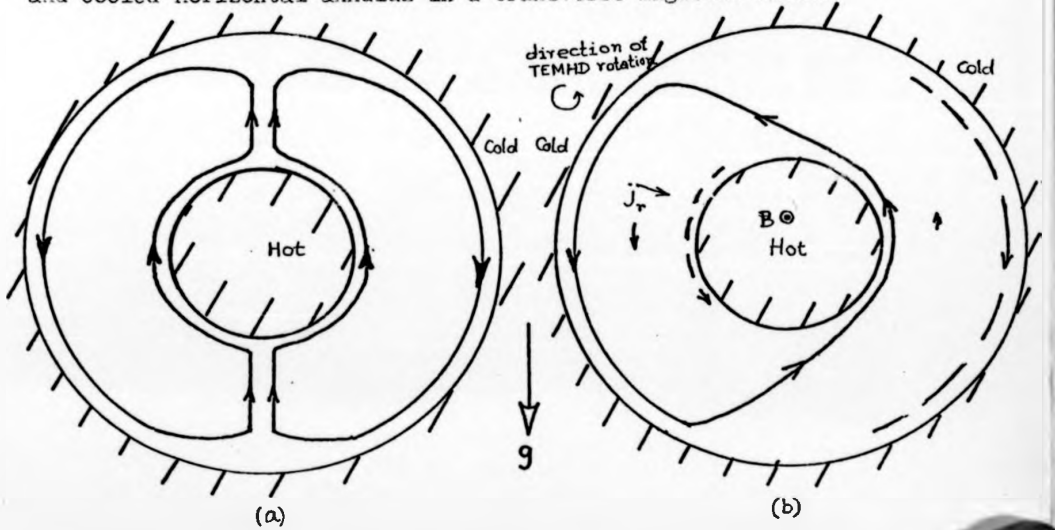

demonstrating the feasibility of TEMHD induced pumping in the lithium blanket is given in this section. To retain the flexibility of dismantling the spiral channels for purposes of later modification that might be warranted due to any unforeseen problem and for cleaning and inspection, the basic structure was made up of individual half sections and held together with tie bars under compression. A completely closed structure fabricated by brazing all around would not have this flexibility,but then the problem of sealing Hg would not be present. To simulate the lithium blanket directly, the inner surface of the annular section of the torus was taken as the hot surface in contrast to the arrangement described in Chapter 6. The tentative use of the device in the Lintott electromagnet I, with a horizontal magnetic field B,allowed only a total space of 7.5 cm lengthwise, out of which the tie bars and the compression end plates occupied a major portion of it. The spiral channels in each module were therefore restricted to 1 cm each in the direction of B (horizontal θ direction). In order to maintain rigidity and avoid deformation under heavy compressional forces, the copper sidewalls of the spiral channels were made of thick (3 mm) copper plates. The spiral channel configuration was formed on the sidewall by brazing a continuous strip of copper 1 cm in height and of 1.5 mm thickness along a contour to be described later. The brazed joints were first cleaned with dilute nitric acid and then made smooth and uniform by rubbing with 'Emery' paper and machining carefully on the milling machine. The spiral structure on the second sidewall was made in an identical fashion so that when it was inverted and placed back to back to the first channel configuration, the two together formed the required inwards and outwards spiralling of the pair

module. It may be noted that the module is capable of reverse mode operation by just changing the direction of rotation (ϕ), for example with a given direction of radial temperature gradient (negative outwards to be specific) by changing the direction of the magnetic field by 180°. The copper sidewalls were first drilled and then machined for the 6.3 cm central recess. The inner cylindrical surface was made out of a 5.5 cm long, 6.3 cm diameter (outer) copper tube (wall thickness of 1.5 mm). The overall outer cylindrical enclosure of the spiral channels was made out of a 15.4 cm diameter (outer) copper pipe with a wall thickness of 3 mm. One of the copper sidewalls with the spiral vaned structure was brazed to one end of each of the above copper pipes so that the copper pipes formed the annular groove of the torus section. Looking from the open end of the annular groove, the spiral vanes were inside the annular enclosure at the closed end. The annular water jacket with a radial spacing of 1 cm was formed at the outer rim between the radially extended sidewall and the 15.4 cm copper tube by brazing copper strips of 1.5 mm thickness, in the peripheral direction first and then at the sidewall end. Two 1.25 cm diameter copper straight tubes were brazed at the holes drilled at the outer rim of the water jacket at 180° apart, so that water from one port can flow down symmetrically through the two halves, and is let out at the other port. Two 0.625 cm diameter copper tubes were joined tangentially to the spiral channel outer ends by placing them carefully in drilled symmetrically placed inclined aligned holes, in two different θ planes corresponding to the two spiral channels, through the water jacket, and then brazing them at the holes for sealing Hg and water. This is the best that could

be done in the limited time, though this changeover of tube cross-section aggravated the entry and exit problem to introduce extra pressure drops during the flow experiments.

The choice of a suitable spiral profile with the right curvature for optimising the pumping effect is difficult. With a large variation of curvature along φ, a constant cross-sectional duct giving complete coverage of the entire annulus section with parallel sidewalls is impossible, and the (smaller) constant cross-sectional duct leads to an increased channel length. A constant cross-sectional channel was adopted (Figure 7.7) by maintaining nearly equal spacing between successive vanes at the same φ (there is a difference between the spacing between vanes at the same φ i.e. Δr, and the spacing measured in the normal direction, but for all practical purposes this difference is small for small $\frac{dr}{rd\varphi}$). With 1 cm spacing between successive vanes and a vane thickness of 1.5 mm four turns could be accommodated in the radial spacing of 4.25 cm. In practice, it was virtually reduced to 3 turns only, as the fourth turn, that is the one closest to the inner boundary of the torus section, was of varying cross-section, and also formed the intermediate connecting (transition) region from one spiral plane to the other.

The two counter spiralling sectional halves were separated from each other by a copper plate (thickness 1.5 mm) shaped to fit in closely between the 15.4 cm and the 6.3 cm diameter copper pipes, with a cutaway section (Figure 7.8) to allow the continuity of the transition zone in the θ direction at the innermost spiral ring near the 6.3 cm diameter copper pipe. The exact position of the middle plate which basically acted as the partition between the two counter-spirals and the alignment of

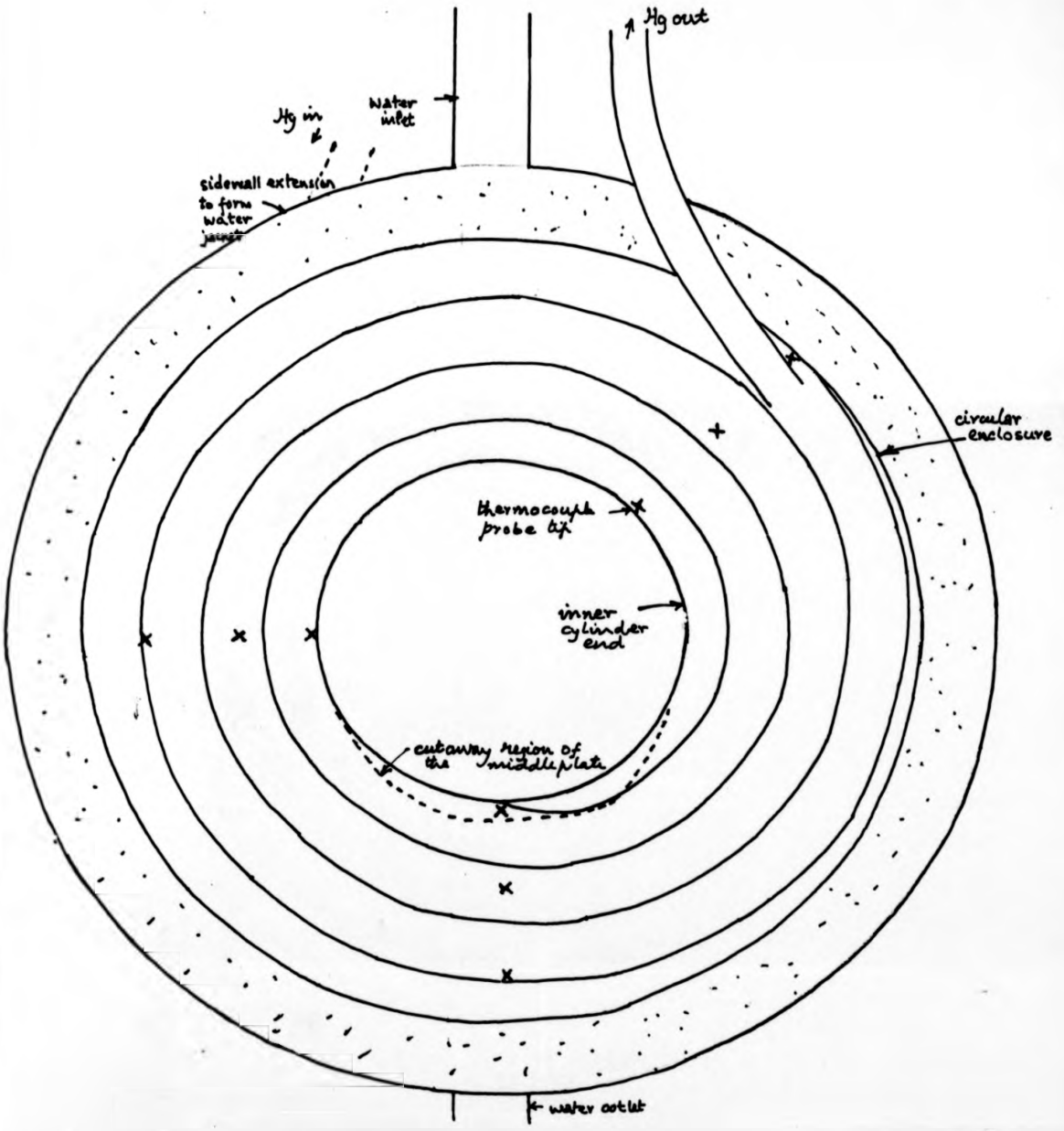

Figure 7.7 The spiral profile of the protoype module. (Full scale diagram)
X - Locations of thermocouple junctions for temperature measurements

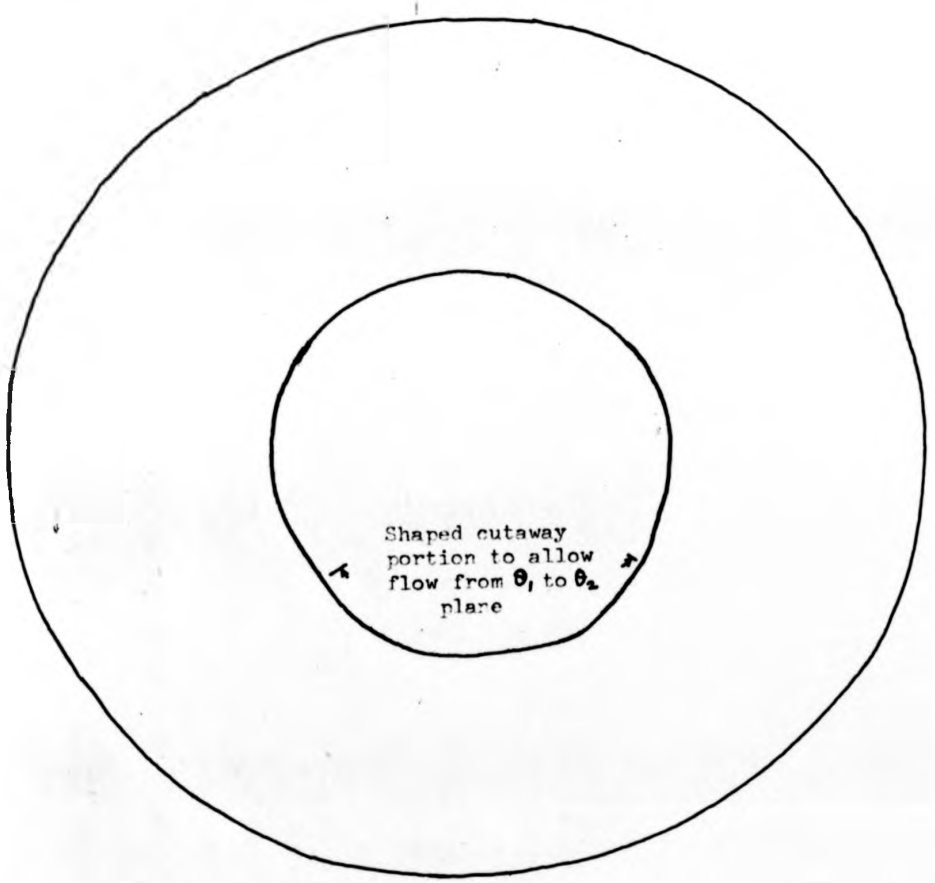

Figure 7.8 The shape of the middle separating copper plate between the half sections of the spiral channel.

placement of the second spiral with respect to the first was made with the help of a fixing pin and alignment grooves located at the outer rim.

The most difficult job in the assembly was in the sealing of Hg at the joints where the second sidewall was attached to the annular torus at the 15.4 cm and the 6.3 cm radii. The best possible arrangement that was finally adopted at the outer rim was to place a continuous (in the φ direction) vulcanised rubber annular ring gasket (punched out of rubber sheet and built up to the required thickness of 1.5 mm by joining layers with glue to match the mechanical tolerance) between the second channel sidewall extension and the flat machined face of the waterjacket sidewall. At the inner radius,a bevelled groove was machined out of the outside surface of the second spiral channel sidewall to house a RM 0595 'O' ring. The electrical contact between the second spiral channel sidewall and the inner and outer cylindrical rims of the torus section was through Hg in the channel,and thus there was a slight asymmetry of the two spiral channels. The assembly was retained in position under compression of the rubber gasket and the 'O' ring by two thick end plates held together with threaded brass rods (0.625 cm diameter) and nuts. Both bakelite and brass endplates were tried for compression,but tightening at the outer rim usually produced a bulge at the central hole, and therefore the 'O' ring was not properly compressed and Hg leaks appeared there. The final arrangement was that of a 1.25 cm thick bakelite endplate at one end, and a combination of 0.625 cm thick brass plate plus 0.625 cm thick tufnol plate at the second spiral channel end. The diameter of the endplates at the outer rim measured 21.5 cm. Initially 8

studs were used, but later they were increased to 14 to make compression more uniform around the rim.

The heater coil was built up on an aluminium tube of 3.75 cm diameter for rigidity. The tube was first securely covered with asbestos and then with MgO and fire clay mixture to build it up to a diameter of 5.90 cm. Mark I heater coil was made with nichrome and Mark II with Kanthal, by winding the resistive wire helically under tension in two symmetrical sections (to facilitate series parallel connection) over the insulator surface. The resistive wire was bonded to the base by applying a fine layer of paste made out of MgO and fire clay which also provided the interturn insulation. The cylindrical surface was checked for uniformity and then a final layer of insulation was provided by wrapping with fibre glass tapes so thatthe coil fitted into the inner bore of the 6.3 cm diameter copper pipe that formed the inner wall of the torus section. It was necessary to have ceramic insulating-blocks at the heater coil connecting leads because of the intense heat generated in the coil. At high heating current, there were always problems at the lead connector as the copper connecting wire ends got charred and burnt out frequently.

Initially the device was operated without any internal measuring probe, but after successful demonstration of static pressure difference and fluid flow, due to TEMHD effect in the spiral channel module, it was felt necessary to probe at least the temperature distribution in the fluid in the interior of the channel. Drilling holes through the sidewalls and blocking them with cement after placing the thermocouples was ruled out because of the inevitable problem of Hg leakage that would follow.

Nine pairs of thermocouples were therefore led through the Hg inlet and outlet ports,and the thermocouple junctions were positioned at φ = 0, 135 and 270^{o} at the inner and the outer rim and at mid-radius. The proper location of the thermocouple junctions was ensured by fixing them in grooves drilled in the spiral vanes. The routing of the thermocouple wire was such as to use the minimal length of the wire inside the channel. The thermocouple wires at the other end were joined to a reference temperature point (ice temperature) and the open ends of the same type of wire (either copper or constantan) were connected to the potentiometer *via* wafer switches for sequential measurement.

7.5 Experiments, Experimental Results and Discussion

The Lintott electromagnet I air gap slot was lined with polythene sheets up to a level 5 cm away from the heater coil to divert any mercury leakage into a tray at the end of the magnet gap. The spiral channel module was held with its axis horizontal by placing it on a wooden V block. The mercury inlet and outlet port tubes were at the vertical top region and were connected *via* PVC tubes to a weir type of mercury reservoir and the inclined tube manometer,in the same manner as described earlier in Chapters 4 and 5.

Static pressure difference due to the interaction of the radial thermoelectric current with the transverse magnetic field could be very easily demonstrated in the double spiral channel module by blocking the flow in the weir type of Hg reservoir in the external connecting loop and measuring the pressure difference across the inlet and outlet ports of the module by the inclined tube manometer. The static pressure difference, Δp,

measured in mm of height of mercury against the magnetic field strength B at various levels of heating current and the cooling water approximately at $8\frac{1}{2}^{o}$ C ($\pm \frac{1}{2}^{o}$ C variation) is shown in Figure 7.9. It may be noted with interest that in contrast to the TEMHD pressure difference characteristic reported for the straight channel experiments in Chapters 4 and 5, with basic thermally stable configuration, where the Δp versus B relationships obey straight line laws, in the case of the spiral channel in a transverse horizontal magnetic field, the Δp versus B relationship is linear only beyond a $B_{cr} \simeq 0.15$ Tesla, below which the relationship is a nonlinear, exponential variation. Maybe this is an indication of the effect of buoyancy at lower value of B, and its suppression at $B > 0.15$ Tesla. The gradient of the Δp versus B curve in the linear zone varies with the heating level which is consistent with the temperature dependence of α_{Cu-Hg}, the thermopower of the Hg-Cu combination.

As remarked earlier, the temperature distribution inside the channel was made with a limited number of thermocouples that could be drawn through the inlet and outlet ports. The exact location of these measuring points are shown in Figure 7.7. On the basis of these limited measurements, at various magnetic field strengths for a fixed level of heating, the profile of isotherms is shown in Figure 7.10 for the stationary state (flow in the external circuit blocked at the weir reservoir of Hg). Temperature oscillations were observed mainly at the hot innermost cylindrical surface for magnetic field strengths < 0.2 Tesla. On the basis of the isotherm profiles drawn with the limited measurement data, the temperature profile across the average radial distance for magnetic fields in the range of 0.2 to 1.25 Tesla is shown in Figure 7.11. The temperature measurements

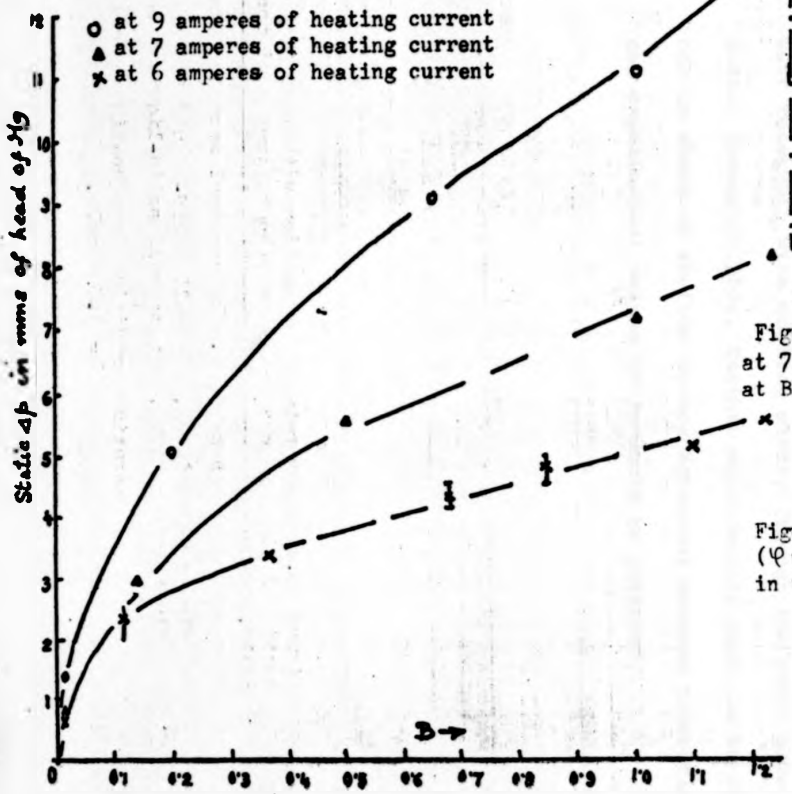

Figure 7.9 The static pressure difference in mms head of Hg across the ends of the spiral channel module against the flux density of the external magnetic field(in Tesla)

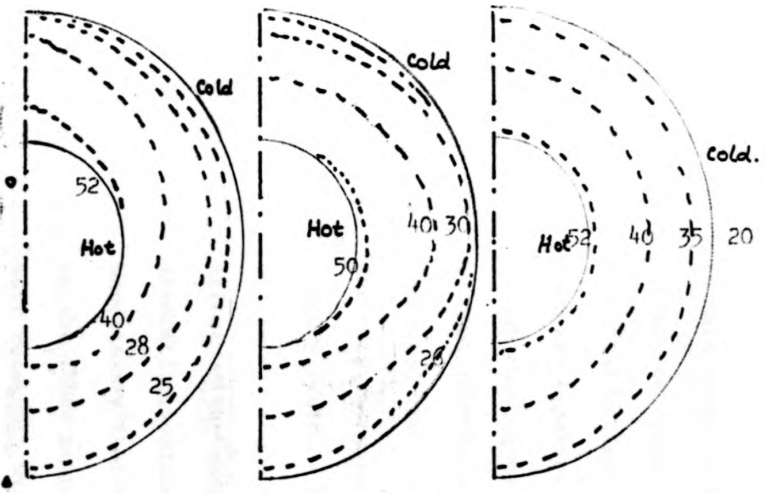

Figure 7.10 Isotherm profiles(°C) at 7 amperes of heating current at B= 0, 0.02and 0.2- 1.2 Tesla

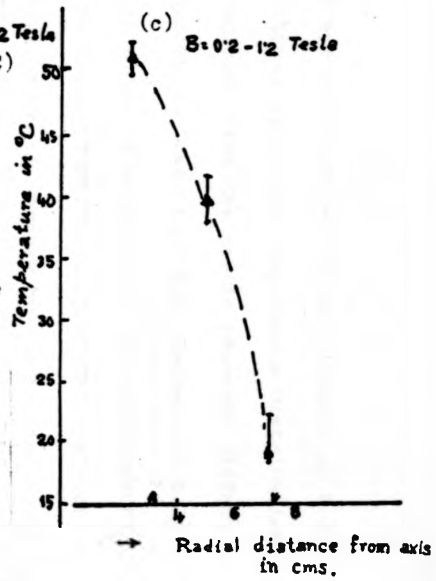

Figure 7.11 Average temperature (φ wise) across the radial space in the spiral channel.

in this range of B are invariant within a tolerance of ± 1%. Theoretical calculations with such temperature distributions in elemental strips indicate that the static pressure difference measured experimentally is lower than the theoretical calculation, though they agree in order of magnitude/within a factor of 2. This discrepancy can be explained by considering leaks between successive channel turns and the contamination of mercury by the brazing material directly in contact with mercury. TEMHD induced pumping of mercury could be easily demonstrated, but the pressure gradient at the end regions (entry and exit effects) and the blocking effect of the thermocouple leads made any comparison with the theoretical values widely different. It is because of this uncertainty that the convective heat transfer characteristic by the TEMHD pumping was not pursued by cooling the Hg in the weir reservoir with cooling water. Though the basic effect is easily demonstrable, further measurements ought to be carried out to check on whether better agreement between theoretical and experimental values of Δp could be obtained.

CHAPTER 8

CONCLUSIONS, CRITICAL EPILOGUE AND SCOPE FOR FURTHER INVESTIGATIONS IN THERMOELECTRIC MAGNETOHYDRODYNAMICS

8.1.1 Conclusions

It should be made clear that the experimental confirmation of TEMHD circulation in non-isothermal liquid metal in metal enclosures does raise the possibility of technological applications in the lithium blanket of magnetically confined TNR's and in melt refining, but in no way does the TEMHD interaction hold any promise at all as a prime energy conversion process due to its very poor efficiency. It is because such an effect does exist inherently in the lithium blanket and in the melt crucible that these effects may be harnessed suitably (e.g. using double spiral channels in the lithium blanket as described in Chapter 7) without having to introduce the TEMHD mechanism powered from external sources. Unless new materials are discovered in which high temperature gradients can be maintained with a low level of thermal energy input,and at the same time these materials possess high electrical conductivity and thermopower (low K, high σ values are contradictory properties of metals by the Wiedemann-Franz law), the energy conversion efficiency would remain insignificant.

The significance of the TEMHD interaction in the laboratory experiments reported in this thesis relies more on the presence of steep temperature gradients rather than high thermopower values of the materials; even though lithium possesses an unusually high thermopower ($\sim$ 25 $\mu v/^{o}$ C) amongst the liquid metals, it is rather small compared to the giant thermopower values possible with semiconductors. It is fortunate that the significance of TEMHD interaction in non-isothermal liquid

metal in metal liners could be demonstrated with Hg in copper channels with the temperature gradients that could be generated in the laboratory models without having to use, say, lithium-platinum (to give high α) combination where the thermopower is at least one order of magnitude higher. That the TEMHD interaction measured either as a static pressure difference Δp or circulation v was indeed due to TEMHD effect was very easily verified by reversing either the direction of the magnetic field or the temperature gradient. Even dirty contaminated Hg showed such characteristics without failure, even though the magnitude of Δp or v was very sensitive to the impurity level.

The investigations reported in Chapters 4,5,6 and 7 do show that a robust, new, accurate method of measuring the thermopower of liquid metals in magnetic fields is possible, using the TEMHD interaction effect measured either as the static pressure difference or the fluid circulation velocity in various types of channel shapes and for various arrangements of heating/cooling and magnetic field orientation. The measurements of TEMHD induced circulation and the static pressure difference have been found to be very sensitive to the presence of impurity levels. This has been checked and confirmed by the conventional thermopower measurements and by determining the impurities. The impurity elements in general fall into two categories, one that increases the intrinsic thermopower value and the other that decreases the thermpower value of the liquid metal. In theory, it is possible to determine the impurity levels in p.p.m., if the impurity elements could be identified completely, by TEMHD measurements. This provides a measure of the purity level in metallurgical refinement processes, and in detecting traces of impurities. It is interesting to note that industrial processes exist where traces

of additives increase the wettability of liquid metals. In recommending the use of TEMHD measurements in determining the thermopower of liquid metals, one may consider the following points: The Δp method is not a self-sufficient measuring method of thermopower; having measured the temperature gradient and the strength of the magnetic field, it is still not sufficient to evaluate the thermopower of the material combination without the knowledge of the electrical conductivities of the materials. Therefore, if the static Δp method of measurement is to be used, a priori knowledge of the electrical conductivities (σ) of the materials is essential, otherwise they have to be measured in a separate experiment. In thermopower evaluation, by measuring TEMHD circulation velocity, no such a priori knowledge or additional measurement of σ is essential. The expression for the mean velocity may be made independent of c, the fluid to wall conductance ratio. It is to be appreciated that such theoretical advantages could be derived only in special channel configurations such as in annular channels entirely in the uniform magnetic field region, so that no pressure gradients are generated at the entry and exit ends of the magnetic and the thermal fields or due to geometrical shape changeover. When $\partial p/\partial z \neq 0$ (z - flow direction), very elaborate compensation is necessary which involves σ and c. In both the methods, unless sufficient care is taken in choosing the right orientation of the temperature gradient and the magnetic field w.r.t the gravity field, detailed account of the nonlinearity of the temperature variation and the nonuniform velocity profile is to be considered.

The importance of proper safeguards against buoyancy induced motion that might modify the TEMHD induced circulation

just mentioned does need further comments on the influence of buoyancy in TEMHD. It may be recalled that even with a stabilizing density gradient in the straight, circular and rectangular cross-sectional channels, temperature measurements in the liquid metal did show temperature oscillations at low magnetic field (B) intensities and only at above a field B_{cr} were the oscillations suppressed. In earlier literature, such temperature oscillations have been mentioned only in the case of laterally heated configurations (free surface measurements only) and construed to be the result of buoyancy induced fluid circulation. The thermal(temperature)oscillations in the straight channels with a basic thermally stable stratification show the importance of instabilities that develop due to minor curvature of the isotherms and the possibility of amplification by small magnetic fields to finite amplitude oscillations with characteristic relaxation times. In the characterisation of a sharp B_{cr} for a given geometrical configuration of the channel with its orientation w.r.t the gravity vector and the magnetic field and heating/cooling conditions, there were indications that very feeble oscillations (that could not be measured properly with the available measurement facilities) persisted in large magnetic fields. It is natural to expect that the increase in magnetic field strength does inhibit buoyancy-induced bulk circulation, but when the characteristic roll dimension or the cell size becomes increasingly small, the magnetic drag is relatively ineffectual and the small scale vorticity is never completely eliminated.

In the lateral heating configuration (Chapter 6), a buoyancy effect is inherently present. In the absence of B,

the effect of buoyancy is to impart to the fluid a characteristic boundary layer structure at the hot and cold sidewalls, where steep temperature gradients exist,with brisk fluid movement in vortex rolls enhancing the heat transfer characteristic. In between these boundary layers, a central zone of stable thermal stratification is set up, and thus a large scale circulation due to buoyancy does not exist in the steady state. The application of a transverse magnetic field at low intensity destroys the stable stratification of the central zone, but is not sufficiently strong to inhibit fluid vorticity. Therefore, in recommending magnetic suppression of thermal oscillations in metallurgical processes of melt refining and crystal growth, it must be borne in mind that magnetic fields greater than B_{cr} that suppress thermal oscillations are to be impressed; otherwise a lower B value might inadvertently increase the thermal oscillations and defeat the purpose of the application of magnetic fields. The temperature profile measurements in the annular channel experiments of Chapter 6 vindicate the fact that,in the central region,the radial temperature gradient has a linear profile, whereas near the sidewall boundary layers the temperature gradient is steep, even with the application of the magnetic field. The increase in the applied magnetic field increases the slope of the still virtually linear temperature profile. A very naturally expected characteristic observed in the annular channel experiments is the increase of the hot wall temperature with the application of the magnetic field, that suppresses buoyancy induced convection for fixed heating/cooling conditions. Cooling water temperature measurements did not show any significant change with the application of the magnetic field, indicating that the amount of

heat transfer is not affected. In contrast, the lowering of the temperature at the hot wall and in the bulk of the liquid metal in the straight channel experiments in Chapters 4 and 5 was not at all expected, and this phenomenon has only been explained by assuming the existence of curvature in the isotherms and its relaxation oscillation with the application of the magnetic field.

The thermal oscillations in a magnetic field $B < B_{cr}$ have a characteristic sinusoidal (dominant first harmonic) variation with a finite time period over the range of 3 to 30 seconds, depending on the intensity of the magnetic field strength. The spiky fluctuations of temperature suggest the presence of impulsive bursts of fluid jets in an otherwise slow motion in cellular vortex rolls. The frequency of the spiky temperature fluctuations increased with higher temperature gradients to greater randomness which was increasingly difficult to suppress, even with the application of the magnetic field.

Apart from the effect of buoyancy (secondary flow and temperature oscillations) and the possibility of impressing a potential difference in the fluid-container assembly uniformly without having to make external discrete connection with connecting leads, the study of TEMHD largely appeared to be rather mundane as the basic characteristics of TEMHD very closely follow the wellknown ordinary MHD studies, though the latter ones are conducted with parameters whose order of magnitude is much greater than in TEMHD. This has been very typically observed in the annular channel experiment of Chapter 6 in the case of the insulated solid-liquid interface at the base wall, giving a velocity profile $\alpha\frac{1}{r}$ which follows from an extension of Hartmann analysis of ordinary MHD to curved channels. Even the boundary

layer thickness at the sidewalls, identifiable from the velocity profiles at the regions where the $\frac{1}{r}$ law of variation is invalidated, agrees with the characteristic dimension $\frac{L}{\sqrt{M}}$ (Shercliff, 1953). However, the Hartmann layer thickness at the base wall extends into the fluid further than L/M.

In the case of the annular channel experiment with all the walls having electrically conducting solid-liquid interfaces, the M shaped velocity profile (section 6.4.4) has the velocity at the sidewalls (parallel to B) orders of magnitude greater than the core velocity for reasons of predominantly steeper temperature gradients at the sidewalls rather than due to the decrease of current flow in the boundary layers (or even the reversal of current flow direction) that characteristically introduces magnetic drag in the core. It is, therefore, possible to have free shear layers in narrow annular channels with totally conducting solid-liquid interface, and it is not essential to consider the mixed interface conductivity at the base wall (section 6.4.3) to investigate TEMHD shear layers. However, the experiments of section 6.4.3 demonstrated shear layers of greater intensity, and the side effect observation proved that a greater magnitude of TEMHD fluid circulation is indeed possible (as indicated by theoretical analysis), with temperature gradient parallel to B rather than temperature gradient configurations transverse to B. The very large TEMHD induced velocity at the outer periphery of the concentrated heating experiment bears evidence of the above fact. The vorticity in the fluid at the shear layers, as measured by the paddle type of pivoted float, can be very easily explained from the slopes of the velocity profiles which themselves in turn obey the ϕ^+ distribution at

the interface according to the temperature distribution. The shear layer may be more readily explained with reference to the flow between two virtual concentric cylinders rotating in the same sense, but with different angular velocities. The extensive temperature distribution measurement in the conducting solid-liquid interface at the bottom wall configuration of the annular channel reveals the existence of zonal adverse temperature gradients inathin boundary layer at the base wall, and might be the additional cause of thermal oscillations in these regions.

In the pursuit of velocity measurements in TEMHD flow, the thermoelectric potential probe, innovated as a modification of the ordinary potential probe to suit the TEMHD environment, proved a very convenient method of measuring temperature and velocity simultaneously. The accuracy of such measurements is questionable at $B < B_{cr}$ for suppressing secondary flow, but was found to be excellent in the magnetic intensity range when the theory of such measurement is valid (balance of thermoelectric and motion induced e.m.f.) as found by calibrating these probes with pitot tubes and the mechanical pivoted float measurements, carried out simultaneously (the measurements with the mechanical probe were very convincing in the way of "seeing is believing"). The use of such thermoelectric potential probes is advantageous, as at higher magnetic fields the TEMHD induced fluid circulation in small temperature gradients becomes so small that pitot tubes and the mechanical measurements with the pivoted float are ineffective. The thermoelectric potential probes are ineffective at very low values of B, when current flow in the bulk of the fluid and the buoyancy driven thermal oscillations make the interpretation and compensation of the fluctuating data very tedious. However, with patience and digital data analysis in

computers, these would be useful in diagnosing the turbulent TEMHD flows. The thermoelectric potential probes, particular example cases of which are simple Hg electrode or copper electrode probes, (with level of purity of Hg maintained or the impurity level maintained uniform, and thermopower previously calibrated), have been preferred instead of using the alternatives, the thermo-anemometric or thermistor probes, because of easier calibration and control, and at least theoretically the thermoelectric potential probe is a better measuring device without having to disturb the measuring environment with heating current from external sources into the sensing element.

The effect of c, the fluid to wall conductance ratio, has been found to corroborate the theoretical characteristics in the measurements of the static pressure differences in the straight channels of circular and rectangular cross-sections. In velocity measurements in TEMHD fluid flow at large B, when there is no pressure gradient in the direction of flow, the parameter c is insignificant. The relevant c parameter in this case is governed by the sidewall secondary boundary layer thickness rather than the absolute channel dimension, and is virtually zero. Thus, even with a very thin wall, a low value of c can be maintained for a significantly large TEMHD induced flow at high B.

Though the TEMHD theory presented in this thesis leans very heavily on high Hartmann number operation, for obvious reasons of avoiding the complex secondary flow, the TEMHD experiments at lower magnetic fields, particularly in the range of 0.02 to 0.04 Tesla where the maximum TEMHD induced circulation was generated, shows the importance of studies in this range of the magnetic field. The transition regions of the velocity variations (magnitude at a particular location as well as the profile

variation with B) throws a significant light on the B_{cr} values when magnetic drag takes over from viscous drag (B_{cr_1}) and when buoyancy induced secondary flow is suppressed to a given degree (B_{cr_2}). The large fluid velocities at such low magnetic fields do confirm the fact that very efficient fluid circulation for heat exchange purposes is possible in liquid metal cooled fast nuclear reactors (fission) with weak permanent magnets installed around fluid channels. It seems very intriguing that,even with the theoretical realisation TEMHD induced velocity $\alpha\frac{1}{B}$ by Rex and others, the practical demonstrations of TEMHD pumping were attempted at 0.398 and 0.78 Tesla. No details of these TEMHD pumping demonstrations are available, and one can sense some amount of frustration in this earlier literature at the failure to demonstrate in practice the theoretically predicted flow at these magnetic field strengths, and the slow fluid circulation that could be obtained did not hold sufficient promise of efficient heat transfer. Instead of lower magnetic field operation, the remedy was sought in the use of materials with higher thermopower values (semimetals and semiconductors). It is particularly interesting to note that,in the models investigated, the maximum velocity occurs at $B \underset{\sim}{} 0.02/0.04$ Tesla, depending on the geometrical dimensions of the model, which happens to be the best estimated field strength in the interior of the earth's molten core,raising the possibility of magneto-strophic balance. Further comments on this possibility is presented in section 8.2.

The nondimensional parameters that arise in the investigation of TEMHD naturally consist of the conventional groups wellknown in ordinary MHD and buoyancy driven flows. They are the Hartmann number M, the interaction parameter N, Reynolds' number Re,

magnetic Reynolds' number R_m, Rayleigh number Ra and the Prandtl number Pr. Other secondary nondimensional groups can be suitably derived from those listed above, e.g. for Gr = Ra/Pr and $\frac{Re}{M^2}$. The new nondimensional parameter proposed in this thesis for characterising the TEMHD flow is $D = \frac{\alpha \Delta T}{\nu B}$, $\Delta T = T_1 - T_2$, which is a measure of the degree of thermoelectric and motion induced (at viscous and inertial force balance) e.m.f. ratio.

In Chapter 7, a new channel configuration has been proposed to utilise the large temperature gradients in the lithium blanket of a TOKAMAK type of magnetically confined TNR. The spiral channel structure has been basically considered from the point of view of steady state operation, but may be also used during the first few minutes of the off time in the pulse type mode of operation. The proposed scheme utilises a small portion of the energy already available in the lithium blanket itself to circulate the fluid, and the heat transfer characteristic is improved by convection. The large temperature gradient also might offer a possibility of isotope separation in lithium (Ott et al, 1964) and segregation of tritium, details of which can be worked out. The TEMHD pumping in the spiral channel has the advantage of reducing the stress in the thin metal conducting channel walls without having to seek a new insulating material compatible with the operation in contact with lithium, over and above that of low additional pumping power that might be necessary at a higher first wall surface density of heat flow. The basic spiral channel may be modified to promote turbulent mixing at the first wall, where ordinary MHD duct flows would make the fluid stagnate, and thus provide very efficient heat extraction. Probably the final arrangement in the blanket would

be a He cooled outer channel near the superconducting magnets, an intermediate lithium spiral channel in the mid-radial space, and a second lithium spiral channel converging in cross-section towards the first wall, to ensure very effective heat extraction from the TNR blanket.

8.1.2 Further comments on the experimental work (a critique)

The experimental investigation in TEMHD reported in this thesis has been very restrictive in the sense that the experimental investigation was confined to the realm of uniform and steady state only, though a few instances of transient processes (build-up and decay with time) and effects of non-uniformity have been indicated. The detailed investigation of nonuniform and unsteady motion has been left out. This is justifiable considering the reality of understanding the steady state operation first before groping in the uncertainty of the complex flow. Much time was spent in the repair of mercury leaks, particularly in the hot environment, and the heater coils, and in cleaning the mercuy by the procedure described in Chapter 3. This may be considered as a necessary wastage, and in the limited time further investigation in TEMHD were severely restricted. The construction of an experimental rig to verify the theoretical prediction of no net flow along the straight channel of circular cross-section with a second harmonic temperature distribution around the periphery had to be abandoned. However, it may be noted that this experiment would have served only academic interest and could be termed as negative experimentation as it would prove that no TEMHD induced net flow is possible in such a configuration. Thus the effort necessary for such experimentation was not felt to be justified.

It would have been otherwise interesting to measure the internal stirring, even though the net flow is zero.

The measurement of secondary flow due to centrifugal and buoyancy induced flow in the annular channels has only been attempted in a casual way; the few measurements that have been reported in this thesis of secondary flow and the free surface profile of Hg do justify the neglect of secondary flow at high Hartmann number.

During the final stage of experimentation, some time has been spent in recording the vortex and wavy motions in the open top annular channels. The peculiarity of the various vortex flow patterns ('free vortex' in the insulated bottom channel core flow; forced vortex and the dramatic higher order vorticity i.e. more than forced vorticity $\omega \propto r^n$, $n > 0$, in the all-conducting wall and the mixed interfacial conductivity at the base wall configurations) have been very easily and convincingly demonstrated, using the paddle type vorticity probe. The apparently very peculiar case of higher order vorticity ($\omega \propto r^n, n > 0$, that has been recorded in movie film is not considered peculiar at all if the temperature distribution at the solid-liquid interface, and the corresponding velocity profiles are compared. The velocity profile has a steep slope starting from a radial position away from the axis (at conductivity transition boundary for the channel with the base wall interface of mixed conductivity), giving a higher order vorticity than the forced vorticity which corresponds to the uniform slope (positive) of the velocity profile from the axis. At low magnetic fields, TEMHD circulation could be made turbulent by increasing the temperature gradient. The turbulent regime was attained through the intermediate stages when streets of longitudinal

vortex rolls and counter-rolls on the top free surface of Hg could be observed in the annular channel experiments. The existence of very slowly rotating wave motion could be demonstrated at the free surface and in oscilloscope recordings, but the recording of these phenomena photographically proved difficult due to the necessity of operating a rotoscope running synchronised to the average fluid rotational speed. The finalisation of these records are left out of this thesis, and will be reported elsewhere. By adjusting the TEMHD parameters, standing waves, eastward or westward drift of waves could be demonstrated. This showed that these wave motions and drifts are general characteristics of all rotating flows (TEMHD induced rotation,in this case,with stationary sidewall cylinders), irrespective of the type of driving force (TEMHD, ordinary MHD or mechanically rotated cylinders).

8.2 Scope for Further Investigations in TEMHD

It has been remarked at the outset of this chapter that the TEMHD system holds no promise as an efficient energy conversion device unless suitable materials are found. However, the investigation in TEMHD reported in this thesis definitely vindicates the worth of exploiting this effect in the metallurgical refinement processes and in the lithium blanket of TNRs. The TEMHD stirring is of central importance in these applications. The academic interest in TEMHD effect should be stimulated from the fact that these interactions are significant, being experimentally measurable under certain conditions, and should not be ignored in the analysis of ordinary MHD in nonisothermal environments at a material property (thermoelectric) sharp

transition interface. It is therefore expected that some attention will be given to further investigation in TEMHD.

To finalise the geometry of the spiral channel module of the lithium blanket, one has to solve the problems of entry and exit of fluid in thermal and magnetic fields, and also the starting and decay processes with time. These probably would be based more or less on numerical solution of the coupled thermal and MHD equations on digital computers rather than through exact analytical solutions or direct experimentation. This area of investigation has been completely ignored in this thesis in order to complete the basic steady state study with a bias towards experimentation. If further TEMHD experiments are conducted to investigate the transient (time dependent), nonuniform TEMHD interactions, it would be advisable to employ multichannel automatic data logging on magnetic tapes so that simultaneous measurements of temperature and velocity at different locations can be fed straight into the computer for data analysis and interpretation. The autocorrelation and cross-correlation of the fluctuating signals magnitude and phase angle would then give better understanding of the fluid motion in rolls under the influence of the temperature gradient, rotation and the magnetic field, and throw some light on the waves and the exact controlling mechanism of their drift. Probably the thermoelectric potential probe would play an important role in such simultaneous measurement of temperature and velocity in TEMHD. Further thoughtsought to be given to the spiral channelsin improving the convective heat transfer process in the lithium blanket by suitable nesting of the spiral channels to incorporate some 'flow coupler' action, so that stress on the sidewalls in the case where external pumping is necessary could

also be further reduced. It may be recalled that the high pumping requirement,due to ordinary MHD effects in the lithium blanket that has so far been a stumbling block, is due to the easy return path(in the conducting wall partition of the torus) in the conducting walls,of the motion induced current flow in the bulk of the liquid. Therefore the idea of incorporating 'flow coupler' circuits is to be assessed critically. The heat transfer processes require elaborate further consideration incorporating neutron heating (most important), radiative heat transfer and heating effects of Bramsstrahlung and α particle energy distribution in the lithium blanket.

The maximum circulation in the annular channel experiments that has been observed at very low magnetic fields of B ∿ 0.02 to 0.04 Tesla raises the question of the importance of TEMHD processes in the maintenance of terrestrial magnetism, though length scales are different. In proposing a TEMHD theory of earth's magnetism, at least the basic origin of the magnetic field is not a matter of speculation as in the fluid motion based linear, weakly asymmetrical or turbulent dynamo theory. It is interesting to note that such a possibility has been explored earlier by Elsasser (1939) and discounted by Inglis (1955).

The author is of the opinion that the thermoelectric properties of materials are not exclusive to the solid or liquid state of the materials, but being an intrinsic property should exist in the gaseous plasma state as well. How significant would be the TEMHD interaction in nonisothermal conducting gaseous environments in enclosures with metallic interface is highly speculative. However, one should not ignore the complex situation in boundary layers at the electrode walls of the

plasma MHD generators, where unexplained large potential drops have been observed due to the nonisothermal nature of the boundary layer along the conversion channel.

The whole basic structure of the TEMHD theory as presented in this thesis is based on low magnetic Reynolds' number. However, if in the lithium blanket of the TNR magnetic self-excitation is made possible through turbulence and α-effect dynamo mechanism, then it would be essential to incorporate induced magnetic field effects into consideration.

Finally, with all humility, it may be pointed out that thermoelectric magnetohydrodynamics forms only a part of the more general galvano-thermo-magnetohydrodynamics, the only other aspect of which, the Hall effect-magnetohydrodynamics interaction has been previously given some importance and attention in plasma magnetohydrodynamics. However small the order of magnitude of the mutual interactions of the thermal, flow, electric and magnetic fields may be, the exact analysis of the overall composite interaction will surely be very complex.

REFERENCES

ACHESON, D.J., (1972)
The critical level for hydrodynamic waves in a rotating fluid.
Journal Fluid Mech., 53, P3, 401-415

ALFVÉN, H. (1950)
Cosmical electrodynamics (2nd ed. 1963)
Clarendon Press, Oxford.

ALTY, C.J.N. (1966)
Magnetohydrodynamic duct flow.
Ph.D. thesis, University of Cambridge.

ALTY, C.J.N. (1971)
Magnetohydrodynamic duct flow in uniform transverse magnetic fields at arbitrary orientation.
Journal Fluid Mech., 48, P3, 429-461.

ARTSIMOVICH, L.A.(1972)
Tokamak devices .
Nuclear Fusion, 12, 215-252.

BATCHELOR, G.K. (1954)
Heat transfer by free convection across a closed cavity between vertical boundaries at different temperatures.
Quart. Applied Math., XII, N3, 209-233.

BAYLIS, J.A. (1966)
Fully developed secondary flow on magnetohydrodynamics.
Ph.D. thesis, University of Cambridge.
(Ref. also JFM 48, P3, 417-428, 1971).

BISHOP, E.H. and CARLEY, C.T. (1966)
Photographic studies of natural convection between concentric cylinders.
Proc. 1966 Heat Trf.Fluid Mech. Inst., 63-78.

BRAGINISKII, S.I. (1959)
Magnetohydrodynamics of weakly conducting fluids.
Zh. Eksp. Theor. Fiz., 37 (Soviet Phys.-JETP 1960), 10, N5, 1005-1014.

BRADLEY, C.C. (1962)
The experimental determination of the thermoelectric power in liquid metals and alloys.
Phil. Mag., 7, 1337-1347.

BRANOVER, G.G. (1967)
Suppression of turbulence in pipes with transverse and longitudinal magnetic fields.
MHD (Russian) 3, 2, 107;(156-157).

BUSSE, F.H. (1970)
Thermal instabilities in rapidly rotating systems
Journal Fluid Mech., 44, P3, 441-460.

CACHARD, M. de and CAUNES, P. (1969)
Thermosiphon à sodium pour irradiation en pile d'éléments combustible.
CEA, Centre d'Études Nucleaires Grenoble Rep., Pi(R), 472-385/69, 1-10.

CARLSON, G.A. and HOFFMAN, M.A. (1971)
Effect of magnetic fields on heat pipes.
Lawrence Radiation Laboratory Rpt. UCRL-72060.

CARLSON, G.A. (1974)
Magnetohydrodynamic pressure drop of lithium flowing in conducting wall pipe in a transverse magnetic field - theory and experiment.
Lawrence Radiation Laboratory Rpt. UCRL-75307.

CHANDRASEKHAR, S. (1961)
Hydrodynamic and hydromagnetic stability.
Clarendon Press, Oxford.

CHANDRASEKHAR, S., ELBERT, D.D. and LEBOVITZ, N.R. (1961)
The stability of viscous flow in a curved channel in the presence of amagnetic field.
Proc. Royal Soc., A264, 155-164.

CHANG, C.C. and LUNDGREN, T.S. (1961)
Duct flow in magnetohydrodynamics.
Zeit. für Angew. Math. und Phys. (ZAMP) 12 (2), 100-114.

CHIANG, C.K. (1974)
The absolute thermopower of some low temperature thermocouple wires in high transverse magnetic fields.
Rev. Sci. Inst. 45, N8, 985-989.

CHIANG, D. and LUNDGREN, T.S. (1967)
Magnetohydrodynamic flow in rectangular duct with perfectly conducting electrodes.
Zeit. für Angew. Math. und Phys. (ZAMP) 18, 92-105.

COWLING, T.G. and SINGH, K.R. (1963)
Thermal convection in magnetohydrodynamics II. Flow in a rectangular box.
Quart. Journal Mech. Appl. Math., 16, 17-31.

COWLING, T.G. (1976)
Magnetohydrodynamics.
Adam Hilgers (1P).

CHRISTIAN, J.W., JAN, J.P., PEARSON, W.B. and TEMPLETON, I.M. (1958)
Thermoelectricity at low temperatrues VI. A redetermination of the absolute scale of thermoelectric power of lead.
Proc. Royal Soc., A245, 213-221.

CRISP, V.H.C., CUSACK, N.E. and KENDALL, P.W. (1970)
The effect of volume changes on the absolute thermoelectric power of some liquid metals.
J. Phys. C. Metal Phys. Suppl. N1. S102-S108.

CULCINSKI, G.L. and CONN, R.W. (1974)
Conceptual design of a 5000 MW (th) D-T Tokamak reactdr.
Fusian Reactor Design Problems; Culham Workshop, 51-77.
IAEA, Vienna.

CUSACK, N. and KENDALL, P. (1958)
The absolute scale of thermoelectric power at high temperature.
Proc. Phys. Soc., 72, 898-901.

CUSACK, N.E. (1963)
The electronic properties of liquid metals.
Rep. Prog. Phys., 26, 361-409.

CUSTER, J.R. and SHAUGHNESSY, E.J. (1977)
Thermoconvective motion of low Prandtl number fluids within a horizontal cylindrical annulus.
Trans. ASME, JHT, 99, 596-602.

DAVIS, G. de VAHL and THOMAS, R.W. (1969)
Natural convection between concentric vertical cylinders.
Phys. Fluids, 12, Supplement II, 198-207.

DONNELLY, R.J. (1958)
Experiments on the stability of viscous flow between rotating cylinders I. Torque measurements.
Proc. Royal Soc. A246, 321-325.

DUTTA GUPTA, P.B. (1977)
Thermoelectromagnetohydrodynamics I.
Research Rept., Dept. of Engineering, University of Warwick.

DUTTA GUPTA, P.B. (1978a)
Thermoelectromagnetohydrodynamics II.
Research Report, Dept. of Engineering, University of Warwick.

DUTTA GUPTA, P.B. (1978b)
Movie film record of TEMHD experiments in annular channels.
University of Warwick (Library).

DWYER, O.E., HLAVAC, P.J. and NIMMO, B.G. (1977)
Eddy diffusivity of heat transfer in the radial direction for turbulent flow of mercury in annuli.
Int. Journal Heat Mass Trf., 20, 141-151.

ELDER, J.W. (1965)
Laminar free convection in a vertical slot.
Journal Fluid Mech., 23, P1, 77-98.

ELSASSER, W.M. (1939)
On the origin of the earth's magnetic field.
Phys. Rev., 55, 489-498.

ENGLISCH, E. (1893)
Thermoelektrische Untersuchungen.
Ann. der Phys. und Chemie, 50, 88-110.

FIELDER, M.L. (1967)
The absolute thermoelectric powers of some liquid alloys.
Adv. Phys., 16, N62, 681-687.

FOWLIS, W.W. (1970)
Techniques and apparatus for the fast and accurate measurement of fluid temperature and flow speed fields.
Rev. Sci. Instr., 41, N4, 570-576.

FRAAS, A.P. (1972)
Analysis of a recirculating lithium blanket designed to give a low MHD pumping power requirement.
Oak Ridge National Laboratory Report. ORNL-TM-3756.

FUJII-E, Y and SUITA, T. (1974)
Blanket cooling with liquid metal as working fluid.
Fusion reactor design problems; Culham workshop, 347-362.
IAEA, Vienna.

FUSSEY, D.E. (1969)
Magneto-viscous effects in combustible plasma.
Ph. D. thesis, University of Warwick.

GARDNER, R.A., UHERKA, K.L. and LYKOUDIS, P.S. (1966)
Influence of a transverse magnetic field on forced convection liquid metal heat transfer.
AIAA Journal, 4, N3, 848-852.

GARDNER, R.A. and LYKOUDIS, P.S. (1971)
Magneto-fluid-mechanic pipe flow in a transverse magnetic field, Part 2. Heat transfer.
Journal Fluid Mech., 48, P1, 129-141.

GEL'FGAT, Yu. M., DOROFEEV, V.S. and SHCHERBININ, E'. V. (1971)
Experimental investigation of the velocity structure of a magnetohydrodynamic flow in a rectangular channel with two conducting walls.
(MHD 7,1,31) MHD, 7,1,26-29.

GILL, A.E. (1974)
A theory of thermal oscillations in liquid metals.
Journal Fluid Mech., 64, P3, 577-588.

GNATYUK, V.V. and PARAMONOVA, T.A. (1971)
Effect of the conductivity of the walls on the velocity profiles in a circular tube.
(MHD 7,1,145), MHD 7,1, 126-128.

GOLD, R.R. (1967)
Effect of wall conductance on MHD flow through finite cross-section channels.
AIAA Journal, 539-544.

GROOT, S.R. de and MAZUR, P. (1962)
Nonequilibrium thermodynamics.
North Holland Pub. Co., Amsterdam.

GUPTA, A.S. (1969)
Combined free and forced covection effects on the magnetohydrodynamic flow through a channel.
Zeit Ang. Math. Phys. (ZAMP), 20, 506-513.

HANCOX, R. and BOOTH, J.A. (1971)
The use of liquid lithium as coolant in a toroidal fusion reactor, Part II. Stress limitations.
Culham Laboratory Report (UKAEA) CLM-R 116.

HEISER, W.H. and SHERCLIFF, J.A. (1965)
A simple demonstration of Hartmann layer.
Journal Fluid Mech., 22, P4, 701-707.

HIDE, R. and ROBERTS, P.H. (1962)
Some elementary problems in magnetohydrodynamics.
Adv. Appl. Mech., V, VII, 215-316.

HIDE, R. (1971)
On geostrophic motion of a nonhomogeneous fluid.
Journal Fluid Mech., 49, P4, 745-751.

HOFFMAN, M.A. and CARLSON, G.A. (1971)
Calculation techniques for estimating the pressure losses for conducting fluid flows in magnetic fields.
Lawrence Radiation Laboratory Rpt., UCRL-51010.

HOLROYD, R.J. (1975)
Magnetohydrodynamic duct flows in nonuniform magnetic fields.
Ph.D. thesis, University of Cambridge.

HUEBNER, R.P. (1966)
Phonon scattering by lattice vacancies in platinum.
Physical Rev., 146, N2 490-501.

HUNT, J.C.R. (1965)
Magnetohydrodynamic flow in rectangular ducts.
Journal Fluid Mech., 21, P4, 577-590.

HUNT, J.C.R. and STEWARTSON, K. (1965)
Magnetohydrodynamic flow in rectangular ducts II.
Journal Fluid Mech., 23, P3, 563-581.

HUNT, J.C.R. (1966)
On the stability of parallel flows with parallel magnetic fields.
Proc. Royal Soc., A293, 342-358.

HUNT, J.C.R. (1967)
Some aspects of magnetohydrodynamics.
Ph.D. thesis, University of Cambridge.

HUNT, J.C.R. and LEIBOVITCH, S. (1967)
Magnetohydrodynamic flow in channels of variable cross-section with strong transverse magnetic fields.
Journal Fluid Mech., 28, P2, 241-260.

HUNT, J.C.R. (1969)
A uniqueness theorem for magnetohydrodynamic duct flows.
Proc. Camb. Phil. Soc., 65, 319-327.

HUNT, J.C.R. and SHERCLIFF, J.A. (1971)
Magnetohydrodynamics at high Hartmann number.
Ann. Rev. Fluid Mech., 3, 37-62.

HUNT, J.C.R. and HANCOX, R. (1971)
The use of liquid lithium as coolant in a toroidal fusion reactor, Part I. Calculation of pumping power.
Culham Laboratory Report (UKAEA) CLM-R 115.

HUNT, J.C.R. and HOLROYD, R.J. (1977)
Applications of laboratory and theoretical MHD duct flow studies in fusion reactor technology.
Culham Laboratory Report (UKAEA) CLM-R 169.

HURLE, D.T.J., JAKEMAN, E., JOHNSON, C.P. (1974)
Convective temperature oscillations in molten gallium.
Journal Fluid Mech., 64, P3, 565-576.

IHARA, S., TAJIMA, K. and MATSUSHIMA, A. (1967)
The flow of conducting fluids in circular pipes with finite conductivity under uniform transverse magnetic fields.
Journal Appl. Mech. V34, Trans. ASME, V89, Series E, 29-36.

INGLIS, D.R. (1955)
Theories of the earth's magnetism.
Rev. Mod. Phys., 27, 212-248.

INTERNATIONAL CRITICAL TABLES of numerical data (Physics, Chemistry and Technology), Vol. VI.
N.R.C., McGraw Hill Book Co. Inc., New York.

IOANNIDES, P., NGUYEN, V.T. and ENDERBY, J.E. (1975)
Measurement of the absolute thermoelectric power of liquid conductors enclosed in metallic tubes.
J. Phys. E: Scientific Instruments, 8, 315-316.

KAMMASH, T. (1975)
Fusion reactor physics: principles and technology.
Ann Arbor Science, 1425 P.O., Ann Arbor, MICH 48106.

KAYE, G.W.C. and LABY, T.H. (1973)
Tables of physical and chemical constants and some mathematical functions.
Longman Press (14 edition).

KUBLANOV, V. and EROKHIN, A. (1974)
On metal motion in a stationary weld pool under the action of electromagnetic forces and gas flow velocity head in arc welding.
Int. Inst. Welding Rpt. (USSR National Committee on Welding, Moscow, 1974).

KULIKOVSKII, A.G. and REGIRER, S.A. (1965)
Influence of the walls on overheating instability in a magneto-hydrodynamic channel.
(Zhurn. Pri. Mekh. Tech. Fiz. N5, 34-39), Journal Appl. Mech. Tech. Phys., N5, 22-25.

KULIKOVSKII, A.G. (1968)
On slow steady flows of conducting fluid with high Hartmann numbers.
Izv. Akad. Nauk. SSSR Mekh. Zhid. i Gaza, 2, 3-10.

KULIKOVSKII, A.G. (1973)
Flows of a conducting incompressible liquid in an arbitrary region with a strong magnetic field.
Izv. Akad. Nauk. SSSR Mech. Zhid. i Gaza, 8, 3, 144 (Fluid dynamics, 8,3, 462-467. Jan. 1975)

LANDECKER, K. (1977)
On power-generating thermojunctions with radial flow of current
Solar energy, 19, 439-443.

LANDER, J.J. (1948)
Measurement of Thomson coefficients for metals at high temperatures and of Peltier coefficients for solid-liquid interfaces of metals.
Phys. Rev. 74, N4, 479-488.

LAUBITZ, M.J. (1969)
Transport properties of pure metals at high temperatures, II. Ag, Au.
Can. Journal Phys., 47, 2633-2644.

LEHNERT, B. (1952)
On the behaviour of an electrically conducting liquid in a magnetic field.
Ark. för Fysik., 5, 69-90.

LEHNERT, B. (1955)
An instability of laminar flow of mercury caused by an external magnetic field.
Proc. Royal Soc., A233, 299-302.

LEHNERT, B. and LITTLE, N.C. (1957)
Experiments on effects of inhomogeneity and obliquity of a magnetic field in inhibiting convection.
Tellus, IX, 97-103.

LUEBKE, E.A. and VANDENBERG, L.B. (1953/4)
Compact reactor power plant with combination heat exchanger-thermoelectric pump.
Knolls Atomic Power Laboratory Rpt., May (U.S. Patent 2748710, 5th June, 1956).

LYON, R.N. (ed.) (1950)
Liquid-metals Handbook. (NAVEXOS P 733).
Atomic Energy Commission, Dept. of the Navy, Washington D.C.

MAKAROV, V.S. and CHERKASSKII, A. Kh. (1969)
Pressure-consumption characteristic and efficiency of a thermo-electromagnetic pump.
(MHD, 5,3, 127-131) MHD 5,3, 84-88.

MALCOLM, D.G. (1968)
Thermo-anemometry in magnetohydrodynamics.
Ph.D. thesis, University of Warwick.

MALCOLM, D.G. (1970)
An investigation of the stability of a magnetohydrodynamic shear layer.
Journal Fluid Mech., 41,3,531-544.

MARWAHA, A.S. and CUSACK, N.E. (1966)
The absolute thermoelectric power of liquid metals.
Phys. Lett., 22, N5, 556.

MARWAHA, A.S. (1967)
The absolute thermoelectric power of polyvalent liquid metals.
Adv. Phys., 16, N62, 617-627.

MOFFATT, H.K. (1964)
Electrically driven steady flows in magnetohydrodynamics.
Proc. 11th Int. Cong. Appl. Mech., Munich, 946.

MOISEEV, N.N. and PETROV, A.A. (1969)
The calculation of free osillations of a liquid in a motionless container.
Adv. Appl. Mech., 9, 91-154.

MORI, Y, UCHIDA, Y. and UKON, T. (1971)
Forced convective heat transfer in a curved channel with a square cross-section.
Int. Journal Heat Mass Trf., 14, 1787-1805.

MURGATROYD, W. (1951)
Improvements in or relating to heat transfer systems.
U.K. Patent Appl. 20911/51.

NIBLETT, E.R. (1958)
The stability of Couette flow in an axial magnetic field.
Can. Journal Phys., 36, 2, 1509-1525.

OTT, A. and LUNDÉN, A. (1964)
Thermal diffusion of isotopes in pure molten lithium metal.
Zeit. Naturförschung, 19A, 822-823.

OSTERLE, J.F. and ANGRIST, S.E. (1964)
The thermoelectric-hydromagnetic pump.
Trans. A.S.M.E., C, JHT, 86, 166-168.

PERLOW, M.A. and DAVIS, K.A. (1965)
Thedevelopment of the SNAP-10 thermoelectric pump.
Space Nuclear Technology Trans. Amer. Nucl. Soc., 8, 160-161;
(also Electrical Rev., 178, 416 (1966)).

POST, R.F. (1976)
Nuclear Fusion.
Annual Rev. Energy, 213-255.

REX, von D. (1961)
Thermoelektrische Pümpen für flüssige Metalle.
VDI Z., 103 (1), 17-19.

ROBERTS, P.H. (1967)
Singularities of Hartmann layers.
Proc. Royal Soc. A300, 94-107.

ROBERTS, R.B. (1977)
The absolute scale of thermoelectricity.
Phil. Mag., 36, N1, 91-107.

SHERCLIFF, J.A. (1953)
Steady motion of conducting fluids in pipes under transverse magnetic fields.
Proc. Camb. Phil. Soc., 49, 136-144.

SHERCLIFF, J.A. (1955)
Problems in magnetohydrodynamics.
Ph.D. thesis, University of Cambridge.

SHERCLIFF, J.A. (1956)
The flow of conducting fluids in circular pipes under transverse magnetic fields.
Journal Fluid Mech., I, 644-666.

SHERCLIFF, J.A. (1962)
The theory of electromagnetic flow measurement.
Cambridge University Press.

SHERCLIFF, J.A. (1964)
A textbook of magnetohydrodynamics.
Pergamon Press.

SHERCLIFF, J.A. (1977)
The current-content of Hartmann layers.
Zeit. Ange. Math. Phys. (ZAMP), 28, 449-466.

SHERCLIFF, J.A., ALTY, C.J.N. and DUTTA GUPTA, P.B. (1978)
Thermoelectric MHD.
Second Bat-Sheva Seminar on MHD.

SHERCLIFF, J.A. (1978)
Personal communication.

SHERCLIFF, J.A. (1979a)
Thermoelectric magnetohydrodynamics.
Journal Fluid Mech., 91, P2, 231-252.

SHERCLIFF. J.A. (1979b)
Thermoelectric magnetohydrodynamics in closed containers.
Phys. Fluids, 22 (4), 635-640.

SMITHELS, C.J. (ed.),(1976)
Metals reference book.
Butterworths, London.

STANBRIDGE, J.R., CARRUTHERS, H.M., KEEN, B.A. and SHOTTER, H.A. (1974)
Design of stainless steel blanket cells for a fusion reactor.
Culham Laboratory Report (UKAEA) CLM- R 127.

TAYLOR, J.B. (1963)
The magnetohydrodynamics of a rotating fluid and the earth's dynamo problem.
Proc. Royal Soc., A274, 274-283.

TRODAHL, H.J. and BLATT, F.J. (1969)
Quantum oscillations in the Peltier effect of Zn.
Phys. Rev., 180, N3, 706-715.

VAHL-DAVIS, G. de and THOMAS, R.W. (1969)
Natural convection between concentric vertical cylinders.
Phys. Fluids, 12, Supplement II, 198-207.

WALKER, J.S. and LUDFORD, G.S.S. (1975)
Magnetohydrodynamic flow in circular expansions with thin conducting walls.
Int. Journal Eng. Sci., 13, 3, 261-269.

WERNER, R.W., CARLSON, G.A., HOVINGH, J., LEE, J.D. and PETERSON, M.A. (1974)
Design studies of mirror machine reactors.
Fusion Reactor Design Problems; Culham Workshop, 171-187.
IAEA, Vienna.

WEAST, R.C. (ed.) (1978)
Handbook of Chemistry and Physics.
C.R.C. Press, Palm Beach, Florida 33409.

WOODS, L.C. (1975)
Thermodynamics of fluid systems.
Clarendon Press, Oxford.

WRIGHT, J.K. (1963)
A temperature instability in magnetohydrodynamic flow.
Proc. Phys. Soc., 81, 498-505.

YOUNG, F.J., HOLCOMB, R.J. and FRAAS, A.P. (1975)
MHD test of a one-sixth scale model of a CTR recirculating lithium blanket.
Oak Ridge Nat. Laboratory Rpt., ORNL TM 4818.

ZIMAN, J.M. (1961)
A theory of the electrical properties of liquid metals I. The monovalent metals.
Phil. Mag., 6, 1013-1034.

ZIMAN, J.M. (1967)
The electron transport properties of pure liquid metals.
Adv. Phys., 16, N62, 551-580.

NOTATION

All notations are explained, as they appear in the text. The general scheme of notation is as follows:-

Vector quantities are shown with a base bar, e.g.

$\underline{B}$ magnetic flux density

$\underline{E}$ electric field

$\underline{j}$ electric current density

$\underline{v}$ fluid velocity

Suffixes indicate quantities as follows:-

C in the core; corresponding to cosine function (in Fourier expansion)

Cr critical value

Cu corresponding to copper

f in the fluid

Hg corresponding to mercury

ijkmn running (integer) variables 1,2,3,.....

r radial component

n normal component

s in the solid, along curves, corresponding to sine function (in Fourier expansion)

w in the wall

x,y,z Cartisian components

θ azimuthal, toroidal component

φ poloidal component

Symbols

A area of cross-section

B magnetic flux densty

C fluid to wall conductance ratio

D nondimensional TEMHD number = $\frac{\alpha T}{\nu B}$

F body force,(e.g. gravitational), arbitrary function

Gr Ra/Pr

$H(r,\theta)$ two dimensional magnetic stream function

I electric current

K thermal conductivity

J_n, Y_n Bessel functions

L dimensional size; length, width, height

M Hartmann number $(\sqrt{\frac{\sigma}{\eta_v}})LB$

N interaction parameter $\frac{M^2}{Re}$

O order of magnitude

P resistance

Pe Péclet number

Pr Prandtl number

Q heat

R radius

Ra Rayleigh number

Re Reynolds number

R_m magnetic Reynolds number

S curvilinear co-ordinate

S_e entropy

T temperature

T_m $(T_2 \sim T_1)/_2$

T_{av} $(T_1 + T_2)/_2$

V mean velocity

W volume

XYZ functions of x,y,z; Cartesian co-ordinates

a channel half width

c fluid to wall conductance ratio $\frac{\sigma_f L_f}{\sigma_w t_w}$

c_p specific heat

e exponential function

f arbitrary function

g gravitational acceleration

h height

j electric current density

k thermal conductivity

n normal direction

p fluid pressure

q heat flow rate/time/volume

r radial co-ordinate

s curvilinear co-ordinate (along solid-liquid interface)

t time

t_w wall thickness

u perturbation velocity

v velocity

w vorticity

x,y,z Cartesian co-ordinates

Γ gamma function

Δ difference

Ω rotational angular velocity

Σ volume

$\textcircled{T}, \textcircled{H}$ perturbation in temperature

α thermoelectric power

β volume expansion coefficient

δ boundary layer thickness

ε energy

ϕ electrical potential

ϕ_α pseudo potential corresponding to thermoelectricity

ϕ^+ $\phi + \phi_\alpha$

θ polar co-ordinate (azimuthal); also toroidal co-ordinate

η_v fluid viscosity

μ permeability (magnetic) of medium $\equiv \mu_{vacuum}$

ρ fluid density

σ electrical conductivity

σ_s surface tension

φ poloidal co-ordinate

ν kinematic viscosity (viscous diffusivity)

η magnetic diffusivity

χ thermal diffusivity

ω angle of inclination; also frequency

Ψ stream function (velocity)

Operators

∇ gradient, divergence

∇^2 $\nabla.\nabla$ $(\equiv \partial^2/\partial x^2+\partial^2/\partial y^2+\partial^2/\partial z^2$ in three dimensional Cartesian co-ordinate system

$\frac{\partial}{\partial x}$ partial derivative w.r.t x

$\frac{d}{dx}$ derivative w.r.t x (primes have been used also)

$\frac{\partial(X,Y)}{\partial(r,\theta)}$ Jacobian notation

N.B. All symbols with numerical suffix refer to arbitrary constants

APPENDIX

TABLE 1

Physical properties of some liquid metals (Discrepancies of data in various literature ignored)

Element	M.P. °C	B.P. °C	Density Kg/m^3 (10^3)	Viscosity $Pa\ s$ (10^{-3}) $\frac{Ns}{m^2}$ (10^{-3})	Cp kJ/ Kg°K	K $\frac{W}{mk}$	Resistivity μΩ-m	Volume expansion β(10^{-6})	α, absolute thermo-power μV/°K at 0° C and (T°C)
Bi	271	1480	10	1.62 (315°C)	150	16.4	1.16	40	-
Cs	29.7	700	1.87	0.607 (50°C)	300	-	0.21	291	-0.9, +6.4 (30°C)
Ga	29.8	2250	6.093 (32°C)	0.59 (1000°C)	-	-	0.24	55	-
Hg	-39	357	13.57 (10°C)	1.59 -	138	8	0.958	180	-4.49
K	64	760	→ 0.807 (149°C)	0.37 -	796	45	0.18	249	-12.9, -14 (65°C)
Li	179	1318	→ 0.5 (204°C)	0.59	4187	38	0.452	168	+10.6, +21.7 (180°C)
Na	97	884	→ 0.9 (204°C)	0.43	1340	80	0.136	213	-5.18, -7.9 (100°C)

(continued)

APPENDIX Table 1 (continued)

Physical properties of some liner materials

	Cu	Fe	Mo	Ni	Nb	Pd	Pt.	Ti	W	V	Zr
M.P. (^{o}C)	1083	1537	2600	1453	2468	1552	1769	1670	3380	1860	1860
Density Kg/m^{3} (10^{3})	8.96	7.87	10.2	8.9	8.6	12	21.45	4.5	19.3	6.1	6.49
Thermal conductivity W/mk	380	50	110	72	44	55	55	13.5	127	22	16
Resistivity $\mu\Omega$-m (500^{o}C)	0.046	0.56	0.176	0.342	0.145 (20^{o}C)	0.275	0.279	1.35	0.18	0.26 (20^{o}C)	0.446 (20^{o}C)
Expansion coefficient $\beta(10^{-6})$ at 500^{o}C	54	42	17	45.5	21 ($0-100^{o}$C)	37	29	28	14	25 ($0-100^{o}$C)	17.7 ($0-100^{o}$C)
α, absolute thermopower at 300^{o}K μV/^{o}K	1.83	15	5.57	-	-	-9.99	-5.28	-	1.07	_	9
at (T^{o}K)	6.91 (1300)	-9 (800)	17.16 (1000)	-18 (273)	-1.5 (500)	-61.48 (2000)	-31.23 (2000)	+7 (400)	19.6 (1400)	1.1 (400)	-6 (800)
					6 (1400)			-3 (950)		9.5 (1300)	

The thermoelectric voltage of various common commercial thermocouples. The reference junction is at 0°C.

Type	Combination
T	Copper-Constantan
J	Iron-Constantan
E	Chromel-Constantan
K	Chromel-Alumel
G*	Tungsten-$^{100}_{95}$W/$^{74}_{74}$Rhenium$_{26}$
C*	Tungsten-$^{100}_{95}$W/$^{95}_{5}$Rhenium$_{26}$
R	Platinum-$^{100}_{100}$Pt/$^{87}_{87}$Rhodium$_{13}$
S	Platinum-$^{100}_{100}$Pt/$^{90}_{90}$Rhodium$_{10}$
B	$^{94}_{94}$/$^{6}_{6}$ - $^{70}_{70}$/$^{30}_{30}$

Constantan 55Cu45Ni
(P) Chromel 90Ni10Cr
Alumel 94Ni3Mn2Al1Si
(X) Chromel 64Ni25Fe11Cr

Data for Nb. reference : {Carter R., Davidson A, Schroeder P. 1970 J. Phy Chem Sol. 31, 2374
{Raag V, Kowger H.V 1965 J. Appl Phy 36, 2045
Fe reference : Blatt F.J., Flood D.J., Rowe V., Schroeder P., Cox J.E. 1967 Phy Rev-Lett 18 395

Supplementary data of α vs T°K

Detailed température dependent physical properties of Hg and Cu: (Lyon, 1950, Marwaha, 1967) T in °C

Mercury	density	$13.546\ (1 - 0.00018(T-20)) \times 10^{3}\ Kg/m^{3}$
	dynamic viscosity	$1.550\ (1 - 0.00303\ (T-20)) \times 10^{-3}\ Ns/m^{2}$
	electrical conductivity	$1.044\ (1 - 0.00090\ (T-20)) \times 10^{6}\ S\ (\mho/m)$
	specific heat capacity	$1.391\ (1 - 0.00017\ (T-20)) \times 10^{2}\ J/Kg^{\circ}K$
	thermal conductivity	$8.694\ (1 - 0.00281\ (T-20))\ W/m^{\circ}K$
	absolute thermal power (at zero pressure)	$2.00 - 23.33 \times 10^{-3}\ (T + 273)\ \mu V/^{\circ}K$
Copper	electrical conductivity	$59.31\ (1 - 0.00403\ (T-20)) \times 10^{6}\ S\ (\mho/m)$
	thermal conductivity	$394\ (1 - 0.00031\ (T-20))\ W/m^{\circ}K$
	absolute thermopower	$0.05 + 5.45 \times 10^{-3}\ (T+273)\ \mu V/^{\circ}K$

Thermistor characteristic

	Po(To)	γ constant	Temperature range	Dissipation constant	Thermal time constant
Miniature bead (151-142)	4.7 KΩ (25°C)	3390	0°C to 125°C	0.7 mW/°C	5 sec
Bead (151-029)	2 KΩ(20°C)	3200	0°C to 300°C	1.2 mW/°C	19 sec

(continued)

Appendix
(continued)

Flowmeter calibration

Volume cc	Time/sec	Flow rate cc/sec	Signal/μV	Flow rate/signal cc/sec-μV
168	60	2.8	450	6.22
266.5	45.2	5.89	950	6.2
200	28	7.14	1160	6.16
230	13.7	16.8	2650	6.37
325.5	15	21.7	3500	6.2
329	12	27.4	4350	6.3

Selection of brazing alloys (Johnson Matthey Metals Limited (81 Hatton Garden, London, EC1P 1AE)

	Nominal composition	Melting range °C Solid	Liquid
'Easy-flo'	50% Ag: Cu: Cd: Zn	620	630
'Easy-flo' No.2	42% Ag: Cu: Cd: Zn	608	617
Silver-copper eutectic	72% Ag: Cu	778	778
Pallabraze 1090*	18% Pd: Cu	1080	1090
Ovobraze 1018*	30% Au: Cu	996	1018
'A' Bronze	96% Cu: Ni: Si	1090	1100
'B' Bronze	97% Cu: Ni: B	1081	1101

*Impurity level in these alloys, which are the most pure in the group, are as follows:-

Impurity	Al	Be	C	Cr	Mn	Ti	Zr	Sb	Bi
p.p.m	5	5	50	10	10	10	5	30	10

Impurity	Cd	Ca	Pb	Li	Mg	Sn	Zn	P
p.p.m	10	30	20	30	30	30	10	100

Plate P.1 The experimental set-up for the circular cross-sectional straight channel TEMHD experiment (Channel II)

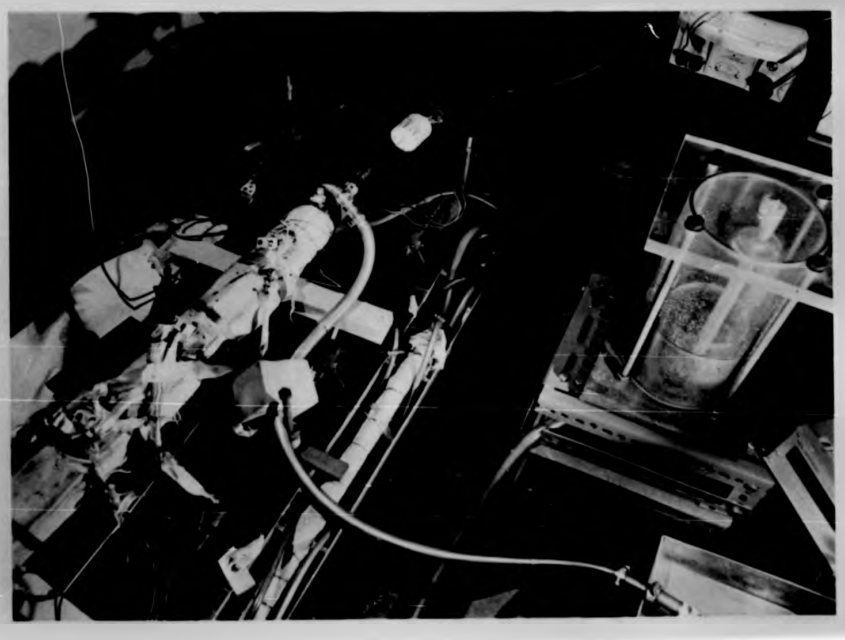

Plate P.2 The circular cross-sectional straight channels. The thermal lagging completely removed and heater insulation partly opened for Channel II.

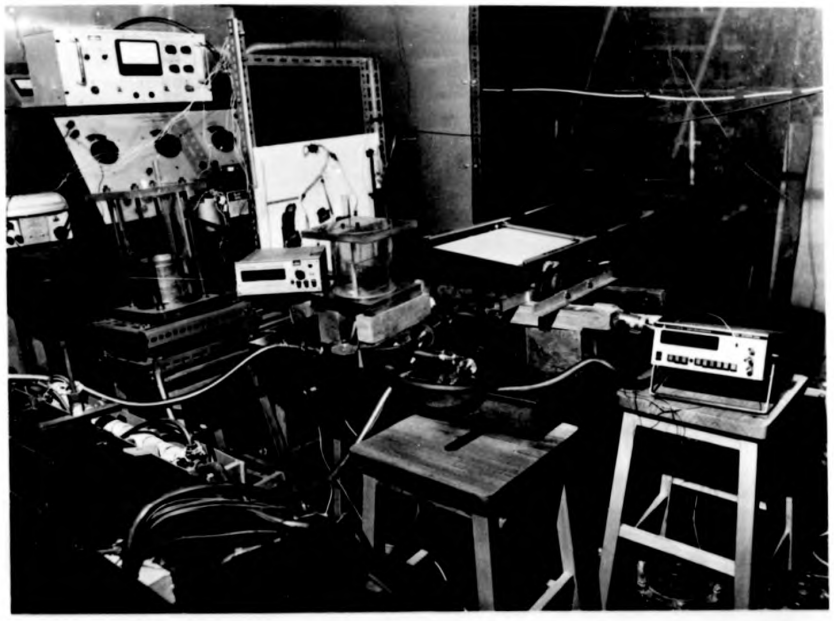

Plate P.1 The experimental set-up for the circular cross-sectional straight channel TEMHD experiment (Channel II)

Plate P.2 The circular cross-sectional straight channel. The thermal lagging completely removed and heater insulation partly opened for Channel II.

Plate P.3 The etch marks on the Mark I annular channel inner surface at the outer periphery.

Plate P.4 Close-up of the etch marks on the Mark I annular channel inner surface at the outer periphery.

Plate P.3 The etch marks on the Mark I annular channel inner surface at the outer periphery.

Plate P.4 Close-up of the etch marks on the Mark I annular channel inner surface at the outer periphery.

Plate P.5 The Mark III annular channel filled up with mercury.

Plate P.6 The Mark II annular channel in the air gap of the Lintott electromagnet II

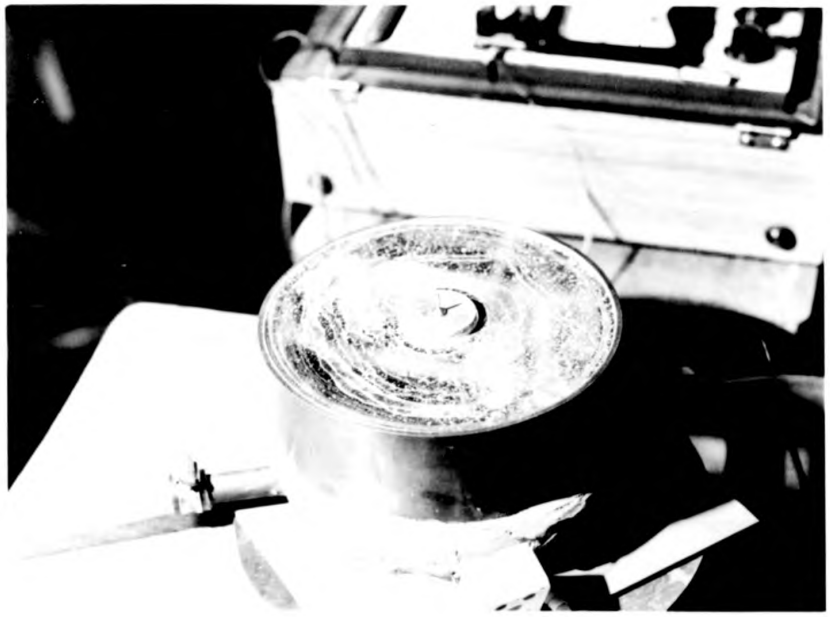

Plate P.5 The Mark III annular channel filled up with mercury.

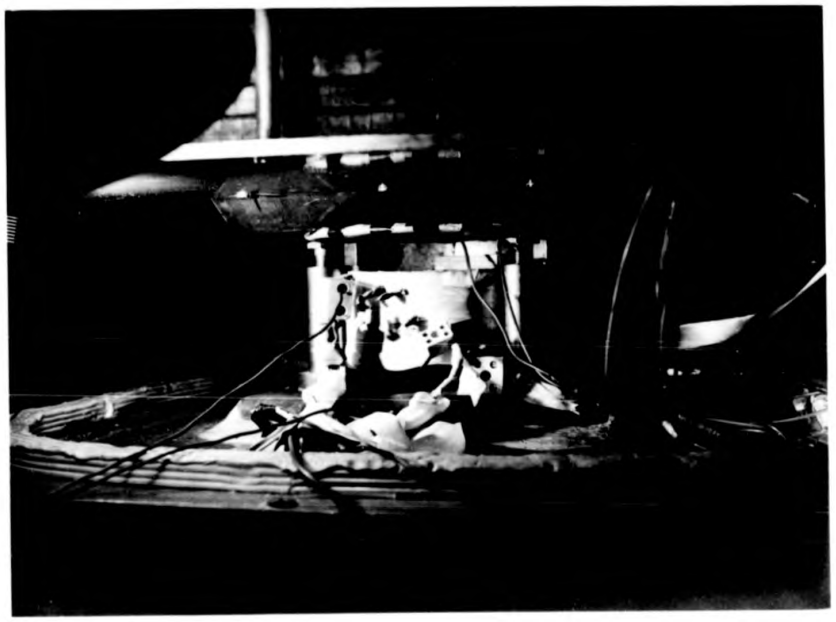

Plate P.6 The Mark II annular channel in the air gap of the Lintott electromagnet II

Plate P.7 The Mark IV annular channel with the heater coil insulation partly opened.

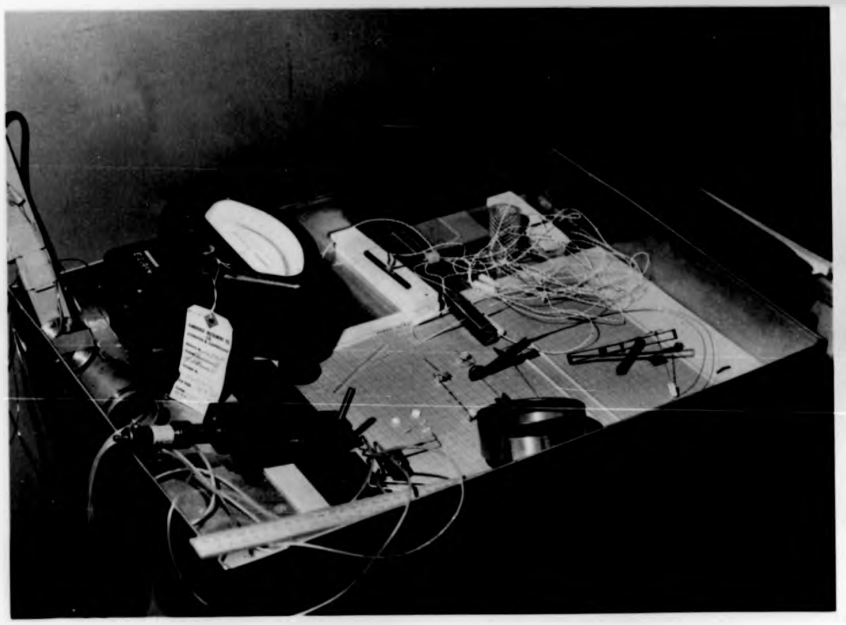

Plate P.8 The various probes.

Plate P.7 The Mark IV annular channel with the heater coil insulation partly opened.

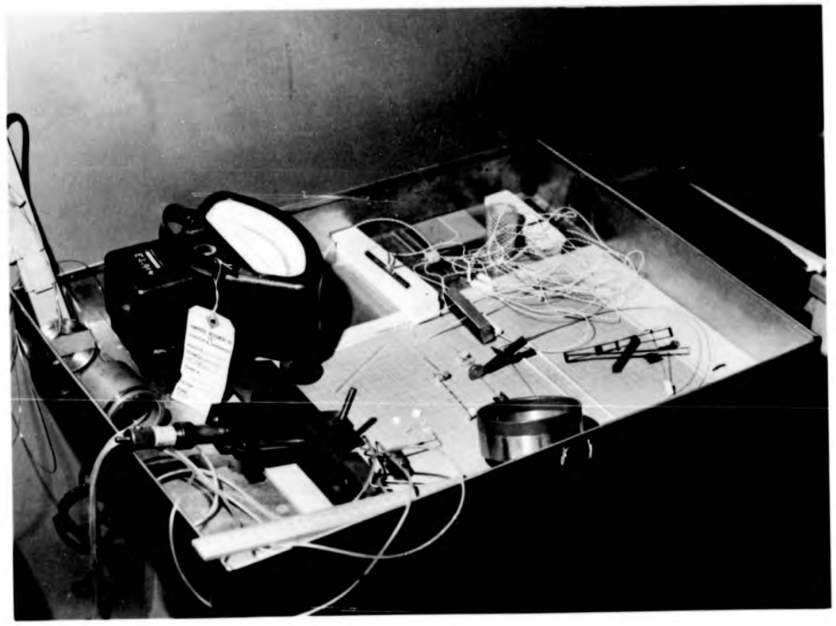

Plate P.8 The various probes.

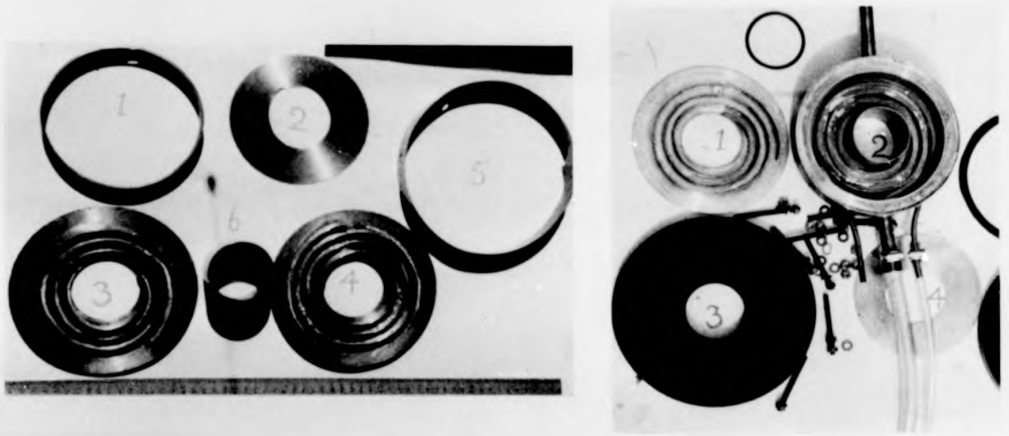

Plate P.9 The spiral channel components during construction

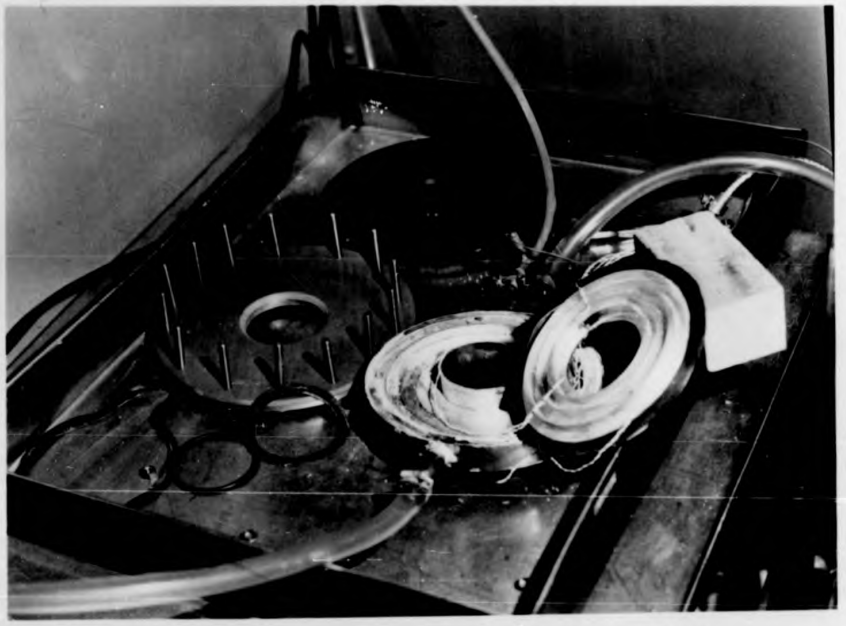

Plate P.10 The spiral channel with thermocouple probes.

Plate P.9 The spiral channel components during construction

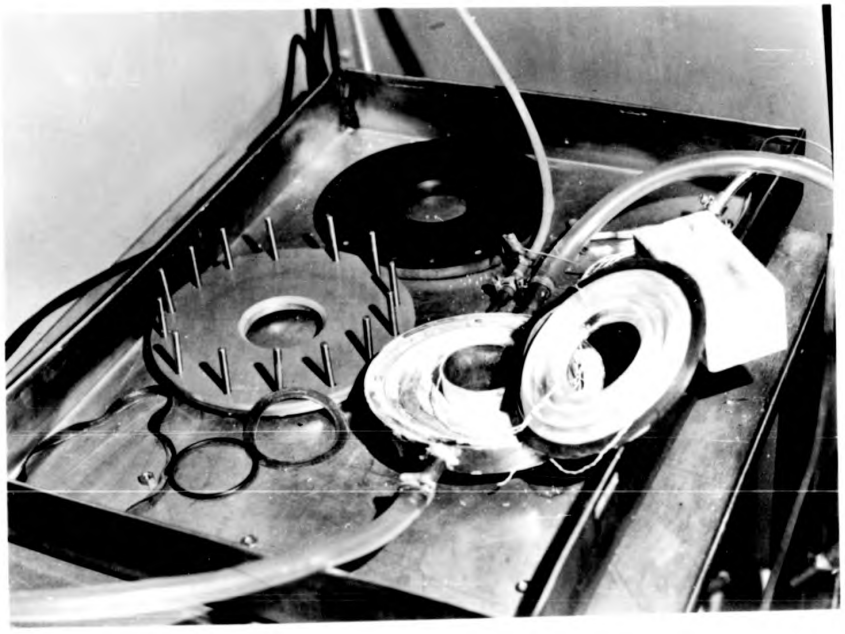

Plate P.10 The spiral channel with thermocouple probes.

'Supplement to Chapters 4 , 5 and 6'
in the form of draft papers prepared for
publication.

Investigations into Experimental Thermoelectric Magneto-hydrodynamics - Part I : Circular cross-sectional straight ducts in transverse magnetic fields.

Abstract

This is the first of the tri logy of papers on experimental Thermoelectric Magnetohydrodynamics in various duct configurations in transverse magnetic fields. In this paper the circular cross-sectional straight duct is considered with a sinusoidal variation of the peripheral temperature distribution that is uniform along the length of the duct so that the experimental results can be compared with the simple analytical solutions possible. In part 2 and 3 of this series of papers, experimental studies on Thermoelectric Magnetohydrodynamics are described in rectangular cross-sectional straight ducts and in annular channels of rectangular cross-section respectively. The experiments are conducted with mercury as the electrically conducting fluid contained in copper ducts with an average thermopower of the combination 7.25 μV/°C in the temperature range of 10°C to 180°C. The measurements include those of pressure gradients and flow velocities at various levels of temperature gradients and magnetic fields. The experimental results for the pressure gradients agree well with the theoretically calculated results but for the velocity measurements, necessary corrections are to be applied for the entry and exit effect and the analysis is valid for high Hartmann number flow only. These measurements also provide a method of thermopower determination of conducting fluids in magnetic fields with sufficient sensitivity to detect impurity/contamination levels in the fluid. Even though

the basic configuration considered is that of the thermally stable stratified fluid, i.e. where buoyancy effects are avoided, detailed temperature measurements in the fluid show that temperature oscillations exist in the fluid, particularly at low magnetic fields. These thermal oscillations are suppressed at high magnetic fields. The build-up process (transients) has also been considered though only casually.

1. Introduction

Electrically conducting liquids can be pumped electromagnetically by $\underline{j} \times \underline{B}$ forces where $\underline{j}$ and $\underline{B}$ refer to the current density and the magnetic field respectively. If the thermoelectric effects drive the current the pumping effect due to such $\underline{j} \times \underline{B}$ forces may be categorised as Thermoelectric-Magnetohydrodynamics (TEMHD). This concept of TEMHD pumping is not new[1-7] — but the practical difficulty in generating significant thermoelectric current has made TEMHD pumping unattractive. This is why no detailed study of the fluid flow interactions with the thermal-electrical-magnetic fields via the thermoelectric effect is available in the literature of the earlier decades. Only recently, the thermoelectric currents are estimated to reach such significant level in the liquid lithium blanket of thermonuclear reactors that the TEMHD effects are considerable and theoretical studies into TEMHD has been undertaken.[8-10] In order to verify the conclusions arrived at theoretically, it is essential to conduct experiments in which significant TEMHD forces could be generated that produce measurable effects in the form of pressure gradients or fluid flow. These measurements provide a new method of determining the thermopower of conducting fluids and may be used to monitor

very effectively the impurity content or the contamination level of the fluid. Special configurations are to be considered to avoid the effect of buoyancy in the essentially non-isothermal environment of TEMHD. The circular cross-sectional straight duct is very important for industrial applications. Therefore in part I of the series of papers, TEMHD of mercury in a circular cross-sectional straight duct of copper, with a sinusoidal peripheral temperature variation (uniform along the duct length) in a transverse magnetic field is considered. The measurements include those of (i) basic temperature distribution, (ii) $\underline{j} \times \underline{B}$ forces that produce pressure gradients and (iii) fluid flow. Section 2 describes the experimental set-up. Section 3 provides the relevant theory while experimental results are presented in section 4. Discussion and conclusion are covered in section 5.

2. Experimental arrangements and measuring systems

2.1 The basic experimental section

The choice of the basic size of the circular cross-sectional straight duct with sinusoidal peripheral temperature distribution was guided by the uniform field space of 1.15 x 0.18 x 0.76 m^3 of the water-cooled 'Lintott' electromagnet I (maximum flux density 1.25 Tesla measured with Hall effect Magnetometers calibrated with NMR facilities) and the availability of commercial copper pipes. Two different sizes of such pipes - (i) 2.55 cm O.D. wall thickness 1.2 mm., length 0.5 m and (ii) 5.25 cm O.D., wall thickness 1.25 mm., length 0.67 m were chosen. Sinusoidal peripheral temperature distribution was maintained by cooling the appropriate part of the

copper surface with water in a built-in copper jacket and heating part of the copper pipe surface with 26 SWG Ni/0.511 mm dia.Kanthal resistive wire heaters of maximum capacity 3.25 KW. The cooling water was made to enter the water jacket at the entry port located at midlength with a maximum rate of 30 litres/min. and was let out through two symmetrically located outlet ports at the two ends of the water jacket with a maximum temperature rise of 1.5°C resulting in an axial temperature gradient of 6°C/m, a mere 0.15% of the corresponding transverse temperature gradient. Water flow rates were measured by Rotameters and temperature measurements were made with thermocouples and mercury-in-glass thermometers. It is important to isolate the heaters electrically from the copper surface though a good rate of heat transfer is to be maintained. This was accomplished by using fibre-glass, MgO and silicone compounds while heat losses were minimised by using fire clay and asbestos cloth and cement. Non-magnetic stainless steel straps kept the heater coils in position. The basic experimental section is placed horizontally in the uniform field region of the electromagnet in such a way that the horizontal magnetic field is perpendicular to both the duct axis and the vertical positive temperature gradient in the fluid that ensures thermal stability.

2.2 The external loop and measurement facilities

The entry and exit sections were made of 'Tufnol' connectors. Pressure taps were also located at these connectors. Pressure difference between such tapping points could be measured by an air-over-fluid-over-mercury inclined tube manometer[11] capable of measuring a pressure difference of 0.025 mm of Hg, when suitably connected via PVC tubes. The

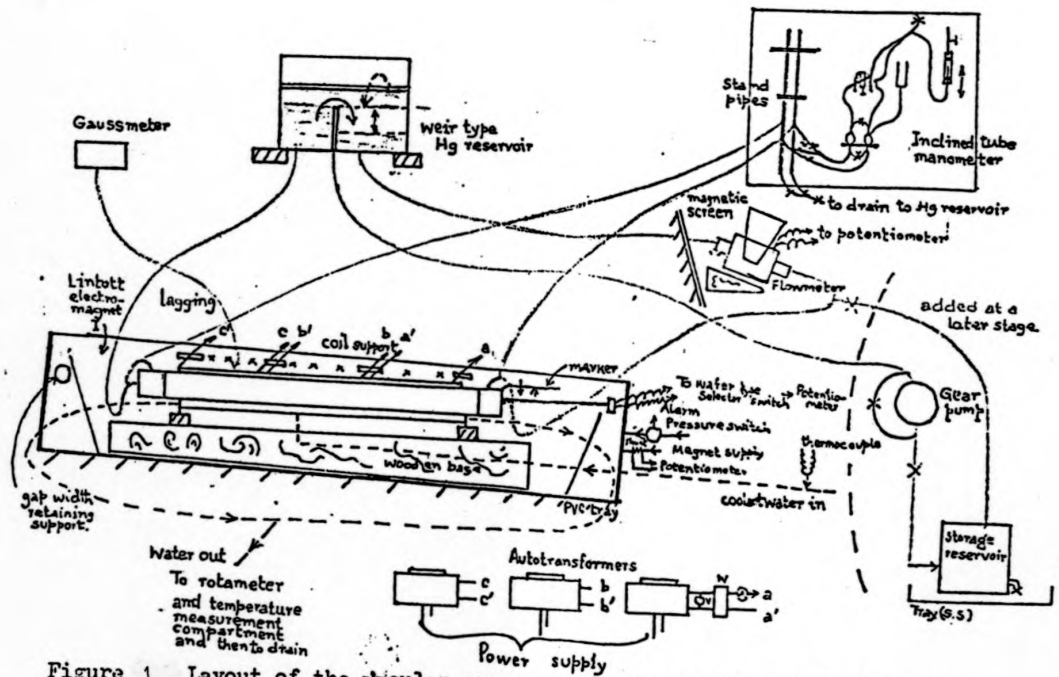

Figure 1 Layout of the circular cross-sectional straight TEMHD channel experiment(Not to scale).

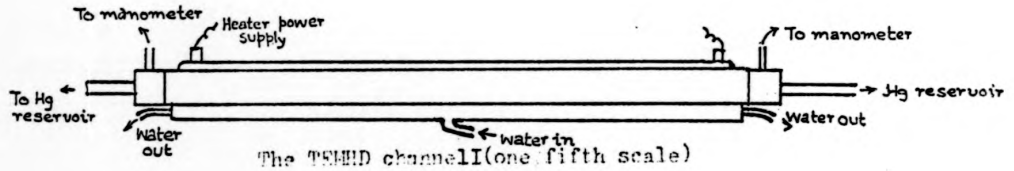

The TEMHD channelI(one fifth scale)

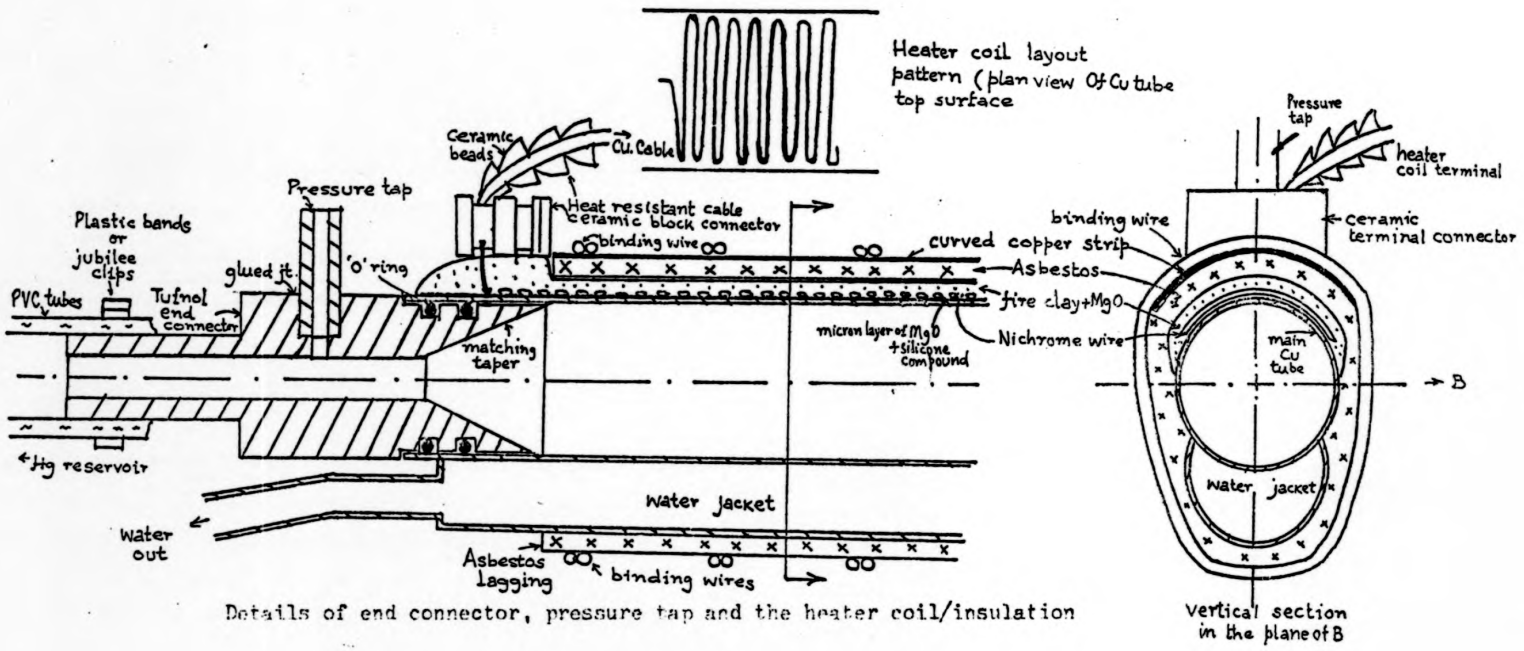

Details of end connector, pressure tap and the heater coil/insulation

Figure 2a The constructional details of the circular cross-sectional channel I for TEMHD experiments.

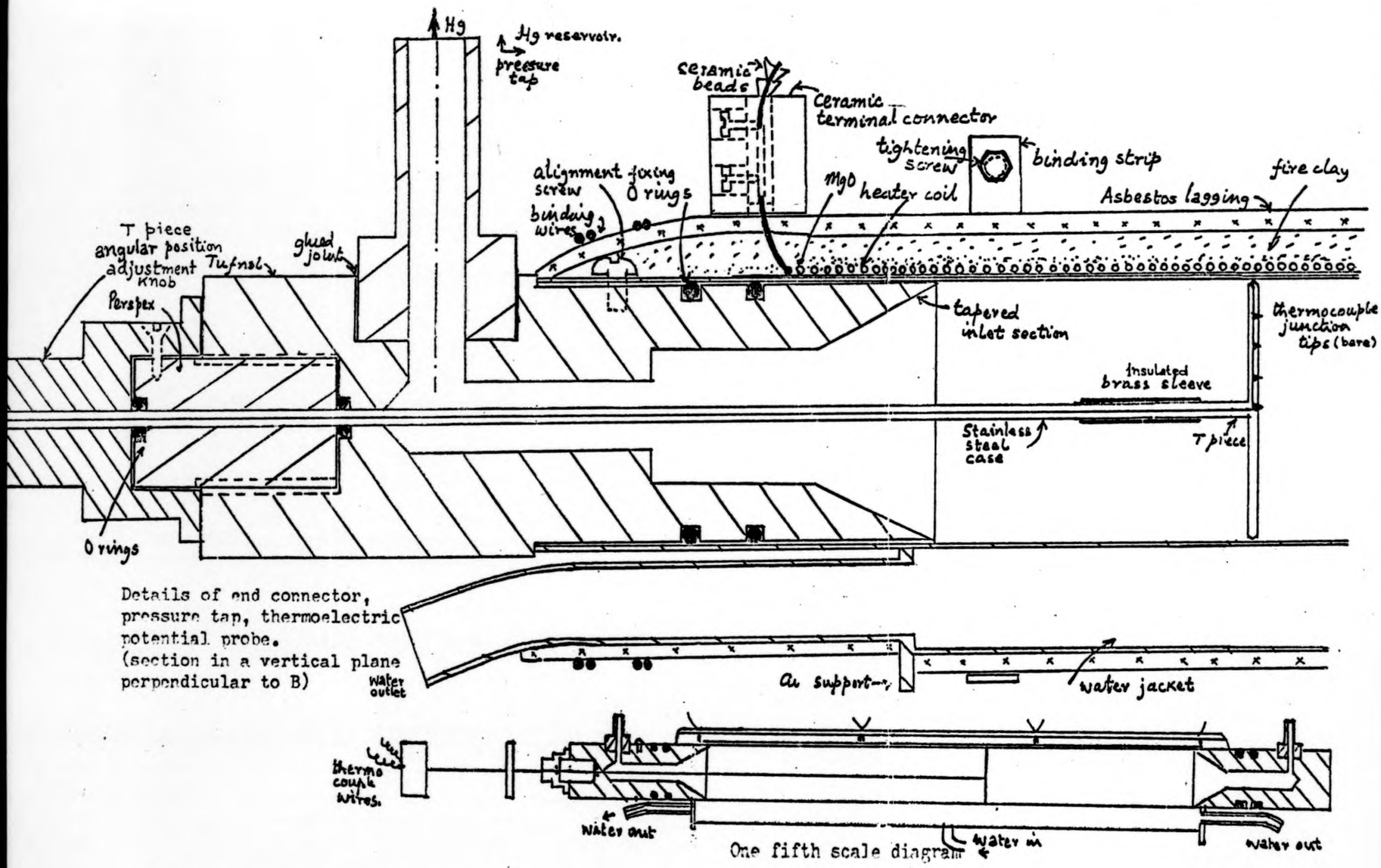

Figure 2b The constructional details of the circular cross-sectional straight channel II for TEMHD experiments.

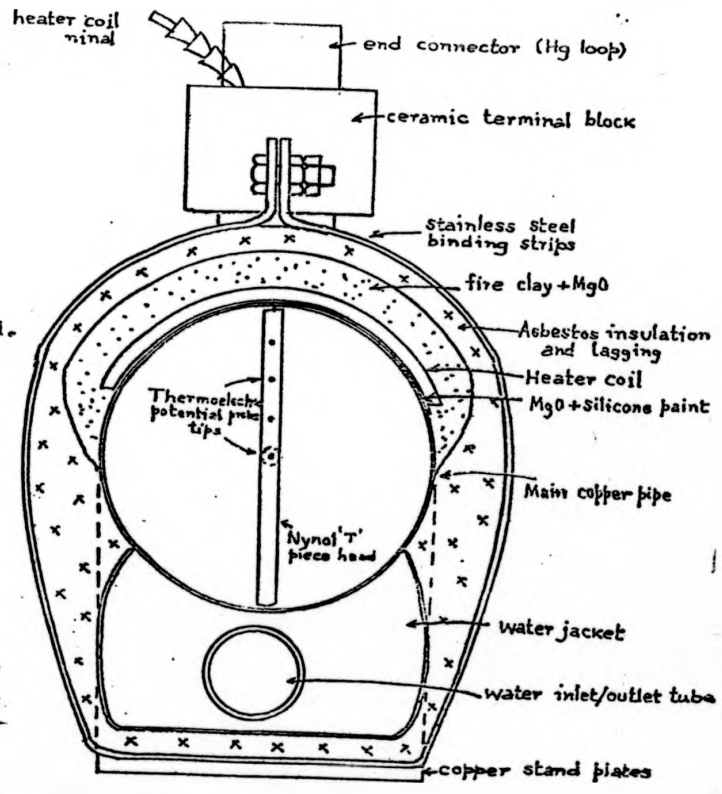

Figure 2b continued. Vertical section in the plane of the magnetic field..

flow loop (Fig. 1) that extended beyond the electromagnetic air gap consisted of PVC tubes, a weir type of mercury reservoir and a filling system and a velocity measurement facility in the form of a calibrated electromagnetic flowmeter (6.25 cc/Sec/mV with 1% accuracy). Connector joints were sealed either with 'O' rings or with glue ('Tensol' cement) and nylon gripping bands/jubilee clips were used to reinforce the seal.

2.3 Special measurement facility

Temperature distribution at the copper surface was measured with an accuracy of ± 0.25°C by a 'Comark' temperature measuring device with the Chromel-Alumel thermocouple tips spot-welded in grooves made into copper at selected positions. In the 5.25 cm O.D. experimental channel, detailed measurement of the temperature in the fluid, at the central 25 cm span length, was made by thermoelectric potential probes. This probe also provided a means of determining either the current density in the fluid when net flow at the weir reservoir was made zero and a pressure difference maintained or that of the fluid flow velocity profile across the diameter transverse to the magnetic field under assumptions of fluid flow without pressure gradients. The probe insertion system (Fig. 2b) is at one of the 'Tufnol' end connectors. Five pairs of ptfe insulated copper-constantan 0.2 mm thermocouple wires were led into the 5.25 cm O.D. copper tube along the central axis through a 3 mm O.D., 2 mm dia. bore rigid stainless steel enclosure. At the probe tip end of the stainless steel tube, a stiff nylon T piece was press-fitted with a brass sleeve

attachment having a slot and a pin arrangement to ensure rigid rotational coupling. The brass sleeve and the stainless steel tube were isolated from contact with mercury by glueing thin PVC sleeves over the metal surface. The tips of the thermocouple potential probes were made bare at the miniature holes in the T piece arm to provide measurements of temperature and potentials at five equally spaced radial positions at a time for a given azimuthal positioning θ. The total length of the two arms of the T piece exactly corresponded to the inner diameter of the copper pipe so that the radial end tips just scratched around the inner surface of the 5.25 cm O.D. copper pipe. The double 'O' ring seals permit the rotation of the T piece, θ position being read on a graduated circular disc outside the copper pipe, as well as the change of the location of the T piece along the axial length, measured by the linear displacement of the indicator away from the 'Tufnol' connector. The five pairs of thermocouple potential probes were numbered and connected either to the 'Pye' potentiometer or to the 'Advance' DVM via wafer selector switches. Temperature measurement with a maximum resolution of 0.1°C is obtained at the corresponding thermocouple wire pair whereas potential difference measurements are obtained between two similar material thermocouple wires from two different thermocouple junction points.

Layout of the experimental set up is shown in Fig. 1. The details of the experimental channels I and II are shown in Fig. 2a and b.

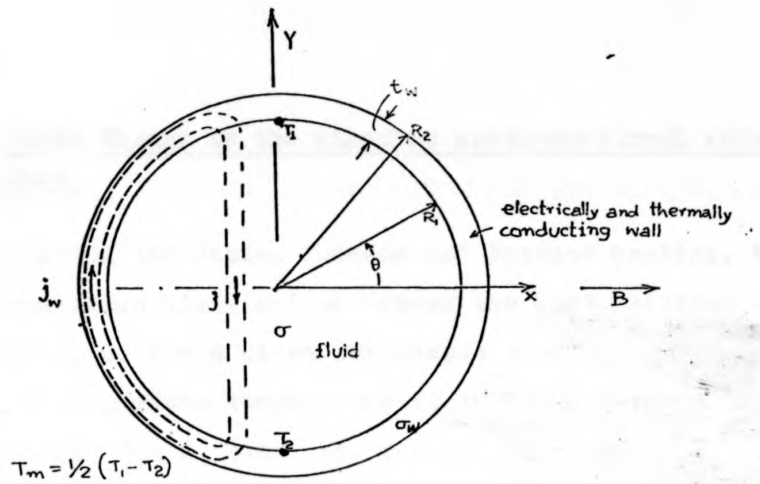

Figure 3 The circular cross-sectional duct with(first harmonic) sinusoidal temperature variation around the periphery.The elemental current path is shown for the simple analysis.

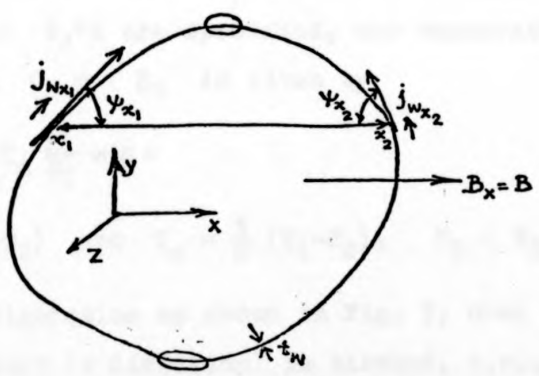

Figure 4 The conducting wall duct for two-dimensional TEMHD flow analysis.

3. TEMHD theory in the circular cross-sectional straight duct.

Ignoring the Joule, Thomson and Peltier heating, the basic temperature distribution across the duct vertical cross-section (Fig. 3) for a given peripheral sinusoidal (first harmonic with maximum temperature at the top) temperature specification $T = A_1 \sin\theta$ at $r = R_2$ is given by

$$T = (A_2 r + \frac{A_3}{r}) \sin\theta \quad \text{in the duct wall}$$

and $T = A_4 r \sin\theta$ in the fluid with A's constants, so that the fluid is thermally stably stratified.

If, however, the top and bottom wall-fluid interface temperatures T_1° and $T_2^\circ K$ are specified, the temperature T in the fluid i.e. in $0 < r < R_1$ is given by

$$T = T_{av} + T_m \frac{r}{R_1} \sin\theta$$

where $T_{av} = \frac{1}{2}(T_1+T_2)$ and $T_m = \frac{1}{2}(T_1-T_2)$, $T_1 < T_2$.

With the configuration as shown in Fig. 3, when the net flow v along the duct (z direction) is blocked, i.e., when $\underline{V} \times \underline{B} = 0$, by symmetry $j_x = 0$.

In the elemental electric circuits shown dotted in Fig.3, neglecting contact resistance at the fluid-wall interface

$$j = j_y = \frac{\alpha_{av} T_m}{R_1 (1 + \frac{\sigma R_1}{\sigma_w t_w})} = \frac{\alpha_{av} T_m}{R_1(1 + c)}$$

where α_{av} is the average thermopower of the fluid-duct material combination in the temperature range (T_1, T_2) assuming

a linear temperature dependence of α , σ the electrical conductivity and c is the fluid to wall conductance ratio. Suffix w refers to the wall.

The interaction of the thermoelectric current j_y and the transverse magnetic field B produces a pressure gradient

$$dp/dz = j_y B = \frac{\sigma \alpha_{av} T_m B}{(1+c) R_1}$$

Following the analysis of Chang and Lundgren,[12] in ordinary MHD, the core velocity when the fluid is allowed to flow in an external dp/dz is given by

$$v_{core} = \frac{\alpha_{av} T_m}{BR_1} - \frac{1+c}{\sigma B^2} \frac{dp}{dz} \quad \frac{(1-y^2/R_1^2)^{\frac{1}{2}}}{(1-y^2/R_1^2)^{\frac{1}{2}} + c/M}$$

$$\rightarrow \frac{\alpha_{av} T_m}{BR_1} - \frac{1+c}{\sigma B^2} \frac{dp}{dz} \quad \text{as } \frac{c}{M} \rightarrow 0$$

where $M = \sqrt{\frac{\sigma}{\eta_v}} BR_1$ is the Hartmann Number with η_v the fluid viscosity.

More general two dimensional analysis of TEMHD in circular cross-sectional straight ducts is given by Shercliff,[9] for a peripheral temperature distribution given by

$$T = T_{av} + \sum_n T_{cn} \cos n\theta + \sum_n T_{sn} \sin n\theta$$

Following Shercliff,[9] the inviscid inertialess flow in the configuration of Fig. 4 gives

$$j_x = \sum_{n \text{ odd only}} \frac{n^2 \alpha_{av} T_{cn} \cos n\theta}{R_1 (c+n)^2 \cos\theta} , = 0 \text{ if } T_{cn} = 0 \text{ n odd only}$$

In such a case velocity v is constant and is independent of x and is given by

$$Bv(y) = \sum_n \frac{n \alpha_{av} T_{sn}}{R_1} \frac{\cos n\theta}{\cos\theta} + \frac{j_y (1+c)}{\sigma}$$

Integrating over the transverse cross-section, the mean velocity V is given by

$$V = \frac{\alpha_{av} T_{s1}}{BR_1} - \frac{1+c}{\sigma B^2} \frac{dp}{dz}$$

For an offset (maximum temperature shifted away from the top position by an azimuthal angle θ') sinusoidal first harmonic peripheral temperature distribution in a horizontal transverse magnetic field

$$\frac{dp}{dz} = \frac{\sigma \alpha_{av} T_m B \cos\theta'}{(1+c) R_1}$$

if the fluid flow v is blocked and buoyancy effects are ignored.

These simple solutions provide easy references for comparing the corresponding experimental results.

4. Experimental Results

4.1. Temperature measurements

Since the basis of TEMHD flow theory outlined in section 3 relies mainly on the first harmonic sinusoidal variation of peripheral temperature that is uniform along the duct length with the maximum temperature at the vertical top location, it is essential to verify how well it could be maintained during experiments.

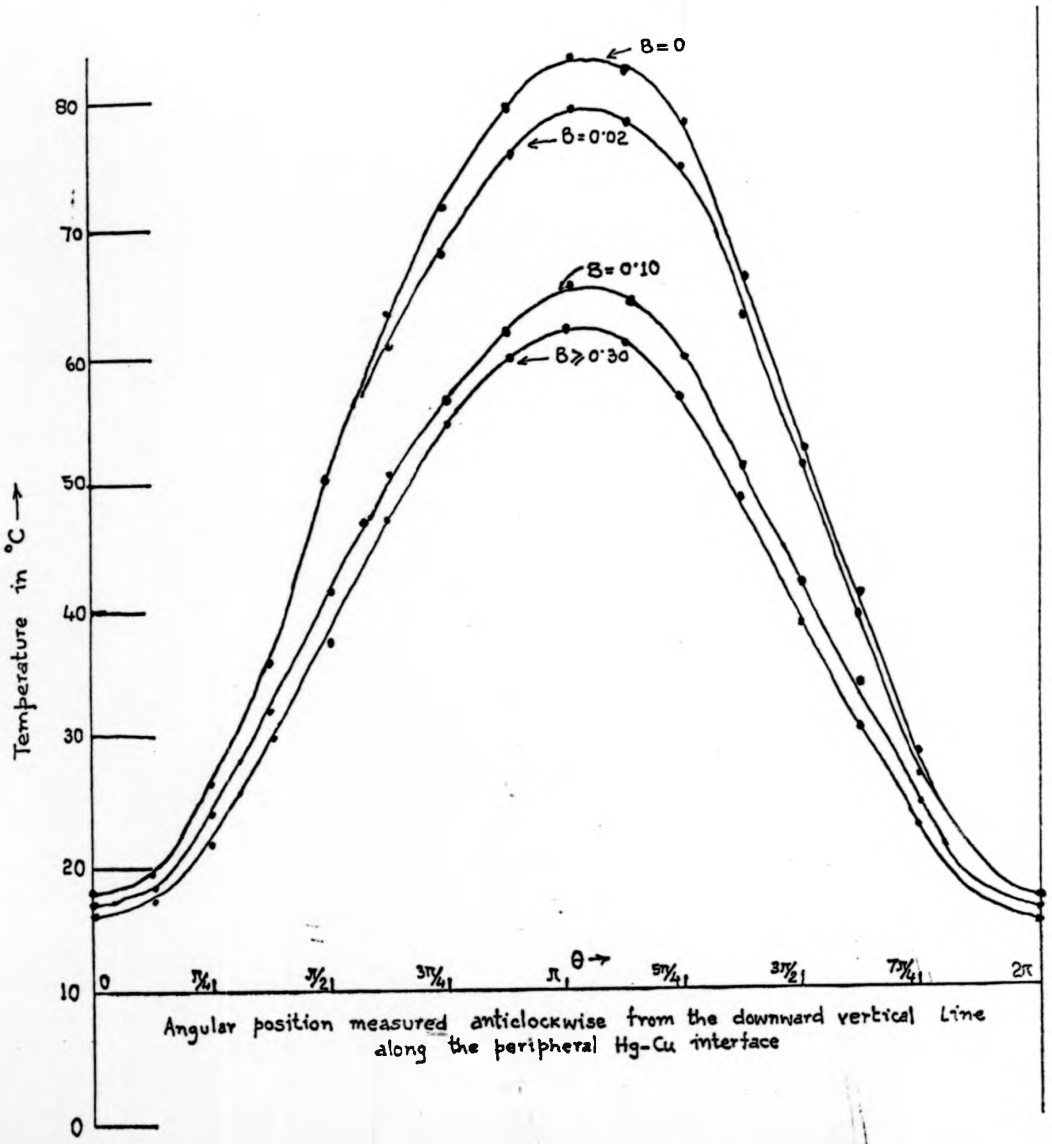

Figure 5. Peripheral temperature distribution in Channel II for a fixed heater current of 3x3 amperes and the cooling water temperature of 16°C at various magnetic flux density B(in Tesla).

The measurement of temperature in the fluid by the thermoelectric potential probe produced remarkably identical temperature distribution across cross-sections at various axial positions in the central 25 cms of channel II for a given magnetic field strength and thermal energy transport (heating and cooling flux). This confirmed the longitudinal parametric invariance. However, though the peripheral temperature distribution for a given thermal energy transport remained sinusoidal at all magnetic field strengths, changes in the magnitude of the transverse magnetic field resulted in a change in values of T_1 and T_2. Fig. 5 shows the variation of the peripheral temperature profile for a heater coil current of 3 x 3 amperes with a cooling water temperature of 16°C in transverse magnetic fields of B = 0, 0.02, 0.1 and $\geq$ 0.3 Tesla when there is no net fluid flow in the z direction. When a particular peripheral temperature profile corresponding to a heater current of 3 x 3.2 amperes and cooling water temperature of 10.75°C at B = 0.5 Tesla was Fourier analysed to evaluate harmonic contents in the form

$$T(\theta) = \frac{a_0}{2} + \sum_{n=1}^{7} \{ a_n \cos n\theta + b_n \sin n\theta \}, \; T \text{ in } °C$$

the harmonic content amplitudes were found as tabulated in Table 1.

Table 1.

Amplitudes of harmonic contents of the peripheral temperature profile in channel II for a heater current of 3 x 3.2 amperes, cooling water temperature of 10.75° and B = 0.5 Tesla.

n	0	1	2	3	4	5	6	7
a_n	82.1	-3.2	-1.1	0.4	0.6	0.8	-0.2	0.3
b_n	0	-31.2	-0.1	1.0	0.6	0.7	0.9	0.6

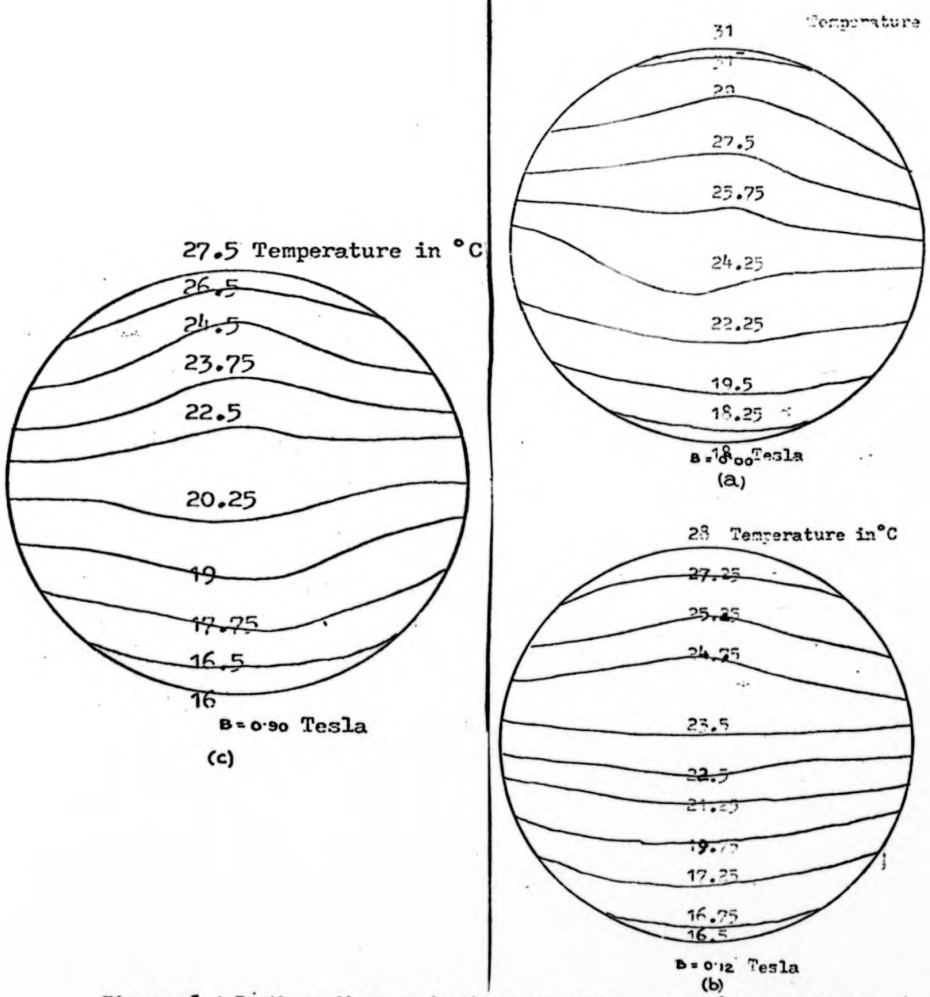

Figure 6. Isotherm diagrams in the cross-section of the channel II for a fixed heating current of 3 x 1.1 amperes (cooling water temperature change < $\frac{1}{2}$°C)

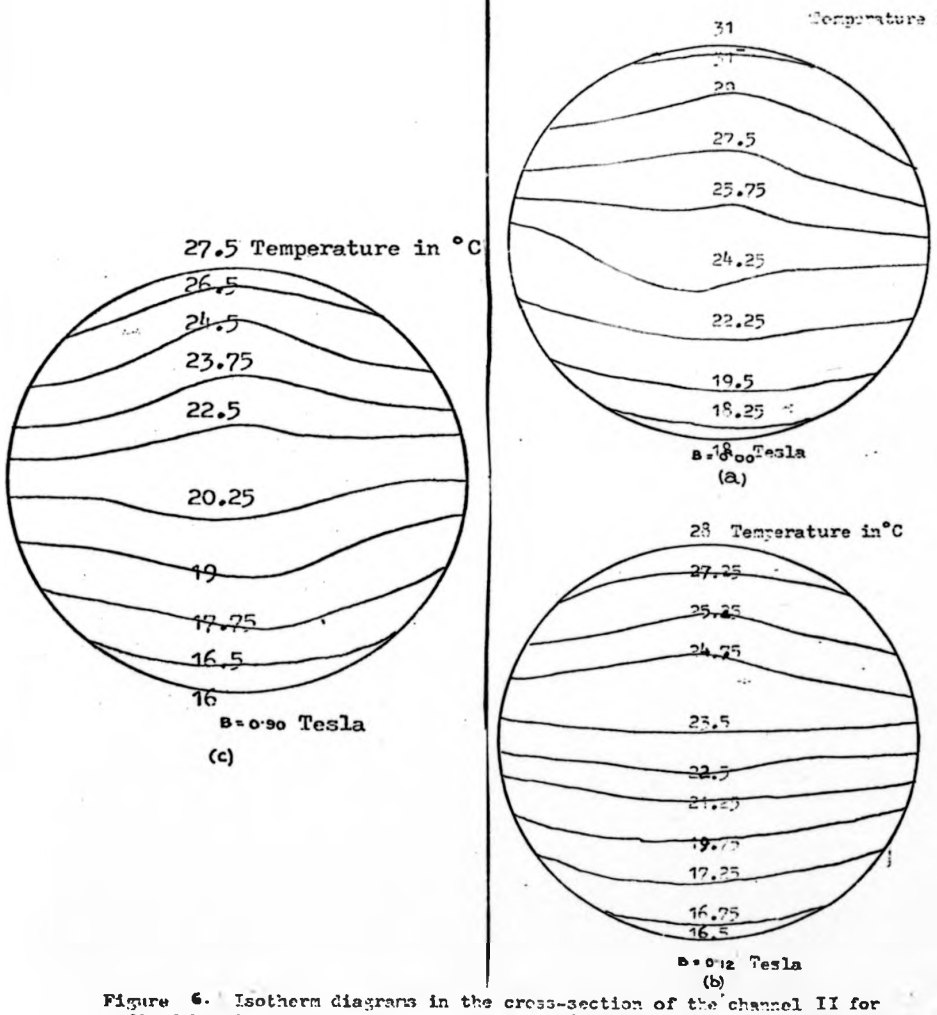

Figure 6. Isotherm diagrams in the cross-section of the channel II for a fixed heating current of 3 x 1.1 amperes (cooling water temperature change $< \frac{1}{2}$°C)

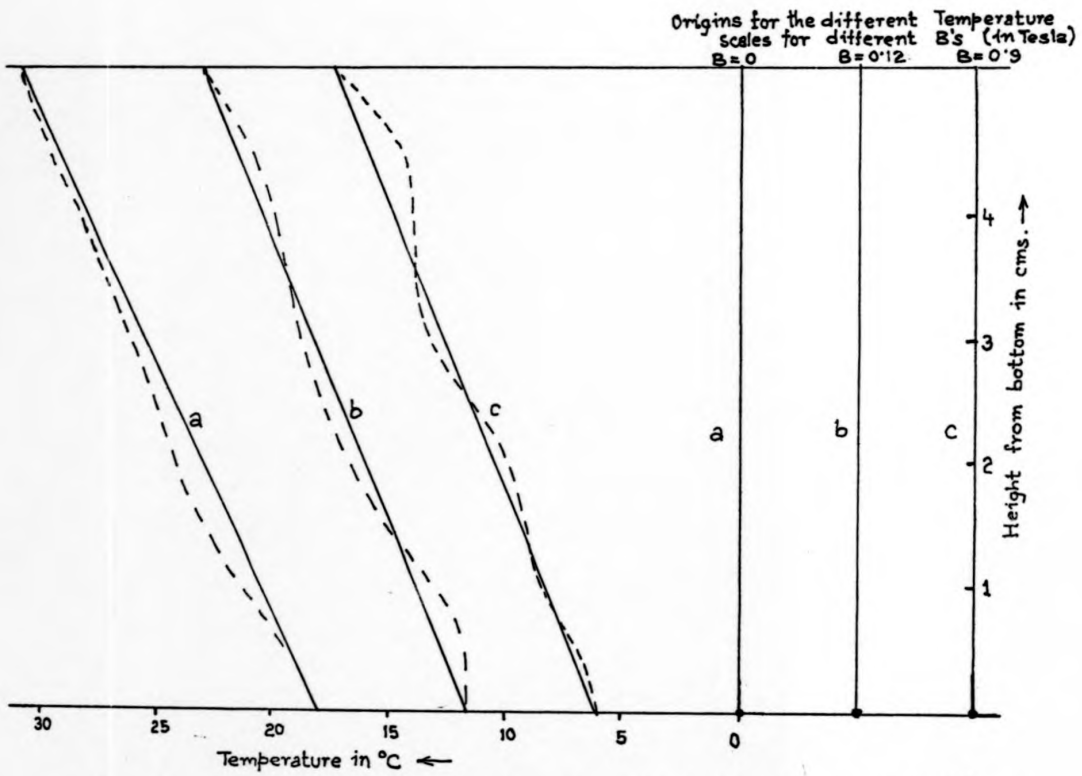

Figure 7. Temperature variation along the vertical diameter in Channel II for a fixed heater current of 3x 1·1 amperes and cooling water temperature variation less than ½°C.

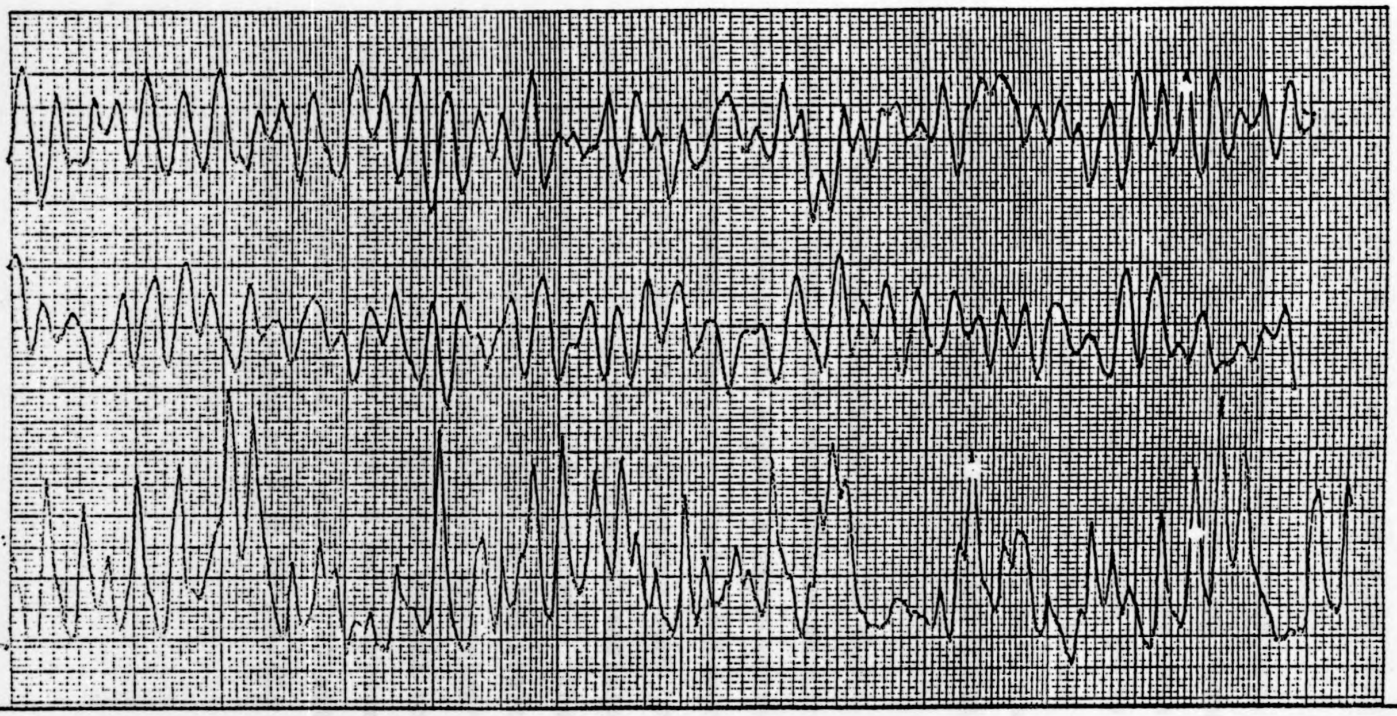

Figure 8 Temporal records of temperature and potential oscillations in the circular cross-sectional channel II in horizontal transverse magnetic field of 0.5 Tesla. The traces move with time from left to right and the time scale (horizontal X direction) is 8 sec/ cm. The Y axis scale is 60 μvolts /cm. Operating condition; 3x3amp heating current. (a) Temperature oscillation at $(R/2, \pi/2)$ (b) Potential oscillation across vertical radius from centre point to $(R/2, \pi/2)$ (c) Temperature oscillation at $(R/2, 5\pi/4)$. Angles measured from the horizontal magnetic field direction (anticlockwise).

The corresponding error due to higher harmonic content in $T_m = 1/2\ (T_1-T_2)$ is only 0.6% while that of $T_{av} = \frac{1}{2}\ (T_1+T_2)$ is 4.5%.

For a given thermal energy transport, the temperature distribution in the fluid has also been observed to change with the transverse magnetic field amplitude when there was no net flow along the duct. Typical isotherm plots for a heater current of 3 x 1.1 ampere and cooling water temperature of 16°C are shown in Fig. 6 for B = 0, 0.12 and 0.9 Tesla. The corresponding temperature distribution along the vertical diameter is shown in Fig. 7.

Temperature measurement in the fluid revealed the existence of temperature oscillations in certain regions of the fluid in transverse magnetic fields above a specific rate of thermal energy transport. While at 3 x 0.5 ampere heater current no such thermal oscillations were present, there were indications that very feeble thermal oscillations started at 3 x 1.1 ampere level of heater current. The maximum temperature fluctuations were confined to two regions ($\pm$ R/2, $\frac{\pi}{2}-\theta$ vertical) but at higher heater current operation oscillations reached the wall-fluid interface as well. Typical thermal oscillation amplitudes are summarised in Table 2 and a typical time-record of temperature oscillations at (R/2, $\pi/2$) with a period of oscillation in the range of 6 to 12 seconds is shown in Fig. 8.

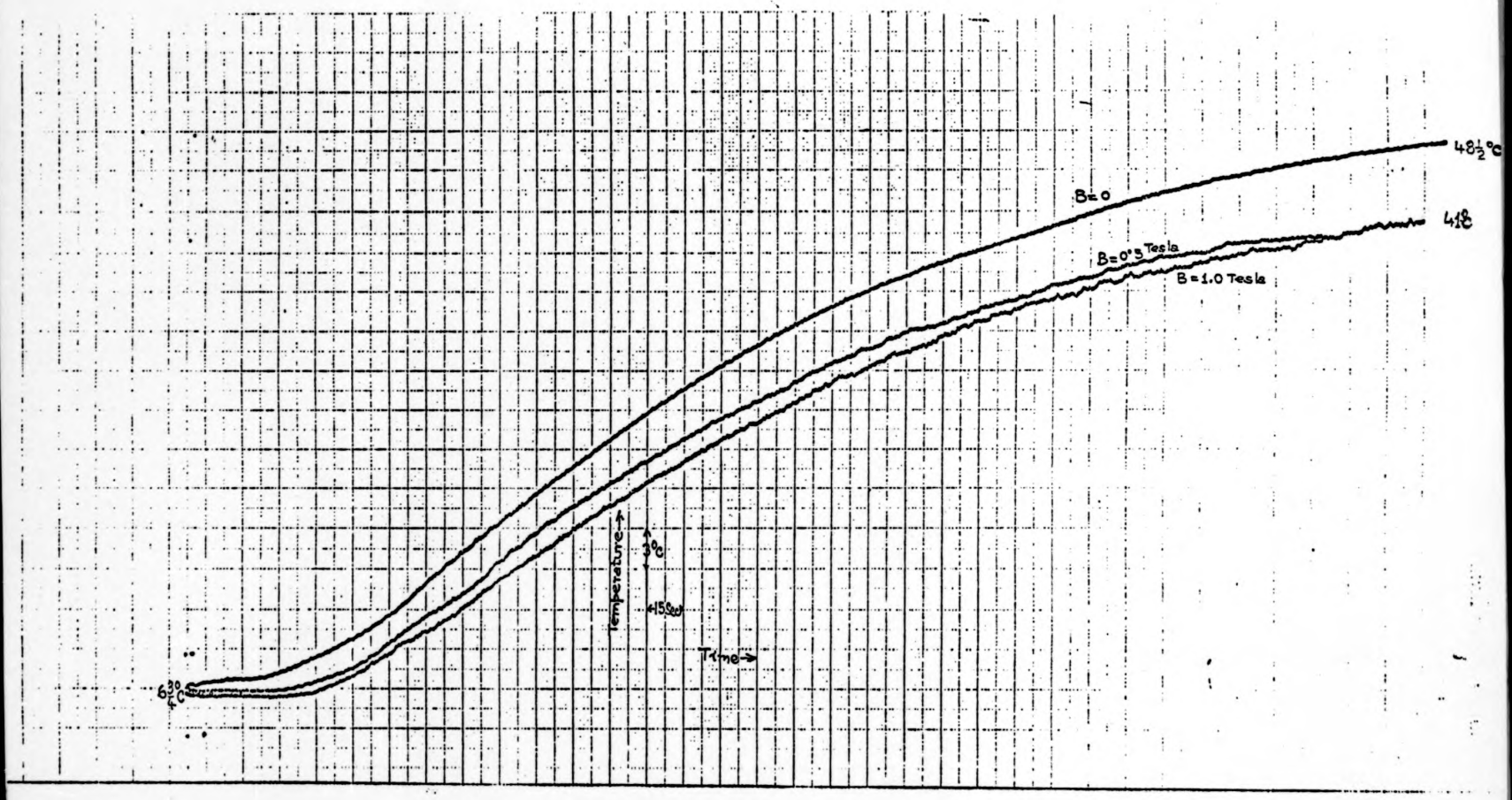

Figure 9 The time record of temperature build up in the circular cross-sectional straight channel II in various steady values of the horizontal transverse magnetic field .Heater current raised suddenly from zero value to 3x3.2 amperes.

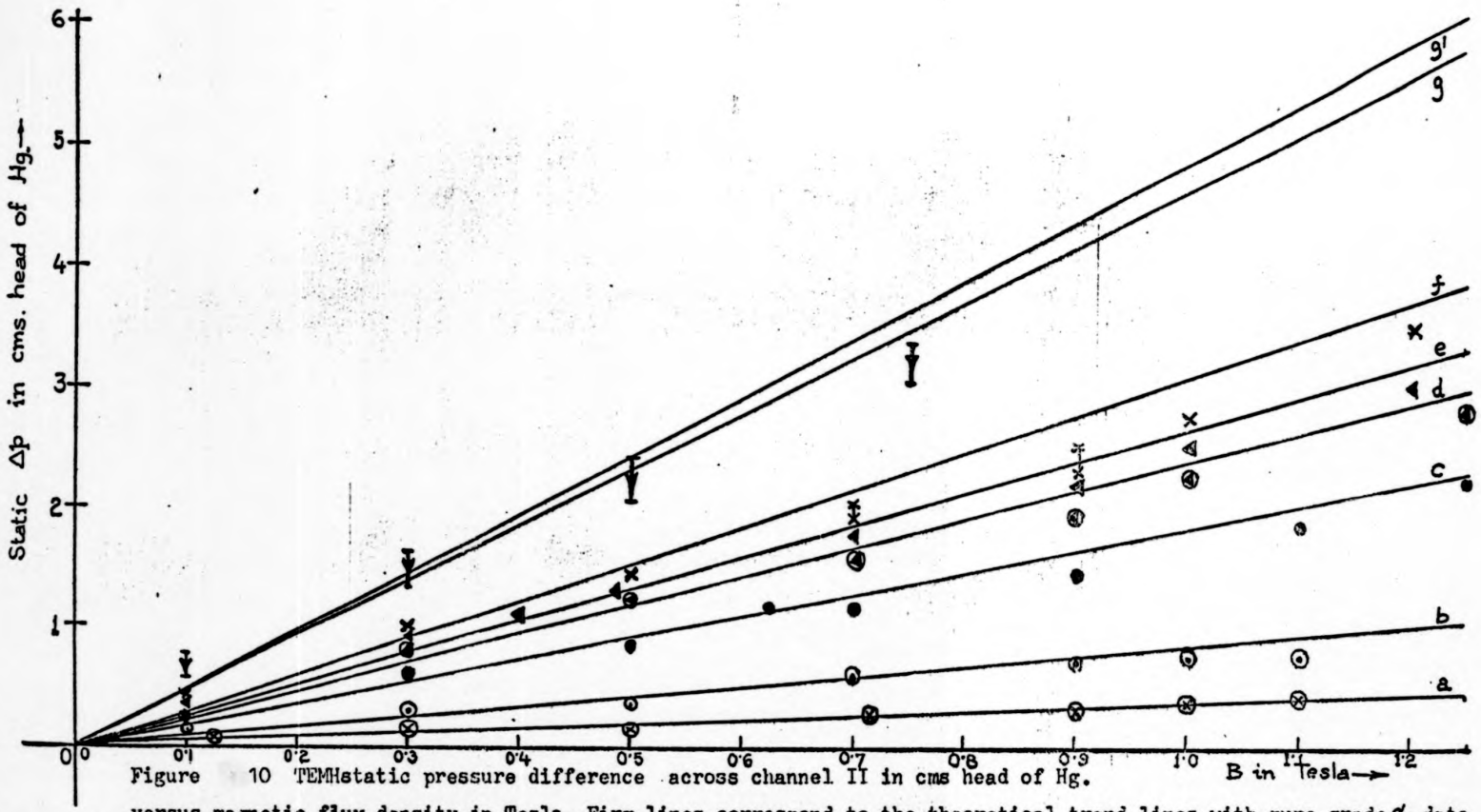

Figure 10 TEMHstatic pressure difference across channel II in cms head of Hg. versus magnetic flux density in Tesla. Firm lines correspond to the theoretical trend lines with pure grade α_{calc} data. Key to the symbols ; (a) ⊗ heater current 1.1amp (b) ⊙ heater current 2 amp (c) ● heater current 3 amp (d) ◐ heater current 3.2 amp (e) ◀ heater current 3.5 amp (f) × heater current 4 amp (g and g') ⚜ heater current 5 amperes. For complete operating conditions refer to Table 3

Table 2

Amplitudes of temperature oscillations in the fluid of channel II.

Heater current	Temperature oscillations (P-P)				
	Location	B=0.02	B=0.1	B=0.5	B > 0.5 Tesla
3 x 3.5 amperes	(R/2, π/2)	2.5°C	2.5°C	0.1°C	-
	Solid fluid interface	-	-	-	-
3 x 4 amperes	(R/2, π/2)	5°C	5°C	5°C	1°C, < 1°C at B=0.9
	Solid fluid interface	1.25°C		0.25°C	-

A typical time record of the temperature build-up in the fluid, for a heater current of 3 x 3.2 amperes, from the instant of power switching on, is shown in Fig. 9 in transverse magnetic fields of B = 0, 0.5 and 1 Tesla. The characteristic time of build up $\simeq$ 4 minutes.

4.2 Pressure measurements

Pressure difference measurements across the basic experimental section of channel II, when there is no net flow along the duct, at different thermal energy transport levels and different amplitudes of the transverse magnetic field form a set of convenient experimental data to compare with the theoretically predicted values. The pressure difference Δp reversed by equal amounts with the reversal of the direction B for a given temperature gradient. Δp readings for a given temperature gradient and B were reproducible within a narrow tolerance of 0.1%. Fig. 10 shows Δp measurements for various heater coil currents against the imposed magnetic flux density. For clarity only a few representation experimental points have

TABLE 3 Experimental operating conditions for Channel II with the corresponding theroetical parameter calculations

Heater current	Supply voltage	B = 0 T_1	T_2	ΔT °C	B ≥ 0.3 Tesla T_1	T_2	ΔT	T_{av} °C	T_m	C	α_{Cu-Hg} $\mu V/_{Th}{}^{\circ}K$	$\Delta h = \frac{\sigma \alpha T_m L}{(1+c) R_1 \rho g} B$
3 x 0.75	3×31	18°	11°	7	-	-	-	-	-	-	-	-(in cm of Hg)
3 x 1.1	3 x 40	32	19.5	13	27.5	16.25	11.25	22 (21.85)	5.5 (5.62)	0.405	6.54	0.392 B
3 x.2	3 x 65/70	47	17.5	29.5	39	16	23	27.5	11.5	0.412	6.698	0.833 B
3 x 3	3 x110	81.5	18	61	65.5	16	48.5	40.25	24.25	0.43	7.06	1.810 B
3 x 3.2	3 x 115/118+	83.5	14	69.5	74.5	11.5	63	43	31.5	0.435	7.144	2.366 B
3.x 3.5	3 x 130	104.5	19	85.5	85	16.5	68.5	51	34.25	0.447	7.374	2.62 B
3 x 4	3 x 145/150	123	19.5	104.5	96	16	80	56	40	0.456	7.517	3.09 B
3 x 5	3 x 188/189	186/189	20	166/169	135/139	18	117/121	76.5/78.5	58.5/60.5	0.495/0.499	8.008/8.165	4.61/4.84 B

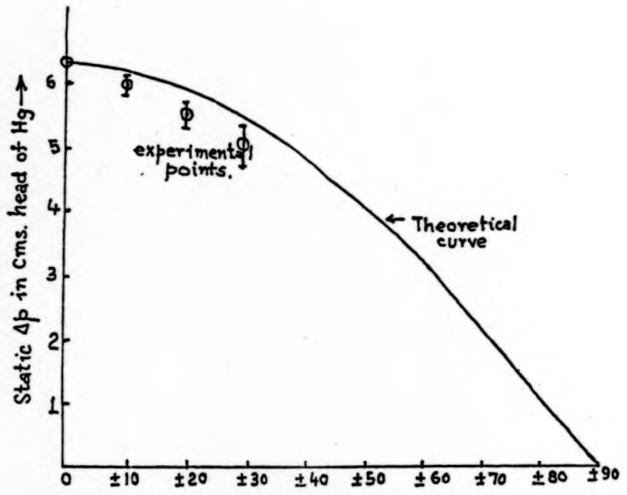

Figure 12. Pressure difference Δp across the channel I pressure taps variation with the inclination of the temperature gradient axis away from the vertical when there is no net flow along the duct. B = 1·2 Tesla, Heater current 5 amp.

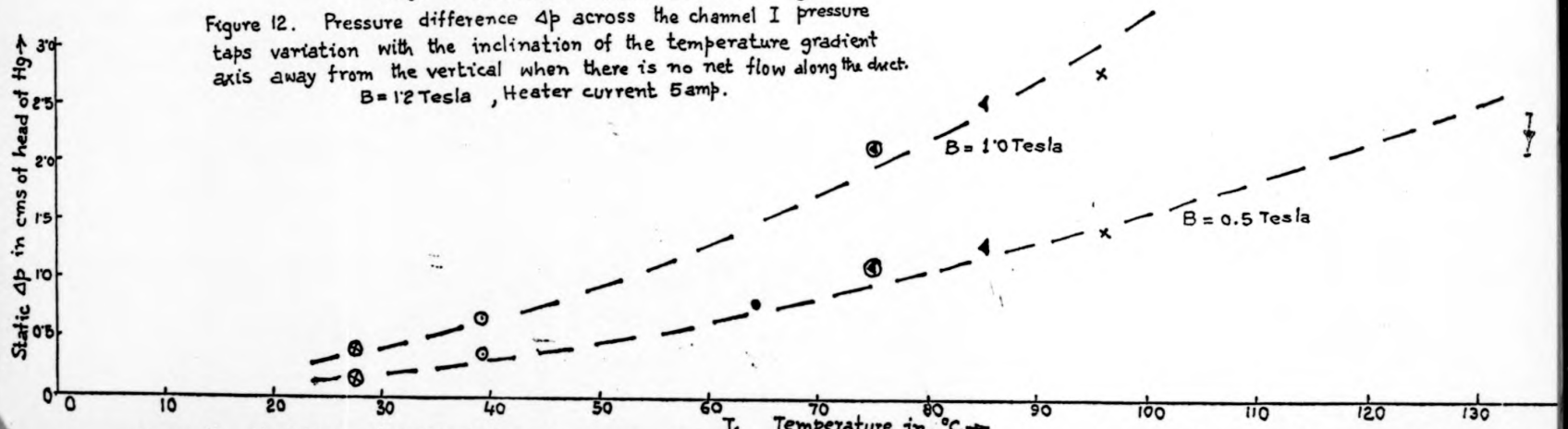

Figure 11. Variation of TEMH Static pressure difference across channel II in cms. head of Hg with the maximum temperature T cooling water $6\frac{1}{2}° \pm 1°$ C. Keys for the experimental points same as in figure 10.

been shown against a background of the theoretical lines based on pure grade $\alpha_{Cu\text{-}Hg}$ value. Table 3 gives the corresponding experimental operating points and the relevant calculations for the theoretical lines. Fig. 11 shows the measured Δp in cms of head of Hg at constant B = 1.0 Tesla and B = 0.5 Tesla against T_1 where variations in cooling water temperature ΔT_2 ($< 2°C$) are ignored.

A few Δp measurements across the basic experimental channel, when there was no net flow along the duct and when the temperature gradient axis was shifted away from the vertical, were made in the channel I experiments. Bar lengths show the spread of the above experimental data in Fig. 12 against a background of the theoretical curve.

To justify the assumption of uniform j_y is section 3, simultaneous measurements of $\phi^+ = \phi + \phi_\alpha$ where grad $\phi_\alpha = \alpha$ grad T and T were carried out across the vertical cross-section, in the fluid, at the heater current level of 3 x 3.2 ampere at B = 0.5 Tesla and cooling water temperature of 10.75°C, when there was no net flow along the duct. From these measurements it is possible to construct the ϕ distribution due to j_y. Table 4 summarizes such j_y evaluation.

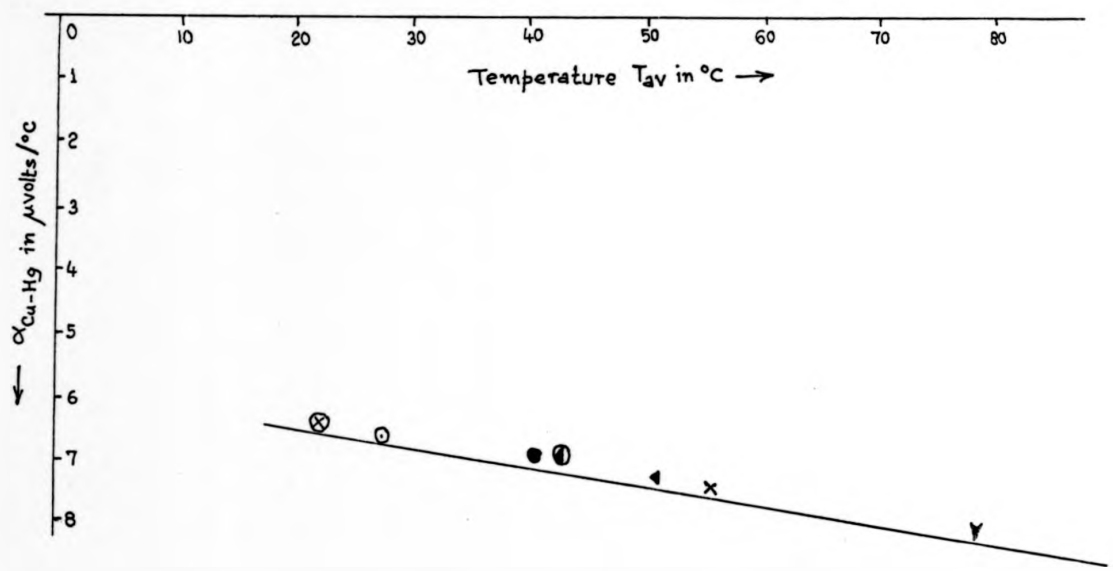

Figure 13. Evaluated average thermopower α_{Cu-Hg}, from the experimental TEMHStatic measurements of Δp vs. B at various T_1 and T_2°C, against T_{av} in °C. Pure grade α_{Cu-Hg} data of Marwaha (1967) is shown by the firm line. Keys for experimental points same as in figure 10.

Table 4

j_y evaluation from ϕ^+, T measurements in channel II for 3 x 3.2 amperes heater current at B = 0.5 Tesla.

Radial Position	Angular Position	Distance cm	$\Delta\phi$ $\mu V_{min/max}$	j_y amp/m^2 min/max
R	0	0	0	indeterminate
R	$\pm \pi/6$	2.515	150,160	6090, 6500
3R/4	$\pm \pi/6$	1.87	100,105	5465, 5740
R	$\pm \pi/4$	3.556	210,215	6035, 6179
R	$\pm \pi/3$	4.35	240,280	5640, 6580
R	$\pm \pi/2$	5.03	305,295	6200, 6000
R	$\pm 2\pi/3$	4.35	240,260	5640, 6180
R	$+ 3\pi/4$	3.556	210,220	6035, 6325
3R/4	$\pm 5\pi/6$	1.87	110,105	6010, 5760
R	$\pm 5\pi/6$	2.515	150,160	6090, 6500
R	π	0	0	indeterminate

j_y as calculated from the theoretical expression

$$j_y = \frac{\sigma \alpha T_m}{(1+c) R}$$

corresponds to a value of 6370 amp/m^2.

Typical time taken to build up the pressure difference Δp is 20 sec.

4.3 Evaluation of α_{Cu-Hg} vs T relationship from pressure measurements

The Δp measurements of subsection 4.2 at various values of B have been utilised to compute the thermopower α_{Cu-Hg} for the range of T_{av} values of the experimental data in Table 3. These calculated values are shown in Fig. 13 as experimental points against the standard data line of pure grade α_{Cu-Hg} available in literature.[13] Two typical spreads

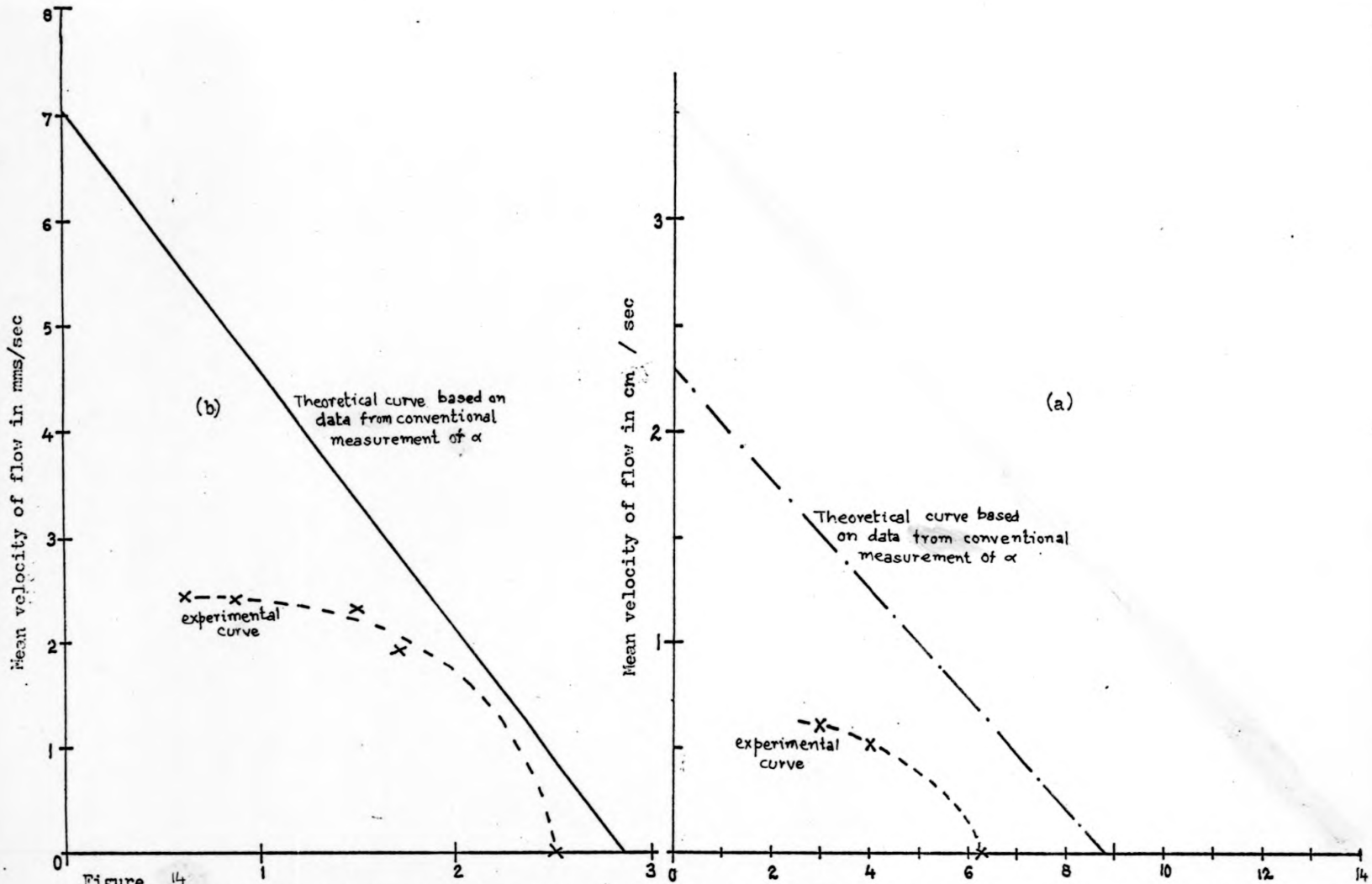

Figure 14
Mean flow rate V versus pressure differenee in cms head of Hg at the Hg weir type of reservoir in (a) Channel I (Heating current 5 amp., B=1.2 Tesla) and (b) Channel II (Heating current 3 x 3.2 amp., B = 1.25 Tesla

of $\propto_{av}(T)$ values are indicated by bar-lengths.

4.4 Flow measurements

TEMHD fluid flow measurements in circular cross-sectional straight ducts fall into two basic categories : (a) mean flow measurements in channels I and II by electromagnetic flowmeters at different Hartmann Numbers for various pressure differences maintained at the weir type mercury reservoir and (b) velocity profile measurement along the vertical diameter of the duct by the thermoelectric potential probes under assumptions of no current flow i.e. at thermoelectric and motion induced e.m.f. balance.

4.41 Mean flow measurements

Steady fluid flow (m^3/sec) with a given pressure difference at the weir type mercury reservoir could be easily achieved by TEMHD forces in both channels I and II. Assuming that the pressure difference at the weir type mercury reservoir results in a uniform pressure gradient across the mercury loop, the theoretical V vs $\triangle p$ relationship is a straight line law. Experimental operating points for channels I and II are shown in Fig. 14a and b respectively at constant values of the Hartmann Number M against the background of the theoretically expected straight line law under the above assumption. The ordinary MHD pressure gradients at the entry and exit sections and for flow in nonuniform magnetic fields,[14] however, invalidates such uniform dp/ds assumption due to the pressure difference at the weir type mercury reservoir alone; since compensation for such nonuniform dp/ds is very tedious to make no effort has been made to do so.

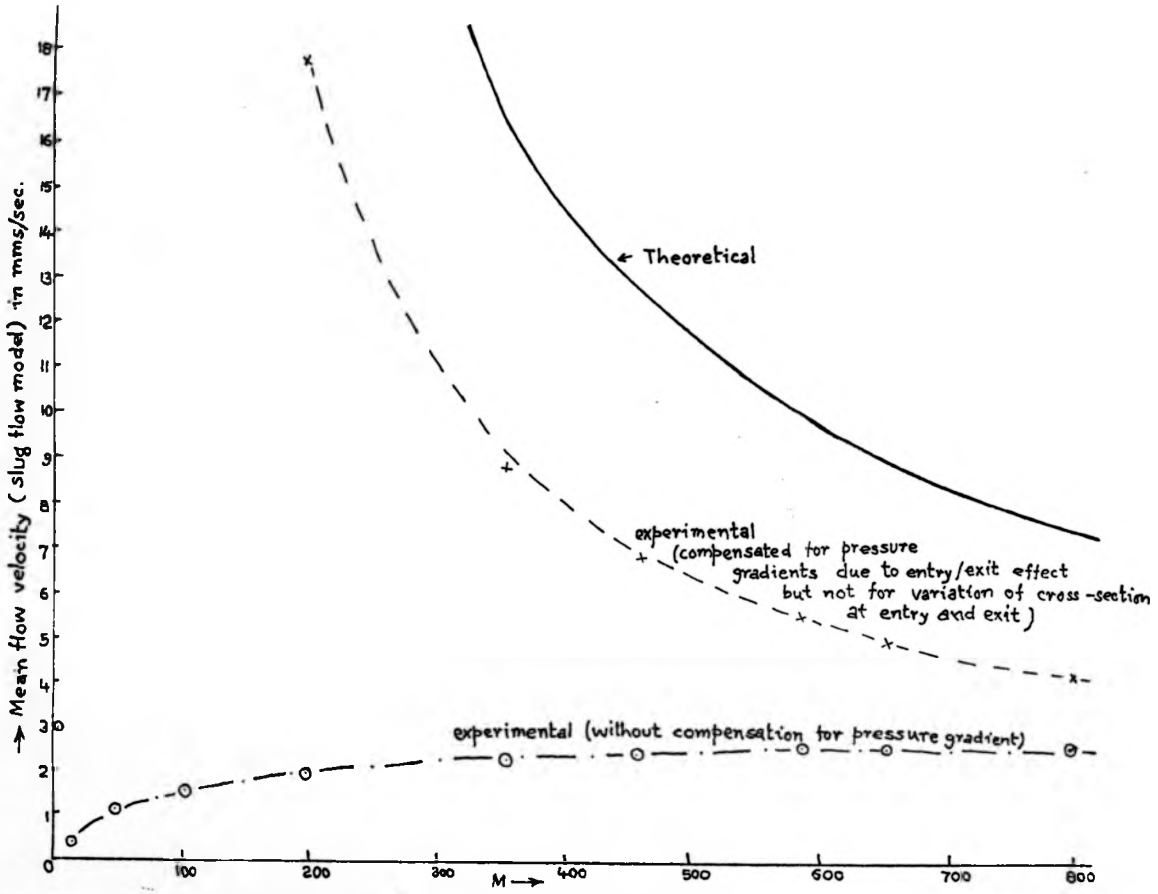

Figure 15. Variation of mean velocity of flow in the circular cross-sectional straight channel II with Hartmann Number M based on channel radius. Heater current 3x3·2 amperes. No pressure difference at the weir type mercury reservoir. — Theoretical curve. —o— Raw experimental V measurement. —x— Experimental curve with pressure difference correction across the channel.

Figure 16 Velocity profile , along the vertical diameter in channel II, evaluated from the T and ϕ^+ measurements at 3 x 3.2 amperes heating current under the assumption of $j_y = 0$.

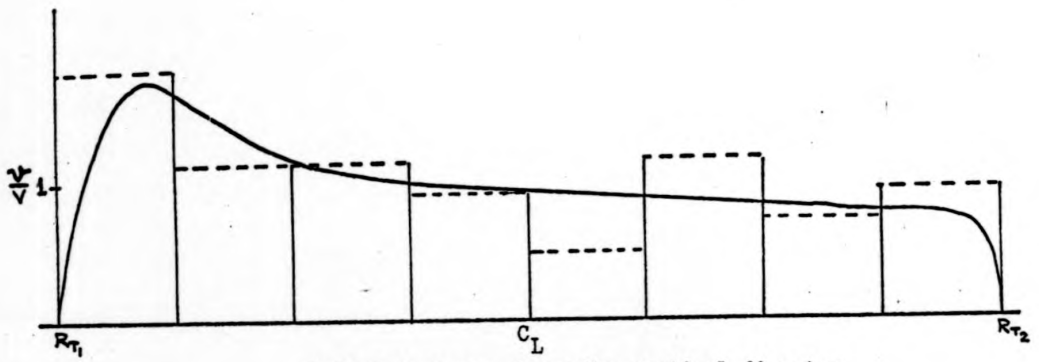

Radial distance along the vertical diameter
of Channel II
(each vertical line corresponds to the
location of the tip of thermoelectric
potential probe)

Experiments were conducted for measuring steady fluid flow (m^3/sec) for a given heater current level of 3 x 3.2 amperes with the weir type mercury reservoir completely filled up to simulate TEMHD flow without dp/dz at various Hartmann Numbers M in channel II. Experimental points (V,M), and the corresponding set partially corrected for the measured pressure differentials across the pressure taps at the two ends of the basic experimental channel length, are shown in Fig. 15 against the background of the theoretical curve. While the uncorrected experimental points do not show the typical flow maximum at a low value of M as expected theoretically [9], the partially corrected set of points do show a velocity maximum at $M \simeq 10$.

The steady mean flow was achieved within a characteristic time of 20 seconds from the instant when magnetic field and thermal flux changes were made.

4.42 Velocity profile measurement

From the measurements of temperature T and potential ϕ' in the fluid in channel II, when a steady TEMHD flow was maintained with the weir type of mercury reservoir completely filled, it is possible to construct the velocity profile along the vertical diameter under assumptions of no current flow in the vertical direction, i.e., $j_y = 0$. One such velocity profile is shown for the heater current of 3 x 3.2 amperes in Fig. 16. In fact the assumption $j_y = 0$ is not true as there was a pressure gradient along the flow direction; but even with a uniform $j_y \neq 0$, this velocity profile should be representative of such flow with a higher velocity at the top hot region.[15] Though the velocity profile along the vertical diameter is

expected to be more interesting than that along the horizontal diameter, it is not possible to construct velocity profiles along the horizontal diameter with T, ϕ^+_{out} measurement data of the existing probe with further modification.

5. Discussion and Conclusions

TEMHD experiments carried out on the circular cross-sectional straight ducts with a sinusoidal peripheral temperature distribution that is uniform along the axial direction in transverse magnetic fields show that significant TEMHD interaction could be generated in the laboratory scale models and the effect of such interactions could also be measured. Reversal of TEMHD flow and of pressure gradients dp/ds with the reversal of the direction of the magnetic field B for a given temperature gradient could be very easily be demonstrated.

For a given thermal flux transport across the channel, the peripheral temperature, and the temperature distribution in the fluid were found to vary with changes in the transverse magnetic field strength $B_\perp$. Heat transfer characteristic is therefore expected to be modified with changes in $B_\perp$ when temperature distribution along the duct periphery is maintained. Even in the basic thermally stable configuration thermal oscillations were observed in the fluid in weak magnetic fields with oscillation periods of the order of 10 sec. This implies oscillating movement of the fluid itself. It is suggested that when joule heating in the fluid is taken into consideration, the isotherms in the fluid are no longer horizontal; particularly near the central zone of the duct vertical cross-

-section perpendicular to the duct axis, the isotherms are more curved. This leads to instability due to buoyancy effect. Time periods of oscillations and the amplitudes of temperature oscillations increase with the increase in $B_\perp$ at lower magnetic field values as a relaxation oscillation mode develops due to the growing destabilising effect of buoyancy and the finite weak stabilising effect of $B_\perp$. However, at higher values of $B_\perp$ greater than a critical value B_{cr}, the stabilising effect of $B_\perp$ dominates over the maximum buoyancy effect, though how well $B_\perp$ is effective in eliminating vorticity due to buoyancy would depend on the size of the rolls.

Higher harmonic content in the peripheral temperature may also cause curvature of the isotherms in the fluid. With the temperature gradient axis away from the vertical, dp/ds measurement data with $V = 0$ show increased uncertainty and fluctuation due to buoyancy effect.

When the buoyancy effect was absent or suppressed, dp/dz and velocity measurements were used even for the determination of the absolute thermopower of the fluid accurately. However, TEMHD fluid flow without pressure gradients are impossible in the experiments described in this paper because of the entry and the exit effects of ordinary MHD. These pressure gradients are great enough to mask the velocity hump at $M \simeq 10$, unless the experimental velocity measurement data are corrected for such pressure gradients. Experimental determination of the exact value of M at which maximum V occurs was also difficult as the magnetic field could not be held

steady at such low values. The velocity hump at such a value of M_1 dependent on C_1 is a characteristic of the flow since the TEMHD driving force is proportional to $B_\perp$ and the MHD drag is proportional to $B_\perp^2$. Simple theoretical estimates suggest that the experimentally observed time to achieve steady state from the instant of thermal and magnetic field adjustment is of the same order (within 10% tolerance).

It is suggested that the thermoelectric potential probe used in the experiments described in this paper would find increasing application in TEMHD experiments. Simultaneous measurements of ϕ^+ and T in the fluid would not only throw light on the current, temperature and velocity distributions in the fluid but correlation analysis of the phase and amplitude of the fluctuating data would provide valuable information about the fluid vorticity and the roll size. By making suitable modification of the thermoelectric potential probe alignment it would be possible to construct the velocity profile across the horizontal diameter in the circular cross-sectional straight duct experiment.

6. Acknowledgements

Acknowledgement is made of the technical help received from Mr. A.E. Webb in the fabrication of the apparatus.

Financial help in the form of a Research Scholarship was provided to P.B. Dutta Gupta by the Commonwealth Scholarship Commission, U.K. at the University of Warwick, Coventry and I.I.T., Kharagpur consented to the leave of absence from their employment during the period of the research work.

References

1. Murgtroyd W. (1951) - Improvements in or relating to heat transfer systems. U.K. Patent Appl. 20911/51.

2. Luebke E.A. and Vandenberg L.B. (1953/4) - Compact reactor power plant with combination heat exchanger - thermoelectric pump. Knolls Atomic Power Laboratory Rpt. (U.S. Patent 2748710, 1956).

3. Rex Von D. (1961) - Thermoelektrische Pümpen für flüssige Metalle. VDI Z., 103(1), 17-19.

4. Osterle J.F. and Angrist S.E. (1964) - The thermoelectric - hydromagnetic pump. Trans. A.S.M.E., C, JHT, 86, 116-168.

5. Perlow M.A. andDavis K.A. (1965) - The development of the SNAP-10 thermoelectric pump. Space Nuclear Technology, Trans. A.N.S., 8, 160-161.

6. Makarov V.S. and Cherkasskii A.Kh. (1969) - Pressure consumption characteristic and efficiency of a thermoelectromagnetic pump. MHD 5, 3, 84-88.

7. Cachard M. de and Cannes P. (1969) - Thermosiphon à sodium pour irradiation en pile d'éléments combustible. CEA, Centre d'Etudes Nucleaires Grenoble Rep., Pi(R), 472-385/69, 1-10.

8. Shercliff, J.A., Alty C.J.N. and Dutta Gupta P.B. (1978) - Thermoelectric MHD. Second Bat-Sheva Seminar on MHD.

9. Shercliff J.A. (1979) - Thermoelectric magnetohydrodynamics. J.F.M. 91, P2, 231-252.

10. Shercliff J.A. (1979) - Thermoelectric magnetohydrodynamics in closed containers. Phy. Fluids, 22 (4), 635-640.

11. Shercliff J.A. (1955) - Problems in magnetohydrodynamics, Ph.D. thesis, University of Cambridge.

12. Chang C.C. and Lundgren T.S. (1961) - Duct flow in magnetohydrodynamics. ZAMP. 12 (2), 100-114.

13. Marwaha A.S. (1967) - The absolute thermoelectric power of polyvalent liquid metals. Adv. Phy. 16, N62, 617-627.

14. Holroyd R.J. (1975) - Magnetohydrodynamic duct flows in nonuniform magnetic fields. Ph.D. thesis, University of Cambridge.

15. Gnatyuk V.V. and Paramonova T.A. (1971) - Effect of the conductivity of the walls on the velocity profiles in a circular tube. MHD 7, 1, 126-128.

Investigations into Experimental Thermoelectric Magneto-hydrodynamics - Part II : Rectangular cross-sectional ducts in transverse magnetic fields.

Abstract

This is the second of the trilogy of papers on experimental 'Thermoelectric Magnetohydrodynamics' (TEMHD) in various duct configurations in transverse magnetic fields. In this paper, the rectangular cross-sectional straight duct is considered with heating at the top horizontal surface and cooling at the bottom that are uniform along the duct length and width in a horizontal uniform magnetic field transverse to the duct axis. The electrically conducting fluid used is mercury and the duct wall material is copper. To avoid uncertainty due to non-uniform temperature gradients, the duct wall-fluid interfaces perpendicular to the magnetic field have been insulated. The measurements reported include those of pressure gradients and fluid flow velocities at various temperature gradients and magnetic field strengths. Experimental results are in good agreement with the theoretically expected characteristics. However, temperature oscillations in the fluid were observed at low values of the magnetic field strength and at high values of temperature gradients. The temperature oscillations were suppressed at transverse magnetic field strengths greater than a critical value. The magnetic field also modified the heat transfer characteristic.

1. Introduction

Significant levels of thermoelectric current $\underline{j}$ in an electrically conducting fluid in transverse magnetic fields $\underline{B}$ produces 'Thermoelectric Magnetohydrodynamic' (TEMHD) body force $\underline{j} \times \underline{B}$. This body force may create pressure gradients in the fluid or affect fluid circulation and may even modify the heat transfer characteristic of the system. This is the principle of TEMHD that has been a subject of detailed theoretical investigation recently[1-3] on the premise that such high values of thermoelectric current may be generated in the lithium blanket of the Fusion reactor. It is essential to conduct experiments to test the theoretical findings and to justify the assumptions involved in the theoretical analysis. Suitable geometrical configurations of the ducts and the orientation of the magnetic field and the temperature gradient are to be considered to avoid the effect of buoyancy in the essentially non-isothermal environment of TEMHD. In part I of this series of papers[4], a circular cross-sectional straight horizontal duct in a transverse horizontal uniform magnetic field has been considered with a sinusoidal peripheral temperature distribution. In this paper, part II in the series, TEMHD in mercury contained in rectangular cross-sectional straight horizontal copper duct in a transverse horizontal magnetic field and with a positive vertical temperature gradient is considered. During the experimentation, the vertical duct wall-fluid interfaces were insulated to avoid any uncertainty due to non-uniform temperature gradients. Section 2 provides the theoretical analysis of TEMHD in rectangular cross-sectional straight ducts. The experimental set-up is described in section 3. The

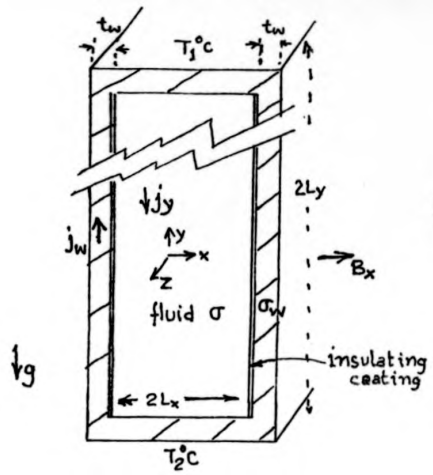

Figure 1. The rectangular cross-sectional straight duct for TEMHD experiments.

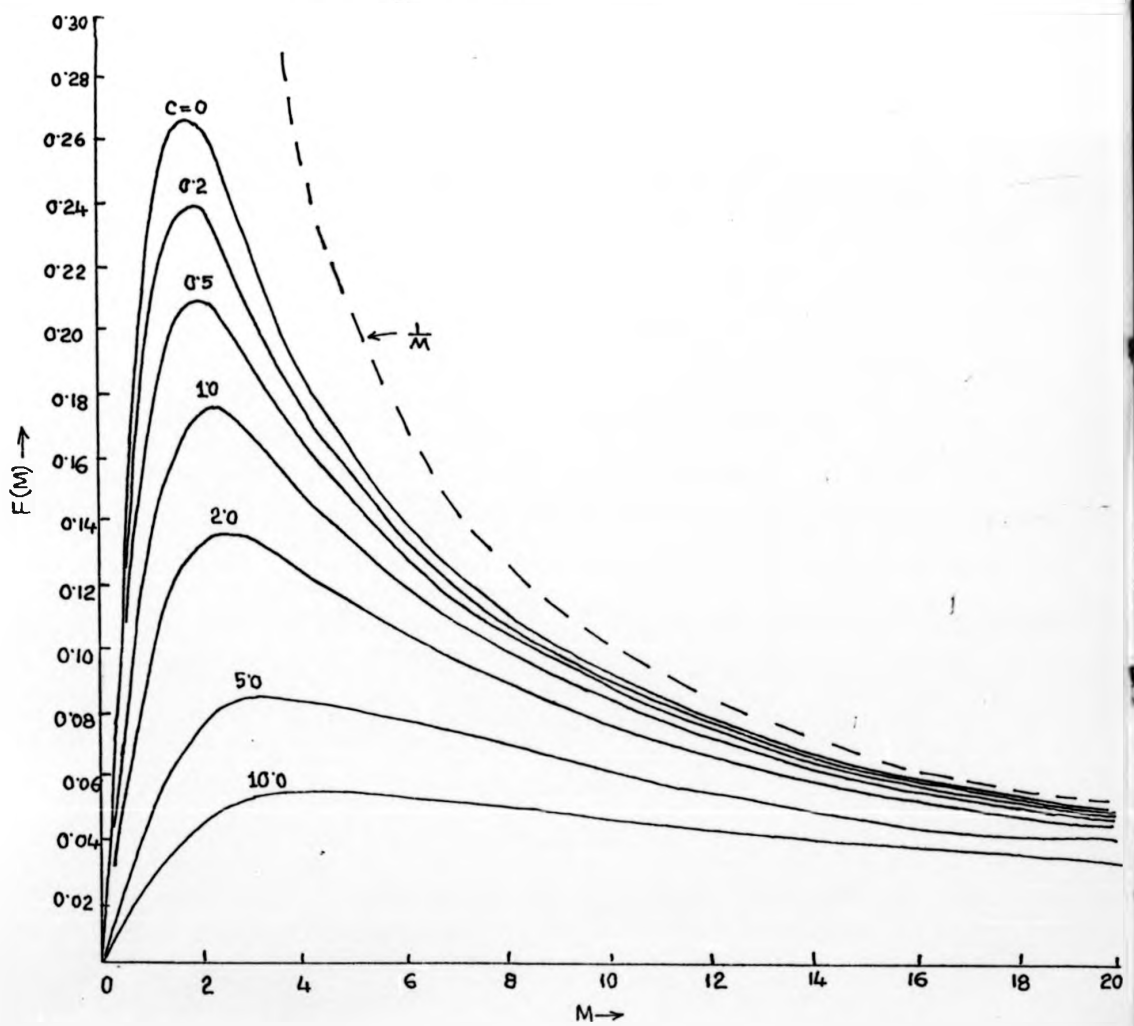

Figure 2. The variation of function F(M) with C and M for flows in rectangular channels of infinite aspect ratio due to TEMHD. F(M) indicates V_z. (Shercliff 1979)

experimental results of temperature, pressure gradient and fluid flow velocity measurements are presented in section 4. Section 5 provides the discussion and relevant conclusions.

2. TEMHD theory in Rectangular Cross-sectional straight ducts

Shercliff[1,2] has analysed the TEMHD flow in a rectangular cross-sectional straight duct with a large aspect ratio (height/width = L_y/L_x , Fig. 1) for a given pressure gradient dp/ds along the duct. The mean flow rate V is given by

$$V = \frac{M - \tanh M}{M + c \tanh M} \left\{ \frac{\alpha}{B} \frac{dT}{dy} - \frac{1+c}{\sigma B^2} \frac{dp}{ds} \right\}$$

where M is the Hartmann Number $\sqrt{\frac{\sigma}{\eta_y}} BL_x$, α is the average thermopower of the wall material — fluid combination, dT/dy is the vertical temperature gradient. B refers to the transverse magnetic field, σ , η_y to the fluid conductivity and viscosity respectively and c refers to the fluid to wall conductance ratio $\frac{\sigma L_x}{\sigma_w t_w}$, L_x being the half width of the channel and t_w, σ_w being the duct wall thickness and conductivity respectively. The (V,M) relationship in Fig. 2 shows a characteristic maximum V at a low value of M, depending on the value of c, when TEMHD driving force (proportional to B) balances the MHD drag (proportional to B^2).

The Hartmann problem in TEMHD may be analysed to give a fluid flow velocity

$$v = \frac{M}{M + c \tanh M} \left\{ \frac{\alpha}{B} \frac{dT}{dy} - \frac{1+c}{\sigma B^2} \frac{dp}{ds} \right\} \left(1 - \frac{\cosh MX/L_x}{\cosh M} \right)$$

The corresponding Hartmann problem in TEMHD with a finite aspect ratio (L_y/L_x) may be analysed by suitably modifying the core flow and boundary layer analysis of

Stewartson and Hunt[5] and that of Chiang and Lundgren[6]. For $M \gg 1$ and ϵ, the mean flow is given by

$$V = \frac{\alpha T_m}{BL_y} - \frac{1+\epsilon}{B^2}\frac{dp}{ds}$$

where $2T_m = T_1 - T_2$; T_1, T_2 being the temperatures at the top and bottom horizontal wall-fluid interfaces respectively and T_m/L_y is the vertical temperature gradient along the channel height $2L_y$.

Under assumptions of uniform j_y and $\frac{dT}{dy}$, the mean TEMHD flow velocity, at large Hartmann Numbers in rectangular cross-sectional ducts with all the walls and the wall-fluid interfaces perfectly conducting, (TEMHD problem corresponding to the problem of ordinary MHD of Chang and Lundgren[7]) is also given by

$$V = \frac{\alpha T_m}{BL_y} - \frac{1+\epsilon}{\sigma B^2}\frac{dp}{ds}$$

When the net flow along the duct axis s is blocked i.e., $V = 0$ TEMHD forces produce a pressure gradient $\frac{dp}{ds} = \frac{\sigma \alpha T_m B}{(1+\epsilon) L_y}$.

3. The Experimental set-up and the measurement system

The basic structure of the experimental channel was made from a rectangular cross-sectional (nominal size 3.81 x 3.09 cm^2, inner bore 2.7 x 2.46 cm^2) copper pipe supplied by the Coventry Metal Bars Ltd. The duct vertical sidewall thickness was 0.55 cm. The other pair of (horizontal) walls of the duct were used as the heating and cooling boundaries and were 0.32 cm thick. A total length of 31 cm (effective length 30 cms) was made up of two symmetrical sections of the

copper duct each 15 cm long with a central insulating gland made of 'Tufnol' 1 cm long separating them. The central insulating gland was designed to accommodate probes for internal measurements of temperature and pressure in the duct.

Two identical heater coils made of 26 SWG Nichrome resistive wire, located over a thin layer of fibre glass and MgO insulation applied on the top horizontal outer surface of the copper duct, provided the heating. The heater coils were enclosed in five clay and Asbestos to reduce heat leak to the atmosphere. The heater coils were held in position with stainless steel straps. The bottom surface was cooled by running water in the two water jackets built on the copper duct sections by brazing extra half-section pieces of the copper channel. The water inlet port was at the middle of each section and the two outlets per section were located symmetrically at the ends of each section. The thick sidewalls of the duct conducted away much of thermal flux and a temperature gradient of 610° K/m only could be maintained at a power input of 6.35 KW/m^2. Thermal energy flow accounting gave a 5% input heat lost to the ambient surrounding through the thermal lagging.

Mercury used for the experiments was of the double distilled purity grade. The vertical sidewalls of the rectangular cross-sectional duct were insulated from the fluid by glueing 0.5 mm thin strips of 'tufnol' to eliminate the possibility of current flow across the vertical wall-fluid interface and the associated fluid vorticity due to non-uniform temperature gradients. The final dimensions of the duct is given in Table 1.

copper duct each 15 cm long with a central insulating gland made of 'Tufnol' 1 cm long separating them. The central insulating gland was designed to accommodate probes for internal measurements of temperature and pressure in the duct.

Two identical heater coils made of 26 SWG Nichrome resistive wire, located over a thin layer of fibre glass and MgO insulation applied on the top horizontal outer surface of the copper duct, provided the heating. The heater coils were enclosed in five clay and Asbestos to reduce heat leak to the atmosphere. The heater coils were held in position with stainless steel straps. The bottom surface was cooled by running water in the two water jackets built on the copper duct sections by brasing extra half-section pieces of the copper channel. The water inlet port was at the middle of each section and the two outlets per section were located symmetrically at the ends of each section. The thick sidewalls of the duct conducted away much of thermal flux and a temperature gradient of 610° K/m only could be maintained at a power input of 6.35 KW/m^2. Thermal energy flow accounting gave a 5% input heat lost to the ambient surrounding through the thermal lagging.

Mercury used for the experiments was of the double distilled purity grade. The vertical sidewalls of the rectangular cross-sectional duct were insulated from the fluid by glueing 0.5 mm thin strips of 'tufnol' to eliminate the possibility of current flow across the vertical wall-fluid interface and the associated fluid vorticity due to non-uniform temperature gradients. The final dimensions of the duct is given in Table 1.

Figure 3 The perspective view of the experimental, rectangular cross-sectional straight duct.

(Heater Coils and the insulation not shown)

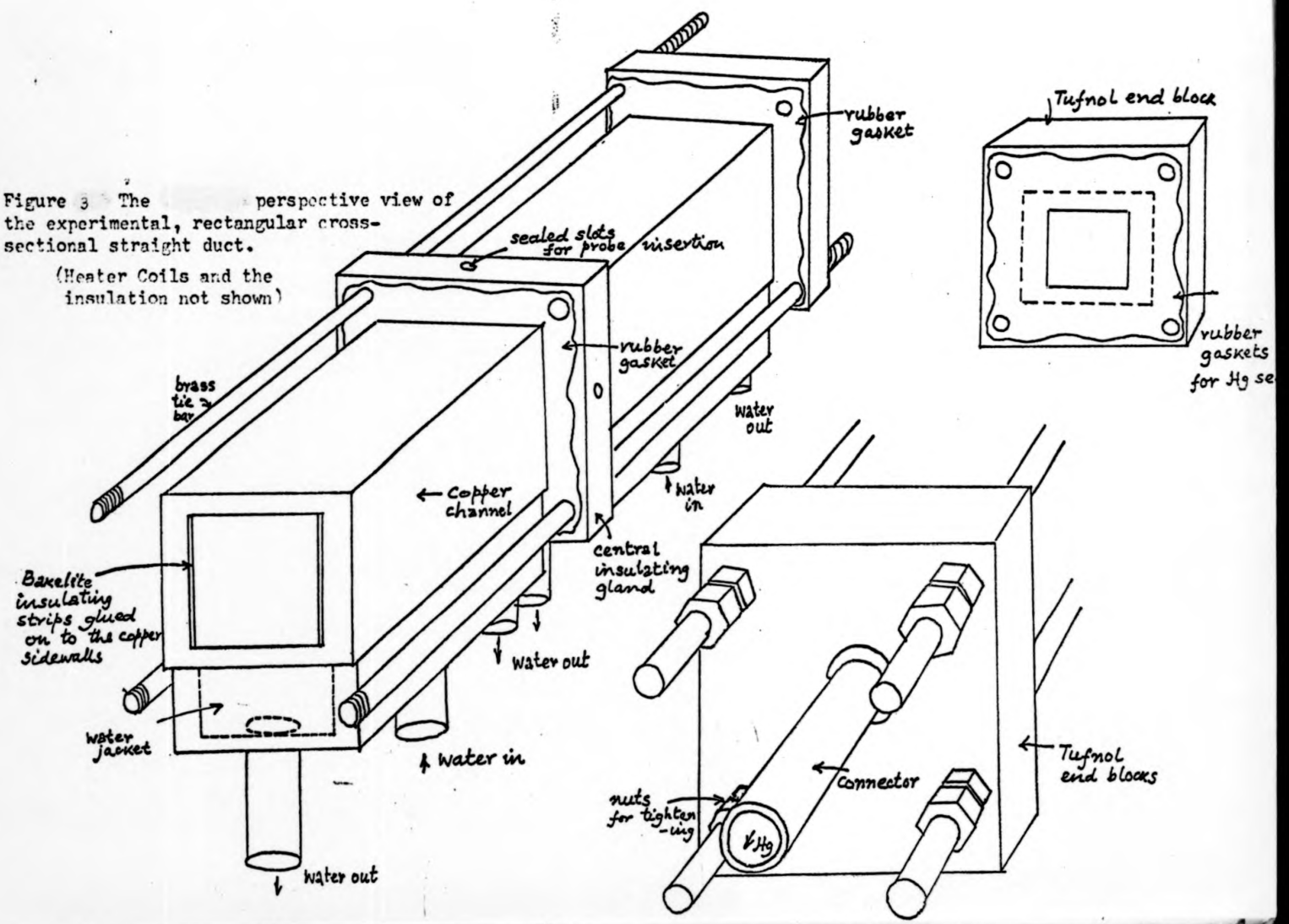

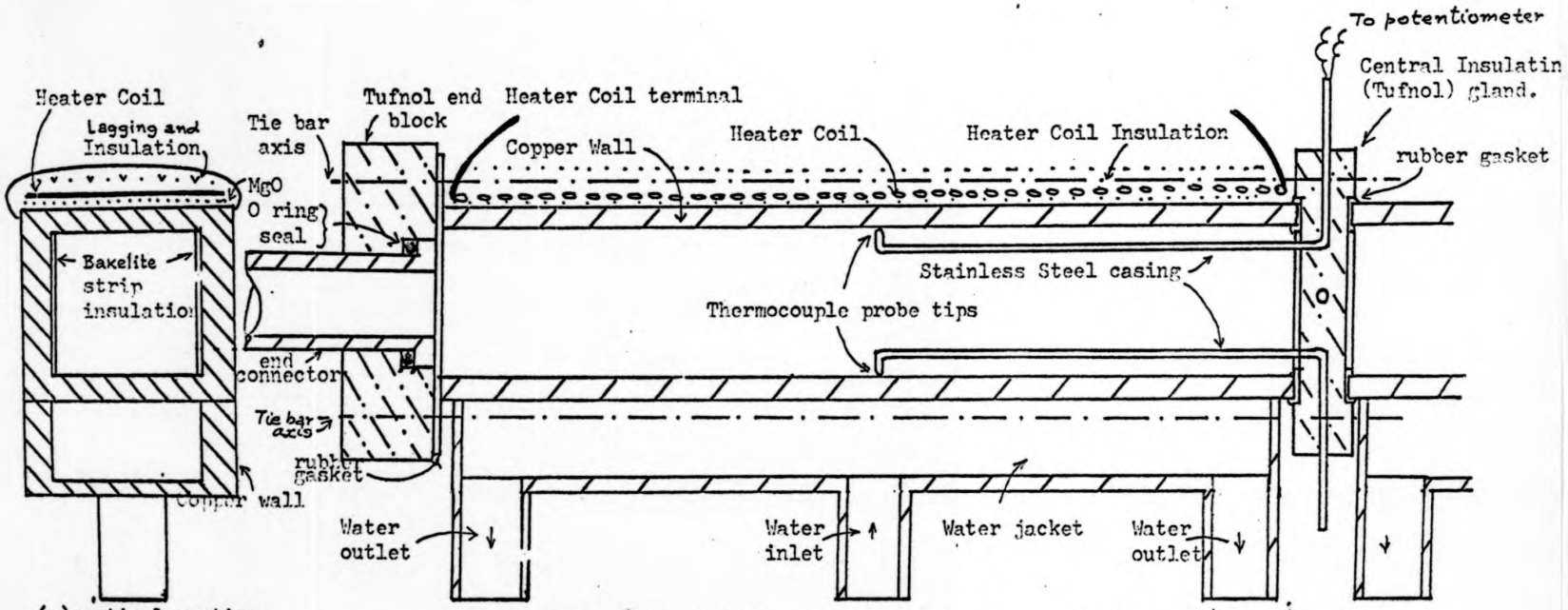

Figure 4 Sectional views of the rectangular cross-sectional straight duct for TEMHD experiment. (Full Scale Diagram)

Table 1

Rectangular cross-sectional straight duct dimensions.

Length/section (Two identical sections)	15 cm	
Inner bore	$2L_y = 2.46$ cm	$2L_x = 2.485$ cm
Outer Size	$2L'_y = 3.10$ cm	$2L'_x = 3.785$ cm
Tolerance of measurement	0.005 cm.	

The end sections of the overall assembly were made of blocks of 'tufnol' with suitable grooves into which round connector tubes were fixed by sealing with 'O' rings and glue. The sealing of Hg at the rectangular peripheries at the end flanges and at the central gland were made with vulcanised rubber gaskets. A partially blown-up perspective view of the assembly is shown in Fig. 3. Sectional view of the assembly is shown in Fig. 4. The assembly of the two half-sections of the copper duct and the central insulating gland were held in position by four brass tie bars.

Two thermoelectric probes (Chromel-Alumel wires insulated by vulcanised rubber sleeves and encased in insulated stainless steel tubes were inserted through the central insulating gland. The tips of the thermoelectric probes were located at the central points of the top and bottom wall-fluid interfaces of one of the half section length of the duct. Pressure taps were located at the central gland and at the end flanges and were connected to the inclined tube manometer for pressure difference measurements.

The assembly of the experimental duct was held horizontally in the air gap space of the water-cooled 'Lintott'

Table 2 Experiment operating conditions in the rectangular cross-sectional duct experiment and evaluation of α to compare with α pure grade

Heater coil Voltage	Current	T_1	T_2	ΔT	T_m	T_{av}	c	σ	Trend line $\Delta h = \frac{\sigma \alpha T_m B \times 0.3}{\rho_{Hg} g (1 + c) L_y}$	$\alpha_{pure\ grade}$	$\alpha_{expt_{av}}$
		^oC									
95	2	20	16	4	2	18	0.0391	1.046	0.2335 B	6.423	6.43
135/140	3	30	21	9	4.5	25.5	0.0401	1.039	0.5387 B	6.64	6.6
160	3.5	33	21	12	6	27	0.0402	1.038	0.7218 B	6.8.	6.6
180	4	37	22	15	7.5	29.5	0.0406	1.035	0.9095 B	6.756	6.75
205	4.5	41	23	18	9	32	0.0409	1.033	1.1003 B	6.825	6.8
230	5	47	25	22	11	36	0.0414	1.029	1.3623 B	6.945	6.9

Rectangular duct

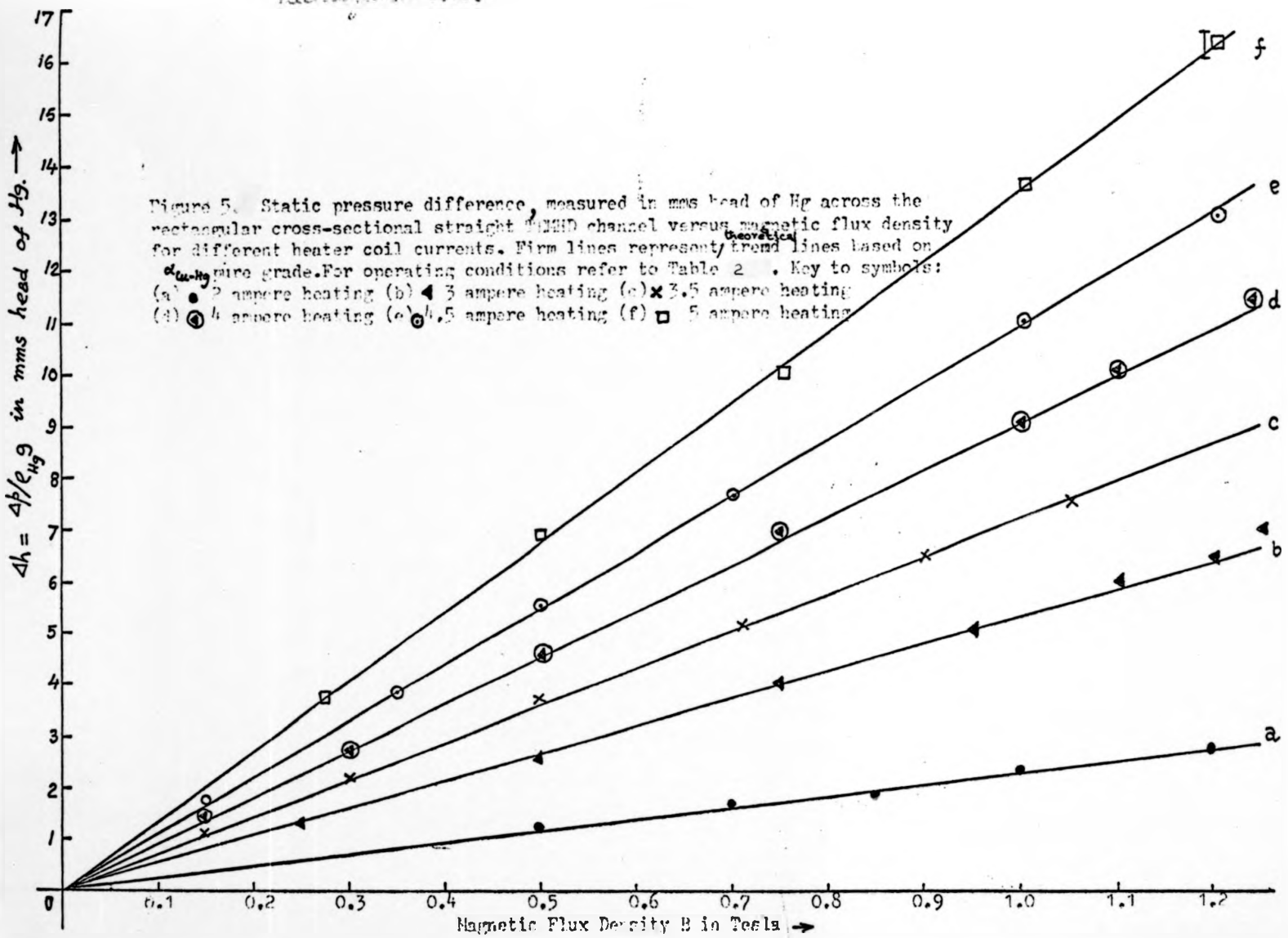

Figure 5. Static pressure difference, measured in mms head of Hg across the rectangular cross-sectional straight duct channel versus magnetic flux density for different heater coil currents. Firm lines represent theoretical trend lines based on $\sigma_{Cu\text{-}Hg}$ wire grade. For operating conditions refer to Table 2 . Key to symbols: (a) ● 2 ampere heating (b) ◀ 3 ampere heating (c) × 3.5 ampere heating (d) ◉ 4 ampere heating (e) ⊙ 4.5 ampere heating (f) □ 5 ampere heating

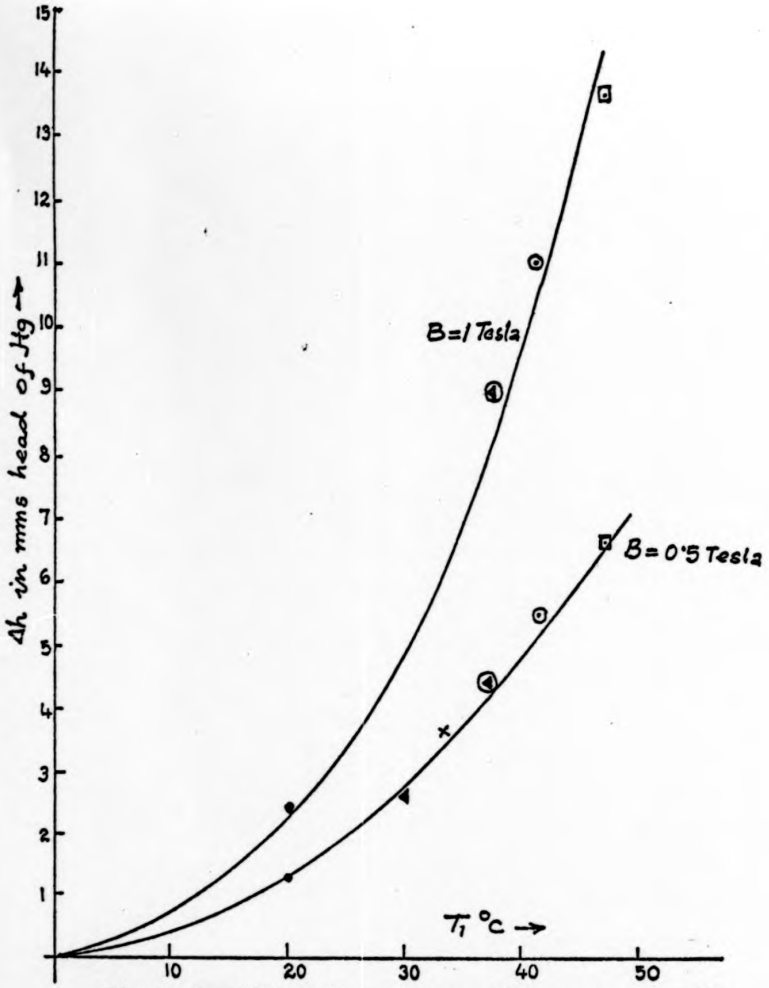

Figure 6 TEMHstatic pressure difference acrossthe rectangular cross-sectional straight channel vs T_1 for B= 0.5 and 1.0 Tesla. Key to symbols refer to figure 5

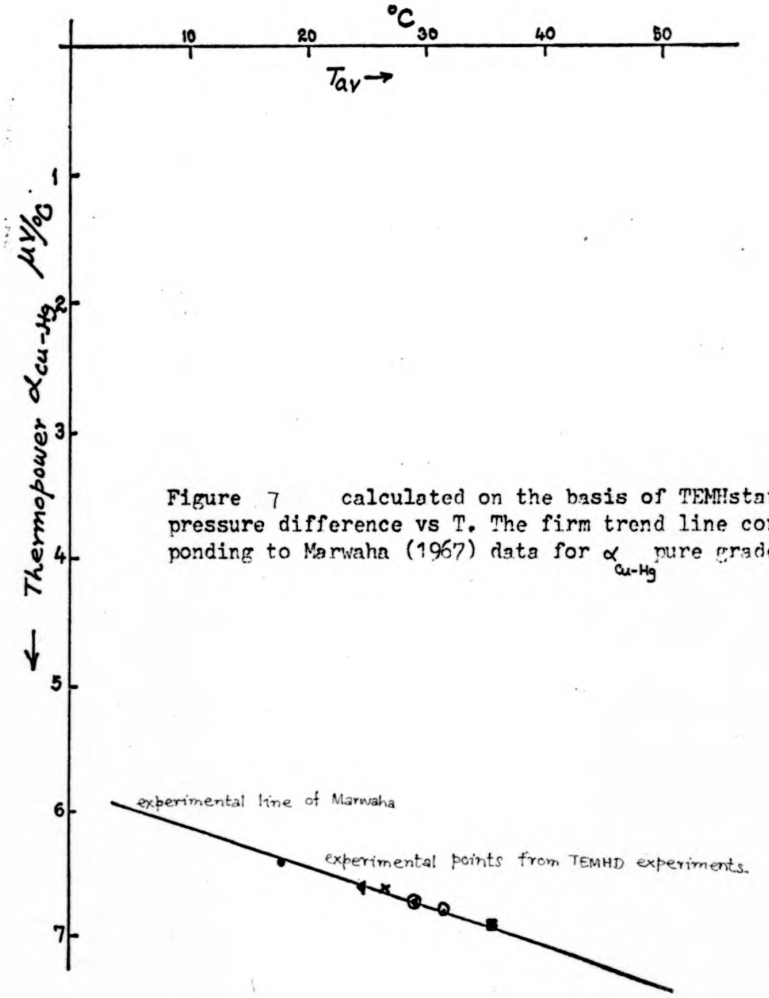

Figure 7 calculated on the basis of TEMHstatic pressure difference vs T. The firm trend line corresponding to Marwaha (1967) data for $\alpha_{Cu\text{-}Hg}$ pure grade.

electromagnet that provided a transverse horizontal magnetic field upto a maximum intensity of 1.25 Tesla. The mercury loop external to the electromagnet consisted of PVC tubes, connectors, an electromagnetic flowmeter and a weir type mercury reservoir with mercury filling system similar to that described in Part I of the series of papers.

4. Experimental Results

4.1 $\frac{dP}{dz}$ vs B, ΔT measurements at V = 0

The pressure difference across the experimental section due to TEMHD forces was measured at the inclined tube manometer, when the levels of Hg at the weir type reservoir were so adjusted that there was no flow of Hg over the weir. Fig. 5 shows the pressure difference in mms of head of Hg for different heating and cooling conditions against the magnetic flux density. The pressure difference readings were reproducible within a tolerance of 3% and agreed consistently when the direction of magnetic flux density B was reversed without altering the magnitude of B. The experimental operating points corresponding to Fig. 5 are summarized in Table 2, which also shows the calculation of Δp based on theoretical calculations with Marwaha[8] data for the pure grade α_{Cu-Hg} These theoretically predicted Δp vs B values are shown as a firm line for each of the different temperature gradient conditions in Fig. 5.

The graphical plots of Δp vs T_1 for the experimentally measured values of Δp and T_1 at constant magnetic flux densities of B = 0.5 and B = 1 Tesla are shown in Fig. 6.

Figure 8 Plot of mean velocity (without pressure drop correction) in the rectangular cross-sectional straight channel in mm/sec against M based on half width of the channel L_x = 1.2425 cm.

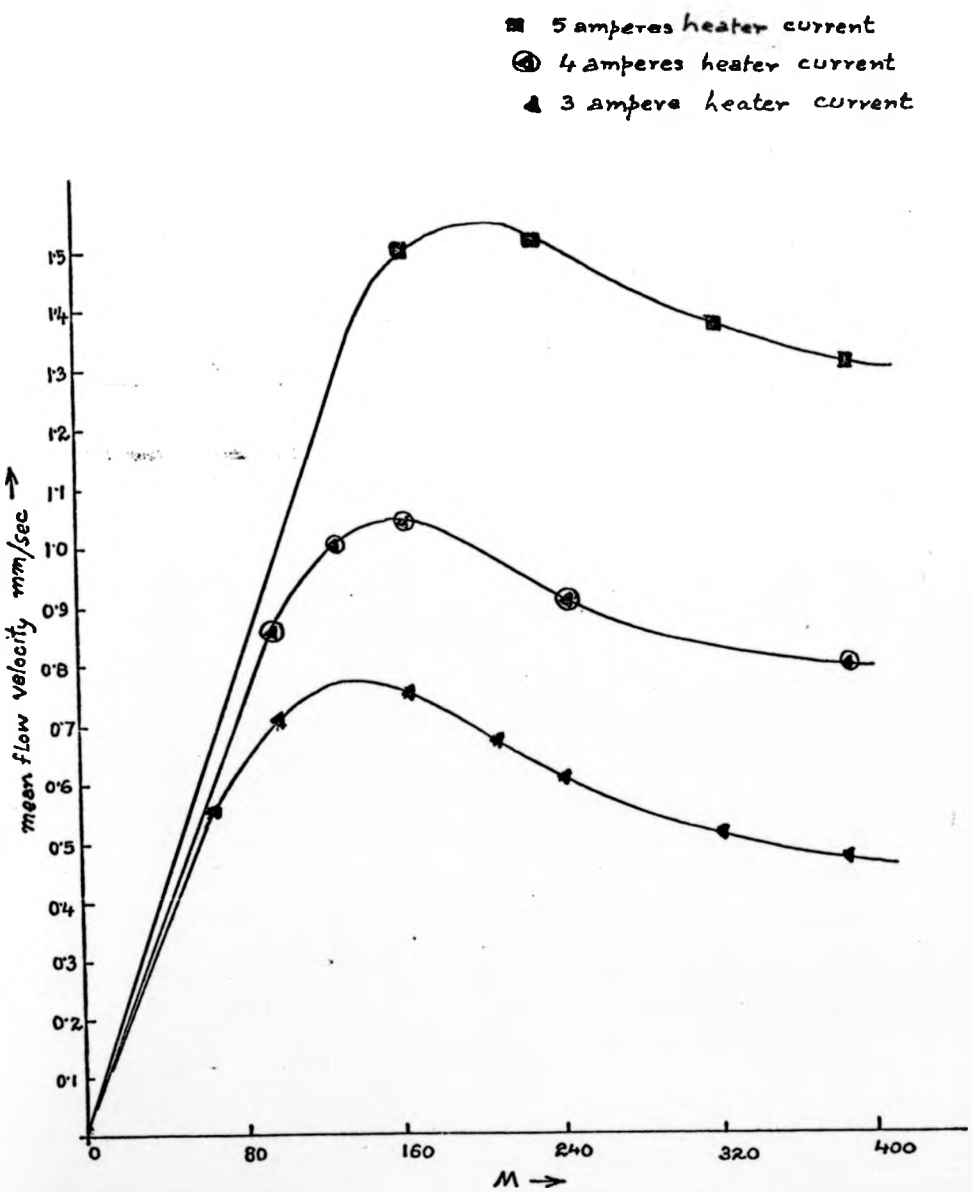

These graphical plots suggest a linear dependence of α on temperature.

4.2 Evaluation of α from $\frac{dp}{ds}$ measurements at V = 0

The extra-ordinarily good fit of the experimental data of Fig. 5 with the theoretically predicted values based on pure grade α_{Cu-Hg} justifies the use of $\frac{dp}{ds}$ measurements as a new way of determining α with the fluid and the wall conductivities known a priori. Fig. 7 shows the calculated values of $\alpha_{Cu-Hg}(T_{av})$ from the experimentally measured $\frac{dp}{ds}$ values at V = 0 and T_1 and T_2 (first set). The Marwaha[8] data (second set) of α_{Cu-Hg} is shown as a firm line in Fig. 7. For the scale used for the plot, these two sets of data cannot be distinguished from each other but the first set of data is within $\pm$ 1.5% of the second set of data of α_{Cu-Hg}.

4.3 Mean flow measurement

Fluid flow rate due to TEMHD forces generated in the rectangular cross-sectional duct was measured by the electromagnetic flowmeter. The flow rate was very low due to the small temperature gradients that could be maintained even at maximum loading of the heater coil. It is difficult to compensate for the pressure gradients due to entry and exit effects and due to flow in non-uniform magnetic fields. The raw (uncompensated for pressure gradients) mean velocity data at various Hartmann Numbers M based on half the channel width L_x = 1.2425 cm. are shown in Fig. 8 for different current loadings of the heater coil when there was no difference in the head of mercury at the weir type reservoir.

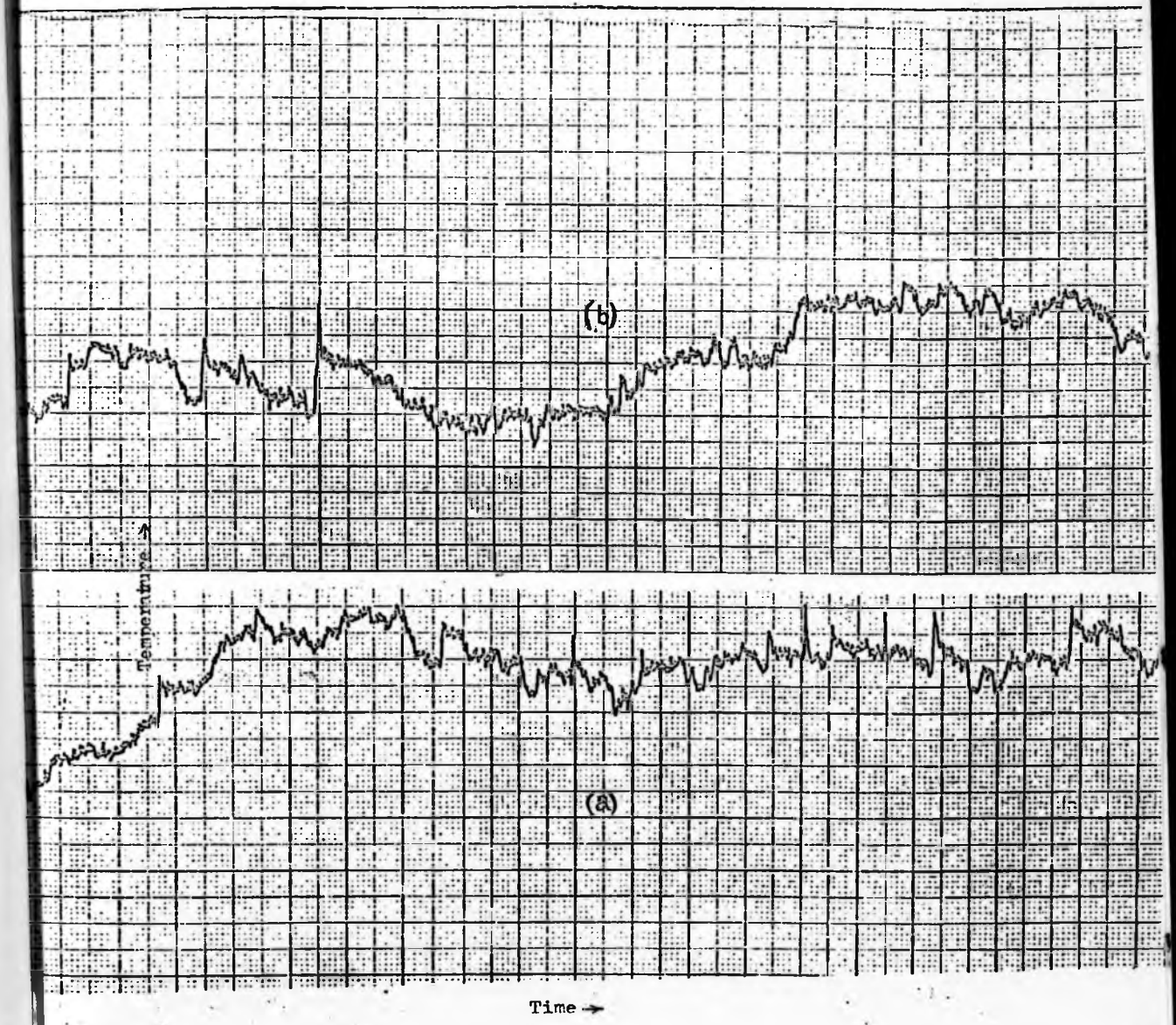

Figure 9 Temperature fluctuation with time in the rectangular cross-sectional straight channel under the influence of the transverse magnetic field. The traces progress from left to right with time with horizontal time scale of 15 sec / cm . The vertical scale corresponds to 1°C / cm.

(a) Fluctuations in T_1, top wall solid-liquid interface temperature and
(b) Fluctuations in T_2, Bottom wall solid-liquid interface temperature.

$T_1 > T_2$

Operating condition 3amp heating current
B= 1.0 Tesla.

4.4 Temperature oscillations

The most surprising observation during the experiments in the rectangular cross-sectional duct was that of the fluctuation in the measurement of T_1 and T_2 at low magnetic fields and at high temperature gradients. A maximum of 2°C to 3°C fluctuation in amplitude representing a $\pm$ 3% variation about the time averaged values of T_1 and T_2 was recorded. These temperature oscillations persisted even at high magnetic flux density of B = 1.2 Tesla though the amplitude of fluctuation was reduced. Typical records of the fluctuations in T_1 and T_2 with time for a heater current of 3 amperes in a transverse magnetic field of 1 Tesla is shown in Fig. 9. Changes in the magnitude of the transverse magnetic field also affected a change in the values of T_1 and T_2 of the order of a maximum of 1° to 2°C. Accurate determination of such temperature changes was virtually impossible as temperatures fluctuated with two superimposed periodic variation.

The characteristic settling time to steady state in the flow measurement and the time to build up in the case of pressure gradient measurements with V = 0 from the instant of magnetic field and temperature gradient adjustment were of the same order in the range of 15 to 20 seconds.

5. Discussion and conclusions

The extra-ordinarily good fit of the experimental data for dp/dz when V = 0 with the theoretically predicted values based on pure grade material properties (σ, α) for the TEMHD experiments in the rectangular cross-sectional duct is in

direct contrast to the lower values of the experimentally measured mean flow rates as compared with the theoretically expected mean flow rates. The main drawback in the case of mean flow rate measurement is that of how accurately the experimentally measured velocity data can be corrected for the inherent pressure gradients in the mercury loop due to entry and exit effects. However, the mean flow rate vs M plots do show a velocity maximum at an intermediate value of M, though the experimental values of M for velocity maxima are much higher than those predicted theoretically. It is true that when the experimental data for the mean flow rate are corrected for the MHD pressure gradients, the corresponding values of M for velocity maxima would shift towards lower values. Velocity profile measurements would have been interesting but it was not possible to do so with the practical difficulty encountered in making the internal measurement probe insertion system leak-proof.

Fluctuations in the measurement of T_1 and T_2 at low magnetic field strengths that persist even at high magnetic flux densities of 1.2 Tesla, though at a reduced amplitude, cannot be explained without the knowledge of isotherm curvature. Thermal instability is theoretically possible when joule heating in the fluid is considered if $\alpha > (1+c)\sqrt{\frac{K}{\sigma x_m}}$ where K refers to the thermal conductivity of the fluid; but this inequality is satisfied only at extremely high temperature T_m. The time records of the fluctuation in T_1 and T_2 show two superimposed modes of periodic fluctuation, the ratio of the periods being 20 and the smaller period spans approximately 12 seconds. From the changes observed in T_1 and T_2 with changes in B for a given thermal flux transport it could be only inferred that fluid eddies due to buoyancy did exist in planes containing

B and perpendicular to the duct axis. It also implies that when fixed T_1 and T_2 values are maintained, magnetic field changes would modify the heat transfer. It would be interesting to have detailed internal measurements in the fluid to determine the isotherm curvature and the fluid vorticity to confirm these inferences.

6. Acknowledgements

Acknowledgement is made of the technical help received from Mr. A.E. Webb in the fabrication of the apparatus.

Financial help in the form of a Research Scholarship was provided to P.B. Dutta Gupta by the Commonwealth Scholarship Commission, U.K. at the University of Warwick, Coventry and I.I.T., Kharagpur consented to the leave of absence from their employment during the period of research work.

References

1. Shercliff J.A., Alty C.J.N. and Dutta Gupta P.B. (1978) - Thermoelectric MHD. Second Bat - Sheva Seminar in MHD.

2. Shercliff J.A. (1979) - Thermoelectric magnetohydrodynamics. J.F.M. 91, P 2, 231-252.

3. Shercliff J.A. (1979) - Thermoelectric magnetohydrodynamics in closed containers. Phy. Fluids, 22(4), 635-640.

4. Dutta Gupta P.B. and Shercliff J.A. - Investigations into Experimental Thermoelectric Magnetohydrodynamics - Part I : Circular cross-sectional straight ducts in transverse magnetic fields - Paper to be submitted for publication.

5. Hunt J.C.R. and Stewartson K. (1965) - Magnetohydrodynamic flow in rectangular ducts II. J.F.M. 23, P3, 563-581.

6. Chiang D. and Lundgren T.S. (1967) - Magnetohydrodynamic flow in rectangular duct with perfectly conducting electrodes. ZAMP 18, 92-105.

7. Cheng C.C. and Lundgren (1961) - Duct flow in magneto-hydrodynamics. ZAMP 12(2), 100-114.

8. Marwaha A.S. (1967) - The absolute thermoelectric power of polyvalent liquid metals. Adv. Phy. 16, N62, 617-627.

Investigations into Experimental Thermoelectric Magnetohydrodynamics - Part III : Annular channels of rectangular cross-section in axial magnetic fields.

Abstract

This is the third and the final part of the trilogy of papers on experimental 'Thermoelectric Magnetohydrodynamics' (TEMHD) in various duct configurations in transverse magnetic fields. In this final part, annular channels of rectangular cross-section (finite aspect ratio) are considered with heating and cooling at the outer and inner vertical cylindrical surfaces respectively in a vertical axial magnetic field. The electrically conducting fluid is mercury and the channel is made of copper. The TEMHD flow is along the torus (endless channel) which is entirely inside the uniform field region of the electromagnet. The top horizontal ends of the channels are left open to allow free surface of mercury for probe insertion and visual measurements. Three different types of wall-fluid interface conductivity at the bottom horizontal wall are considered : (a) totally insulating (b) partly insulating and partly conducting and (c) totally conducting. The measurements reported in this paper include those of the azimuthal velocity of the fluid due to TEMHD forces and the secondary flow due to curvature and buoyancy inherently present in the system, at various temperature gradients and magnetic field strengths. Extensive temperature measurements in the fluid have been made to obtain temperature distribution patterns in the fluid that explains the mode of heat transfer. Measurements of thermal oscillations in the fluid at high temperature gradients and low Hartmann Numbers are also included. A few measurements of the

transient TEMHD flow during sudden magnetic field changes are reported.

1. Introduction

'Thermoelectric Magnetohydrodynamic' (TEMHD) body force $\underline{j} \times \underline{B}$ is generated in the fluid due to the interaction of the thermoelectric current $\underline{j}$ in the fluid and the external magnetic field $\underline{B}$. This body force may be significant enough in the lithium blanket of a magnetically confined thermonuclear reactor where large temperature gradients exist to induce fluid circulation that might affect the heat transfer characteristic. On this premise, detailed theoretical studies[1-3] on TEMHD have been carried out recently. Experimental investigations on TEMHD in various geometrical configurations of ducts with different magnetic field orientations to the duct axis are reported in this series of papers. In part I[4] of the series of papers, TEMHD in a circular cross-sectional straight horizontal duct with sinusoidal peripheral temperature distribution in a transverse magnetic field has been considered. TEMHD in a rectangular cross-sectional horizontal straight duct in horizontal magnetic fields transverse to the duct axis has been presented in Part II[5]. In this final part III in the series, experimental investigations into TEMHD in annular channels of rectangular cross-section of finite aspect ratio in an axial vertical magnetic field are reported. The electrically conducting fluid is mercury and the channel is made of copper. Heating and cooling arrangements are at the outer and inner vertical cylindrical surfaces respectively so that the TEMHD fluid flow is along the torus (endless channel) which is entirely inside the uniform field region of the electro-

-magnet. This configuration thus permits TEMHD fluid flow without pressure gradients which was impossible to obtain in the configurations of Part I and II of this series of papers. The top horizontal ends of the annular channels are left open to have free surface of mercury for the convenience of probe insertion for internal measurements in the fluid and visual measurements at the free surface. Three different types of wall-fluid interface conductivity at the bottom horizontal wall are considered. Type I has a totally insulating wall-fluid interface at the bottom wall that gives the azimuthal fluid flow velocity, due to TEMHD, as an inverse functional form of the radial distance. In type II the wall-fluid interface at the bottom wall is partly insulating and partly conducting so that by maintaining a radial temperature gradient proportional to the radial distance over the conducting bottom wall-fluid interface, two different azimuthal velocity profiles are generated giving a shear layer at the changeover region of the bottom wall-fluid interface conductivities. Type III has a totally conducting wall-fluid interface at the bottom wall. The curvature of the torus and the horizontal temperature gradient used in the experiments with the annular channels generate secondary flow.

In section 2, a brief treatment is given to the theoretical analysis of TEMHD in annular channels with rectangular cross-section in axial vertical magnetic fields. The three types of channels used for the experiments and the experimental set up are described in section 3. The special measurement system is presented in section 4 while the experimental results are reported in section 5. Section 6 covers the discussion and the conclusions.

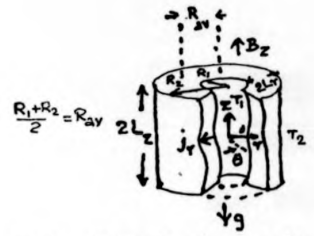

Figure 1. The basic annular channel configuration and the co-ordinate system.

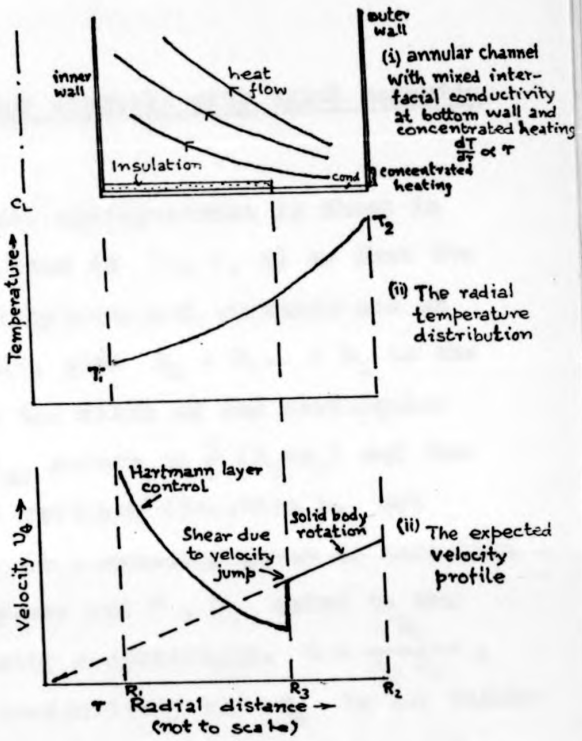

Figure 2. (i), (ii), (iii). The schematic diagram showing the free shear layer generation by TEMHD in a mixed conductivity solid-fluid interfacial bottom walled annular channel with concentrated heating $\frac{dT}{dr}$ oc r.

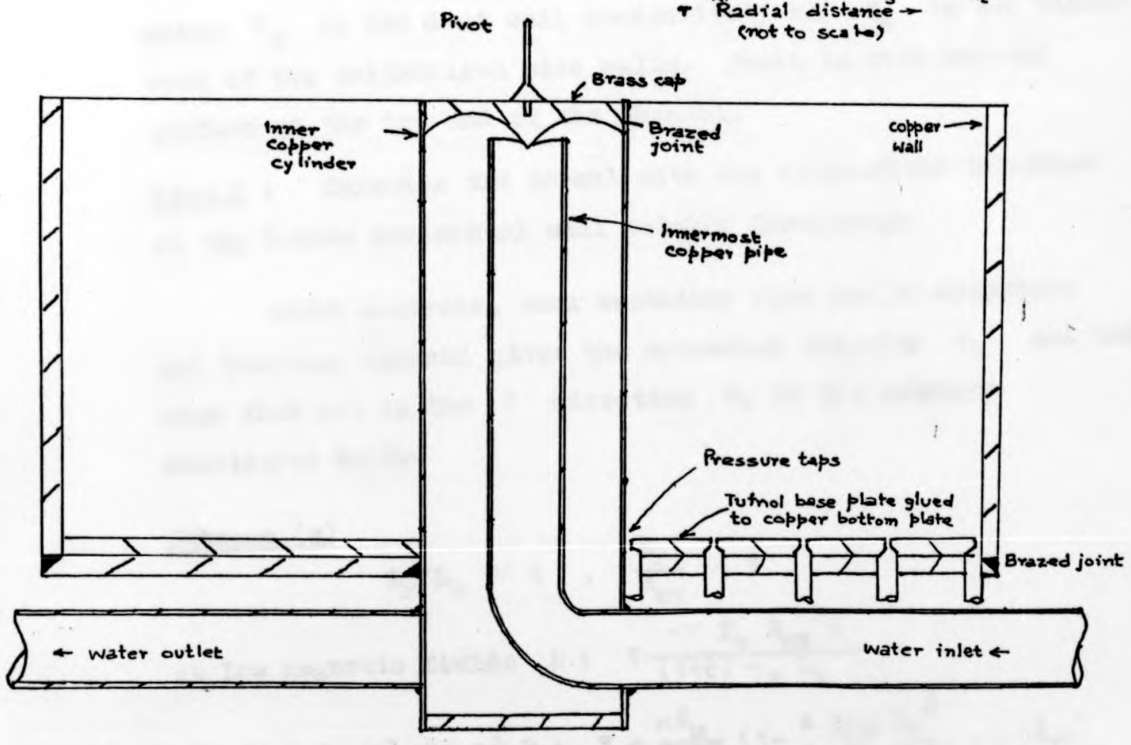

Figure 3. Full scale vertical section through the radial line of pressure taps of the mark II annular channel with insulated solid-liquid interface at the bottom wall.

2. TEMHD theory in annular channels with axial magnetic fields

The basic annular channel configuration is shown in Fig.1 where the co-ordinate system is (r, θ, z) so that the hot (T_2°C) and the cold (T_1°C) cylindrical surfaces are at $r = R_2$ and $r = R_1$ respectively, with $R_2 > R_1$. $2L_z$ is the height and $2L_r = R_2 - R_1$ is the width of the rectangular cross-section of the duct. R_{av} refers to $\frac{1}{2}(R_1+R_2)$ and the magnetic field $B_z = B$ is in the vertical direction z. Let $2T_m = T_2 - T_1$. The azimuthal (θ) symmetry gives no variation in θ. Let α be the thermopower and σ, η_v refer to the fluid conductivity and viscosity respectively. $C = \frac{\sigma L_r}{\sigma_w t_w}$, where σ_w is the duct wall conductivity and t_w is the thickness of the cylindrical side walls. There is free mercury surface at the top end of the channel.

Case I : Consider the channel with the solid-fluid interface at the bottom horizontal wall totally insulating.

TEMHD analysis, when secondary flow due to curvature and buoyancy is ignored gives the azimuthal velocity v_θ and the mean flow rate in the θ direction, V_θ in the subcases considered below.

Subcase (a)

$$L_r/L_z \ll 1 \quad , \quad \frac{L_r}{R_{av}} \ll 1$$

at low magnetic fields B : $$V = \frac{\alpha\sigma T_m R_{av}^2 B}{(1+c)\eta_v L_r}$$

at moderate values of B : $$V = \frac{\alpha T_m}{L_r B}\left(1 - \frac{8}{15}\frac{1+c}{M^2}\frac{L_r^2}{R_{av}}2 + O\left(\frac{1}{M^4}\right)\right)$$

where M is the Hartmannn Number $\sqrt{\frac{\sigma}{\eta_v}}\, B\, L_r$

At high magnetic fields i.e. as $M \to \infty$

$$V \to \frac{\alpha T_w}{L_r B}$$

v_θ is of the form

$v_\theta = A_1\, r \ln r + A_2 r + \frac{A_3}{r}$ where A's are constants.

Subcase (b)

$L_r \simeq L_z$, $L_r < R_{av}$

TEMHD analysis, at high Hartmann Numbers M, by applying Thevenin's theorem to the thermoelectric potential and the cylindrical side walls and following a core and boundary layer type of flow analysis similar to Baylis [6] and Hunt [7] , gives

$$V = \frac{\alpha T_w}{L_r B} \left\{ 1 + \frac{1+c}{M} + \frac{0.956\left(\frac{1}{R_1} + \frac{1}{R_2}\right) L_z}{M^{3/2} \ln \frac{R_2}{R_1}} + 0\left(\frac{1}{M^2}\right) \right\}$$

If $M \gg 1$, c. $\frac{L_z}{R_1}$ and L_z/R_2 ,

$$V \to \frac{\alpha T_w}{L_r B}$$

v_θ in the core is of the form

$v_\theta = \frac{A_1}{r}$ where A_1 is a constant.

Subcase (c)

$L_z \ll L_r$, $L_r < R_{av}$

v_θ in the core is given by

$$v_\theta = \frac{2\alpha T_m}{rB\left(1 + \frac{2\tanh M}{M} \ln \frac{r_2}{r_1}\right)} \left\{ 1 - \frac{\cosh \frac{Mz}{L_z}}{\cosh M} \right\}$$

Analysis of the buoyancy induced circulation (single cell vortex only i.e., $\frac{T_m}{L_z}$ small) of the fluid in the absence of thermoelectric current with a stress free top mercury surface (i.e. $dv/dz = 0$ at $z = 2L_z$) and no slip at the bottom boundary (i.e., $v = 0$ at $z = 0$) gives

$$v_r = \frac{\rho g \beta \frac{T_m}{L_r} (2L_z)^3}{\eta_v M^2} \left[Z + \frac{\sinh MZ \left\{ M + \left(\frac{M^2}{2} - 1\right) \sinh M \right\}}{M(\sinh M - M\cosh M)} + \frac{\left\{ 1 + \left(\frac{M^2}{2} - 1\right)\cosh M \right\} (1 - \cosh MZ)}{M(\sinh M - M\cosh M)} \right]$$

where ρ, β are the density and the thermal volume expansion coefficient of the fluid and g refers to the acceleration due to gravity.

Using this value of v_r, the heat transfer analysis gives the temperature distribution in the central core

$$T = T_{av} + A_{12} f_1 \left(\frac{T_m}{L_r}, M\right) f_2(z)$$

where A_{12} is a constant and $f_1 \left(\frac{T_m}{L_r}, M\right)$, $f_2(z)$ are functions of $(T_m/L_r, M)$ and z respectively.

This shows a stable thermal stratification in the core.

At the boundary layers

$$T \simeq T_{av} + r \frac{T_m}{L_r}$$

Case II

Solid-fluid interface at the bottom horizontal wall is insulating in the span $r = R_1$ to $r = R_3$ and is conducting in the span $r = R_3$ to $r = R_2$ where $R_1 < R_3 < R_2$. Heating and cooling at $r = R_2$ and at $r = R_1$ are such as to give $\frac{dT}{dr} \propto r$.

TEMHD analysis ignoring secondary flow due to curvature and buoyancy with $L_2 \simeq L_3$ and $L_2 \ll R_{av}$ gives for flow in the core

$$v_\theta = \frac{A_1}{r} \quad \text{in} \quad R_1 < r < R_3$$

and $v_\theta = A_2 r$ in $R_3 < r < R_2$ where A's are constants.

Then a free shear layer is expected as shown in Fig. 2.

Case III

Solid-fluid interface at the bottom horizontal wall is totally conducting.

TEMHD analysis, without secondary flow gives the azimuthal velocity in the core

$$v_\theta \simeq \frac{A_1}{r} \quad \text{with } A_1 \text{ a constant.}$$

3. The Experimental set up and the channels

3.1 The magnetic field system

The vertical magnetic field B_z was provided by the 'Lintott' II watercooled electromagnet with a maximum flux density of 0.9 Tesla with an air gap space of 15 cm. Extra mild steel attachments at the pole faces gave a uniform B_z over

a 15 cm diametral area in horizontal planes within a tolerance of 1% of B_g. The magnetic fields in the θ and the radial directions were less than 0.5% and 1% of B_g respectively.

3.2 The experimental channels

The annular channels of rectangular cross-section and with an open end to allow free surface of mercury were fabricated from 3 mm thick copper plates and commercial pipes of 15.4, 5.4, 3.2 and 1.25 cm diameter. The radius ratio R_2/R_1 was maintained near the value 4.5 to give maximum thermoelectric current in the fluid for a given temperature difference, T_2-T_1. The heights and the radius ratios of the four different channels used are : Mark I, 10 cm, 7.5/2.7; Mark II and III, 7.5 cm, 7.5/1.6; Mark IV, 3.2 cm, 7.5/1.6.

The bottom wall of the channel was formed by brazing a 3 mm thick copper plate, 15.4 cm diameter, with a matching 5.4/3.2 cm diameter hole drilled at the centre, onto the 5.4/3.2 cm diameter copper pipe at 2.5 cm from the end and at the end of the 15.4 cm diameter copper pipe. The bottom wall was made accurately parallel to the blocked end surface of the 5.4/3.2 cm copper pipe at a distance of 2.5 cm. The blocked end surface of the 5.4/3.2 cm copper pipe served as the support to the apparatus. The 2.5 cm end length of the 5.4/3.2 cm pipe also served the requirements of manifolding of the cooling water inlet-outlet system. The cooling system is shown in Fig. 3 where a third copper pipe of 1.25 cm diameter is held co-axially by brazing the 90° bent inlet section to the 5.4/3.2 cm diameter copper pipe with a symmetrical placement with respect to the bottom 2.5 cm region. Cooling water flowing through the 1.25 cm

diameter copper pipe was let out through the annular space between the 5.4/3.2 cm and the 1.25 cm diameter copper pipes by having a clearance between the open top end of the 1.25 cm diameter pipe and the closed top end of the 5.4/3.2 cm copper pipe. The cooling water outlet tube was also of 1.25 cm diameter and was located horizontally aligned with the inlet tube. The outlet tube was manifolded into the 2.5 cm bottom end zone of the 5.4/3.2 cm copper tube by brazing.

The insulating wall-fluid interface at the bottom wall in annular channels, Mark I and II, was provided by fixing a 3 mm thick 'tufnol' matched annular ring type disc with 'araldite' glue to the upper surface of the bottom wall. Five pressure taps were provided by drilling 1 mm diameter holes through the 'tufnol'-'araldite'-copper thickness at symmetrically located positions along a radial line for measurements of Δp with the inclined tube manometer. Later, these holes for pressure taps were sealed with 'araldite'.

At the inner zone ($R_1 < r < R_3$) of the upper surface of the bottom copper wall of Mark III channel, a uniform coating of 0.2 mm thick PVC paint was applied to give an insulating wall to fluid interface. At the outer zone ($R_3 < r < R_2$) the copper wall to fluid interface was conducting. No pressure taps were provided at the bottom wall of Mark III channel.

For the annular channel Mark IV, the wall to fluid interface was totally conducting.

A central pivot was fixed on the closed top surface of the 5.4/3.2 cm pipe to hold the rotating paddle type of vorticity - velocity measurement probe in Mark II and III channels.

3.3 The heating system

Heating at the outer curved surface at $r = R_2$ was done with coils made of 26 SWG Nichrome/0.511 mm diameter Kanthal resistive heating wires. Heater coils were electrically insulated by fibre glass and then bonded to the outer surface of the 15.4 cm diameter copper pipe with silicone compound and MgO fillings. Fire clay was used for external setting. The final thermal lagging was provided by wrapping Asbestos cloth around the coil embedded in fire clay. The heating arrangement for the Mark I, II and IV channels was uniformly distributed over the outer cylindrical surface at $r = R_2$ while for the Mark III channel, concentrated heating at the bottom end of the outer cylindrical surface was made by a short length heater coil.

The maximum heat transfer to the cooling water was only 85% of the input heat, due to the heat loss from the top free surface of mercury to the ambient surrounding as compared to that of 95% in the totally lagged system of the experimental arrangements with straight ducts of Part I and II of the series of papers.

4. The Experimental measurement system

Pressure difference measurements were carried out by using pitot tubes and the air-over fluid-over Hg type of inclined tube manometer. Velocity measurements were made by using both pitot tubes and potential probes. These measurements were done precisely as detailed in the paper of Malcolm[8] and Hunt[7]. A simple (r,s) positioning device for the probes was used.

The non-isothermal environment of the system required the velocity and vorticity measurements in the fluid. For this

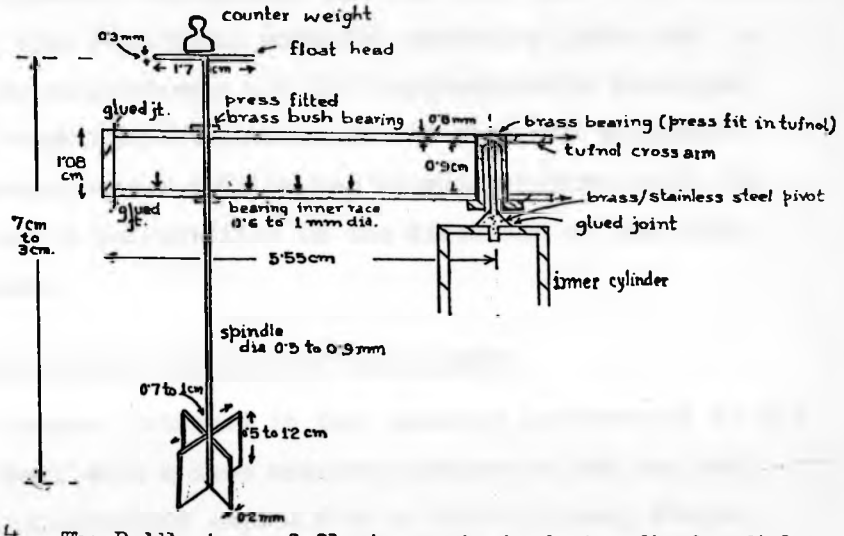

Figure 4 The Paddle type of float, constrained at a fixed radial location w.r.t. the central axis, on the pivoted cross arm. Only one set of brass bush bearings for the float spindle is shown for clarity, other positions are marked ↓

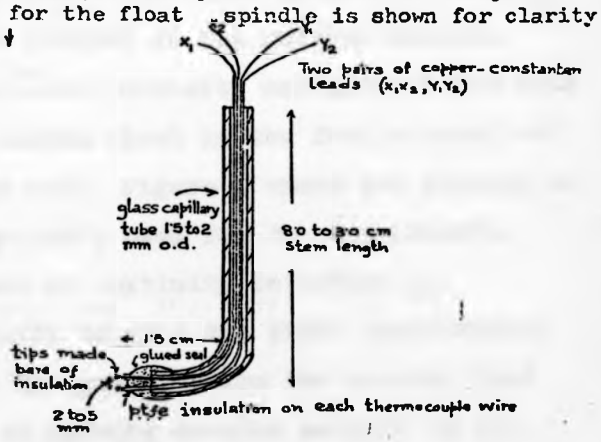

Figure 5 The thermoelectric potential probe. Potentiometer connection to the pair of terminals (i) X_1X_2 (ii) Y_1Y_2 (iii) either X_1Y_1 or X_2Y_2.

purpose two special measurement systems were used : (a) mechanical, paddle type rotational velocity vorticity probe for v_θ and vorticity measurements and (b) thermoelectric potential probes for temperature measurements and also for velocity/vorticity measurements outside the boundary layers under the assumption of no current flow in the direction of the probe tip separation.

4.1 The mechanical velocity-vorticity probe

The primary interest in the velocity measurement in the annular channel with a free mercury surface at the top end being that of azimuthal motion due to TEMHD forces, floats constrained at a particular radial location by fixing it along a radial arm which itself is pivoted at the annulus central axis, were developed. The fluid vorticity measurement was also possible by modifying the simple float in the form a cross arm type of paddle at its lower end. Figure 4 shows the details of one such velocity-vorticity probe used for the experiments. The principle of this method of vorticity detection is similar to that of Heiser and Shercliff[9] but the design details differ in order to suit the TEMHD environment. The depth of the float and the paddle below the mercury free surface could be adjusted by putting counter weights on the detachable head (a flat platform) at the top of the float spindle. The float spindle was maintained vertical with the help of two brass bearings aligned vertically with a spacing of 1 cm between them. Brass bearings located at 2.3, 3.0, 3.75, 4.45 and 5.2 cm radial distances from the central axis permitted the location of the float at these positions. In addition, measurements could be done at 2.5, 2.75, 3.2, 3.65,

4, 5, 6.3 and 7.1 cm radial positions with other radial 'tunfol' arms. The float spindle was free to spin about its own axis while the pivoted radial arm rotated around the central pivot due to the azimuthal drag on the float by fluid circulation. Painting the top of the spindle head black and white with a pointer indicator permitted the observation of the state of the paddle alignment to reveal the fluid vorticity in the vertical direction. The float spindle diameters ranged from 0.05 to 0.09 cm. The central pivot was conical shape with a vertex semi-angle of 60° while the matching part of the bearing had a corresponding slope of 75°. Low friction allowed accurate flow measurements upto a rotational speed of 1 rev/120 seconds.

4.2 Thermoelectric potential probes

Thermoelectric potential probes are potential probes (fig 5) with each of the probe wire tips replaced by a thermocouple junction so that simultaneous measurement of temperature, temperature gradient, potential ϕ^+ where grad ϕ^+ = α grad T + $\underline{E}$ = α grad T - grad ϕ , and potential gradients can be made. Under assumptions of no current flow, fluid flow velocity can be determined from the $\Delta\phi^+$, T measurements as reported in Part I of the series of papers.

5. The Experimental Results

5.1 Experimental measurements on the Mark I and II annular channels

The following experimental results were obtained on the Mark II annular channel in general. One case of the measurement results in the Mark I annular channel is also reported and has

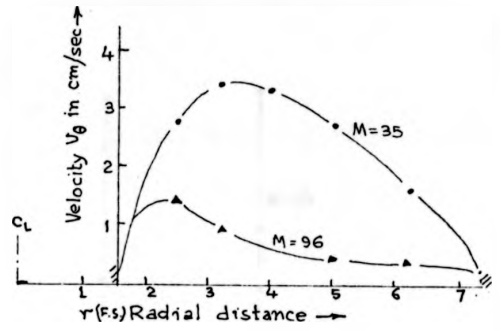

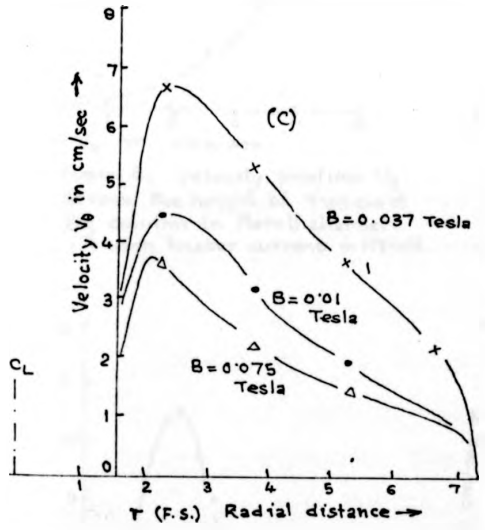

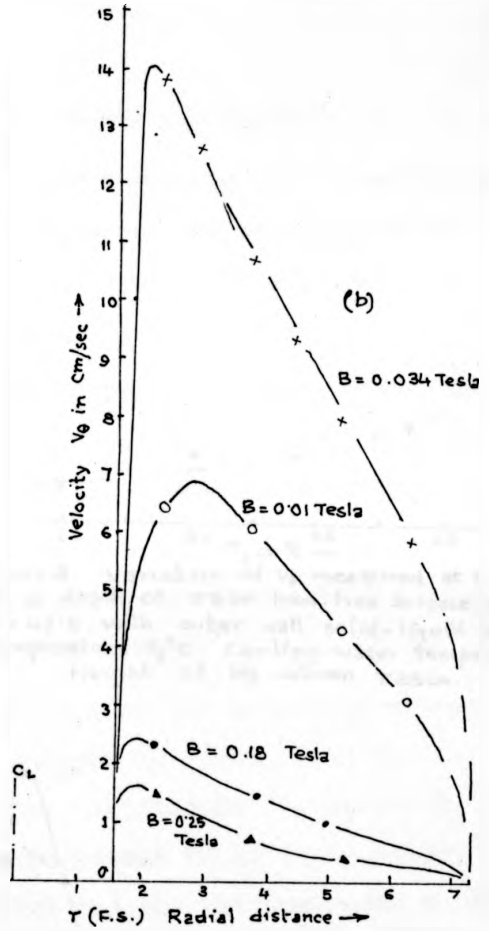

Figure 6. Radial profiles of v_θ in the Mark II annular channel. Height of Hg column 7·25cm is the basis of Hartmann Number M. (a) Heater coil HY 1·7amp (b) Heater coil KL, 1amp. (c) Heater coil 1·5 amp.

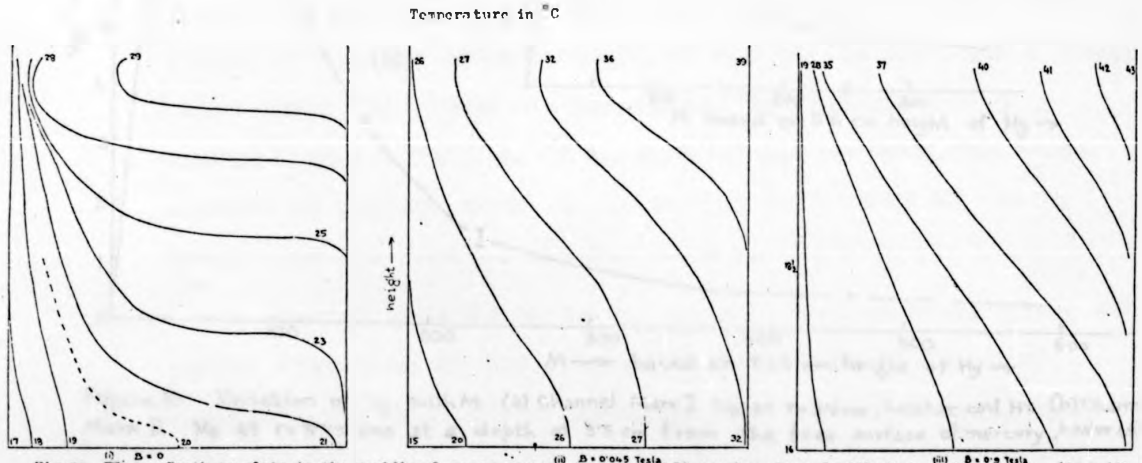

Figure 7 Isotherm plots in the meridional cross-section in the MarkII annular channel with distributed heating (1amp.AC wir

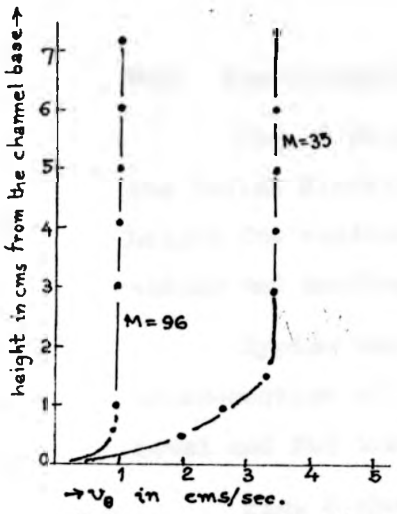

Figure 8. Velocity profiles v_θ across the height of 7·25 cm of Hg column in Mark II channel. 1·7 amp heater current in HY coil.

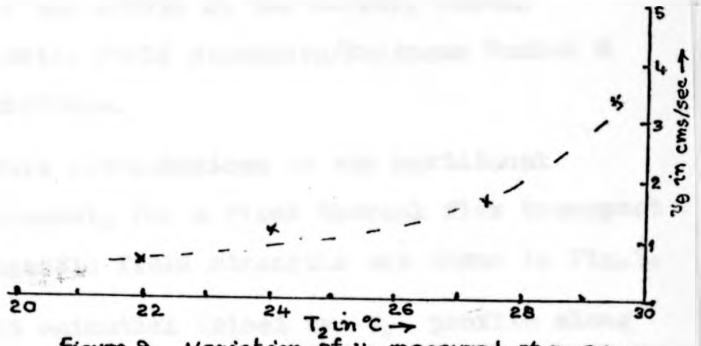

Figure 9. Variation of v_θ measured at r = 3·2 cm at a depth of 3·5 cm from free surface at a fixed M = 42·5 with outer wall solid-liquid interface temperature T_2°C. Cooling water temperature 10°C. Height of Hg column 7·25 cm.

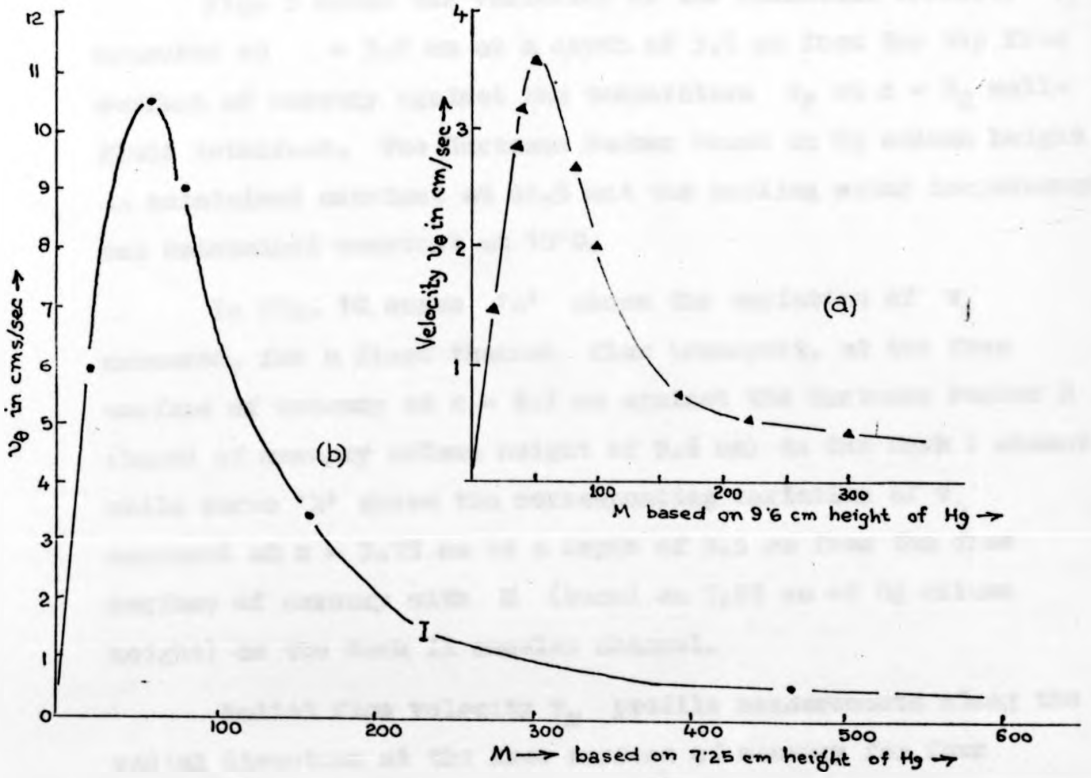

Figure 10. Variation of v_θ with M (a) Channel Mark I v_θ at r = 5·1 cm, heater coil HY (b) Channel Mark II v_θ at r = 3·75 cms at a depth of 3·5 cm from the free surface of mercury, heater coil KL.

been specifically mentioned 'Mark I channel'.

Fig. 6 shows the azimuthal velocity v_θ profile along the radial direction at the middle of the mercury column height for various magnetic field strenghts/Hartmann Number M values and heating conditions.

Typical temperature distributions in the meridional cross-section of the channel, for a fixed thermal flux transport level and for three magnetic field strengths are shown in Fig.7.

Fig. 8 shows the azimuthal velocity v_θ profile along the height of the mercury column at two different Hartmann Numbers for a given thermal flux input.

Fig. 9 shows the variation of the azimuthal velocity v_θ measured at r = 3.2 cm at a depth of 3.5 cm from the top free surface of mercury against the temperature T_2 at $r = R_2$ wall-fluid interface. The Hartmann Number based on Hg column height was maintained constant at 42.5 and the cooling water temperature was maintained constant at 10°C.

In Fig. 10, curve 'a' shows the variation of v_θ measured, for a fixed thermal flux transport, at the free surface of mercury at r = 5.1 cm against the Hartmann Number M (based of mercury column height of 9.6 cm) in the Mark I channel while curve 'b' shows the corresponding variation of v_θ measured at r = 3.75 cm at a depth of 3.5 cm from the free surface of mercury with M (based on 7.25 cm of Hg column height) on the Mark II annular channel.

Radial flow velocity v_r profile measurements along the radial direction at the free surface of mercury for four different magnetic field strengths and a fixed thermal input

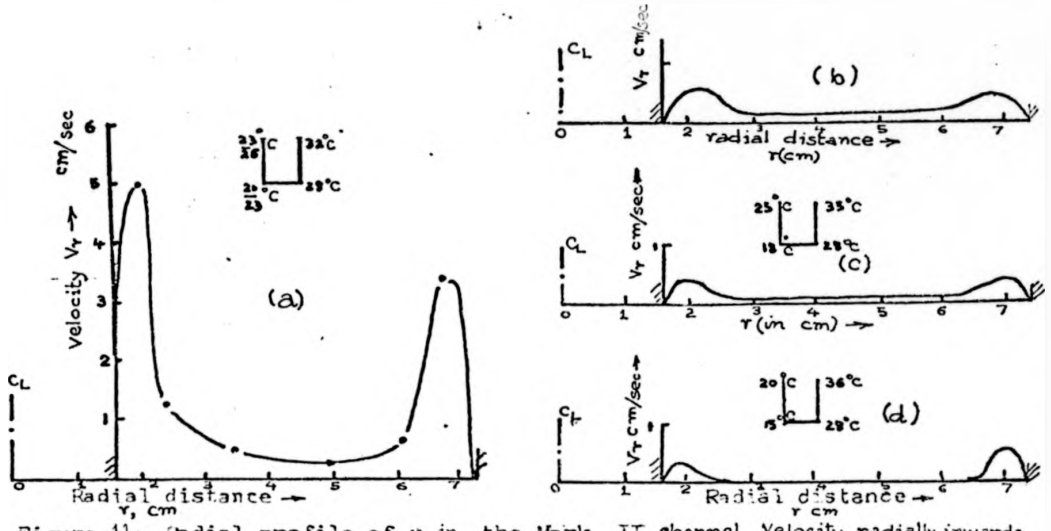

Figure 11. Radial profile of v_r in the Mark II channel. Velocity radially inwards.
(a)B=0 (b) B= 0.02 Tesla (c) B=0.1 Tesla (d) B=0.35Tesla

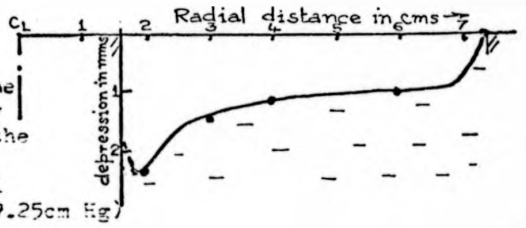

Figure 12. The shape of the free surface of Hg shown by the measure of depth from the highest meniscus level at M=64 in the Mark II channel (I_{ht}=1.5 amp, KL 4sections, 7.25cm Hg)

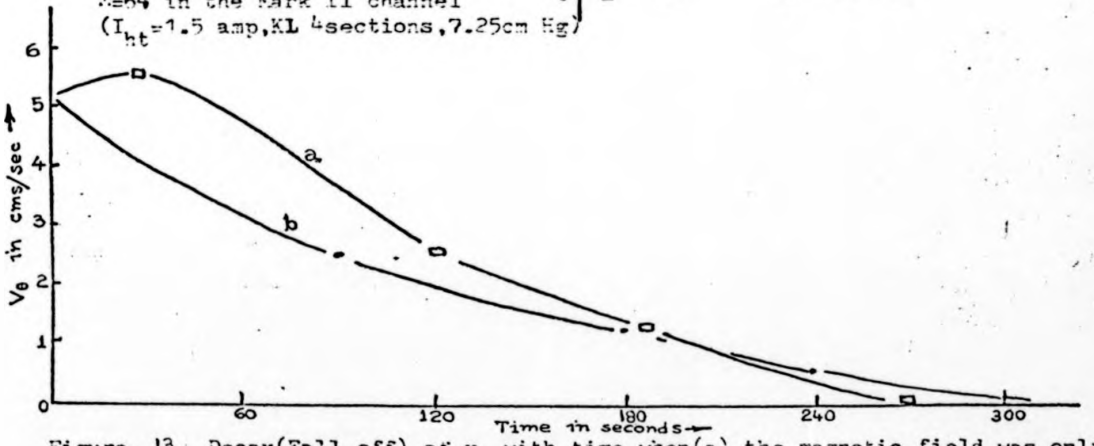

Figure 13. Decay(Fall off) of v_θ with time when(a) the magnetic field was only switched off from steady state (b) the heater supply only was switched off in the Mark II channel. Initial steady state B=0.045 Tesla and 1 amp. of distributed heating in the four sections of the Kanthal heater wire.

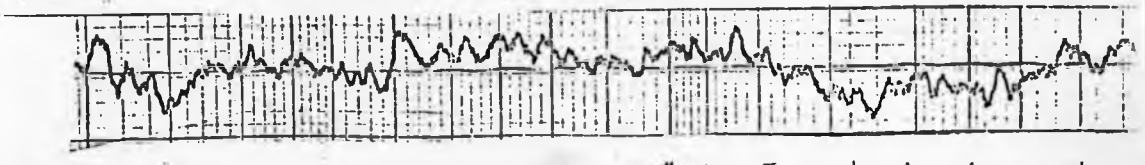

Figure 14. Steady state temperature oscillations in the Mark II annular channel measured 3 mms away from the inner wall at a depth of 3.5 cms from the Hg free surface. The trace moves from left to right ; 15 sec per cm. Amplitude scale 1°C per cm. Heater KL, 1 ampere.

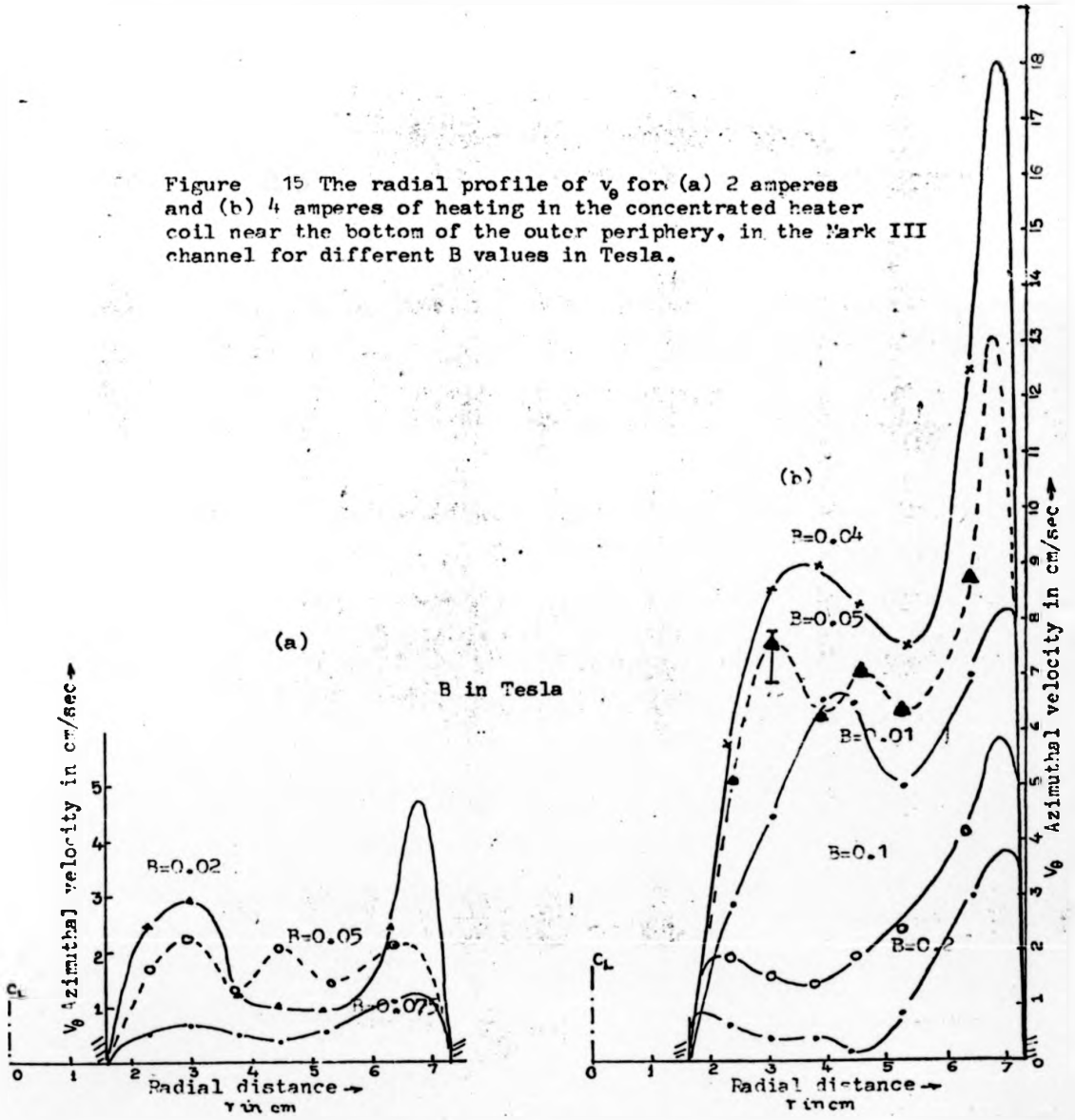

Figure 15 The radial profile of v_θ for (a) 2 amperes and (b) 4 amperes of heating in the concentrated heater coil near the bottom of the outer periphery, in the Mark III channel for different B values in Tesla.

Figure 3.15 (continued) The radial profile of v_θ for (c) 3 amp and (d) 5 amp. of heating current in the concentrated heater coil near the bottom of the outer periphery, in the Mark III channel for different B values in Tesla.

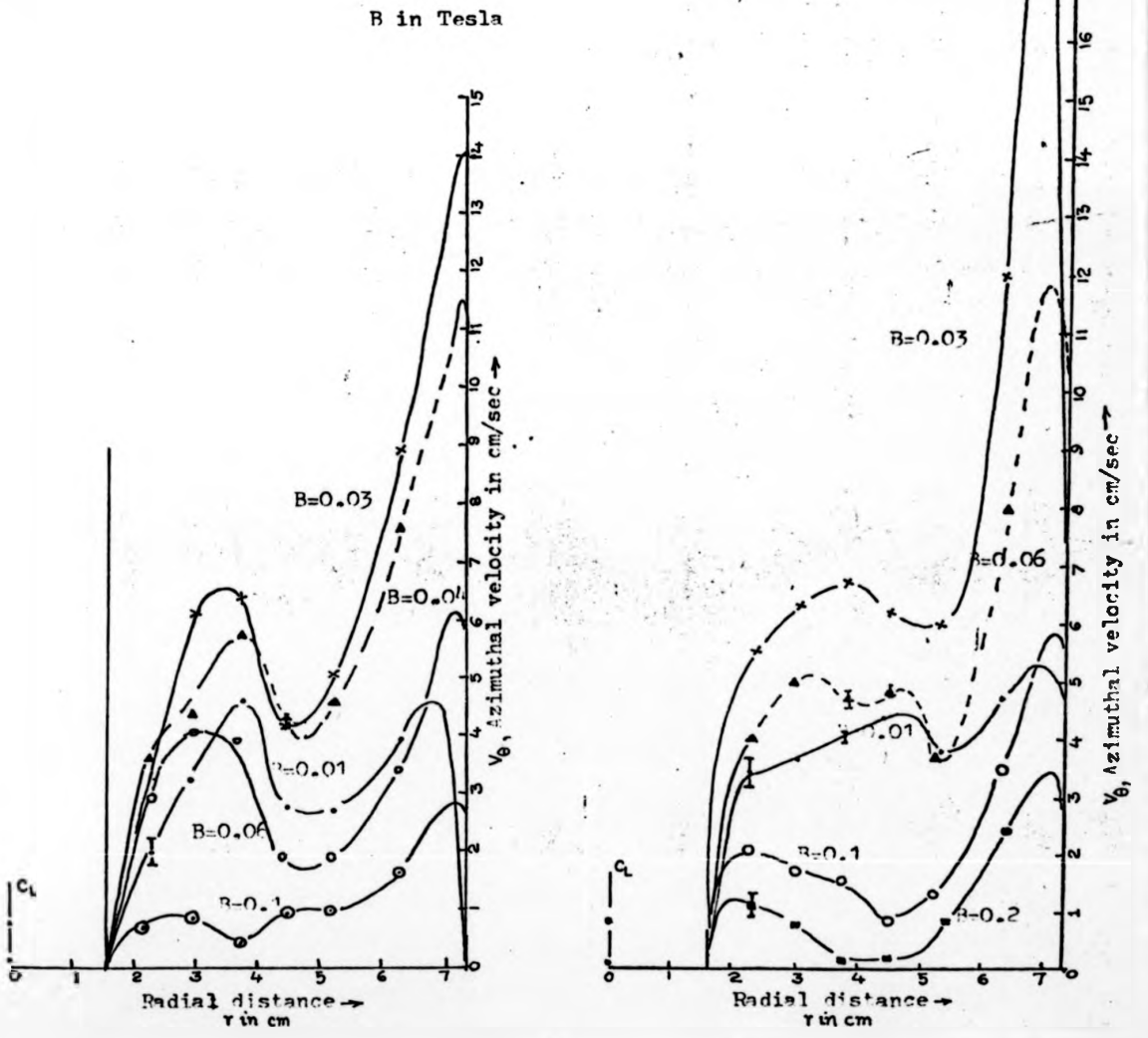

level are shown in Fig. 11 a-d. Insets show the temperature levels at the corners of the meridional cross-section.

The free surface of mercury is not horizontal and a typical measurement of the free surface of mercury is shown in Fig. 12.

Fig. 13 shows the instantaneous measurements of asimuthal velocity v_θ at a fixed location in the central region of the fluid as time advances from the instant when (a) the steady magnetic field strength of B = 0.045 Tesla is suddenly switched off or (b) the heater power is suddenly switched off, with an otherwise fixed thermal/magnetic equilibrium maintained.

Fig. 14 shows a typical record of the temperature oscillation in the fluid at a point 3 mms. away from the inner cylinder and at depth of 3.5 cm from the free surface of mercury with time. The thermal flux input level and the cooling water temperature were maintained constant.

Vorticity measurements showed that the TEMHD fluid flow in the central core region corresponded to a free vortex.

5.2 Experimental measurements on the Mark III annular channel

To investigate the possiblity of free shear layer occurring in the fluid at the region of wall-fluid interface conductivity change at the bottom wall of the Mark III annular channel the asimuthal velocity v_θ profile along the radial direction was measured. Fig. 15 shows the experimental v_θ measurements in the fluid away from the Hartmann layer, for different strengths of the vertical magnetic field B and heater coil currents, against the radial position of measurement.

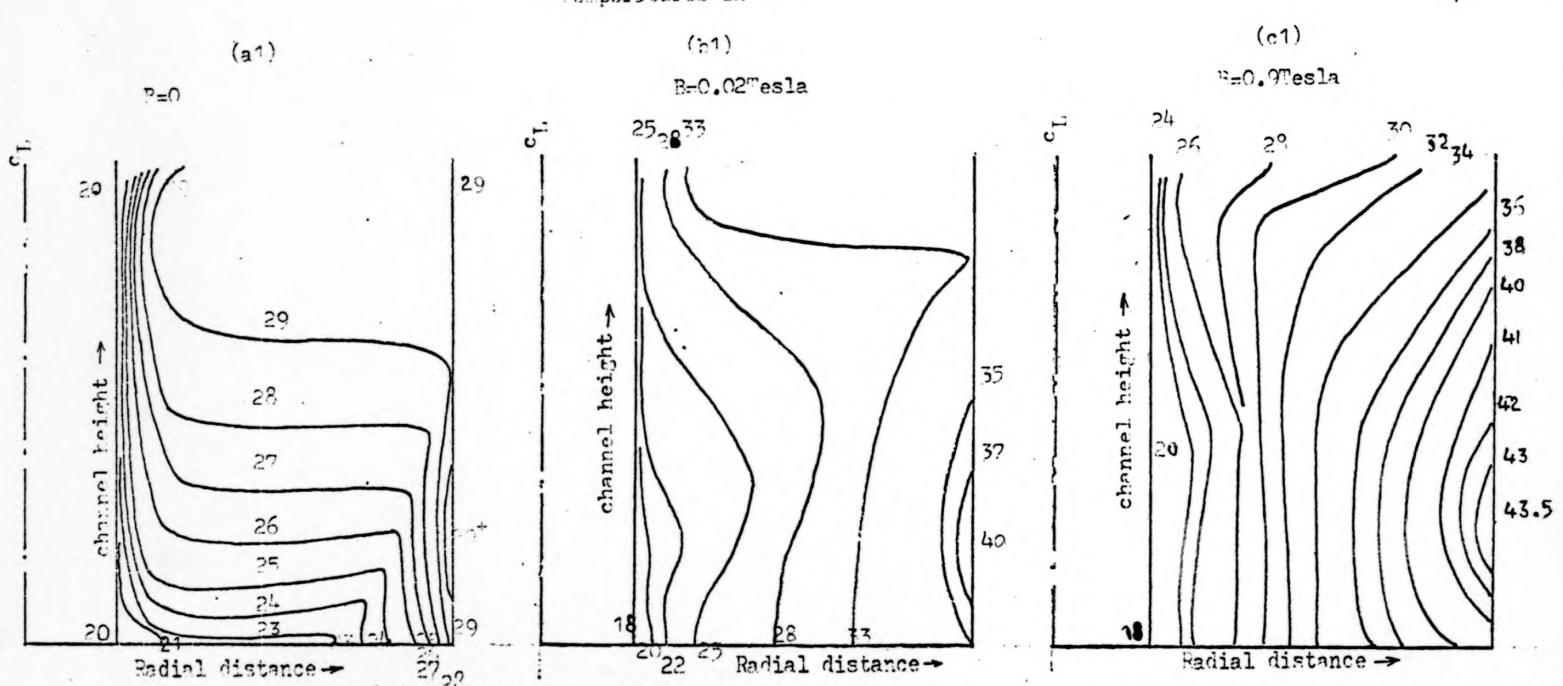

Figure 6 Isotherm (in °C) plots in the meridional planes (rectangular cross-sectional) in the Mark III annular channel with concentrated heating at the outer periphery bottom boundary and mixed interfacial conductivity at the bottom wall. Heating current 3 amp. at 72 volts. Cooling water flow rate 15 litres per minute.
(a1) B=0 (b1) B= 0.02 Tesla (c1) B=0.9 Tesla

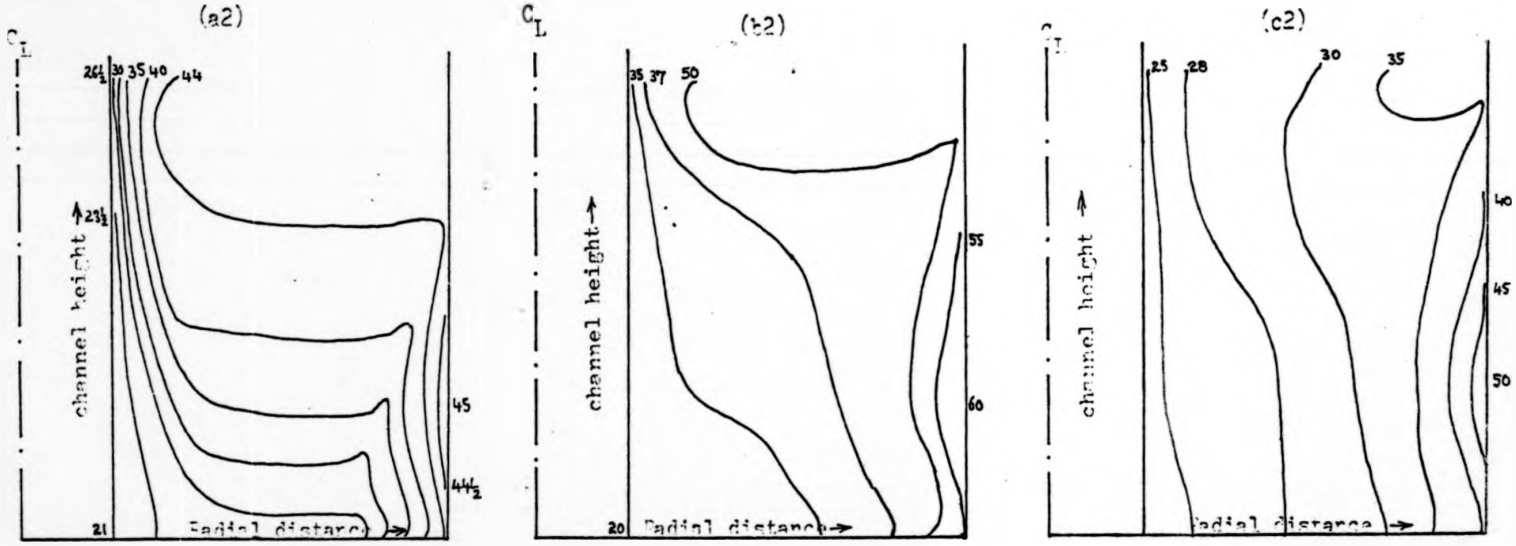

Figure 6 - (continued) Isotherm plots in the meridional planes (rectangular cross-sectional) in the Mark III annular channel with concentrated heating at the outer periphery bottom boundary and mixed interfacial conductivity at the bottom wall. Heating current 5 amperes (a2) B=0 (b2) B=0.02 Tesla (c2) B=0.2 Tesla. Temperatures in $^{\circ}$C

Mark III annular channel with partly conducting(O) and partly insulating (i) interface at the base wall .(Concentrated heating with 3 amperes flowing in the heater coil at channel bottom outer rim.)

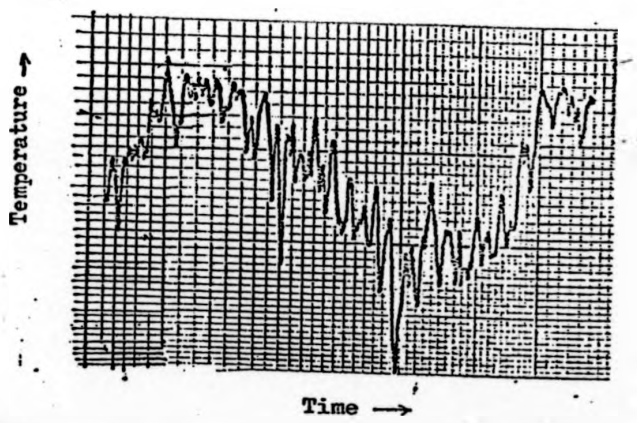

Figure 17 Record of temperature oscillation by the Hewlett-Packard XY plotter . Position of the copper-constantan thermocouple probe tip inside Hg at r= 1.89 cm and at a depth of 3.5 cms from the free surface of Hg. The trace moves with time from left to right . Horizontal time scale 8sec / cm and the vertical scale corresponds to 60 μV / cm which is approximately equivalent to 1.5 °C / cm.

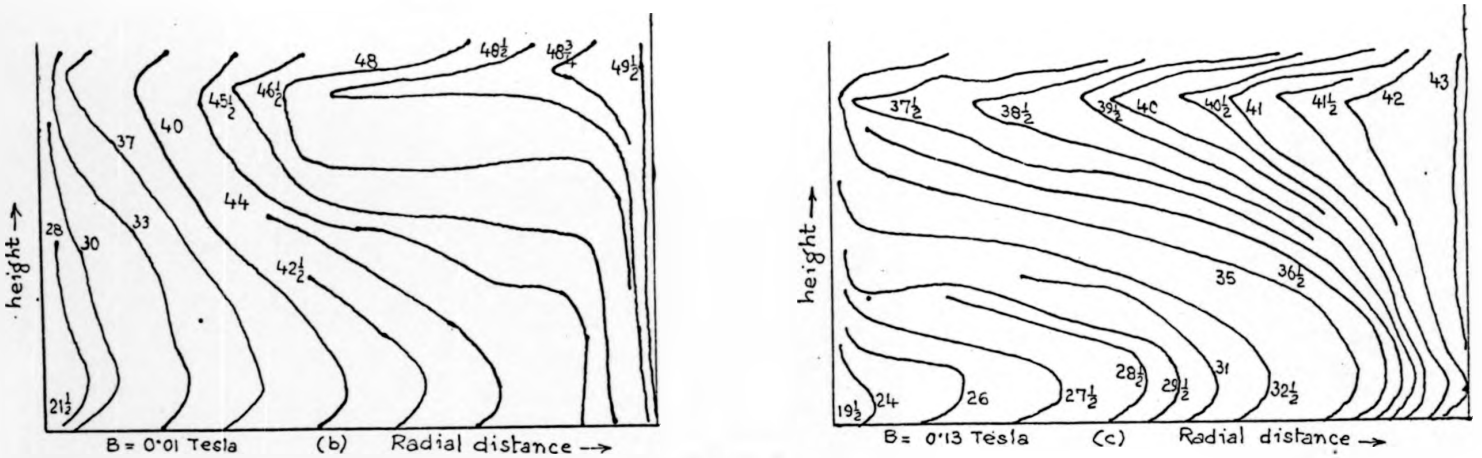

Figure 18. Detailed isotherm plots, in the meridional planes of the Mark IV annular channel with uniformly distributed heating at the outer periphery for 3.1 amperes heating current and (a) B = 0 (b) B = 0.01 Tesla (c) B = 0.13 Tesla (d) B = 0.45 Tesla (scale : Double Full Sc.)

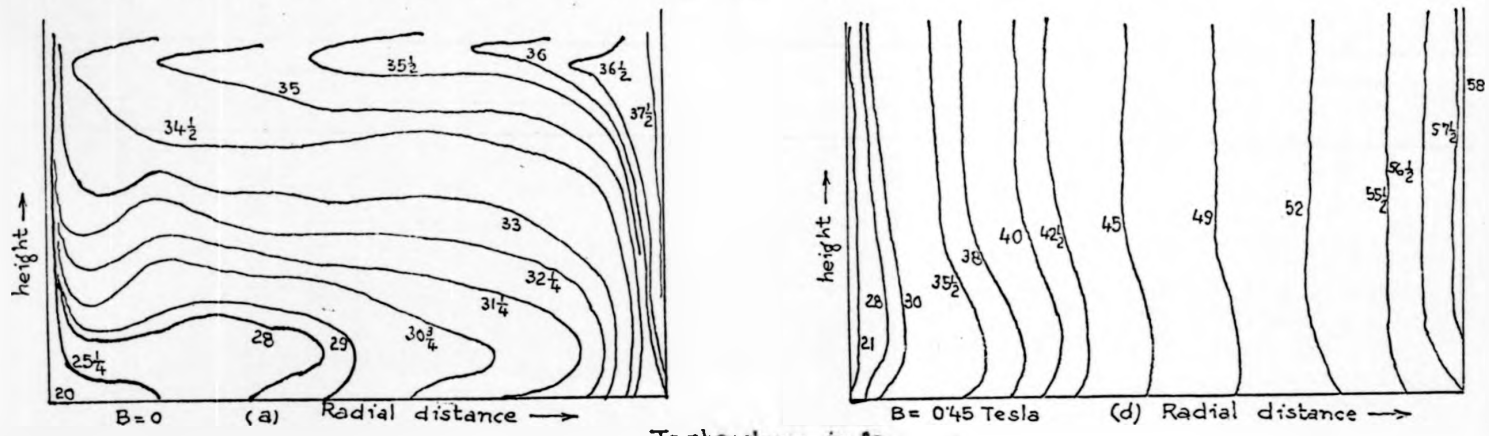

Temperatures in °C

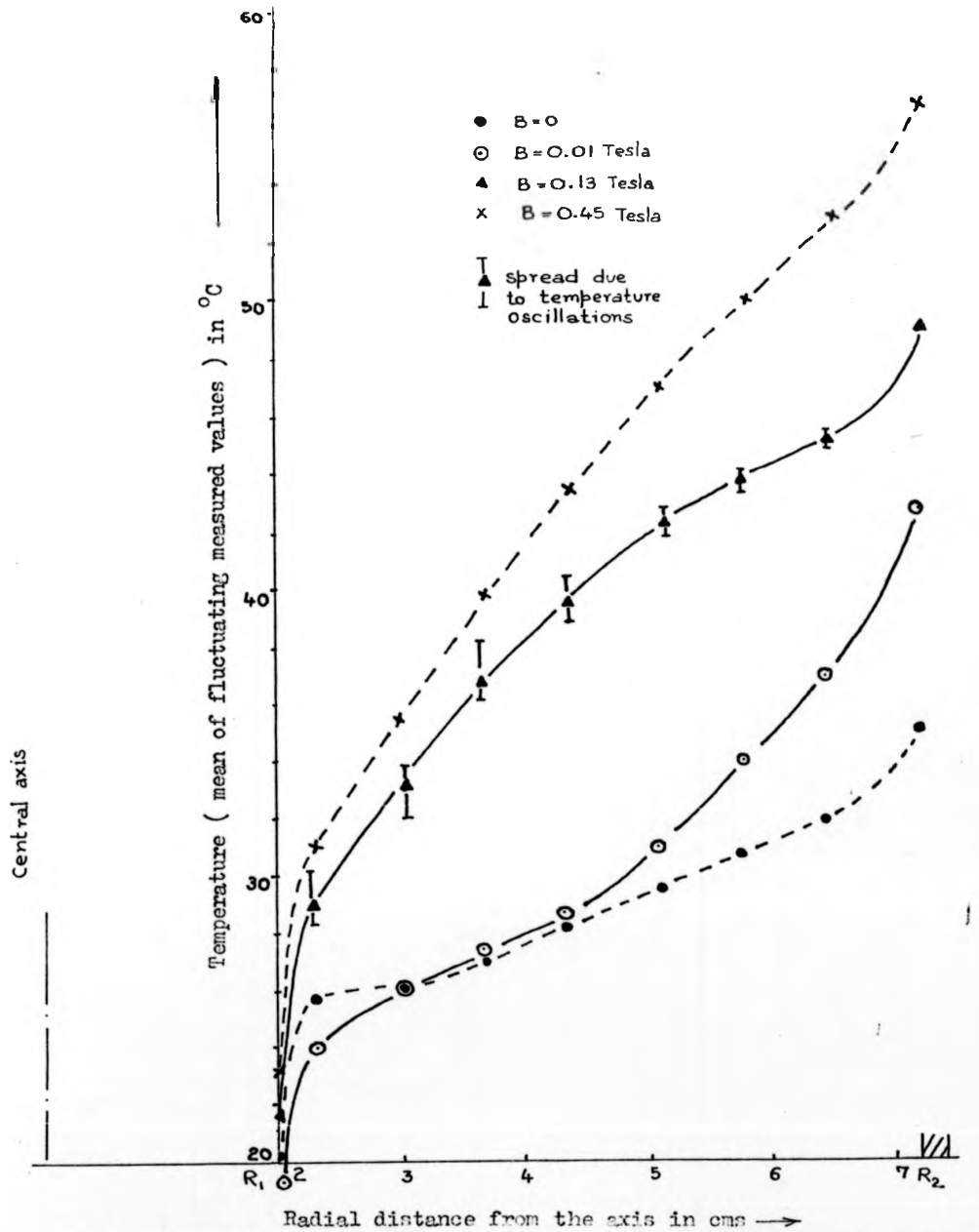

Figure 19 Temperature(in ^{0}C) profile along the radial span at the base of the MarkIV annular channel for 3.2 amperes of heater current (uniform vertical distribution) and at magnetic flux densities of 0 ,0.01,0.13and 0.45 Tesla.

To confirm the results of figure 15, the vorticity probes were used to show a free vortex at the inner radial zone ($R_1 \leq r \leq R_3$) at the bottom of which the wall-fluid interface was insulating and a forced vortex at the outer radial zone ($R_3 \leq r \leq R_2$), the corresponding bottom wall-fluid interface being electrically conducting, and a dT/dr maintained by concentrated heating.

Fig. 16 shows the typical temperature distributions, in the form of isotherm lines in the meridional cross-section of the Mark III annular channel for a fixed level of thermal flux input and a constant temperature cooling water system when the magnetic field strength was maintained constant at three different values.

Fig. 17 shows a typical record of the temperature oscillation in the fluid at a location of r = 1.89 cm and a depth of 3.5 cms from the free surface of mercury with time. The thermal flux input level and the cooling water temperature were maintained constant and an otherwise steady state operation achieved.

5.3 Experimental measurements on the Mark IV annular channel.

Experimental results obtained with the Mark IV annular channel are summarised as follows : Fig. 18 shows the detailed temperature distribution in the meridional cross-section of the fluid for a fixed thermal input and cooling water temperature at different constant values of the magnetic field.

Fig. 19 shows the temperature profile along the radial span at the base of the annular channel for a fixed thermal input and a constant cooling water temperature and for various

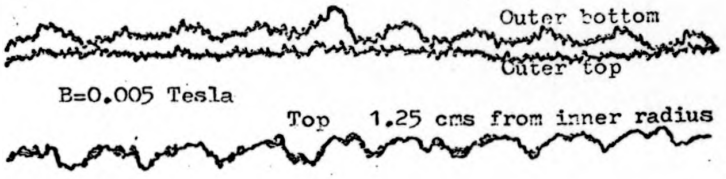

(a)

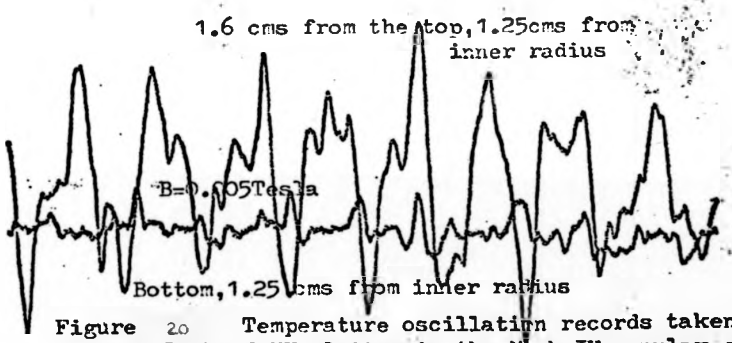

Figure 20 Temperature oscillation records taken with the Hewlett-Packard XY plotter in the Mark IV annular channel I_{ht}=3 amp at 150 volts. The trace proceeds with time from left to right at the speed of 4sec/cm. Amplitude scale 40uV/cm

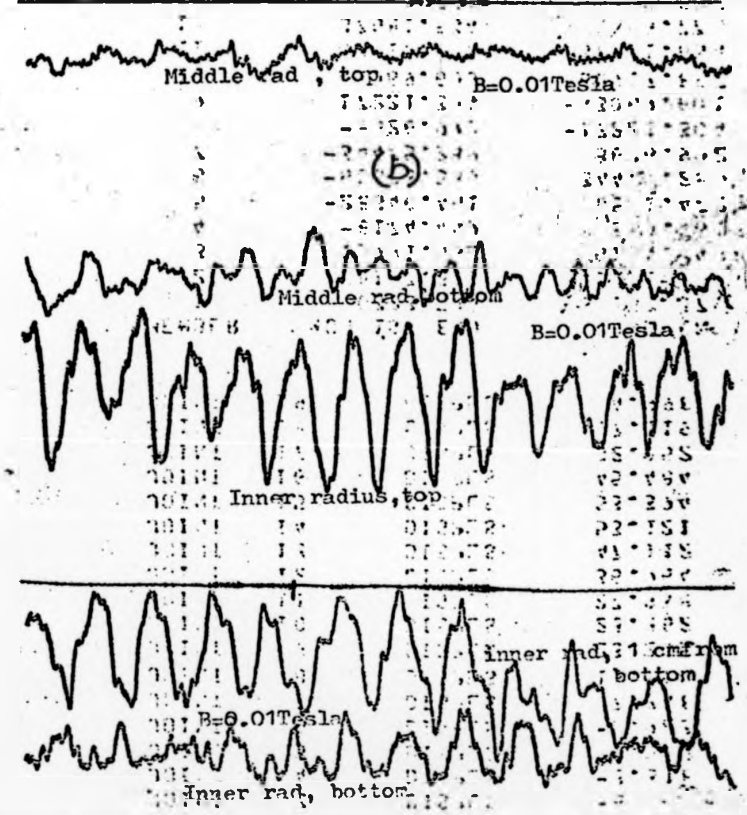

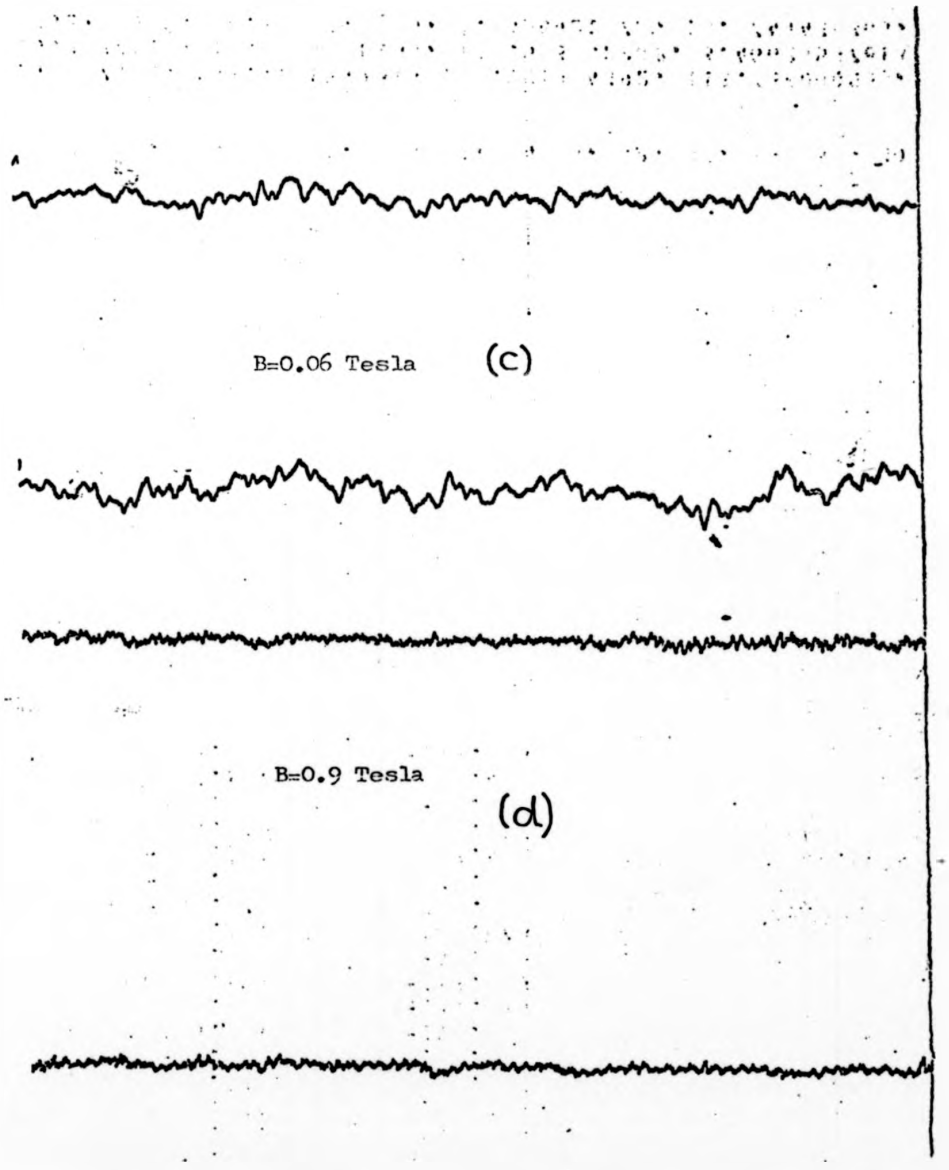

Figure 20 (continued) Typical records of temperaure oscillations in Hg. in the Mark IV annular channel at B=0.06 Tesla and B = 0.9 Tesla For legends refer to Figure 6.26 (a)

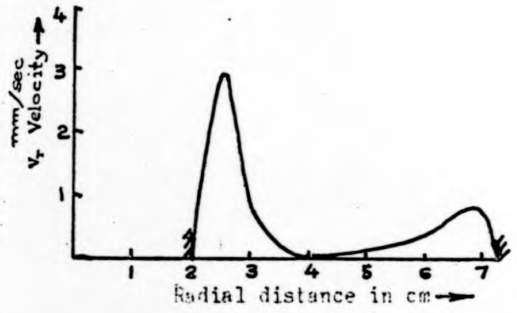

Figure 20 Radial profile of v_r at B=0.005 Tesla with 2amperes of distributed heating current in the Mark IV annular channel

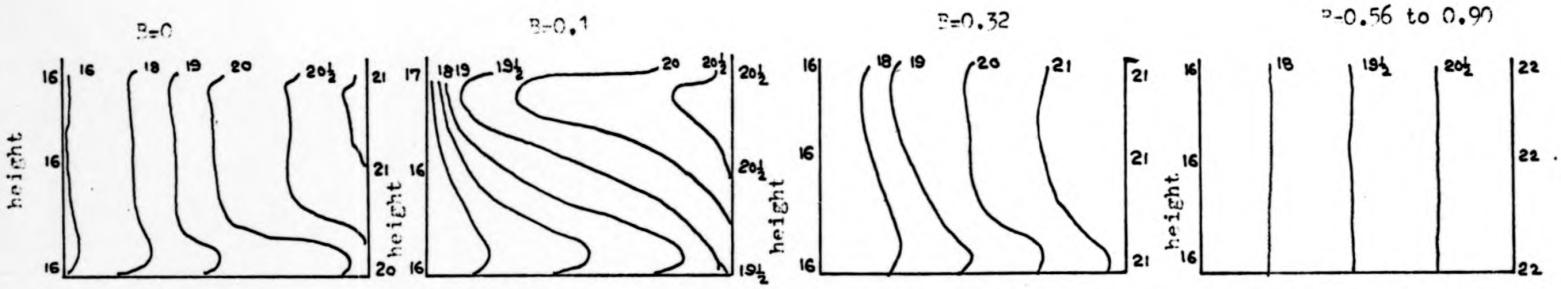

Figure .22 a.Isotherm plots in the meridional plane of the Mark IV channel for 1 amp. distributed heating current. T in °C , Full scale diagram, B in Tesla

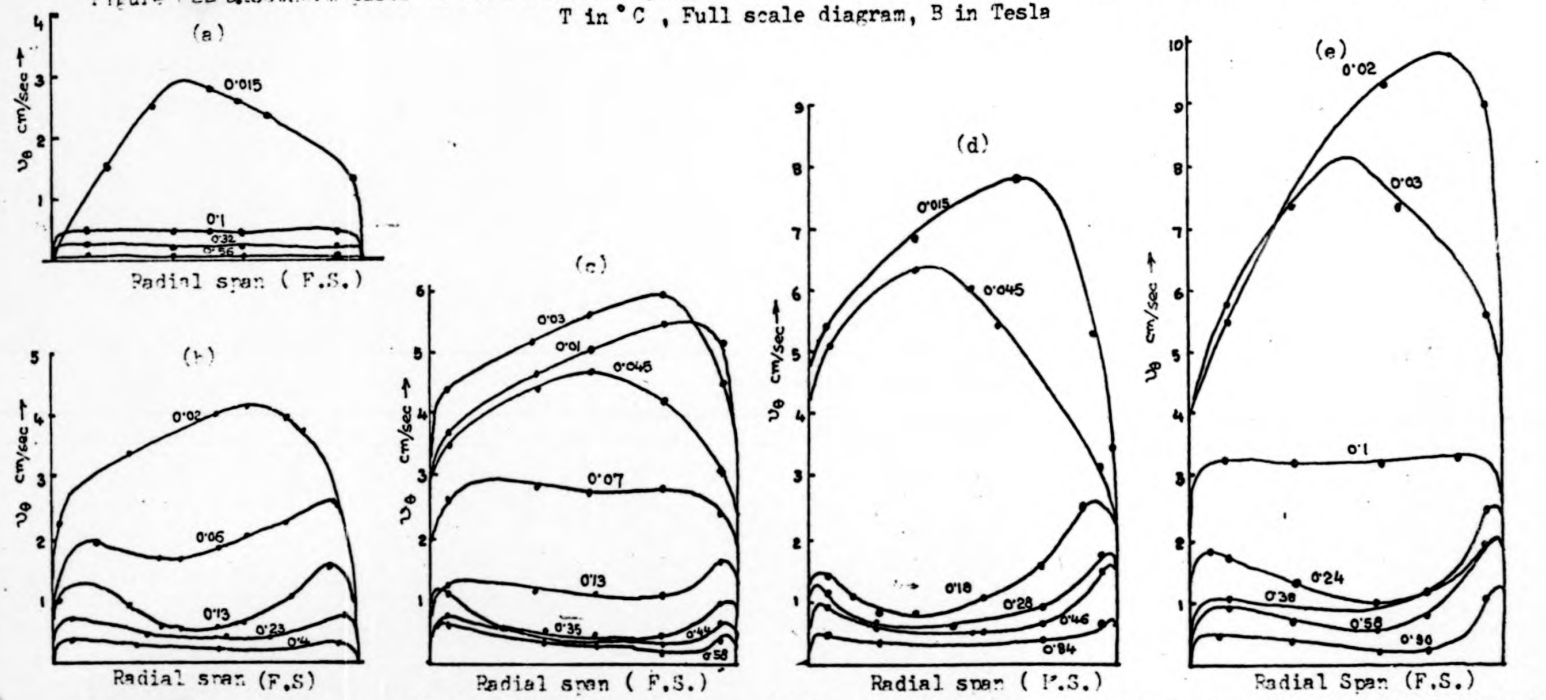

Figure .22 The radial profiles of v measured in the Mark IV annular channel at uniformly distributed heating current of (a) 1 amp. (b) 1.5 amp. (c) 2 amp. (d) 2.5 amp (e) 3 amp. The magnetic flux density in Tesla is marked along the curves.

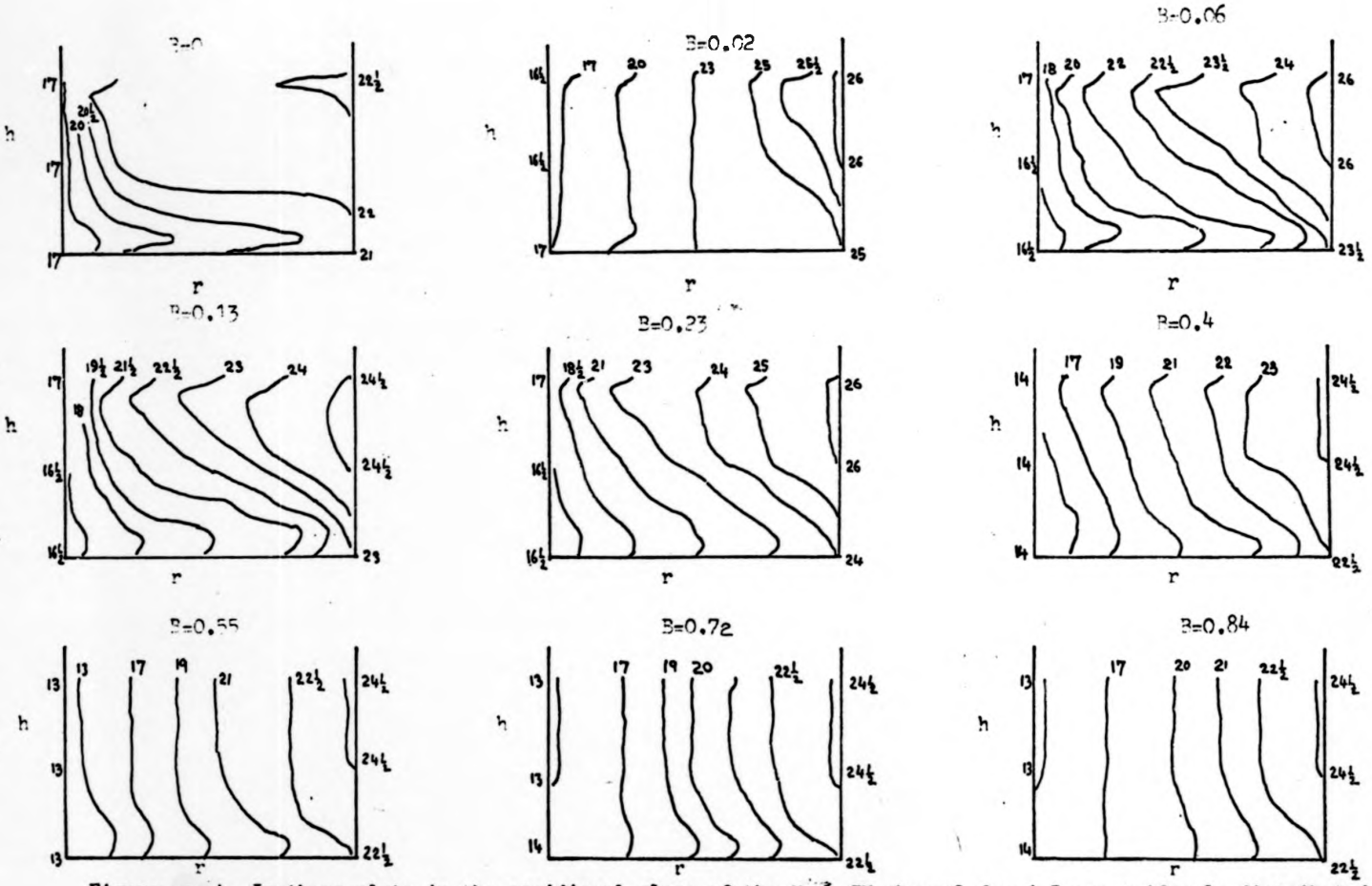

Figure 22 b. Isotherm plots in the meridional plane of the Mark IV channel for 1.5 amp uniformly distributed heating current. T in °C, Full scale diagram , B in Tesla (r - Radial span, h- Height.)

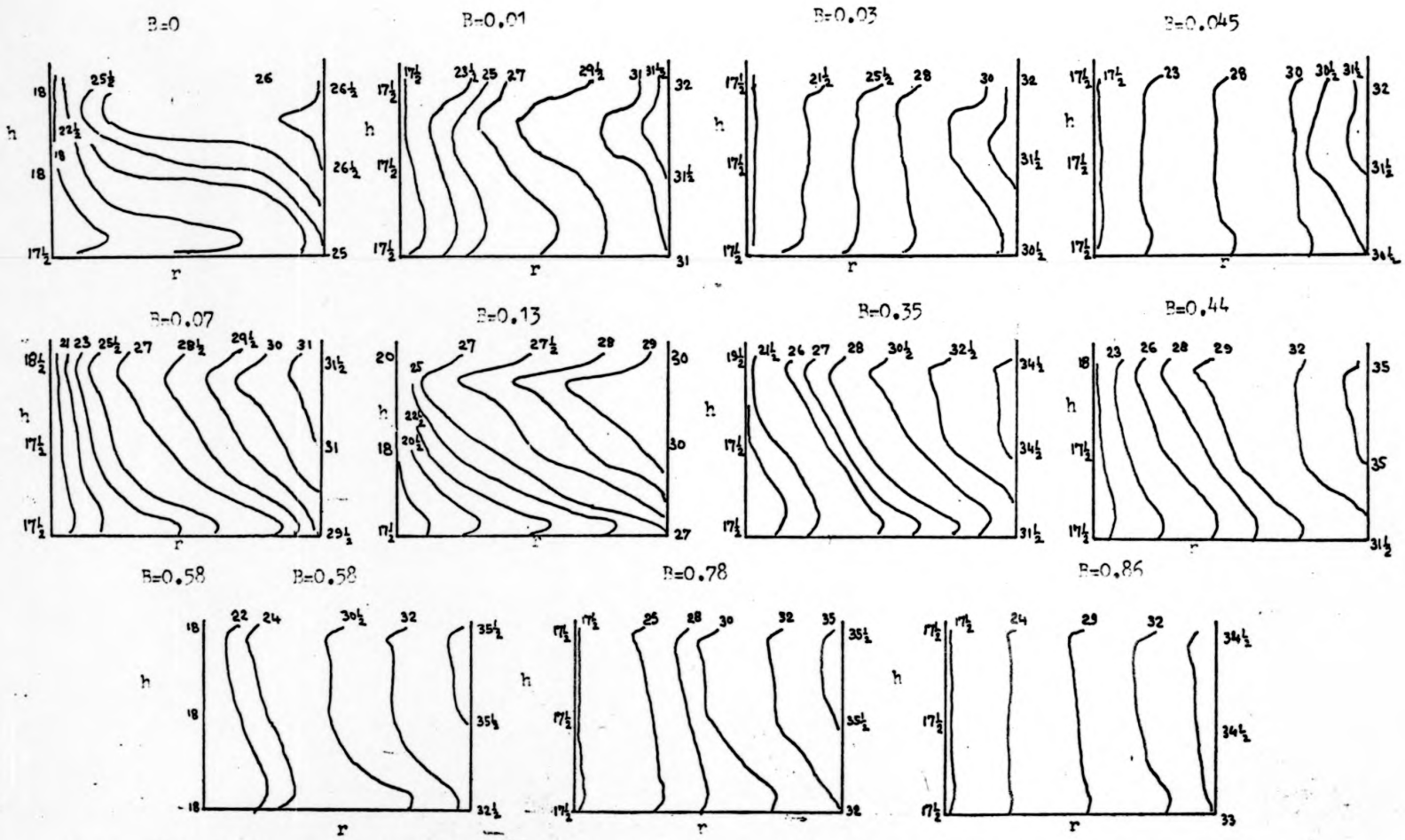

Figure 22 c. Isotherm plots in the meridional plane of the Mark IV channel for 2 amp uniformly distributed heating current. T in °C, Full scale diagram , B in Tesla . (r - Radial span , h - height .)

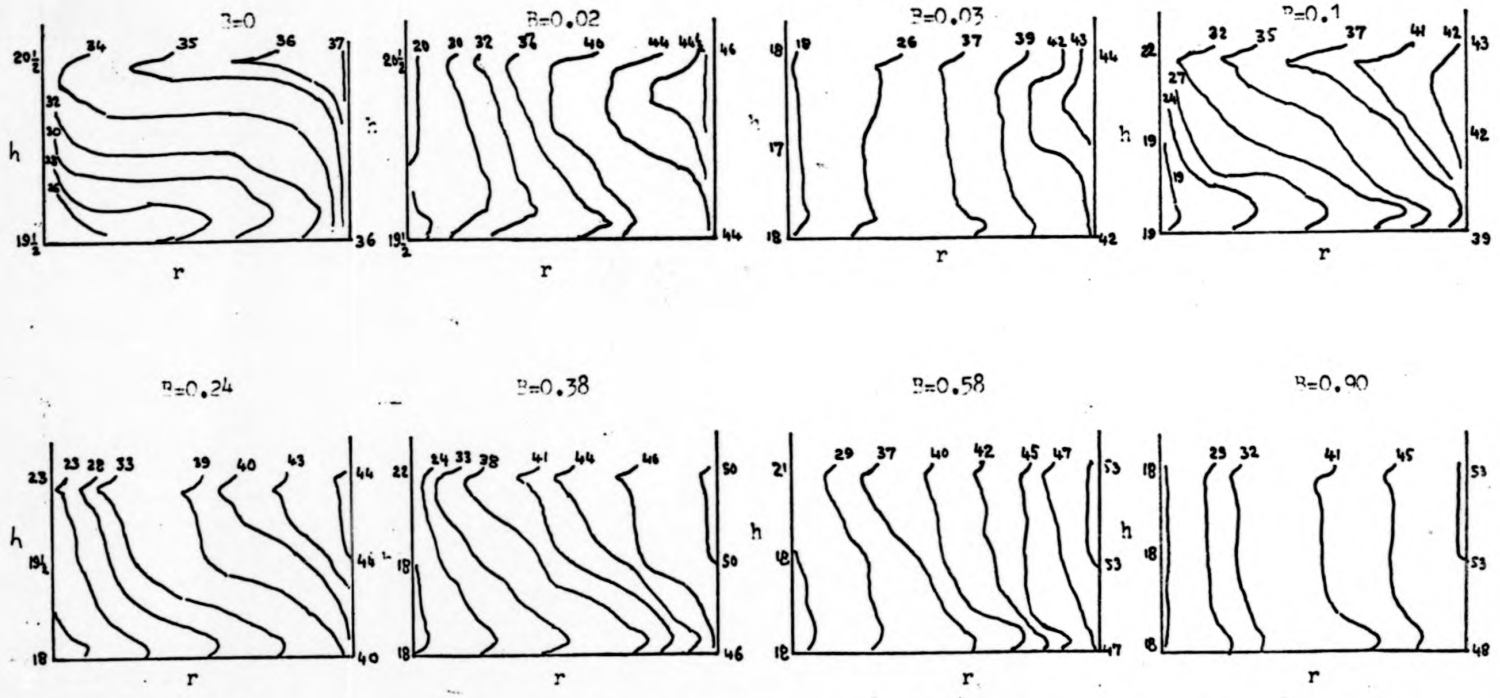

Figure 22 d. Isotherm plots in the meridional plane of the Mark IV channel for 3 amp uniformly distributed heating current. T in °C, Full scale diagram , B in Tesla . (r- Radial span , h - Height .)

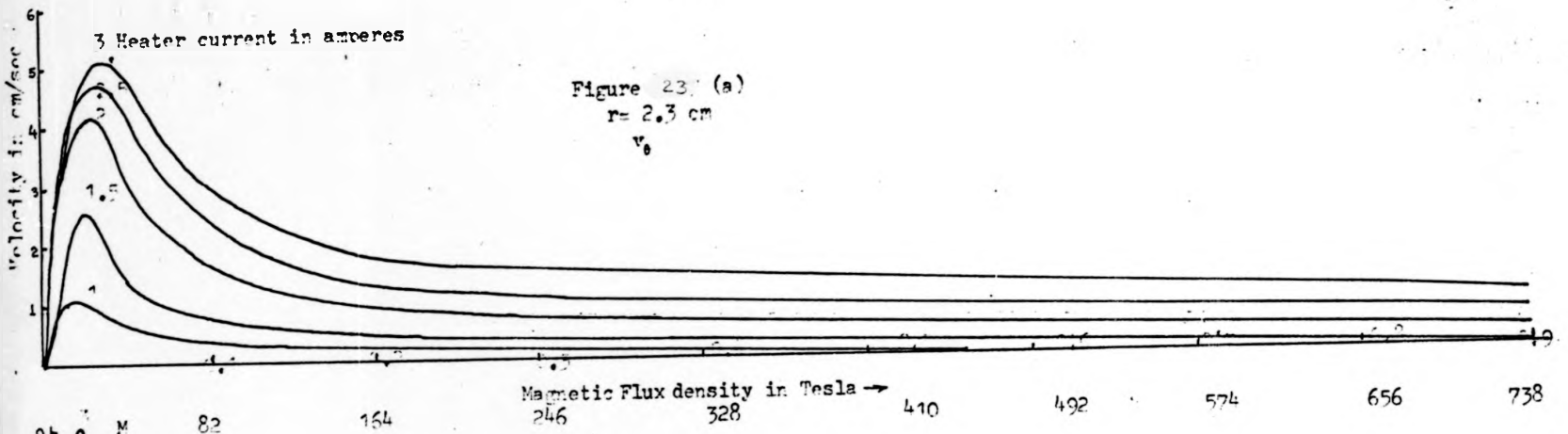

Figure 23 (a)
r= 2.3 cm
V_θ

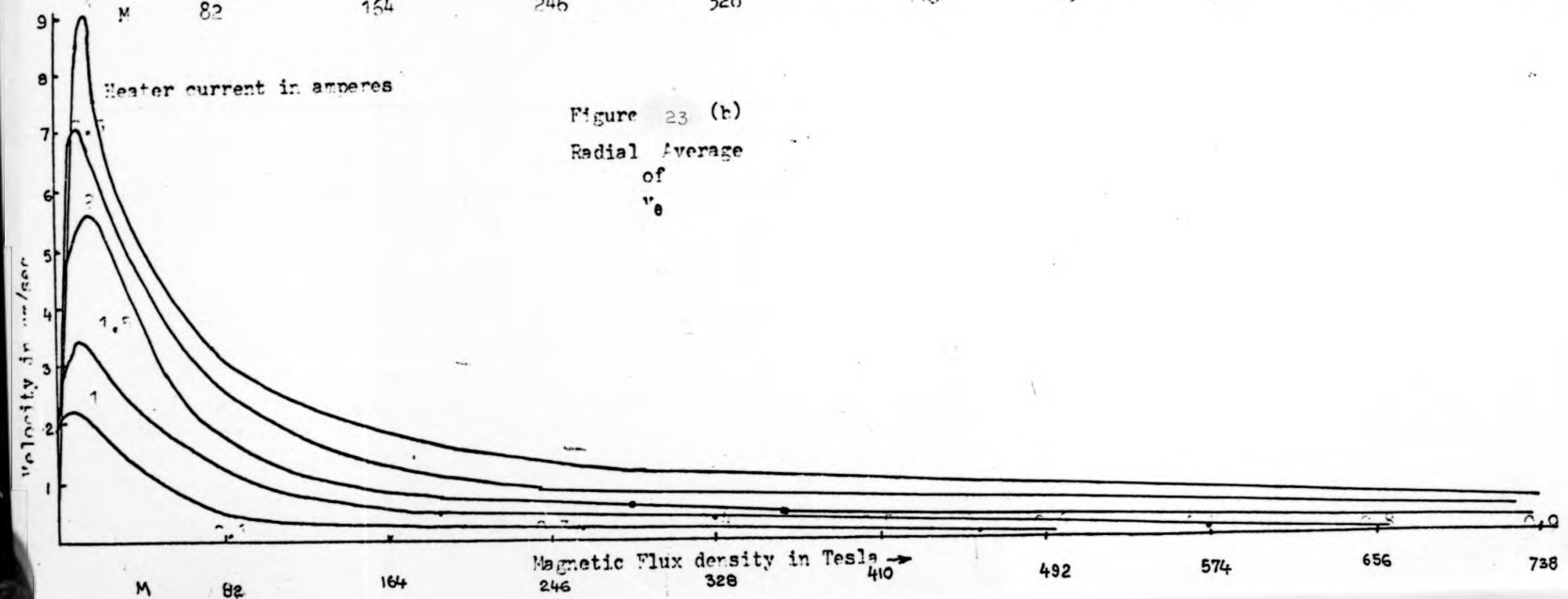

Figure 23 (b)
Radial Average
of
V_θ

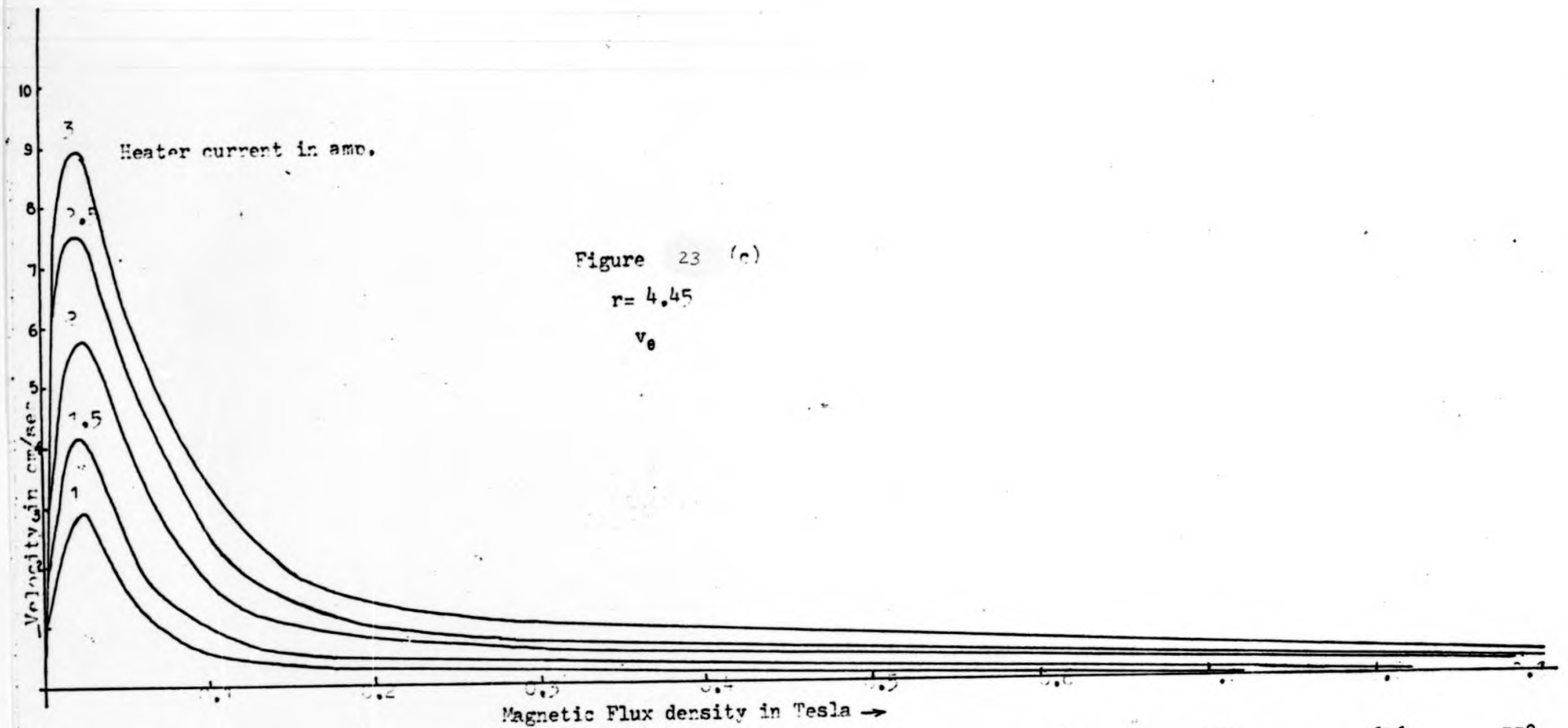

Figure 23 (c)

r= 4.45

v_θ

Figure 6.27 (a , b , c) Velocity plots against magnetic flux density B / Hartmann number (based on 3.15 cm- mean height) for the Mark IV annular channel at various values of steady heater current .

(a) v_θ measured at r=2.3cm (b) V, radial average of v_θ (c) v_θ measured at r= 4.45 cm

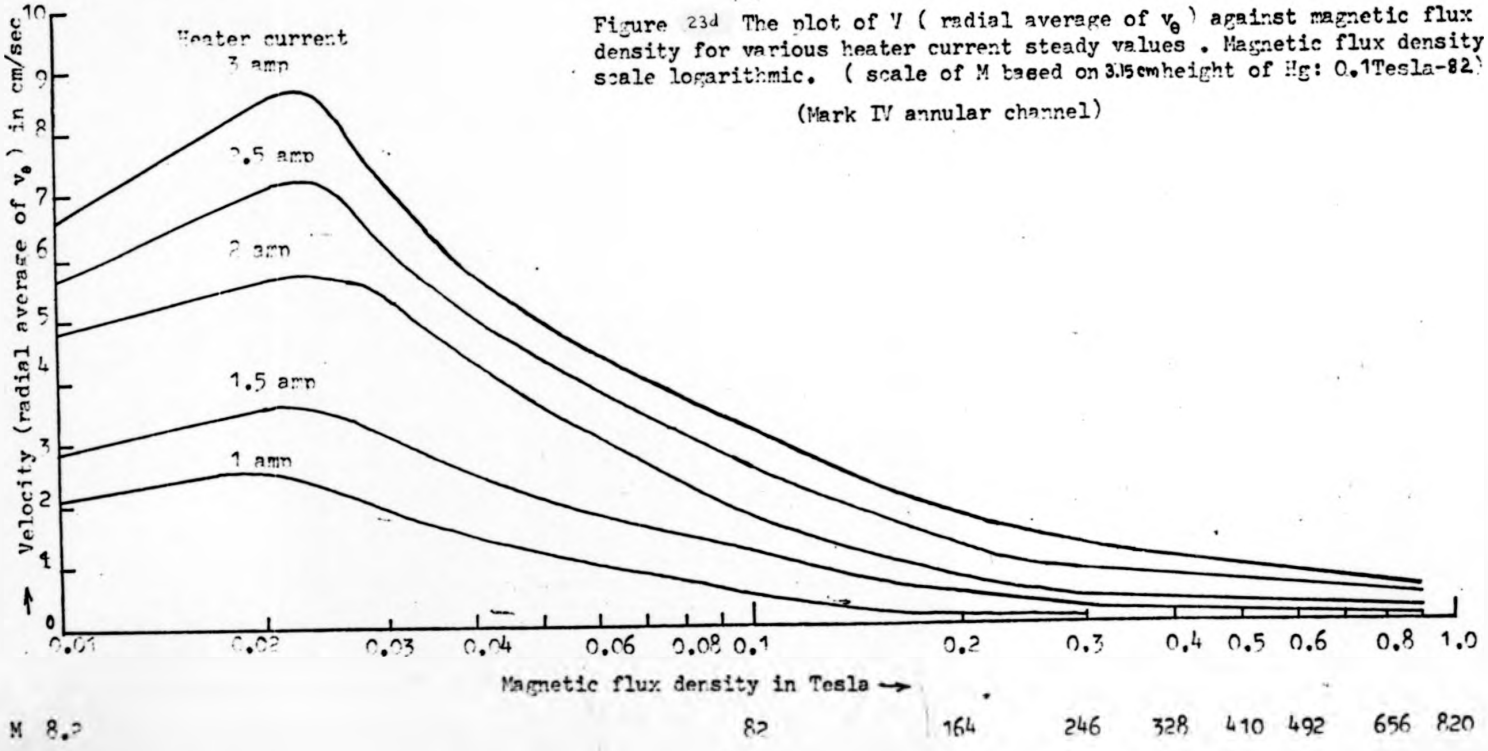

Figure 234 The plot of V (radial average of v_θ) against magnetic flux density for various heater current steady values . Magnetic flux density scale logarithmic. (scale of M based on 3.15cm height of Hg: 0.1Tesla-82)

(Mark IV annular channel)

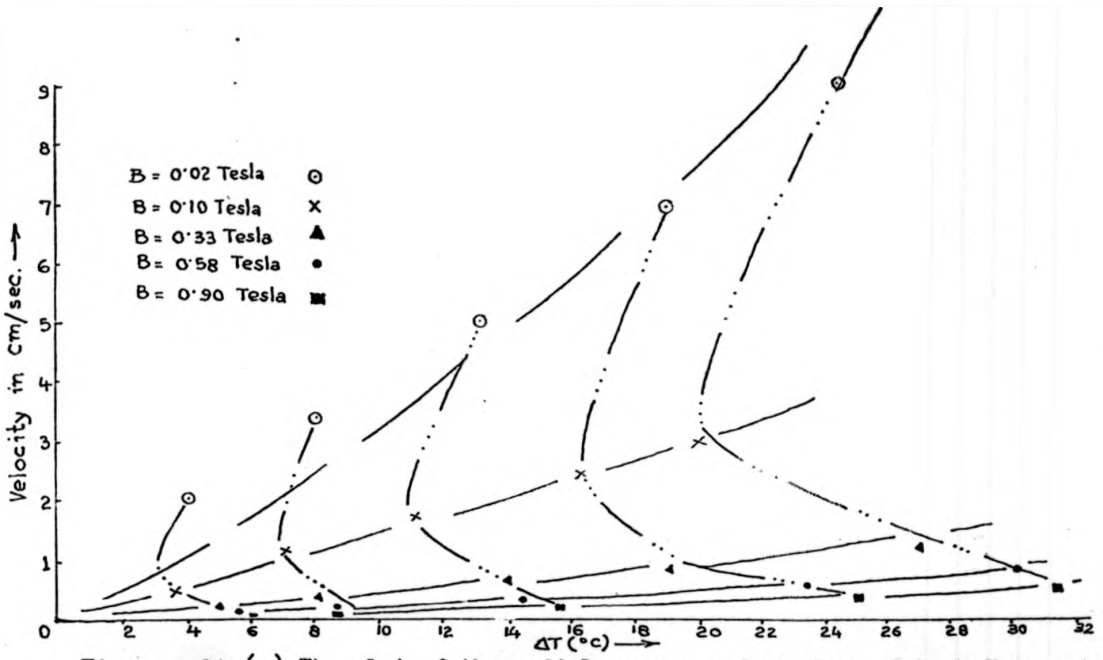

Figure 24 (a) The plot of the radial average value of v_θ against Temperature difference in the Mark IV annular channel . (Cooling water at 18°C).

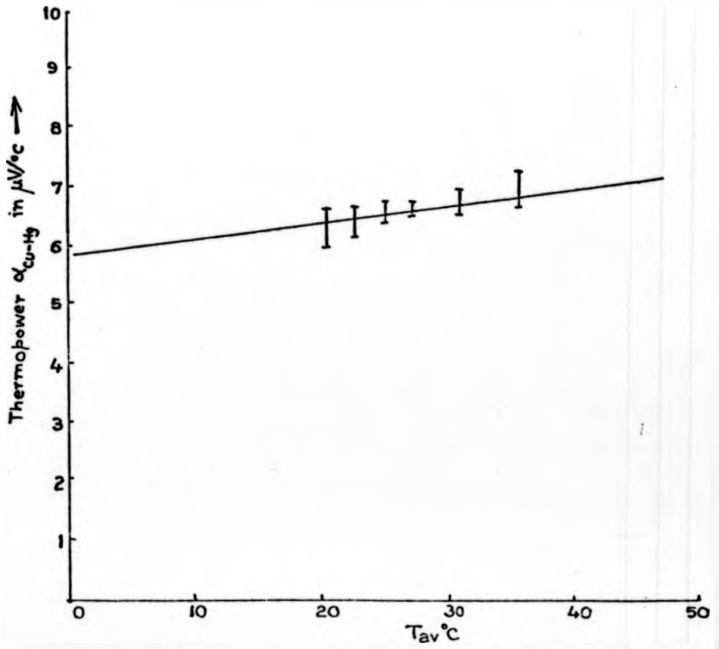

Figure 24b Plot of the thermopower α_{Cu-Hg} values calculated from the velocity measurement data of figure 6.29 (the spread in α for a given T_{av} with different B is shown by bar height) as a function of T_{av} in the Mark IV annular channel. The firm line corresponds to Marwaha data

fixed values of the magnetic field strength. Linear rays and a reference logarithmic curve have been superimposed on the plot for the comparison of the corresponding gradients of the temperature profiles.

Fig. 20 shows typical records of the temperature oscillations at different locations in the fluid for a fixed thermal input and a constant cooling water temperature at various constant values of the vertical magnetic field strength.

Fig. 21 shows a typical radial velocity v_r profile along the radial distance for a vertical magnetic field strength of B = 0.005 Tesla and a fixed thermal input corresponding to 2 amperes in the heater coil.

Fig. 22 shows the azimuthal velocity v_θ profile along the radial direction for different fixed heating conditions at $r = R_2$ and a constant cooling water temperature for various fixed values of the vertical magnetic field strength. The corresponding temperature distributions in the meridional cross-section of the fluid are also shown in Fig. 22.

Fig. 23 shows the plots of the azimuthal velocity v_θ measurements at fixed heater coil currents and a constant level of the cooling water temperature at fixed radial locations on the free surface of mercury against the vertical magnetic field strength/Hartmann Number based on the mercury column height.

Fig. 24a shows the plot of the radial averages of v_θ measurements at the top free surface of mercury against temperature difference $\Delta T = T_2 - T_1$ for a fixed cooling water temperature of 18°C and for different fixed values of the magnetic field strength.

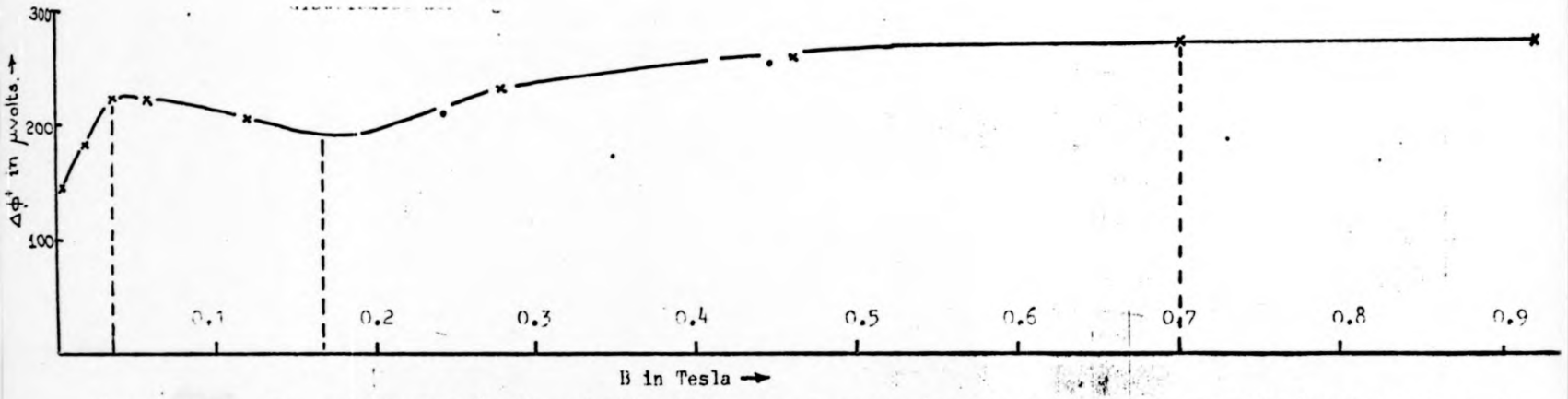

Figure 25 The variation of $\Delta\phi^{+}$, the potential difference measured across the total radial span of Hg (with Hg electrode potential probe) with the magnetic flux density in the Mark IV annular channel heated at the outer and cooled at the inner rim.

Based on the experimental results of v_θ measurements for different heating conditions as given in figure 24a the calculated thermopower α_{Cu-Hg} values (the spread of α for a given T_{av} for different B shown by bar height) against T_{av} are shown in figure 24b against the background of the Marwaha thermopower data (shown by the firm line).

The variation of $\Delta\phi^+$, the potential difference measured across the total radial span of mercury with a mercury electrode potential probe, with the magnetic flux density, for a fixed thermal input and a constant cooling water temperature is shown in figure 25.

6. Discussion and conclusions

The main conclusion derived from the experiments with the annular channels of rectangular cross-section is that TEMHD interactions in laboratory scale models are significant enough so as to be measureable. This is in keeping with the conclusions arrived at in Part I and II of the series of papers. However, it has been shown in Part III that TEMHD fluid flow without pressure gradients is possible and such velocity measurements can be done. This was not possible in the experimental arrangements of Part I and II without compensating for the pressure gradients introduced by entry and exit effects of MHD.

Azimuthal velocity v_θ profile measurements along the horizontal radial span agrees qualitatively with the theoretically predicted characteristic at all magnetic field strengths but the mean flow rate values (V) agree only at high Hartmann Numbers only for which the theoretical calculations are valid. Thus $v_\theta \propto \frac{1}{r}$ is

the core of the fluid in the Hartmann layer controlled flow in the Mark I and II channels and $v_\theta \propto r$ at the conducting wall-fluid interface of the bottom wall in Mark III and IV annular channels when a temperature gradient dT/dr proportional to r could be maintained. Both quantitative and qualitative agreement of the velocity v_θ measurements with the theoretical predictions, at large Hartmann Numbers, permit the determination of α_{Cu-Hg} and the thermopower of the conducting fluid at various temperatures and these values are accurate within a $\pm$ 4% tolerance of the Marwaha data, even when compensation for the changes in T_1 and T_2 values at different magnetic field strengths are not applied. With compensation, the thermopower determination by velocity measurements is within $\pm \frac{1}{2}$% tolerance of the Marwaha data. Determination of thermopower from the TEMHD velocity measurements without pressure gradients at high Hartmann Numbers is more advantageous as compared to those of thermopower determination from the TEMHD pressure gradient measurements with $V = 0$ as reported in Part I and II, as no separate determination of the conductivities of the fluid and the wall materials (s) is essential.

Since the experimental v_θ profiles agree with the theoretical predictions at all values of the magnetic field with the wall-fluid interface at the bottom wall either conducting or insulating, the free shear layer in the fluid at the interface conductivity change-over region does occur as was measured by the vorticity probes in the Mark III annular channel when a temperature gradient dT/dr proportional to r was maintained at the conducting interface region by

concentrated heating. In fact the nature of vorticity could be controlled by controlling dT/dr dependence on r when the bottom wall-fluid interface was conducting and was confirmed by the vorticity measurements by the paddle type mechanical vorticity probe.

The measurements of the azimuthal velocity v_θ along r and the depths of the fluid column shows boundary layers at the solid walls as expected from the theoretical calculations. However, the Hartmann layer thickness, though decreased with increase of the Hartmann Number M, was three to four times greater than the theoretically predicted values; the boundary layer thickness at the curved walls was of the same order as $\frac{1}{\sqrt{M}}$, the theoretically expected value.

In contrast to the experimental arrangements of Part I and II of the series of papers, the configuration of Part III has secondary flows inherent in the fluid due to buoyancy effect and the curvature of the flow. However, measurements of v_z shows that in the vertical magnetic field, v_z is at least an order of magnitude less than v_θ because secondary flow is suppressed by the magnetic field. At high Hartmann Number v_θ is small enough to generate any secondary flow due to curvature. Thus the assumptions of neglecting secondary flow at high Hartmann Numbers are justified in the core of the fluid. However, measurements of v_z at the curved wall boundary layers show that $v_z \simeq 0\ (v_\theta)$.

Temperature measurements in the meridional cross-section of the fluid in the Mark II and IV annular channels,

show that in the absence of the vertical magnetic field a stable thermal stratification exist " at the central region. For a given thermal flux input level and a fixed cooling water temperature the wall-fluid interface temperature at $r = R_2$ increased with the switching on of the magnetic field. This is understandable from the standpoint that secondary flow is affected by the magnetic field and therefore the heat transfer characteristic is changed. Two different transition levels in heat transfer with changes in the magnetic field strength may be observed in the experimental results in that slight increase in B from the zero level increases the temperature T_2 to T_2', further increase in B lowers the temperature to T_2'' slightly ($T_2 < T_2'' < T_2'$) and finally at much higher B, $T_2''' > T_2'$. As the magnetic field strength is increased the isotherms become more and more vertical and the thermal stratification is lost. The transverse magnetic field suppresses the destabilizing effect of buoyancy but how well it can suppress it depends on the roll size. As the roll size decreases the effectiveness of the transverse magnetic in suppressing vorticity decreases. This is evident from the temperature oscillations in the fluid even at high magnetic field strengths of B = 0.9 Tesla even though the amplitude of temperature oscillations reduced with increase of the magnetic field strength. The difference in the mode of heat transfer in the bottom copper wall (by conduction only) and that in the fluid (by conduction and convection) for the Mark IV channel with a conducting bottom interface gives diverse temperature gradients in the fluid near the bottom wall and the

show that in the absence of the vertical magnetic field a stable thermal stratification exist " at the central region. For a given thermal flux input level and a fixed cooling water temperature the wall-fluid interface temperature at $r = R_2$ increased with the switching on of the magnetic field. This is understandable from the standpoint that secondary flow is affected by the magnetic field and therefore the heat transfer characteristic is changed. Two different transition levels in heat transfer with changes in the magnetic field strength may be observed in the experimental results in that slight increase in B from the zero level increases the temperature T_2 to T_2', further increase in B lowers the temperature to T_2'' slightly ($T_2 < T_2'' < T_2'$) and finally at much higher B, $T_2''' > T_2'$. As the magnetic field strength is increased the isotherms become more and more vertical and the thermal stratification is lost. The transverse magnetic field suppresses the destabilizing effect of buoyancy but how well it can suppress it depends on the roll size. As the roll size decreases the effectiveness of the transverse magnetic in suppressing vorticity decreases. This is evident from the temperature oscillations in the fluid even at high magnetic field strengths of B = 0.9 Tesla even though the amplitude of temperature oscillations reduced with increase of the magnetic field strength. The difference in the mode of heat transfer in the bottom copper wall (by conduction only) and that in the fluid (by conduction and convection) for the Mark IV channel with a conducting bottom interface gives adverse temperature gradients in the fluid near the bottom wall and the

temperature oscillations in that region are the most pronounced ones. The period of temperature oscillation ranges from 3 to 30 seconds, showing the presence of different modes of fluid verticity.

The experimentally measured asimuthal velocity v_θ at any radial location increases with the Hartmann Number M initially, reaches a maximum at $M \simeq 10\text{-}15$ and then decreases at higher values of M. This is perfectly in agreement with the theory as at lower B, the TEMHD driving force dominates against viscous drag only whereas at a higher B the magneto-hydrodynamic drag proportional to B^2 dominates over the TEMHD driving force proportional to B. The Hartmann Number M at which the maximum v_θ occurs with changes inM is much closer to the value of $M \simeq 2\text{-}3$ in the TEMHD analysis of Shercliff in rectangular channels with infinite aspect ratio, as compared to the experimental values of $M \simeq O(100)$ in the experiments of Part I and II, where accurate compensation for pressure gradients could not be applied. The slopes of the experimental curve of v_θ vs M suggests three operational ranges of M giving two critical transition value of B, B_{cr1} and B_{cr2}, which identify the three ranges of M as (i) increasing high valuesof v_θ, low magnetic drag a low value of B, v_r due to buoyancy (flow inwards) opposes that due to curvature, (ii) decreasing values of v_θ at intermediate values of B due to increasing magnetic drag, with the secondary flow due to curvature decreasing and (iii) low values of v_θ with no secondary flow at high Hartmann Numbers. This corroborates with the three operational regions of M with respect to the changes in

the temperature at the curved wall-fluid interface for a fixed thermal input and constant cooling water temperature. $\Delta\phi^+$ -M measurements also imply such postulates. This suggests the adoption of a new nondimensional number $D = \alpha \Delta T / \nu B$ where $\Delta T = T_2 - T_1$ and ν is the kinematic viscosity of the fluid.

The experimental results of v_θ measurements with sudden switching off of either (a) the magnetic field or (b) the heater power when the thermal flux level or the magnetic field is maintained constant respectively are in agreement with the theoretically expected characteristic. Since a magnetic field decay passes through a corresponding value of M for v_θ maximum the hump in the v_θ - t curve (a) is in order whereas otherwise there is an exponential decrement only.

Pitot tube measurements are ineffective at large values of M as v_θ decreases, whereas the thermoelectric potential probe measurements were ineffective at lower values of M. The mechanical velocity-vorticity probe measurements were effective over both these ranges of M and covered the entire range of operational values of M. Since free fluid surface may not be available in TEMHD experiments in general and as the theoretical investigations in TEMHD as at present available apply to high Hartmann Numbers, it is implied that the thermoelectric potential probe would find increasing application in experimental TEMHD. In particular, the simultaneous measurements of T, Φ^+ oscillations at different regions of the fluid might offer proper explanation of the fluid vorticity pattern when the correlation analysis of the amplitude and phase of the oscillations is carried out.

7. Acknowledgements

Acknowledgement is made of the technical help received from Mr. A.E. Webb in the fabrication of the apparatus.

Financial help in the form of a Research Scholarship was provided to P.B. Dutta Gupta by the Commonwealth Scholarship Commission, U.K. at the University of Warwick, Coventry and I.I.T., Kharagpur consented to the leave of absence from their employment during the period of research work.

References :

1. Shercliff J.A., Alty C.J.N. and Dutta Gupta P.B. (1978) - Thermoelectric MHD. Second Bat-Sheva Seminar in MHD.
2. Shercliff J.A. (1979) - Thermoelectric magnetohydrodynamics, J.F.M. 91, P 2, 231-252.
3. Shercliff J.A. (1979) - Thermoelectric magnetohydrodynamics in closed containers. Phy. Fluids, 22(4), 635-640.
4. Dutta Gupta P.B. and Shercliff J.A. - Investigations into Experimental Thermoelectric Magnetohydrodynamics - Part I : Circular cross-sectional straight ducts in transverse magnetic fields - Paper to be submitted for publication.
5. Dutta Gupta P.B. and Shercliff J.A. - Investigations into Experimental Thermoelectric Magnetohydrodynamics - Part II : Rectangular cross-sectional straight ducts in transverse magnetic fields - Paper to be submitted for publication.
6. Baylis J.A. (1966) - Fully developed secondary flow on magnetohydrodynamics. Ph.D. thesis, University of Cambridge.
7. Hunt J.C.R. (1967) - Some aspects of magnetohydrodynamics. Ph.D. thesis, University of Cambridge.
8. Malcolm D.G. (1968) - Thermoanemometry in magnetohydrodynamics, Ph.D. thesis, University of Warwick.

9. Heiser W.H. and Shercliff J.A. (1965) - A simple demonstration of Hartmann layer. J.F.M. 22, P4, 701-707

10. Marwaha A.S. (1967) - The absolute thermoelectric power of polyvalent liquid metals. Adv. Phys. 16, N 62, 617-627.

11. Elder J.W. (1965) - Laminar free convection in a vertical slot. J.F.M. 23, P 1, 77-98.